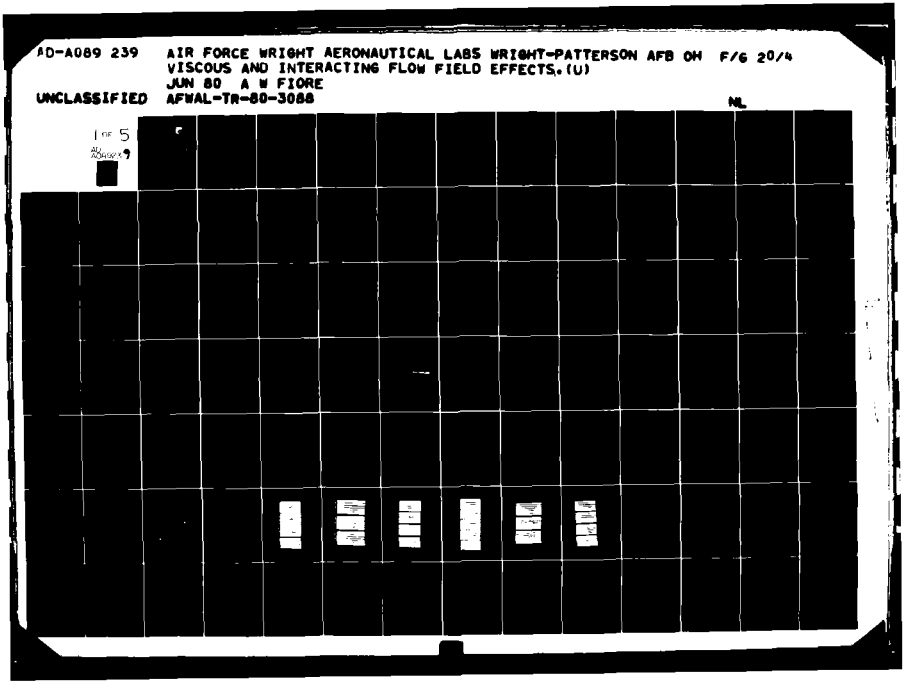

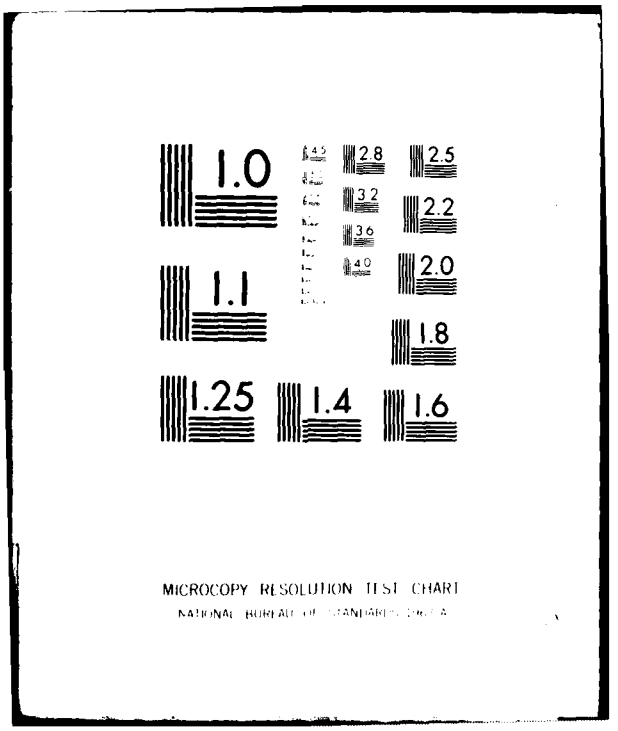

AFWAL
TR-80-3088

LEVEL II

VISCOUS AND INTERACTING FLOW FIELD EFFECTS
Proceedings of the 5th U. S. Air Force and the Federal Republic of Germany Data Exchange Agreement Meeting

DR. ANTHONY W. FIORE
U.S.A.F. PROJECT OFFICER AND EDITOR
AEROMECHANICS DIVISION

JUNE 1980

TECHNICAL REPORT AFFDL-TR-80-3088
Technical Proceedings Report for period April 1979 – April 1980

Approved for public release; distribution unlimited.

AIR FORCE WRIGHT AERONAUTICAL LABORATORIES
FLIGHT DYNAMICS LABORATORY
AIR FORCE SYSTEMS COMMAND
WRIGHT-PATTERSON AIR FORCE BASE, OHIO 45433

NOTICE

When Government drawings, specifications, or other data are used for any purpose other than in connection with a definitely related Government procurement operation, the United States Government thereby incurs no responsibility nor any obligation whatsoever; and the fact that the government may have formulated, furnished, or in any way supplied the said drawings, specifications, or other data, is not to be regarded by implication or otherwise as in any manner licensing the holder or any other person or corporation, or conveying any rights or permission to manufacture use, or sell any patented invention that may in any way be related thereto.

This report has been reviewed by the Office of Public Affairs (ASD/PA) and is releasable to the National Technical Information Service (NTIS). At NTIS, it will be available to the general public, including foreign nations.

This technical report has been reviewed and is approved for publication.

Anthony W. Fiore

DR. ANTHONY W. FIORE
U.S.A.F. Project Officer
Aeromechanics Division

Melvin L. Buck

MR. MELVIN L. BUCK
Chief, High Speed Aerodynamics Group
Aeromechanics Division

PETER J. BUTKEWICZ
Colonel, USAF
Chief, Aeromechanics Division

"If your address has changed, if you wish to be removed from our mailing list, or if the addressee is no longer employed by your organization, please notify AFWAL/FIMG, W-PAFB, Ohio 45433 to help us maintain a current mailing list."

Copies of this report should not be returned unless return is required by security considerations, contractual obligations, or notice on a specific document.

AIR FORCE/56780/26 August 1980 — 240

UNCLASSIFIED

SECURITY CLASSIFICATION OF THIS PAGE *(When Data Entered)*

REPORT DOCUMENTATION PAGE	READ INSTRUCTIONS BEFORE COMPLETING FORM
1. REPORT NUMBER: AFWAL-TR-80-3088 / 2. GOVT ACCESSION NO.: AD-A089239	3. RECIPIENT'S CATALOG NUMBER:
4. TITLE *(and Subtitle)*: Viscous and Interacting Flow Field Effects	5. TYPE OF REPORT & PERIOD COVERED: Technical Proceedings Report April 1979 - April 1980
	6. PERFORMING ORG. REPORT NUMBER:
7. AUTHOR(s): Dr. Anthony W. Fiore, USAF Project Officer and Editor	8. CONTRACT OR GRANT NUMBER(s):
9. PERFORMING ORGANIZATION NAME AND ADDRESS: Aeromechanics Division, Flight Dynamics Laboratory, WPAFB, OH 45433	10. PROGRAM ELEMENT, PROJECT, TASK AREA & WORK UNIT NUMBERS: MWDDEA-AF-75-G-7440
11. CONTROLLING OFFICE NAME AND ADDRESS: Aeromechanics Division, Flight Dynamics Laboratory, WPAFB, OH 45433	12. REPORT DATE: June 1980
	13. NUMBER OF PAGES: 420
14. MONITORING AGENCY NAME & ADDRESS *(if different from Controlling Office)*	15. SECURITY CLASS. *(of this report)*: Unclassified
	15a. DECLASSIFICATION/DOWNGRADING SCHEDULE

16. DISTRIBUTION STATEMENT *(of this Report)*

Approved for public release; distribution unlimited.

17. DISTRIBUTION STATEMENT *(of the abstract entered in Block 20, if different from Report)*

18. SUPPLEMENTARY NOTES

Proceedings of the 5th U.S. Air Force/Federal Republic of Germany Data Exchange Agreement Meeting, 15/17 April 1980, U.S. Naval Academy, Annoplis, Maryland.

19. KEY WORDS *(Continue on reverse side if necessary and identify by block number)*

Turbulent Boundary layers	Viscous interaction
Transonics	Fluid dynamics
Numerical Methods	Separated flows
High Reynolds Number	Subsonic
	Supersonic

20. ABSTRACT *(Continue on reverse side if necessary and identify by block number)*

In 1975 the U.S. Air Force and the Federal Republic of Germany signed a Data Exchange Agreement Numbered AF-75-G-7440 entitled "Viscous and Interacting Flow Fields". The purpose was to exchange data in the area of boundary layer research. It included both experimental and theoretical boundary layer research at speeds from subsonic to hypersonic Mach numbers in the presence of laminar, transitional, and turbulent boundary layers. The main effort in recent years has been on turbulent boundary layers, both attached

DD FORM 1 JAN 73 1473 EDITION OF 1 NOV 65 IS OBSOLETE

UNCLASSIFIED

SECURITY CLASSIFICATION OF THIS PAGE *(When Data Entered)*

and separated in the presence of such parameters as pressure gradients, wall temperature, surface roughness, etc. The research presented in this report covers the period April 1979 to April 1980 with the results presented on 16/18 April 1980 in a meeting held at the U.S Naval Academy in Annapolis Maryland. In the United States the research was conducted in various Department of Defense, N.A.S.A., Aircraft Corporations, and University laboratories. In the Federal Republic of Germany it was done in the various DFVLR, Industrial, and University research centers.

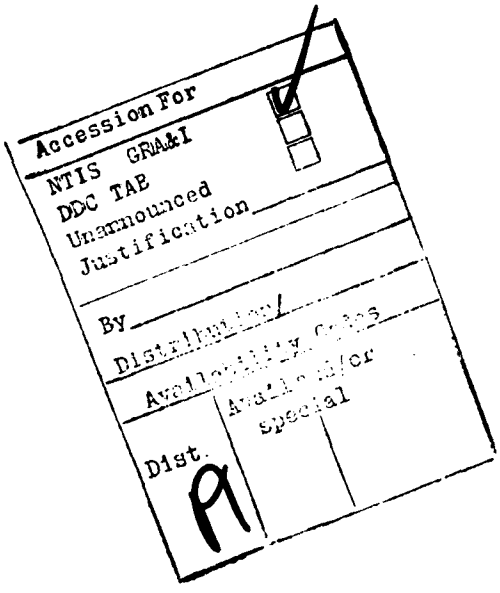

FOREWORD

The 5th U.S. Air Force/Federal Republic of Germany Data Exchange Agreement Meeting entitled "Viscous and Interacting Flow Fields" numbered MWDDEA AF-75-G-7440 was sponsored by the Air Force Flight Dynamics Laboratory and hosted by the U.S. Navy with Dr Joseph Gillerlain of the U.S. Naval Academy as organizer. It was held on 15/18 April 1980 at the U.S. Naval Academy in Annapolis Maryland. This report contains the detailed proceedings of that meeting. It contains both theoretical and experimental results covering a great variety of topics in the area of boundary layer research. The speed range is from subsonic to hypersonic Mach numbers. The types of boundary layers were laminar, transitional, and turbulent; both fully attached and separated. Similar problems in the area of hydrodynamics are also included.

The Air Force wishes to thank Dr Joseph Gillerlain of the U.S. Naval Academy for his efforts in preparing the meeting. Thanks is also extended to the Superintendent of the Naval Academy for the use of his facilities. In addition the Air Force wishes to thank the following Naval personnel for their efforts: Mr William C. Volz of the Naval System Command, Drs W.J. Glowacki and W. Yanta along with Mr R.L.P. Voisnet of the Naval Surface Weapons Center. Finally the Air Force wishes to thank all the participants from the Federal Republic of Germany for their scientific contributions and for coming such a long distance for this meeting.

The contribution from the United States was research performed within the Air Force Flight Dynamics Laboratory, the U.S. Navy, the U.S. Army, N.A.S.A., and various American Aircraft Companies and Universities.

The contributions from the Federal Republic of Germany were from such organizations as the DFVLR-AVA-Göttingen, DFVLR-Linden Höke, the Universities of Berlin, Karlsruke, and Hamberg and such aircraft corporations as VFW-Fokker and Dornier.

The research reported was conducted in the period April 1979 to April 1980.

TABLE OF CONTENTS

TABLE OF CONTENTS, CONT.

TABLE OF CONTENTS, CONCLUDED

5th U. S. - German DEA Meeting
16-18 April 1980
U. S. Naval Academy
Annapolis, Maryland 21402

List of Participants

Name	Organization
Bartels, F. Dr.	David M. Taylor Naval Ship Research and Development Center Bethesda, Maryland 20084 USA
Cebeci, T., Dr.	Douglas Aircraft Company Code 36-81 3855 Lakewood Blvd. Long Beach, California 90840 USA
Chien, K.-Y., Dr.	Naval Surface Weapons Center White Oak Laboratory Silver Spring, Maryland 20910 USA
Danberg, J. E., Prof.	Dept. Mechanical & Aerospace Engineering University of Delaware 107 Evans Hall Newark, Delaware 19711 USA
Dolling, D., Dr.	Princeton University Dept. of Mechanical & Aerospace Engineering James Forrestal Campus Princeton, New Jersey 08540 USA
Dvorak, F. A., Dr.	Analytical Methods, Inc. 100-116th Avenue S.E. Bellevue, Washington 98004 USA

ame	Organization
re, A. W., Dr.	Air Force Flight Dynamics Laboratory AFWAL/FIMG Wright-Patterson Air Force Base Dayton, Ohio 45433 USA
Gersten, K., Prof. Dr.	Ruhr-Universität Bochum Inst.f.Thermo- u. Fluiddynamik Universitätsstr. 150 IB D 4630 Bochum University Federal Republic of Germany
Gillerlain, J., Prof.	Mechanical Engineering Department U. S. Naval Academy Annapolis, Maryland 21402 USA
Glowacki, W. J., Dr.	Naval Surface Weapons Center White Oak Laboratory Silver Spring, Maryland 20910 USA
Granville, P., Dr.	David W. Taylor Naval Ship Research and Development Center Bethesda, Maryland 20084 USA
Granger, R., Prof.	Mechanical Engineering Department U. S. Naval Academy Annapolis, Maryland 21402 USA
Hankey, W., Dr.	Air Force Flight Dynamics Laboratory AFWAL/FIM Wright-Patterson Air Force Base Dayton, Ohio 45433 USA

Name	Organization
Hill, J., Dr.	Naval Surface Weapons Center White Oak Laboratory Silver Spring, Maryland 20910 USA
Hsieh, T., Dr.	Naval Surface Weapons Center White Oak Laboratory Silver Spring, Maryland 20910 USA
Inger, G., Prof.	Virginia Polytechnic Institute and State University Aerospace and Ocean Engineering Blacksburg, Virginia 24061 USA
Johnson, B., Prof.	Naval Systems Engineering Department U. S. Naval Academy Annapolis, Maryland 21402 USA
Kreplin, H.-P., Dr.	DFVLR-AVA Inst.f.Experimentelle Strömungsmechn. Bunsenstr. 10 D 3400 Göttingen Federal Republic of Germany
Lea, G., Dr.	Program Director Fluid Mechanics Program National Science Foundation Washington, D.C. 20550 USA
Lemmerman, L., Dr.	Lockheed-Georgia Marietta, Georgia 30060 USA
Lugt, H., Dr.	David W. Taylor Naval Ship Research and Development Center Bethesda, Maryland 20084 USA

Name	Organization
McLean, J., Dr.	Boeing Commercial Airplane Company P.O. Box 3707 Seattle, Washington 98124 USA
Meier, H. U., Dr.	DFVLR-AVA Inst.f.Experimentelle Strömungsmechn. Bunsenstr. 10 D 3400 Göttingen Federal Republic of Germany
Melnik, W., Prof	Aerospace Engineering Department University of Maryland College Park, Maryland 20742 USA
Müller, U., Dr.	NASA-Ames Research Center Moffett Field, California 94035 USA
Nietubicz, C., Mr.	U. S. Army Ballistics Research Laboratory Aberdeen Proving Ground, Maryland 21005 USA
Rotta, J. C., Dr.	DFVLR-AVA Inst.f.Experimentelle Strömungsmechn. Zeppelinstr. 3 D 3400 Göttingen Federal Republic of Germany
Schindel, L., Dr.	Naval Surface Weapons Center White Oak Laboratory Silver Spring, Maryland 20910 USA
Schlie, R., Dr.	Naval Surface Weapons Center White Oak Laboratory Silver Spring, Maryland 20910 USA

Schneider, G., Dr.	DFVLR-AVA Inst.f.Theoretische Strömungsmechn. Bunsenstr. 10 D 3400 Göttingen Federal Republic of Germany
Schot, J., Dr.	David W. Taylor Naval Ship Research and Development Center Head, Numerical Mechanics Division Bethesda, Maryland 20084 USA
Shoaff, R., LCDR	David W. Taylor Naval Ship Research and Development Center Bethesda, Maryland 20084 USA
Stock, H., Dr.	Dornier GmbH Postfach 14 20 D 7990 Friedrichshafen Federal Republic of Germany
Sturek, W., Dr.	U. S. Army Ballistics Research Laboratory Chief, Aerodynamics Research Branch Aberdeen Proving Ground, Maryland 21005 USA
Tai, T. C., Dr.	David W. Taylor Naval Ship Research and Development Center Bethesda, Maryland 20084 USA
Thiede, P., Prof. Dr.	VFW-Fokker GmbH Hünefeldstr. 1-5 D 2800 Bremen Federal Republic of Germany
Thrasher, F., Dr.	David W. Taylor Naval Ship Research and Development Center Bethesda, Maryland 20084 USA

Name	Organization
Van Tuyl, A., Dr.	Naval Surface Weapons Center White Oak Laboratory Silver Spring, Maryland 20910 USA
Viets, H., Prof.	Wright State University Dayton, Ohio 45409 USA
Voisinet, R., Mr.	Naval Surface Weapons Center Head, Project Engineering Section White Oak Laboratory Silver Spring, Maryland 20910 USA
Volz, W., Mr.	Naval Air Systems Command AIR-320C Washington, D.C. 20361 USA
Walz, A., Prof. Dr.	Am Kurzarm 7 D 7830 Emmendingen Federal Republic of Germany
Wieghardt, K., Prof. Dr.	Universität Hamburg Institut fur Schiffbau Lämmersieth 90 D 2000 Hamburg 60 Federal Republic of Germany
Yanta, W., Dr.	Naval Surface Weapons Center White Oak Laboratory Silver Spring, Maryland 20910 USA
Zien, T. F., Dr.	Naval Surface Weapons Center Head, Applied Mathematics Branch White Oak Laboratory Silver Spring, Maryland 20910 USA

THE MODELLING OF AIRFOIL SEPARATION IN SUBSONIC AND TRANSONIC FLOW

by

Frank A. Dvorak and Brian Maskew
Analytical Methods, Inc.
Bellevue, Washington 98004

Abstract

A free shear layer model for separation has been developed which enables one to calculate the flow about airfoils up to and beyond the stall. The calculation procedure involves iteration between viscous and inviscid flows. The separation region is modelled in the inviscid flow analysis using free vortex sheets whose shapes are determined by iteration. The outer iteration employs boundary layer calculations to determine the location of separation. In subsonic flow the inviscid flow field is calculated using a panel method based on linearly varying vortex and source singularities. Viscous effects are introduced via the surface transpiration approach. In transonic flow a finite-difference procedure employing the velocity potential is used to determine the airfoil flow field. In the transonic case, the separation region is modelled by sheets of discontinuous velocity potential gradient. A direct analogy exists between the free vortex sheet model for separation in the subsonic case, and the discontinuity sheet model in the transonic case. The subsonic method has been compared with experiment for a wide range of airfoil types. The stall behavior for airfoils with trailing-edge or leading-edge separation is predicted quite well, while thin airfoil or long bubble stall is poorly predicted. The method has been applied at angles of attack through ninety degrees with excellent results. The transonic method is in a much earlier stange of development, but results to data are very encouraging.

Introduction

Boundary layer separation is one of the least understood but most important of fluid flow phenomena affecting aerodynamic forces and moments. Its accurate modelling is essential to the estimation of airborne vehicle performance. Currently, reliance is placed on wind tunnel tests to determine the consequences of separation; a procedure which is not entirely free of doubt because of Reynolds number effects. Successful theoretical modelling of separation is limited to a small number of special cases, one of which is two-dimensional turbulent boundary layer separation from airfoils or diffusers. The first successful model for trailing-edge separation was developed by

---

The authors gratefully acknowledge the support given by the U.S. Army Research Office, Research Triangle Park, N.C., for this work under Contracts DAAG29-76-C-0019 and DAAG29-79-C-0004.

Jacob (1). With Jacob's model, the separation region is simulated using source fluid, the distribution of which is chosen to give constant pressure everywhere in the separation region. In general, the method predicts the upstream pressure distribution in a satisfactory manner, although agreement with experiment for base pressure level is not consistent.

Recently a separation model has been developed by Analytical Methods, Inc. which replaces the source distribution in the separation zone by a vortex wake model. This model is described in some detail in (2), but is discussed herein for reasons of completeness.

Separation Model--Subsonic Flow

An approximate model of the flow about an airfoil with a region of separation is shown in Figure 1. It is assumed that:

(i) The boundary layer and free shear layers do not have significant thickness and, hence, can be represented as slip surfaces; that is, streamlines across which there exists a jump in velocity.

(ii) The wake region does not have significant vorticity and has constant total pressure (lower than the free-stream total pressure). It is, therefore, taken to be a potential flow region.

The flow field in the potential flow is obtained using linearly varying vortex singularities distributed on planar panels. The wake is represented by sheets of vorticity shed at the separation points.

The mathematical problem is to find the vorticity sheet strength such that the appropriate boundary conditions are met. The position of the vorticity sheet representing the free shear layer is not known a priori.

Approximations For the Free Shear Layer

(i) Wake Shape

Initially, the streamlines are not known, and so the shapes of the free shear layers must be obtained iteratively starting from an initial assumption. Earlier calculations in which the vortex sheet shapes were obtained by iteration suggested an initial shape as follows. The upper and lower sheets are represented by parabolic curves passing from the separation poins to a common point downstream. The slope at the upstream end is the mean between the free stream direction and the local surface slope. (Indications from further calculations are that this starting slope should be streamwise for calculations beyond the stall.) Once the wake calculation begins, the initial slope and downstream position of each wake is determined by iteration. The final wake position represents the separating streamline.

(ii) Wake Length

Early calculations indicated that the results were sensitive to the length of the free vortex sheets. Good correlation with experimental results was obtained only with relatively short wakes; i.e., wakes extending .1c to .2c beyond the trailing edge. Such a model appears reasonable in the light of experimental evidence: the separated wake does, in fact, close quickly downstream of the trailing edge, as a result of the strong entrainment process brought about by the rotation in the free shear layers (see (3)). On the basis of several comparisons with experiment, a simple correlation was obtained for the wake length as a function of the airfoil thickness to chord ratio. This is discussed in detail in (2).

(iii) Wake Pressure

The approximation of zero static pressure drop across the free shear layer is used to obtain an expression for the total pressure in the wake in terms of the strength of the free vortex sheets. Considering the upper shear layer, if the average velocity in the layer is denoted by

$$\overline{V} = \tfrac{1}{2}\left(V_{outer} + V_{inner} \right)$$

then

$$V_{outer} = \overline{V} + \gamma_U/2, \text{ and}$$

$$V_{inner} = \overline{V} - \gamma_U/2,$$

since the vorticity, $\gamma_U = V_{outer} - V_{inner}$, on the upper sheet. (The vorticity in the lower shear layer is $\gamma_L = V_{inner} - V_{outer}$.)

The jump in total pressure across the shear layer is then

$$\begin{aligned} \Delta H &= H_{inner} - H_{outer} \\ &= \left\{ p_{inner} + \tfrac{1}{2}\rho \left(\overline{V} - \gamma_U/2 \right)^2 \right\} \\ &\quad - \left\{ p_{outer} + \tfrac{1}{2}\rho \left(\overline{V} + \gamma_U/2 \right)^2 \right\} \\ &= -\rho \overline{V} \gamma_U = \rho \overline{V} \gamma_L \, . \end{aligned}$$

given the boundary condition that the static pressure, p, has no jump in value across the shear layer.

Since the wake has constant total pressure (assumption (ii)), the jump in total pressure across the free shear layer is the same everywhere.

Once the vorticity strengths of the individual panels representing the airfoil and of the vorticity sheets representing the wake are determined, the velocity at any point in the flow field can be calculated.

The pressures are calculated from the velocities according to the Bernoulli equation which is expressed non-dimensionally as

$$C_p = 1 - \left(\frac{V}{V_\infty}\right)^2 + \frac{\Delta H}{q_\infty}$$

where $C_p = \frac{p - p_\infty}{q_\infty}$, $q_\infty = \frac{1}{2}\rho V_\infty^2$, and ΔH = increase in total pressure over that at infinity. Note that $\Delta H = 0$ everywhere except in the wake region for which it was previously shown that $\Delta H = \rho \bar{V} \gamma_L$.

Calculation Procedure

The overall calculation procedure is shown in Figure 2, and involves two separate iteration loops.

(i) Wake Shape Iteration

The iteration loop for wake shape is the inner loop and involves the potential flow analysis only. Within this loop the separation points are fixed. The separation points may be located anywhere on a surface panel; they are not restricted to panel edge points.

The wake shape is calculated as follows. Using the previous vorticity distribution, velocities are calculated at the panel mid-points on the free vortex sheets. The new wake shape is then determined by piecewise integration, starting at the separation points. The upper and lower sheet downstream end points, which were coincident in the initial wake, are allowed to move independently in subsequent iterations. At each iteration, the wake influence coefficients at the surface control points are recalculated, and a new potential flow solution is obtained.

The number of wake iterations is an input parameter in the current version of the program; typically, however, it has been found that three wake iterations are sufficient to produce a converged solution.

(ii) Viscous/Potential Flow Iteration

This outer iteration loop takes the potential flow pressure distribution over to the boundary layer analysis and returns with the separation points and with the boundary layer source distribution. The source distribution is determined directly from the boundary layer solution as

$$\sigma = \frac{d}{ds} (U_e \delta^*),$$

where U_e is the streamwise potential flow velocity at the edge of the boundary layer, and δ^* is the displacement thickness. The addition of this source distribution modifies the normal velocity, V_N, at each panel control point. The sources are set to zero in the separated region.

The program generates a new wake shape using the new separation points together with information from the previous iterated wake. A new potential flow solution is then obtained, and so on. The outer iteration is terminated when the change in C_ℓ is below 1%. A limit of eight iterations is currently imposed within the program.

Boundary Layer Methods

The boundary layer development on an arbitrarily-shaped two-dimensional lifting configuration with separated flow is very complex. A thorough and exact calculation of this development is properly the domain of the time-dependent solution to the general Navier Stokes equations. Unfortunately, the computer does not yet exist which is capable of handling such a problem in a reasonable time at a reasonable cost. Such a calculation is not, therefore, of practical interest to the aerodynamicist. Less difficult or costly are the finite-difference boundary layer programs now in existence. The amount of computer time required for each calculation still prohibits their use in an analysis procedure of the type reported herein. Having made the above evaluation, one must conclude that if the objective is a viscosity-dependent calculation procedure of practical use to the aerodynamicist for $C_{\ell_{max}}$ analysis, and, possibly, for preliminary design, the method must be relatively simple to use and economic of computer time. This can only be achieved if integral boundary layer methods are used. In two dimensions, integral methods are typically about 100 times faster than finite-difference methods. They can, however, be expected to break down in the region of separation where none of the boundary layer methods (including three-dimensional) can be expected to be valid. It is anticipated, therefore, that integral methods will suffice for most applications of interest to the aerodynamicist for $C_{\ell_{max}}$ prediction.

In those cases of special interest to the aerodynamicist, such as the effect of area suction for boundary layer control or of roughness (rivets, etc.) on $C_{\ell_{max}}$, alternative boundary layer calculation modules are available. These methods are called as needed into the overall calculation procedure. A brief discription of the boundary layer methods is given in the following paragraphs.

The laminar boundary layer development is calculated by Curle's method (4), an adaption of the well known method of Thwaites (5). The calculation proceeds either to laminar separation or to the end of the airfoil--whichever occurs first. The calculated boundary layer development is then interrogated to determine if transition, laminar separation or forced transition (boundary layer tripping) has taken place. If any of these phenomena have occurred, the downstream flow is assumed to be turbulent.

Methods for the calculation of turbulent boundary layers in two dimensions have been developed by many investigators. A review of these methods was made at a conference held in 1968 at Stanford University (6). One of the methods, an integral method by Nash and Hicks (7) compared very favorably with the more complex finite-difference methods. Now, several years later, the method remains an excellent approach for application to the current problem both in terms of accuracy and speed.

If surface roughness or area suction are of interest, an alternate turbulent boundary layer method developed by Dvorak (8) and (9) can be called. This method is capable of predicting the downstream development and skin friction drag of a turbulent boundary layer over a rough surface, or a surface with area suction boundary layer control.

Turbulent boundary layer separation is predicted by either the Nash and Hicks or Dvorak methods when the calculated local skin friction coefficient reaches zero.

Discussion of Results

The method was applied to a GA(W)-1 airfoil. This section shape represents a difficult test case and pressure distributions are available from experiments at NASA-Langley for a range of incidence.

The first set of results, Figures 3 through 5, are for a Reynolds number of 6.3×10^6 with a boundary layer trip at .08c. Figure 3 shows a very good agreement between the calculated and experimental pressure distribution at 20.05° incidence. The calculation took six viscous/potential flow iterations, each with three wake shape iterations. For comparison, the attached potential flow solution at this incidence is also plotted, and indicates the large change in pressures due to the separated flow.

The wake shape history for a 21.14° incidence is shown in Figure 4, and indicates very good convergence characteristics. Lift and pitching moment characteristics show excellent agreement with experiment, Figure 5. The previous calculations show considerable improvement over a previous Lockheed/NASA-Langley calculation. The attached potential flow solution is included in Figure 5 to put into perspective the magnitude of the change achieved by the new method.

Figure 6 shows the lift characteristics for the GA(W)-1 airfoil at a Reynolds number of 2.1 x 10^6. The calculations give good agreement with experiment up to $C_{\ell_{max}}$, but the turnover in the curve occurs 2 to 3 degrees later than in the experiment.

Additional comparisons were made with experiment for several airfoils. Shown on Figures 7 and 8 are the results for the lift characteristics for the airfoils tested by McCullough and Gault (10). In the case of the NACA 63009 airfoil, the program predicts a trailing-edge stall while experimentally the airfoil stalls from the leading edge. As shown in Figure 7, a slight modification to the laminar separation reattachment criterion leads to a much improved correlation with experiment. This points out the need for a better understanding of the laminar separation bubble bursting phenomenon.

Comparisons between theory and experiment for the lift characteristics of the NACA 4412 at a series of Reynolds numbers are shown on Figures 9, 10 and 11. A summary of the predicted and experimental $C_{\ell_{max}}$ variation with Reynolds number is shown in Figure 12. The calculated values agree very closely with the experimental curve from (11). Calculations for lower Reynolds numbers were attempted, but problems with the laminar separation bubble bursting criterion produced inconsistent results.

A series of calculations were made to demonstrate the capability of the analysis method over a wide range of angles of attack. Figure 13 shows the calculated wake shape for a NACA 0012 airfoil at 90 degrees to the free stream. The corresponding pressure distribution is given in Figure 14. The calculated lift and drag coefficients are 0.25 (.15) and 2.1(2.08 - 2.3), respectively. These values compare well with measured lift and drag coefficients given in the enclosed brackets. Figure 15 shows a comparison between measured and calculated lift coefficients for the NACA 0012 airfoil from 0 degrees through 90 degrees angle of attack. The agreement is surprisingly good. A summary plot of calculated versus experimental $C_{\ell_{max}}$ for a series of different airfoils is shown on Figure 16.

Separation Model--Transonic Flow

In the transonic flow case, the wake model is analogous to that used in the subsonic case. Specifically, there exists a direct analog between the vorticity sheet wake model and the velocity potential (ϕ) discontinuity sheet model. The gradient in ϕ with repsect to surface distance, s, i.e., $\partial\phi/\partial s$, at the separation points, both upper and lower surface, must be equal in magnitude as required by the Kutta condition. The additional requirement is that the entire ϕ-discontinuity sheet representing the wake must retain the value of $\partial\phi/\partial s$ at separation. Just as in the vorticity model where there is a jump in tangential velocity across the wake sheet, in the ϕ field there must be a jump in ϕ across the discontinuity sheet. The corrrect path of the separating wake sheet is found by iteration; that is, the actual values of $\partial\phi/\partial n$ on the wake sheet from the previous iteration are used to determine the new wake location. A new ϕ field solution is then obtained, and so on, until the solution has converged for a wake path having the requirement that $\partial\phi/\partial n = 0$ across the

discontinuity sheet. The requirement for a converged solution is that with all other conditions satisfied, the circulation should have attained a converged value.

Potential Flow Model

Initially a pilot code was generated to solve the full potential version of the equations of motion for flow about a circular cylinder using a line over-relaxation finite-difference technique. With the separation point known, the pilot code gives results in excellent agreement with experiment (see Figure 17). The separation model was then incorporated into a transonic code developed by Jameson (12). A compressible integral boundary layer program consisting of the laminar method of Cohen and Reshotko (13) and the turbulent lag-entrainment method of Green et al. (14) has been coupled to the potential flow program.

Results for the circular cylinder are compared with experiment and with the pilot code in Figure 17. A further comparison is shown in Figure 18 for the GA(W)-1 airfoil at 19.06° angle of attack. The measure of agreement is very encouraging.

Conclusions

The results of comparisons with experiment, including those presented in this paper lead to the following conclusions.

(i) The basic analysis method predicts both the lift curve and the maximum lift coefficient quite accurately for a wide variety of airfoils over a range of Reynolds numbers.

(ii) Post-stall behavior is best predicted for the trailing-edge type of stall.

(iii) Leading-edge and thin airfoil stall prediction could be considerably improved by a better laminar separation bubble bursting criterion.

(iv) The use of vortex sheets to represent the separated flow boundaries suggests that the model will be applicable to unsteady flows.

(v) The extension to the transonic case has lead to very good agreement with experiment, at least for the lower Mach number, high angle-of-attack regime.

References

1. Jacob, K., "Computation of Separated, Incompressible Flow Around Airfoils and Determination of Maximum Lift", AVA Report 66, A, 62, 1967.

2. Maskew, B. and Dvorak, F.A., "The Prediction of $C_{\ell_{max}}$ Using a Separated Flow Model", Proceedings 33rd Annual Forum of the American Helicopter Soceity, Washington, D.C., May 1977. Also J. Amer. Hel. Soc., April 1978.

3. Seetharam, H.C. and Wentz, W.H., "Experimental Studies of Flow Separation and Stalling on a Two-Dimensonal Airfoil at Low Speeds", NASA CR-2560, 1975.

4. Curle, H., "A Two-Parameter Method for Calculating the Two-Dimensional Incompressible Laminar Boundary Layer", J. R. Aero. Soc., Vol. 71, 1967.

5. Thwaites, B., "Approximate Calculation of the Laminar Boundary Layer", Aero. Quart., Vol. I, 1949.

6. Kline, S.J., Morkovin, M.V., Sovran, G. and Cockrell, D.J., "Computation of Turbulent Boundary Layers", Proceedings 1968 AFOSR-IFP Stanford Conference, Stanford University Press, Stanford, California, 1969.

7. Nash, J.F. and Hicks, J.G., "An Integral Method Including the Effect of Upstream History on the Turbulent Shear Stress", Proceedings Computation of Turbulent Boundary Layers--1968 AFOSR-IFP Stanford Conference, Vol. 1, Stanford University Department of Mechanical Engineering, Stanford, California.

8. Dvorak, F.A., "The Calculation of Turbulent Boundary Layers on Rough Surfaces in Pressure Gradient", AIAA J., Vol. 7, No. 9, September 1969.

9. Dvorak, F.A., "The Calculation of Compressible Turbulent Boundary Layers with Roughness and Heat Transfer", AIAA J., Vol. 10, No. 11, November 1972.

10. McCullough, G.B. and Gault, D.E., "Examples of Three Representative Types of Airfoil Section Stall at Low Speed", NACA Tech. Note 2502, 1951.

11. Pinkerton, R.N., "The Variation with Reynolds Number of Pressure Distribution over an Airfoil Section", NACA Report No. 613.

12. Jameson, A., "Iterative Solution of Transonic Flows Over Airfoils and Wings, Including Flows at Mach 1", Communications of Pure and Applied Math, Vol. 27, pp. 283-309, 1974.

13. Cohen, C.B. and Reshotko, E., "The Compressible Laminar Boundary Layer with Heat Transfer and Arbitrary Pressure Gradient", NACA 1294, 1956.

14. Green, J.E., et al., "Prediction of Turbulent Boundary Layers and Wakes in Compressible Flow by a Lag-Entrainment Method", RAE TR-72231, January 1973.

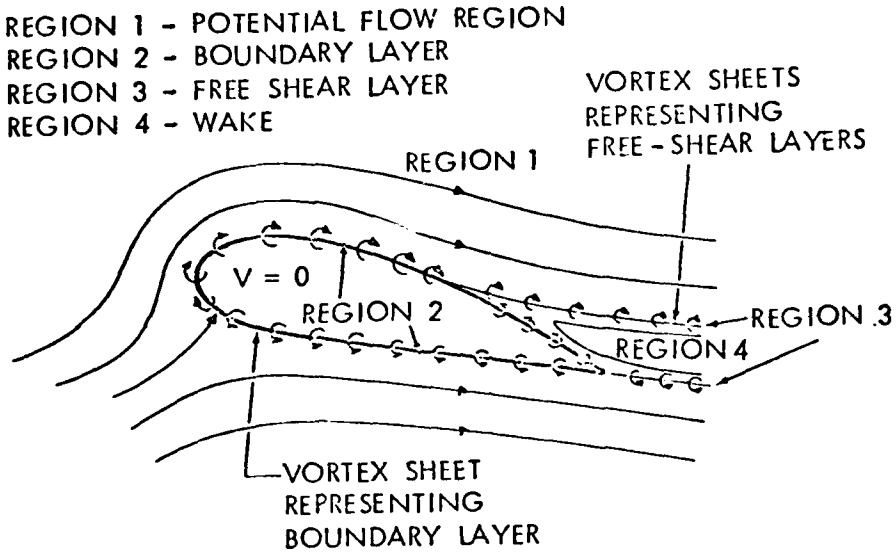

Fig. 1. Mathematical Flow Model.

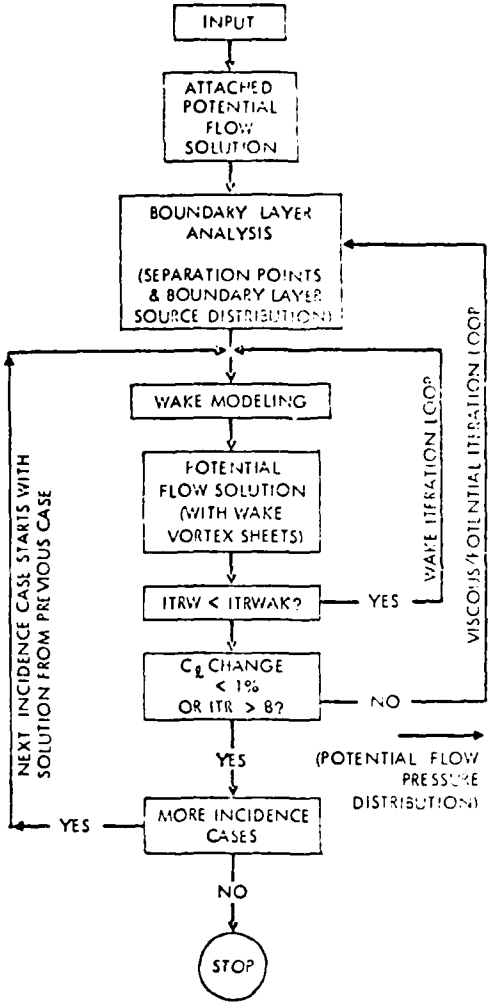

Fig. 2. Calculation Procedure.

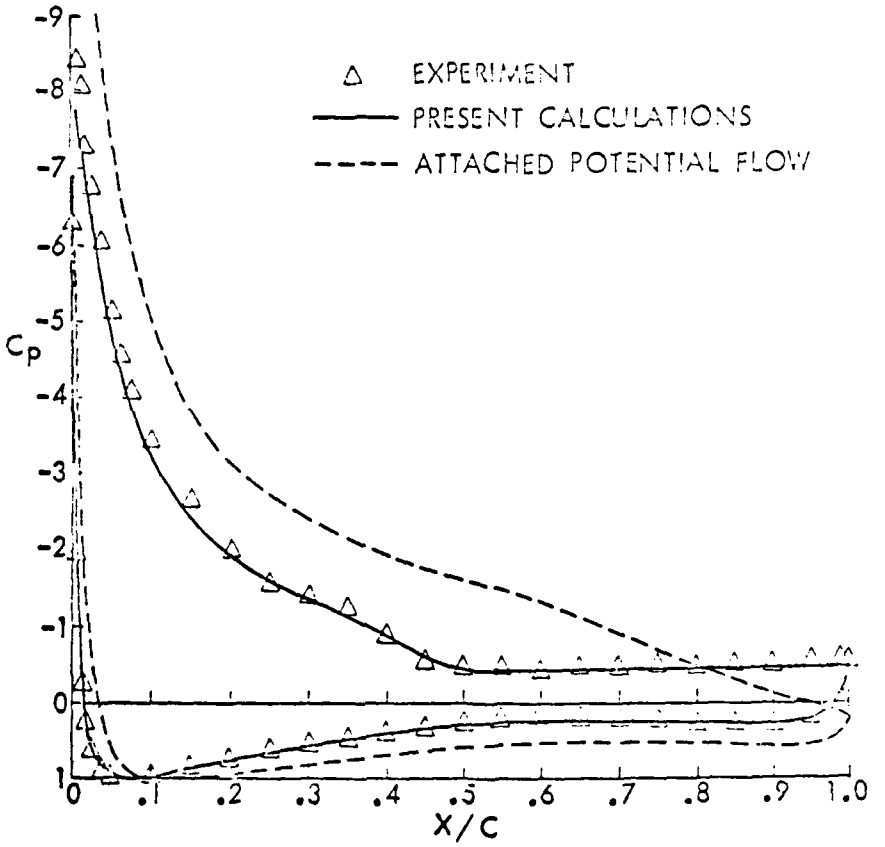

Fig. 3. Comparison of Calculated and Experimental Pressure Distributions on a GA(W)-1 Airfoil Post Stall; Re = 6.3×10^6, $\alpha = 20.05^{\circ}$.

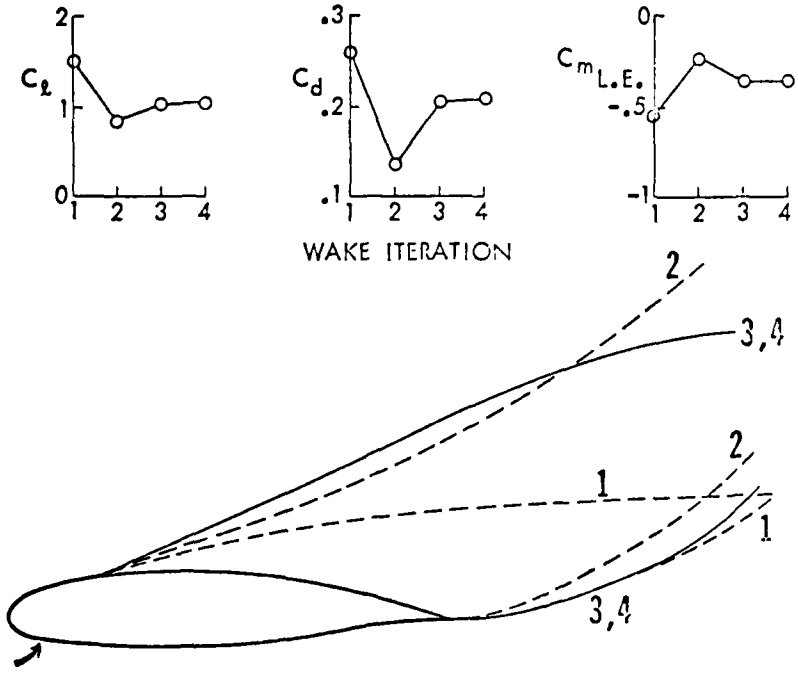

Fig. 4. Typical Wake Shape Iteration Characteristics for an Angle-of-Attack Beyond the Stall.

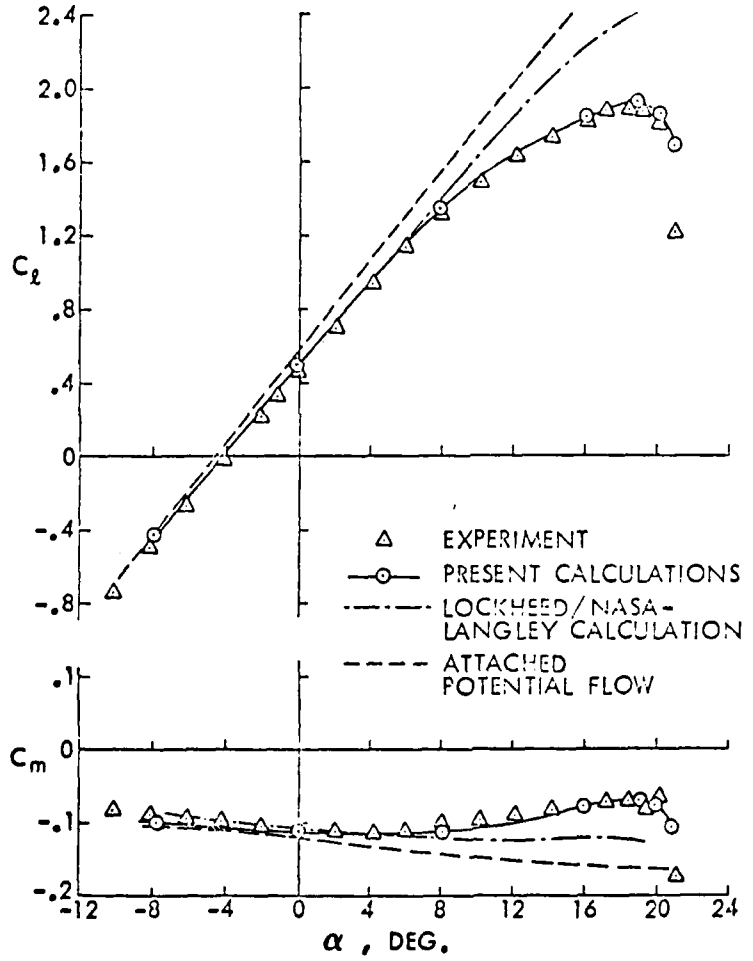

Fig. 5. Comparisons of Calculated and Experimental Lift and Pitching Moment Characteristics for the GA(W)-1 Airfoil: Re = 6.3×10^6.

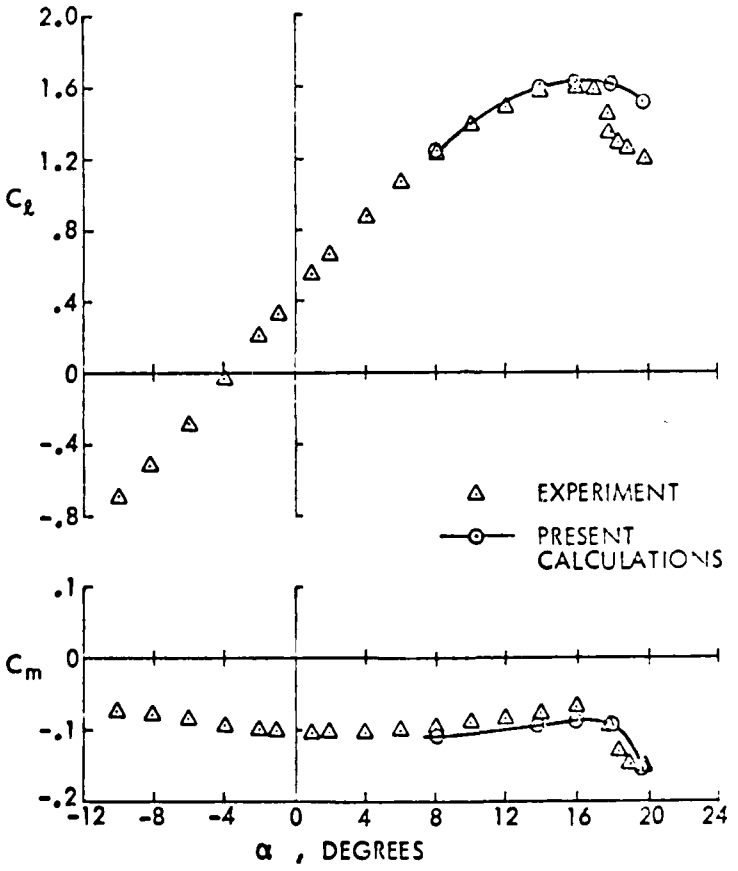

Fig. 6. Comparisons of Calculated and Experimental Lift and Pitching Moment Characteristics for the GA(W)-1 Airfoil: Re = 2.1 x 10^6.

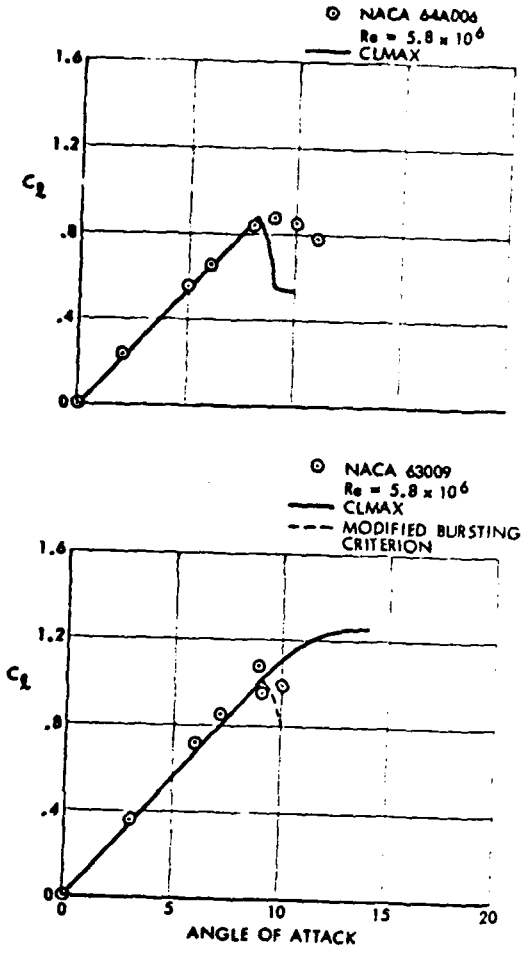

Fig. 7. Comparison of Calculated and Experimental Lift Characteristics.

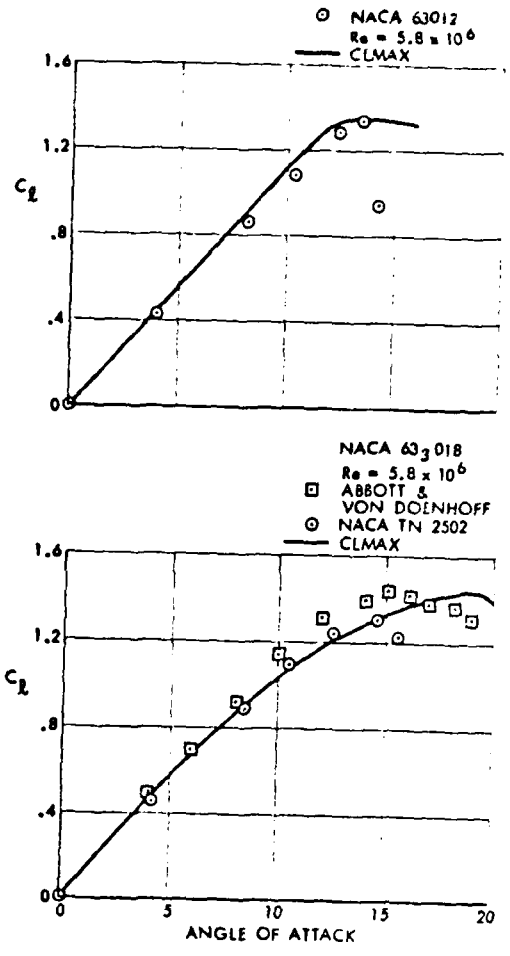

Fig. 8. Comparison of Calculated and Experimental Lift Characteristics.

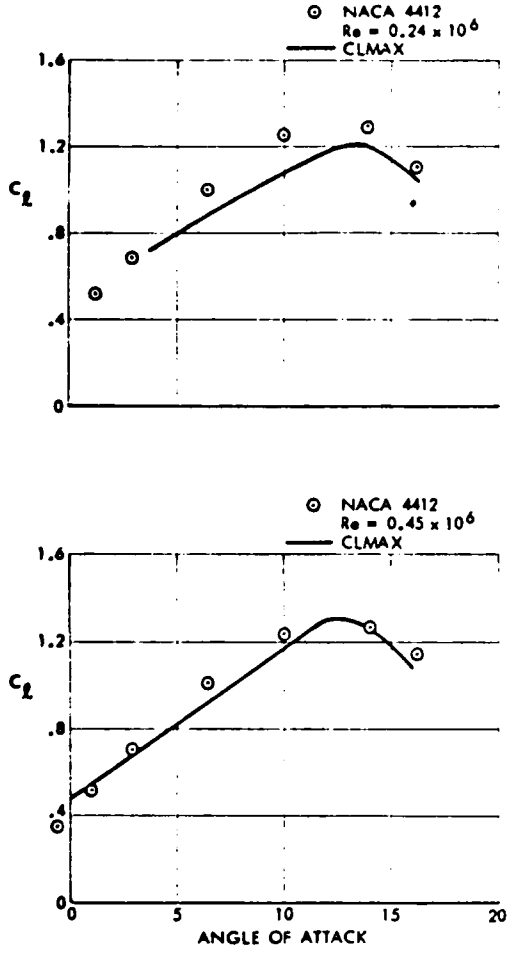

Fig. 9. Comparison of Calculated and Experimental Lift Characteristics.

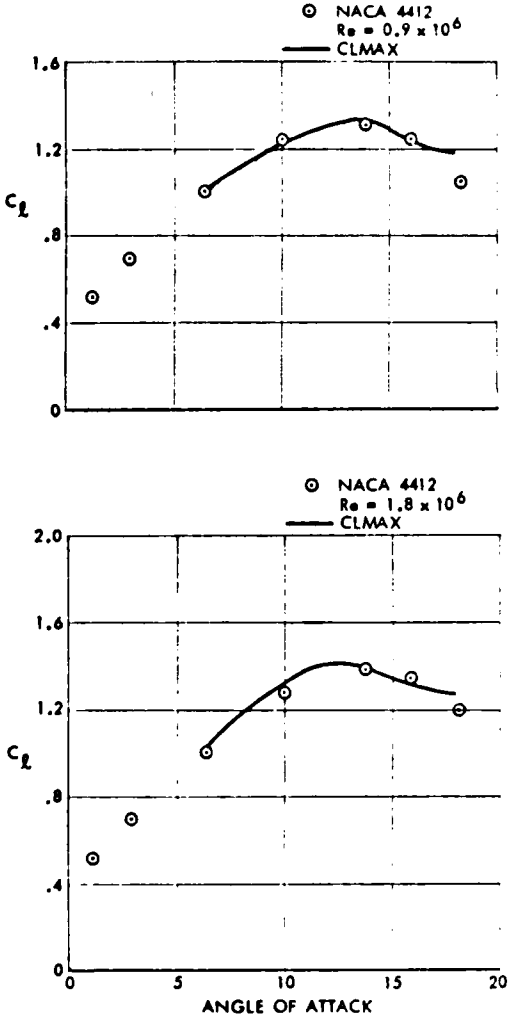

Fig. 10. Comparison of Calculated and Experimental Lift Characteristics.

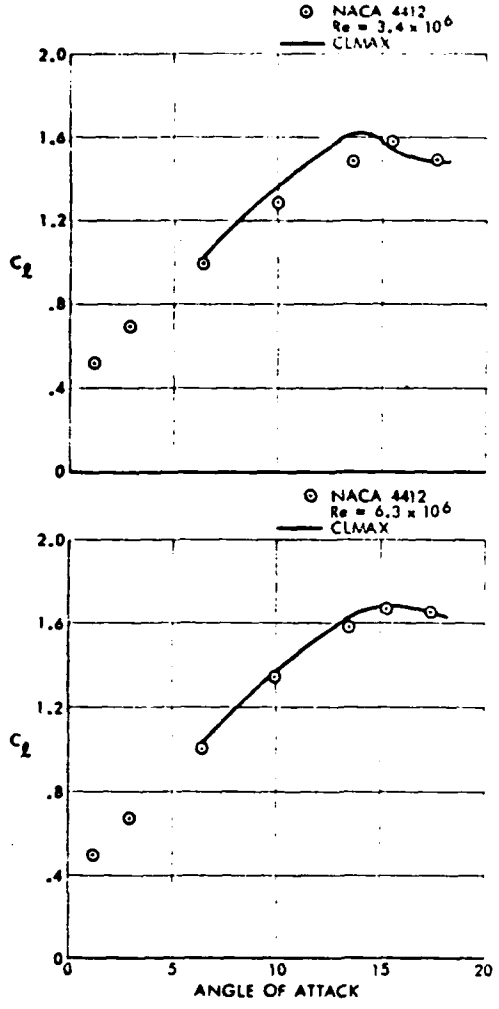

Fig. 11. Comparison of Calculated and Experimental Lift Characteristics.

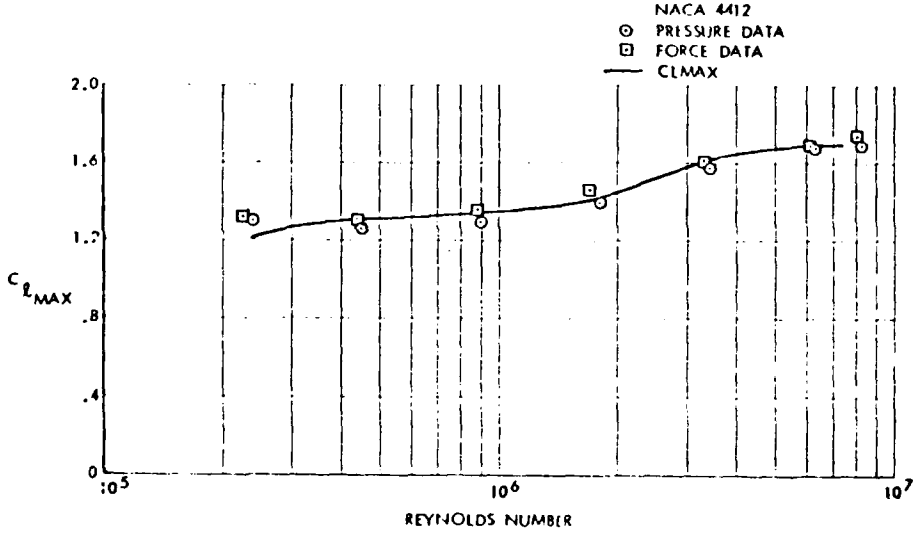

Fig. 12. Comparison of Calculated and Experimental $C_{\ell_{max}}$ Variation with Reynolds Number for the NACA 4412 Airfoil.

Figure 14.

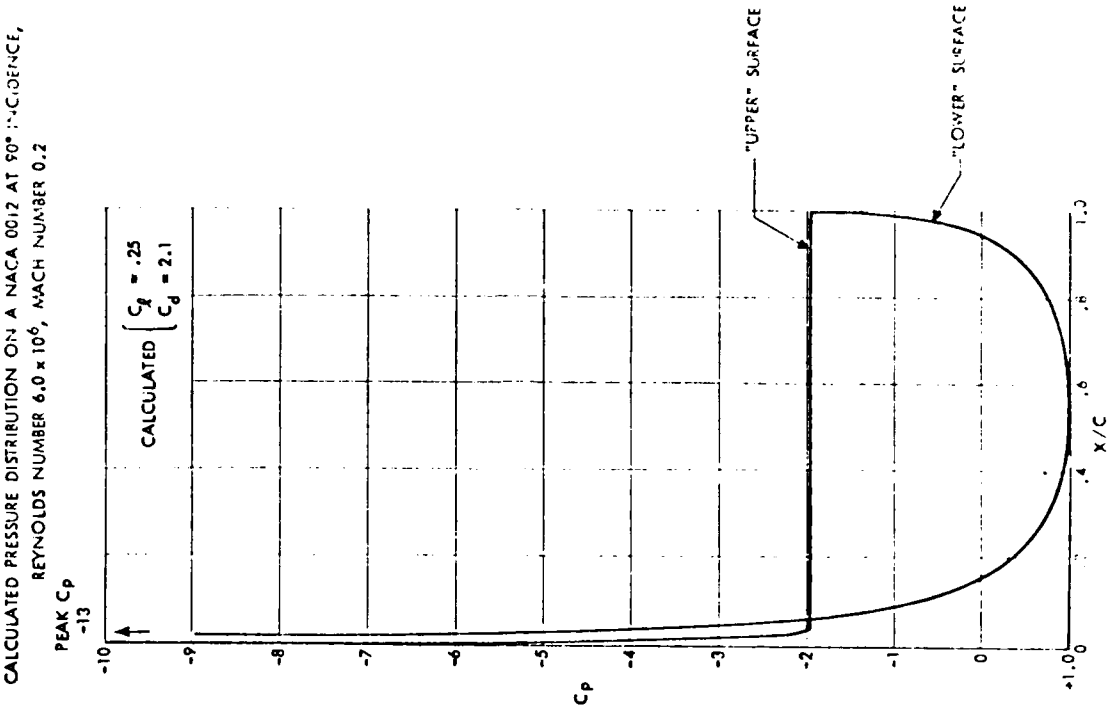

Figure 13.

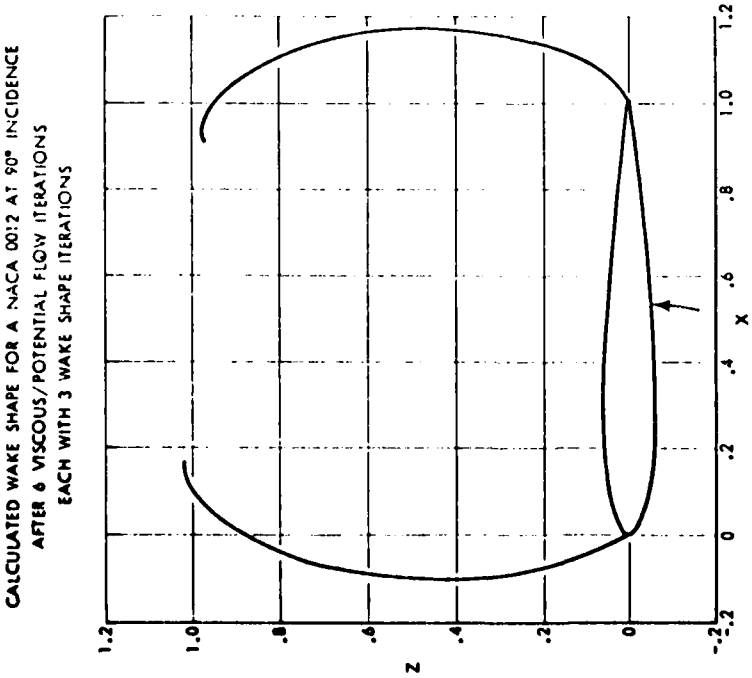

Figure 15.

COMPARISON OF CALCULATED AND EXPERIMENTAL LIFT CHARACTERISTICS FOR A NACA 0012 AIRFOIL, REYNOLDS NUMBER 6.0×10^6, MACH NUMBER 0.2

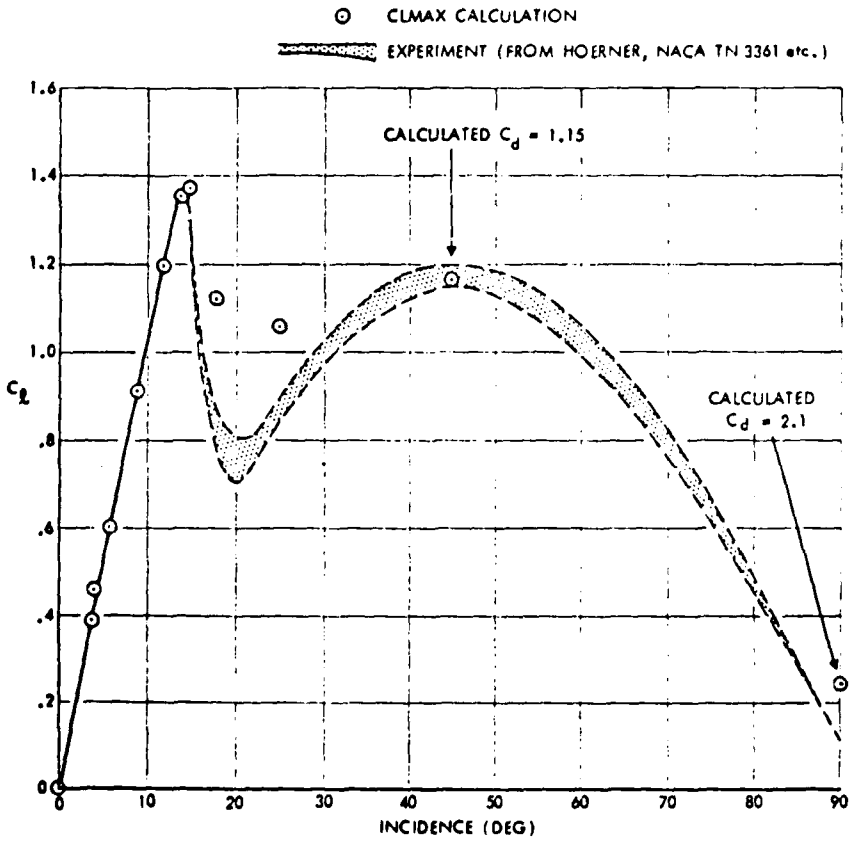

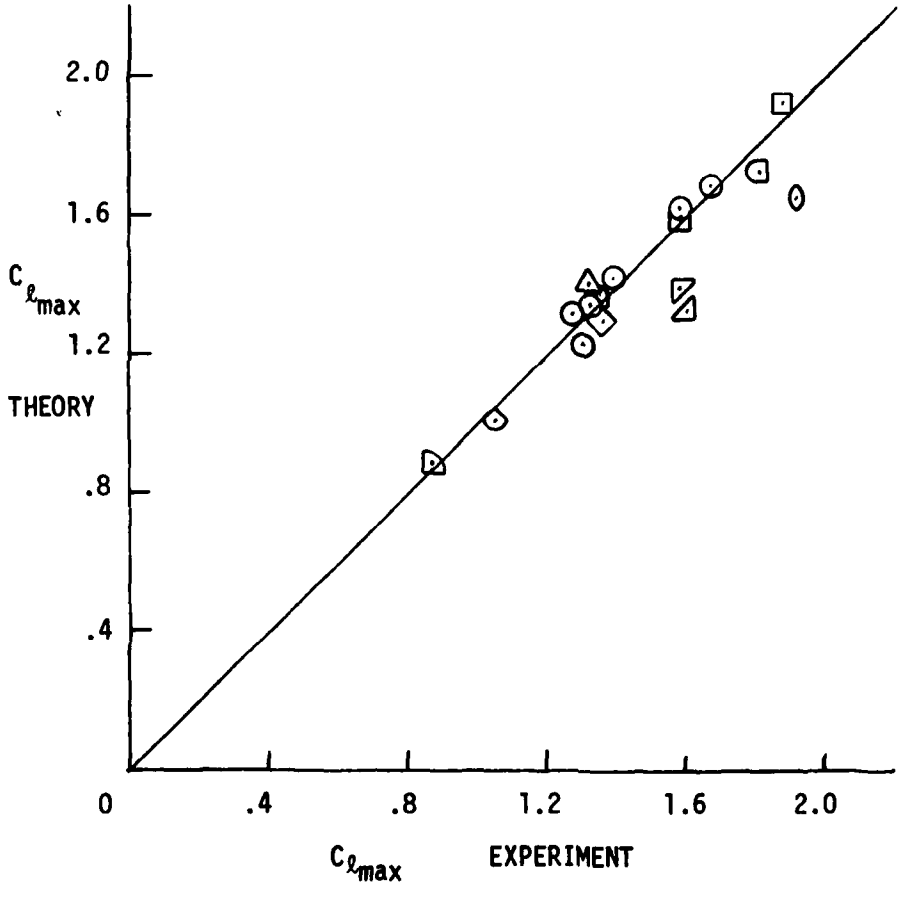

Figure 16. Comparison of Program CLMAX with Experiment.

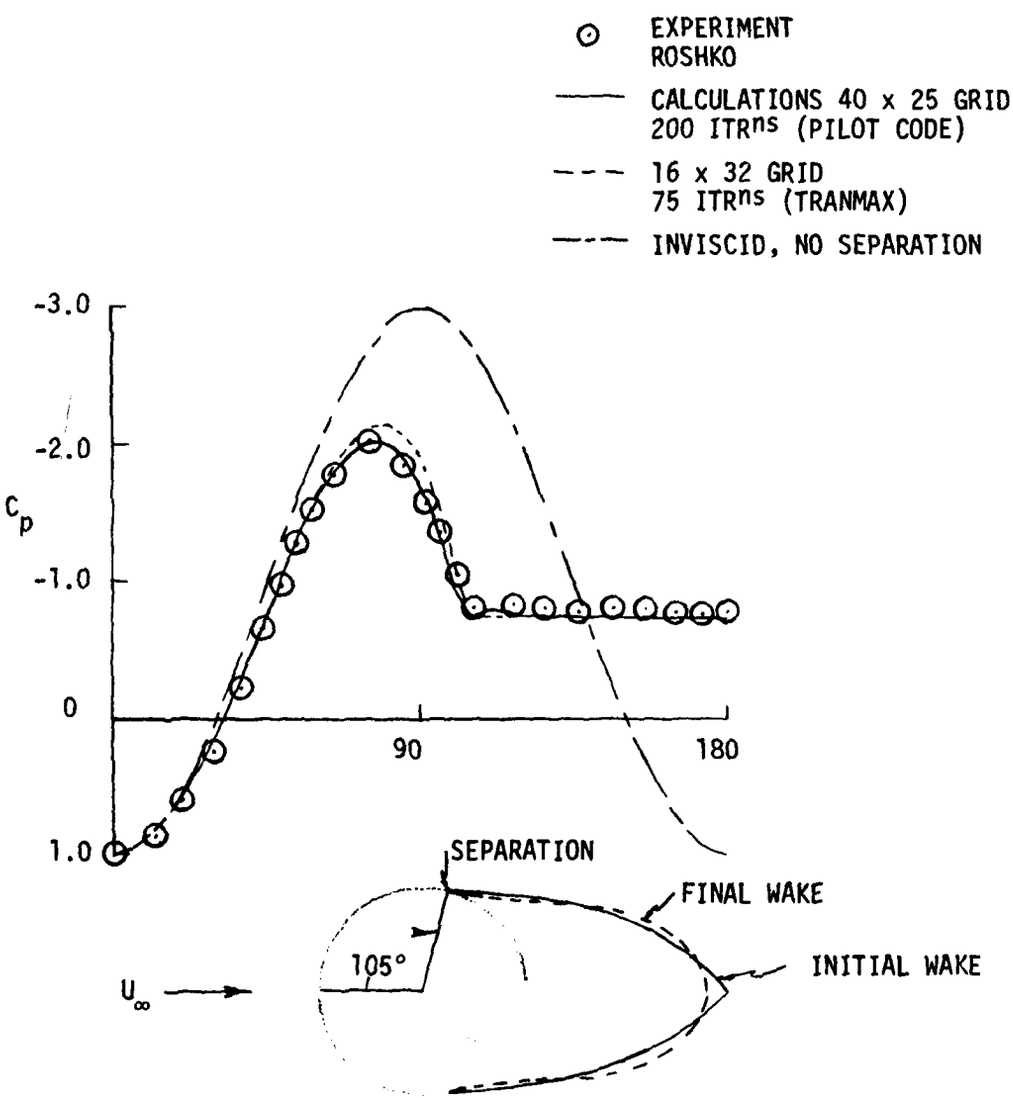

Figure 17. Comparison of Calculated and Experimental Pressure Distributions on a Circular Cylinder; Re = 8.4 x 10^6.

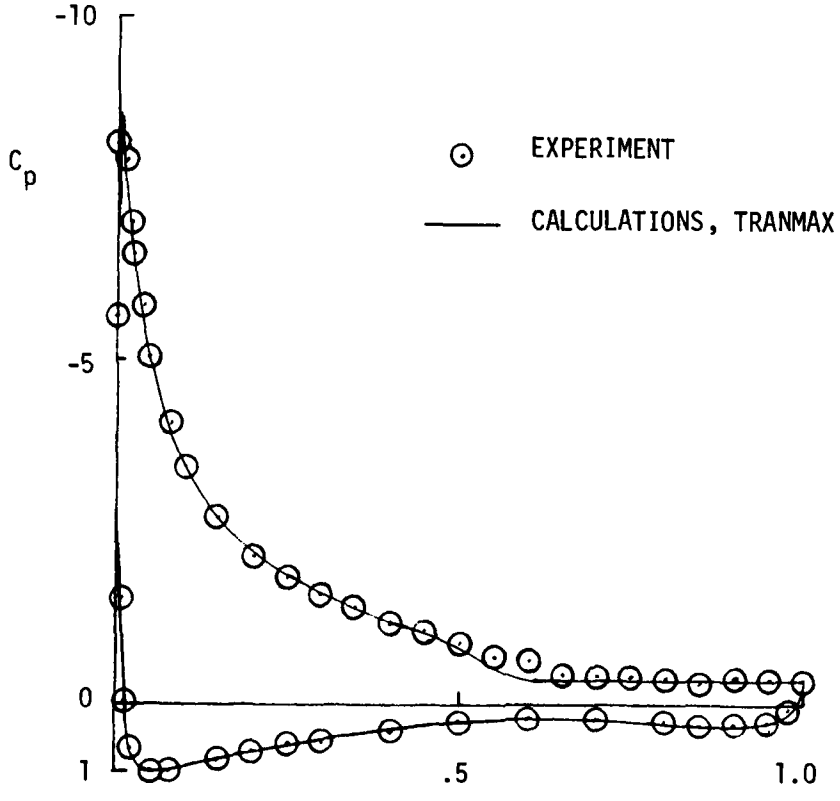

Figure 18. Comparison of Calculated and Experimental Pressure Distributions on a GA(W)-1 Airfoil; Re = 6.3 x 10^6, α = 19.06°, M_∞ = .20.

THEORETICAL DETERMINATION OF THREE-DIMENSIONAL FLOW SEPARATION

Tsze C. Tai*
David W. Taylor Naval Ship Research and Development Center
Bethesda, Maryland, U.S.A.

Abstract

A streamline approach for determining the free vortex-layer type, three-dimensional flow separation is presented. The procedure is based on the Maskell postulation about separation patterns in three dimensions. The line of separation is determined by the envelope of merging streamlines inside the viscous layer. The required streamlines are calculated by three ordinary differential equations, using inviscid pressures along with proper viscous damping parameters. The method is illustrated by two examples, a prolate spheroid in an incompressible flow and a spherically blunted cone at hypersonic speed, both at moderate angles of attack. Comparisons of the theoretical results with experiments and a three-dimensional boundary-layer solution are made.

Nomenclature

a,b	major and minor axes of an ellipsoid
e	eccentricity
f	local body radial distance from the centerline
g_{ij}, g^{ij}	metric tensor for body geometry
h_1, h_2	metric coefficients for coordinates ξ, β
ℓ	length of a body
M	Mach number
P	static pressure
R	nose radius
S	distance along a streamline measured from the stagnation point
u, v, w	velocity components in body-oriented coordinates
V	velocity
x, ϕ, z	body-oriented nonorthogonal coordinates
$\bar{x}$, $\bar{y}$, $\bar{z}$	Cartesian coordinates
α	angle of attack
γ	ratio of specific heats
θ	streamline angle
λ	coefficient for friction model
μ	viscosity
ξ, β, ζ	streamwise coordinates
ρ	density
$-\rho\overline{u'w'}$, $-\rho\overline{v'w'}$	Reynolds stresses
τ	shearing stress

Subscripts

i	initial condition
o	stagnation
1,2	x,ϕ direction
∞	freestream

This research was sponsored by the Naval Air Systems Command (AIR-320D, AIRTASK 9R023-02-000) under the cognizance of D. Kirkpatrick. The author is indebted to K. C. Wang of San Diego State University, S. de los Santos, M. Martin, and H. J. Lugt of DTNSRDC for their useful discussions and comments, and to D. G. Rousseau for his assistance in computer programming.

*Research Aerospace Engineer, Aviation and Surface Effects Department.

Introduction

The criterion for flow separation in three dimensions is radically different from the conventional concept based on two-dimensional flows, where separation takes place as the skin friction vanishes. In three-dimensional flows, the vanishing of skin friction in either or both directions cannot be used to define a flow separation. Instead, the concept of the envelope of limiting streamlines as the separation line, has been developed. First suggested by Eichelbrenner and Ondart,[1] the envelope idea was further explored by Maskell,[2] based on general flow observations and supported by Wang[3] from the standpoint of numerical results. A comprehensive review of the subject was given by Wang.[4]

Maskell[2] postulated two basic forms of separation patterns in three dimensions -- a bubble and a free vortex (or shear) layer. In the case of a bubble, the surface of separation encloses fluid which is not part of the main stream but is carried along with the body surface. In the case of a vortex layer, both sides of the separation surface are filled with the main stream fluid. Although each displays a different flow structure, the line of separation is generally identified as an envelope of the limiting streamlines. In reality, a combination of both types of flow separation with a bubble and a free vortex layer is most likely to exist.

The Maskell descriptions, which are representations of experimental observations, are found by Wang[4] to be consistent with the three-dimensional boundary-layer theory. Wang[4] introduced an open-and-closed separation concept, however. In a closed separation, the separated region is inaccessible to the upstream flow. For an open separation, on the other hand, the limiting streamlines on both sides of the separation line stem from the same front stagnation point; the separated region is accessible to the upstream flow. Physically, therefore, Wang's closed-type separation corresponds to Maskell's bubble type, and the open-type separation corresponds to the vortex-layer type. The open separation concept, which is relatively new, has been substantiated by recent measurements made by Meier et al.[5] and Han and Patel.[6]

Formation of Vortex-Layer-Type Separation

Of particular importance is the vortex-layer-type separation (or the open type) which covers a wide class of flows of practical interest. Flows around a body of revolution, at angles of attack that often model spacecraft,[7] missiles,[8] and submarine configurations[9] in maneuver, fall into this category. Also, free vortices over a wing-body combination[10] or in a ship stern[11] are generated by the vortex-layer-type separation due to merging of streamlines which originated from a common upstream flow. The phenomenon is unique in three-dimensional flows.

Maskell's postulation on the free vortex-layer-type separation pattern is shown in Fig. 1, which is based on description given in Ref. 12. It is

noted that above the limiting streamlines, there lie the inviscid streamlines. Since the limiting streamlines and the inviscid streamlines are both influenced by the surface pressure distribution and the deviation between the two is strictly of a boundary-layer nature, it is proper to suggest that the limiting streamlines are eventually dictated by the streamlines above them. The line of separation, which is an envelope of the limiting streamlines, therefore, can be determined approximately by the loci of merging streamlines inside or at the edge of the boundary layer. These streamlines, however, must be calculated accurately based on realistic pressure distributions containing physical properties that have direct bearing on the flow behavior. Experimental or empirical pressure distributions or theoretical pressures obtained by means of viscous-inviscid interactions involving not only attached flow but also separation are considered to possess such physical properties. If pure inviscid pressures are used, proper viscous damping terms should be incorporated to simulate the real flow.

In the present analysis, a method is developed to determine the vortex-type separation by the envelope of merging streamlines inside or at the edge of the boundary layer. An exact, yet simple method for determining the inviscid streamline geometry over general three-dimensional bodies has been developed. To trace the streamline inside the boundary layer, the method is extended to viscous flows by adding a friction model. The latter is particularly useful when realistic pressure distribution is not available.

Inviscid Streamline Equations

A. General Three-Dimensional Body

Few analyses have been developed in the literature to obtain the inviscid streamline geometry.[13-16] Here we will consider an exact method using nonorthogonal systems.[17] In body-oriented nonorthogonal coordinates (x,ϕ,z), the inviscid momentum equations for the flow over the surface of a general three-dimensional body can be written as follows.[17]

x - Momentum

$$u\frac{\partial u}{\partial x}+\frac{v}{g_{22}^{1/2}}\frac{\partial u}{\partial \phi}+\left(\frac{uvg^{12}}{g_{22}^{1/2}}-\frac{v^2g^{11}}{2g_{22}}\right)\frac{\partial g_{22}}{\partial x}$$

$$+\frac{v^2g^{12}}{2g_{22}}\frac{\partial g_{22}}{\partial \phi}+u^2g^{12}\frac{\partial g_{12}}{\partial x}+\frac{v^2g^{11}}{g_{22}}\frac{\partial g_{12}}{\partial \phi}$$

$$=-\frac{1}{\rho}g^{11}\frac{\partial P}{\partial x}+g^{12}\frac{\partial P}{\partial \phi} \qquad (1)$$

ϕ - Momentum

$$u\frac{\partial v}{\partial x}+\frac{v}{g_{22}^{1/2}}\frac{\partial v}{\partial \phi}+\left[uv\left(g^{22}-\frac{1}{2g_{22}}\right)-\frac{v^2g^{12}}{2g_{22}^{1/2}}\right]\frac{\partial g_{22}}{\partial x}$$

$$+\frac{v^2}{2g_{22}^{1/2}}\left(g^{22}-\frac{1}{g_{22}}\right)\frac{\partial g_{22}}{\partial \phi}+u^2g_{22}^{1/2}g^{22}\frac{\partial g_{12}}{\partial x}$$

$$+\frac{v^2g^{12}}{g_{22}^{1/2}}\frac{\partial g_{12}}{\partial \phi}=-\frac{g_{22}}{\rho}\left(g^{12}\frac{\partial P}{\partial x}+g^{22}\frac{\partial P}{\partial \phi}\right) \qquad (2)$$

where x is the distance along the body surface of a constant ϕ plane, ϕ is the azimuthal angle measured from the most windward line, and z is normal to the surface (see Fig. 2). The velocity components u and v are measured along the surface in x and ϕ directions, respectively, and P and ρ are the static pressure and density, respectively. The g_{ij} is the metric tensor for the body geometry and g^{ij} is the conjugate metric tensor of g_{ij}. Their expressions are given in Ref. 17.

The geometry of any streamline emanating from the stagnation point may be expressed as $\phi=\phi(x,\beta)$, where β is constant along a streamline. The coordinates are related to the velocity components through the relation, with the aid of the following sketch:

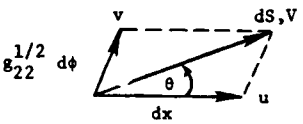

$$u:dx=v:g_{22}^{1/2}d\phi$$

$$\frac{g_{22}^{1/2}d\phi}{dx}=\frac{v}{u} \qquad (3)$$

Defining D/Dx as the substantial derivative, or derivative along a streamline, Eq. (3) can be written in the form

$$\frac{D\phi}{Dx}=\frac{v}{g_{22}^{1/2}u} \qquad (4)$$

Differentiate the above equation with respect to x to get

$$\frac{D^2\phi}{Dx^2}=\frac{1}{g_{22}^{1/2}}\left[\frac{u\frac{Dv}{Dx}-v\frac{Du}{Dx}}{u^2}-\frac{v}{2u}\frac{1}{g_{22}}\frac{Dg_{22}}{Dx}\right] \qquad (5)$$

Also, introduce a variable θ, the angle between the tangent of local streamline and the x-axis by the relation

$$\theta=\arccos\left[\frac{1+g_{12}\frac{D\phi}{Dx}}{\sqrt{1+g_{22}\left(\frac{D\phi}{Dx}\right)^2+2g_{12}\frac{D\phi}{Dx}}}\right] \qquad (6)$$

Differentiating Eq. (6) with respect to x along a streamline and rearranging, there yields

$$\frac{D^2\phi}{Dx^2} = \frac{\sin\theta\left[1 + 2g_{12}t + g_{22}t^2\right]^{3/2}\frac{D\theta}{Dx}}{(g_{22} - g_{12}^2)\,t} - \frac{\left[(1 + g_{12}t)\frac{Dg_{22}}{Dx} - 2(g_{12} + g_{22}t)\frac{Dg_{12}}{Dx}\right]t}{2(g_{22} - g_{12}^2)\,t} \tag{7}$$

where $t = D\phi/Dx$. Equating Eqs. (5) and (7), yields

$$\frac{D\theta}{Dx} = Q\left(x, \phi, u, v, \frac{Du}{Dx}, \frac{Dv}{Dx}\right) \tag{8}$$

Integration of Eq. (8) gives the local direction of a streamline. For streamlines in the nose region that first move forward from the stagnation point and then bend towards the leeside, the Dx term experiences zero movement adjacent to the turning point. It causes the derivative to approach infinity. To amend such a numerical problem, the length of the streamline S is used as the independent variable instead of x. Accordingly, Eq. (8) is recast in the form

$$\frac{D\theta}{DS} = \frac{D\theta}{Dx}\frac{Dx}{DS} = R\left(x, \phi, u, v, \frac{Du}{Dx}, \frac{Dv}{Dx}\right) \tag{9}$$

The expressions for the total derivatives Du/Dx and Dv/Dx in Eq. (9) are obtained from Eqs. (1) and (2) in conjunction with the following relations

$$\frac{Du}{Dx} = \frac{\partial u}{\partial x}\frac{Dx}{Dx} + \frac{\partial u}{\partial \phi}\frac{D\phi}{Dx} = \frac{\partial u}{\partial x} + \frac{v}{ug_{22}^{1/2}}\frac{\partial u}{\partial \phi} \tag{10}$$

Rearranging Eq. (1) and substituting in Eq. (10), there results

$$\frac{Du}{Dx} = -\left(\frac{vg^{12}}{g_{22}^{1/2}} - \frac{v^2g^{11}}{2ug_{22}}\right)\frac{\partial g_{22}}{\partial x} - \frac{v^2g^{12}}{2ug_{22}}\frac{\partial g_{22}}{\partial \phi} - ug^{12}\frac{\partial g_{12}}{\partial x} - \frac{v^2g^{11}}{ug_{22}}\frac{\partial g_{12}}{\partial \phi} - \frac{1}{\rho u}\left(g^{11}\frac{\partial P}{\partial x} + g^{12}\frac{\partial P}{\partial \phi}\right) \tag{11}$$

In a similar manner, Eq. (2) gives

$$\frac{Dv}{Dx} = \frac{\partial v}{\partial x} + \frac{v}{ug_{22}^{1/2}}\frac{\partial v}{\partial \phi} = -\left[v\left(g^{22} - \frac{1}{2g_{22}}\right) - \frac{v^2g^{12}}{2ug_{22}^{1/2}}\right]\frac{\partial g_{22}}{\partial x} - \frac{v^2}{2ug_{22}^{1/2}}\left(g^{22} - \frac{1}{g_{22}}\right)\frac{\partial g_{22}}{\partial \phi} - ug_{22}^{1/2}g^{22}\frac{\partial g_{12}}{\partial x} - \frac{v^2g^{12}}{ug_{22}^{1/2}}\frac{\partial g_{12}}{\partial \phi} - \frac{g_{22}^{1/2}}{\rho u}\left(g^{12}\frac{\partial P}{\partial x} + g^{22}\frac{\partial P}{\partial \phi}\right) \tag{12}$$

Furthermore, that

$$\frac{v}{u} = g_{22}^{1/2}\frac{D\phi}{Dx} \qquad \text{bis (4)}$$

and

$$u^2 = \frac{\gamma M^2 P}{\rho}\frac{1}{1 + g_{12}\frac{D\phi}{Dx} + g_{22}\left(\frac{D\phi}{Dx}\right)^2} \tag{13}$$

Using Eqs. (11) through (13), Eq. (9) can be completed to read

$$\frac{D\theta}{DS} = \frac{1}{\sqrt{(\varepsilon^2 + g_{12}\varepsilon\sigma + g_{22}\sigma^2)\,(g_{22} - g_{12}^{1/2})}} \times \left\{\frac{1}{\gamma M^2 P}\left[(g_{12}\varepsilon + g_{22}\sigma)\frac{\partial P}{\partial x} - (\varepsilon + g_{12}\sigma)\frac{\partial P}{\partial \phi}\right] - \frac{\sigma}{2}\frac{\partial g_{22}}{\partial x} - \varepsilon\frac{\partial g_{12}}{\partial x}\right\} \tag{14}$$

The geometrical relations between the x and S, and ϕ and S are

$$\frac{Dx}{DS} = \frac{\varepsilon}{\sqrt{\varepsilon^2 + g_{22}\sigma^2 + 2g_{12}\sigma\varepsilon}} \tag{15}$$

$$\frac{D\phi}{DS} = \frac{\sigma}{\sqrt{\varepsilon^2 + g_{22}\sigma^2 + 2g_{12}\sigma\varepsilon}} \tag{16}$$

where

$$\epsilon = g_{22}\cos^2\theta - g_{12}^2 \tag{17}$$

$$\sigma = g_{12}\sin^2\theta + (g_{22} - g_{12}^2)\sin\theta\cos\theta \tag{18}$$

Equations (14) through (16) constitute a set of first-order, ordinary differential equations for determining the geometry of a chosen streamline from the known pressure distribution. The method is considered exact in the sense that no approximations have been made in the process of derivation and provided that exact expressions for the pressure gradients can be incorporated. The streamline pattern so calculated, strongly depends upon the input pressure distribution. The more realistic is the input pressure distribution, the more realistic is the streamline geometry, including the streamline merging for determining the three-dimensional flow separation to be further discussed later.

B. Body of Revolution at Incidence

For a body of revolution at incidence, where the x and ϕ coordinates can be set orthogonal, simplification can be achieved by letting

$$\left.\begin{aligned} g_{12} &= \frac{\partial g_{12}}{\partial x} = \frac{\partial g_{12}}{\partial \phi} = \frac{\partial g_{22}}{\partial \phi} = 0 \\ g_{22} &= f^2 \end{aligned}\right\} \text{ orthogonal system only}$$

Eqs. (1) and (2) are reduced to the form:

x - Momentum (orthogonal system only)

$$u\frac{\partial u}{\partial x} + \frac{v}{f}\frac{\partial u}{\partial \phi} - \frac{v^2}{f}\frac{df}{dx} = -\frac{1}{\rho}\frac{\partial P}{\partial x} \tag{19}$$

ϕ - Momentum (orthogonal system only)

$$u\frac{\partial v}{\partial x} + \frac{v}{f}\frac{\partial v}{\partial \phi} + \frac{uv}{f}\frac{df}{dx} = -\frac{1}{\rho f}\frac{\partial P}{\partial \phi} \tag{20}$$

Following the same procedure, Eqs. (19) and (20) can be reduced to ordinary forms for calculating the streamline geometry of a body of revolution at incidence

$$\left(\frac{D\theta}{DS}\right)_{orth.} = \frac{1}{\gamma M^2 P}\left(\frac{\partial P}{\partial x}\sin\theta - \frac{1}{f}\frac{\partial P}{\partial \phi}\cos\theta\right) - \frac{1}{f}\frac{df}{dx}\sin\theta \tag{21}$$

$$\left(\frac{D\phi}{DS}\right)_{orth.} = \frac{\sin\theta}{f} \tag{22}$$

$$\left(\frac{Dx}{DS}\right)_{orth.} = \cos\theta \tag{23}$$

Streamlines in a Boundary Layer

A. Equations for Viscous Streamlines

Many times a realistic pressure distribution is not available. To simulate the physical flow, so that the three-dimensional flow separation can be detected, it is necessary to consider streamlines inside the boundary layer; see Fig. 3. Without losing generality, a body of revolution at incidence will be considered as an illustration. The equations of motion that govern a three-dimensional boundary layer flow can be written as follows

x - Momentum

$$u\frac{\partial u}{\partial x} + \frac{v}{f}\frac{\partial u}{\partial \phi} + w\frac{\partial u}{\partial z} - \frac{v^2}{f}\frac{df}{dx} = -\frac{1}{\rho}\left(\frac{\partial P}{\partial x} - \frac{\partial \tau_1}{\partial z}\right) \tag{24}$$

ϕ - Momentum

$$u\frac{\partial v}{\partial x} + \frac{v}{f}\frac{\partial v}{\partial \phi} + w\frac{\partial v}{\partial z} + \frac{uv}{f}\frac{df}{dx} = -\frac{1}{\rho}\left(\frac{\partial P}{f\partial \phi} - \frac{\partial \tau_2}{\partial z}\right) \tag{25}$$

where τ_1 and τ_2 are the shearing stresses in x and ϕ directions, respectively, i.e.,

$$\tau_1 = \mu\frac{\partial u}{\partial z} - \rho\overline{u'w'} \tag{26}$$

$$\tau_2 = \mu\frac{\partial v}{\partial z} - \rho\overline{v'w'} \tag{27}$$

The substantial derivatives along a streamline inside a three-dimensional boundary layer are

$$\frac{Du}{Dx} = \frac{\partial u}{\partial x} + \frac{v}{uf}\frac{\partial u}{\partial \phi} + \frac{w}{u}\frac{\partial u}{\partial z} \tag{28}$$

$$\frac{Dv}{Dx} = \frac{\partial v}{\partial x} + \frac{v}{uf}\frac{\partial v}{\partial \phi} + \frac{w}{u}\frac{\partial v}{\partial z} \tag{29}$$

It indicates that additional z-component terms can be absorbed in the total derivatives in the derivation of the streamline equations. Following the same procedure as for the inviscid case, the resulting ordinary equations for calculating the streamline geometry inside the boundary layer are

$$\left(\frac{D\theta}{DS}\right)_{viscous} = \frac{1}{\gamma M^2 P}\left[\left(\frac{\partial P}{\partial x} - \frac{\partial \tau_1}{\partial z}\right)\sin\theta - \left(\frac{1}{f}\frac{\partial P}{\partial \phi} - \frac{\partial \tau_2}{\partial z}\right)\cos\theta\right] - \frac{1}{f}\frac{df}{dx}\sin\theta \tag{30}$$

$$\left(\frac{D\phi}{DS}\right)_{viscous} = \frac{\sin\theta}{f} \tag{31}$$

$$\left(\frac{Dx}{DS}\right)_{viscous} = \cos\theta \tag{32}$$

Note that terms in parentheses in Eq. (30) represent the effective pressure gradients for computing θ.

B. Friction Model

The addition of friction terms $\partial\tau_1/\partial z$ and $\partial\tau_2/\partial z$ makes the system (30) through (32) not readily solvable even if the pressure values are provided. A proper determination of these terms, of course, is to solve the three-dimensional boundary-layer equations. Even that, the solution involves turbulence modeling which has been a problem for many years. It is attempted, therefore, to model these friction terms without solving the complex three-dimensional boundary-layer problem.

First, consider that in a boundary-layer flow, the friction force is of comparable order of magnitude with the inertia force. Schlichting[18] suggested that for a flat plate, the friction force per unit volume can be estimated by the condition of equality of the friction and inertia forces:

$$\frac{\partial\tau}{\partial z} \sim \frac{\rho V^2}{\ell} \quad \text{(for a flat plate)}$$

where ℓ is the characteristic length of the body in question. It is assumed that the flow under consideration is locally similar to that over a flat plate and that other influences can be absorbed in an empirical relation:

$$\frac{\partial\tau}{\partial z} = \bar{\lambda}\frac{\rho V^2}{\ell} = \bar{\lambda}\frac{\rho V_\infty^2}{\ell}\left(\frac{V}{V_\infty}\right)^2 = \lambda\left(\frac{V}{V_\infty}\right)^2 \tag{33}$$

Then, the friction component in the x-direction can be written as

$$\frac{\partial\tau_1}{\partial z} = \frac{\partial}{\partial z}\left(\mu\frac{\partial u}{\partial z} - \rho\overline{u'w'}\right) = \lambda_1\left(\frac{u}{V_\infty}\right)^2 \tag{34}$$

and that in the ϕ-direction

$$\frac{\partial\tau_2}{\partial z} = \frac{\partial}{\partial z}\left(\mu\frac{\partial v}{\partial z} - \rho\overline{v'w'}\right) = \lambda_2\left(\frac{v}{V_\infty}\right)^2 \tag{35}$$

The parameter λ could be a function of Reynolds number, Mach number, pressure gradient, and possibly, the angle of attack. To simplify the approach, it is assumed that λ takes on the following form

$$\lambda_1 = a_1 + b_1\frac{\bar{x}}{\ell} \tag{36}$$

and

$$\lambda_2 = a_2 + b_2\phi \tag{37}$$

where a_1, b_1, a_2, and b_2 are constants to be determined experimentally. It is noted that near the wall, the sign for λ is directly affected by the velocity profile, which is ultimately dominated by the pressure gradient.[18] These closure statements, which merely represent a working formula, are far from complete. Further improvement might have to be pursued in a similar way for modeling the turbulence in usual boundary-layer computations.

Determination of Three-Dimensional Flow Separation

With the streamline method available, the flow separation can be approximately determined by merging streamlines at the edge of or inside the boundary layer, depending on the particular pressure distribution used. If a realistic pressure distribution is available, i.e., experimental or empirical pressure distribution, or theoretical pressures obtained by means of viscous-inviscid interactions, the simple inviscid streamline approach can be employed. For the case of a pure inviscid pressure, then the streamlines must be calculated with proper viscous terms included. The former will be illustrated by the case of a spherically blunted cone at an angle of attack at a hypersonic speed and the latter demonstrated by a prolate spheroid at moderate incidences in an incompressible flow. In both cases, the streamlines are computed by the initial value technique. That is, all the streamlines originate from the forward stagnation point and the envelope of merging streamlines is traced out by the interception of streamlines from windward and leeward sides. Once two streamlines intercept, it is assumed that they immediately leave the surface, resulting in a flow separation.

A. Determination of Flow Separation over a Spherically Blunted Cone at Incidence

In hypersonic flows, a typical configuration frequently considered in the past is the spherically blunted cone. Experimental and theoretical pressure distributions for the case of a 9-deg half-angle cone at $M_\infty = 18$ and specific angles of attack were made available by Knox and Lewis.[19] The body geometry can be expressed as follows; see Fig. 4.

For spherical cap:

$$\frac{f}{R} = \sqrt{2\left(\frac{\bar{x}}{R}\right) - \left(\frac{\bar{x}}{R}\right)^2} \tag{38}$$

For the cone:

$$\frac{f}{R} = \sec\psi + \frac{\bar{x} - R}{R}\tan\psi \tag{39}$$

where ψ is the cone half angle.

To obtain the pressure gradients required by the the present method, the empirical interpolation formula suggested by Zakkay[20] is employed

$$\frac{P}{P_o} = \left(\frac{P}{P_o}\right)_{\alpha=0} + \bar{A}\alpha\cos\phi + \bar{B} + \bar{C}\alpha^3\cos 2\phi$$

which can be recast into the form:

$$\frac{P}{P_o} = A\cos\phi + B + C\cos 2\phi \tag{40}$$

where A, B, and C are functions of x only, that can be determined by collocating the pressure dat along ϕ = 0 deg, 90 deg, and 180 deg meridian lines. The pressure gradients are

$$\frac{\partial}{\partial x}\left(\frac{P}{P_o}\right) = \frac{dA}{dx}\cos\phi + \frac{dB}{dx} + \frac{dC}{dx}\cos 2\phi \qquad (41)$$

$$\frac{\partial}{\partial \phi}\left(\frac{P}{P_o}\right) = -A\sin\phi - 2C\sin 2\phi \qquad (42)$$

Pressure solution by the method of characteristics on ϕ = 0 deg, 90 deg, and 180 deg meridian lines at M_∞ = 18 and α = 10 deg are taken from Ref. 19, which were then curve fitted with a polynomial to form A, B, and C. The theoretical pressure values were used with empiricism built into the interpolation formulas, Eq. (40). A comparison between the interpolated and the original theoretical pressure distributions is shown in Fig. 5.

Equations (40) through (42), together with body geometry equations and the isentropic relation between the local Mach number and pressure, constitute all the terms needed for the right-hand side of Eqs. (21) through (23) for calculating streamlines. To start the calculation, the initial conditions are determined by the exact geometrical relations on the spherical cap; see Fig. 6.

$$x_i = \cos^{-1}(\cos\alpha\cos S_i - \sin\alpha\sin S_i\cos\beta)$$

$$\phi_i = \sin^{-1}(\sin S_i \sin\beta / \sin x_i)$$

$$\theta_i = \sin^{-1}(\sin\alpha\sin\beta / \sin x_i) \qquad (43)$$

For a spherical body, these exact relations hold everywhere. It is, therefore, convenient to apply these relations right at the juncture and initiate the integration there. The integration of Eqs. (21) through (23) can be accurately performed by using a fourth-order Runge-Kutta scheme to give the location of the streamline in terms of coordinates x and ϕ, and its direction measured with respect to the x axis. The calculated streamlines are designated by β values which run from 0 to 180; β = 0 for the most windward line. The three-dimensional flow separation then can be determined by tracing the envelope of inviscid streamlines.

B. Determination of Flow Separation over a Prolate Spheroid at Incidence

The flow separation over a prolate spheroid (ellipsoid) at specific incidences has been investigated both theoretically[4] and experimentally.[5,6] It is a good case for comparison purposes. Also, since a closed form potential flow solution is available for this body, it is convenient to illustrate the viscous procedure proposed earlier in the present paper.

With the major and minor axes of the ellipsoid defined by a and b, respectively, the body coordinate is given by (see Fig. 7):

$$f = b\sqrt{1 - (\bar{x}/a - 1)^2} \qquad (44)$$

The surface pressure can be expressed by

$$P = P_\infty + \frac{\gamma M_\infty^2 P_\infty}{2}\left(1 - \frac{u^2}{V_\infty^2} - \frac{v^2}{V_\infty^2}\right) \qquad (45)$$

The required velocity components are given by Wang[21] based on the potential flow solution

$$\frac{u}{V_\infty} = \frac{1}{(1 - e^2\bar{x}^2)^{1/2}}\left[(1 + k_a)(\cos\alpha)(2\bar{x} - \bar{x}^2)^{1/2} + (b/a)(1 + k_c)(\sin\alpha)(\bar{x} - 1)\cos\phi\right] \qquad (46)$$

$$\frac{v}{V_\infty} = (1 + k_c)\sin\alpha\sin\phi \qquad (47)$$

where α is the incidence and e is the eccentricity given by

$$e = \sqrt{1 - \frac{b^2}{a^2}} \qquad (48)$$

Parameters k_a and k_c are the axial and cross coefficients of virtual mass defined by

$$k_a = \left[\frac{1}{2e}\ln\frac{1+e}{1-e} - 1\right]\Big/\left[\frac{1}{1-e^2} - \frac{1}{2e}\ln\frac{1+e}{1-e}\right] \qquad (49)$$

and

$$k_c = \frac{1}{1 + 2k_a} \qquad (50)$$

The pressure gradients are readily obtained through the following relations

$$\frac{\partial P}{\partial x} = -\gamma M_\infty^2 P_\infty \frac{u}{V_\infty}\left[\frac{2\bar{x} - \bar{x}^2}{1 - e^2(\bar{x} - 1)^2}\right]^{1/2}\frac{\partial}{\partial \bar{x}}\left(\frac{u}{V_\infty}\right) \qquad (51)$$

$$\frac{\partial P}{\partial \phi} = -\gamma M_\infty^2 P_\infty\left[\frac{u}{V_\infty}\frac{\partial}{\partial\phi}\left(\frac{u}{V_\infty}\right) + \frac{v}{V_\infty}\frac{\partial}{\partial\phi}\left(\frac{v}{V_\infty}\right)\right] \qquad (52)$$

For this particular case in which the inviscid velocity components are known everywhere, the local inviscid streamline angle θ is also known

$$\theta = \tan^{-1}\left(\frac{v}{u}\right) \qquad (53)$$

Equation (53) is useful for (a) testing the accuracy of the system, Eqs. (21) through (23), by comparing the integrated θ value against the exact value and (b) providing the initial condition for calculation of viscous streamlines using Eqs. (30) through (32).

The viscous streamline equations, Eqs. (30) through (32), with the aid of Eqs. (44) through (52) and the proper friction model, can then be integrated using a fourth-order Runge-Kutta scheme. The initial condition for θ is evaluated by Eq. (53) at a point close to the forward stagnation point. Similar to the previous case, the calculated streamlines are designated by β values which run from 0 to 180; β = 0 for the most windward line. The three-dimensional flow separation can be then determined by tracing the merge of viscous streamlines.

Results and Discussion

The procedure described in the previous section has been coded in FORTRAN using a CDC 6600/6700 computer. Each case, either the spherically blunted cone or the ellipsoid, takes less than 150 statements and occupies a very limited storage. Because of its small size, the program was subsequently converted to the BASIC language using a Tektronix desk-top computer. The latter has instant graphic capability to facilitate evaluation of the friction model.

A. Spherically Blunted Cone at α = 10 Degrees

The results of a 9-deg spherically blunted cone at M_∞ = 18 and α = 10 deg are shown in Fig. 8. All the streamlines are labelled with β values; β = 0 for the most windward line. The streamlines in the upper leeward region turn back to the windside because of flow retardation caused by the empirical nature of the pressure gradient employed. The flow exhibits vortex-layer-type (open type) separation resulting from streamline merging. The line of separation is easily traced using the envelope concept. A remarkable resemblance between the present result and Fig. 15c of Ref. 4 is observed. This same case was considered by the author earlier.[22] However, then the reason for leeside streamlines bending toward windside was not identified. As a consequence, those streamlines for $\beta > 90$ deg were not published; see Fig. 12 of Ref. 22.

B. Prolate Spheroid at Incidences

In the case of a prolate spheroid at incidences in an incompressible flow, both the inviscid approach (streamlines at the edge of boundary layer) and the viscous approach (streamlines inside the boundary layer) were examined numerically.

Using the inviscid approach with pure potential flow pressures, the calculated streamlines monotonically approach the apex of the leeward side; see Fig. 9. The integrated values for the streamline angle θ agree very closely with those exact values given by Eq. (53). It serves as a test case for validating the method.

The viscous approach was first investigated with a very simple friction model. Constant viscous parameters ($\tau_1 = \tau_2 = 5$) were assigned for the case of a prolate spheroid (a/b = 4) at α = 30 deg. The result is shown in Fig. 10. It indicates that streamlines in the leeward side turn back to the windward side and then encounter those directly from the windside and, therefore, form a flow separation. The trend is consistent with the previous case. The line of separation is determined by the envelope of merging streamlines. The level of agreement between the present result and the experimental data is comparable to that between the three-dimensional boundary-layer solution and the experiment; see Fig. 11. The results, in general, depend on the magnitude of the damping parameters used. Figure 11 also reveals the effect of the friction model. A slightly improved location of the line of separation can be found as a consequence of change of values of empirical parameters.

Finally, the present viscous result is further compared with recent experimental data provided by Meier et al.[5] Empirical constants for the friction model were adjusted so that the theoretically determined separation pattern matches that of the experimental one. This is depicted in Fig. 12 for an a/b = 6 prolate spheroid at α = 30 deg. The constants were found as follows:

$$a_1 = 3.0 \qquad b_1 = 5.0$$

$$a_2 = 5.0 \qquad b_2 = -0.02$$

for Eqs. (36) and (37). The set represents one of many possible combinations. In general, the parameter τ is affected by the nature of the boundary layer, the compressibility, the velocity profile and possibly, the angle of attack. The first three may be represented by the Reynolds number, the Mach number, and the pressure gradient. A physically oriented friction model is yet to be developed in the future.

Concluding Remarks

A streamline approach for determining the free vortex-layer-type, three-dimensional flow separation is developed. Both inviscid and viscous approaches were considered. For the inviscid method, the more realistic are the input surface pressures, the more realistic are the streamline and, therefore, the separation patterns. Experimental or empirical pressure distributions or theoretical pressures, obtained by means of viscous-inviscid interactions, are considered to possess such physical properties.

The viscous approach allows use of pure inviscid pressures along with proper viscous damping. The accuracy of the new, simple method depends on the ability of modeling the friction force in the boundary layer. An approximate model based on the equality condition between the friction and inertia forces works reasonably well for the case of a prolate spheroid at incidence. The model needs to be improved with more considerations from a boundary-layer point of view.

Nevertheless, because of its simplicity and small computation requirement, the present approach may become a useful tool to facilitate computation of viscous-inviscid interactions with flow separation in three dimensions and to predict the interference drag involving free vortices resulting from flow separation.

References

1. Eichelbrenner, E. A. and Oudart, A., "Methode de Calcul de la Couche Limite Tridimensionnelle. Application a un Corps Fusele Incline sur le Vent," ONERE Publication 76, Paris, France, 1955.

2. Maskell, E. C., "Flow Separation in Three Dimensions," RAE Report Aero 2565, Royal Aircraft Establishment, Bedford, England, Nov 1955.

3. Wang, K.C., "Separation Patterns of Boundary Layers over an Inclined Body of Revolution," AIAA J., Vol. 10, pp. 1044-1050, Aug 1972.

4. Wang, K.C., "Separation of Three-Dimensional Flow," MML TR-76-54C, Martin Marietta, Baltimore, Maryland, Aug 1976.

5. Kreplin, H. P., Vollmers, H., and Meier, H. U., "Experimental Determination of Wall Shear Stress Vectors on an Inclined Prolate Spheroid," Paper presented at the 5th U.S.-W. Germany DEA Meeting on "Viscous and Interacting Flow Field Effects," Annapolis, MD, Apr 1980.

6. Han, T. and Patel, V. C., "Flow Separation on a Spheroid at Incidence," J. Fluid Mechanics, Vol. 92, Part 4, pp. 643-657, 1979.

7. Stetson, K. F. and Friberg, E. G., "Surface Conditions in the Leeward Region of a Blunt Cone at Angle of Attack in Hypersonic Flow," ARL-69-0114, Aerospace Research Lab, Wright-Patterson Air Force Base, Dayton, Ohio, Jul 1969.

8. Nielsen, J. N., "Missile Aerodynamics - Past, Present, Future," AIAA Paper 79-1819, presented as Wright Brothers Lectureship in Aeronautics at AIAA Aircraft Systems and Technology Meeting, New York, N.Y., Aug 1979.

9. Martin, M., "Private Communications," David Taylor Naval Ship Research and Development Center, Bethesda, Maryland, May 1980.

10. Grosche, F. R., "Wind Tunnel Investigation of the Vortex System Near an Inclined Body of Revolution With and Without Wings," AGARD CP-71, 1970.

11. Tanaka, H. and Ueda, T., "Study on the Structure of Ship Vortices Generated by Full Sterns," Proceedings of 12th Symposium on Naval Hydrodynamics, Washington, D.C., Jun 1978.

12. Rosenhead, L., (editor) "Laminar Boundary Layers," Oxford University Press, Oxford, England, pp. 488-491, 1963.

13. Harris, E. L., "Determination of Streamlines on a Sphere-Cone at Angles of Attack from the Measured Surface Pressure Distribution," Naval Ordnance Laboratory Report NOL TR-63-37, Feb 1963.

14. Maikapar, G. I., "Calculation of Streamlines with a Known Pressure Distribution on the Surface of a Rigid Body," Journal of Applied Mathematics and Mechanics, Jan 1965.

15. DeJarnette, F. R., "Calculation of Inviscid Surface Streamlines and Heat Transfer on Shuttle Type Configurations," NASA CR-111921, Aug 1971.

16. Rakich, J. V. and Lanfranco, M. J., "Numerical Computation of Space Shuttle Laminar Heating and Surface Streamlines," J. Spacecraft, Vol. 14, No. 5, pp. 265-272, May 1977.

17. Tai, T. C., "Determination of Streamline Geometry and Equivalent Radius over Arbitrary Bodies with Application to Three-Dimensional Drag Problem," David Taylor Naval Ship R&D Center, Bethesda, Maryland, DTNSRDC-79/80, Dec 1979.

18. Schlichting, H., "Boundary Layer Theory," 4th English Edition, McGraw-Hill, New York, p. 25 and pp. 113-114, 1960.

19. Knox, E. C. and Lewis, C. H., "A Comparison of Experimental and Theoretically Predicted Pressure Distributions and Force and Stability Coefficients for a Spherically Blunted Cone at M_∞ = 18 and Angle of Attack," ARO, Inc., AEDC-TR-65-234, Feb 1966.

20. Zakkay, V., "Pressure and Laminar Heat Transfer Results in Three-Dimensional Hypersonic Flow," WADC TN 58-182, ASTIA Document Number AD 155-679, Sep 1958.

21. Wang, K. C., "Boundary Layer over a Blunt Body at High Incidence with an Open-Type of Separation," Proc. R. Soc. London A 340, pp. 33-55, 1974.

22. Tai, T. C., "Laminar and Turbulent Convective Heat Transfer Over Bodies at an Angle of Attack," Ph.D Thesis, Virginia Polytechnic Institute, Blacksburg, Virginia, Oct 1968.

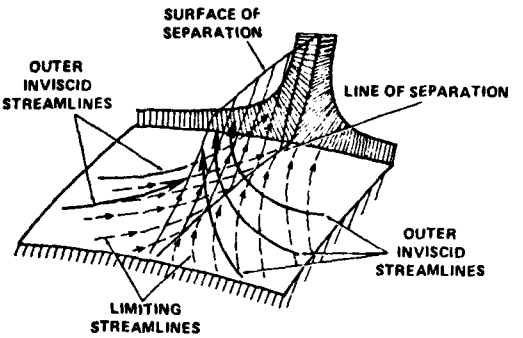

Fig. 1 - Maskell's Postulation on Three-Dimensional Flow Separation Forming a Free-Vortex Layer

NOTE: $\bar{x}, \bar{y}, \bar{z}$ – CARTESIAN COORDINATES
x, ϕ, z – NONORTHOGONAL CURVILINEAR COORDINATES
ξ, β, ζ – STREAMWISE COORDINATES

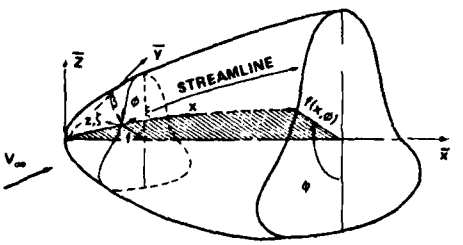

Fig. 2 - Coordinate Systems for a General Three-Dimensional Body

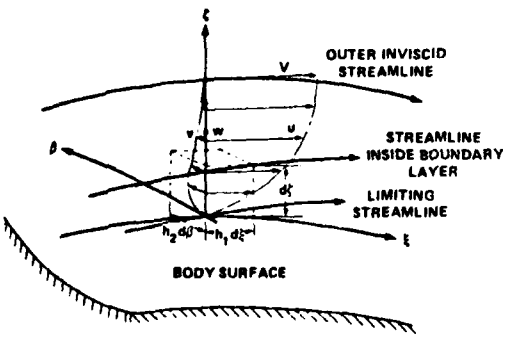

Fig. 3 - Streamlines in a Boundary Layer

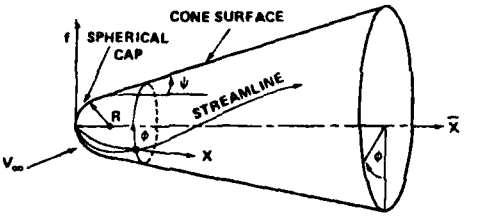

Fig. 4 - Geometry of a Spherically Blunted Cone

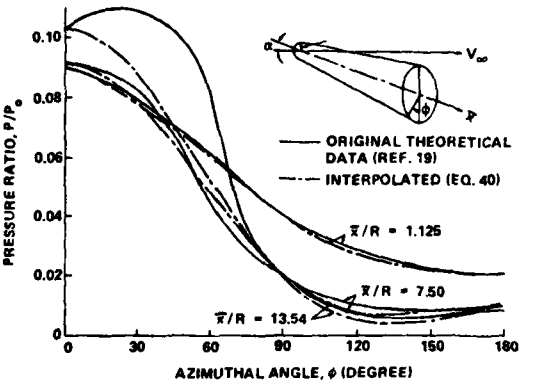

Fig. 5 - Pressure Distributions Over a 9-Degree Half-Angle Spherically Blunted Cone at $M_\infty \approx 18$ and $\alpha = 10^o$

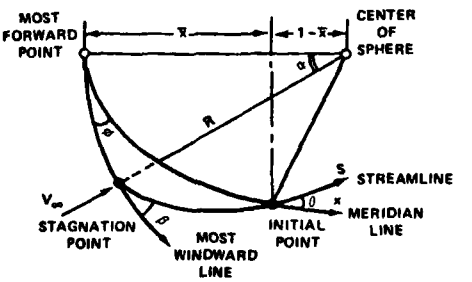

Fig. 6 - Initial Conditions on a Spherical Cap

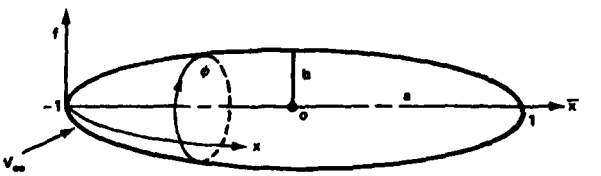

Fig. 7 - Geometry of a Prolate Spheroid

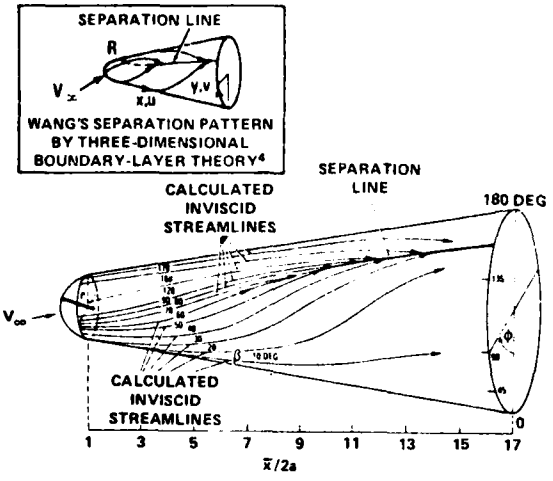

Fig. 8 - Separation Line Over a 9-Degree Half-Angle Spherically Blunted Cone at $M_\infty = 18$ and $\alpha = 10^o$

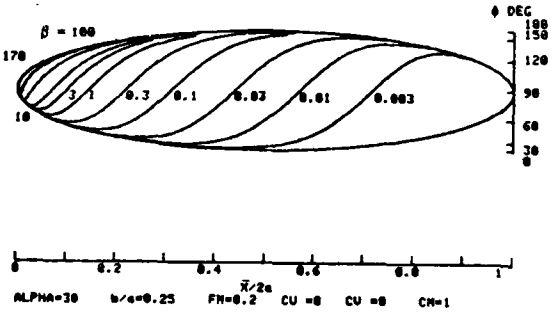

Fig. 9 - Inviscid Streamlines Over a Prolate Spheroid Calculated by Using Potential Flow Pressure Distribution

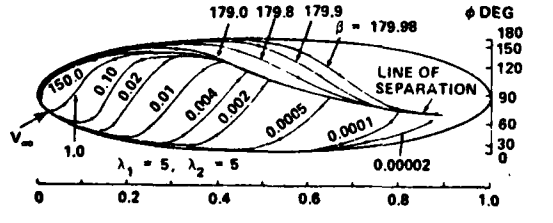

Fig. 10 - Line of Separation Determined by Merging Streamlines Over a Prolate Spheroid (a/b = 4) at α = 30 Degrees

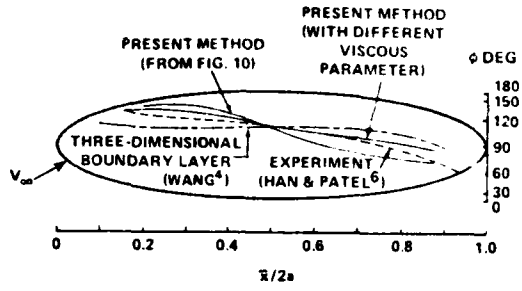

Fig. 11 - Comparison of the Location of Line of Separation

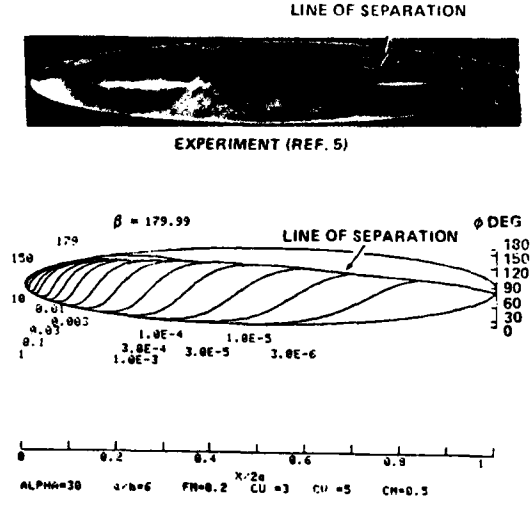

Fig. 12 - Correlation of Separation Patterns Over a Prolate Spheroid (a/b = 6) at α = 30 Degrees

ANALYSIS OF SELF-EXCITED OSCILLATIONS IN FLUID FLOWS

W. L. Hankey* and J. S. Shang**
Air Force Flight Dynamics Laboratory
Wright-Patterson Air Force Base, Ohio

Abstract

A class of self-excited oscillations in fluid flows has been analyzed. It was shown that the source of the instability is a separated shear layer with an inflection point in the velocity profile. The larger the extent of separation, the greater the amplification of the instability. Separated flows possess a natural frequency for which they are most likely excited and are stable on either side of that frequency. Self-excitation results when a feedback mechanism occurs within the flow field and pressure waves travel upstream through the subsonic separated flow to the origin of the initial disturbance. All frequency modes of oscillation can be predicted from a simple formula attributed to Rossiter. Resonance occurs when one of the feedback frequencies is near the natural frequency of the shear layer.

Navier-Stokes solutions were obtained for open cavity oscillations and spike tipped body buzz. Encouraging agreement with experiment resulted that reinforced understanding of the phenomenon. Inlet buzz was also investigated and found to be caused by a similar instability in a separated shear layer for subcritical flow rates.

Nomenclature

a_o	stagnation speed of sound
A	amplifier transfer function
B	feedback loop transfer function
c	complex wave speed
c_r	propagation velocity
c_i	amplification factor
f	frequency
i	$\sqrt{-1}$
k	$\frac{c_r}{U_e}$ = dimensionless propagation velocity
L	length
M_o	$\frac{U_e}{a_o}$ = Mach number based on stagnation sound speed
P	period
t	time
u,v,w	Cartesian velocity components
x,y,z	Cartesian coordinates
α	wave number
δ	shear layer thickness
θ	phase angle
ν	kinematic viscosity
ϕ	fluctuation amplitude function
ω	$2\pi f$ = angular frequency

Introduction

A self-excited oscillation is one in which the force that sustains the motion is created by the motion itself; when the motion ceases the alternating force disappears[1]. (In a forced vibration, the alternating force exists independently of the motion and persists even when the motion is stopped.) Self-excited oscillations are encountered in mechanical and aero-mechanical systems as well as in other fields. Some examples are nose wheel shimmy, machine chatter, chalk screech, galloping transmission lines, Karman vortex trails, wing flutter and inlet buzz.

Den Hartog[1] analyzes self-excited oscillations of mechanical systems with particular attention given to the damping term. Consider a spring-mass system with viscous damping for which the motion may be described as follows:

$$m\ddot{x} + c\dot{x} + kx = 0$$

The solution to this equation for constant coefficients is

$$x = x_o e^{\frac{-ct}{2m}} \cos(\omega t + \theta)$$

The natural frequency of the system is

$$\omega = [\frac{k}{m} (1 - \frac{c^2}{4km})]^{\frac{1}{2}}$$

Given an initial disturbance, the motion will grow or decay depending upon the sign of the damping term (c). Negative damping ($c < 0$) is necessary to produce a self-excited oscillation. For this linear analysis, the disturbance will be amplified and grow without bound. In nature, however, non-linear effects occur and and both negative and positive damping exist during portions of the oscillation so that a "limit-cycle" can result. A balance is reached between energy production and dissipation so that the net work is zero during one cycle. This steady state periodic solution is the self-excited oscillation that we observe in nature for a simple mechanical system.

The analysis for fluid flows is analagous to the mechanical system. For an incompressible two dimensional flow, the governing equations are linearized by assuming small perturbations of the following form[2]:

$$v' = \phi(y)\, e^{i\alpha(x - ct)}$$

This results in the Rayleigh equation (which is a degenerate Orr-Sommerfeld equation appropriate for large Reynolds numbers)

$$\phi'' - (\alpha^2 + \frac{\bar{U}''}{\bar{U} - c})\, \phi = 0$$

* Senior Scientist, Flight Mechanics Division, Associate Fellow, AIAA
** Aerospace Engineer, Flight Mechanics Division, Associate Fellow, AIAA

with boundary conditions as follows:

$$\phi(0) = 0 \quad ; \quad \phi(\infty) = 0$$

$\bar{U}(y)$ is the mean velocity component in the x direction, and c is complex.

$$c = c_r + i\, c_i$$

Here c_r is the propagation speed of the wave and c_i determines the degree of damping or amplification depending upon its sign.

For prescribed values of $\bar{U}$ this is an eigenvalue problem in which $c(\alpha)$ can be obtained subject to satisfying the boundary conditions. The resulting solution takes on the following form:

$$v' = \phi e^{\alpha c_i t}\, e^{i\alpha(x - c_r t)}$$

For positive values of c_i a self-excited oscillation occurs which is equivalent to a negative damping case. Rayleigh[3] first investigated this type of flow and proved that velocity profiles with inflection points are unstable. In order to further explore this fact, a class of separated flows was analyzed. The stability of Stewartson's Lower Branch solutions of the Falkner-Skan equation was investigated (Fig 1). The Rayleigh equation was solved for several different values of the pressure gradient parameter, β, for the entire range of separated flows from incipient to a free shear layer[4]. Figure 2 presents the values of the amplification factor for the unstable frequency range. (Note $f_\alpha = \bar{\alpha}\, c_r/2\pi\delta$). For reference purposes, these amplification factors are nearly two orders of magnitude greater than the more familiar Tollmien-Schlichting waves[2]. The propagation speed (c_r) for the disturbances was generally between 0.4 and 0.9 of $\bar{U}_e$ (Fig 3). Therefore, one can deduce from these results that self-excited oscillations do exist (positive c_i) over a very limited frequency range for similar separated laminar boundary layers. By analogy, the frequency for which maximum c_i occurs can be viewed as the natural frequency of the shear layer. This corresponds to the most probable Strouhal Number likely to occur for periodic disturbances and is always numerically less than unity. In Ref 5, compressibility effects of a free shear layer were investigated and the instability was found to diminish as Mach number increased (Fig 4). Although only one class of flows with inflection points has been examined, one is tempted to generalize these findings for all separated flows. One can speculate that (1) separated flows become more unstable in progressing from incipient to fully separated; (2) separated flows possess a relatively low natural frequency for which they are most likely to be self-excited and are stable on either side of that frequency; (3) the instability diminishes as Mach number increases. Based upon these hypotheses, one can embark upon an analysis of self-excited flow problems.

To investigate these flows in detail the Reynolds averaged Navier-Stokes equations will be required. Use of the Reynolds averaged Navier-Stokes equation to numerically simulate unsteady buffeting was demonstrated by Levy[6]. Steger and Bailey[7] used these same equations to simulate aileron buzz. Chapman[8] showed that unsteady practical problems can be solved with the Reynolds averaged equations provided that the frequencies of interest are two orders of magnitude below the mean frequency of the turbulent eddies. This generally implies that the Strouhal Number ($\frac{fL}{U_e}$) be less than unity.

One of the first numerical examples of a self-excited oscillation was the time-dependent computation of a stalled airfoil by Hodge[9]. In Fig 5, a series of eddies is observed on the upper side of the airfoil where the flow experiences an adverse pressure gradient. These eddies grow and are shed in a regular periodic manner as shown in Fig 6. The numerical values of $c_r = 0.4$ and $c_i = 0.07$ for this flow are within the range of values obtained from linear theory (Figs 2 and 3). Note that the flow is under a favorable pressure gradient on the lower surface and of course no instability occurs. In Fig 7, the velocity vector field shows inflection points only on the upper surface of the airfoil. It is, therefore, concluded that numerical methods can be used successfully to analyze self-excited oscillations.

Feedback Mechanism

Separated flows were shown to possess a natural frequency for which small disturbances are highly amplified over a limited frequency range. For a significant self-excited oscillation to persist, a feedback mechanism is required in which signals in the natural frequency range are returned to the shear layer origin and then selectively reamplified. The mechanism considered here is a pressure wave (acoustical signal) which travels upstream through the subsonic separated shear layer. Three cases will be discussed which are physically dissimilar but generically related to the same physical phenomenon, i.e., a large separated unstable shear layer with an acoustical feedback mechanism. These cases are open cavity resonance, spike buzz and inlet buzz. All of these examples contain a fluid amplifier (separated flow) and a feedback mechanism (upstream acoustical propagation).

A. Frequency of Disturbance

The frequency of a self-excited oscillation can now be predicted based upon the previous statements. A forward traveling pressure wave disturbance propagates at speed, c_r, until it reaches a reflection surface at length L. After reflection, an acoustical rearward traveling wave returns at sonic speed, a_o, through the subsonic separated shear layer (Fig 9). The cycle is then repeated. The period of this disturbance can be deduced easily from the figure.

$$P_1 = \frac{L}{c_r} + \frac{L}{a_o}$$

Since multiple waves are possible, the frequency (and higher harmonics) may be determined as follows:

$$f_m = \frac{m}{P_1} = \frac{mU_e}{L(M_o + k^{-1})}$$

This is the modified Rossiter[11,12] equation (for $\alpha = 0$) in which

$$M_o = \frac{U_e}{a_o} \quad ; \quad k = \frac{c_r}{U_e} \quad ; \quad m = \text{mode number (integer)}$$

It may be informative at this point to compare a fluid dynamic oscillator with an electronic oscillator[10]. In an electronic circuit an amplifier with a feedback loop will oscillate under certain conditions. This instability can be readily determined by examining the transfer functions. If A in Figure 10 is the transfer function (a complex number) of the amplifier and B is the transfer function of the feedback loop then the overall gain is as follows:

$$\text{Gain} = \frac{A}{1 - AB}$$

The existence of a frequency for which the return ratio, AB, equals unity is a sufficient condition for an instability and is hence the criterion for a sustained oscillation.

$$\text{If } A = \frac{\hat{P}\, e^{i(\alpha_1 L - \omega t)}}{\hat{P}\, e^{-i\omega t}} = e^{i\alpha_1 L} \; ; \; \omega = \alpha_1 c_r$$

and

$$B = \frac{\hat{P}\, e^{-i\omega t}}{\hat{P}\, e^{i(-\alpha_2 L - \omega t)}} = e^{i\alpha_2 L} \; ; \; \omega = \alpha_2 a_o$$

At resonance, $AB = e^{i(\alpha_1 + \alpha_2)L} = 1 = e^{i2\pi m}$

(m = integer)

This relationship produces two results from equating the real and imaginary parts of this equation.

(1) Real Part:

$$(\alpha_1 + \alpha_2)L = 2\pi m \quad \text{or}$$

$$f = \frac{mU_e}{L(M_o + k^{-1})}$$

which is identical to Rossiter's equation

(2) Imaginary Part:

$$\left(\frac{c_i}{c_r}\right)_1 + \left(\frac{c_i}{a_o}\right)_2 = 0$$

This indicates that the net damping is zero during one cycle.

We therefore, conclude that a fluid dynamic oscillator may exist when amplification occurs ($c_i > 0$) in the flowfield with a feedback mechanism. However, sustained oscillations will result only for very specific phase relationships. We will later see that this is consistent with both the experimental and numerical results.

In summary, any oscillator possesses three main features, i.e., an amplifier, a feedback loop and tuned operation with positive feedback at the correct phase.

B. Resonance

A self-excited oscillation occurs (analogous to a resonant state for forces oscillations) when one of the Rossiter frequencies (f_m) exists near the natural frequency of the shear layer (f_α). These signals will be selectively amplified while all other frequencies will decay. The amplified signals will continue to grow until a limit cycle is achieved.

Several points concerning resonance should be made. First, since the fundamental Rossiter frequency must be less than the natural frequency range of the shear layer for resonance to occur, it is therefore possible to design a system to eliminate resonance (Fig 10).

For example:

$$f_m > f_\alpha \quad \text{design requirement}$$

$$\frac{mU_e}{L(M_o + k^{-1})} > \frac{\bar{\alpha}\, c_r}{2\pi\delta}$$

or since minimum m = 1

$$\frac{L}{\delta} < \frac{2\pi}{\bar{\alpha}_{max}(1 + kM_o)}$$

By decreasing the characteristic length of the shear layer, this "length resonance mode" may be eliminated.

Another point of interest is that the predominate frequency mode can jump from one value of the fundamental to another integer value as flow parameters are varied. The scientific community has studied edgetones for some time and observed a shift in frequency with Reynolds number[13] (Fig 11). This fact can be explained readily by examination of the natural frequency for this case.

$$f_m = (f_\alpha)_{opt.} \text{ at maximum } c_i$$

$$\frac{mU_e}{L(M_o + k^{-1})} = \frac{\alpha_{opt.}\, c_r}{2\pi\delta}$$

or

$$m_{opt} = \frac{(1 + kM_o)\nu}{2\pi\delta}\left(\frac{U_e L}{\nu}\right)$$

The frequency mode will therefore increase with Reynolds number (provided the remaining quantities in the relationship are not changed significantly). Since only discrete values are possible the dominant frequency must jump with Reynolds number, as shown in Fig 11, rather than vary continuously. Three cases of self-excited oscillations will now be discussed, i.e., cavity, spiked body, and inlet.

Open Cavity

Transonic flow over an open cavity has been investigated experimentally by many investigators

and found to produce severe pressure oscillations under certain conditions[11,12,14,15]. The flow obviously has an inflection point as shown in the velocity vector plot (Fig 12) from a numerical computation[16]. A linear stability analysis predicts a natural frequency of this shear flow of

$$f_\alpha = \frac{\alpha_{opt}\, c_r}{2\pi\delta} \simeq 200 \text{ Hz}$$

with Rossiter feedback frequencies of

$$f_m = \frac{mU_e}{L(M_o + k^{-1})} = 115m \text{ Hz}$$

Fig 13 shows the amplification factor for this flow. Also shown in Fig 13 is the experimental spectral analysis[15] confirming the existence of Rossiter frequency modes and the fact that only the unstable range of frequencies are amplified. A numerical solution of the Reynolds averaged Navier-Stokes equations for the open cavity[16] produced a self-excited oscillation which qualitatively reproduced the intensity of the pressure disturbance. The spectral distribution for this case, shown in Fig 15, was also found to be in agreement with linear stability theory.

Spiked Body Buzz

Spike-tipped bodies at supersonic speeds are noted for producing violent buzz under a restricted range of spike lengths[17]. Fig 16 shows the experimental pressure intensity for different spike lengths at a Mach of 3. Also shown in Fig 17 is the predicted Rossiter frequencies (f_m) for the first three modes compared with the experimental frequencies[18].

The agreement observed indicates the validity of the wave analysis of Rossiter. However, as observed in Fig 16, these frequencies only occur between 20 and 45 mm spike lengths. Oscillations are not encountered at other lengths. As noted previously, resonance will not occur (even though separation exists) when $f_m > f_\alpha$ or $\frac{\bar{\alpha}(1 + M_o k)L}{2\pi\delta} < 1$. This appears to be the situation for this case.

Fig 18 displays velocity profiles for spike lengths for which numerical calculations were performed in Ref 19. For the spike length of 13mm, the shock wave is detached and subsonic flow completely envelops the spike. The numerical results show that $\frac{L_s}{\delta} = 1.5$, thereby creating a condition for which $\frac{\bar{\alpha}(1 + M_o k)L}{\pi\delta} < 1$ or $f_m > f_\alpha$; hence the short spikes are stable. Alternatively the numerical calculations show that $\frac{L}{\delta} = 9$ for the 38mm spike[19], which creates a condition where $f_m < f_\alpha$ and results in resonance. Numerical computations have not been performed for spike lengths greater than 45 mm, however, as the spike length is further increased, δ increases and M becomes supersonic causing a dramatic decrease in α_{max} (see Fig 4). Separation will not occur at the spike tip but only over a restricted portion of the spike ($L_s < L$).

All of these changes tend to increase f_m/f_α. When f_m suddenly exceeds f_α (as shown in Fig 10) resonance will cease causing a discontinuous cut-off of pressure intensity as observed in Fig 16. Although the separated region is still unstable, only random tunnel turbulence will be amplified, and no commensurable frequency modes will appear. The wind tunnel data supports this conclusion[17].

The numerical results for the spike length of 38mm are shown in Figs 19-22. These results confirm the hypothesis that large regions of separated flow exist during resonance (Fig 19) that a limit cycle is achieved in which the shock wave oscillates between the weak and strong shock solution, the wave form of the numerical results duplicate the experimental measurements, (Fig 20), the frequencies are commensurable (Fig 21) and that pressure waves are propagated upstream at acoustical speed (Fig 22) to close the feedback loop.

Inlet Buzz

Experimental evidence of instabilities encountered in supersonic inlets has been available for many years[20-25]. In spite of these observations, no reliable prediction method of inlet buzz exists and no completely satisfactory explanation of the phenomenon is available.

A supersonic inlet operating at subcritical flow conditions is believed to possess the two features necessary for buzz, i.e. a large region of separated flow and a downstream interface to reflect acoustical signals. When an inlet with a supersonic diffuser is throttled back to subcritical flow conditions a second throat occurs at the throttle. The normal shock is expelled from the diffuser causing separation on the centerbody. If the boundary layer never reattaches on the center body a flow field similar to the open cavity results. Pressure waves are reflected from the second throat and returned to the shear layer origin. This separated layer is known to be unstable and is the principal cause of the oscillation. Standing waves will occur in the duct with the natural frequency of the shear layer. During buzz of an inlet the downstream end appears to behave as a closed end (even though small flow rates still exist) and produces an antinode in the pressure wave[23,25]. If the upstream end behaves as an open end, antisymmetric modes will occur and all harmonics will be odd. If the upstream end behaves as a closed end, only symmetric modes will occur and all harmonics will be even.

Two very significant results can be obtained from a standing wave analysis[26]. First, the measured frequencies should be commensurable in which harmonics occur at exact integer values of the fundamental frequency. Secondly, antisymmetric (m = odd) or symmetric (m = even) mode shapes occur in the inlet duct if a standing wave exists. This analysis cannot predict which mode to expect but restricts the solution to a limited selection of eigenvalues. One can also anticipate frequency modes to jump discretely, in a quantum fashion, as flow conditions are changed by different throttle settings.

To examine the validity of the standing wave analysis, the frequency was predicted for six experimental cases of buzz. Table I lists these cases with the last column showing a correlation of the

measured frequency divided by the predicted fundamental frequency, i.e., $m = 4Lf/a$. These results give a strong indication that buzz occurs primarily in the antisymmetric mode ($m = 1$, odd). The error in frequency for all cases is less than 20% which is encouraging considering the simplicity of the method. Buzz is believed to occur when one of the frequency modes occurs near the natural frequency of the shear layer. To confirm this hypothesis the reduced frequency was estimated for the same cases of buzz tabulated previously in Table I. These results, also presented in Table I, show buzz occurs at a reduced frequency at the appropriate values of natural frequency displayed in Fig 2 ($0 < \bar{\alpha} < .2$), thereby reinforcing the hypothesis that massive separation in the duct is the source of the instability. This preliminary analysis is hoped to be useful in conducting a Navier-Stokes computation of inlet buzz.

TABLE I

INLET FREQUENCY DATA

Data	M	L ft	f Hz	m=4Lf/a	R inch	$\bar{\alpha}$
Connors[22]	1.87	8.0	29	1.03	4	.12
Trimpi[23]	1.9	13.0	18	1.04	2	.04
Sterbentz[24]	1.98	7.87	28	.98	4	.12
		9.17	20	.82	8	.17
		15.6	13	.90	8	.11
Nagashima[25]	2.0	2.2	110	1.07	.8	.09

Conclusions

Self-excited fluid flows have been analyzed. Numerical solutions of the time dependent Navier-Stokes equations have produced encouraging agreement with experimental results. It was shown that the source of the instability is a separated shear layer with an inflection point in the velocity profile. Separated flows possess a natural frequency at which small disturbances are highly amplified over a limited frequency range. A fluid dynamic oscillator exists when positive feedback occurs with the correct phase relationship.

These statements now appear obvious. However, as a point of reflection, all previous papers on buzz surveyed by the authors have started with the wrong equations. In all cases irrotational flow was assumed (i.e., linearized potential or acoustical wave equations) which completely eliminated the Rayleigh instability. The investigators were doomed to failure even before any calculations were ever performed. The rotational equations must be used which admit a maximum in vorticity, i.e., the source of the instability. Only then it is possible to obtain useful information; even by linearizing, as long as the double-valued character of the vorticity is retained[27].

References

1. Den Hartog, J.P., Mechanical Vibrations, McGraw-Hill Book Co., Inc, 1947.

2. Schlichting, H., Boundary Layer Theory, Pergamon Press, N.Y., 1955.

3. Rayleigh, Lord, "On the Stability or Instability of Certain Fluid Motion", Scientific Papers, Vol 1, pp. 474-484, Cambridge University Press, 1880.

4. Verma, G., Hankey, W., and Scherr, S., "Stability Analysis of the Lower Branch Solutions of the Falkner-Skan Equations", AFFDL-TR-79-3116, July 1979.

5. Roscoe, D. and Hankey, W., "Stability of Compressible Shear Layers", AFWAL-TR-80-3016, April 1980.

6. Levy, L.L., Jr., "Experimental and Computational Steady and Unsteady Transonic Flows About a Thick Air Foil", AIAA J., Vol 16, No. 6, pp 564-572, June 1978.

7. Steger J. and Bailey, H., "Calculation of Transonic Aileron Buzz", AIAA Paper 79-0134, Jan 1979.

8. Chapman, D.R., "Computational Aerodynamics Development and Outlook", Dryden Lectureship in Research AIAA Paper 79-0129, 17th Aerospace Sciences Meeting, New Orleans, Jan 1979.

9. Hodge, J.K. and Cooper, W.H., "Solution of Navier-Stokes Equations for Airfoils at Angle of Attack Near Stall," AFFDL-TM-77-94FXM, Nov 1977.

10. Glasford, G.M., Linear Analysis of Electronic Circuits, Addison-Wesley, 1965.

11. Rossiter, J.E., Wind-Tunnel Experiment on the Flow Over Rectangular Cavities at Subsonic and Transonic Speeds, R & M No.3438, British ARC, Oct 1964.

12. Heller, H., Holmes G., Covert E., "Flow-Induced Pressure Oscillations in Shallow Cavities," AFFDL-TR-70-104, Dec 1970.

13. Charaud, R.D. and Powell, Some Experiments Concerning the Hole and Ring Tone, A. J., Acoust. Soc. AM. 37 902-11 (1965).

14. Heller, H. and Bliss, D., "Aerodynamically Induced Pressure Oscillations in Cavities: Physical Mechanisms and Suppression Concepts", AFFDL-TR-74-133, WPAFB, Ohio, 1974.

15. Maurer, O. "Investigation and Reduction of Weapons Bay Pressure Oscillations Expected in the B-1 Aircraft," AFFDL-TM-74-101, WPAFB, Ohio, 1974.

16. Hankey, W., and Shang, J., "The Numerical Solution of Pressure Oscillations in an Open Cavity," AIAA Paper, 79-0136, 17th Aerospace Science Meeting, New Orleans, Jan 1979.

17. Harney, D.J., "Oscillating Shocks on Spiked Nose Tips at Mach 3", AFFDL-TM-79-9-FX, 1979.

18. Hankey, W., Hunter, L. and Harney, D., "Self-Sustained Oscillations on Spiked Tipped Bodies at Mach 3", AFFDL-TM-79-23-FXM, Jan 1979.

19. Shang, J., and Smith, R. and Hankey, W., "Flow Oscillations of Spike-Tipped Bodies", AIAA Paper 80-0062.

20. Oswatitsch, K.: Der Druckruckgewinn bei Geschossen mit Ruckstossantrieb bei hohen Uberschallgeschwindigkeiten, Bericht Nr 1005, Gottingen 1944, (Also NACA TM 1140).

21. Ferri, A. and Nucci, L., "The Origin of Aerodynamic Instability of Supersonic Inlets at Subcritical Conditions," NACA RM L 50K30, 1951.

22. Connors, J.F., "Effect of Ram Jet Pressure Pulsations on Supersonic-Diffuser Performance," NACA RM E50H22, 1950.

23. Trimpi, R.L, "An Analysis of Buzzing in Supersonic Ram Jets by a Modified One-Dimensional Non Stationary Wave Theory," NACA TN 3695, 1956.

24. Sterbentz, W.H. and Davids, J., "Amplitude of Supersonic Diffuser Flow Pulsations," NACA TN 3572, 1955.

25. Nagashima, T., Obokata, T. and Asanuma, T., "Experiment of Supersoni Air Intake Buzz," Rept No. 481, University of Tokyo, 1972.

26. Hankey, W., "Analysis of Inlet Buzz,". AFWAL-TM-FIMM-1980.

27. Lin. C.C., "The Theory of Hydrodynamic Stability," Cambridge University Press (1955).

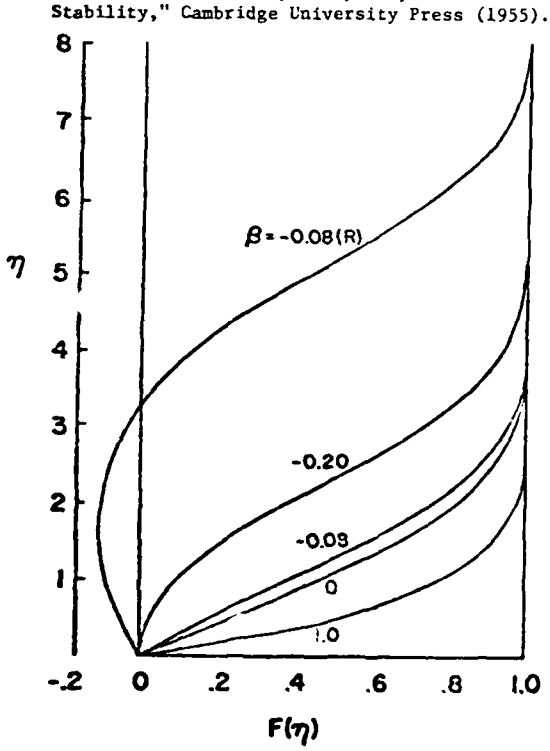

Fig 1. Similar Velocity Profiles for Falkner-Skan Flow

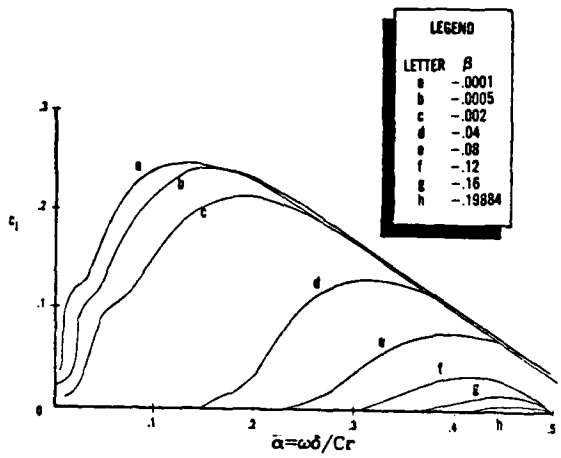

Fig 2. Amplification Factor vs. Wave Number for Various β (Ref. 4)

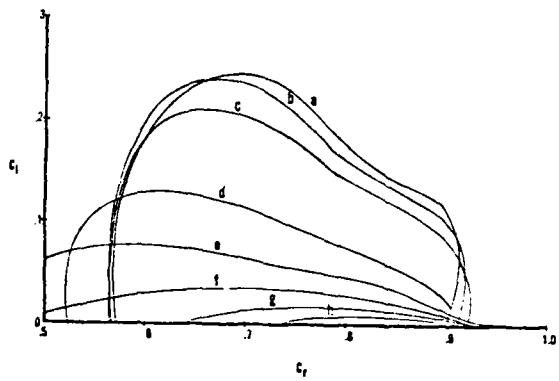

Fig 3. c_i vs. c_r for Various β (Ref. 4)

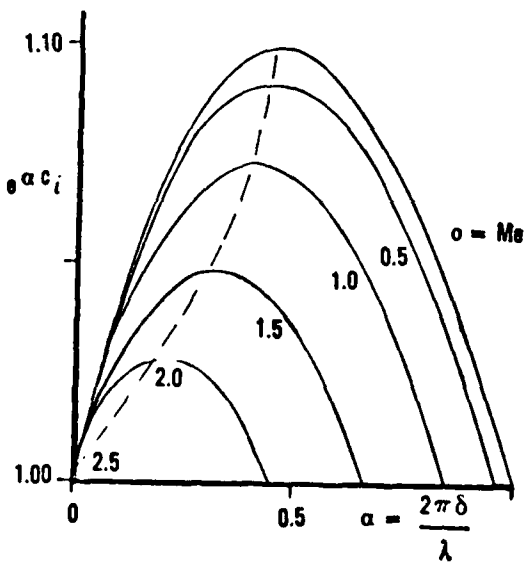

Fig 4. Influence of Mach Number on the Amplification Factor (Ref. 5)

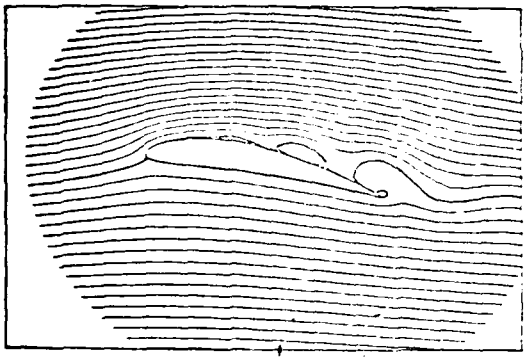

Fig 5. Instantaneous Streamline Distribution Over NACA 6412 Airfoil (Ref. 9)

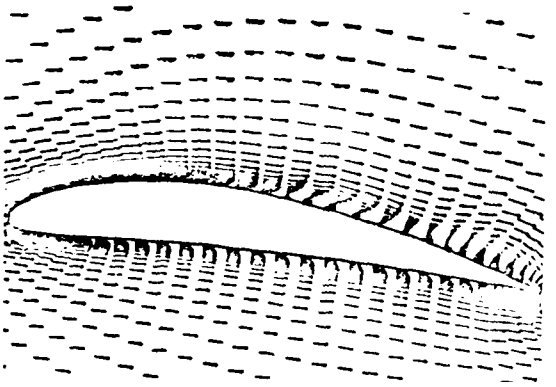

Fig 7. Velocity Field Over NACA 6412 Airfoil Depicting Inflection Points (Ref. 9)

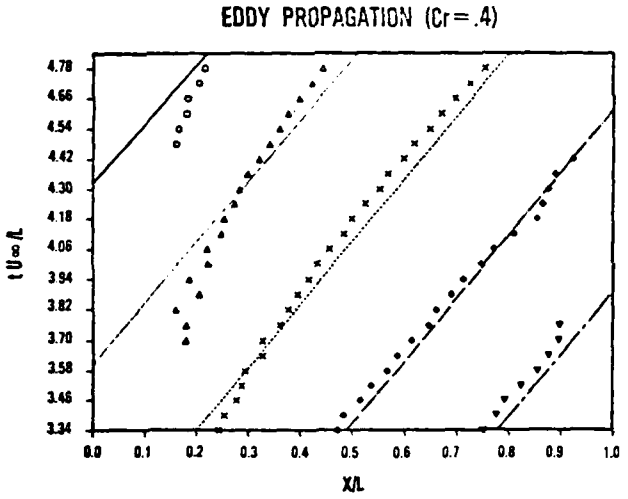

Fig 6a. Wave Diagram of Shedding Eddies for Airfoil (Ref. 9)

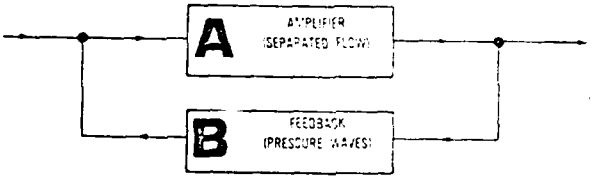

Fig 8. Diagram of Oscillator with Feedback

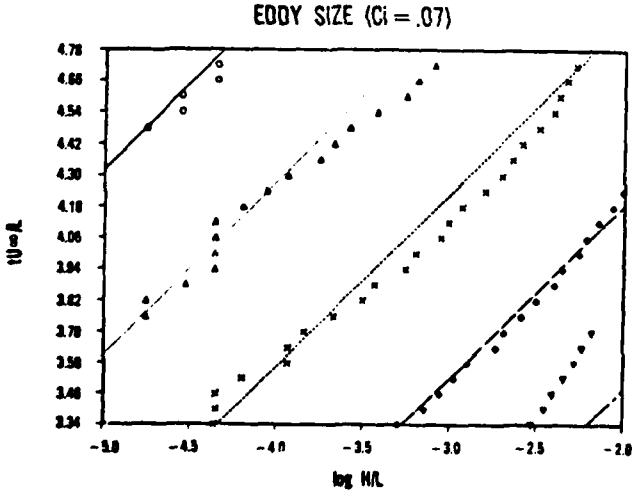

Fig 6b. Growth Rate of Shedding Eddies for Airfoil (Ref. 9)

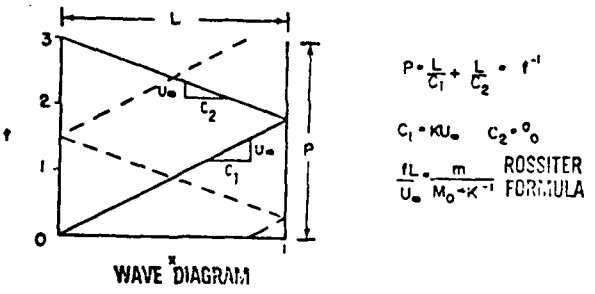

Fig 9. Wave Diagram for Pressure Oscillation

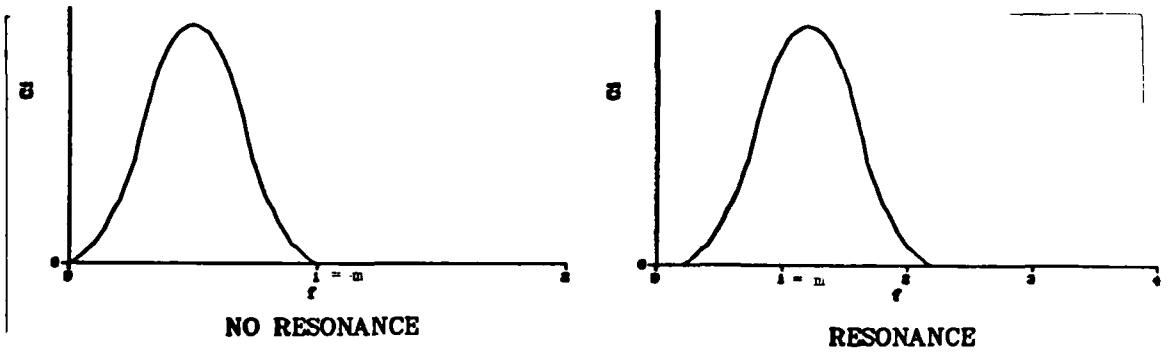

Fig 10. Criterion for Resonance

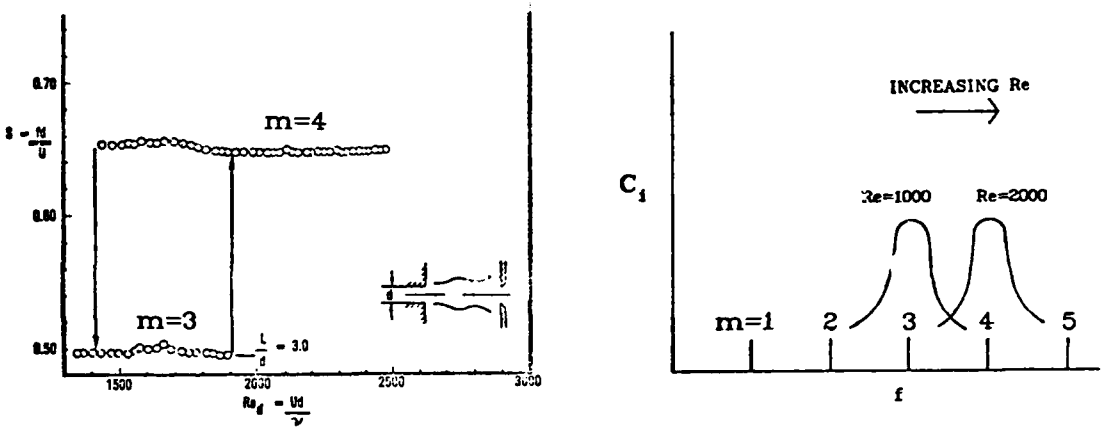

Fig 11. Jumps in Strouhal Number for Edge Tones (Ref. 12)

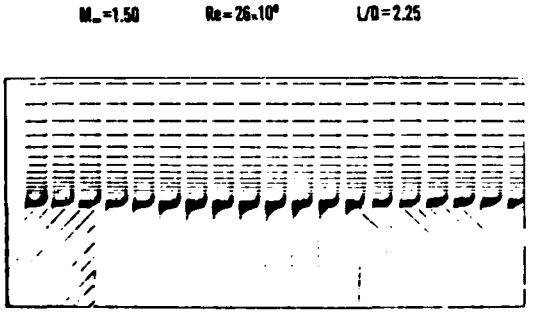

Fig 12. Velocity Distribution for Flow Over an Open Cavity (Ref 16)

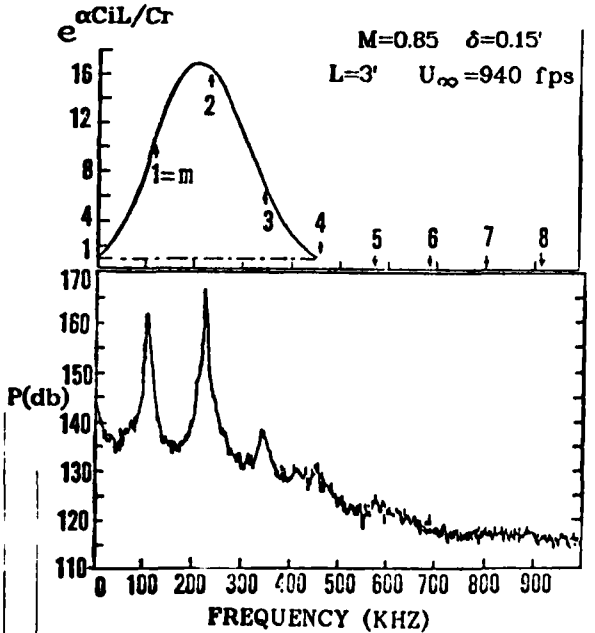

Fig 13. Comparison of Predicted (Ref. 16) and Experimental (Ref. 15) Spectral Analysis for Open Cavity

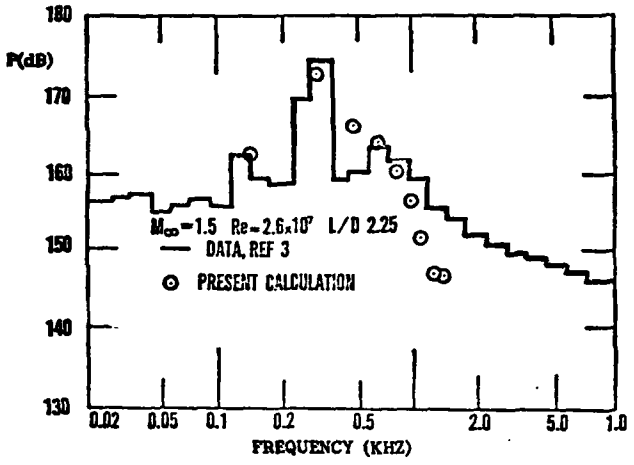

Fig 14. Spectral Analysis for the Numerical Solution of the Open Cavity

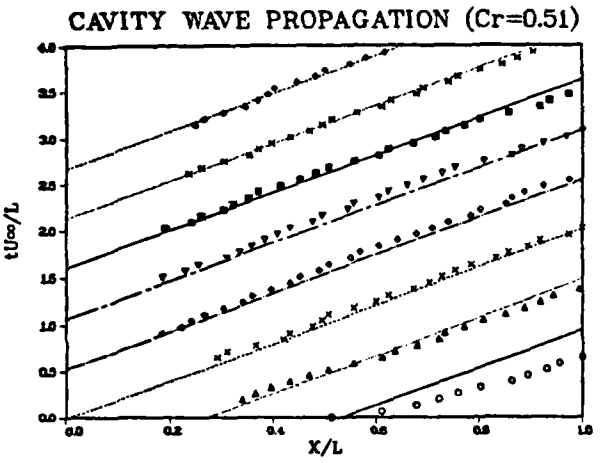

Fig 15. Wave Diagram for the Numerical Solution of the Open Cavity

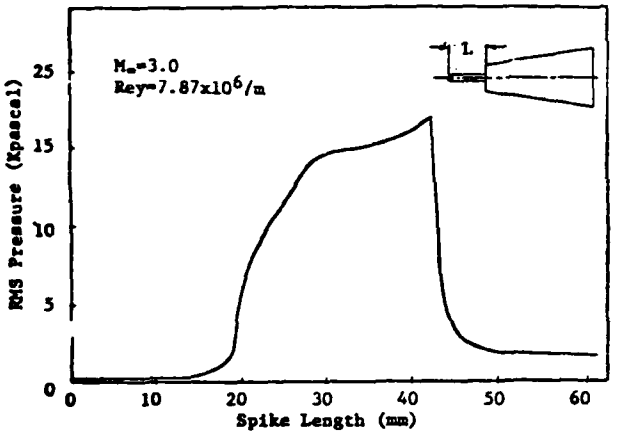

Fig 16. RMS Pressure Level for Spike Buzz

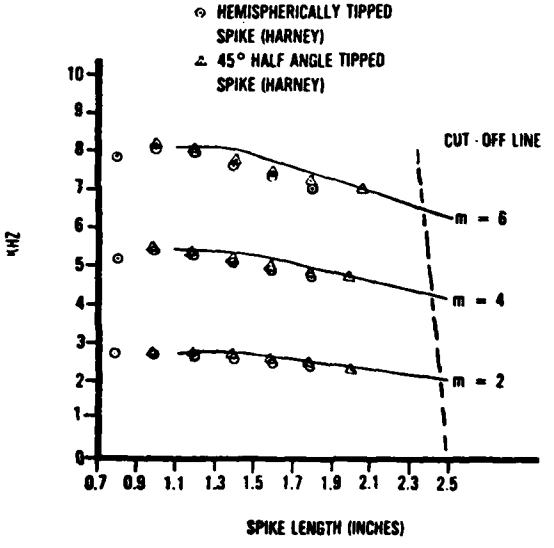

Fig 17. Frequency Mode Prediction for Spike-Tipped Body

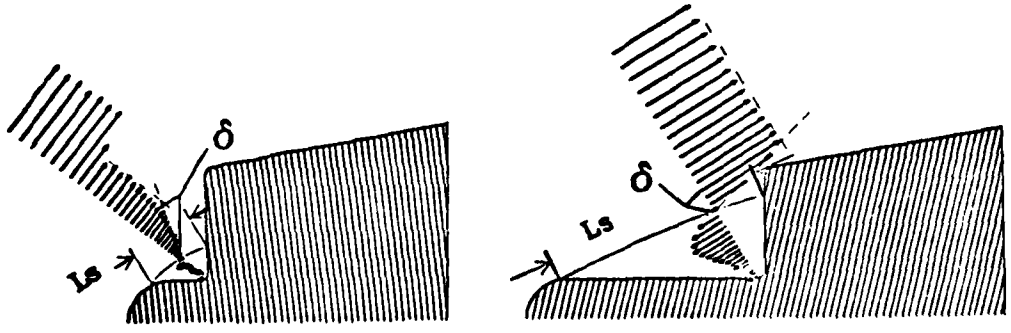

Fig 18. Velocity Profiles Over Spikes Depicting Inflection Points

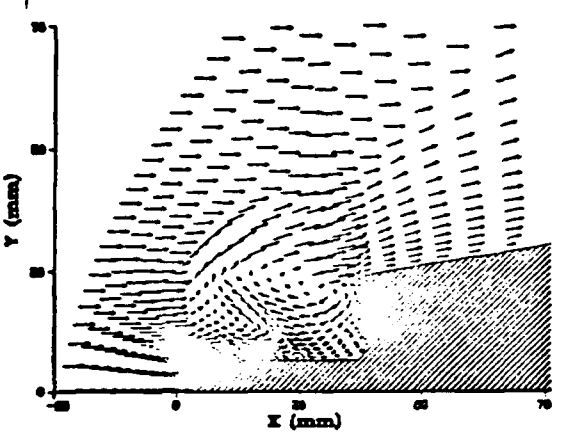

Fig 19. Instantaneous Velocity Field Over Spike-Tipped Body

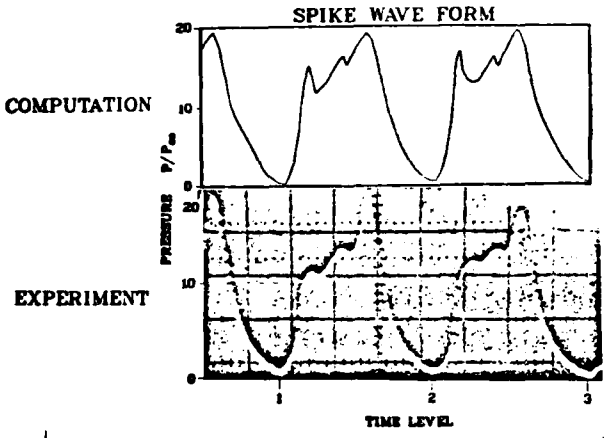

Fig 20. Comparison of Predicted and Experimental Wave Forms for Spike-Buzz

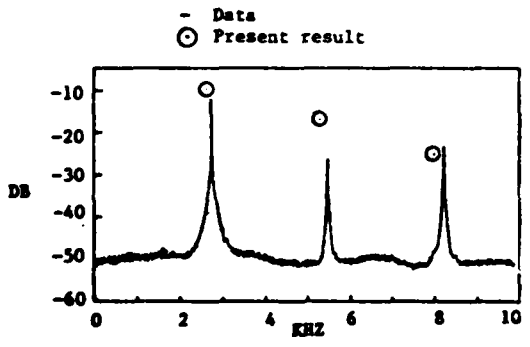

Fig 21. Comparison of Predicted and Experimental Spectral Analysis for Spike-Buzz

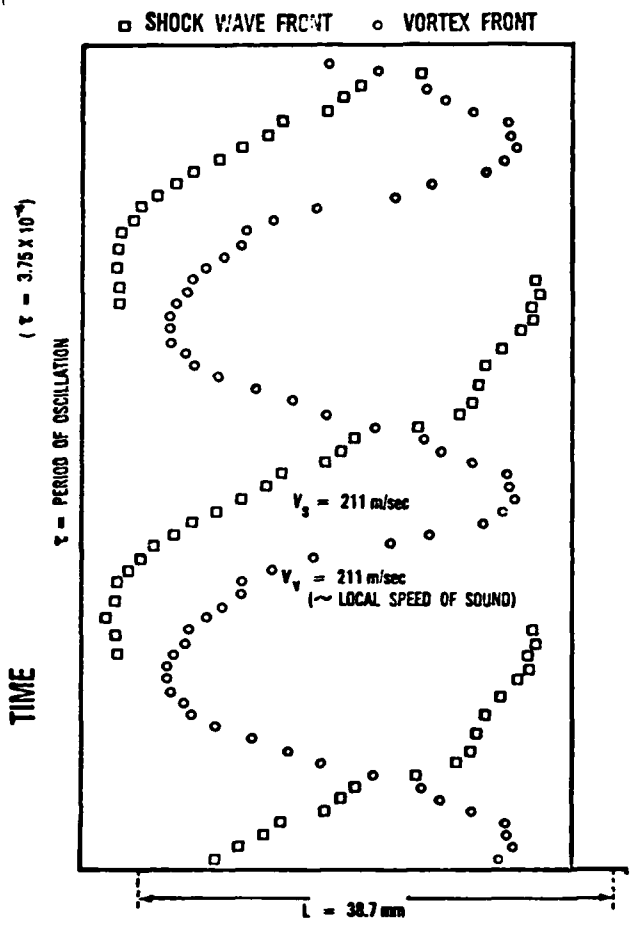

Fig 22. Wave Diagram of Spike-Buzz for Numerical Computation

Forced Vortices Near a Wall[+]

Hermann Viets[*], Michael Piatt[**] and Mont Ball[***]
Wright State University, Dayton, Ohio

Introduction

The existence of large scale, unsteady structures in flows which are nominally steady has been noted by Roshko and others[1]. These structures are currently under intense investigation due to their relationship to the turbulence structure and eventually to computational analysis, perhaps employing an eddy viscosity. The coherent structures seem to have a strong effect on the transport properties of flow systems. Their effect is yet amplified by the fact that they survive and remain coherent for very large characteristic flow times[2].

Of course, large scale flow structures have often been employed to enhance the momentum transfer between various flow regions. The common vortex generators found on aircraft wings produced streamwise vorticity in order to energize the boundary layer and thereby avoid separation. Large scale streamwise vorticity has also been employed to enhance the mixing of a jet with the surrounding fluid[3,4]. Perhaps more effective but certainly more difficult to produce is the generation of transverse vortices in the jet, lying parallel to the plane of the jet exit. Such structures have been produced by acoustical bombardment[5], mechanical interference[6] and fluidic switching[7,8] and significantly improve the mixing rates.

The purpose of the present investigation is to examine the generation of transverse vortices near a wall and their effect on the overall flow. The

---

+ Supported in part by Grant No. 78-3525 from the Air Force Office of Scientific Research, Monitored by George Catalano, A.F. Flight Dynamics Laboratory.

* Professor, Associate Fellow AIAA

** Graduate Student

***Senior Technician

mechanical vortex generator is shown in Figure 1 and consists of a simple cam shaped rotor. The flow is from left to right as shown and the rotor turns in the counter-clockwise sense. Each time the rotor surface discontinuity is exposed to the flow, a vortex is generated in a manner similar to the generation of a starting vortex by a rapidly accelerated airfoil section. The vortex then is swept downstream by the flow and causes the transfer of momentum in the vicinity of the wall.

Potential Applications

The vortex generation device shown in Figure 1 has been tested in several flow geometries related to potential applications of the technique. Three of these geometries are shown in Figure 2 and described below.

Figure 2a shows the rotor mounted near the leading edge of an airfoil. The vortices produced are swept over the airfoil and have been shown to energize the boundary layer and thus delay separation until a higher angle of attack[9]. The positioning of the rotor in this geometry actually arose from studying the vortex structure above an airfoil oscillating sinusoidally about a mean angle of attack. Application to aircraft could potentially allow landing at higher angles of attack and hence lower airspeeds.

The flow over the rearward facing ramp, shown in Figure 2b, is also energized by a rotor located just upstream of the start of the ramp. The use of the unsteady vortex generator makes it possible to increase the ramp angle beyond the value at which separation normally occurs[10]. Potential application of such a device might reduce vehicle wake size to reduce drag or allow the operation of wider angle diffusers.

In both the airfoil and ramp applications, the advantage of the rotor technique is primarily the improvement of the time averaged flow, even though the flow must be unsteady to produce this benefit. In the case of the rearward

facing step (Figure 2c), the primary benefit is the actual time dependency produced by the rotor. The objective is to increase the interaction between the recirculation region behind the step and the remainder of the flowfield. The rotor causes the recirculation region length to pulsate and has potential application to the improvement of dump combustors[11].

Flow Visualization Results

The rotor shape shown in Figure 1 was originally a simple spiral in which the rotor surface gradually transitioned from a smaller radius to a larger one and then abruptly returned to the smaller radius. Then the step from the larger to smaller radius was undercut in order to produce a cusp at the rotor tip and thus improve the vortex generation process.

The flow structure produced by the spinning cam shaped rotor may be clearly seen by employing smoke flow visualization. The smoke is generated by dripping kerosine on an inclined resistance heater. The vaporized kerosine is released through tubes located at the tunnel inlet and entrained into the test section. The following photographs are obtained by the use of a strobe light so they indicate the instantaneous position of the smoke lines. Since the flow is unsteady, these lines are not streamlines but rather streaklines. Their interpretation is less straightforeward since their position represents the integrated effect of everything upstream. However, in this case the interpretation is considerably simplified by the fact that the flow can be observed dynamically. This is achieved by allowing a small frequency difference between the rotor and the strobe light,which effectively produces a slow motion version of the flowfield. The significance attributed to the following figures is guided by this dynamic view of the flow.

The tunnel itself is an open circuit low velocity, low turbulence tunnel with a dozen inlet screens to break up the large scale motions in the entrained

air. The velocity in the test section is uniform within 4% without the rotor activated. The boundary layer thickness is less than .64 cm. (.25 inch). The velocity at the rotor position is 11.6 m/sec (38.1 ft/sec) and the rotor extends a distance of 2.54 cm (1 inch) into the flow in its fully extended position as shown in Figure 1. The resulting Reynolds Number is 1.98×10^4, based on the rotor size and free stream velocity. Of course, the Reynolds Number will change with relative velocity between the rotor tip and the freestream.

Six rotor speeds were examined by the flow visualization technique in order to examine the effect of generation frequency and vortex strength. The significant parameters are listed in Table 1.

Typical of the desired vortex generation is the result shown in Figure 3 for a rotor speed of 3000 rpm. The strobe lighted photographs have been arranged in the order of their occurrence, from top to bottom. As the rotor tip sweeps from right to left, the first hint of the vortex produced is seen in the lowest smoke line which begins to curl up in Figure 3a. By Figure 3b the rotor tip has disappeared and the vortex is evident, slightly farther downstream. The streaklines still appear to be relatively laminar but in Figure 3c the vortex flow appears to be turbulent with a smaller scale structure visible. By Figure 3d the size of the vortex structure has grown considerably and it has translated downstream as well as rising, higher above the surface of the plate. Its position yet farther downstream is shown in Figures 3a, b and c where its continued growth and interaction with the outer streaklines is evident. In summary, the vortex is produced by the rotor shape, grows and transitions to a turbulent state and is convected downstream. Its energization of the boundary layer flow can be inferred from the results cited in the preceding sections.

The tip of the rotor is moving in the upstream direction in the previous case and a strong vortex is apparent. Turning the rotor in the opposite direction at the same speed (i.e. - 3000 rpm) generates vorticies at the same frequency

and rotating in the same sense. This indicates that the relative velocity between the rotor and freestream is still in the same sense. For this case the relative velocity in Table 1 is in the opposite sense, indicating that the local streamwise velocity is slightly increased by the presence of the rotor. In general, for rotation in the clockwise direction the strength of the vortex is greatly reduced by the lowered relative velocity. Such a case is shown in Figure 4 for various rotor positions. The vortex is clearly formed, stays near the wall and eventually bursts into turbulence. The interaction with the stream is minor due to the weakness of the vortex.

Decreasing the rotor speed to +2000 rpm in Figure 5, produces a somewhat weaker vortex than the +3000 rpm case of Figure 3. The rolling up of the flow is very pronounced but the disturbance is not as strong. Turning the rotor in the clockwise sense so that the tip moves in the same direction as the free stream velocity, results in a stronger vortex in this case (Figure 6, ω = -2000 rpm) than that produced in Figure 4 (ω = -3000 rpm). This is simply due to the fact that the relative velocity is increased between the rotor and the freestream.

Further results, Figures 7 and 8, compare the case of rotation at $\pm$ 1000 rpm. Again, the frequency of vortex generation is the same with rotation in either sense, but for this speed the vorticies are rather weak in either case. Neither disturbance is very large and the curling up of the streakline is not very evident. The magnitude of the disturbance appears to be roughly the same in either case.

Thus the flow visualization results clearly show the existence of a vortex structure downstream of the spinning rotor. The frequency of generation depends upon the rotational frequency since each rotation produces one vortex. The strength of the vortex depends upon the relative velocity between the motion of the cusp tip and the free stream velocity.

Quantitative Results

The flow geometry described above is examined quantitatively by employing a hot wire anemometer. A Flow Corporation (Now Datametrics) Model 900 constant temperature anemometer is employed in conjunction with a pair of Thermo Systems Inc. linearizers. Since the instantaneous velocity field is required to study the vortices and their effect, the hot wire signal must be conditioned so that the only velocity recorded is at a predetermined phase angle of the rotor's motion. The technique is to mount a magnetic pickup on the shaft of the rotor, so that the position of the rotor is known. As shown schematically in Figure 9, the triggering signal from the magnetic pickup is electronically manipulated and used to arm a Schmitt trigger which in turn controls a sample and hold circuit. The hot wire continuously samples the flow velocity, but the signals are only recorded when the rotor is in a particular orientation. Thus, all data recorded with the sampling electronics at a given setting apply to the same position of the rotor and the data is instantaneous (as long as the cycles are sufficiently repeatable).

Combining the streamwise, u, and transverse, v, velocities, the entire flowfield can be depicted by plotting the magnitude of the total velocity and its orientation as the length and angle of vector arrows in a field. Such a field is shown in Figure 10, where the rotor is in the $\theta = 0°$ (i.e. the maximum extension) position. The velocity vectors shown are the instantaneous values at that particular phase position of the rotor.

Examining Figure 10, there is no evidence of the existence of a vortex in the flowfield. However, in order to see the coherent motion of a portion of matter, the observer should be in a frame of reference moving with its center of mass[12]. In the field of Figure 10, this can be accomplished by simply subtracting the velocity of the center of the particular vortex. Of course, the location of the vortex center is unknown, so the process involves some trial and error.

However, the flow structure which leads to a vortex can be isolated. It consists of a curved instantaneous streamline in the vicinity of which the magnitudes of the velocity vectors simultaneously increase with distance from the center of curvature of the streamline.

By the above method the approximate location of the vortex center may be located. In Figure 10a, for example, the instantaneous streamlines are highly curved and appear to satisfy the necessary form at a streamwise location $\bar{X} = 7.5$. Choosing an intermediate streamwise velocity from this profile and subtracting it from all the velocities in the field reveals the structure of the vortex, Figure 10b. Its center is located at approximately $\bar{X} = 7.5$, $\bar{Y} = 3.5$. No other vortex is apparent.

One third of a cycle later, the rotor is instantaneously positioned at an angle $\theta = 120°$ as shown in Figure 11a. At this time, the vortex located at $\bar{X} = 7.5$ for $\theta = 0°$ must be located farther downstream. The anticipated structure is found and the transformed structure (obtained by subtracting a velocity 11.8 m/sec) is shown in Figure 11b, clearly illustrating a vortex centered at $\bar{X} \cong 10.5$, $\bar{Y} = 4.75$.

Searching the field of Figure 11a, it appears that another vortex may be present very close to the rotor position itself. The velocity profiles are taken as continuous profiles, so additional detail is shown in Figure 11c. Identifying the typical structure and subtracting a velocity of 130.0 m/sec results in Figure 11d where the vortex is evident at a location $\bar{X} \cong 1.5$, $\bar{Y} = 1.25$. That this vortex was not observed in the $\theta = 0°$ case indicates that it was not yet large enough to be identified.

One third of a cycle later, the rotor is in the $\theta = 240°$ position. The flowfield corresponding to this time is shown in Figure 12a. Searching for the typical structure described above, it is apparent that two vortex structures are

present. Subtracting streamline velocities of 13.0 m/sec and 11.0 m/sec reveals vortices at locations $\bar{X}$ = 4.5, $\bar{Y}$ = 2.0 and $\bar{X}$ = 13, $\bar{Y}$ = 5.75 as shown in Figures 12b and 12c respectively.

Of course the various vortex structures illustrated above are really the same vortex observed at different times as it is swept downstream. The various positions and phase angles are plotted in Figure 13 and show the trajectory of the vortex to be an almost linear rise after its structure is established. Based on the trajectory, the translational velocity of the vortex is approximately constant and equal to the undisturbed freestream velocity, 11.6 m/sec (38.1 ft/sec). The average translational velocity, based on the positions and phase angle shown, is 10.7 m/sec.

The trajectory of the vortex, as shown in Figure 13, also explains why the vortex generator is so effective even if it is submerged within a boundary layer as in Reference 10. The vortex is created with a very small core which grows rapidly and it rises out of the boundary layer. Thus the scale of its influence becomes larger as it moves downstream and it moves into a better position from which to energize the boundary layer.

The influence of the vortex on the streamwise velocity is shown in Figure 14. The streamwise velocity profiles are plotted along with the position of the instantaneous vortex. The vortex clearly produces an overshoot in the velocity profile; that is, a velocity higher than anywhere else in the field. This overshoot must be the result of the vortex since the rotor is turning in the wrong direction to generate such a streamwise increase. In addition, the vortex flow produces a flow to the wall which energizes the boundary layer.

Analytically, Theisen[13] has examined the character of boundary layers and wakes with discrete vortex structures. In agreement with experimental observations,

he derived a separation criterion which is related to the flow intermittency and burst frequencies. Such a method could be especially useful in the optimization of a vortex generator from the point of view of frequency, once the optimum shape has been found. Walker and Abbott[14] have analyzed the case of a vortex moving near a wall. Unfortunately, their vortex rotates in the opposite sense. Nevertheless, the implications of some of their results parallel those above.

The identification of the vortex structures in the present case is rather straight-forward since the forced time dependent flow is so strong. If the unsteadiness is weaker compared to the mean flow, the structure may be more difficult to distinquish. A method to handle this situation has been developed by Bethke and Viets[15] employing a discrete Fourier Transform. The locations of the individual vortices may then be deduced from the angles produced in the transformed plane.

Another interesting aspect of the velocity profiles of Figure 14 is the apparent potential for viscous drag reduction. The existence of the vortex in the field lowers the velocity near the wall below that which would normally exist. In this way the velocity gradient at the wall is reduced, as is the instantaneous viscous drag. The effect of this reduction on the mean viscous drag is currently being investigated. The entire situation is reminiscent of the use of a vortex sheet to produce the required boundary condition in potential flow.

Conclusions

The results presented above show the generation and subsequent dynamics of the unsteady vortices produced by a mechanical rotor operating near a wall.

The very large scale vorticity and structure shown here has two main applications. One is to explain the success achieved with vortex generators in various applications. The second is to use these readily identifiable structures in order to test methods of determining large scale vortex structures in nominally "steady" boundary layers. Success in identifying the large scale steady structures would then allow the modeling of a real steady turbulent boundary layer with both its large scale structure and small scale viscous structure.

References

1. Roshko, A., "Structure of Turbulent Shear Flows: A New Look," AIAA Journal, Vol. 14, No. 10, 1976, pp. 1349-1357.

2. Papailiou, D.D. and Lykondis, P.S., "Turbulent Vortex Streets and the Mechanism of Entrainment," J.F.M., Vol. 62, 1974, pp. 11-31.

3. Quinn, B., "Compact Ejector Thrust Augmentation," J. Aircraft, Vol. 10, No. 8, August 1973, pp. 481-486.

4. Bevilaqua, P.M. and Toms, H.L., Jr., "A Comparison Test of the Hypermixing Nozzle," U.S.A.F. Aerospace Research Laboratories Report TR-74-0006, January 1974.

5. Crow, S.C. and Champagne, F.H., "Orderly Structure in Jet Turbulence," J.F.M., Vol. 48, Part 3, 1971, pp. 547-591.

6. Binder, G. and Favre-Marinet, M., "Mixing Improvement in Pulsating Turbulent Jets," ASME Symposium on Fluid Mechanics of Mixing, June, 1973.

7. Viets, H., "Flip-Flop Jet Nozzle," AIAA Journal, Vol. 13, No. 10, Oct. 1975, pp. 1375-1379.

8. Piatt, M. and Viets, H., "Conditioned Sampling in an Unsteady Jet," AIAA Paper No. 79-1857, AIAA Aircraft Systems and Technology Mtg., New York City, Aug. 1979.

9. Viets, H., Piatt, M. and Ball, M., "Unsteady Wing Boundary Layer Energization," AIAA Paper No. 79-1631, AIAA Atmospheric Flight Mechanics Conf., Boulder, Colo., Aug. 1979.

10. Viets, H., Piatt, M. and Ball, M., "Boundary Layer Control By Unsteady Vortex Generation," in Aerodynamics of Transportation, Morel, T. and Dalton, C. (Eds.), Published by ASME, June 1979.

11. Viets, H. and Piatt, M., "Induced Unsteady Flow in a Dump Combustor," Presented at the Seventh International Colloquium on Gasdynamics of Explosions and Reactive Systems, Göttingen, Germany, Aug. 1979 (to be

published in the AIAA Progress in Astronautics Series).

12. Viets, H., "Coherent Structures in Time Dependent Shear Flows," AGARD CP-271, AGARD/NATO Conference on Turbulent Boundary Layers--Experiments, Theory and Modelling, The Hague, Netherlands, Sept. 1979.

13. Theisen, J.G., "A New Turbulent Boundary Layer Separation Criterion Based on Flow Dynamics," Lockheed Georgia Company, Report LG78ER0007, March 1978.

14. Walker, J.D.A. and Abbott, D.E., "Implications of the Structure of the Viscous Wall Layer," Turbulence in Internal Flows, (Murthy, Ed.), Hemisphere, 1977.

15. Bethke, R.J. and Viets, H., "Data Analysis to Identify Coherent Flow Structures," AIAA Paper No. 80-1561, AIAA 7th Atmospheric Flight Mechanics Conference, Danvers, Mass., Aug. 1980.

Table 1

Figure No.	RPM	V_{rel}(m/sec)	V_{rel}/V_∞	$Re(x10^4)$ $Re = \rho \frac{V_{rel}H}{\mu}$
4	3000	23.60	2.03	4.02
5	-3000	-.42	-.03	.015
6	2000	19.61	1.69	3.35
7	-2000	3.64	.31	.61
8	1000	15.61	1.34	2.65
9	-1000	7.63	.66	1.31

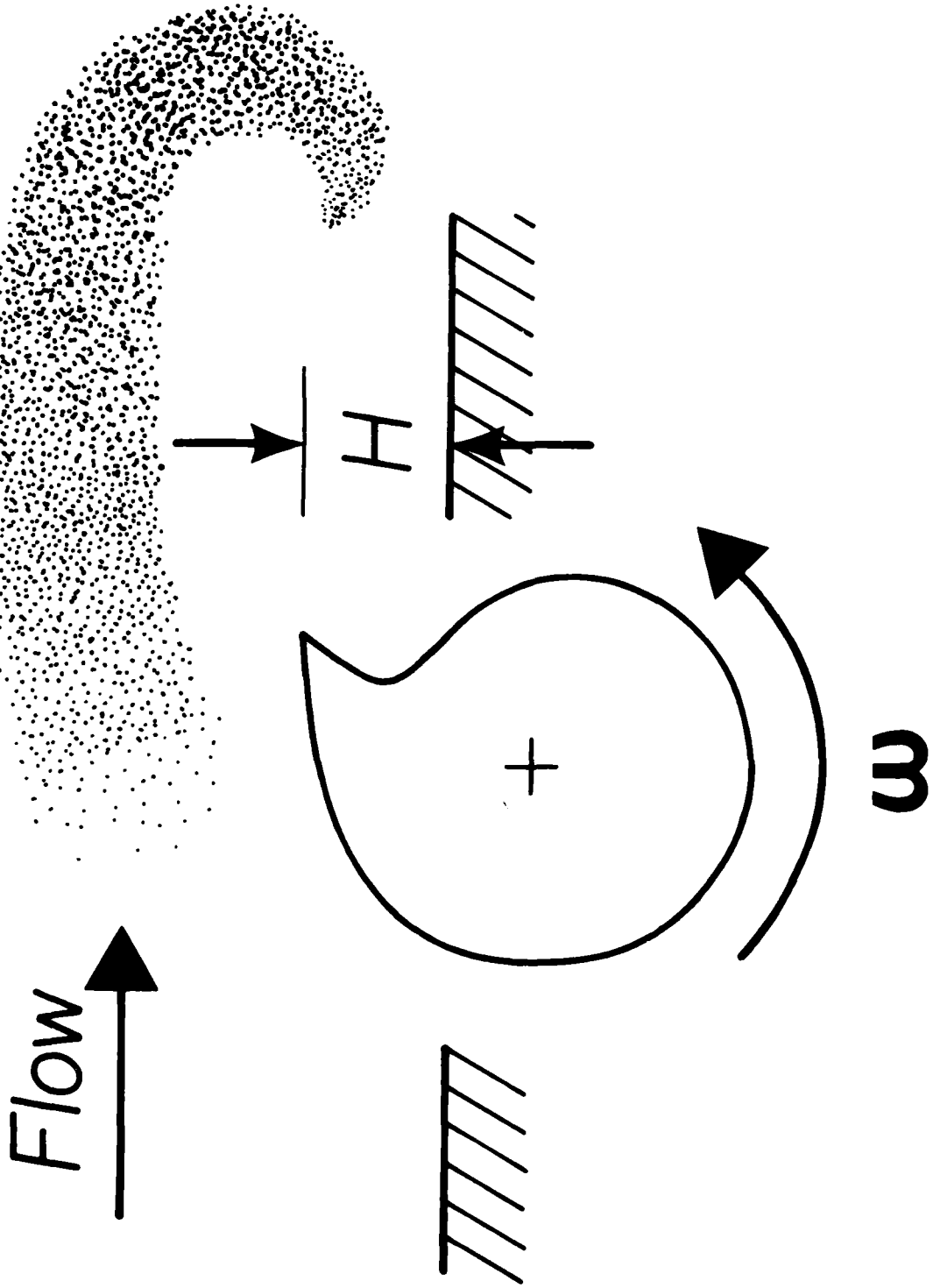

Figure 1. Schematic of the vortex generator.

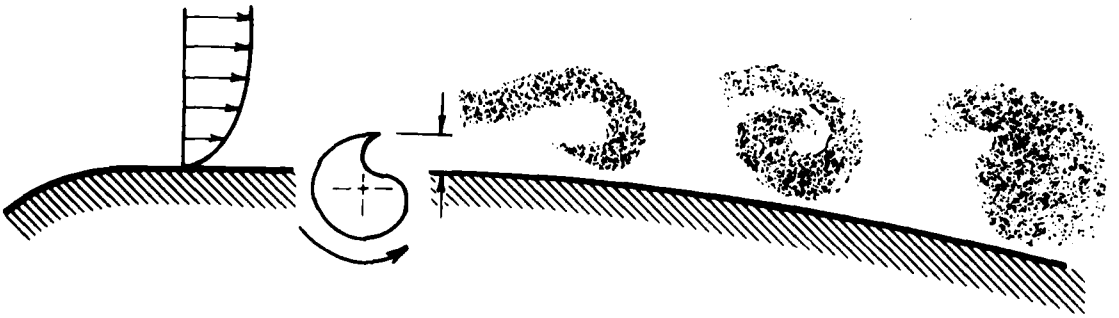

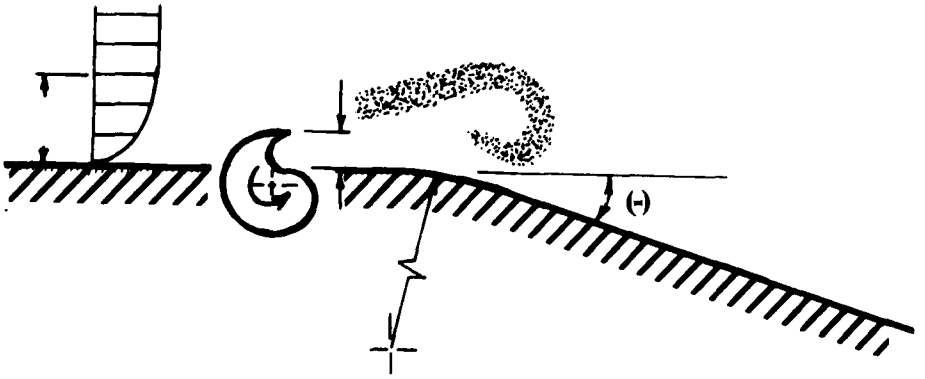

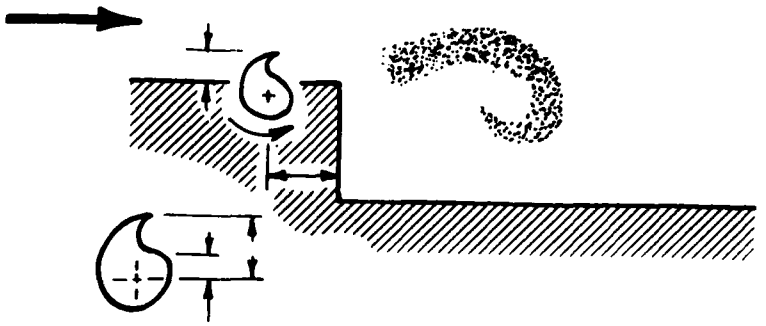

Figure 2. Potential applications of unsteady flows.

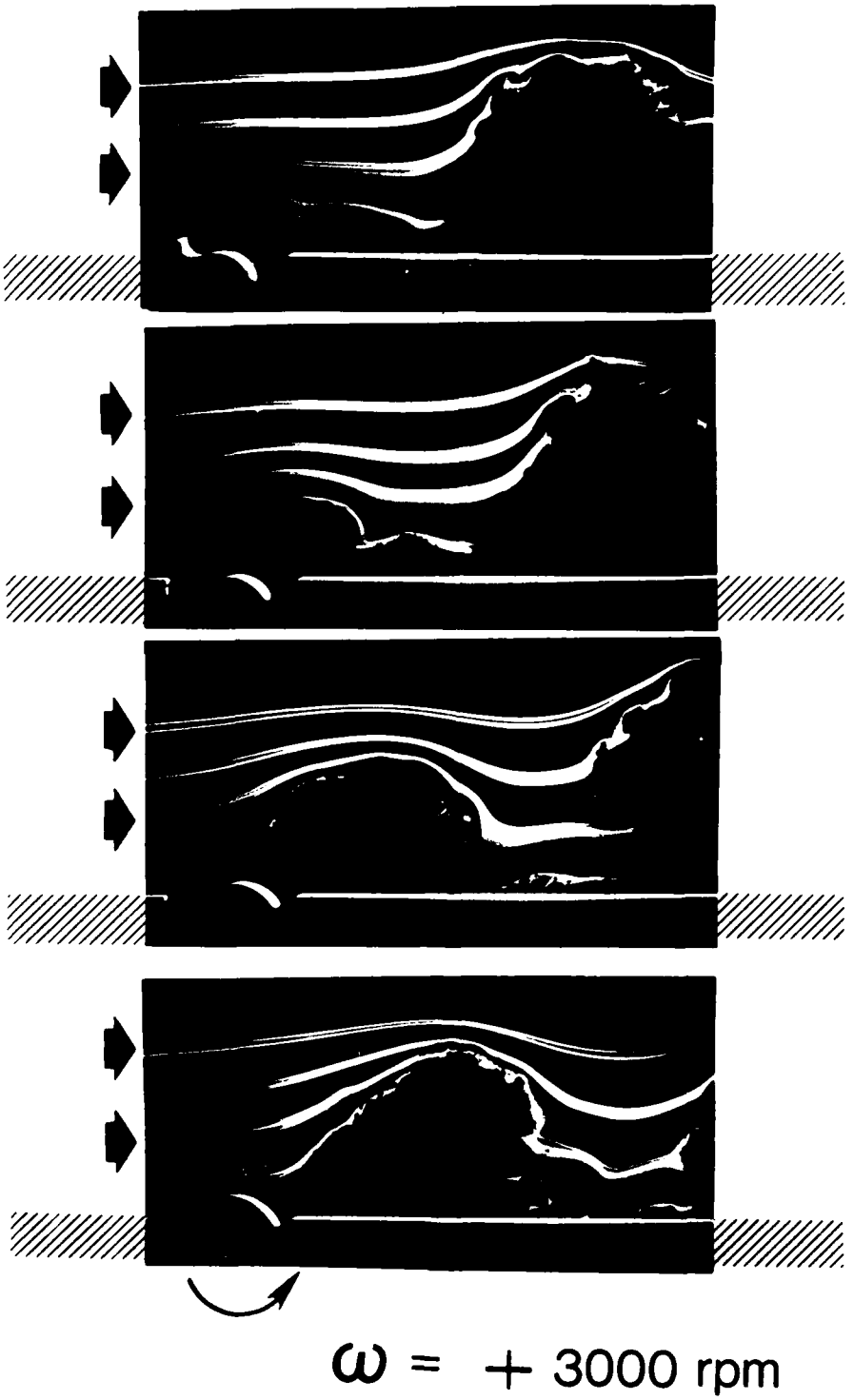

Figure 3. Flow visualization of vortex structure produced by the vortex generator with ω = 3000 rpm.

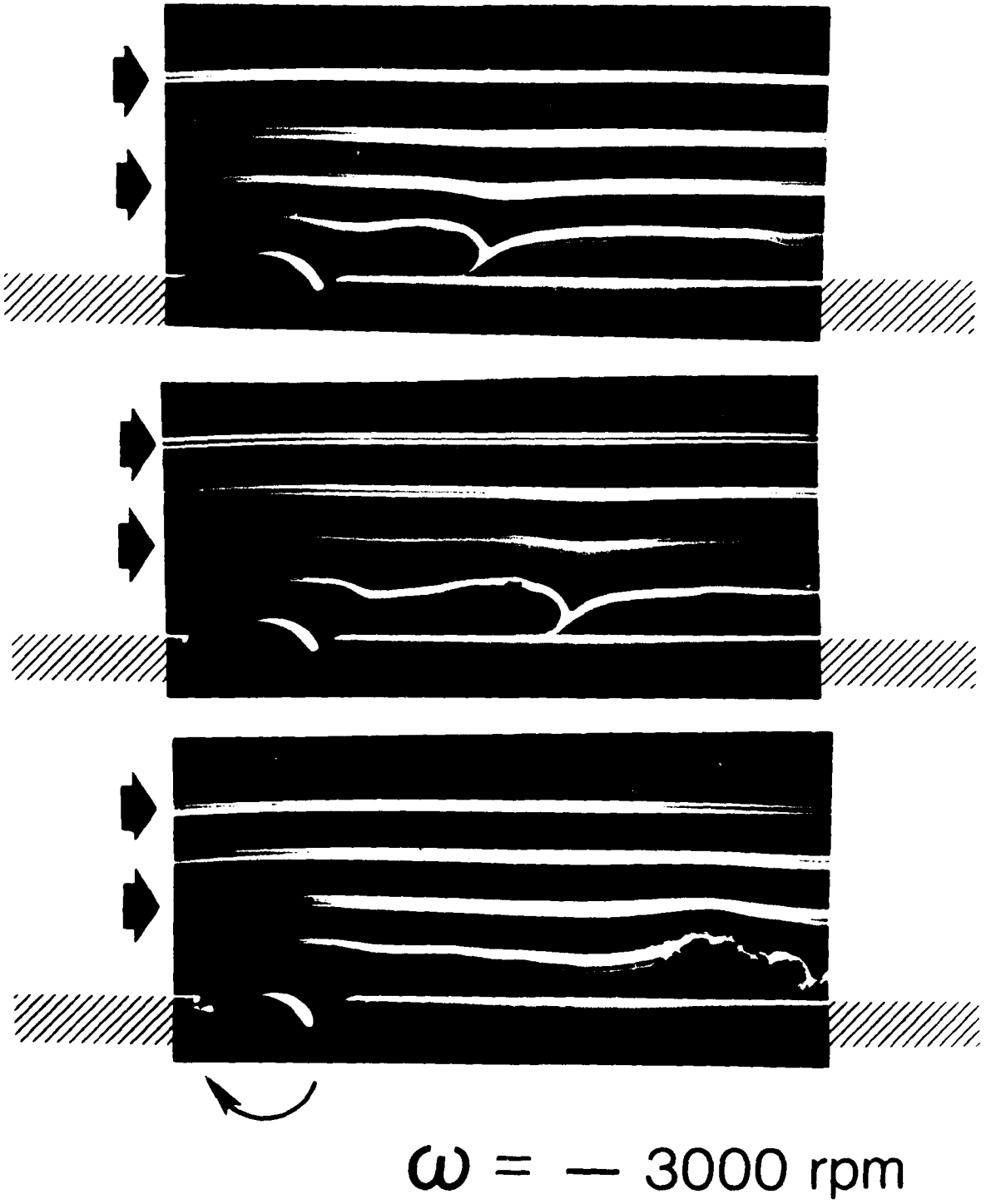

Figure 4. Flow visualization of vortex structure produced by the [illegible] generator with -3000 rpm.

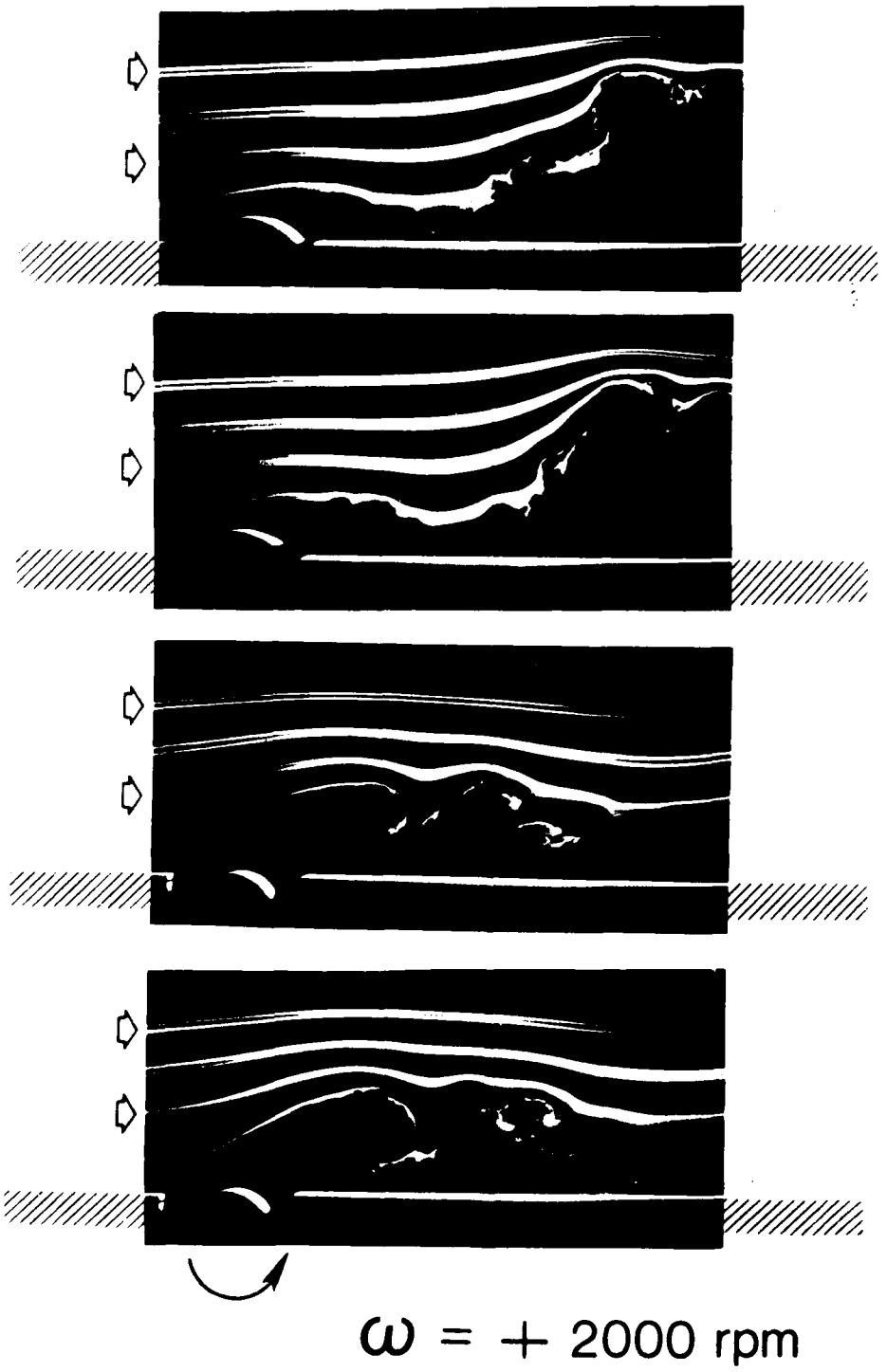

Figure [illegible]. Flow visualization of vortex structure produced by the vortex generator with [illegible] rpm.

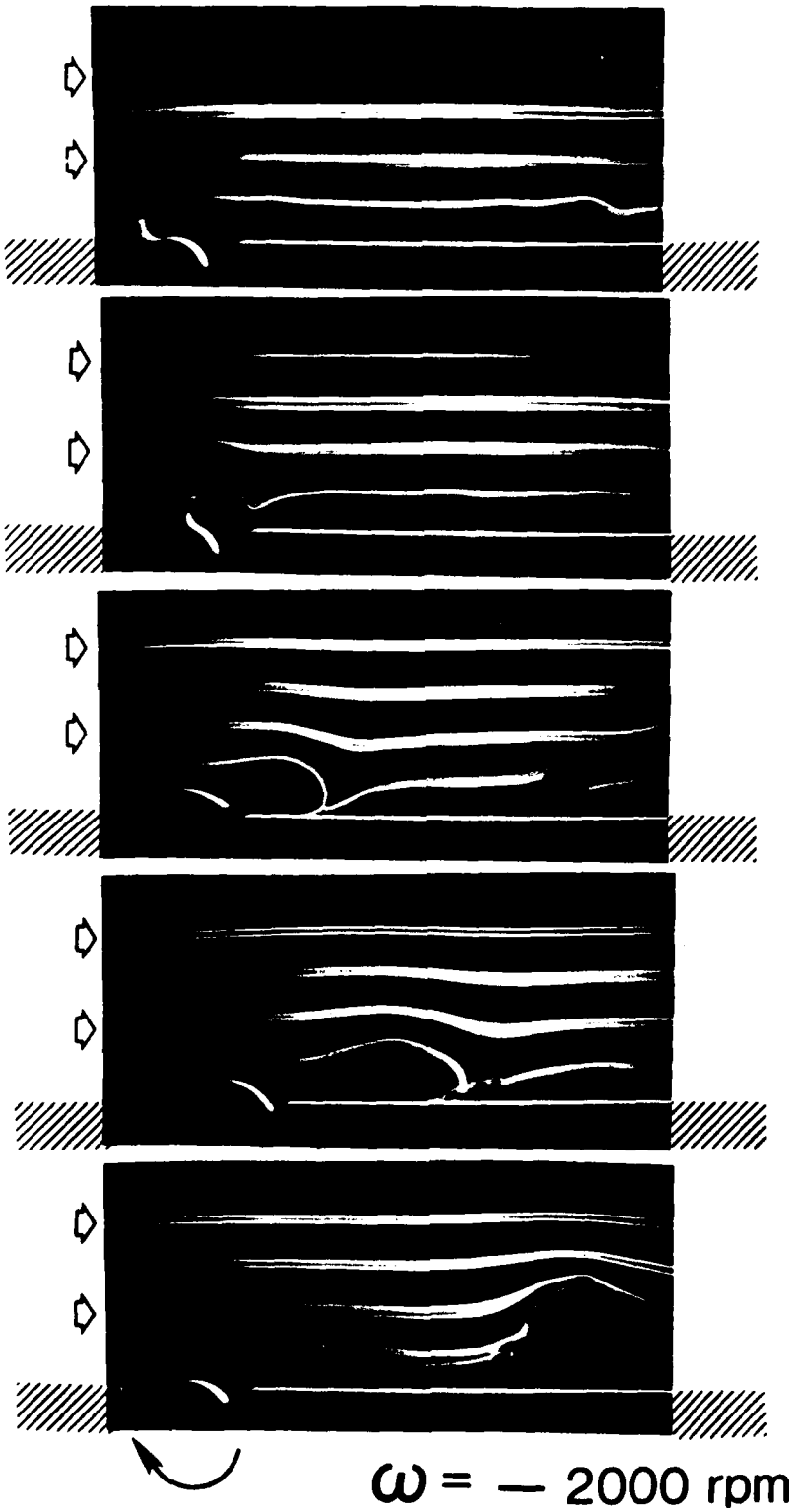

Figure 6. Flow visualization of vortex structure produced by the vortex generator with ω = -2000 rpm.

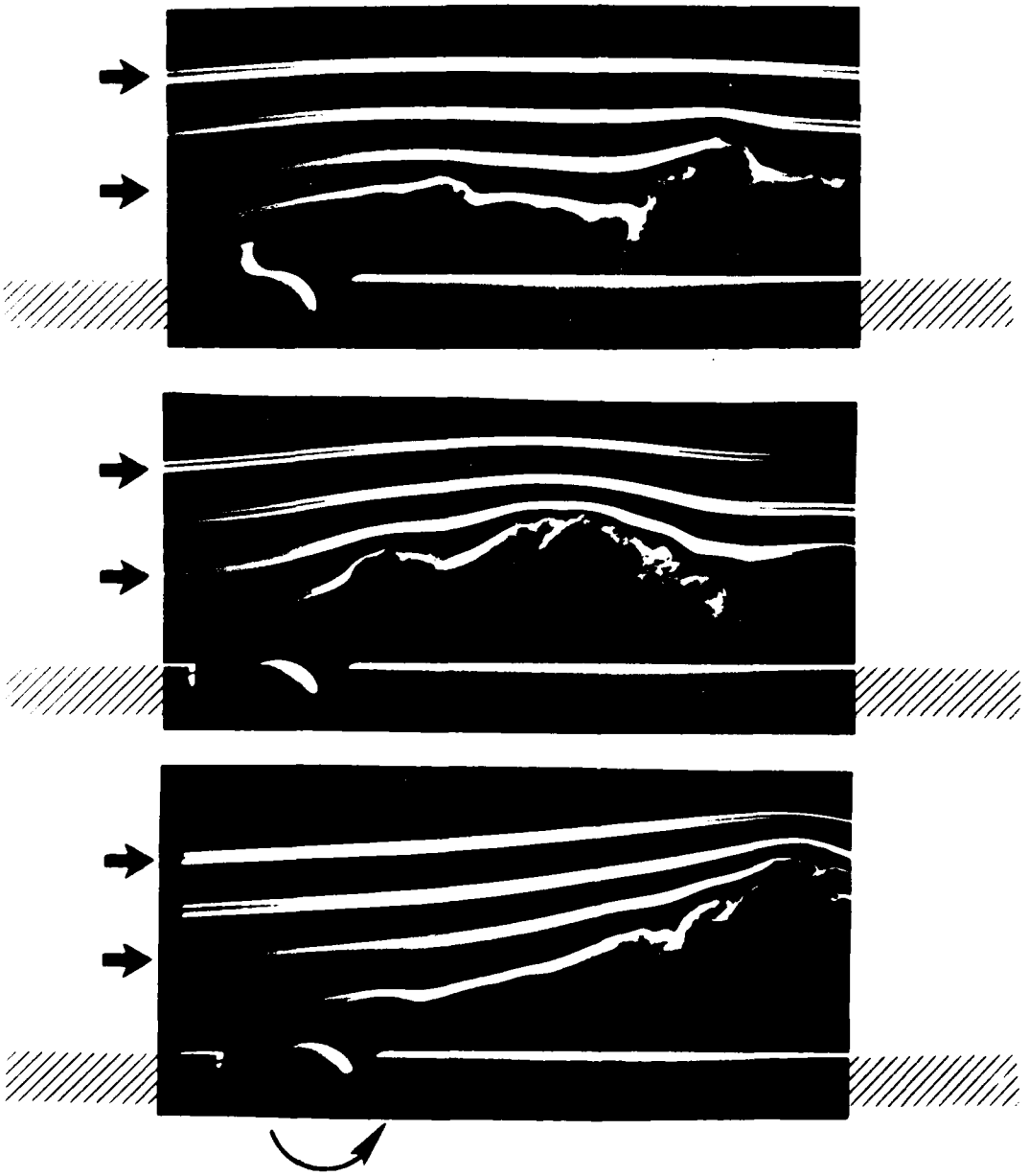

$\omega = +\ 1000$ rpm

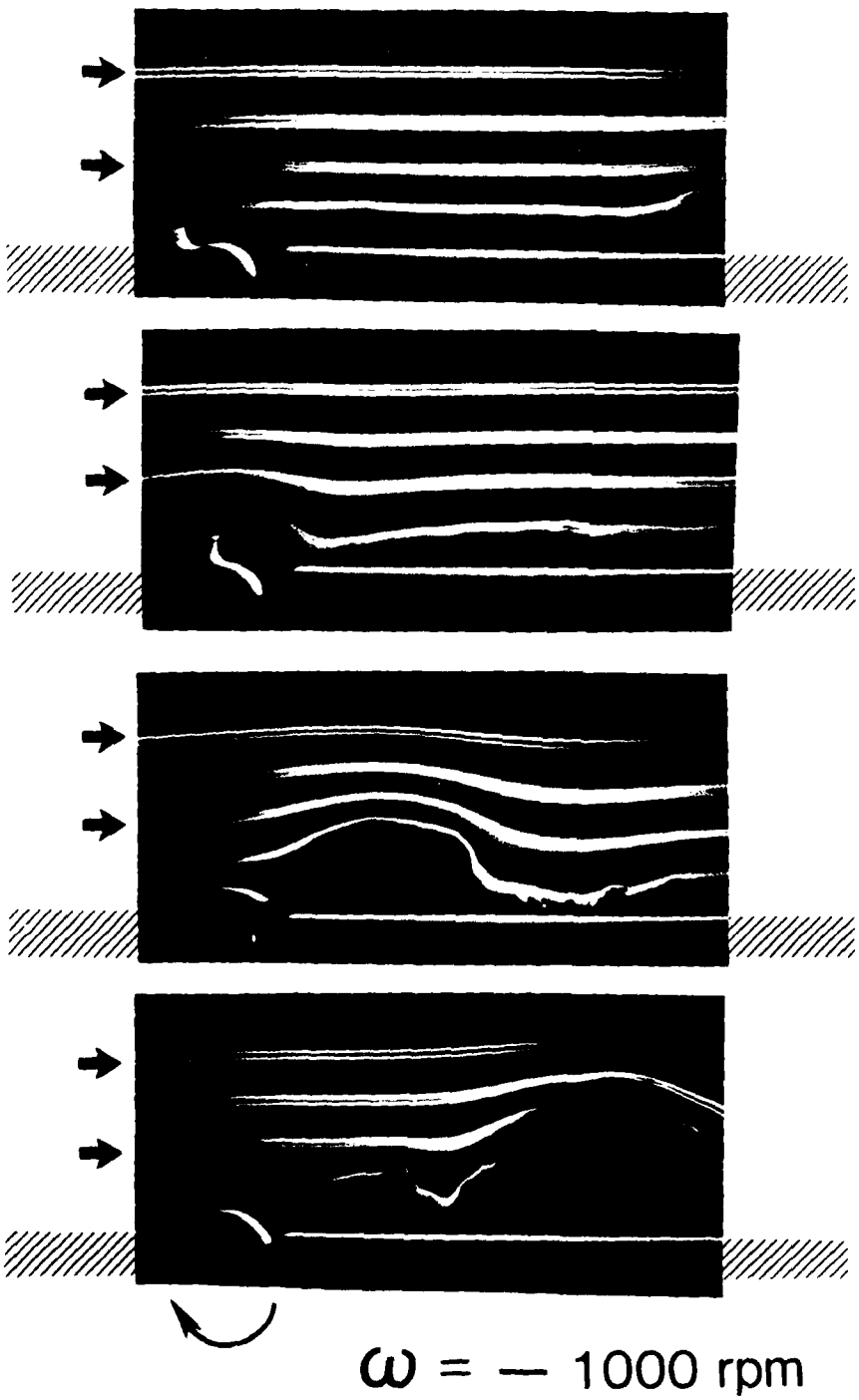

Figure 8. Flow visualization of vortex structure produced by the vortex generator with $\omega = -1000$ rpm.

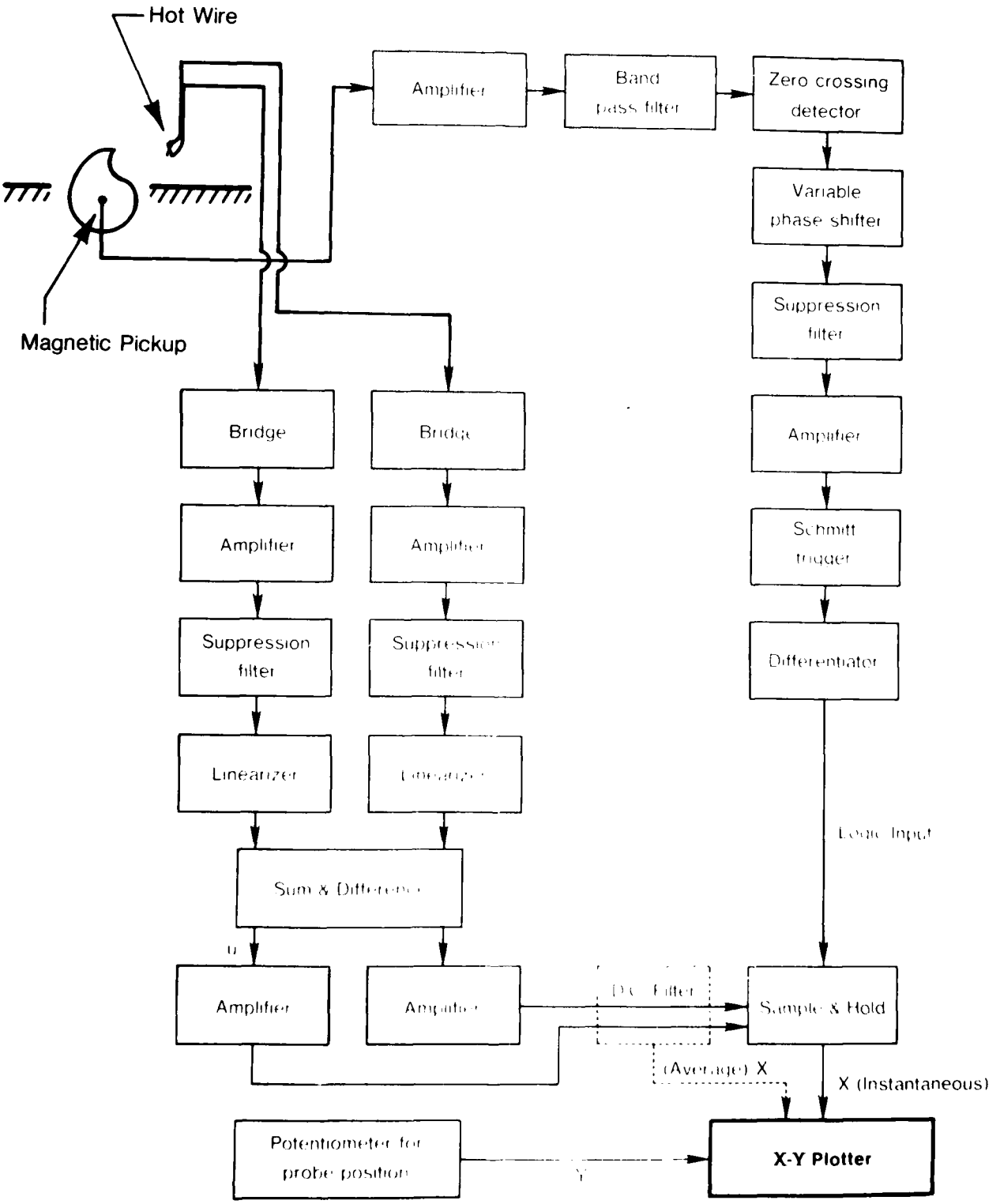

Figure 9. Schematic of conditioned sampling apparatus.

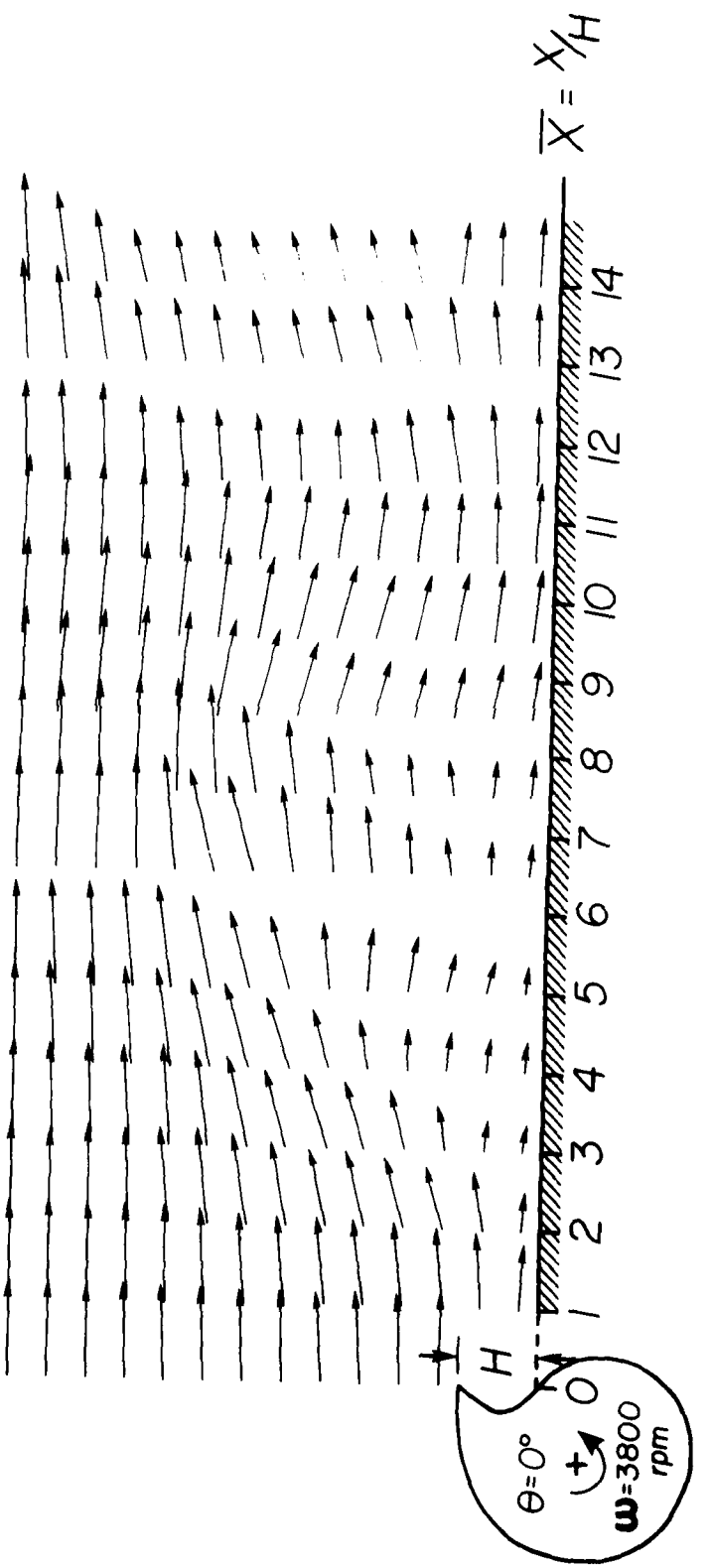

Figure 10a. Instantaneous velocity field with the rotor fully extended in the $\theta = 0°$ position.

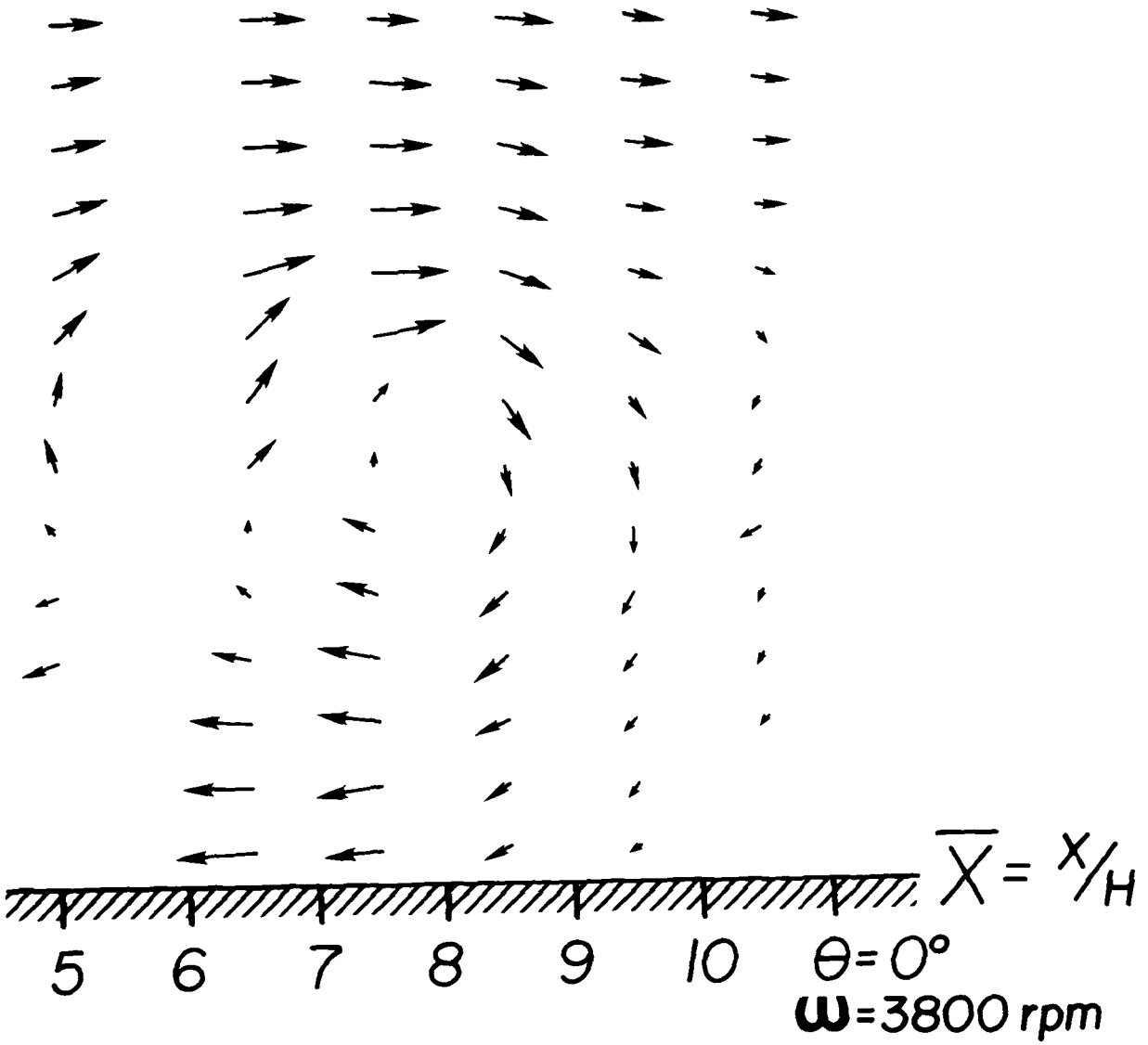

Figure 10b. Identification of a vortex structure in a reference frame moving at 11.5 m/sec.

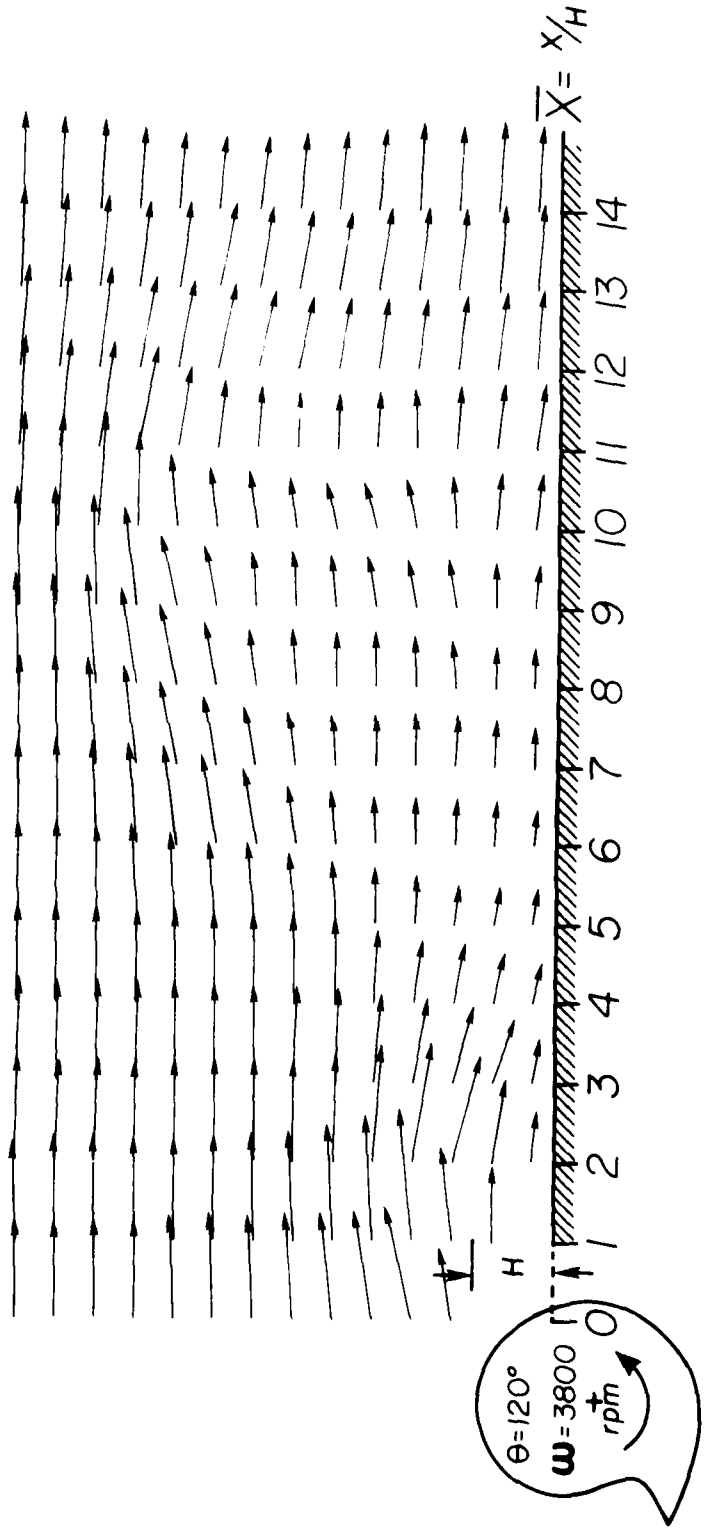

Figure 11a. Instantaneous velocity field with the rotor in the θ = 120° position.

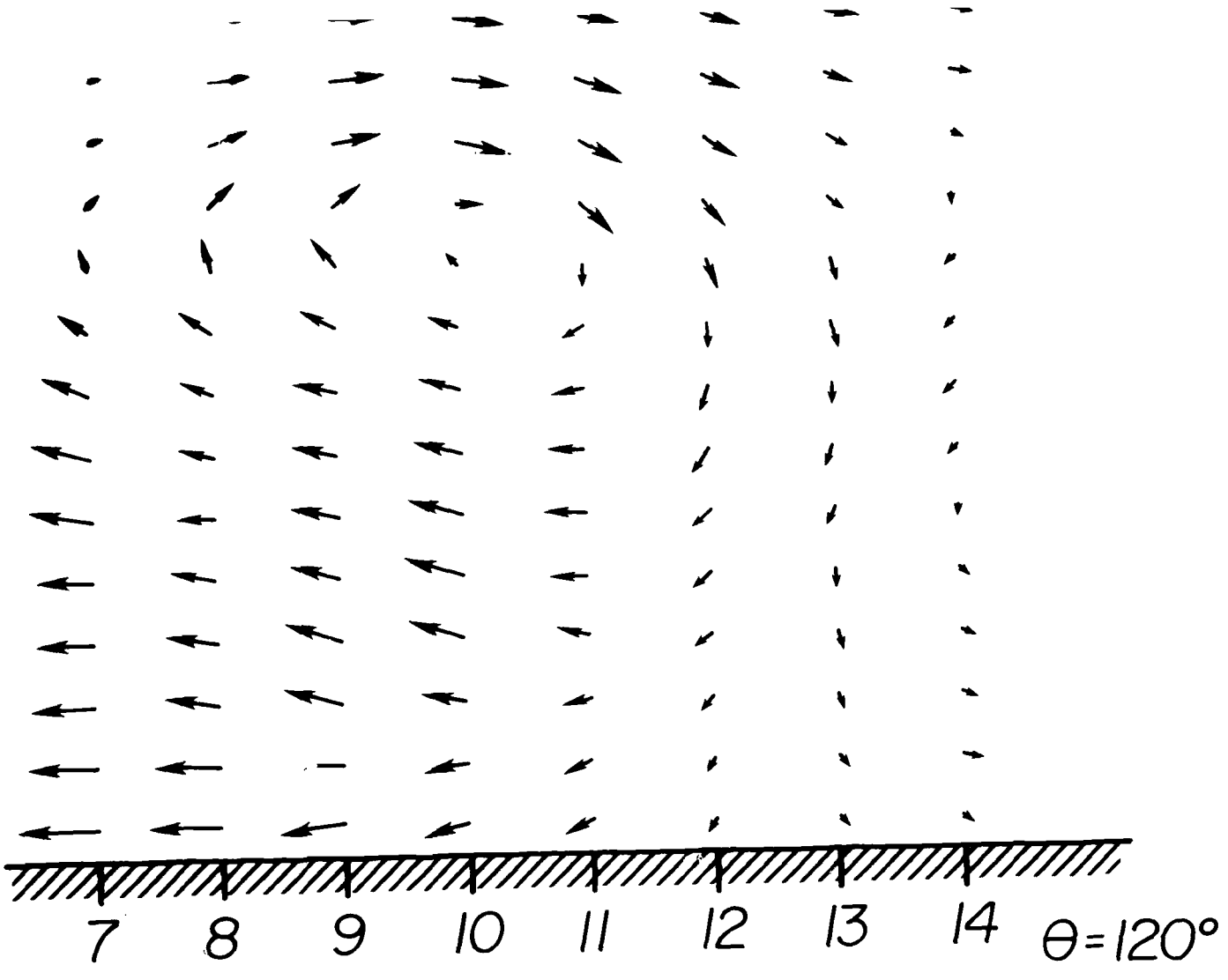

Figure 11b. Identification of a vortex structure in a reference frame moving at m/sec.

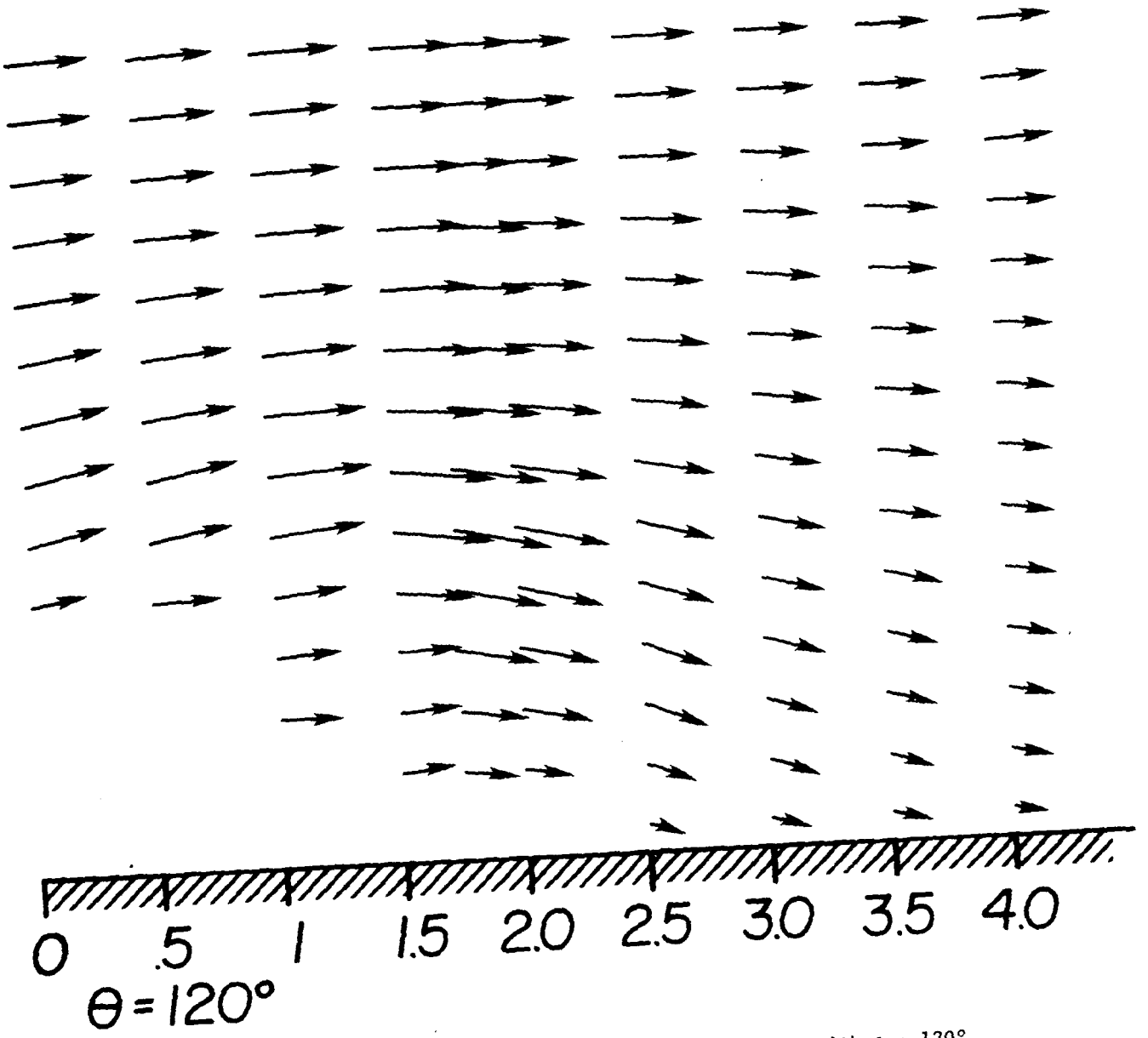

Figure 11c. More detail of the flow near the rotor with θ = 120°.

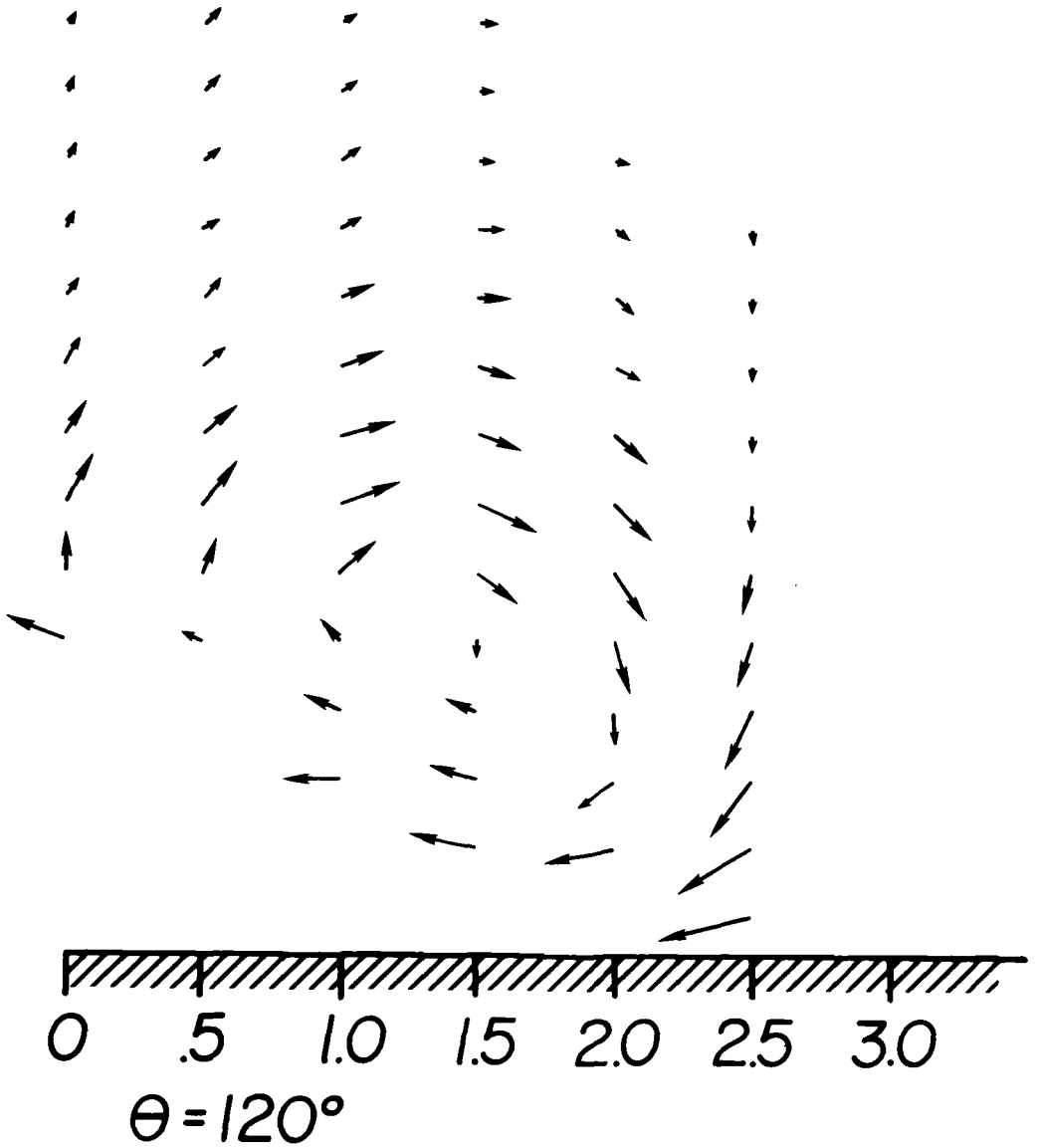

Figure 11d. Identification of a vortex structure in the flowfield of Figure 11c.

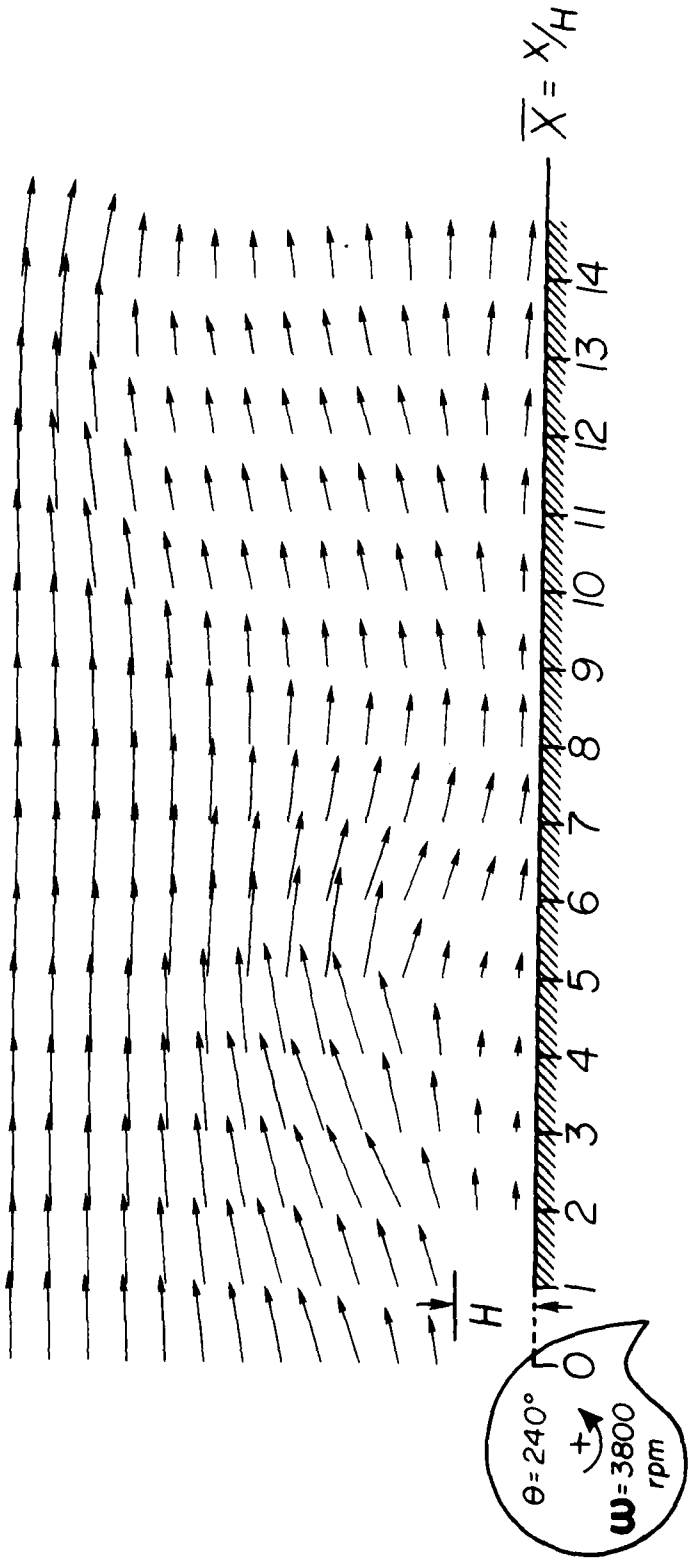

Figure 12a. Instantaneous velocity field with the rotor in the $\theta = 240°$ orientation.

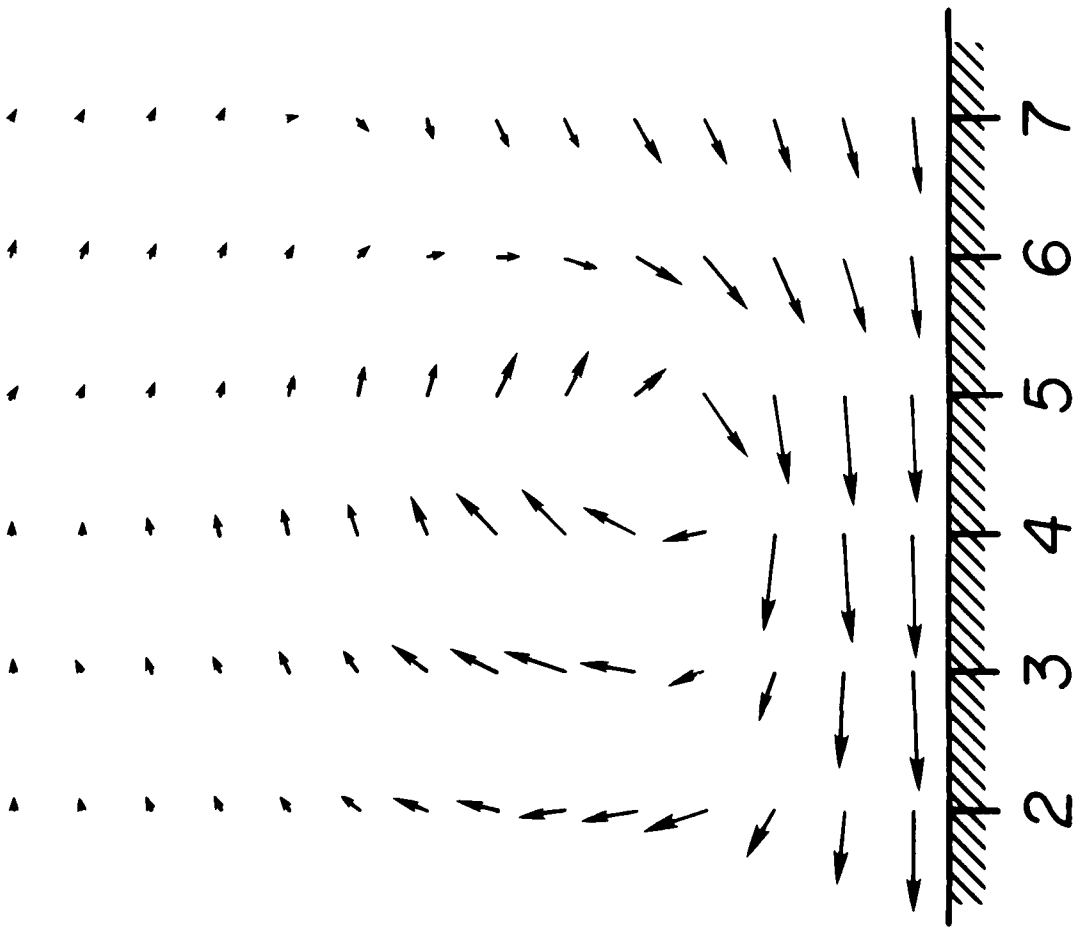

Figure 12b. Identification of a vortex structure in the flowfield of Figure 12a at $\bar{x} = 4.5$, $\bar{y} = 2.0$.

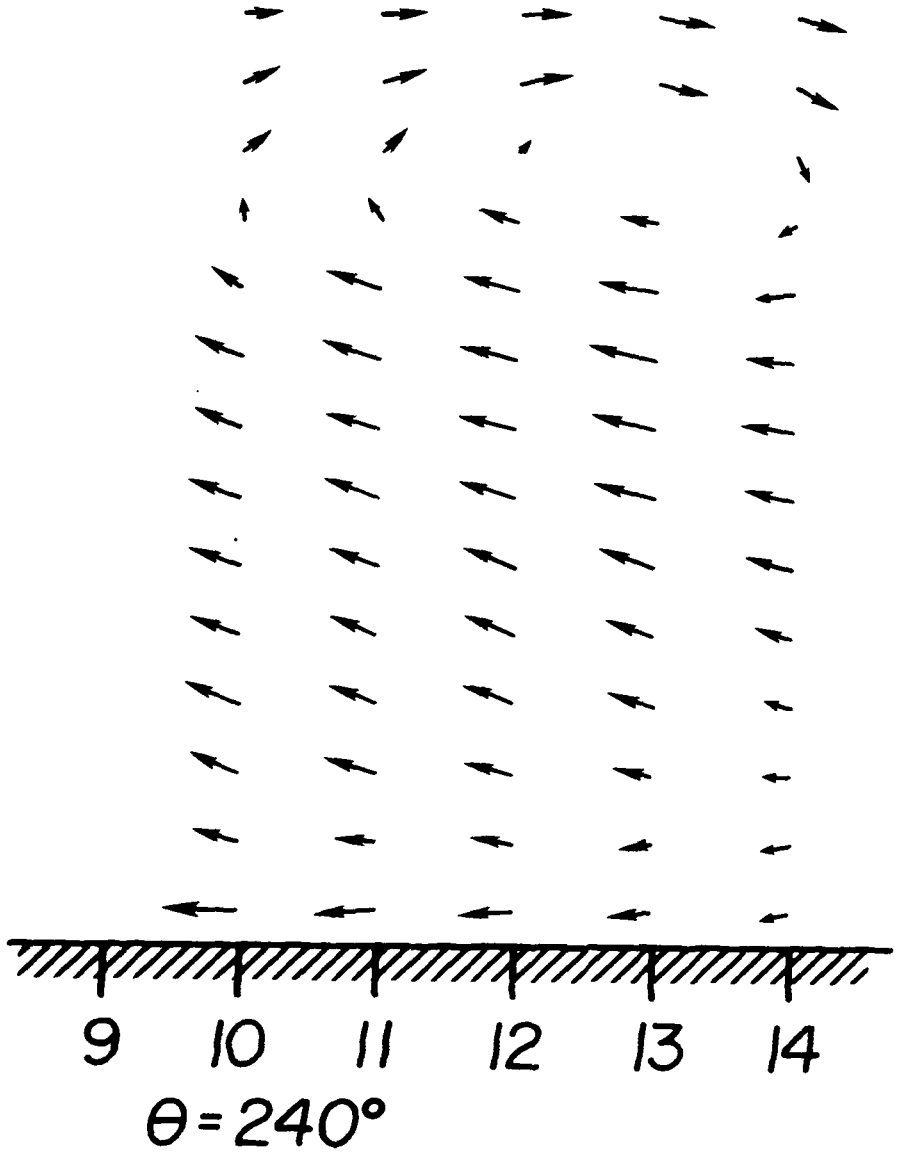

Figure 12c. Identification of a vortex structure in the flowfield of Figure 12a at $\bar{x}$ = 13.0, $\bar{y}$ = 5.75.

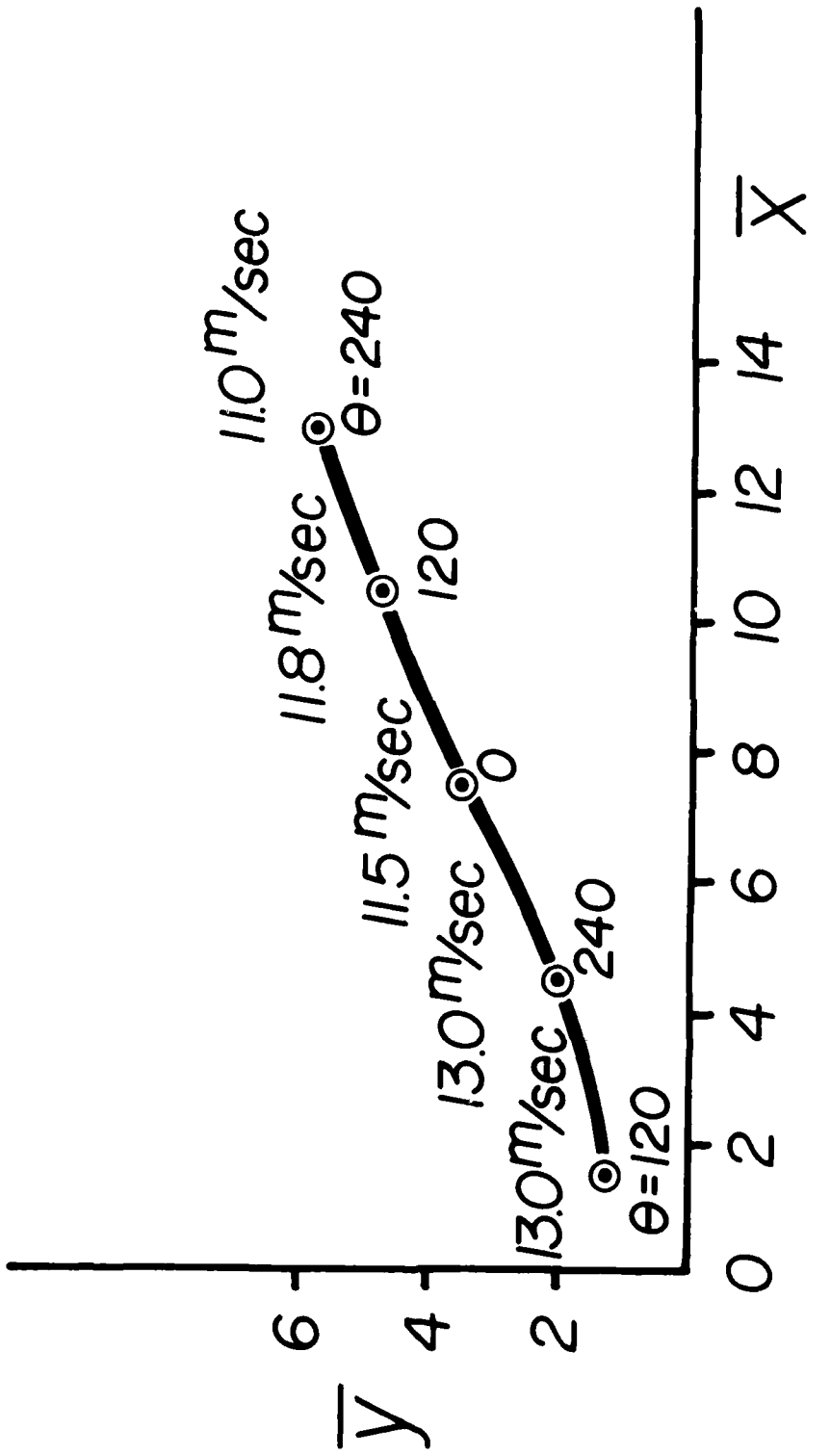

Figure 13. Trajectory of the vortex center as it moves downstream.

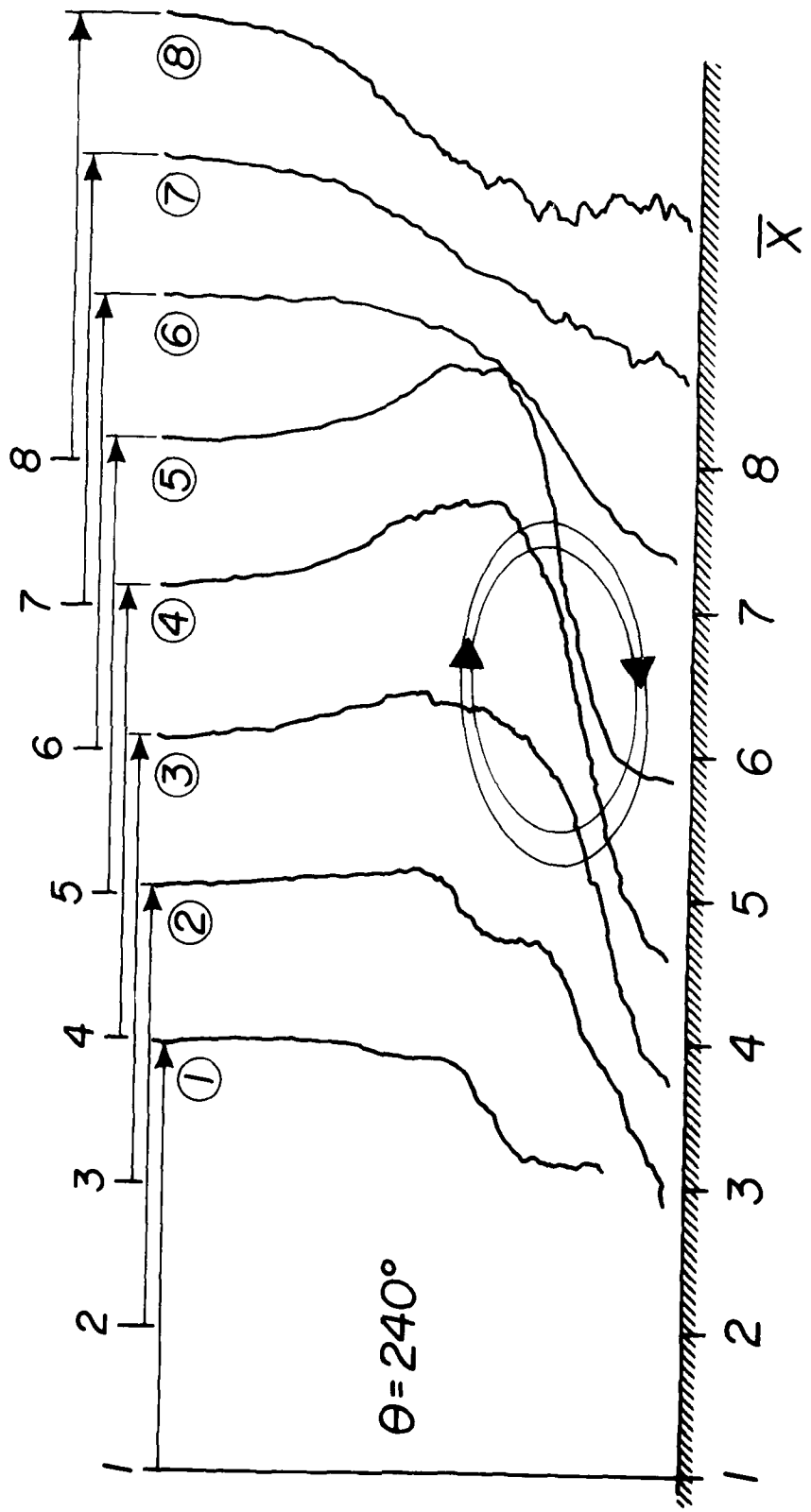

Figure 14. Influence of the Vortex on the Streamwise Velocity Profiles.

THREEDIMENSIONAL MEASUREMENTS NEAR THE STERN OF A DOUBLE MODEL OF A SHIP

J.Kux and K. Wieghardt
Institut für Schiffbau
der Universität Hamburg[+)]

1. Introduction

To supplement previous wind tunnel tests on the double model of a full ship the mean velocity field of the stern flow including the wake is investigated now with a five hole tube in several planes x = const (x in length direction) at a 3 by 3 mm grid in y-direction (sidewards) and z-direction (upwards). Whereas even a threedimensional boundary layer test is just a peep along an oblique ray into the jungle, the aim now is a general survey of the details of the mean flow. We know that vorticity is produced along the parallel midship with the vector $\vec{\omega} = \text{rot } \vec{v}$ directed girthwise around the main section and perpendicular to the main velocity or x-direction. Yet, lateron in the wake we usually find what looks like a strong longitudinal vortex pair, even when the bilge is well rounded off (as with our model) so that no bilge vortices are formed by separation there. Hence, the old question is: how are the vorticity lines bent and bundled?

2. Experimental apparatus

The double model of a full ship (length 2.74 m, breadth o.4o4 m. depth o.148 m) is suspended in the windtunnel with a slotted wall test section (diameter 1.2 m); speed is around 27 m/s giving a Reynolds number of $5 \cdot 1o^6$. Sections in the stern region are shown in Fig.1.

[+)] Support by Bundesministerium der Verteidigung and Deutsche Forschungsgemeinschaft is gratefully acknowledged.

A five hole tube (diameter 2.6 to 3 mm) is held always in x-direction; only tests with a positive pressure in the front hole are evaluated,- hence the blank regions near the body in Fig.2 to 5. Comparison with LDV-measurements had shown the reliability of this five hole tube as long as turbulent fluctuations are not excessive. From calibration the dimensionless velocities $u,v,w = U_{1,2,3}/U_\infty$ are found and the static pressure $p/\varrho U_\infty^2$. By graphical, resp.linear numerical differentiation in x- resp. y and z-direction all nine gradients of the mean velocities can be determined and the vorticity components $\omega_1 = w_y - v_z$, $\omega_2 = u_z - w_x$ and $\omega_3 = v_x - u_y$ $\left[1/m\right]$.

Unfortunately, continuity equation is not everywhere fulfilled correctly. Besides to numerical errors and turbulent fluctuations this might be due to the fact that any finite tube will somewhat straighten the flow in its neighbourhood. Hence, LDV-tests would be preferable but also more expensive, of course.

3. Preliminary results

Examples of the secondary, upwards and inwards flow in a transverse plane are plotted in Figs.2 to 7. Obviously, they suggest the existence of a longitudinal vorticity component ω_1 at least near and after the stern; lines of ω_1=const are shown in Figs.8 to 11, together with isotachs u = o.5, o.7 and o.9.*) At the end of the parallel midship, at x = -853 mm measured from the stern post, the highest values of ω_1 are near the bilge, yet, they are still smaller than 5/m. Near the stern and in the wake, at $-157 \leq x \leq 200$ mm, the maximum value of ω_1 is about the same in all sections, a little over 2o/m.

Near the "waterline" there is negative vorticity as well,

*) The line u = o.9 is distorted by the wake of a span wire below the keel.

though only of the order of -5/m. This might be due to a draw back of the double model technique where a more or less sharp edge on the waterline is unavoidable. Whenever the main flow has a turbulent fluctuation downwards there will be some separation on this edge and a vortex spiral with negative rotation (clockwise as seen from behind) is build up. Since we measure only time averages we find the upper part of the test section contaminated with such negative vorticity, and the secondary flow pushes this flow material towards the model hull.

In the wake a strange interaction between the measured starboard vorticity region and the opposite backboard region at x = 1oo mm is to be seen in Figs.6 and 11b. At x = 2oo mm the flow at the lower end of the vorticity region has become asymmetric in Fig.7. Since the testing time for a complete section with about 1ooo points was about one week, it is, in any case, amazing how regular and repeatable this weak secondary mean flow turns out to be.

Of the other two components of vorticity we can give a few examples only because differentiation in x-direction is not yet computerized. Figs.12 a and b show that even in the wake (at x = 1oo mm) longitudinal rotation ω_l is not the main component. Outside the core of the vorticity region the angle between velocity and vorticity is usually about 80°. This is also to be seen from Table I where the three ω-components are calculated at the point z = 0, y = 42 mm (marked in Fig.1) for four sections at x = -63, -53, -38 and -19 mm. At greater distances from the body (i.e.for increasing x) the angle $\sphericalangle\, \vec{v},\vec{\omega}$ approaches 90° and the two acceleration terms in $\vec{a} = \text{grad}\, \vec{v}^2/2 - \vec{v} \times \vec{\omega}$ almost cancel each other to give - with the small pressure gradient - small Reynolds stresses. Hence, the vorticity lines there are spirals with low pitch.

4. Comparison with tests in water

At Hamburg Towing Tank, HSVA, J.Laudan has made LDV-measurements of the nominal wake just in front of the propeller plane of a towed model (length 7.846 m, C_B = o.7544, Re = $12.4 \cdot 1o^6$) without propeller. Evaluation of these tests gives Fig.13 for the axial vorticity ω_1. Unfortunately, since for these tests the propeller was taken off together with its boss, there is now a strong separation region with positive ω_1 (anticlockwise) which should not be here at the port side. Hence, this is certainly not typical. On the model in the wind tunnel a cone (120^o) simulates the stern post tail.

A first rough guess for the order of magnitude of mean vorticity ($\omega_{2,3}$) produced in the boundary layer would be U_∞/δ with δ = boundary layer thickness. Along a plate δ is - after tests by K.G.Winter and L.Gaudet up to Re = $2 \cdot 1o^8$ - (RAE Techn Rep. 7o251, 197o):

$$\delta = o.o85 \; L \; Re^{-o.1} \pm 3\ \% \text{ for } 1o^6 \leqslant Re \leqslant 1o^9.$$

This would give for $|\omega| \sim 1/\delta$

wind tunnel	towing tank (model scale 1:26)	ship
L = 2.74 m	7.846 m	2o4 m
U_∞ = 27 m/s	1.82 m/s	9.28 m/s
ν = $15 \cdot 1o^{-6}$ m^2/s	$1.15 \cdot 1o^{-6}$ m^2/s	$1.15 \cdot 1o^{-6}$ m^2/s
Re = $5 \cdot 1o^6$	$12.4 \cdot 1o^6$	$1.65 \cdot 1o^9$
$1/\delta$ = 20/m	7.7/m	o.5/m.

By chance, these figures[+)] correspond not only to the order of magnitude but rather directly to the experimental findings for the maximum of ω_1 in air and in water. Hence, at least for the extrapolation model to ship this simple rule should be good enough.

[+)] for $1/\delta$

5. Conclusions

The original aim to retrace vorticity lines to their origin on the model and to find separation regions has not been reached because the axially directed five hole tube does not give reliable data near the body. These blank regions should be investigated rather by hot wires.

Further computation of all three vorticity components in the whole field - except near to the wall - will give a more realistic view of the main flow there.

Last not least, all test data are available, of course, to check calculation methods.

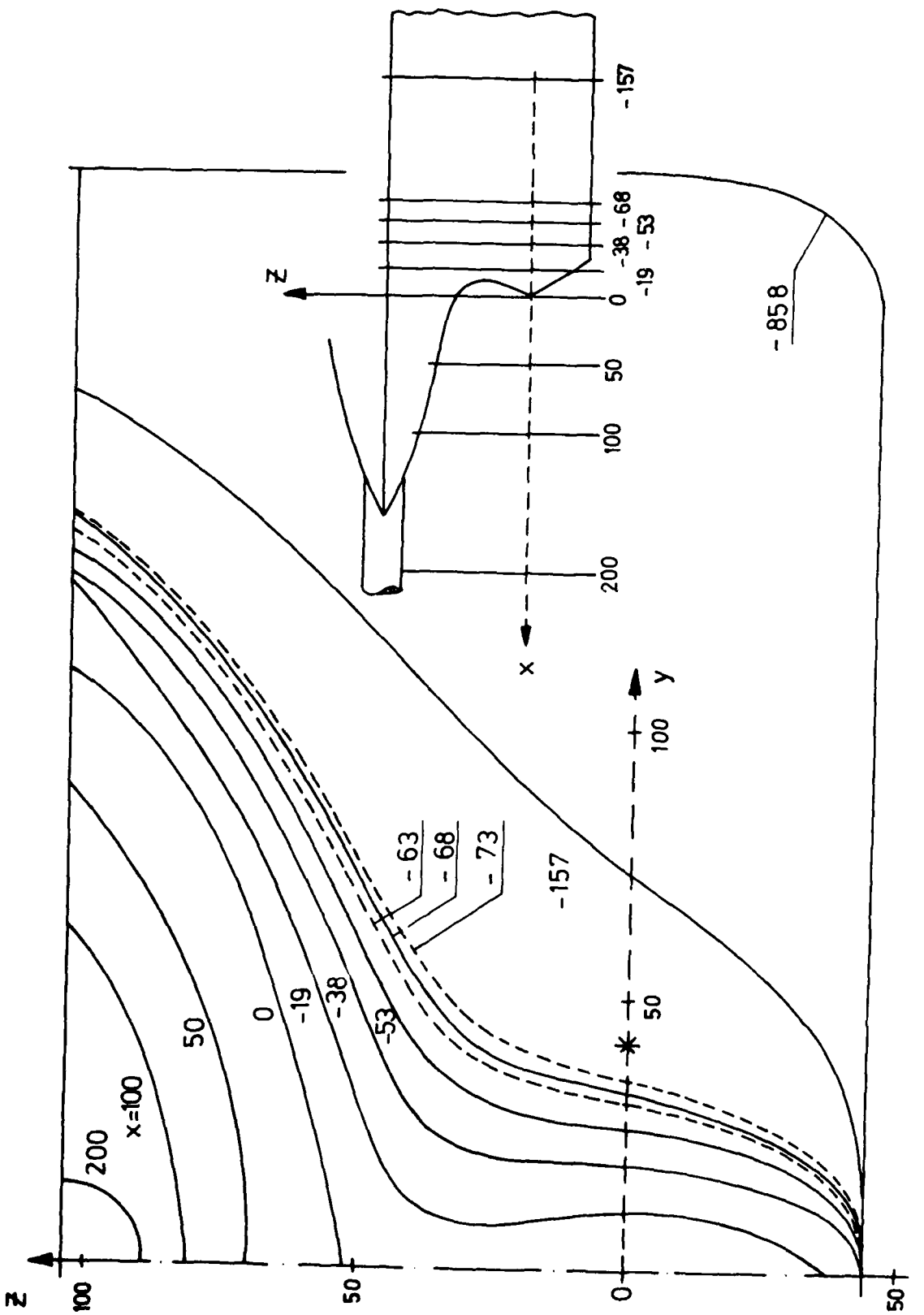

Fig.1 Transverse sections in the test planes x = const near the stern
x in axial direction, y sidewards (starboard), z upward.

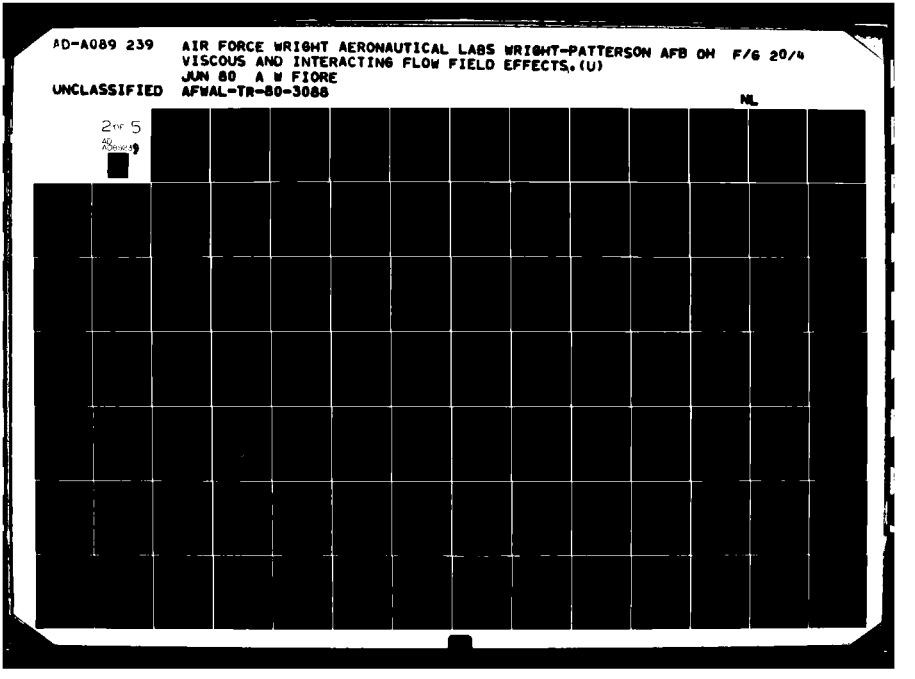

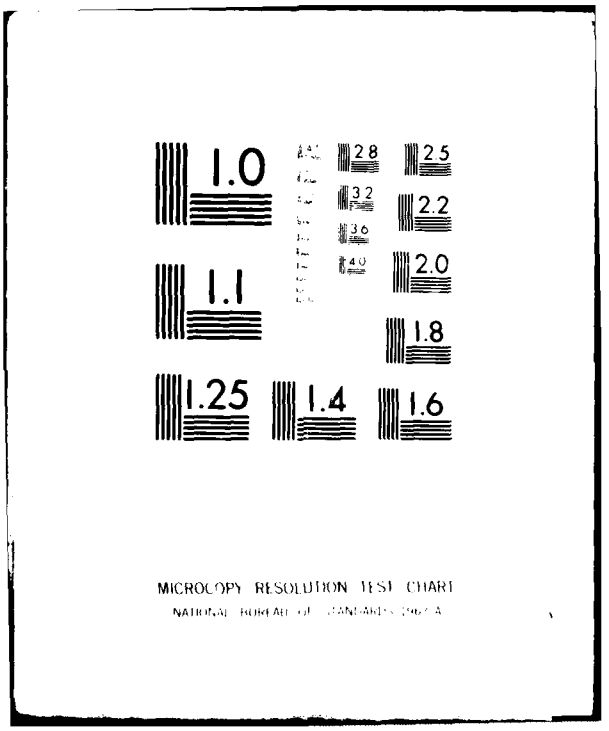

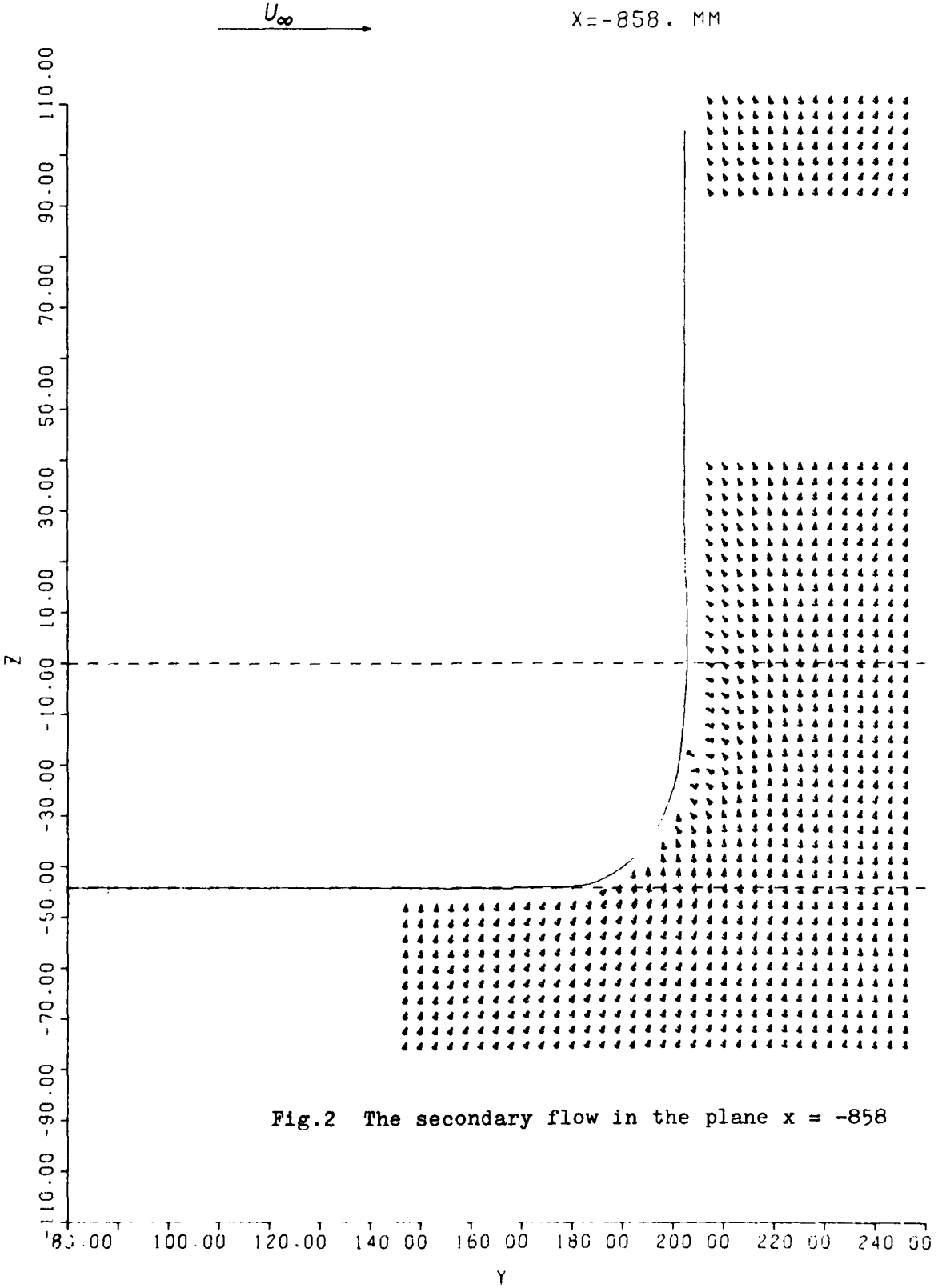

Fig.2 The secondary flow in the plane x = -858

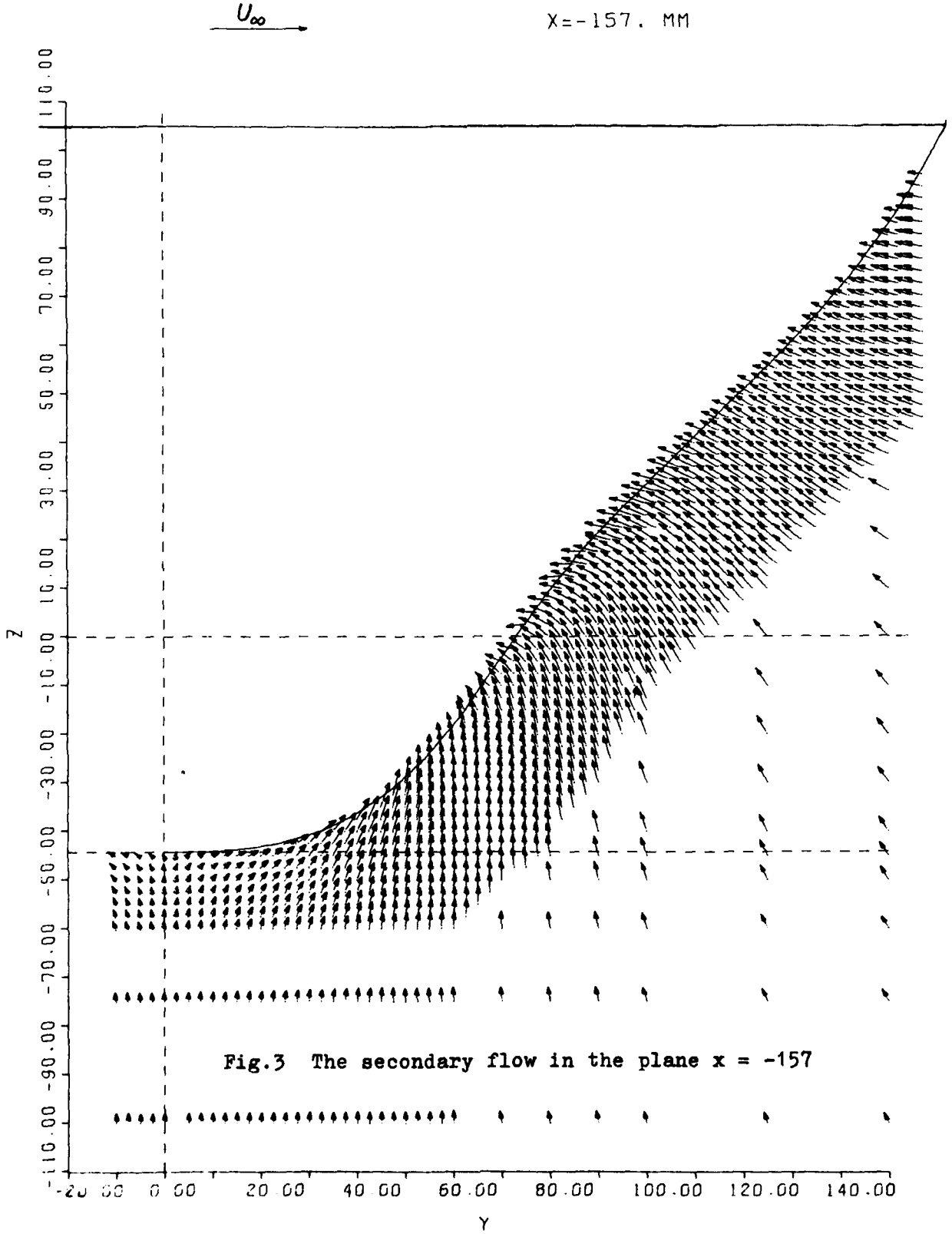

Fig.3 The secondary flow in the plane x = -157

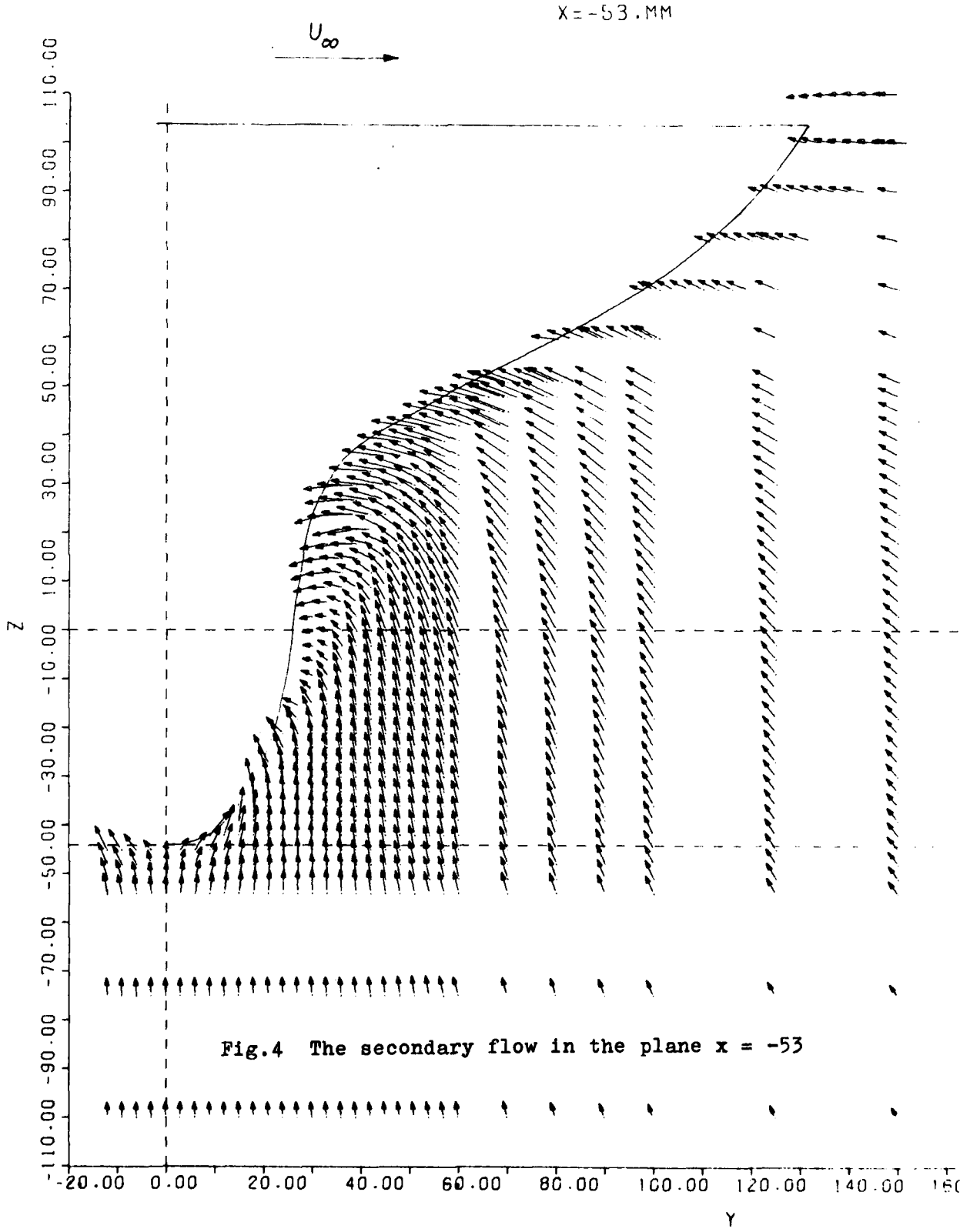

Fig.4 The secondary flow in the plane x = -53

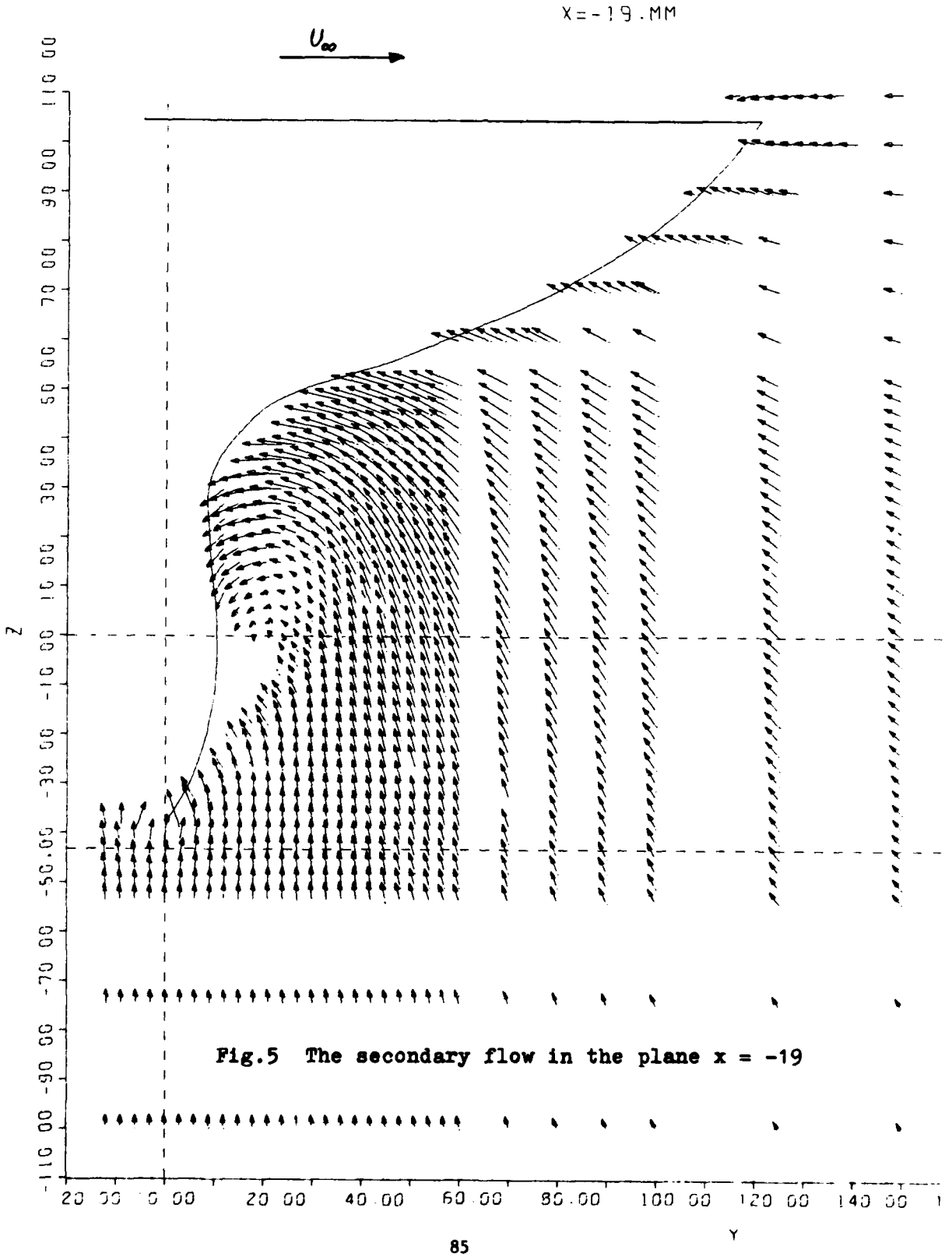

Fig.5 The secondary flow in the plane x = -19

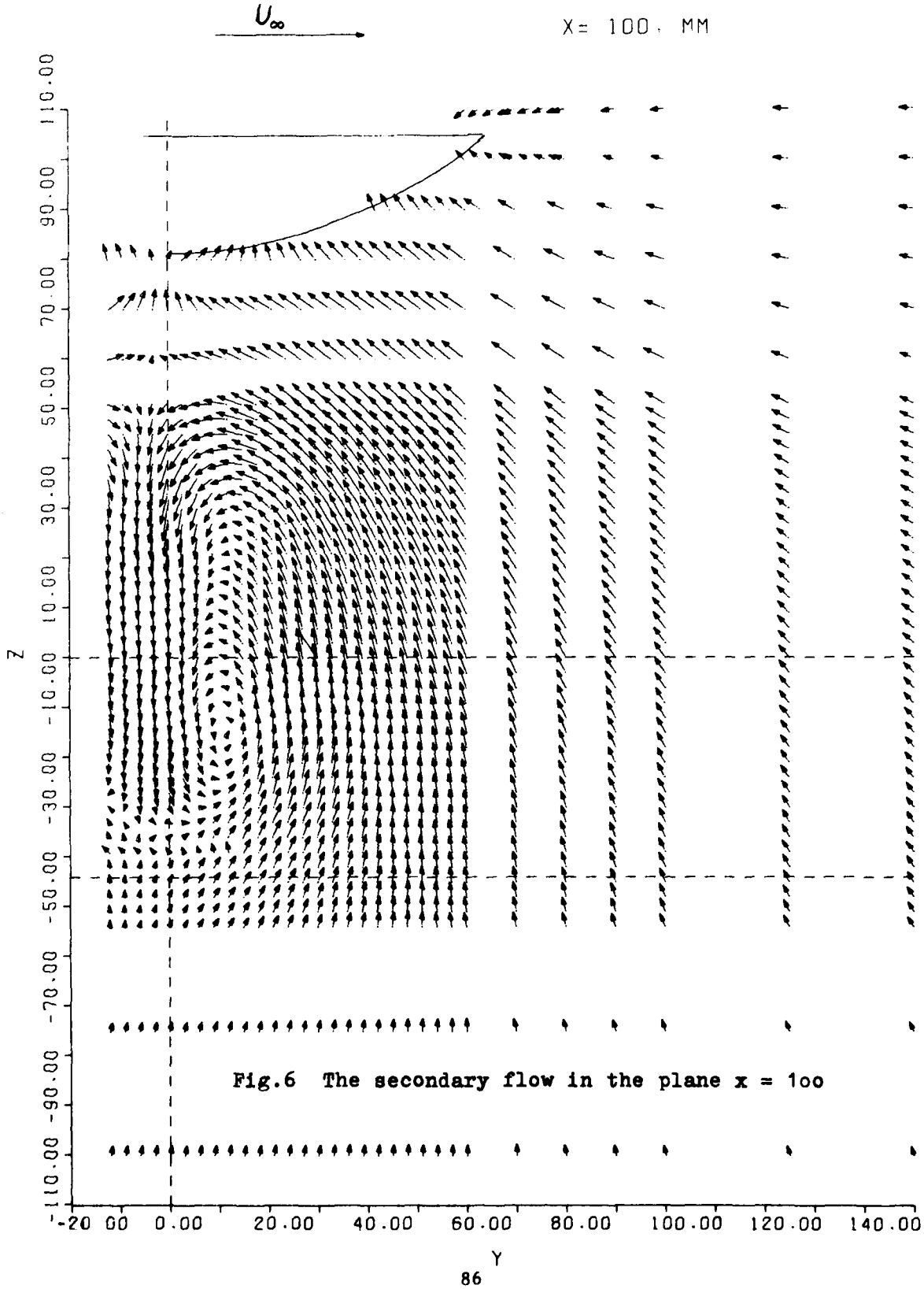

Fig.6 The secondary flow in the plane x = 1oo

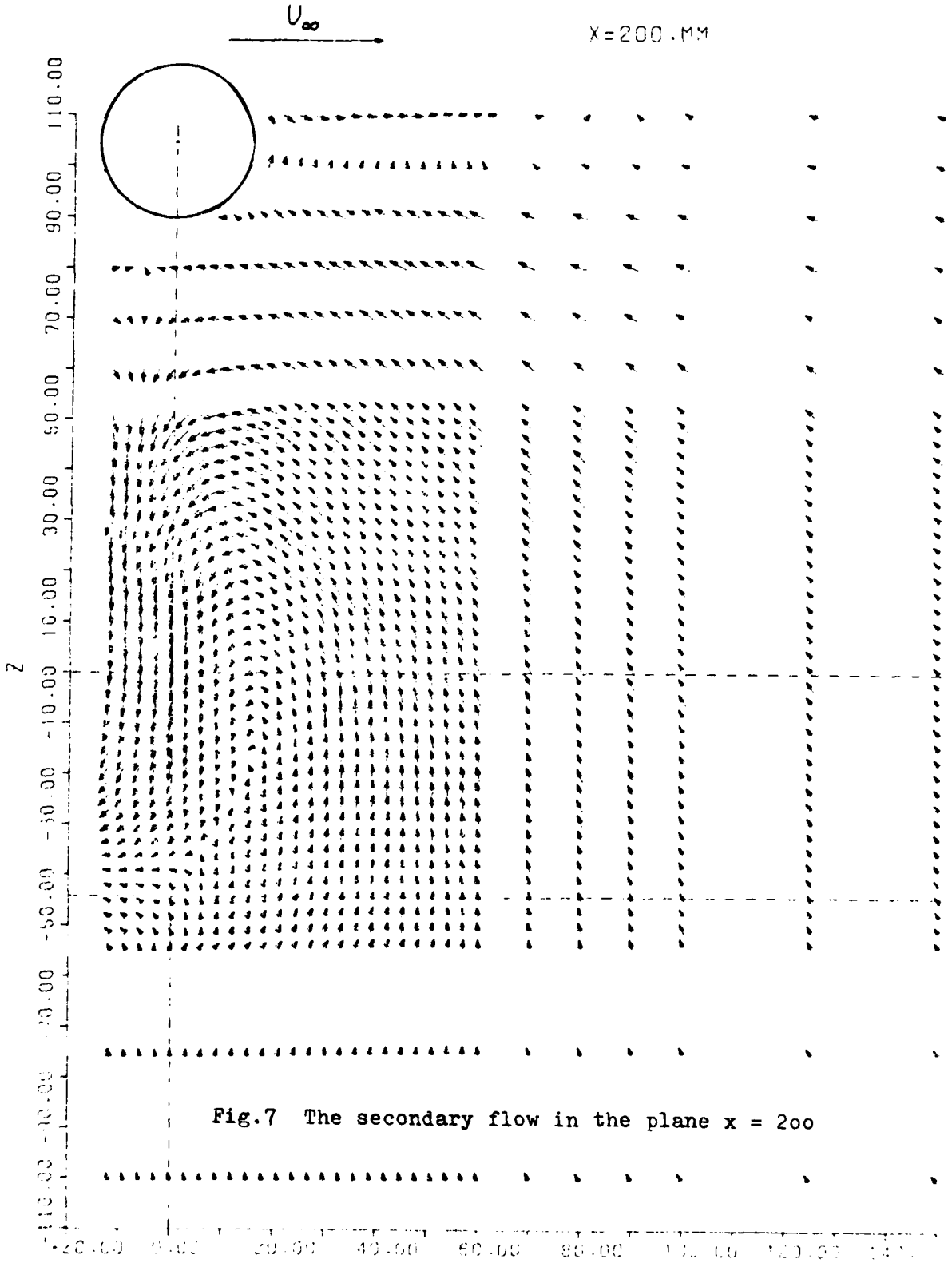

Fig.7 The secondary flow in the plane x = 2oo

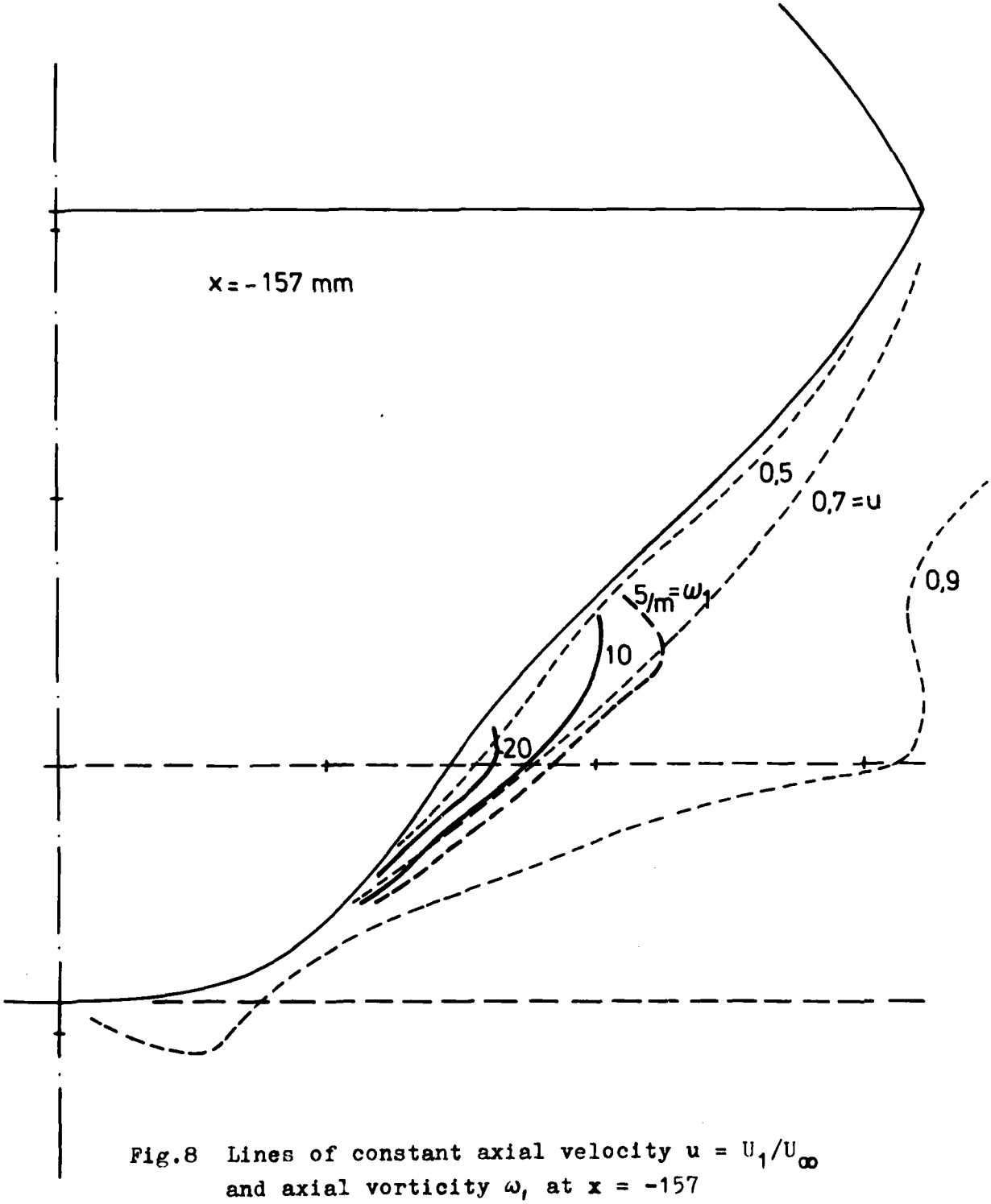

Fig.8 Lines of constant axial velocity $u = U_1/U_\infty$ and axial vorticity ω_1 at x = -157

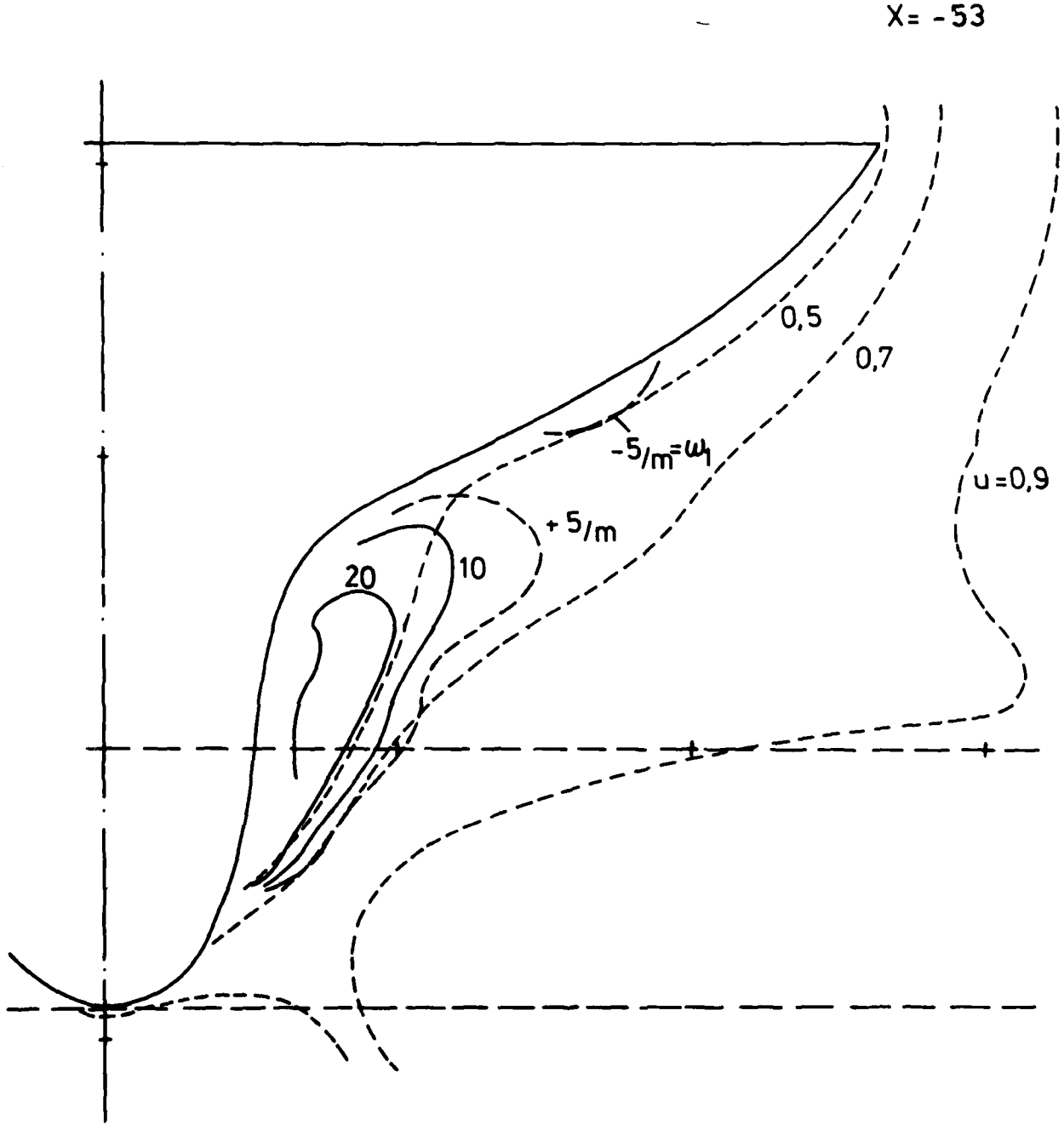

Fig. 9 Lines of constant axial velocity $u=U_1/U_\infty$ and axial vorticity ω_1 at section x= -53 .

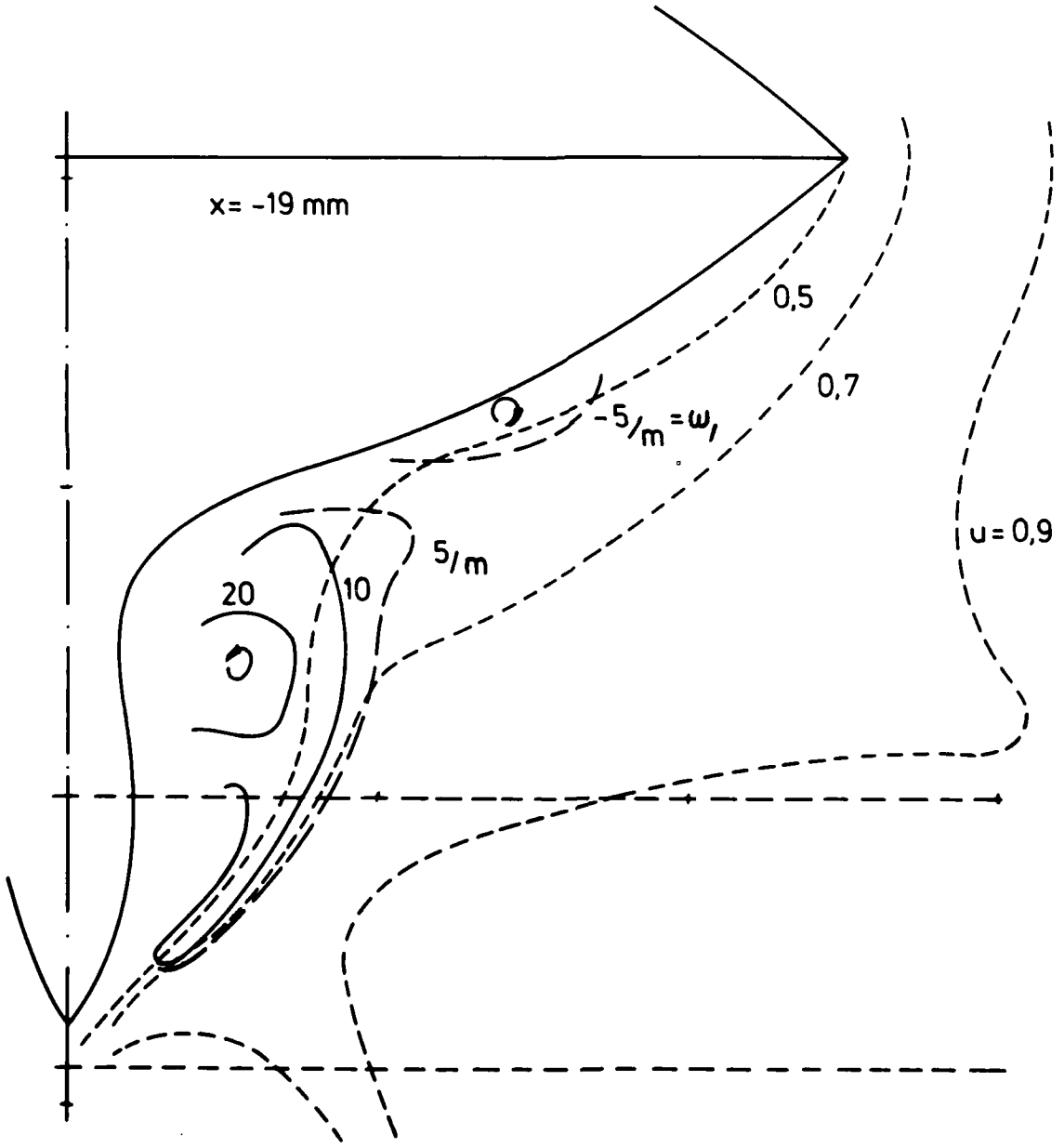

Fig.1o Lines of constant axial velocity $u = U_1/U_\infty$ and axial vorticity ω, at x = -19

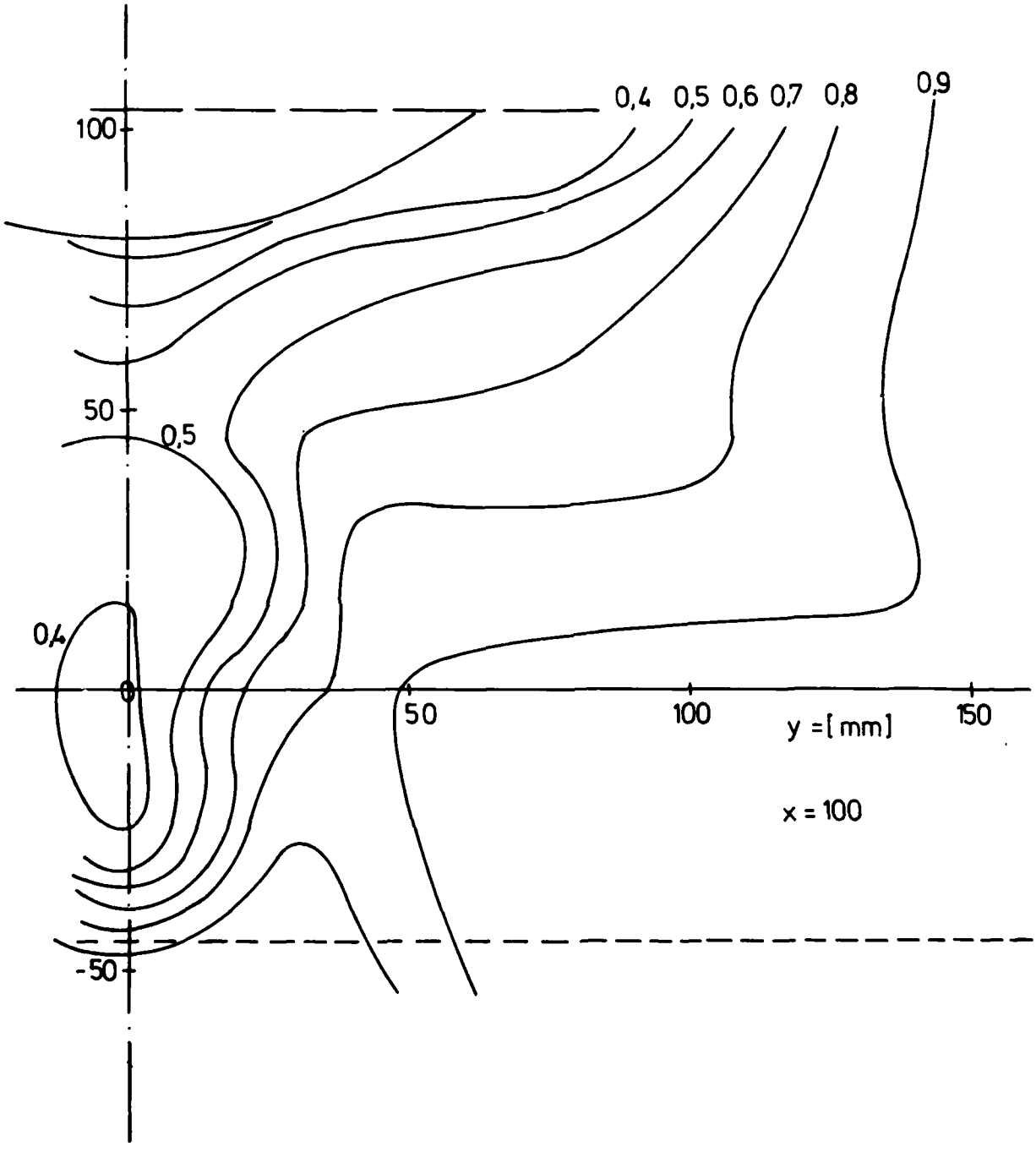

Fig.11 a Lines of constant axial velocity $u = U_1/U_\infty$ at x = 1oo

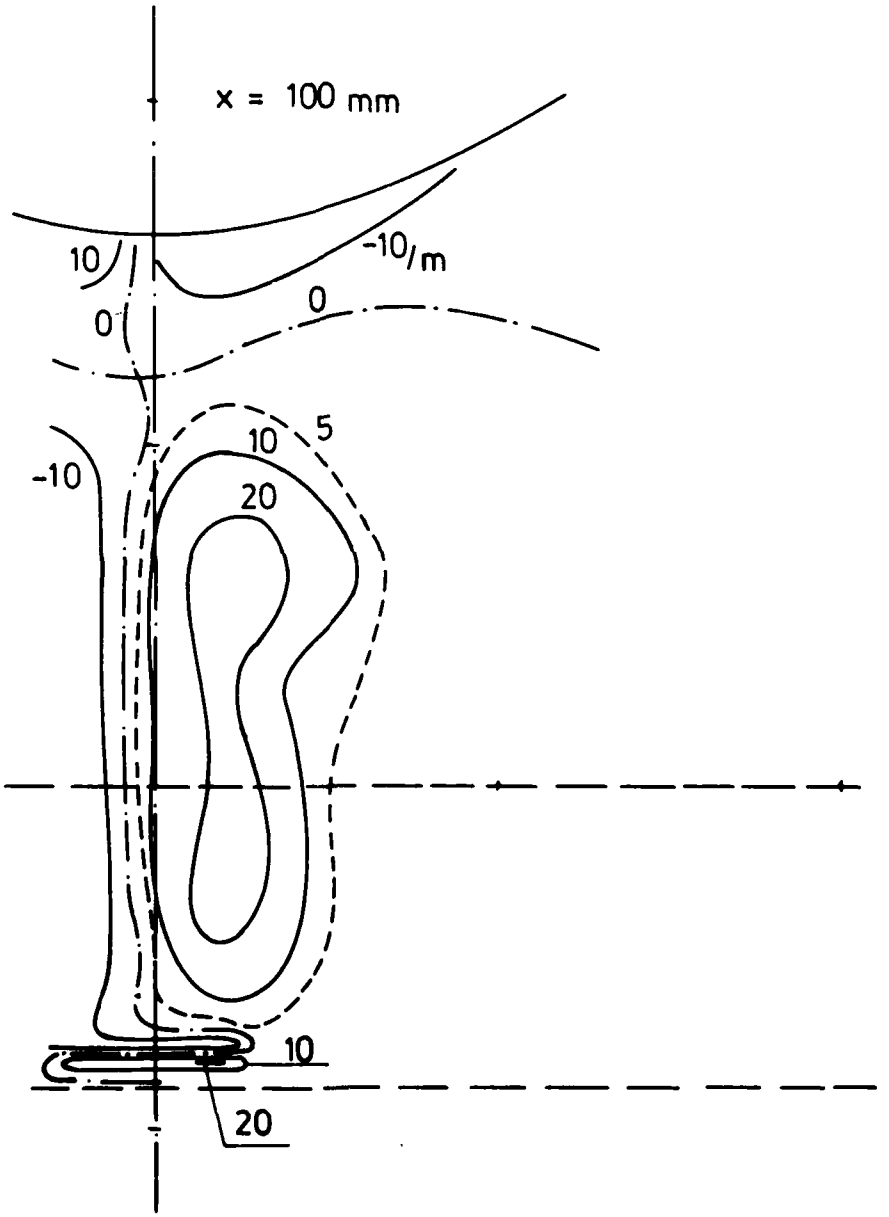

Fig.11 b Lines of constant axial vorticity at x = 1oo

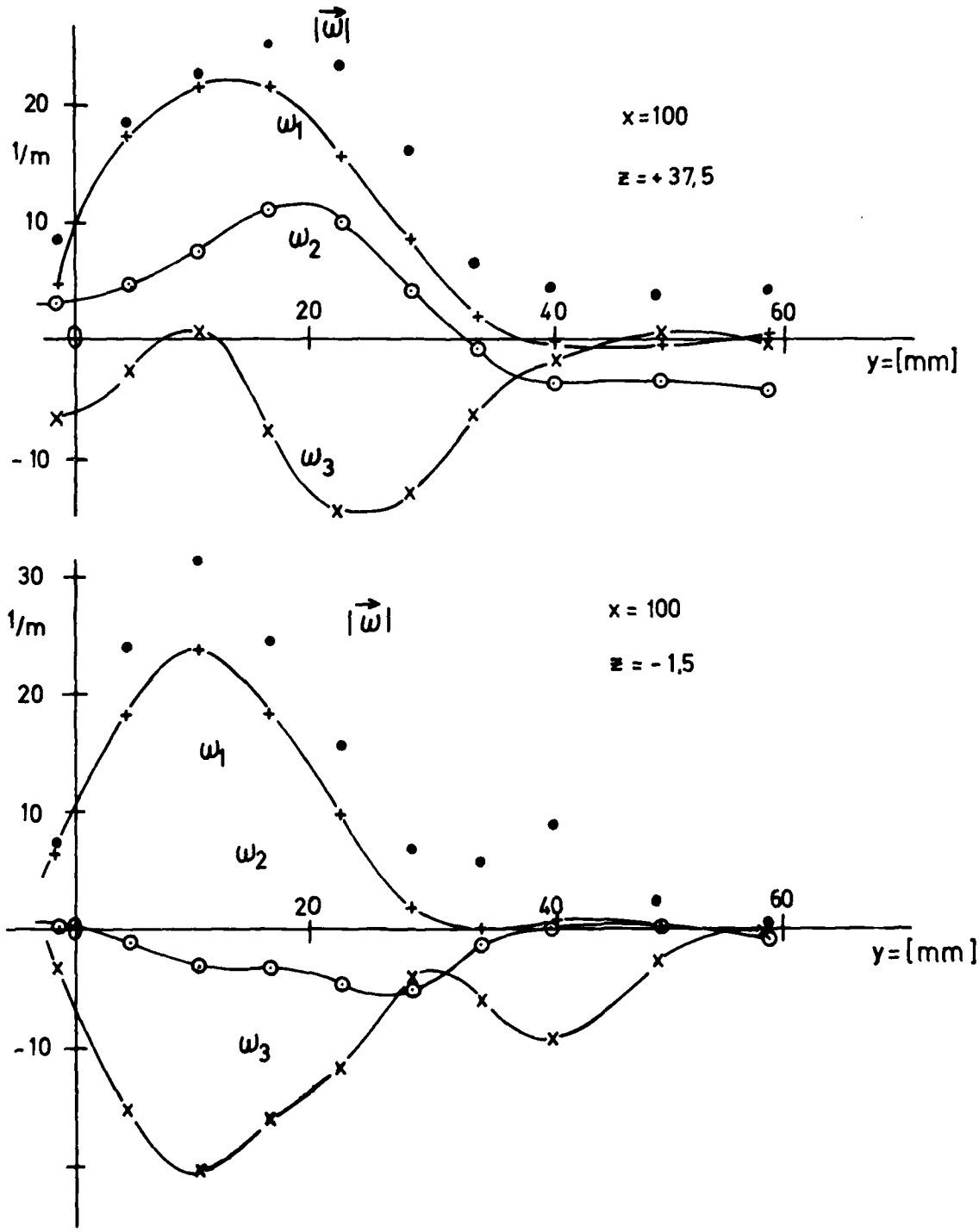

Fig.12 a All three vorticity components at x = 1oo, z = 37.5 and z = -1.5

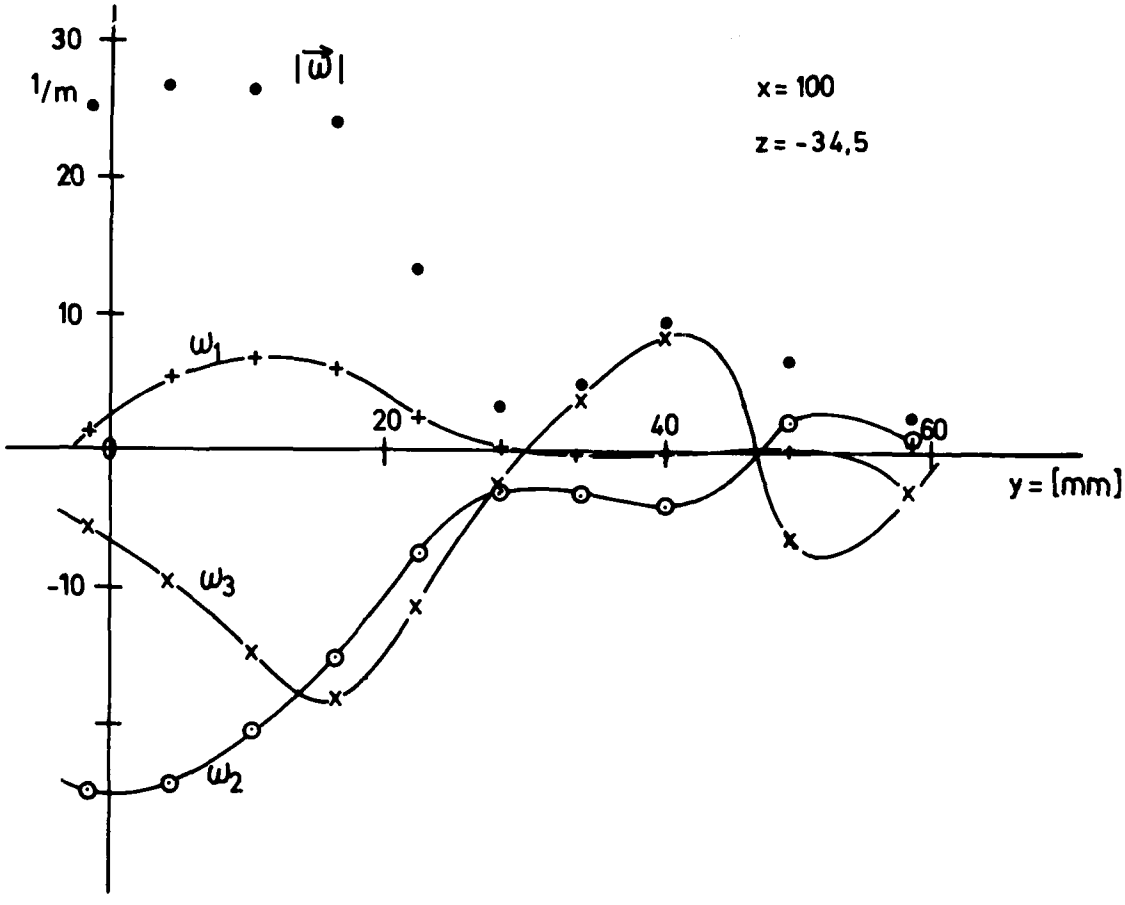

Fig.12 b All three vorticity components
at x = 1oo and z = -34.5

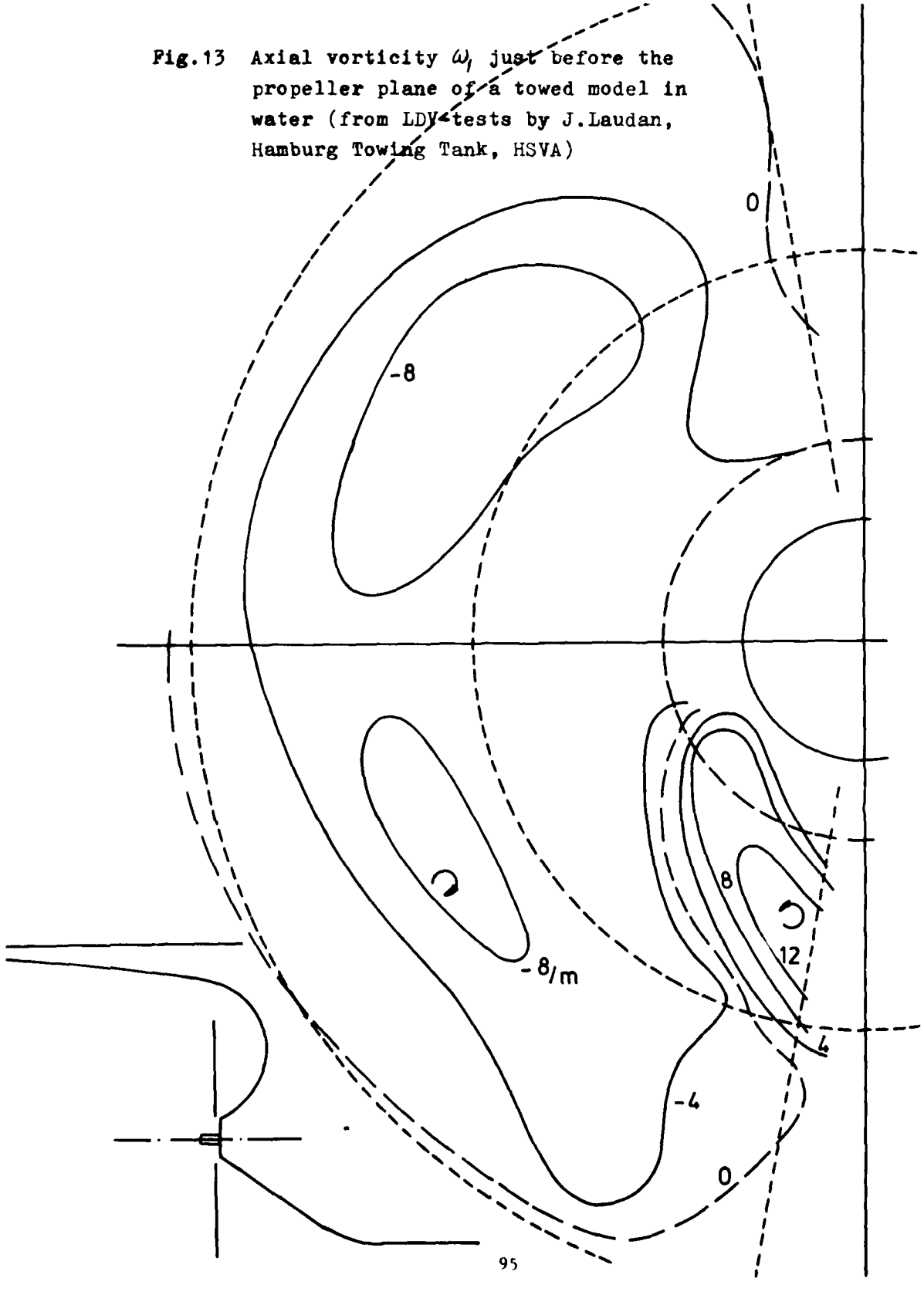

Fig.13 Axial vorticity ω_1 just before the propeller plane of a towed model in water (from LDV-tests by J.Laudan, Hamburg Towing Tank, HSVA)

x [mm]	$\vec{v} = \vec{U}/U_\infty$ $\lvert\vec{v}\rvert$ [—]	grad $\vec{v}^2/2$ $\lvert\text{grad}\,\vec{v}^2/2\rvert$ [1/m]	$\vec{\omega}$ $\lvert\vec{\omega}\rvert$ [1/m]	$\vec{v}\times\vec{\omega}$ $\lvert\vec{v}\times\vec{\omega}\rvert$ [1/m]	$\vec{a}$ $\lvert\vec{a}\rvert$ [1/m]	grad $p/\rho U_\infty^2$ [1/m]	$\frac{\lvert\vec{v}\times\vec{\omega}\rvert}{\lvert\text{grad}\,\vec{v}^2/2\rvert}$ $\sphericalangle\,\vec{v},\vec{\omega}$ $\sphericalangle\,x,\vec{v}$ $\sphericalangle\,x,\vec{\omega}$
-19	0.719	2.59	5.0	3.88	-1.29	0.34	1.052
	-0.067	15.18	-10.5	15.80	-0.62	-0.3	87.7°
	0.240	-7.00	-20.3	-7.22	0.22	0.6	19.1°
	0.761	16.92	23.4	17.80	1.45		77.1°
-38	0.609	4.32	11.5	6.06	-1.74	0.41	1.026
	-0.068	20.12	-17.4	20.62	-0.50	-0.3	85.2°
	0.234	-10.13	-29.5	-9.82	-0.48	~0	21.8°
	0.656	23.01	36.1	23.6	1.87		71.4°
-53	0.501	4.13	18.4	5.92	-1.79	0.76	1.015
	-0.079	18.37	-18.3	18.47	-0.10	~0	77.7°
	0.195	-8.34	-29.7	-7.71	-0.63	-0.65	22.8°
	0.543	20.59	39.4	20.9	1.90		62.2°
-63	0.410	3.60	25.5	5.73	-2.13	1.0	0.929
	-0.110	16.87	-21.6	15.23	1.64	~0	61.7°
	0.113	-7.31	-30.1	-6.07	-1.24	-0.9	21.0°
	0.439	18.73	45.0	17.4	2.96		55.5°

Table I

At z = 0, y = 42 mm and $-63 \leqslant x \leqslant -19$ mm (cf.Fig.1): mean velocity $\vec{v} = \vec{U}/U_\infty$, vorticity $\vec{\omega} = \text{rot}\,\vec{v}$, mean acceleration $\vec{a}$, pressure gradient and the angles between velocity, vorticity and axial direction x. (N.B.The vorticity measure $\lvert\vec{v}\times\vec{\omega}\rvert/\lvert\text{grad}\,\vec{v}^2/2\rvert$ seems to increase with wall distance.)

Survey on Integral Methods for Turbulent Boundary Layers with Prehistory Phenomena

by Alfred WALZ
Technical Universities of Berlin and Karlsruhe

1. Introduction

In the Wake Region of Turbulent Boundary Layers large scale eddies are convecting their turbulent energy downstream with a small rate of dissipation and, consequently, with a long life-time. In the "Law-of-the-Wall-Region", however, the prevailing very small eddies are dissipating their energy within very short time, i.e. about locally. Both layers are continuously interacting with regard to mass, momentum, and energy. For a given steady-state streamwise pressure distribution $p(x)$ in many cases an equilibrium situation between these two layers is approached after a certain flow length. Sudden and/or strong streamwise changes of $p(x)$ may generate a so-called "Prehistory Effect" in such a manner that the wake turbulent energy will be dissipated with a remarkable time delay far downstream of the location x where it was generated. The process of streamwise decay of such a prehistory situation may be observed and described by the streamwise variation of the thicknesses δ_{II} (Law-of-Wall) and δ_{III} (Wake) and the correlated dissipation integral fractions. With δ_I as the laminar sublayer thickness the total boundary thickness is $\delta = \delta_I + \delta_{II} + \delta_{III}$.

Hence, the ratios δ_I/δ, δ_{II}/δ, δ_{III}/δ or - by physical reasons - the related displacement thickness ratios δ_{1I}/δ, δ_{1II}/δ, δ_{1III}/δ should be used (at least implicitly) as physical parameters for a "Three Layer Hypothetical Velocity Profile" representing a universal turbulent boundary layer including the laminar sublayer. An analytic representation of such a universal velocity profile with 3 or 4 rather well known universal constants was proposed by WALZ [1] with use of integral conditions for momentum, mechanical and thermal energy. NEUBERT-WALZ [2] [3] justified the effectiveness and practical feasability of the above prediction procedure.

Surprisingly good agreement with experimental findings in cases with strong prehistory effects have been found for two-dimensional cases but including compressibility effects up to $M = 7$.

From these results we may conclude that the use of the integral conditions for mechanical and thermal energy is an inevitable pre-condition for having the physical key to account for the detailed dissipation phenomena through all of the 3 velocity Profile layers.

This successful check in the 2D-case encourages to make a further step into the 3D-case. The well known MAGER-JOHNSTON-principles for coupling main and cross flow characteristics will be applied in a generalized form as proposed by GEROPP [4] and prepared by WALZ [5] recently in combination with the "Three-Layer-Concept" for turbulent Boundary Layers.

There are good reasons for getting in this way an accurate and economic prediction method for actual 3D-turbulent and compressible boundary layer problems.

2. Physical Considerations on a hypothetical Three-Layer-Velocity Profile

By reasons of physical transparency let us, as a first step, consider the Three-Layer-Profile shown in Fig. 1 without interaction between the 3 layers, hence, for the one dimension y ("Schichtenströmung").

I. Laminar Sublayer

With $u_\tau = \sqrt{\tau_w/\rho_w}$ and $c_f = 2\tau_w/\rho_\delta u_\delta^2$ we have

$$\frac{u_I(y)}{u_\tau} = \frac{\rho_w u_\tau y}{\mu_w} = \eta^* \tag{1}$$

as linear course of u_I with y within $0 < y < \delta_I$ $(0 < \eta^* < 15)$. For the thickness δ_I yields approximately

$$\delta_I \approx 15\ \mu_w/\sqrt{\rho_w \tau_w}\ . \tag{2}$$

For being able to make use, later on, of the "Wall-Condition" (which involves the two variables x and y, hence, two dimensions)

$$(3) \qquad \left(\frac{\partial \tau}{\partial y}\right)_{y=0} = \left[\frac{\partial}{\partial y}\left(\mu \frac{\partial u}{\partial y}\right)\right]_{y=0} = \frac{dp}{dx} = - \rho_\delta u_\delta \frac{du_\delta}{dx} ,$$

the statement (1) must be generalized by adding a square term. Thus, we write, accomplishing (1),

$$(4),(5) \qquad \frac{u_I(x,y)}{u_\tau} = \eta^* + k\eta^{*2} , \quad k(x) = \frac{du_\delta/dx}{u_\delta} \frac{\rho_\delta}{\rho_w} \frac{\delta}{2c_f \eta^*_\delta} .$$

This generalization will also be important for predictions at high Re-Number and/or strong heating of the wall. In both cases the laminar sublayer may become remarkably thick.

II. Turbulent Wall-Law-Region

PRANDTL's logarithmic law, valid for $\tau_{II} = \tau_w = \text{const}$, and for $\delta_I < y < \delta_{II}$, is adopted:

$$(6) \qquad \frac{u_{II}(y)}{u_\tau} = b \ln \eta^* + c \quad \text{with} \quad b = 2.5, \quad c = 5.1 .$$

For establishing an analytic statement for the whole boundary layer ($0 < y < \delta$) without the singularity $u \to -\infty$ for $y \to 0$ we modify (6) by writing

$$(7) \qquad \frac{u_{II}(y)}{u_\tau} = b \ln(\eta^* + 1) + c \quad \text{for} \quad \eta^* > 15$$

which involves small deviations from (6) but which remain within the few percent permissible limits of empirical errors. We note that u_{II}, as well as u_{III} in the next paragraph, are time-averaged values.

III. Wake-Region

Here we adopt HINZE's simplified cos-interpolation of COLE's empirical Wake-Law:

$$\frac{u_{III}(y)}{u_\delta} = \frac{1}{2}(1 - \cos \pi\eta); \quad \boxed{\eta = \frac{y}{\delta}} \quad , \quad \delta_I + \delta_{II} < y < \delta \tag{8}$$

with

$$\delta_{III} = \delta - (\delta_I + \delta_{II}) \ . \tag{9}$$

3. Analytical matching of the three Layers I, II, III for a presentation of the velocity profile in the two dimensions x, y

This matching is realized first of all by fulfilling physically important boundary conditions at the wall ($y = 0$) and at the outer edge of the boundary layer ($y = \delta$) automatically:

$$\begin{aligned} &y = 0: \quad u = 0 \ , \qquad \tau = \tau_w(x) = \left(\mu \frac{\partial u}{\partial y}\right)_{y=0} \\ &y = \delta: \quad u = u_\delta(x) \ ; \quad \tau = \tau_\delta(\neq 0) \end{aligned} \tag{10}$$

We make the statement

$$\boxed{\frac{u(x,y)}{u_\delta(x)} = \sqrt{c_f/2}\,[f_I + f_{II}] + f_{III}} \ . \tag{11}$$

The functions f_I, f_{II}, f_{III} are mainly related to the specific velocity contributions of the 3 Layers respectively, but also fulfil the requirements of the boundary conditions (10).

In complete details we write

$$f_I(x,y) = e^{-a\eta^*}[(1 - ac - b)\eta^* + k\eta^{*2} - c] \tag{12}$$

(13) $$f_{II}(x,y) = b \ln(\eta^* + 1) + c$$

(14) $$f_{III}(x,y) = \frac{1}{2}(1 - \cos \pi\eta)\{1 - \sqrt{c_f/2}[b \ln(\eta_\delta^* + 1) + c]\}$$

The "Buffer Layer Constant" $a = 0.3$ in the damping factor $e^{-a\eta^*}$ for the laminar sublayer is derived from Fig. 2 (REICHARDT's experiments, Fig. 2). The function $k(x)$ is defined by (5) and the universal constants b and c are taken from (6). The automatic accomplishment of the boundary conditions (10) can easily be verified.

4. The Shear-Stress distribution in the 3 Layer Concept

There exists a unique correlation between the shear-stress and the laminar sublayer I:

(15) $$\tau_I(x,y) = \mu \frac{\partial u}{\partial y}$$

with $\mu = \mu\{T(x,y)\}$ as molecular viscosity .

By accepting PRANDTL's logarithmic wall-law velocity distribution (6) or eq. (7) the assumption

(16) $$\tau_{II} = \tau_I = \tau_w \approx \text{const}$$

must be made by reasons of physical coherence. More (realistic) complexity, however, may be involved in the course of τ_I and τ_{II} if the wall condition (3), in connection with eq. (4), should be satisfied. In this more general case the pressure gradient dp/dx (or the corresponding outer edge velocity gradient du_δ/dx) is involved in the statement (11). Calculations which imply this generalized velocity profile statement are just under way. The prediction examples shown later, however, have been based upon the assumption (16).

The shear-stress τ_{III} in the wake region needs empirical inputs which cannot be covered by eqs. (11) and (14) alone. We have

(17) $$\tau_{III} = \varepsilon_{III}\left(\frac{\partial u}{\partial y}\right)_{III+II}$$

where the eddy-viscosity ε_{III} has to be extracted from a Wake-Turbulence modeling. NEUBERT-WALZ [2] [3] used the MAISE-McDONALD [6] model

(18) $$\varepsilon_{III} = \alpha_1 \rho u_\delta \delta_1 (1 + \alpha_2 \eta^{\alpha_3})^{\alpha_4} \quad ; \quad \rho = \rho(p,T)$$

where δ_1 is the total displacement thickness and the 4 empirical constants are

(19) $$\alpha_1 = 0.0168,\ \alpha_2 = 5.5,\ \alpha_3 = 6,\ \alpha_4 = -1$$

for all calculations reported in chapter 9.

For further development of the present prediction method we will prefer PRANDTL's simple wake Eddy Viscosity statement

(20) $$\varepsilon_{III} = d\, u_\delta \left[1 - (f_{III})_\xi\right] \rho(\delta_1)_{III} \quad ; \quad \rho = \rho(p,T)$$

with only one empirical constant $d \approx 0.014$. We can proceed in this way because the thickness δ_{III} of the Wake Layer as well as the velocity u_{III} at the distance $y = \delta - \delta_{III}$ may be obtained analytically from (11) through (14) (as we will see later).

5. Advantages of a comprehensive analytic interpolation formula like (11) through (14)

For the use of Integral Conditions of Mass, Momentum, Energy (mechanical as well as thermal) and higher order momentum conditions (if needed) across the whole boundary layer thickness $\delta = \delta_I + \delta_{II} + \delta_{III}$ the integral quantities like δ_1, δ_2, δ_3, δ_4 and others (displacement, momentum-loss, energy-loss, density-loss thicknesses, respectively) can be obtained by simple integrations. In this way a detailed information

about the contributions for instance to the displacement thickness of the 3 layers is separately obtained. The same is true for the contributions to the Dissipation-Integral. Thus a chance to include the "Prehistory Effects" into the prediction method, without need of an additional prehistory model, is opened. For the Wake Region III due to the cos-velocity shape we know by integration that yields $\delta_{III} = 2\delta_{1III}$.

The choice of characteristical boundary layer parameters is widely free. Parameters like

$$c_f(x) = 2\frac{\tau_w}{\rho_\delta u_\delta^2}\,, \quad R_{\delta_2}(x) = \frac{\rho_\delta u_\delta \delta_2}{\mu_w}\,, \quad \delta_1 = \int_0^\delta \left(1 - \frac{\rho u}{\rho_\delta u_\delta}\right) dy\,;$$

(21)
$$\delta_2 = \int_0^\delta \frac{\rho u}{\rho_\delta u_\delta}\left(1 - \frac{u}{u_\delta}\right) dy\,; \quad \delta_3 = \int_0^\delta \frac{\rho u}{\rho_\delta u_\delta}\left[1 - \left(\frac{u}{u_\delta}\right)^2\right] dy\,;$$

$$\delta_4 = \int_0^\delta \frac{\rho u}{\rho_\delta u_\delta}\left(\frac{\rho_\delta}{\rho} - 1\right) dy\,; \quad \frac{\delta_1}{\delta_2} = H_{12}\,; \quad \frac{\delta_3}{\delta_2} = H_{32}\,; \quad \frac{\delta_4}{\delta_2} = H_{42}$$

as well as analytically interpolated ratios of those parameters are commonly used. The 3 Layer Concept offers additional parameters like

(22),(23)
$$\frac{\delta_{1III}}{\delta} = \int_0^\delta \left(1 - \frac{\rho}{\rho_\delta} f_{III}\right) dy/\delta\,; \quad (f_{III})_\delta = \left(\frac{\Delta u \text{ wake}}{u_\delta}\right)_{max}\,.$$

These parameters (22), (23) indicate the contribution of the wake phenomena to the displacement thickness $\delta_1 = \delta_{1I} + \delta_{1II} + \delta_{1III}$ or to the maximum velocity u_δ at the outer edge of the boundary layer respectively.

It must be pointed out here that no special empirical relationships between parameters as defined above are needed. This is possible because the statement (11) through (14) with (22), (23) provides a coherent summary of all empirical inputs. NEUBERT-WALZ [2] found that any additional interpolation formula as mostly used in connection with integral conditions, i.e. $c_f = c_f(H_{12}, R_{\delta_2})$, $H_{12} = f(H_{32}, R_{\delta_2})$, may be a dangerous

source of avoidable errors within the computational scheme which are due only to an undetected incoherence of different empirical inputs.

One of the most important features which are incorporated in the statements (11) through (14) with (22), (23) is a physically detailed definition of the dissipation integral

$$(24) \qquad c_D = \frac{1}{\rho_\delta u_\delta^3}\int_0^\delta u\frac{\partial \tau}{\partial y}\,dy = \frac{1}{\rho_\delta u_\delta^3}\left[(u\tau)_0^\delta - \int_0^\delta \tau\frac{\partial u}{\partial y}\,dy\right] = \frac{1}{\rho_\delta u_\delta^3}\left(u_\delta\tau_\delta - \int_0^{u_\delta}\tau\,du\right).$$

The evaluation of this integral term which occurs in the integral conditions of mechanical and thermal energy (see eq. (30)) has to be performed with use of the relations (15) to (20), thus warranting the inclusion of "Prehistory effects" if such effects are existing due to a given pressure distribution. We note that the value of the shear-stress τ_δ depends on the definition of δ. It will vanish only outside of the Intermittency region.

7. The set of Integral Conditions for the 2D-case including compressibility

With reference to WALZ [1] (page 90, eq. (3.39)) we adopt for PRANDTL-Number $Pr \approx 1$ (turbulent air Boundary Layer) the following simultaneous set of ν different ordinary differential equations, all of them based upon PRANDTL's classical B.L.-Equation with ν as a kind of "Momentum Number", which may be chosen arbitrarely (i.e., $\nu = 0, 1, 2, 3, \ldots n \ldots \infty$)

$$(25) \qquad \frac{df_\nu}{dx} + f_\nu\left(2 + \nu - \frac{g_\nu}{f_\nu} - M_\delta^2\right)\frac{1}{u_\mathcal{E}}\frac{du_\mathcal{E}}{dx} + e_\nu + h_\nu = 0$$

with

$$(26),(27) \qquad e_\nu = (\nu+1)\int_0^\delta \left(\frac{u}{u_\delta}\right)^\nu \frac{\partial}{\partial y}\left(\frac{\tau}{\rho_\delta u_\delta^2}\right)dy \;;\quad f_\nu = \int_0^\delta \frac{\rho u}{\rho_\delta u_\delta}\left[1 - \left(\frac{u}{u_\delta}\right)^{\nu+1}\right]dy$$

$$(28),(29) \qquad g_\nu = (\nu+1)\int_0^\delta \frac{\rho u}{\rho_\delta u_\delta}\left[\frac{\rho_\delta}{\rho}\left(\frac{u}{u_\delta}\right)^{\nu-1} - 1\right]dy \;;\quad h_\nu = 0 \quad (\text{for } \nu \neq \infty) \;;$$

(30) $$M_\delta(x) = \frac{u_\delta(x)}{a_\delta(x)}\ , \quad a_\delta = \text{Velocity of sound.}$$

For $\nu = 0$ we obtain the Integral Condition for Momentum with $e_0 = -c_f/2$; $f_0 = \delta_2$; $g_0 = \delta_1$.

For $\nu = 1$ we get the Integral Condition for the mechanical Energies with

(31) $$e_1 = \frac{2}{\rho_\delta u_\delta^3} \int_0^\delta u \frac{\partial \tau}{\partial y}\, dy = 2D \quad \text{(Dissipation Integral (23))}$$

(32) $$f_1 = \delta_3$$

(33) $$g_1 = 2\delta_4$$

For PRANDTL-Number $Pr \approx 1$ (which is suitable for turbulent Boundary Layers) the flow and temperature field are coupled by a well known closed solution of the linear partial differential equation for the total enthalpy (total energy)

$$H(x,y) = c_p T + \frac{u^2}{2} \quad (c_p = \text{specific heat at constant pressure})$$

which writes in terms of the temperature T

(34) $$\boxed{\frac{T}{T_\delta} = A + B\frac{u}{u_\delta} + C\left(\frac{u}{u_\delta}\right)^2}\ ; \quad A = \frac{T_w}{T_\delta}\ ;\ B = \frac{T_e - T_w}{T_\delta};\ C = -r\,\frac{\kappa-1}{2}M_\delta^2$$

$\kappa = c_p/c_v$; r = Recovery Factor ≈ 1 for $Pr \approx 1$

Hence, the temperature $T(x,y)$ and density $\rho(x,y)$ are known with u/u_δ for given MACH-Number and heat transfer conditions if the system of ordinary differential equations (25) is solved simultaneously with (34) on the basis of (11) through (14). It is important to point out that the

inclusion of the compressible case by use of (34) introduces no unknowns additional to those chosen for the velocity field, but it involves the knowledge of the MACH-Number $M_\delta(x)$ and the wall temperature $T_W(x)$.

8. Choice of practical Parameters (unknowns) of the Velocity Field as Function of x only

8.1. Relative Boundary Layer Thicknesses:

$$\delta_1/\delta, \quad \delta_2/\delta, \quad \delta_3/\delta, \quad \frac{\delta_{1I}}{\delta}, \quad \frac{\delta_{1III}}{\delta}, \quad \boxed{H_{12} = \frac{\delta_1}{\delta_2}}, \quad H_{32} = \frac{\delta_3}{\delta_2}$$

8.2. Physical Technical Quantities:

$$\boxed{R_{\delta_2} = \frac{\rho_\delta u_\delta \delta_2}{\mu_W}}, \quad \boxed{c_f = 2\,\frac{\tau_W}{\rho_\delta u_\delta^2}}, \quad \boxed{\Pi = \frac{\delta_1}{\tau_W}\frac{dp}{dx}}.$$

The line-surrounded quantities have been selected by NEUBERT-WALZ [2] and used for calculating typical examples, where Prehistory effects have been expected in the related experiments. Further improvement will probably achieved by use of the POHLHAUSEN-ROTTA-CLAUSER-Parameter Π, especially in the compressible case with thick laminar sublayers.

9. Results for 2D-cases

The Figs. 6 to 10 are showing the comparison of some experimental and theoretical results predicted by the method in its present preliminary state of development. The prediction of the essential boundary layer parameters in the presence of strong prehistory effects may be considered as surprisingly good.

10. The 3D-case

For a first approach to this problem the suggestions of GEROPP [4] will be followed. We assume a unique coupling between a main flow direction with the velocity component u (ξ-direction) and the cross flow component w (η-direction) in an orthogonal curvilinear coordinate system ξ,η.

Generalizing JOHNSTON's [7] procedure, GEROPP writes

$$\frac{w}{u_\delta} = c_1 \frac{u}{u_\delta}\left(1 - \frac{u}{u_\delta}\right) \tag{35}$$

with c_1 as a parameter of the cross-flow profile. For further generalization he makes the cross flow statement

$$\frac{w}{u_\delta} = c_1 \frac{u}{u_\delta}\left(1 - \frac{u}{u_\delta}\right) + c_2 \eta (1 - \eta)^{c_3} \quad ,$$

where c_1, c_2 and c_3 are three cross-flow shape parameters which may be determined by Integral Conditions and/or wall conditions in the η-direction.

The related formalism to get these equations may be suppressed here refering to GEROPP's analysis [4].

The main progressive feature of the work started in this direction is the automatic transfer of the Three-Layer Concept into the turbulent cross-flow phenomena. It may be expected that the progress observed in 2D-applications will also be achieved in the 3D-case.

References

[1] WALZ, A., Boundary Layers of Flow and Temperature, Page 115, The MIT Press, Cambridge, Mass. USA (1969)

[2] NEUBERT, W., WALZ, A., Beitrag zur Berechnung zweidimensionaler kompressibler turbulenter Grenzschichten mit Integralbedingungen, Festschrift zum 60. Geburtstag von Prof. Dr.-Ing. E. TRUCKENBRODT, München 1977

[3] NEUBERT, W., Ein Transformationskonzept zur Berechnung turbulenter kompressibler Grenzschichten, DLR-FB 77-16, S. 177-184

[4] GEROPP, D., Entwicklung und Erprobung eines dreidimensionalen Grenzschichtreihenverfahrens, insbesondere für Rümpfe beliebiger Querschnittsform, Interner Bericht Nr. G 1/70, Univ. Karlsruhe, Abt. Strömungsgrenzschichten (1971)

[5] WALZ, A., Beitrag zur Theorie und praktischen Berechnung dreidimensionaler Strömungs- und Temperaturfelder, Forsch.-Ber. aus der Wehrtechnik BMVg-FBWT-75-22 und 78-4 (1975 und 1978)

[6] MAISE, G., McDONALD, H., Mixing Length and Kinematic Eddy Viscosity in a compressible Boundary Layer. AIAA Journ., Vol. 6, No. 1, 1968

[7] JOHNSTON, J.P., The turbulent boundary layer at a plane of symmetry in a three-dimensional flow. Journ. of Basic Engineering, Series D, Trans. ASME 82, 1960

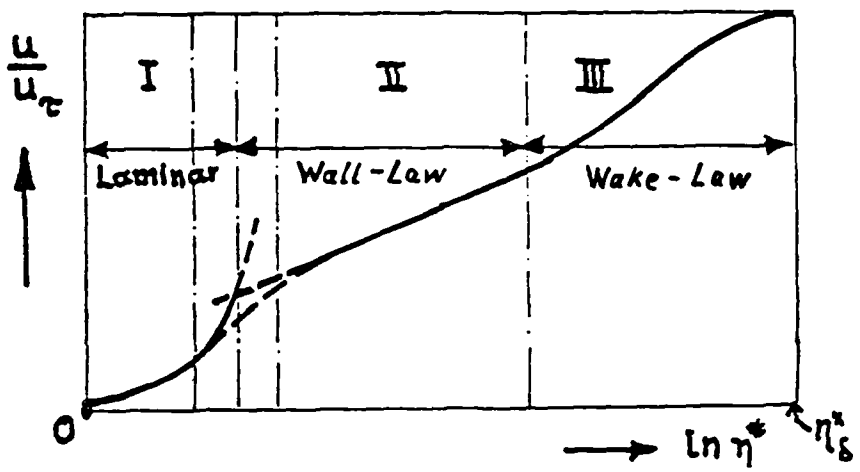

FIG. 1
Three Layer-Modell for turb. Boundary Layer

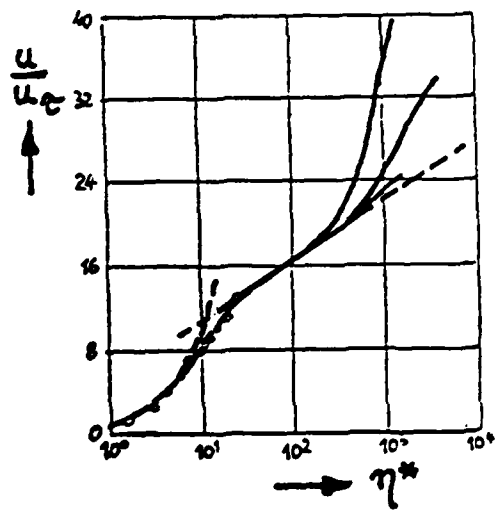

FIG. 2
Typical experimental course of $\frac{u}{u_\tau}(\eta^*)$
o Experimental Data according to Reichardt

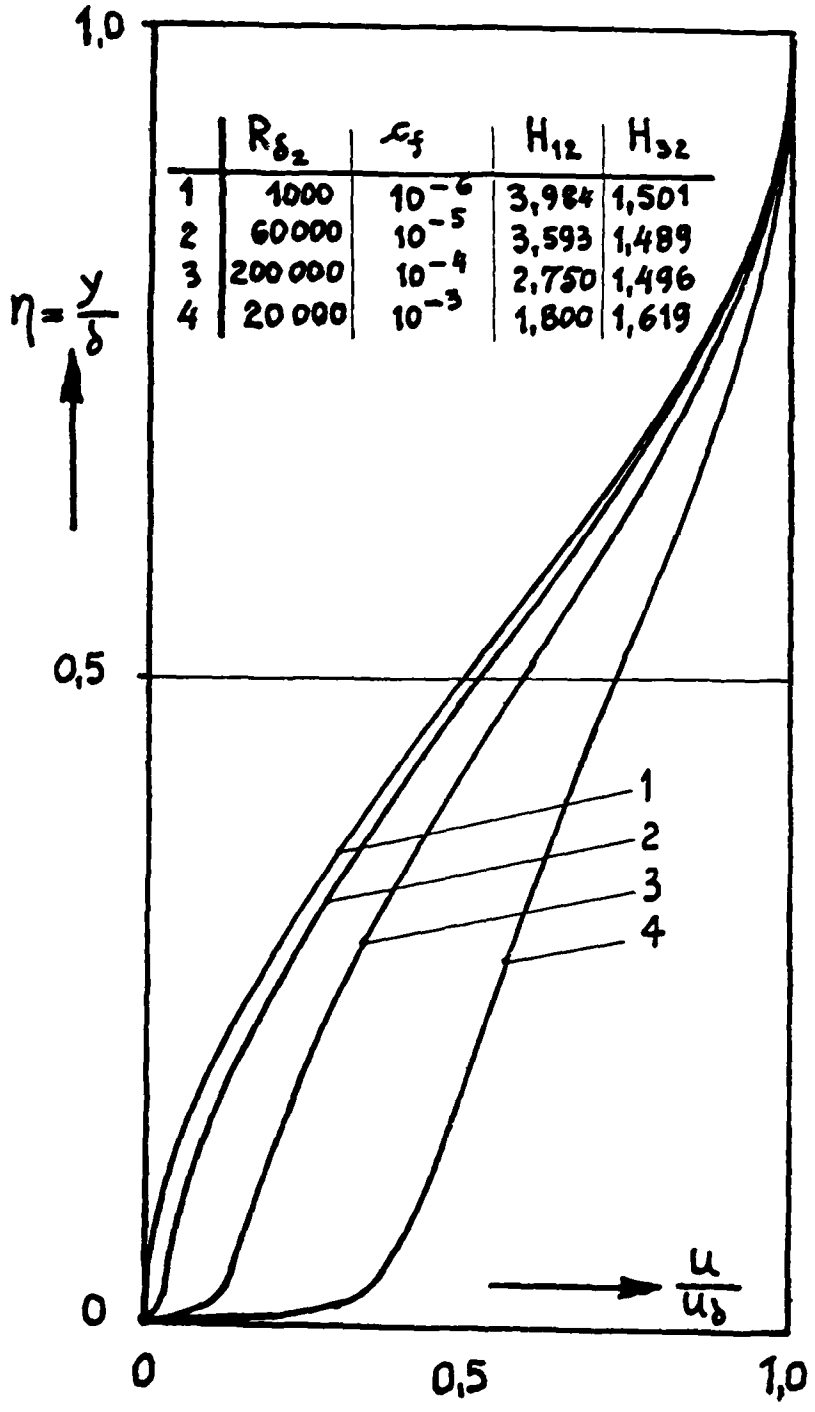

	R_{δ_2}	c_f	H_{12}	H_{32}
1	1000	10^{-6}	3,984	1,501
2	60000	10^{-5}	3,593	1,489
3	200000	10^{-4}	2,750	1,496
4	20000	10^{-3}	1,800	1,619

Typical Shapes of Velocity Profiles according to the Three-Layer Concept (for ϱ=const, μ= const)

FIG.3

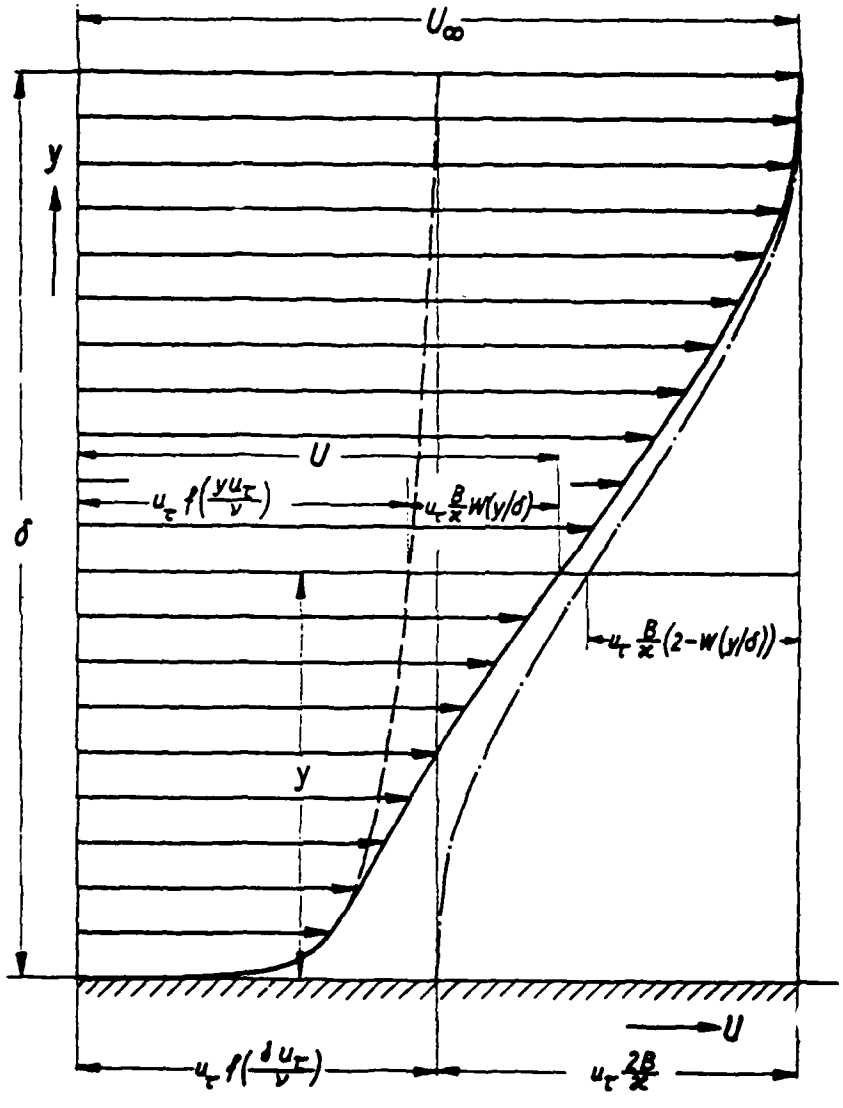

FIGURE 13

Hypothetical velocity profile of turbulent boundary layer

——— total mean velocity profile
— — — velocity distribution according to the law of the wall, Eq. (2)
—·— velocity distribution of wake flow.

FIG. 4 Two-Layer Velocity Profile (COLES - ROTTA)

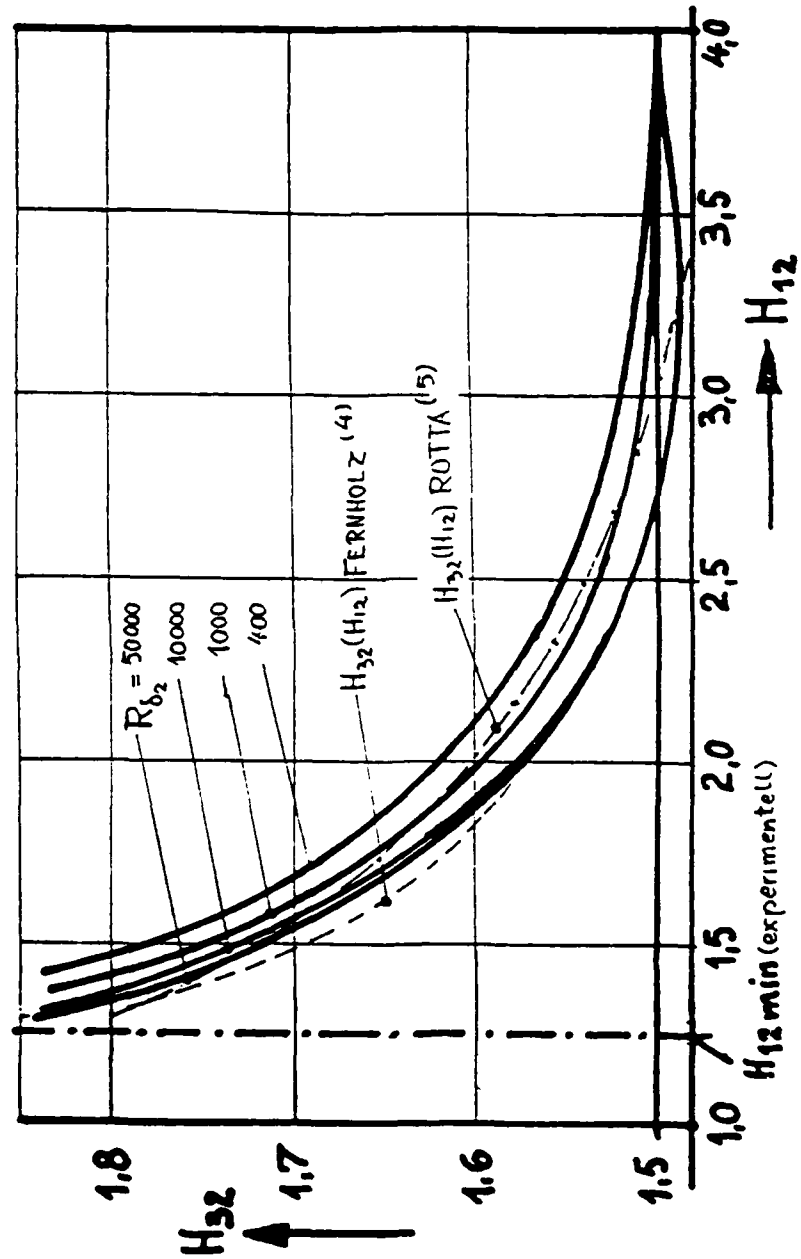

FIG.5 Correlation $H_{32} = f(H_{12}, R_{b_2})$ from Equ. (11) through (14)

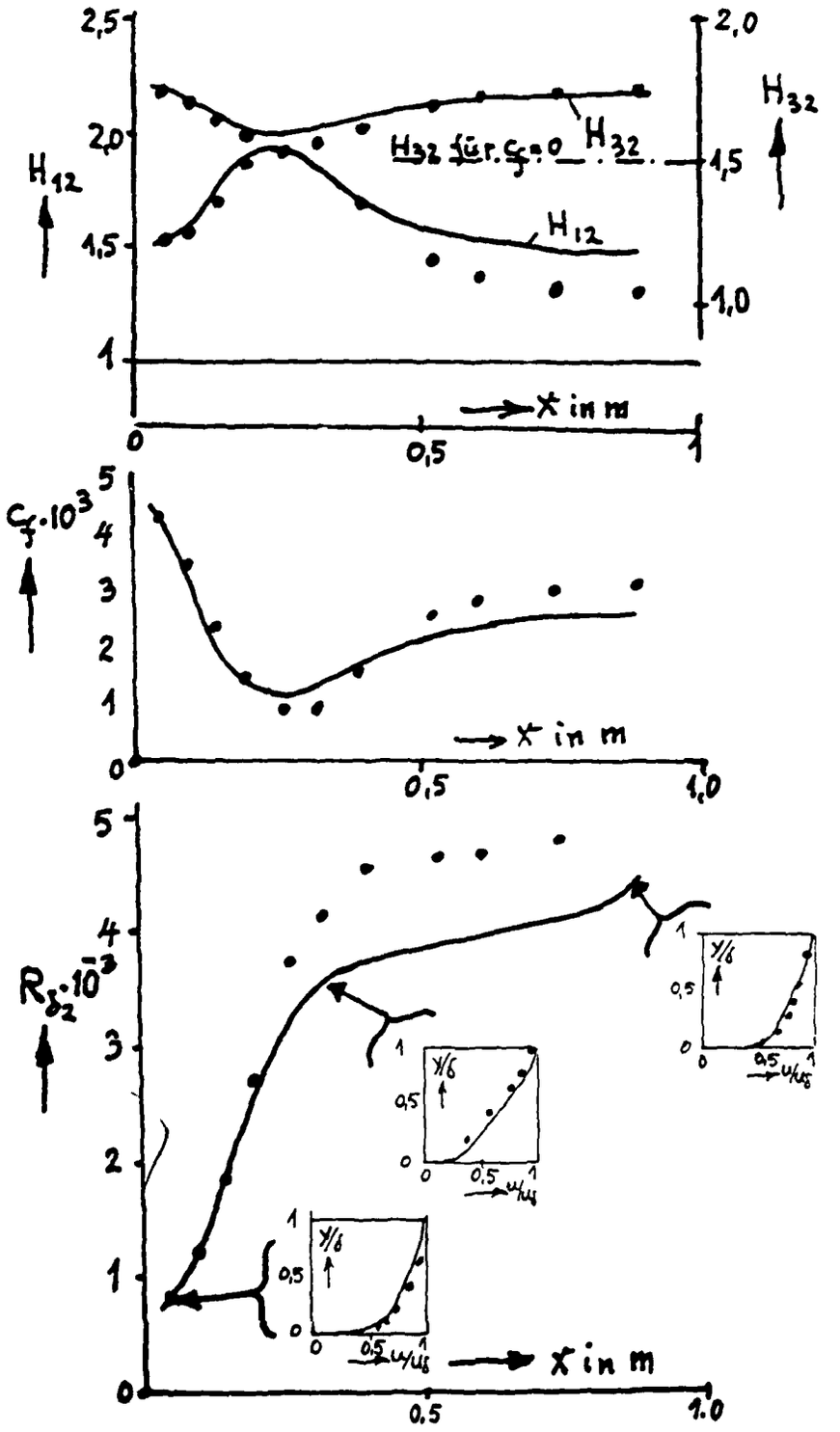

FIG.6 *Example with Pressure Increase and Decrease*

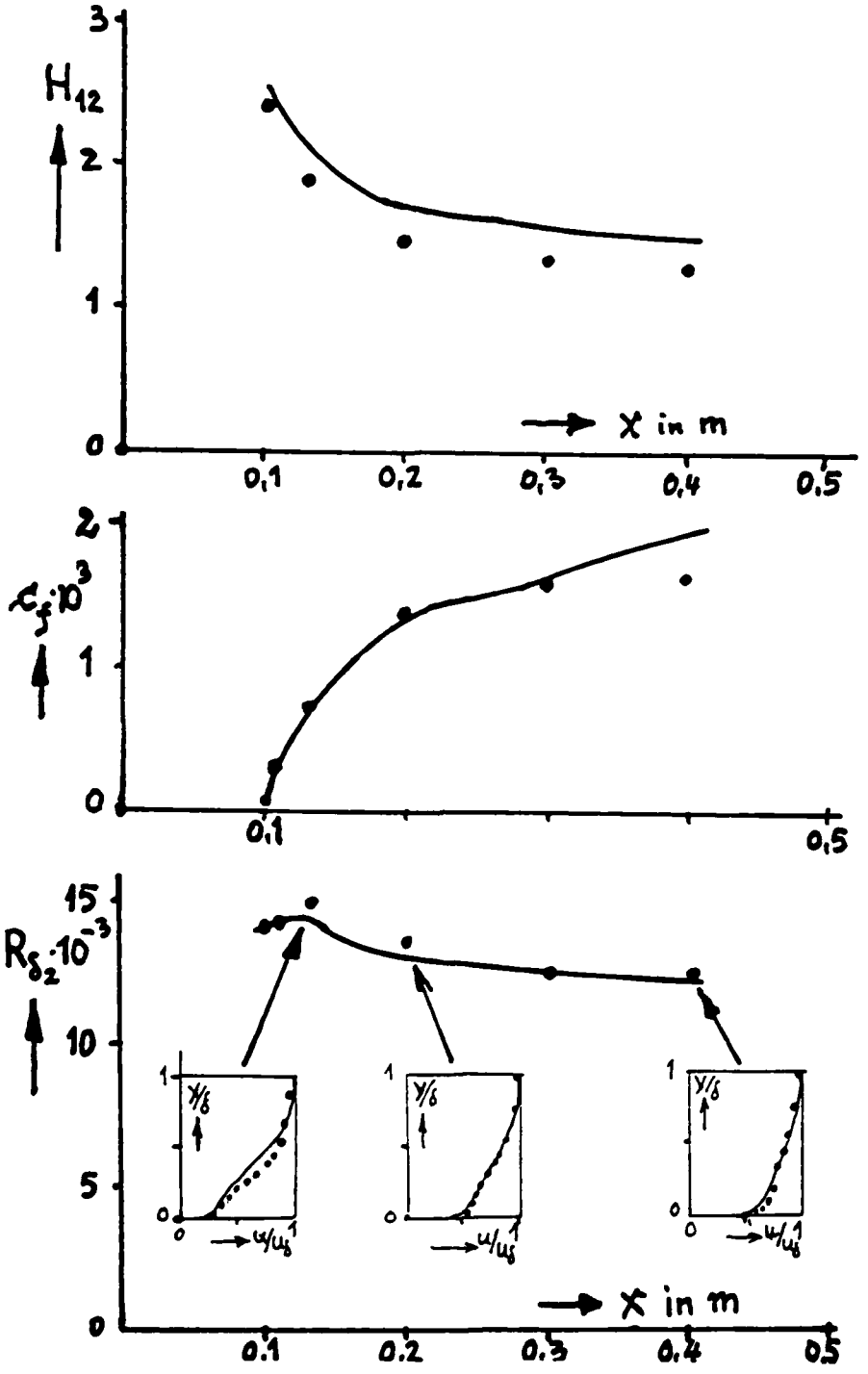

FIG.7 Reattaching Boundary Layer, Step at $\frac{x}{l} = 0.1$

- Experiments Wauschkuhn, P., Vasantra Ram, V.

— Present Theory

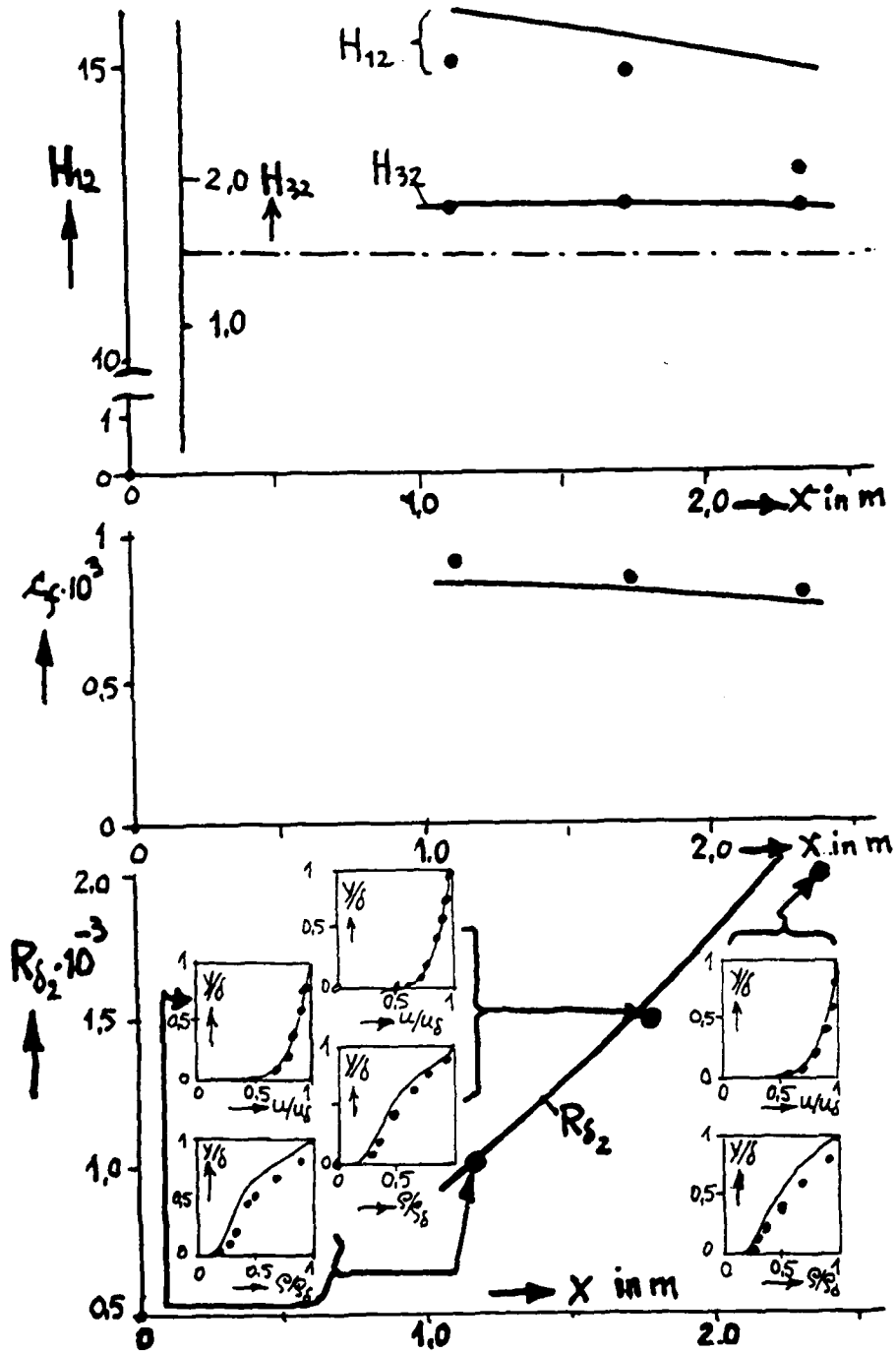

FIG. 8 Axial Flow along a Zylinder, $\frac{dp}{dx} = 0$, $M_\delta = 7.2$, $\frac{T_w}{T_e} = 0.5$

- Experiments
- Calculations

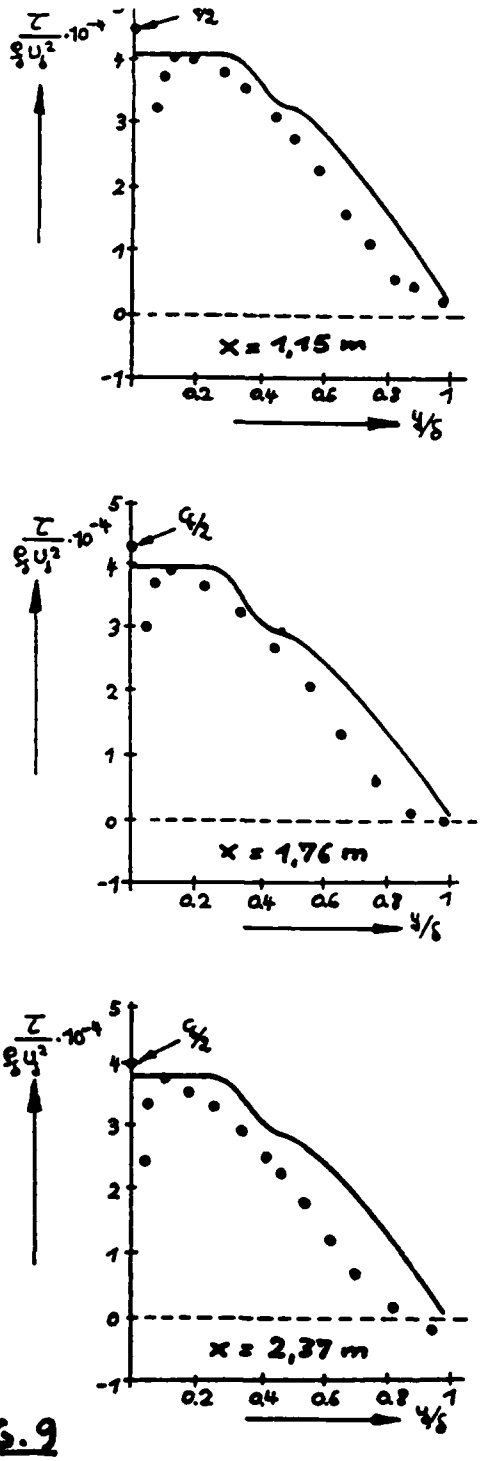

Experiments

– Present Theory, Total Shear-Stress

FIG. 9

Axial Flow along a Zylinder
Comparison of calculated and experimental Shear-Stress Values

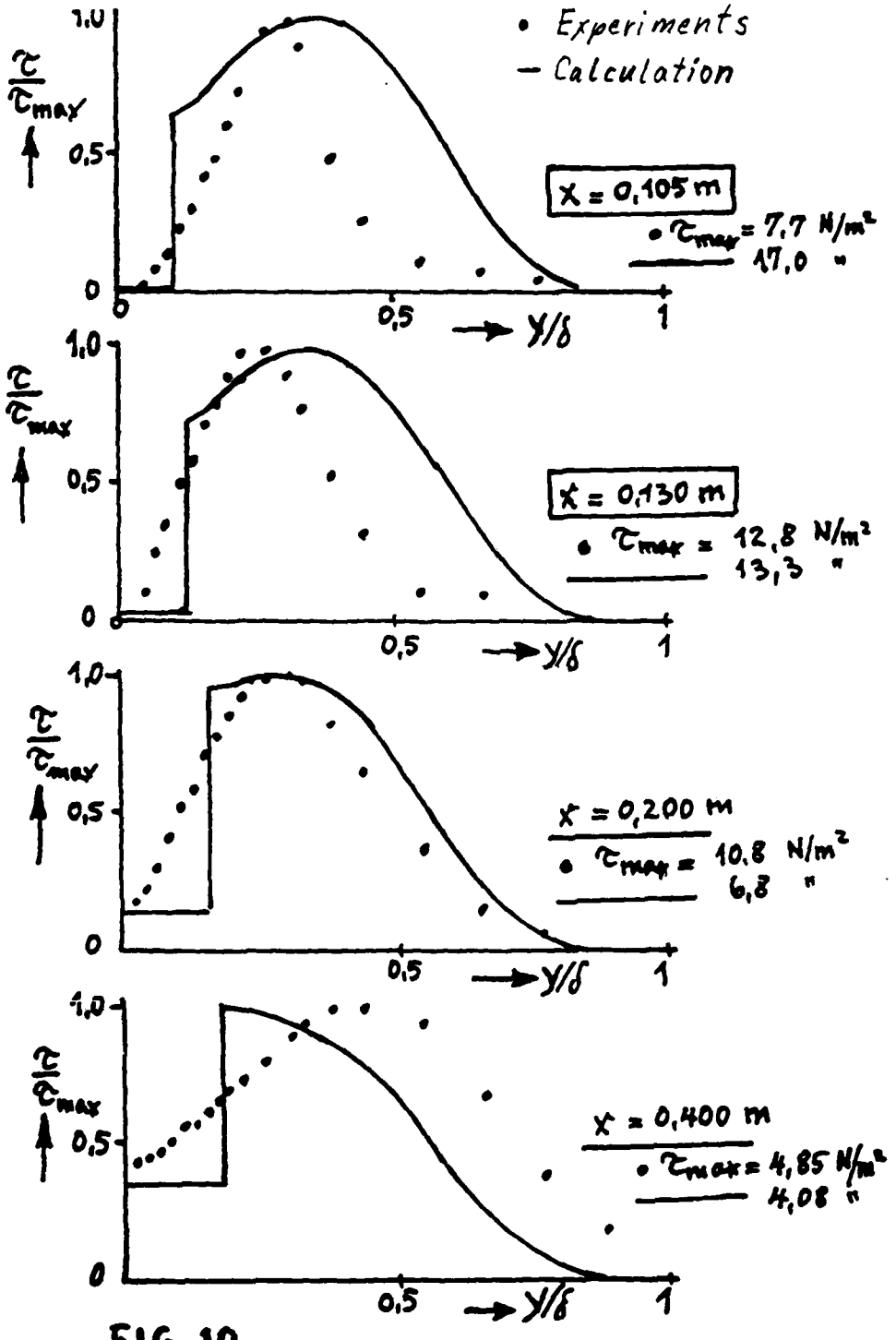

FIG. 10

Comparison of messured and predicted Shear-Stress Profiles at different Stations x

A THEORETICAL TREATMENT OF THE FREE STREAM TURBULENCE EFFECTS ON THE TURBULENT BOUNDARY LAYER

J. C. Rotta

Institut für Experimentelle Strömungsmechanik
DFVLR-AVA, Göttingen

Abstract

The effect of free stream turbulence on the turbulent boundary layer is theoretically attacked using second order moment closure assumptions for the turbulence equations. The free stream turbulence field is assumed to be homogeneous with respect to planes normal to the direction of the undisturbed flow and is described by the intensity and the integral length scale. The partial differential equations for the two-dimensional flat plate boundary layer are integrated using a finite difference procedure. Numerical results of the development of the boundary layer are shown and the effect of intensity and length scale on the velocity profiles is discussed.

Nomenclature

$C = 5,2$	Constant, Eq. (16)
$c_f = 2\tau_w/\rho U_\infty^2$	local skin friction coefficient
$E = \left(\frac{\overline{u^2}+\overline{v^2}+\overline{w^2}}{2}\right)$	kinetic energy of turbulence
L	integral length scale, Eq. (9)
L_x	longitudinal integral length scale, Eq.(10)
$H_{12} = \delta_1/\delta_2$	form parameter
$Re_2 = U_\infty \delta_2/\nu$	momentum loss thickness Reynolds number
Tu	free stream turbulence intensity, Eq. (7)
U, V	mean velocities components
u, v, w	fluctuating velocity components
$u_\tau = (\tau_w/\rho)^{1/2}$	shear stress velocity
x, y	Cartesian coordinates, x in direction of mean flow
$\delta_1 = \int_{o_\infty}^{\infty}(1 - U/U_\infty)dy$	dispacement thickness
$\delta_2 = \int_{o}^{\infty}\frac{U}{U_\infty}(1-\frac{U}{U_\infty})dy$	momentum loss thickness
δ	thickness of boundary layer (δ = y at which U = 0.999 U_∞)

$\kappa = 0{,}41$	von Kármán constant
ν	kinematic viscosity
ϱ	density

Subcripts

w	conditions at the wall ($y = 0$)
∞	free stream conditions ($y \longrightarrow \infty$)
0	conditions at $x = 0$
1	conditions at $x = 1$

An overbar denotes a time average

1. Introduction

The wellknown fact that free stream turbulence affects not only laminar turbulent transition, but also the turbulent boundary layer, has been stated for the first time, as far as I know, by K. Wieghardt in his paper [1] published in 1944, in which he reported on measurements in the turbulent boundary layer on a flat plate behind a turbulence generating grid. Many further measurements have been made by various investigators since that time. The problem is of importance with regard to the interpretation of tests in windtunnels, the stream of which is not free of turbulent fluctuations.

In most of the known publications, the variation of characteristic boundary layer parameters like local skin friction coefficient and velocity profile shape parameter are correlated with the intensity of the free stream turbulence. Actually, the turbulence field is characterized by a variety of statistical parameters, the most important of which is the integral length scale, besides the intensity.

An experimental investigation of the two parameters, intensity and integral length scale, has been made by H.U. Meier and H.-P. Kreplin [2], suggesting that the magnitude of the integral length scale has a major effect on the development of the turbulent boundary layer.

The present paper reports on an attempt to predict the effect of the free stream turbulence field on the development of the two-dimensional flat plate turbulent boundary layer using a finite difference method to solve the partial differential equations of a second order closure turbulence model. The free stream turbulence field is described by the intensity and integral length scale, such that the investigation will give an answer about the effect of these two quantities on the turbulent boundary layer.

2. Differential Equations

The solution of the problem is based on simultaneous integration of the partial differential equations for mean flow, Reynolds shear stress, kinetic energy of turbulence, and length scale. The equations present a second order moment closure and have been successfully applied to free shear flows, pipe and channel

flow, as well as two-dimensional boundary layers [3, 4, 5]. In the case of a two-dimensional boundary layer at incompressible constant pressure flow of high Reynolds numbers, the equations read as follows:

Continuity of mean flow

$$(1) \qquad \frac{\partial U}{\partial x} + \frac{\partial V}{\partial y} = 0,$$

momentum of mean flow

$$(2) \qquad U \frac{\partial U}{\partial x} + V \frac{\partial U}{\partial y} = - \frac{\partial \overline{uv}}{\partial y},$$

Reynolds shear stress

$$(3) \qquad U \frac{\partial \overline{uv}}{\partial x} + V \frac{\partial \overline{uv}}{\partial y} = - a_p E \frac{\partial U}{\partial y} - k_p c \frac{E^{1/2}}{L} \overline{uv} + \frac{\partial}{\partial y}\left(k_{q\tau} E^{1/2} L \frac{\partial \overline{uv}}{\partial y}\right),$$

kinetic energy of turbulence

$$(4) \qquad U \frac{\partial E}{\partial x} + V \frac{\partial E}{\partial y} = -\overline{uv} \frac{\partial U}{\partial y} - c \frac{E^{3/2}}{L} + \frac{\partial}{\partial y}(k_q E^{1/2} L \frac{\partial E}{\partial y}),$$

product of integral length scale and kinetic energy of turbulence

$$(5) \quad U \frac{\partial (EL)}{\partial x} + V \frac{\partial (EL)}{\partial y} = -\overline{uv} \left(\zeta \frac{\partial U}{\partial y} L + \zeta_3 \frac{\partial^3 U}{\partial y^3} L^3\right) - \frac{\partial \overline{uv}}{\partial y} \zeta_2 L^3 \frac{\partial^2 U}{\partial y^2}$$

$$- c_L c E^{3/2} + \frac{\partial}{\partial y}\left[E^{1/2} L (k_q L \frac{\partial E}{\partial y} + k_{qL} E \frac{\partial L}{\partial y})\right].$$

In the latter equation, which is referred to as the length scale equation for brevity, the first term on the left hand side is the simplified form $U\partial(EL)/\partial x$, which is used instead of

$\partial(UEL)/\partial x$ as originally derived [6]. The advantage of using the simplified form for boundary layers with pressure gradients was shown by R. Voges [5]. In accordance with previous applications of the equations the following values and relationships are used for the empirical coefficients

$$
(6)\quad \begin{cases}
a_p = 0.2 \\
c = 0.165 \\
k_p = a_p c^{-4/3} \\
c_L = 0.8 \\
\zeta = 0.98 \\
\zeta_2 = 1.2 \\
\zeta_3 = -1.5 \\
k_q = 0.25 + 0.55(y/\delta)^2(3-2y/\delta) \\
k_{q\tau} = 0.25 + 0.35(y/\delta)^2(3-2y]/\delta) \\
k_{qL} = (c_L - \zeta)/\kappa^2 - 2\zeta_3)c \\
\kappa = 0.41.
\end{cases}
$$

The equations (2) to (5) are valid for high Reynolds number flow.

3. The Field of Free Stream Turbulence

The field of the free stream turbulence is assumed to be homogeneous with respect to planes normal to the free stream direction (x-direction) and is described by two parameters, viz. the kinetic energy of the fluctuating velocity, E_∞, and the integral length scale L_∞. Both quantities vary with x in accordance with the law of decay. Generally, the intensity, defined as

$$(7) \qquad Tu = \left[(\overline{u^2} + \overline{v^2} + \overline{w^2})/3\right]^{1/2} / U_\infty,$$

where u, v, w are the velocity fluctuations, is used as a measure of wind tunnel turbulence. By definition, this intensity is related to the kinetic energy of turbulence through

$$(8) \qquad Tu = (2E_\infty/3)^{1/2}/U_\infty.$$

The product of kinetic energy and length scale, used in Eq. (5), is defined as the integral of the transverse two-point correlation function, multiplied by 3/16:

$$(9) \qquad EL = \frac{3}{16}\int_{-y}^{\Delta y=\infty} \left[\overline{u(y)u(y+\Delta y)} + \overline{v(y)v(y+\Delta y)} + \overline{w(y)w(y+\Delta y)}\right] d(\Delta y)$$

The same definition holds for $E_\infty L_\infty$. With the experimental investigation by H.U. Meier and H.-P. Kreplin [2], the longitudinal integral length scale,

$$(10) \qquad L_x = \frac{U_\infty}{\overline{u^2}} \int_0^\infty \overline{u(t)u(t+\Delta t)}\, d(\Delta t),$$

is determined from the integral of the autocorrelation function,

where t is the time. Provided, the relationships of isotropic turbulence and Taylor's hypothesis can be applied, the length scale of the present investigations is related to L_x by

$$L = L_x/2. \tag{11}$$

Outside the boundary layer, the kinetic energy equation (4) and the length scale equation (5) reduce to

$$U_\infty \frac{\partial E_\infty}{\partial x} = - c \frac{E_\infty^{3/2}}{L_\infty}, \tag{12}$$

$$U_\infty \frac{\partial (E_\infty L_\infty)}{\partial x} = - c_L c \, E_\infty^{3/2}. \tag{13}$$

With $c_L = 0.8$, the equations have the solution

$$E_\infty = E_{\infty r} \left(\frac{x}{x_r}\right)^{-10/7}, \tag{14}$$

$$L_\infty = L_{\infty r} \left(\frac{x}{x_r}\right)^{2/7}, \tag{15}$$

corresponding to the decay law of an isotropic turbulence field, which satisfies Loitsianskii's invariant, where $E_{\infty r}$ and $L_{\infty r}$ are the quantities at position of reference, x_r, and x is measured from the virtual origin of the free stream turbulence, which is not identical with the starting position of the boundary layer calculation.

4. Boundary Conditions and Initial Distributions

The formulation of the boundary conditions at the solid wall have been discussed by the author [7]. The important fact is, that the flow close to the surface is strongly affected by the viscosity, which does not appear in the equations. Since the thickness of sublayer, directly influenced by the viscosity, is small as compared with the boundary layer thickness, when the Reynolds number is high, it may be permissible, to extrapolate the mean velocity distribution according to the law of the wall,

$$U = u_\tau \left[\frac{1}{\kappa} \ln (y u_\tau / \nu) + C \right], \tag{16}$$

down to the distance $y = y_w$, where $U = 0$ according to Eq. (16). This distance is

$$y_w = \frac{\nu}{u_\tau} e^{-\kappa C} \approx 0.12 \nu / u_\tau . \tag{17}$$

In the region $0 \leq y \leq y_w$, $U \equiv 0$ is assumed. In addition, at $y = y_w$ it is put

$$E_w = e^{-2/3} u_\tau^2 , \tag{18}$$

$$\left(\frac{\partial \overline{uv}}{\partial y} \right)_w = 0 . \tag{19}$$

The value of $-(\overline{uv})_w$ at $y = y_w$ is considered to correspond to the wall shear stress

$$-(\overline{uv})_w = \frac{\tau_w}{\rho} = u_\tau^2 . \tag{20}$$

At the outer edge, the relevant flow quantities approach the

following values:

$$
\begin{aligned}
&U \longrightarrow U_\infty \\
&\overline{uv} \longrightarrow 0 \\
&E \longrightarrow E_\infty \\
&L \longrightarrow L_\infty .
\end{aligned}
\tag{21}
$$

The integration of the parabolic differential equations start from a set of initial distributions of the dependent variables, to be given at the position $x = x_o$. These initial distributions are determined as follows: First a set of distributions for a boundary layer without free stream turbulence is constructed, which satisfy given values of $Re_2 = u\delta_2/\nu$, δ_2 and H_{12}. The mean velocity profile consists of the logarithmic law of the wall, Eq. (16), to which a wake function after Coles is added. The distribution of the length scale is approximated by a hyperbolic tangens function and the shear stresses are calculated with Prandtl's mixing length formula. The kinetic energy of turbulence is assumed to be proportional to the shear stress according to

$$E = -\overline{uv}\, c^{-2/3}. \tag{22}$$

In order to satisfy the boundary conditions for E and EL in accordance with Eqs. (21) contributions of the form

$$\Delta E = E_\infty (y/\delta)^2 \, (3 - 2y/\delta), \tag{23}$$

$$\Delta(EL) = E_\infty L_\infty (y/\delta)^3 \, (4 - 3\, y/\delta) \tag{24}$$

are added, such that smooth initial distributions are obtained.

An explicit finite difference scheme is used to integrate the partial differential equations by an iterative procedure. For each iteration the differential equations are integrated one after the other in the order

Continity Eq. (1),
Energy Eq. (4),
Length scale Eq. (5),
Shear stress Eq. (3),
Momentum Eq. (2).

5. Results

It is expected that the results will depend to a certain extent on the initial distributions of U, E, L, and $-\overline{uv}$. This effect will become smaller and smaller with growing distance from the starting position. For the present numerical results the following conditions are chosen, which are in gross agreement with the conditions, at which Meier's and Kreplin's [2] experiments were made. The length of the flat plate is 1 m and the fully turbulent boundary layer starts at the leading edge ($x = 0$) with a momentum loss thickness of $\delta_2 = 0.71$ mm, a momentum loss thickness Reynolds number of $Re_2 = 2690$, and a form parameter $H_{12} \approx 1.41$. Thus the integration of the boundary layer equations extends over a range of roughly 1400 times the initial momemtum loss thickness. The plate Reynolds number is $U_\infty x_1/\nu \approx 3.8 \times 10^6$.

The investigations concentrate on small free stream turbulence

intensities up to Tu $\approx$ 1 p.c. and relatively small length scales up to $L_\infty \approx 4$ mm. The procedure of making the calculations is to prescribe certain values Tu_1 and $L_{\infty 1}$ of the free stream turbulence at the end of the plate, x = 1 m, which can be varied independently within certain limits. The initial values at x = 0 can then be calculated from the decay law, Eqs. (12) to (15).

Fig. 1 shows for two flow cases the distributions of mean velocity, turbulent energy, and length scale as functions of the distance from the plate at the initial position x = 0 and at the end of the integration range, x = 1 m. The set of curves 1 represents the results for the calculation with zero free stream turbulence. At x = 1 m the boundary layer thickness is $\delta \approx 20$ mm and is about three times as thick as its initial value at x = 0. The momentum loss thickness Reynolds number is $Re_2 \approx 7700$ and the form parameter $H_{12} = 1.35$. This value of H_{12} is in fair agreement with known measurements; e.g. K. Wieghardt has obtained $H_{12} = 1.356$ at $Re_2 = 8170$ (see Ref. [8]).

The other calculation (curves 2) given in Fig. 1 is for a free stream turbulence intensity of $Tu_1 = 1$ p.c. and a length scale $L_{\infty\,1} = 3{,}2$ mm at x = 1 m. The initial mean velocity profile is the same as in the previous case, the initial distributions of kinetic energy and length scale are modified as to satisfy the outer boundary conditions corresponding to Tu $\approx$ 1.5 p.c. and $L_\infty \approx$ 2.7 mm. At x = 1 m the boundary layer is significantly thicker and the mean velocity profile has a fuller shape when compared with the case of zero free stream turbulence. The distribution of the length scale has a small maximum near the edge of the boundary layer and decreases gradually towards the plate.

In order to demonstrate the effect of the length scale of the free stream turbulence, the results of two other cases are plotted in a similar manner in Fig. 2. The free stream turbulence intensity is Tu_1 = 0.8 p.c. for both cases and the length scale is $L_{\infty 1}$ = 1.28 mm and 3.73 mm respectively at x = 1 m. At x = 0 the values are Tu ≈ 3.8 p.c., L_∞ = 0.69 mm, and Tu ≈ 1 p.c., $L_\infty \approx 3.36$ mm respectively. The initial mean velocity profiles are in both cases the same as before. With the greater length scale a fuller shape of the mean velocity profile is produced at x = 1 m. The length scale distribution of this case (2) is similar to that of Fig. 1, case (2). In the case (1) at x = 1 m, the length scale is greater over a major part inside the boundary layer than its free stream value.

Of practical importance is the detailed investigation of the influence of the two free stream turbulence parameters on relevant boundary layer parameters like form parameter, skin friction etc.. Fig. 3 to 6 show the variation of the form parameter, the momentum loss thickness, the local skin friction coefficient, and the total thickness of the boundary layer as a function of the length scale L_∞, for various values of the intensity at position x = 1 m. The data of each run, which are represented by spots, are the results of an integration over more than hundred steps, and for each step, three or more iterations have been made. This is the reason for the scatter of the points. Higher accuracy of the computations is certainly desirable, but this requires longer computing time. Faired curves are drawn through the points of equal turbulence intensity, except for the skin friction coefficient, the scatter of which is high. However, the general trend can clearly be recognized. In qualitative agreement with experimental results, the form parameter decreases while the momentum loss thickness and skin friction coefficient

increases, when the turbulence intensity increases. The influence of the free stream turbulence length scale is small at low turbulence intensity. But with increasing turbulence intensity, the influence of the free stream length scale increases considerably. The thickness of the boundary layer increases strongly with intensity and length scale of the free stream turbulence as a consequence of decreasing form parameter and increasing momentum loss thickness.

The practice of the experimentalists to correlate the effect of the free stream turbulence on the turbulent boundary layer with the local intensity, neglects not only the effect of the structure but also the inhomogenity of the free stream turbulence field in flow direction, which is caused by the decay of the turbulence. The rate of decay, on the other hand, depends on the length scale. In order to give an idea, the ratio of turbulence intensities at x = 0 to that at x = 1 m is shown in Fig. 7 as a function of the length scale, $L_{\infty 1}$, and the intensity at x = 1 m. As is seen, the ratio Tu_0/Tu_1 is high if Tu_1 is high and $L_{\infty 1}$ is small.

The length scale of the free stream turbulence grows in flow direction, but usually not as fast as the boundary layer thickness. Consequently the ratio L_∞/δ, which is plotted in Fig. 8 versus $L_{\infty 1}$, has its greatest value near the leading edge of the plate, whereas L_∞/δ has much smaller values at x = 1 m. Remarkable is that at station x = 1 m and for greater turbulence intensity the ratio L_∞/δ has a maximum, when plotted over $L_{\infty 1}$. This means, increasing $L_{\infty 1}$ beyond a certain limit increases the boundary layer thickness so rapidly that the ratio L_∞/δ becomes smaller again.

Fig. 9 shows the development of the form parameter, H_{12}, the free stream turbulence intensity, Tu_1, and the length scale ratio L_∞/δ along the coordinate x. In the case of the zero free stream turbulence, the form parameter decreases slightly downstream in the wellknown manner. For $Tu_1 = 0.008$, the curves of H_{12}, beginning at ≈ 1.41, first decrease rapidly to a minimum at $x \approx 0.4$ m and than rise again. This suggests that the increase in H_{12} on the rear part of the plate, where the influence of the initial distributions has vanished, is caused by the decrease of the free stream turbulence intensity and length scale ratio. This supposition is confirmed by another computation with the same free stream turbulence field ($Tu_1 = 0.008$, $L_{\infty 1} = 3.73$ mm), which started with $H_{12} = 1.33$ instead of $H_{12} \approx 1.41$. It is seen that the development is very different in this case, which is represented by dotted lines in Fig. 9. The form parameter H_{12} rises first to a maximum and than decreases to a minimum at $x \approx 0.5$ m. But farther downstream, the two curves, belonging to the same free stream turbulence field, come close together. The remaining discrepancy may be attributed to the lack of accuracy of the calculation method already mentioned. The characteristics of the initial distributions seem to have faded away after an integration over a distance of 600 to 800 times the initial momentum loss thickness according to these computations.

6. Concluding Remarks

From the present investigations it can be concluded that the effects of the free stream turbulence on the turbulent boundary layer can be calculated, in principle, with a second order closure turbulence model. The effect of free stream turbulence which manifests itself in fuller mean velocity profiles, higher skin friction coefficients and greater boundary layer thicknesses, increases with intensity and integral length scale in the range of Tu_1 and $L_{\infty 1}$ values covered by the present computations. The results agree qualitatively with experiments. However, more investigations are needed before general conclusions can be drawn, especially since the presented computations suffer from some lack of accuracy.

Acknowledgement

This research is supported by the Deutsche Forschungsgemeinschaft, Bad Godesberg

References

1 Wieghardt, K. Über die turbulente Strömung in Rohr und längs einer Platte. ZAMM 24, 1944, 294-296.

2 Meier, H.U. and Kreplin, H.-P., Influence of Freestream Turbulence on Boundary-Layer Development.
AIAA Journal Vol 18, 1980, 11-15

3 Vollmers, H.and Rotta, J.C., Similar Solutions of the Mean Velocity Turbulent Energy and Length Scale Equation.
AIAA Journal Vol. 15, 1977, 714-720.

4 Meineke, E., Berechnung freier turbulenter Scherströmungen mit einem Drei-Gleichungs-Turbulenzmodell von J.C. Rotta. Deutsche Forschungs- und Versuchsanstalt für Luft- und Raumfahrt, DLR-FB 77-60, 1977.

5 Voges, R., Berechnung turbulenter Wandgrenzschichten mit Zwei-Gleichungs-Turbulenzmodellen. Dissertation Technische Universität München, 1978.

6 Rotta, J.C., Turbulente Strömungen. Stuttgart 1972.

7 Rotta, J.C., Prediction of Turbulent Shear Flow Using the Transport Equation for Turbulence Energy and Turbulence Length Scale. Von Karman Institute for Fluid Dynamics, Brussels, Lecture Series 76, 1975.

8 Coles, D.E. and Hirst E.A., Computation of Turbulent Boundary Layers - 1968. AFORSR-IFP-Stanford Conference, Vol. II, Compiled Data, 1968.

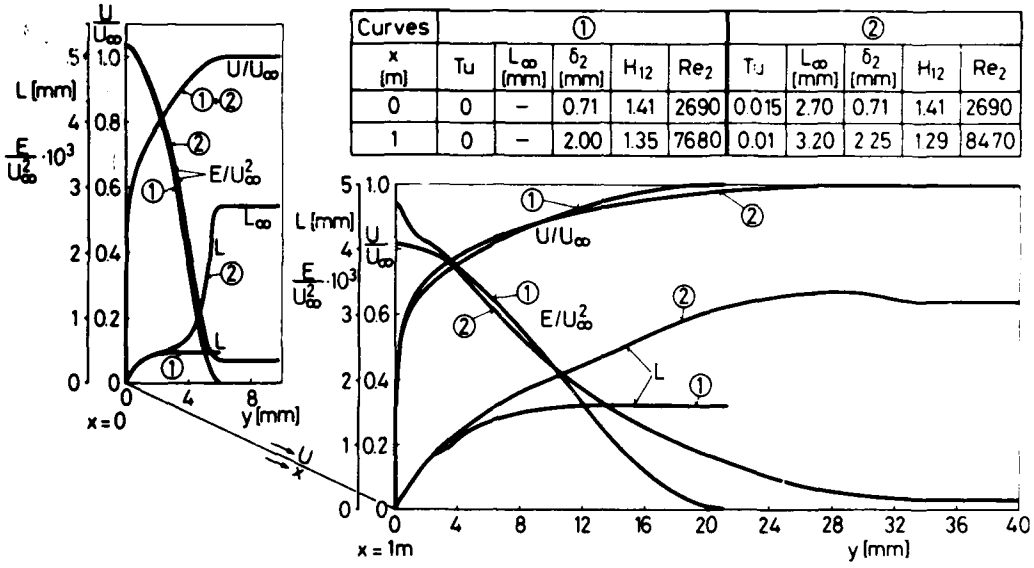

Curves	①					②				
x [m]	Tu	L_∞ [mm]	δ_2 [mm]	H_{12}	Re_2	Tu	L_∞ [mm]	δ_2 [mm]	H_{12}	Re_2
0	0	–	0.71	1.41	2690	0.015	2.70	0.71	1.41	2690
1	0	–	2.00	1.35	7680	0.01	3.20	2.25	1.29	8470

Fig. 1 Development of the turbulent boundary layer profiles without and with free stream turbulence

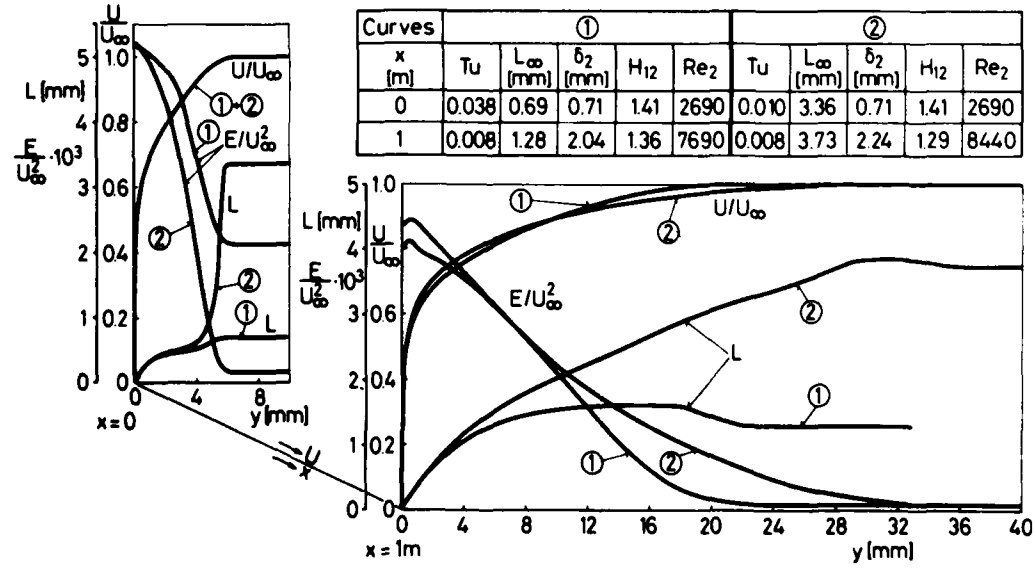

Curves	①					②				
x [m]	Tu	L_∞ [mm]	δ_2 [mm]	H_{12}	Re_2	Tu	L_∞ [mm]	δ_2 [mm]	H_{12}	Re_2
0	0.038	0.69	0.71	1.41	2690	0.010	3.36	0.71	1.41	2690
1	0.008	1.28	2.04	1.36	7690	0.008	3.73	2.24	1.29	8440

Fig. 2 Development of the turbulent boundary layer profiles with free stream turbulence of different length scales

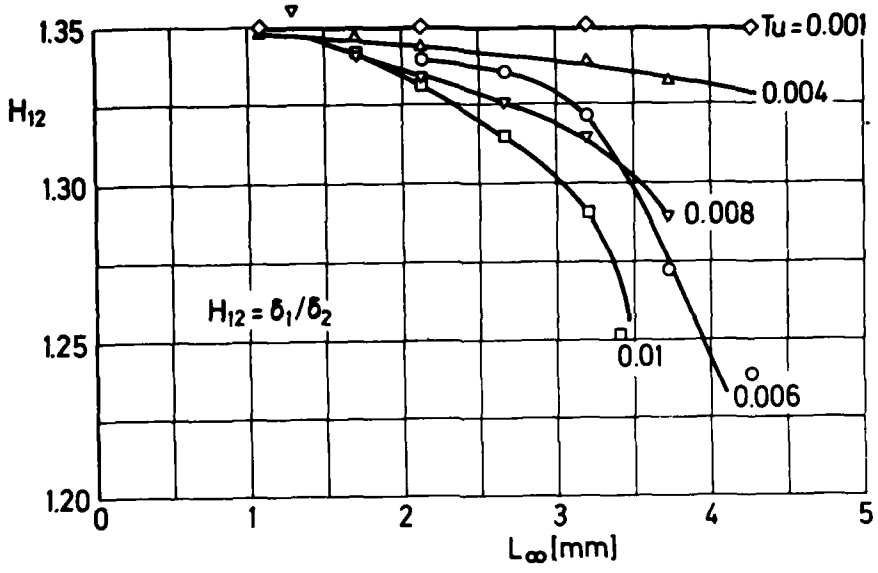

Fig. 3 Variation of the form parameter with intensity and length scale of free stream turbulence at station x = 1 m

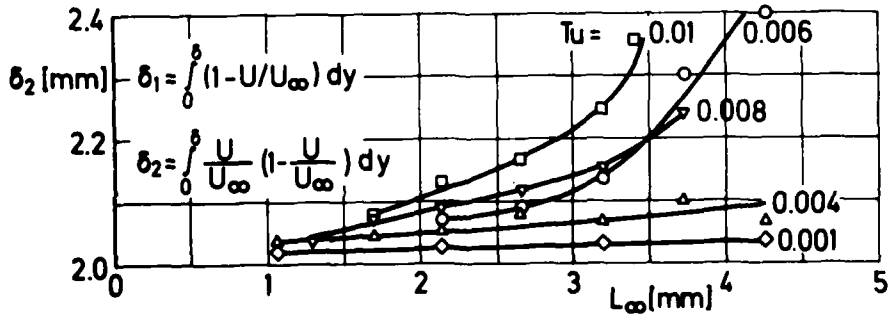

Fig. 4 Variation of the momentum loss thickness with intensity and length scale of free stream turbulence at station x = 1 m

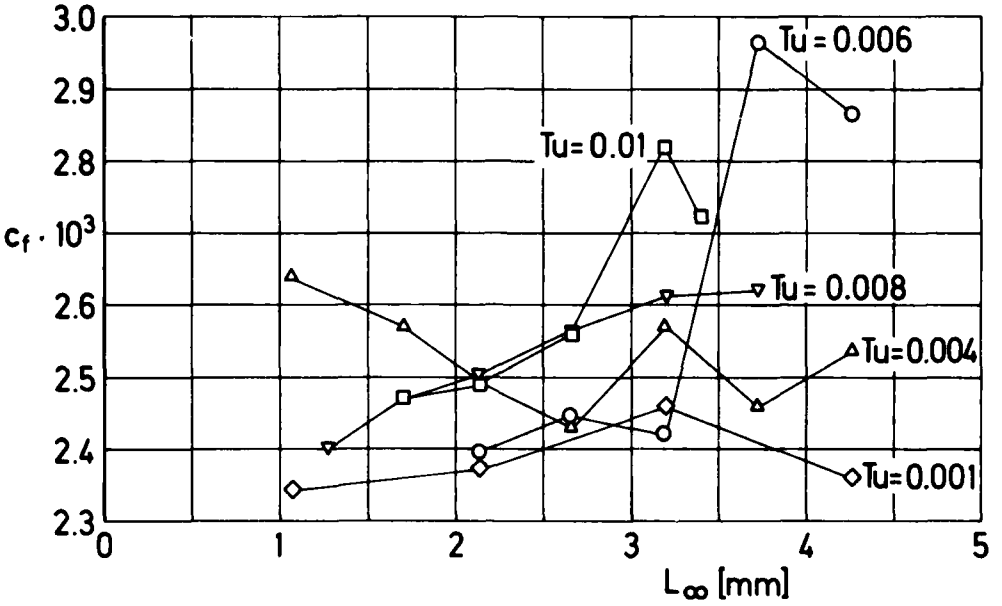

Fig. 5 Variation of the local skin friction coefficient with intensity and length scale of free stream turbulence at station x = 1 m

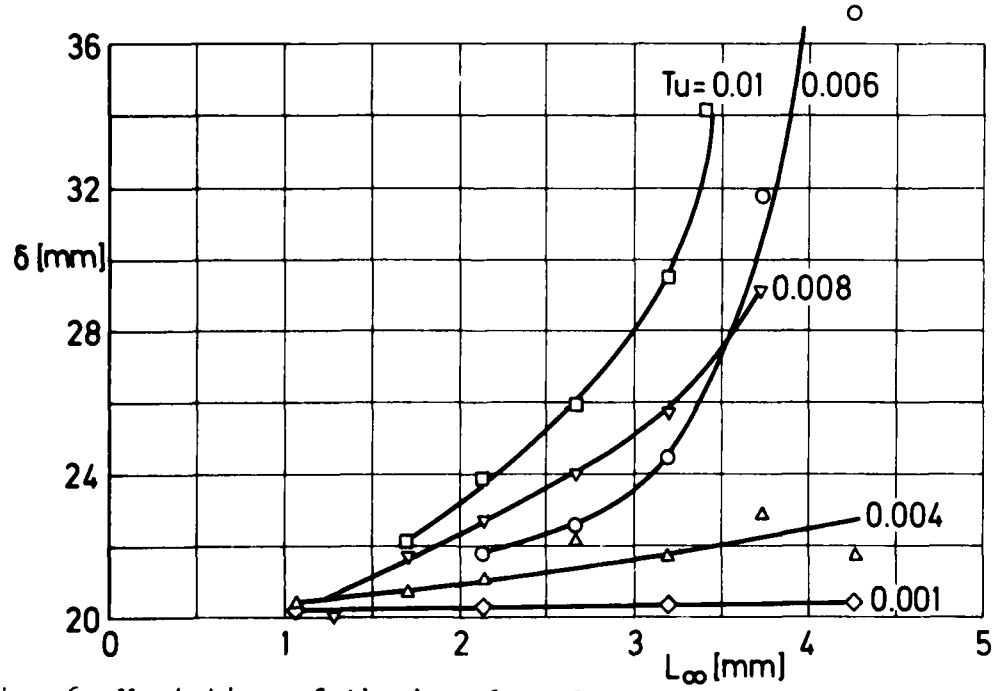

Fig. 6 Variation of the boundary layer thickness with intensity and length scale of free stream turbulence at station x = 1 m

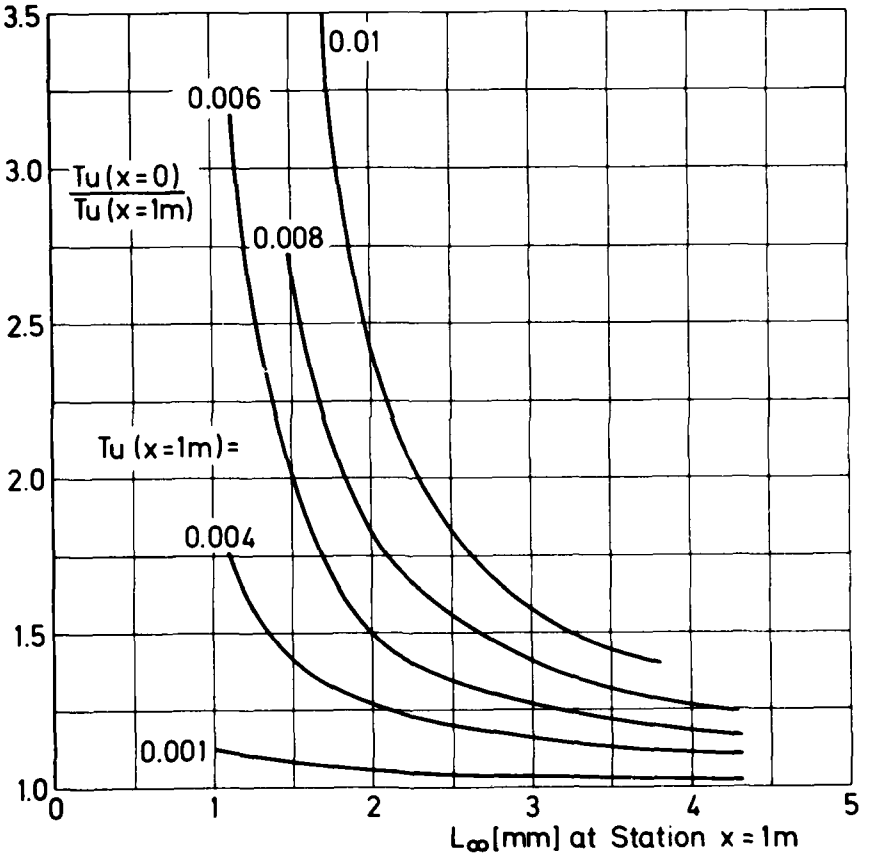

Fig. 7 Ratio of free stream turbulence intensities at x = 0 and x = 1 m as a function of Tu_1 and $L_{\infty 1}$

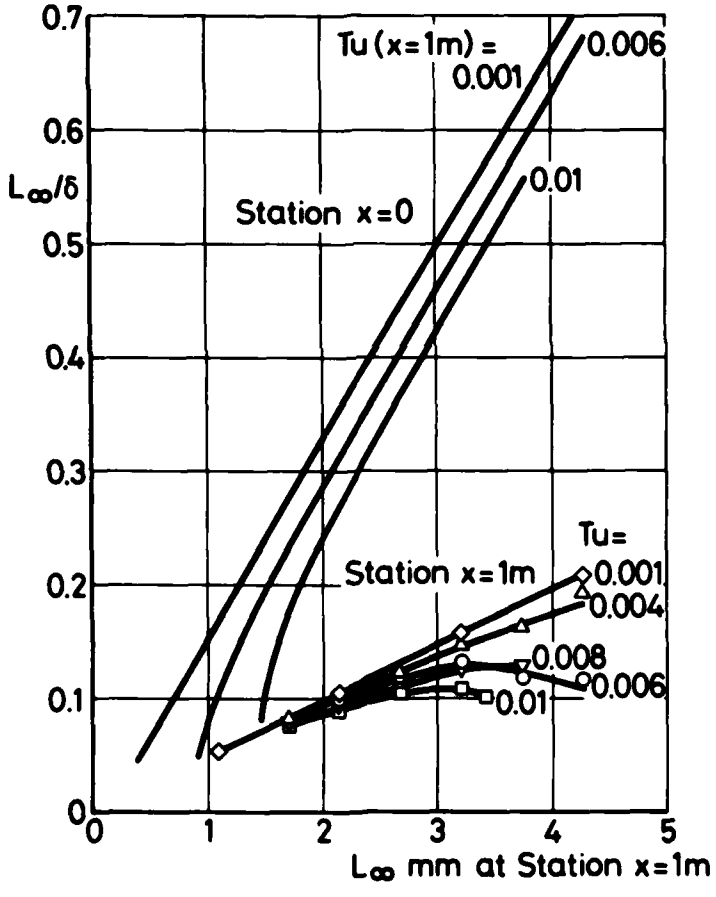

Fig. 8 Length scale ratio of free stream turbulence L_∞/δ at stations x = 0 and x = 1 m

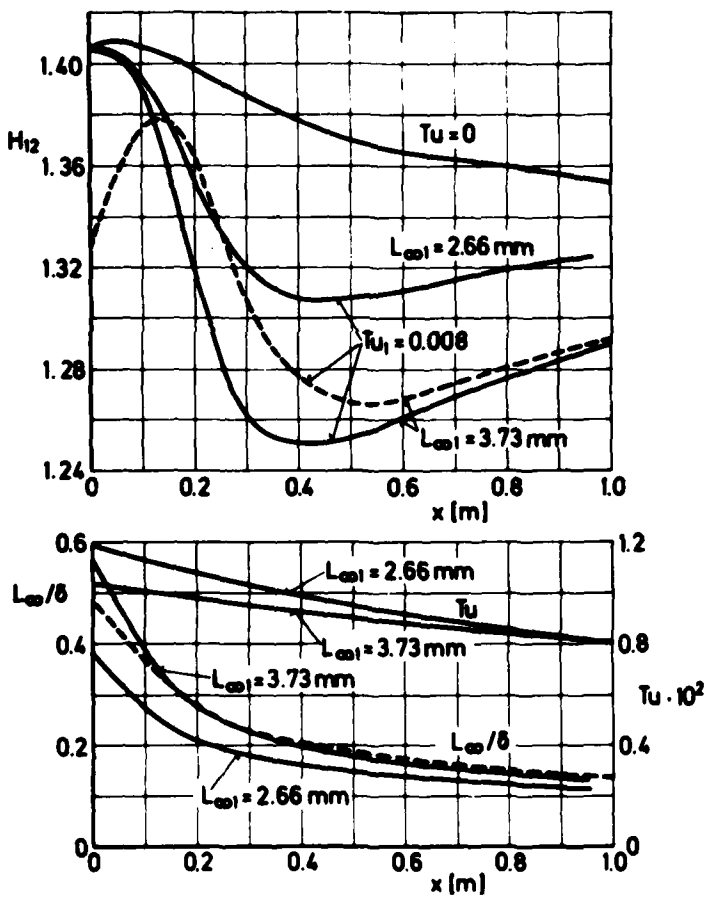

Fig. 9 Variation of form parameter, H_{12}, intensity, Tu, and length scale ratio L_∞/δ along the plate

THEORETICAL STUDY OF VISCOUS DAMPING OF TURBULENCE IN THE LAW OF THE WALL REGION†

G. R. Inger*

Virginia Polytechnic Institute and State University
Blacksburg, VA 24061

1. INTRODUCTION

Although widely used, the well-known viscous damping factor relationship for turbulent eddy shear stress near a wall, proposed by Van Driest[1] and later popularized and extended in various ways by Cebeci,[2] has in fact only a very rough heuristic basis without any solid theoretical foundation. It is therefore of fundamental and practical importance to establish a basic theory of this damping problem in the case of smooth non-porous incompressible flat plate flow, not only to better understand the limitations of the Van Driest model but also to provide the correct foundation for treating more complicated flow problems involving streamwise pressure gradients, surface roughness and wall mass transfer effects. We have undertaken such a study based on the fundamental Navier-Stokes equations and the properties of the Law of the Wall region; the present paper reports on its progress.

Our approach is essentially an extension and modification of the earlier small disturbance studies of turbulent fluctuation behavior near a wall by Sternberg[3] and by Shubert and Corcos[4]. We show that certain alterations of this work, including a different treatment of asymptotic boundary conditions far from the surface and the added enforcement of the basic Law of the Wall similitude properties, lead to a two-point value problem governing the decaying Reynolds stress field approaching the wall which shows promise as the desired theoretical model of the damping process.

2. BRIEF REVIEW OF PREVIOUS WORK

The basic problem we address, illustrated schematically in Fig. 1, can be stated as follows: given a velocity fluctuation field within the fully-turbulent portion of the Law of the Wall region adjacent to a smooth impermeable surface, develope from first principles a theory of how the average turbulent Reynolds stress associated with this field damps out toward the surface due to the action of viscosity and the no-slip condition. We confine attention here to the simplest prototype version of the problem, namely to a high Reynolds number mean flow with zero streamwise pressure gradient that contains a two-dimensional turbulent fluctuation field (it is of course recognized that this field is in reality significantly three-dimensional and ultimately must be so-treated if the present preliminary study yields promising results).

Van Driests[1] original description of the damping process was based on a

---

* Professor of Aerospace and Ocean Engineering.

† Presented to the 1980 U.S.A.F. - F.R.G. DEA Meeting, U. S. Naval Academy, Annapolis, Md., April 17.

purely heuristic analogy with the classical Stokes oscillating plane problem; as schematically summarized in Fig. 2, this approach does not satisfy even the continuity equation for the fluctuation field. Not-withstanding its wide-spread success it is thus not based on any kind of proper theory and hence cannot be soundly extended without even more such heuristic assumptions. For these reasons, we deem it highly desireable to better understand the damping process with a more proper theory of the problem.

Subsequently, Sternberg[3] in a pioneering effort constructed such a theory for a highly simplified small disturbance model of the disturbance flow in which the mean velocity profile was taken to be linear and the pressure gradient plus all inertia effects of the disturbance field were neglected (see Fig. 3). In spite of the resulting poor description of Reynolds stress damping outside the very thin inner laminar sublayer portion of the Law of the Wall region, this work remains very useful as a starting point and an appraisal of the viability of a small disturbance-analysis approach. Sternbergs work was subsequently generalized appreciably by Schubert and Concos[4] to remove many (but not all - see below) of the aforementioned limitations, with evidently even more promising results; curiously, however, the resulting Reynolds stress solutions were not examined in sufficient detail to enable an interpretation in the spirit of a better model of the Van Driest damping problem. The primary limitation on this work would appear to be an overly-simplified model of the mean Law of the Wall velocity profile and its proper coupling via the mean eddy stress to the companion fluctuation field problem.

It should be noted that we do not consider the role of the highly three-dimensional structured turbulent bursts and their associated "sweeps" which are known to occur periodically in the wall region with period $t \sim 5\delta/U_e$; rather, in the same spirit as the work by Walker et al[5], we deal only with the essentially random fluctuation field problem that is presumed to exist during the intervals between such short-lived bursts.

3. FORMULATION OF THE THEORETICAL MODEL

3.1 Assumptions

The incompressible two-dimensional Navier-Stokes equations are presumed to govern the unsteady total turbulent motion at each instant. In the usual fashion this motion is taken to be composed of statistically random fluctuations $u'(x,y,t)$, $v'(x,y,t)$, $p'(x,y,t)$ about a steady mean flow $\bar{u} = U_0(x,y)$, $\bar{v}=V_0(x,y)$, $\bar{p}=P_0(x,y)$ where those latter values involve the influence of the turbulent eddy (Reynolds) stresses $\overline{U'^2}$, $\overline{V'^2}$ and (especially) $\overline{u'v'}$.

We consider high Reynolds number boundary layer-type flows with negligable streamwise pressure gradient that are far removed from incipient separation. In such a case, the mean flow in Law of the Wall region close to the surface is accurately described by $p_0 \simeq$ constant, $V_0 \simeq 0$ with $U_0 = U_0(y)$ governed by

$$\nu \frac{dU_0}{dy} + (-\overline{u'v'}) = \tau_{w_0}/\rho \qquad (1)$$

while the corresponding instantaneous turbulent fluctuation field (after the mean motion has been subtracted out) is governed by the equations

$$\frac{\partial u'}{\partial x} + \frac{\partial v'}{\partial y} = 0 \tag{2}$$

$$\frac{\partial u'}{\partial t} + U_0 \frac{\partial u'}{\partial x} + v' \frac{dU_0}{dy} + \frac{1}{\rho}\frac{\partial p'}{\partial x} = \nu \frac{\partial^2 u'}{\partial y^2} + \frac{\partial}{\partial y}\left(\overline{u'v'} - u'v'\right) \tag{3}$$

$$\frac{\partial v'}{\partial t} + U_0 \frac{\partial v'}{\partial x} + \frac{1}{\rho}\frac{\partial p'}{\partial y} = \nu \frac{\partial^2 v'}{\partial y^2} + \frac{\partial}{\partial y}\left(-v'^2\right) \tag{4}$$

To simplify the analysis while still retaining the essential physics of the problem we further introduce two simplifying assumptions associated with the relative thinness of the damping region and its proximity to the wall: (a) we take $\partial p'/\partial y \simeq 0$ with $p' \simeq p'(x,t)$ given by the fully-turbulent-region, thereby eliminating the need for Eq. 4 ; (b) we linearize the disturbance problem by neglecting the last non-linear turbulent shear term in Eq. 3. For the high Reynolds number conditions of interest, the validity and limitations of these approximations have been discussed in detail by Schubert and Corcos[4] and hence need not be examined here; suffice it to say that the resulting small disturbance relations retain the main physical elements of the damping problem under investigation. In addition, we follow both Ref. 3 and 4 by representing the imposed turbulent fluctuation field as simple time - and streamwise - periodic functions with a single characteristic wavelength $\lambda_x = 2\pi/k$ and convection speed U_c (which is <u>not</u> in general equal to the local mean flow velocity[3]). Thus we take

$$u' = \text{Real}\left[u(y)\, e^{ik(x-U_c t)}\right] \tag{5}$$

$$v' = \text{Real}\left[v(y)\, e^{ik(x-U_c t)}\right] \tag{6}$$

$$p' = p_e \cos(kx - kU_c t) \tag{7}$$

where p_e is a given real number, and seek to find the y-variation of the real and imaginary parts of the complex damping functions $u = u_r + iu_i$, $v = v_r + iv_i$ inward across the Law of the Wall region. Corresponding to Eqs. (5), (6), we <u>note</u> that averaging over one or more periods yields the correlation value $\overline{u'v'} = 1/2\,(u_r v_r + u_i v_i)$.

3.2 The Resulting Boundary Value Problem

The aforementioned simplifying assumptions thus yield from Eqs. (1)-(4) the following set of governing ordinary differential equations:

$$ikU + \frac{dV}{dy} = 0 \tag{8}$$

$$ik(U_0 - U_c)U + \frac{dU_0}{dy}V + \frac{ik p_e}{\rho} = \nu \frac{d^2 U}{dy^2} \tag{9}$$

$$\frac{dU_0}{dy} - \frac{1}{2}(U_r V_r + U_i V_i) = \tau_{w_0}/\mu \tag{10}$$

At this point we note that Eqs. (8) and (9) can be combined to eliminate p_e and U and obtain the following equivalent equation in V alone:

$$(U_0 - U_c)\frac{d^2V}{dy^2} - \frac{d^2U_0}{dy^2}V = \frac{-iV}{k}\frac{d^4V}{dy^4} \tag{11}$$

while from (8) and (10) the corresponding total shear equation becomes

$$\frac{dU_0}{dy} + V_r\frac{dV_i}{dy} - V_i\frac{dV_r}{dy} = \tau_{w_0}/\mu \tag{12}$$

Now Eqs. (11) and (12) constitute a coupled fourth order differential system in V which thus requires four boundary conditions plus a single condition on U_0. Three are provided by the no slip conditions on the impermeable wall that $V(o) = 0$, $U_0(o) = 0$ and $U(o) = dV/dy(o) = 0$. Another is provided by evaluating the differential equation (9) itself at the wall; in terms of V this yields

$$d^3V/dy^3(0) = k^2 p_e/\mu \tag{13}$$

The remaining condition is obtained by requiring that the effects of viscosity vanish in the outer logarithmic mean flow region "far" from the wall; that is, from Eq. (11) we require that $V \to V_{inv}$ for $U_\tau y/\nu >> 1$ where $\rho U_\tau^2 \equiv \tau_{wo}$ and V_{inv} satisfies

$$(U_{0,ASYM} - U_c)\frac{d^2V_{INV}}{dy^2} = \frac{d^2U_{0,ASYM}}{dy^2}V_{INV} \tag{14A}$$

with[6]

$$U_{0,ASYM} = U_\tau[C + .41\ln(U_\tau y/\nu)] \tag{14B}$$

This is to be applied as a homogeneous boundary condition on the solution to (11) at a y large enough to insure (consistent with Eq. 14B) that the first term in Eq. (12) becomes negligible compared to the other terms.

We thus have to do with a fourth order homogeneous split boundary value problem for V wherein the driving disturbance mechanism appears solely in the single inner boundary condition (13) due to the imposed pressure fluctuation level*. Owing to the eddy stress coupling term in Eq. (12), however, our problem is <u>not</u> linear inspite of the linearized form of the V-Equation (11); this plus our satisfaction of the proper logarithmic mean flow profile (14B)

* This is as it should be: "the turbulent pressure fluctuation leaves its footprint on the wall".[3]

far from the wall are the major points of improvement over the earlier work of Schubert and Corcos.[4]

3.3 Law of the Wall Similitude Considerations

Before solving the aforementioned boundary value problem, it is appropriate and revealing to first introduce the implications of the similitude properties pertaining to turbulent flow in the Law of the Wall region. Now it is a well-established result of dimensional analysis and experiment[6,7] that the mean velocity and Reynolds stress profiles in the absence of pressure gradient or mass transfer possess the fundamental similitude property that

$$U_o^* \equiv U_o/U_\tau = f(y^*) \tag{15A}$$

$$\overline{u'v'}/U_\tau^2 = g(y^*) \tag{15B}$$

with $y^* \equiv U_\tau y/\nu$ and where f and g are functions containing only universal constants (e.g., the "Karman constant" K = .41). In particular, f and g have logarithmic and constant form, respectively, in the fully turbulent region $y^* >> 1$, whereas $f \sim y^*$ and $g \sim y^{*4}$, respectively, in the laminar sublayer very close to the wall. Furthermore, Yaglom[7] suggests that the same type of similitude applies to the fluctuation field as well, and indeed this may be inferred from the strong influence of U_o and (especially) the non-linear Reynolds stress coupling effect contained in the above disturbance problem equations. Thus a detailed examination of these equations when rewritten in terms of U_o^* and y^* shows that appropriately - non-dimensionalized U and V variables must be functions only of the single independent variable y^* involving at most universal constants.

We are thus led to introduce the non-dimensional fluctuation velocity components $U^* = U/U_{ref}$, $V^* = V/V_{ref}$ in terms of reference speeds U_{ref}, V_{ref} which by virtue of imposing the aforementioned similude requirements on Eqs. (8) and (10) must satisfy the relations $U_{ref} = (U_\tau/\nu k)\, V_{ref}$ and $U_{ref} V_{ref} = 2U_\tau^2$. The resulting appropriate non-dimensional problem for $V^*(y^*)$ is then obtained from Eqs. (11) - (13) as follows:

$$(\lambda_c - U_o^*)\frac{d^2V^*}{dy^{*2}} + \frac{d^2U_o^*}{dy^{*2}}V^* = i\lambda_\nu \frac{d^4V^*}{dy^{*4}} \tag{16}$$

$$\frac{dU_o^*}{dy^*} + V_R^*\frac{dV_I^*}{dy^*} - V_I^*\frac{dV_R^*}{dy^*} = 1 \tag{17}$$

with

$$\frac{d^3V^*}{dy^{*3}}(0) = \lambda_p/\lambda_\nu \tag{18}$$

where each of the parameters

$$\lambda_c \equiv U_c/U_\tau \tag{19A}$$

$$\lambda_\nu \equiv U_\tau/k\nu \tag{19B}$$

$$\lambda_p \equiv P_e/\rho U_\tau^2 \tag{19C}$$

must be universal constants across the Law of the Wall region. These similitude constraints [which we re-emphasize follow from the non-linear Reynolds stress coupling effect in Eq. (12) plus the wall boundary condition (13)] imply that only those fluctuation fields satisfying Eqs. (19) are physically compatible with the Law of the Wall. They further imply that k and U_c must each vary with Reynolds number; for, if λ_c and λ_v are to remain constant, then $U_c \sim U_\tau \sim \sqrt{C_{fo}}$ and $k \sim U_\tau/\nu \sim \sqrt{C_{fo}}$ so both in fact must decrease slowly with increasing Reynolds number. This appears to be in rough agreement with experimental trends.[4] Likewise, the requirement of constant $p_e/\rho U_\tau^2$ is also supported by experimental observation.

4. SOLUTION RESULTS

As of this writing, the necessarily - numerical solution of the above non-dimensional boundary value problem is just being set up so that complete results are not yet available. However, an important analytical property of the solution can be noted for the Reynolds stress decay approaching the wall.

Making the physically - reasonable assumption that both real and imaginary parts of V^* are analytic functions of y^* as $y^* \to 0$ and thus expanding them in Taylor series away from the wall, we have upon noting the inner boundary conditions that

$$V_r^* = C_2 y^{*2} + C_3 y^{*3} + \cdots \tag{20A}$$

$$V_i^* = D_2 y^{*2} + D_3 y^{*3} + \cdots \tag{20B}$$

where the two pairs of constants (C_2,C_3; D_2, D_3) are the basic unknown "initial" values in terms of which the coefficients of higher order terms in Eqs. 20 can be found from the differential Eq. (16) itself. Then using (20A) we immediately obtain the corresponding non-dimensional Reynolds stress behavior (see Eq. (17):

$$V_r^* \frac{dV_i^*}{dy^*} - V_i^* \frac{dV_r^*}{dy^*} = 2\underbrace{(C_2 D_2 - D_2 C_2)}_{0} y^{*3} + (C_3 D_2 - D_3 C_2) y^{*4} + \cdots \tag{21}$$

that is, the Reynolds stress damps out like y^3 deep within the laminar sublayer. This result is in qualitative agreement with experiment (including the very data used by Van Driest[1] to validate his damping rule) and is independent of the particular values of C_2, C_3, D_2 and D_3.

Acknowledgement

This research is supported by NASA under Grant NSG-1589 with Dr. Jerry Hefner as technical monitor.

REFERENCES

1. Van Driest, E. R., "On Turbulent Flow Near a Wall," Jour. of Aero. Sci. 1956, pp. 1007-1011.

2. Cebeci, T. and A.M.O. Smith, "Analysis of Turbulent Boundary Layers," Academic Press, N. Y., 1974.

3. Sternberg, J., Jour. of Fluid Mech. 13, 1965, pp. 241-271.

4. Schubert, G. and G. M. Corcos, Jour. Fluid Mech. 29, 1967, pp. 113-135.

5. Walker, J. D. A., D. E. Abbott and R. K. Scharnhorst, "On The Nominally Steady Two-Dimensional Time-Mean Turbulent Boundary Layer," Purdue University Tech. Report CFMTR-76-1 (AFOSR TR-76-0489), Feb. 1976.

6. White, F. M., Viscous Fluid Flow, McGraw-Hill, pp. 470-477.

7. Yaglom, A. M., "Similarity Laws for Constant Pressure and Pressure Gradient Wall Flows," Annual Rev. of Fluid Mech. 1979. pp. 505-540.

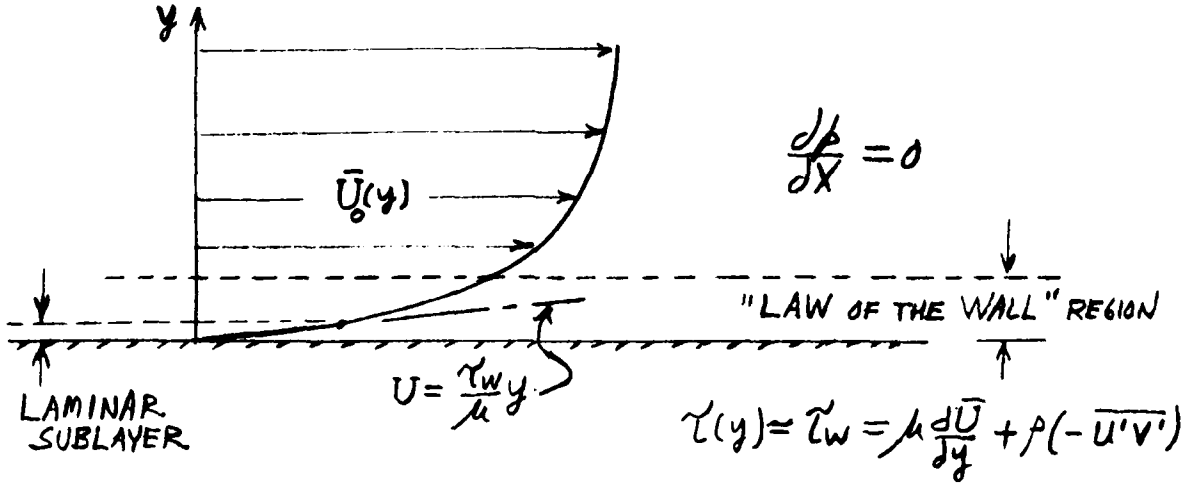

THE FUNDAMENTAL PROBLEM

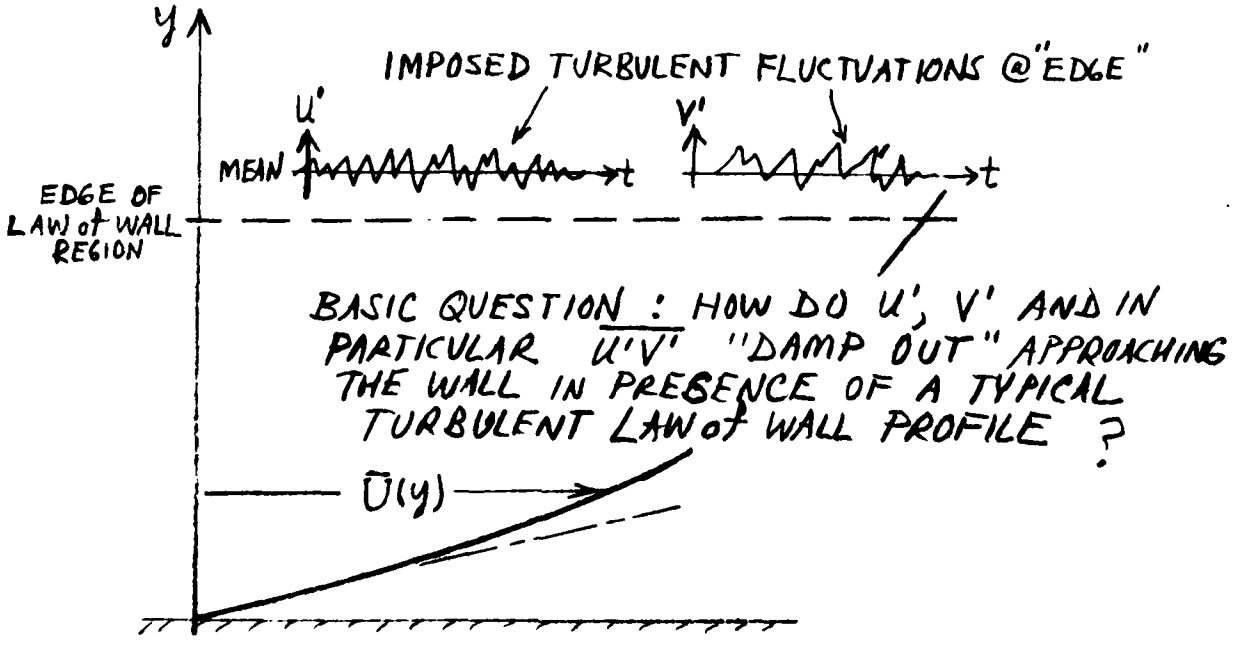

FIG. 1

Van Driest's Heuristic Solution (1956)

(a) A-Priori Analogy with the Stokes Oscillating Infinite Plane Solution:

$$u' \approx u'(\infty)\left(1 - e^{-Ky}\right)$$

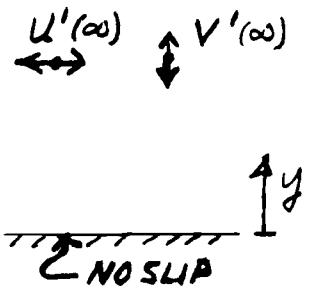

(b) Assumes $v' \sim u'$; CONTINUITY EQ^N FOR FLUCTUATION FIELD IGNORED

RESULT :

$$\overline{u'v'} = \underbrace{\overline{u'v'(\infty)}}_{\text{FULLY-TURB. VALUE}} \cdot \left(1 - e^{-y/A}\right)^2$$

with the constant "A" chosen to fit data

FIG. 2

Sternberg's Simplified Linearized Theory (1961)

Solve (Neglected terms struck through)

$$\frac{\partial u'}{\partial t} \simeq \nu \frac{\partial^2 u'}{\partial y^2} - \frac{1}{\rho}\cancel{\frac{\partial p}{\partial x}} - U_0\cancel{\frac{\partial u'}{\partial x}} - v'\cancel{\frac{dU_0}{dy}}$$

(THE RAYLEIGH PROBLEM)

and $\partial v'/\partial y + \partial u'/\partial x = 0$

within $U_0 \simeq \tau_w y/\mu$

(NOTE: SOLUTION OBTAINED ASSUMING SIMPLE HARMONIC FORM
$u' \sim e^{K_x x - \beta t} \cdot F(y)$)

RESULT:

$$\overline{u'v'} = \overline{u'v'(\infty)}\left\{(1 - e^{-y/c})^2 + 2\left(1 - \frac{y}{c}\sin\frac{y}{c} - \cos\frac{y}{c}\right)e^{-y/c}\right\}$$

FIG. 3

Further Studies of a Low-Reynolds-Number Turbulence Model

Kuei-Yuan Chien

Naval Surface Weapons Center
Silver Spring, Maryland USA

Abstract

This paper presents the results based on a slight modification of our low-Reynolds-number turbulence model described at the 1979 DEA meeting. The new model was applied to a channel flow and to a boundary-layer flow over a flat plate. Results were compared with the model of Jones and Launder and with measurements. For the cases considered, present theory not only yields better predictions of the peak turbulent kinetic energy, but requires about one tenth of the computer time of the theory of Jones and Launder. Finally, some preliminary findings based on the idea of using stability theory results as the initial data for the present turbulence model for transition studies are also presented.

1. Introduction

A low-Reynolds-number turbulence model in which two partial differential equations were used to describe the development of the turbulent kinetic energy and its rate of dissipation was described in Ref. 1. A key assumption was that the eddy viscosity ν_t behaves as y^4 near the wall $y = 0$. Although generally good agreement was found between the theory and experiments, the theory overpredicted the flat-plate mean velocity distribution for $y^+ \sim 30$ to 200. This fact suggests that the theory underpredicts the eddy viscosity distribution in the near-wall region. In such a region, there is little difference between channel and boundary-layer flows. The turbulent shear stress, given by the relation

$$-\overline{u'v'} = \nu_t \frac{\partial u}{\partial y} \tag{1}$$

is plotted in Fig. 1 where the solid lines are theoretical predictions of Ref. 1 and the symbols represent experimental data of Laufer (Ref. 2), Eckelmann (Ref. 3), and Schildknecht, Miller and Meier (Ref. 4). (The notations are identical to those of Ref. 1.) Because of the compensating effect of the two terms on the right hand side of Eq. (1), the predictions and measurements are seen to agree quite well for $y^+ \gtrsim 30$. Despite this compensating effect, the theory significantly underpredicts the turbulent shear stress distribution for $y^+ < 15$. Consequently, the behavior of the turbulence model very close to the wall needs to be modified. This is given in Sec. 2. Results of the new model will be compared with the available experimental data and with the model of Jones and Launder in Sec. 3. Finally, some preliminary findings based on the idea of using the linear stability theory results as the initial data for the present model for calculations at lower Reynolds numbers will be briefly discussed.

2. The Turbulence Model

The basic approach is the same as that of Ref. 1, namely, by adding the kinematic viscosity to the turbulent diffusivity in equations of high-Reynolds-number form (Eqs. (1) and (2) of Ref. 1) to account for the effect of molecular diffusion, and by adding the "wall" dissipation terms to represent the true finite rate of energy dissipation at a solid wall. Therefore, the behavior $\varepsilon \sim y^2$ near $y = 0$ is preserved. This ensures the desired requirement that the turbulence length scale $\sim k^{3/2}/\varepsilon \sim y$ since $k \sim y^2$ near $y = 0$.

Three modifications have been introduced into our previous turbulence model (Ref. 1). First, the dissipation term in the ε-equation is modified to fit the data of the decaying homogeneous grid turbulence at both high and low Reynolds numbers. Secondly, the behavior of the eddy viscosity near the wall is kept as $\nu_t \sim y^3$. Lastly, the "wall" dissipation term in the k-equation is not being damped. The details can be found in Ref. 5, and the governing equations are:

$$\frac{Dk}{Dt} = \frac{\partial}{\partial y}[(\nu+\nu_t)\frac{\partial k}{\partial y}] + \nu_t(\frac{\partial u}{\partial y})^2 - \varepsilon - \frac{2\nu k}{y^2} \tag{2}$$

$$\frac{D\varepsilon}{Dt} = \frac{\partial}{\partial y}[(\nu + \frac{\nu_t}{\sigma})\frac{\partial \varepsilon}{\partial y}] + c_1 \frac{\varepsilon}{k} \nu_t(\frac{\partial u}{\partial y})^2 - \frac{\varepsilon}{k}[c_2 f\varepsilon + \frac{2\nu k}{y^2} \exp(-\frac{u_* y}{2\nu})] \tag{3}$$

$$\nu_t = c_\mu \frac{k^2}{\varepsilon} [1 - \exp(-c_3 u_* y/\nu)] \tag{4}$$

where (Ref. 6)

$$f = 1 - \frac{0.4}{1.8} e^{-(k^2/6\nu\varepsilon)^2}$$

Expanding Eqs. (2) to (4) near $y = 0$, one may confirm that $\nu_t \sim y^3$ and the "wall" dissipation terms exactly balance the molecular diffusion terms at $y = 0$. As explained in Ref. 5, the values for the various constants are:

$c_\mu = 0.09$, $c_1 = 1.35$, $c_2 = 1.8$, $c_3 = 0.0115$ and $\sigma = 1.3$. Note also that in the exponential (damping) term of Eq. (3), the constant value of $\frac{1}{2}$, which was used in our initial study (Ref. 7), has been kept unchanged.

3. Turbulent Results

The above set of equations was applied to the fully developed channel flow problem and solved by the time-dependent marching technique using the Crank-Nicolson finite difference method. The near-wall turbulent shear stress distribution of the present prediction is compared with the measurements of Laufer (Refs. 2 and 8), Eckelmann (Ref. 3) and Schildknecht, et al (Ref. 4) in Fig. 2. Comparing to Fig. 1, it is clear that the present model has removed the deficiency of our previous model; the agreement between the present theory and the measurements is extremely good for all values of y^+. As shown in Ref. 5, this is true for the whole channel width.

A more critical evaluation of the present model is a comparison of the turbulent kinetic energy distribution in the near-wall region. In addition to the channel measurements of Refs. 2, 9 and 10, the pipe flow data of Laufer (Ref. 8) and that of Schildknecht, Miller and Meier (Ref. 4) are also included in Fig. 3. Also shown in Fig. 3 are the present predictions at Re = 3850, 15200 and 30800, respectively. Because of the large amount of scatter among all the data, a definitive conclusion on the accuracy of the present theory is difficult to draw. Present model yields predictions that seem to capture the general shape and lie within the band of the data.

To provide a proper perspective, the turbulence model of Jones and Launder (JL) (Ref. 11) was inserted into our computer program and calculations were carried out. The corresponding turbulent kinetic energy results are compared with the same set of experimental data in Fig. 4. It is clear that

the degree of agreement here is worse than that shown in Fig. 3. A somewhat surprising but important finding is the much longer computer time required by the JL model as compared to the present model. For the cases considered, present model requires only about one tenth of the computer time of the JL model.

Eqs. (2) to (4) with the same constants have also been applied to the problem of a turbulent boundary layer flow over a flat plate. These equations and the continuity and the momentum equations were solved by the same marching technique (in x) using the Crank-Nicolson finite-difference method. The calculated distribution of the skin friction c_f as a function of the Reynolds number based on the momentum thickness $R_{e\theta}$ is compared with the measurements of Smith and Walker (Ref. 12) and of Wieghardt and Tillmann (Ref. 13), and with the correlation formula of Coles (Ref. 14) and that of Karman and Schoenherr (Ref. 15) in Fig. 5. The agreement is seen to be extremely good.

The calculated nondimensional velocity $u^+(\equiv u/u_*)$ at $R_{e\theta} = 7700$ is plotted against y^+ in Fig. 6. Also shown are the measurements of Klebanoff (Ref. 16) at the same $R_{e\theta}$ and that of Wieghardt and Tillmann (Ref. 13) at $R_{e\theta} = 7170$ and 8170, respectively. It is clear from Fig. 6 that the overprediction of Ref. 1 has been corrected and the agreement between theory and experiments is very good.

The distribution of the turbulent kinetic energy (normalized by the free-stream velocity squared) across the flat-plate boundary layer as predicted by the present model at $R_{e\theta} = 7700$ is compared in Fig. 7 with Klebanoff's data (Ref. 16) at the same Reynolds number (y = 0 is at the wall and $y/\delta = 1$ is at the boundary layer edge). The theory predicts a very sharp increase of the turbulent kinetic energy from zero at the wall to a peak at $y/\delta \approx 0.0089$, and

then an almost equally rapid drop followed by a much slower decline. Although Klebanoff's data do not locate the peak exactly, the agreement with the theory is very good.

Calculations using the same numerical scheme but based on the JL model (Ref. 11) have also been carried out. Results indicate again that the computer time required by the JL model is about ten times that of the present model. To cut down the computational cost, the results of the JL model shown below have been started at $R_{e\theta}$ = 5250 using the results of the present model at that location as the initial conditions. The influence of the initial conditions died down rather quickly and the calculated c_f distribution is also included in Fig. 5. It is seen that the agreement is quite good although the JL model yields a prediction that is slightly lower than the data and the present theory. The calculated u^+ distribution at $R_{e\theta}$ = 7700 based on the JL model, as shown in Fig. 6, is in good agreement with the present model and with the data. On the other hand, similar to the channel flow results, the turbulent kinetic energy distribution of the JL model as shown in Fig. 7 is seen to yield a peak value that is considerably lower than both the measurements and the present theory.

4. Transition Study

Because of the general success of the present model in providing detailed descriptions of the turbulence structure such as the turbulent kinetic energy and the shear stress distributions, it is natural to investigate the applicability of the model at much lower Reynolds numbers where the flow may be transitional. This line of approach has been pursued by several investigators (Refs. 17-19). Near the beginning of transition caused by small disturbances where linear stability theory is valid, the disturbance frequency is an important parameter

of the problem. Therefore, a key question faced by applying turbulence-model equations to transition studies is the manifestation of the frequency effect in the calculation. This is achieved in the present study by using the results of linear stability theory as the initial conditions for Eqs. (2) and (3).

Linear stability of parallel flows has been considered by many investigators. A summary of calculations for a flat-plate boundary layer is given by Jordinson (Ref. 20). In the stability theory the perturbation is assumed to be periodic both in space and in time. The wave number α and the frequency β are made dimensionless using the freestream velocity Ue and the displacement thickness of the Blasius boundary layer δ^*. Since the effect of nonparallelism is small at a Reynolds number R (based on δ^*) of 1000 (Ref. 21), the tabulated eigenfunction solution of Jordinson (Ref. 20) for R = 998 and β = 0.1122 is used to generate the initial conditions for the present model. The point lies inside the neutral stability curve and the real and imaginary parts of the wave number are, respectively, α_r = 0.3086, α_i = -0.0057. Turbulent shear stress $-\overline{u'v'}$, kinetic energy k, and the true rate of energy dissipation D are calculated from the definitions, with the required differentiations accomplished using 4th order accurate finite-difference formulae. The Blasius velocity profile is used in conjunction with Eq. (1) to determine ν_t, and ε is calculated from the relation

$$D = \varepsilon + \frac{2\nu k}{y^2} \tag{5}$$

Substituting these results into Eq. (4), one may determine c_3 which is now not only different from its value for the fully turbulent case, but a function of y as well. This is perhaps not surprising since eigenfunctions at different values of β will in principle yield different

distributions of c_3. One should note that while quantities such as k, ε, and ν_t as calculated in the above manner still depend on one parameter (which may be taken as the freestream turbulence intensity), c_3 as calculated from Eq. (4) is uniquely determined. One may map out the frequency dependence of c_3 from eigenfunction solutions of the stability theory at different values of R and β. In the present paper, however, we shall make only one comparison with the linear stability theory (Ref. 20) and experiment (Ref. 22).

A quantity of interest is the amplification curve at constant frequency F ($\equiv\beta/R$), which is traditionally expressed as $\ell n(A/A_0)$ where A is the perturbation amplitude at R and A_0 the corresponding quantity at R_0 which is a point on branch I of the neutral stability curve. For our model, $A \approx \sqrt{k}$. Without the relation $c_3(\beta,R)$, we cannot compute the amplification curve as a function of R. However, its slope at R = 998 can be calculated since now the distribution of c_3 can be kept frozen and A_0 is immaterial. The value of $10^3\, d\ell n(A/A_0)/dR$ as determined from the stability theory and the experiment is 3.3 and 2.9, respectively (Fig. 7 of Ref. 22), and the corresponding value as calculated from the present model is 3.6. In view of the relatively low value of R, the agreement is indeed quite encouraging.

Concluding Remarks

A low-Reynolds-number turbulence model has been developed and applied to the channel flow and boundary-layer flow. Comparisons between the present theory and the various experimental measurements have been made and good agreement has been found to be generally the case. Calculations based on the JL model indicate that it underpredicts the turbulent kinetic energy peak considerably. Preliminary calculation based on the idea of using stability theory results as the initial data for the present turbulence model for transition studies is quite encouraging.

Acknowledgment

This work was sponsored by the Naval Air Systems Command, Task No. 9R02302003 (Boundary Layer Research) under the cognizance of Mr. W. C. Volz (AIR 320C).

References

1. K.-Y. Chien, "Progress toward a Transport Model for Transitional/Turbulent Flow Predictions," US/FRG Data Exchange Agreement Meeting, 24-26 April 1979, West Germany; BMVG-FBWT 79-31, pp. 548-566.
2. J. Laufer, "Investigation of Turbulent Flow in a Two-Dimensional Channel," NACA Rept. 1053, 1951.
3. H. Eckelmann, "The Structure of the Viscous Sublayer and the Adjacent Wall Region in a Turbulent Channel Flow," J. Fluid Mechanics, Vol. 65, p. 439, 1974.
4. M. Schildknecht, J. A. Miller and G. E. A. Meier, "The Influence of Suction on the Structure of Turbulence in Fully Developed Pipe Flow," J. Fluid Mechanics, Vol. 90, p. 67, 1979.
5. K.-Y. Chien, "Predictions of Channel and Boundary Layer Flows with a Low-Reynolds-Number Two-Equation Model of Turbulence," AIAA 18th Aerospace Sciences Meeting, 14-16 January 1980, Paper No. 80-0134.
6. K. Hanjalic and B. E. Launder, "Contribution Towards a Reynolds-Stress Closure for Low-Reynolds-Number Turbulence," J. Fluid Mechanics, Vol. 74, p. 593, 1976.
7. K.-Y. Chien, "On the Modelling of Turbulence Near a Solid Wall," paper presented at the Navy/Air Force Science and Engineering Symposium, San Diego, Calif., Oct. 17-19, 1978.

8. J. Laufer, "The Structure of Turbulence in Fully Developed Pipe Flow," NACA Rept. 1174, 1954.

9. J. A. Clark, "A Study of Incompressible Turbulent Boundary Layers in Channel Flow," J. Basic Eng., Vol. 90, p. 455, 1968.

10. H.-P. Kreplin and H. Eckelmann, "Behavior of the Three Fluctuating Velocity Components in the Wall Region of a Turbulent Channel Flow," Physics of Fluids, Vol. 22, p. 1233, 1979.

11. W. P. Jones and B. E. Launder, "The Prediction of Laminarization with a 2-Equation Model of Turbulence," Int. J. Heat Mass Transfer, Vol. 15, p. 301, 1972.

12. D. W. Smith and J. H. Walker, "Skin-Friction Measurements in Incompressible Flow," NASA TR R-26, 1959.

13. K. Wieghardt and W. Tillmann, "On the Turbulent Friction Layer for Rising Pressure," NACA TM 1314, 1951.

14. D. E. Coles, "The turbulent boundary layer in a compressible fluid." The Rand Corporation Report R-403-PR, 1962.

15. E. J. Hopkins and M. Inouye, "An Evaluation of Theories for Predicting Turbulent Skin Friction and Heat Transfer on Flat Plates at Supersonic and Hypersonic Mach Numbers," AIAA Journal, Vol. 9, p. 993, 1971.

16. P. S. Klebanoff, "Characteristics of Turbulence in a Boundary Layer with Zero Pressure Gradient," NACA Rept. 1247, 1955.

17. C. duP. Donaldson, "A Computer Study of an Analytical Model of Boundary Layer Transition," AIAA Journal, Vol. 7, p. 271, 1969.

18. D. C. Wilcox, "Turbulence-Model Transition Predictions," AIAA Journal, Vol. 13, p. 241, 1975.

19. M. L. Finson, "On the Application of Second-Order Closure Models to Boundary Layer Transition," AGARD-CP-224, paper no. 23, 1977.

20. R. Jordinson, "The Flat Plate Boundary Layer. Part 1. Numerical Integration of the Orr-Sommerfeld Equation," J. Fluid Mechanics, vol. 43, p. 801, 1970.

21. W. S. Saric and A. H. Nayfeh, "Nonparallel Stability of Boundary-layer Flows," Physics of Fluids, Vol. 18, p. 945, 1975.

22. J. A. Ross, F. H. Barnes, J. G. Burns and M. A. S. Ross, "The Flat Plate Boundary Layer. Part 3. Comparison of Theory with Experiment," J. Fluid Mechanics, Vol. 43, p. 819, 1970.

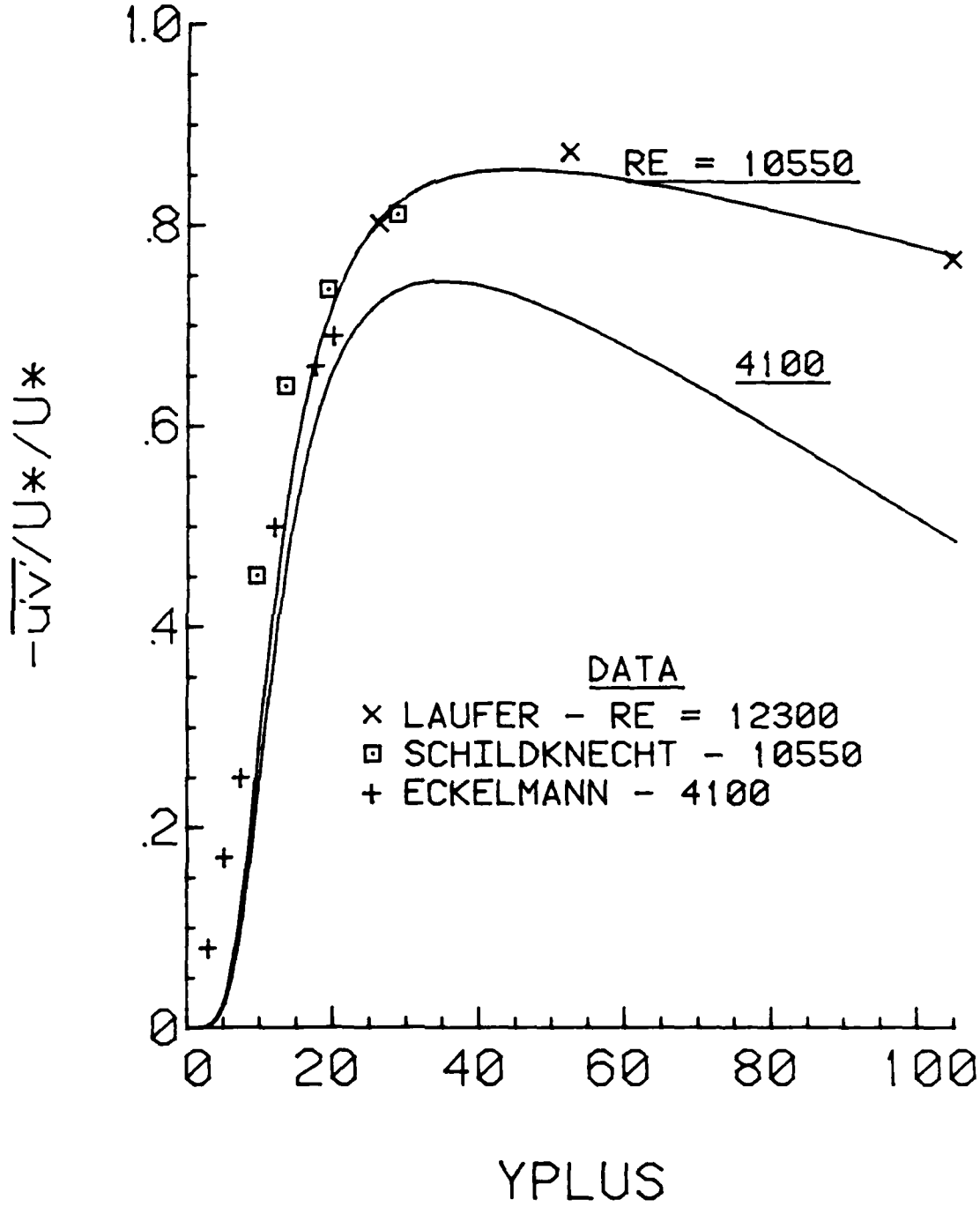

Fig. 1 Comparison of turbulent shear stress data near the channel wall with 1979 model.

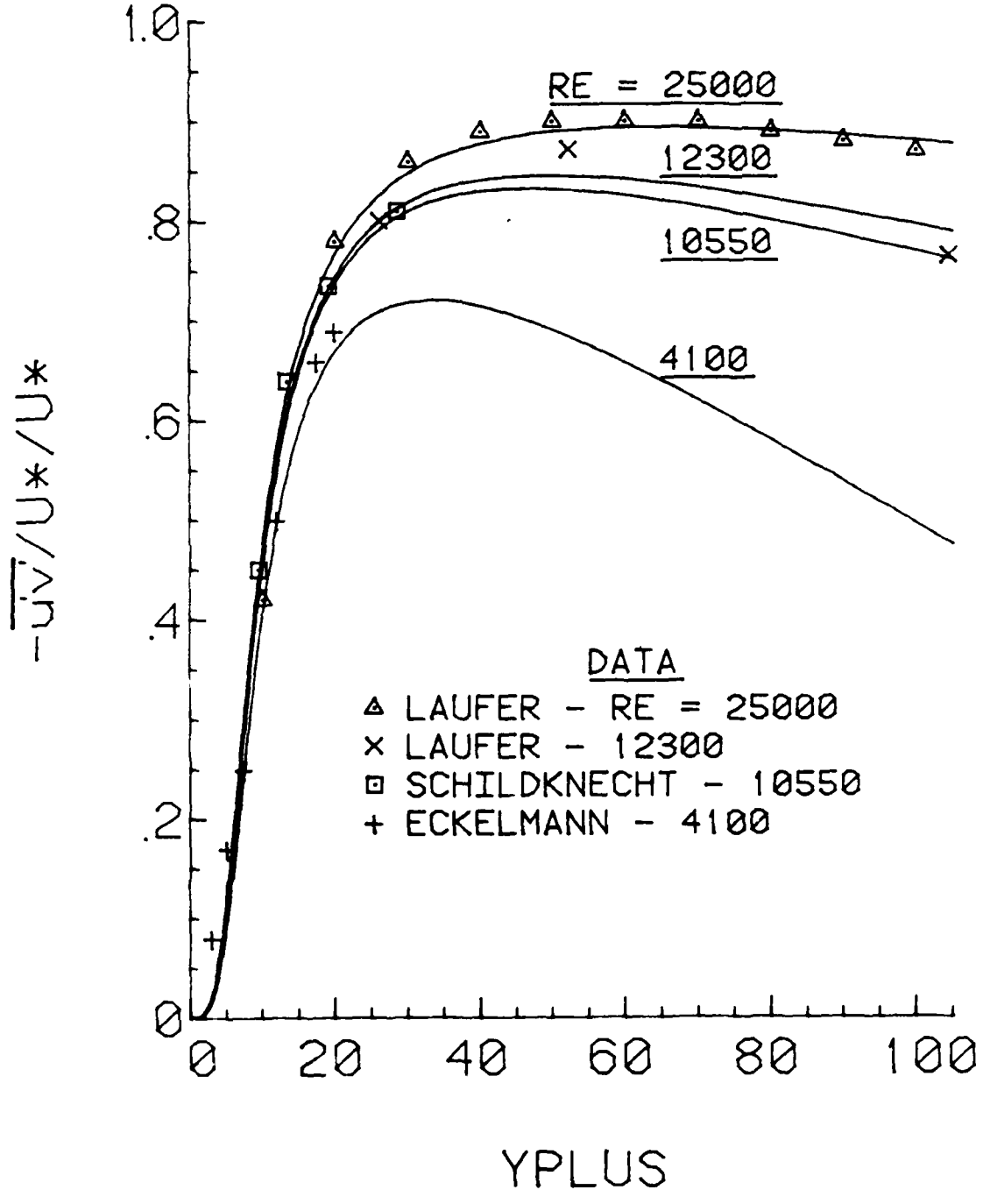

Fig. 2 Comparison of turbulent shear stress data near the channel wall with the present theory.

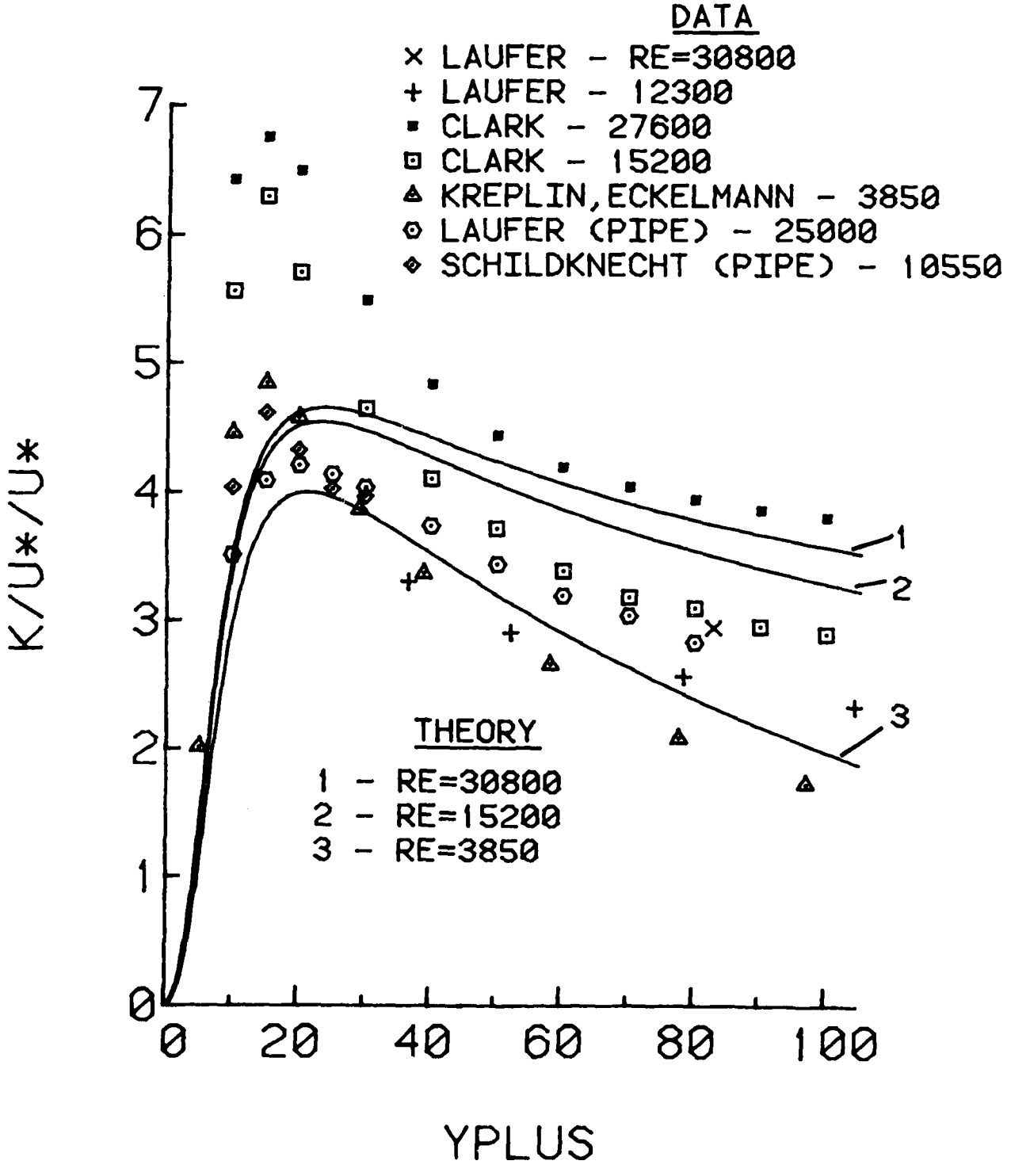

...n of turbulent kinetic energy data near the ... wall with the present theory.

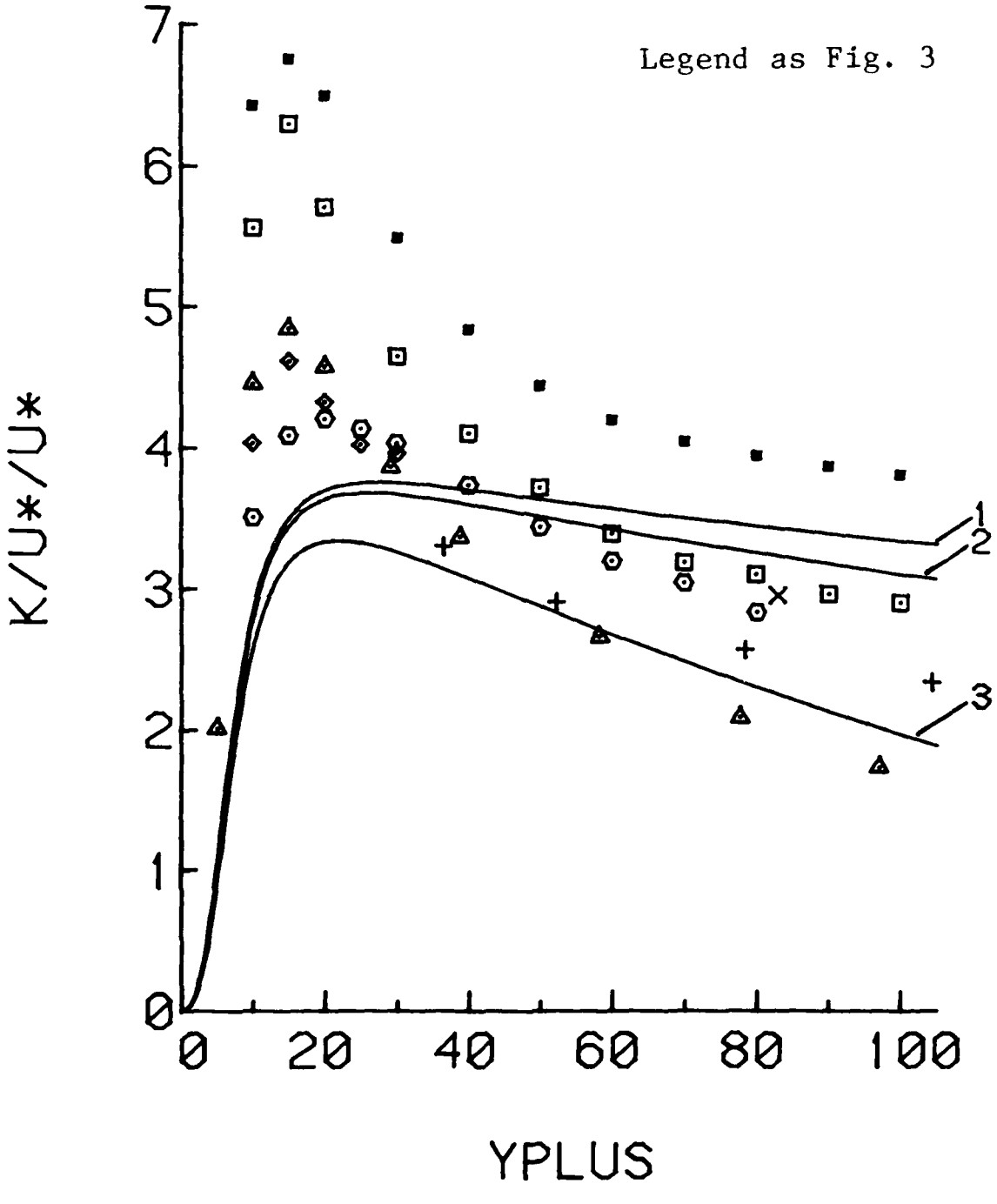

Fig. 4 Comparison of turbulent kinetic energy data near the channel wall with the theory of Jones and Launder.

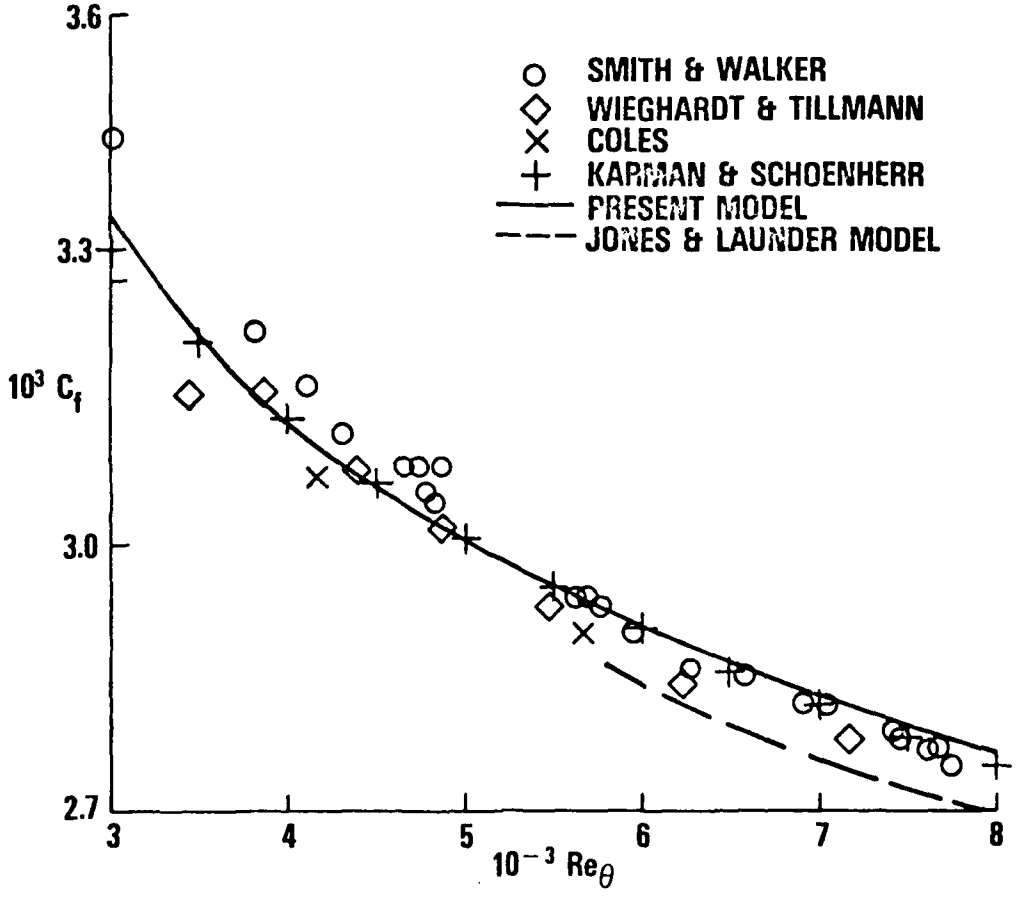

Fig. 5 Flat-plate skin friction distribution.

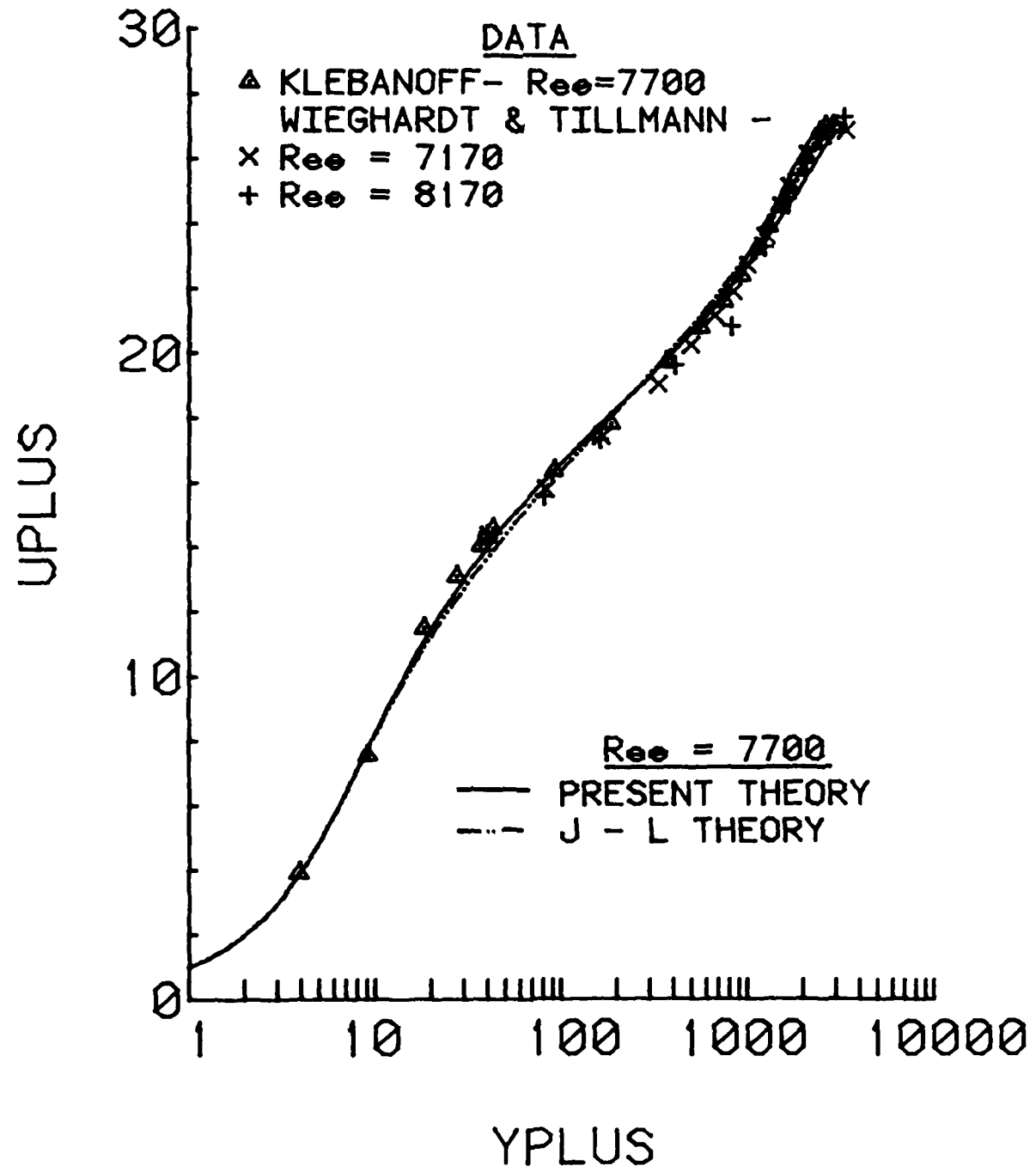

Fig. 6 Velocity distribution across the boundary layer.

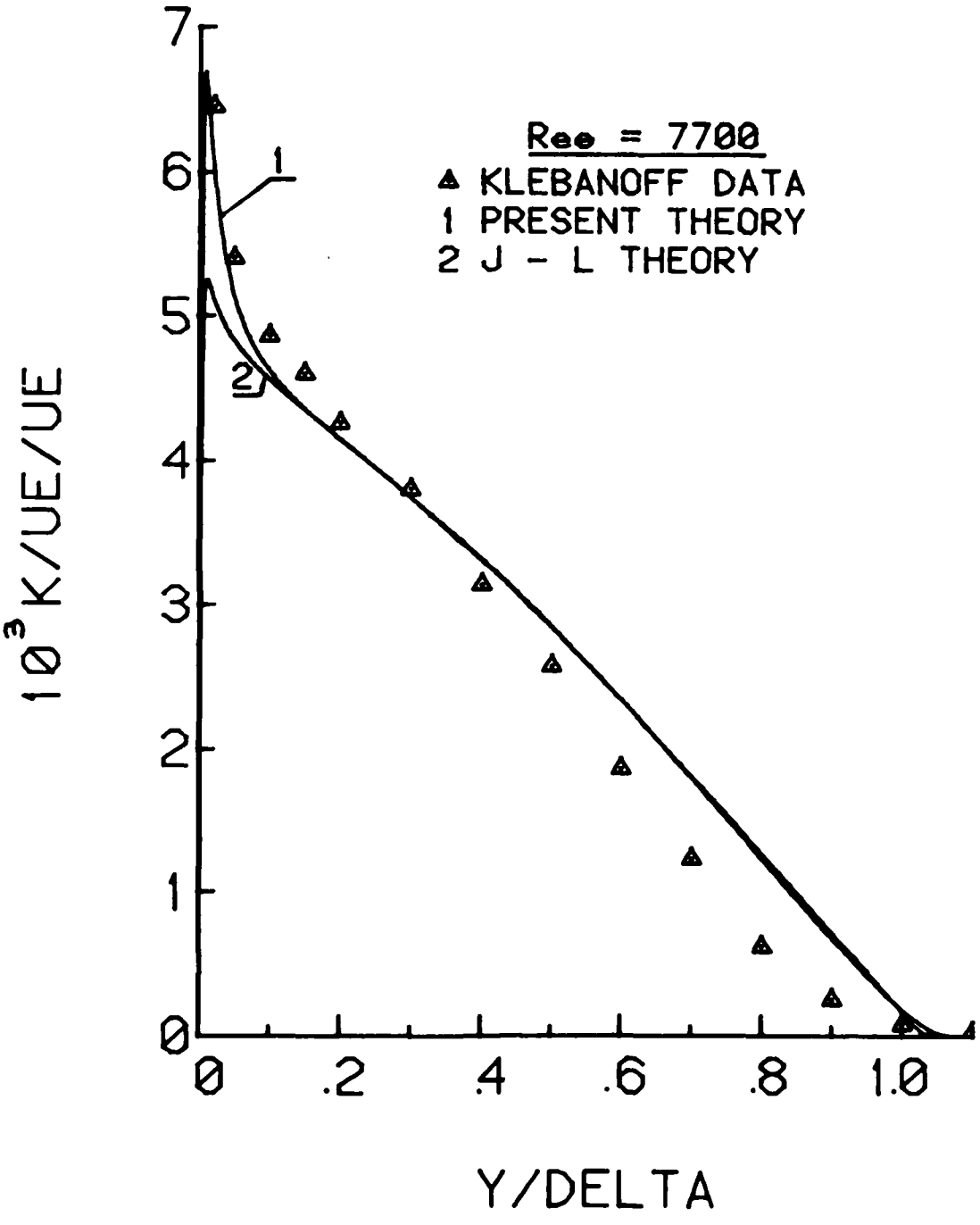

Fig. 7 Turbulent kinetic energy distribution across the boundary layer.

EXPERIMENTAL STUDY OF BOUNDARY LAYER VELOCITY PROFILES ON A PROLATE SPHEROID AT LOW INCIDENCE IN THE CROSS SECTION $x_o/L = 0.64$

H.U. Meier and H.-P. Kreplin
DEUTSCHE FORSCHUNGS- UND VERSUCHSANSTALT
FÜR LUFT- UND RAUMFAHRT E.V.
Institut für Experimentelle Strömungsmechanik
Bunsenstraße 10, D-3400 Göttingen

Summary

The mean velocity distributions and cross flow angles in three-dimensional boundary layer profiles, developing on a 1 : 6 prolate spheroid, were measured at an angle of incidence $\alpha = 10°$, and a free stream velocity of $U_\infty = 45$ m/s. The boundary layer profiles were investigated at a fixed cross section $x_o/L = 0.64$ and at different circumferential angles φ applying a Three-Hole-Direction Probe. The profiles were analysed and the results compared with previous information obtained from hot film surface probe measurements and oil flow patterns.

Nomenclature

a, b	half axes of prolate spheroid
c_f	skin friction coefficient, $c_f = \frac{2\tau_w}{\rho U_\infty 2}$
c_p	pressure coefficient, $c_p = \frac{p_w - p_s}{q_\infty}$
H_{12}	shape parameter, Eq. (5)
L	model length, $L = 2a$
$p_{1,3}$	pressure at 3-hole probe, $\Delta p = p_1 - p_3$, Fig. 2
p_2	total pressure measured with 3-hole probe
p_s	static pressure
p_w	static pressure measured at surface
q	dynamic pressure, $q = \frac{\rho}{2} u_r^2$
T_∞	free stream temperature
u,w	velocity components in x,z plane, Eqs. (2a,b)
u_r	resultant velocity in x,z plane, Eq. (1)
u_τ	shear stress velocity, $u_\tau = (\tau_w/\rho)^{1/2}$
U_e, W_e, U_{re}	values of u, w, u_r at $y = \delta$
U_∞	free stream velocity
x, y, z	cartesian co-ordinates, Fig. 1
x_o, y_o, z_o	model orientated co-ordinates, Fig. 1

α	angle of incidence
γ	crossflow angle (yaw), Fig. 1
δ	boundary layer thickness
δ_{1r}	'displacement' thickness, Eq. (3)
δ_{2r}	'momentum' thickness, Eq. (4)
ρ	density in free stream
τ_w	wall shear stress
φ	circumferential model angle

1. Introduction

Prediction of the boundary layer development on a body of revolution is a severe test for both the experimentalist as well as the theoretician. This is because the flow is characterized by:

- laminar-turbulent boundary layer transition,
- strong crossflow with regions of negative flow direction,
- separation of threedimensional, laminar or turbulent, boundary layer,
- formation of longitudinal vortices,
- flow reversal.

In order to attack these complicated flow problems, a theoretical and experimental study of the flow over a prolate spheroid is being investigated at the DFVLR. The first experiments were aimed at the determination of the pressure distribution and at the regions of boundary layer transition and separation. This was to provide foundamental input information for the calculations. A summary of these experimental results is given in Refs. [1] and [2].

The purpose of the present investigation is to evaluate the application of a conventional 3-hole probe for the determination of the mean velocity distribution and of the flow direction in the boundary layer developing on the prolate spheroid at low incidence.

2. Test Set Up and Data Reduction Procedure

The windtunnel model and the test set up in a 3 m x 3 m Low Speed Windtunnel of the DFVLR are described in detail in papers [1]and [3], presented at the '1978 and 1979 DEA meetings'. Inside the prolate spheroid a probe traversing mechanism is installed

and allows to displace the probe tip in the perpendicular direction relative to the model surface. Investigating the flow field, perpendicular to the model, a conical surface is generated as the model turns around its longitudinal axis. The co-ordinate system chosen for the data reduction is a local cartesian co-ordinate system (Fig. 1).

The boundary layer measurements were carried out applying a 3-hole direction-probe (Fig. 2), which allows the determination of the magnitude and the direction of the local velocity. The directional sensitivity with respect to the angle of incidence α and the yaw angle γ was obtained in a twodimensional channel flow of the DFVLR Low Turbulence Wind Tunnel. This calibration was checked during the tests positioning the probe in the free stream while the angle of incidence of the prolate spheroid was zero. In Fig. 3 the directional sensitivity of the 3-hole probe for yaw angles of $\gamma = \pm 30°$ and angles of incidence up to $\alpha = 10°$ is shown. The results indicate that the directional sensitivity is almost independent of the angle of incidence, as far as they are representative of our test conditions. This is no longer true, when the total pressure measurement (p_2) is analysed. The uncorrected pressure difference $p_2 - p_s$, non-dimensionalized with the dynamic pressure, obtained from the free stream conditions, changes considerably for $\alpha = 10°$, as the probe is inclined with respect to the tunnel axis. However, for a first approximation in the boundary layer, the streamlines are parallel to the model surface which implies that the corrections can be assumed to be small. Due to the fact that during this test no upwash angles were measured in the boundary layers, an "α-correction" was not applied in the data reduction procedure. At this stage of investigation the static pressure was measured at the model surface and assumed to be constant through the whole boundary layers thickness. An error could have been revealed, here, if the boundary layer close to the separation is investigated. For this reason the effect will be later tested experimentally. The local velocity in the boundary layer was calculated from the measured quantities, applying the Bernoulli equation and the following data reduction procedure was applied:

$$\frac{p_1 - p_3}{p_2 - p_s} = \frac{\Delta p}{p_2 - p_s} \longrightarrow \text{crossflow angle } \gamma \quad \text{(Fig. 3)}.$$

Using the calibration curve in Fig. 4, one obtains by means of γ above the corrected local dynamic pressure q. The magnitude of the local velocity can be calculated from the relation:

$$u_r = \sqrt{\frac{2q}{\rho}} .$$

The density ρ can be derived from the equation of state for ideal gases, if the tunnel temperature T_∞ is known. The edge of the boundary layer was assumed to be in the region where the local dynamic pressure q became constant. This assumption will be proven by calculating the velocity at the boundary layer edge on the basis of measured wall pressure, applying the Euler equations. If the local velocity u_r and the crossflow angle are known, the velocity components in the x, z plane can be respectively calculated from:

$$u = u_r \cos \gamma \qquad (2\ a)$$

$$w = u_r \sin \gamma \qquad (2\ b)$$

It is known that the physical interpretation of the integral values, obtained from threedimensional boundary layer velocity profiles, is somewhat difficult. However, for the present investigation ($\alpha = 10°$) the crossflow angles measured were relatively small, i.e. $\gamma < 20°$. For this reason 'displacement' and 'momentum' thicknesses were calculated on the basis of the local resultant velocities:

$$\delta_{1r} = \int_0^{y=\delta} \left(1 - \frac{u_r}{U_{re}}\right) dy \qquad (3)$$

$$\delta_{2r} = \int_0^{y=\delta} \frac{u_r}{U_{re}} \left(1 - \frac{u_r}{U_{re}}\right) dy \qquad (4)$$

With these quantities the shape parameter,

$$H_{12} = \frac{\delta_{1r}}{\delta_{2r}}, \qquad (5)$$

is obtained, which will lead to interesting information on the separation region of the boundary layer.

In order to prove the wall shear stress values, obtained from the surface hot film measurements, the boundary layer velocity profiles were analysed. Section 4 demonstrates that the application of a twodimensional profile analysis, for threedimensional velocity profiles with relatively small cross-flow, is justified and leads to small differences in the resultant local wall shear stress values. The procedure of the profile analysis is described in detail in Ref. [4]. Essentially, velocity profiles are constructed on the basis of the Law of Wall and two Wake Functions. Then wall shear stress and the boundary layer thickness have to be determined in such a way that the calculated profile is in the best possible agreement with the experimental profile. This is accomplished by requiring the Root Mean Square deviation between the two profiles becomes a minimum.

4. Results and Discussion

Results shown below are for the prolate spheroid at an incidence of $\alpha = 10°$. This test case was chosen because the theoretical inviscid pressure distribution (Ref. [5]) indicates over large positions of the body only small deviations from the measured one. This is demonstrated in Fig. 5.

Boundary layer velocity profiles were measured only at the cross section $x_o/2a = 0.64$ at a free stream velocity of $U_\infty = 45$ m/s. Figures 6 - 9 present boundary layer velocity and corresponding crossflow angle profiles for different circumferential angles

Fig. 6 illustrates that the u_r-profiles, starting from the windward symmetry plane $\varphi = 0°$, become steeper and thicker for increasing angles of φ. This effect is quite pronounced in the regions with negative crossflow (Fig. 8). Reversed circumferential flow begins to occur at angles between 135° and 140°, as indicated in Figs. 7 and 9.*) Above $\varphi = 150°$ and up to $\varphi = 180°$, the u_r-profiles become still fuller which consequently results in an increase of the local wall shear stress. This is shown in Fig. 13. The maximum negative crossflow angle at the surface was found to be $\gamma = -4{,}8°$ at a circumferential angle of $\varphi = 160°$. The measured profile development is qualitatively in agreement with calculated laminar boundary layer velocity profiles by K. C. Wang [6] for a 1 : 4 prolate spheroid at an angle of incidence $\alpha = 6°$.

In Figs. 10a - 10d u_r-velocity profiles are plotted in the x - y plane and the corresponding crossflow angles are projected onto the x - z plane, in order to demonstrate the distortion of the profiles. At the circumferential angles $\varphi = 0°$ and 90° the profiles are not twisted, and consequently can be analysed as twodimensional boundary layer profiles. At $\varphi = 140°$ and 160° the crossflow at the surface becomes zero or negative and the profiles show a significant distortion. In Fig. 11 u and w velocity profiles are plotted for different angles φ. The local velocity components are non-dimensionalised by their values at the boundary layer edge. With increasing angle φ the crossflow component at the surface becomes negative as it was indicated by the corresponding γ -distributions. A flow visualisation of the surface 'limiting' streamlines is compared with the wall shear stress measurements, (Fig. 12). Although the oil flow pattern is of a poor clarity, an agreement of crossflow angle for $\varphi = 90°$ with the hot film and profile measurements is possible to recognize.

*) It is assumed that the flow angle measured at the smallest wall distance of y = 0.25 mm, is not changing towards the wall.

The flow visualisation, as well as the calculated streamlines based on the measured wall shear distributions Fig. 5 in Ref.[2], do not indicate an open separation line in the cross section $x_o/2a = 0.64$. The open separation line found in [7]was observed at low Reynolds numbers ($Re = U_\infty 2a/\nu = 8 \times 10^4$) where the boundary layer flow can be expected to be laminar over the whole model. In our test at the cross section $x_o/2a = 0.64$ the boundary layer flow was fully turbulent ($Re = 7.2 \times 10^6$) and lead to a different flow pattern Ref.[1] . The boundary layer measurements, however, indicated negative crossflow for circumferential angles $\varphi > 140°$. In this region ($\varphi \approx 140°$) the shape parameter H_{12}, calculated from the resultant velocity profiles, reaches a maximum (Fig. 13) and the circumferential shear stress component τ_w becomes zero. As found from the laminar boundary layer calculations [8], the measurements confirm the observation that the wall shear stress $\tau_{w\varphi}$ becomes zero at smaller circumferential angles corresponding to the wall shear stress minimum. A comparison of the wall shear stress vectors measured with the surface hot film probe [2], and derived from boundary layer profile measurements, shows an excellent agreement. In Fig. 14 it is demonstrated that the boundary layer analysis leads to almost identical results, if the velocity profile of u_r and the corresponding u-component are compared with calculated profiles based on the Law of the Wall and two additional Wake Functions. For crossflow angles $\gamma < 20°$ the determined skin-friction coefficients differ only by a few per cent.

Summary and Conclusions

A 3-hole direction probe was successfully applied for measurements of mean velocity distributions in threedimensional turbulent boundary layers, developing on a prolate spheroid at low incidence. The derived crossflow angles and local wall shear stress values are in agreement with previous results obtained from surface hot film measurements.

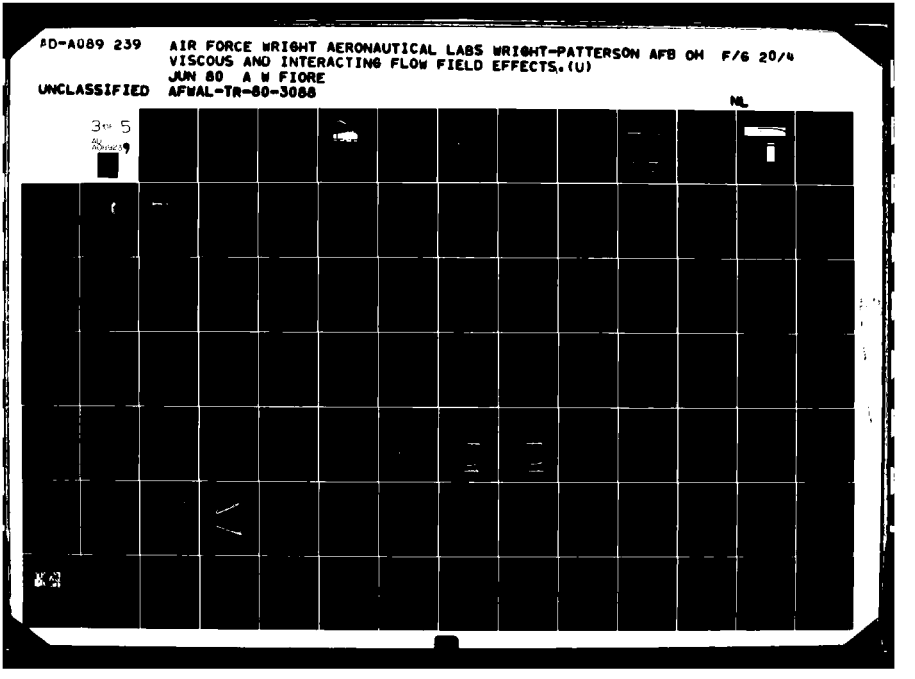

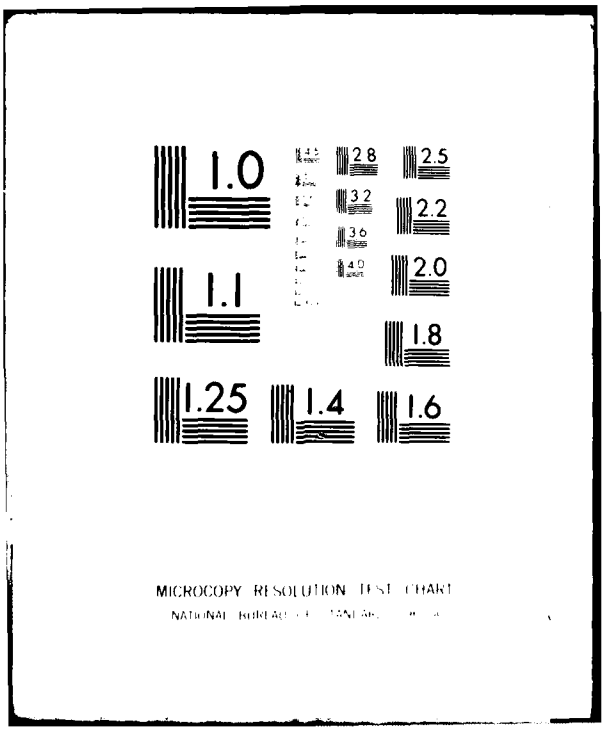

Further investigations will concentrate on boundary layer investigation in regions where the circumferential wall shear stress becomes zero and negative crossflow occurs. In this flow regime the described measuring technique can be applied with sufficient accuracy for even high angles of incidence and certainly will lead to interesting new results.

5. References

[1] Meier, H.U., Kreplin, H.-P.
"Experimental investigation of the transition and separation phenomena on a body of revolution"
Proc. 2nd Symposium on "Turbulent Shear Flows", July 2-4, 1979, Imperial College, London, pp. 15.1 - 15.7, 1979
see also: Proc. 4th US-FRG DEA Meeting "Viscous and Interacting Flow Field Effects"
Forschungsbericht aus der Wehrtechnik BMVg-FBWT 29-31, pp. 258 - 273, 1979

[2] Kreplin, H.-P., Vollmers, H., Meier, H.U.
Experimental determination of wall stress vectors on an inclined prolate spheroid"
Proc. 5th US-FRG DEA Meeting "Viscous and Interacting Flow Field Effects", Naval Academy, Annapolis/Maryland, April 16-18, 1980, to be published

[3] Meier, H.U., Kreplin, H.-P.
"Pressure distributions and flow visualisations on an ellipsoid 1 : 6 designed for threedimensional boundary layer investigations"
Proc. 7th US-FRG DEA-Meeting "Boundary Layer Effects", Air Force Flight Dynamics Laboratory, Technical Report AFFDL-TR-78-111, pp. 197-208, 1978

[4] Meier, H.U.
"The response of turbulent boundary layers to small turbulence levels in the external free stream"
Proc. The Tenth Congress on the International Council of the Aeronautical Scienes, October 3-8, 1976, Ottawa/Canada, ICAS-Paper No. 76-05, 1976

[5] Geißler, W.
"Berechnung der Potentialströmung um rotationssymmetrische Rümpfe, Ringprofile und Triebwerkseinläufe"
Z. Flugwiss. Vol. 20, pp. 257-262, 1972

[6] Wang, K.C.
"Boundary layer over a blunt body at low incidence with circumferential reversed flow"
J. Fluid Mech. Vol. 72, pp. 49-65, 1975

[7] Taeyoung Han, Patel, V.C.
"Flow separation on a spheroid at incidence"
J. Fluid Mech. Vol. 92, pp. 643-657, 1979

[8] Cebeci, T., Khattab, A.A., Stewartson, K.
"Prediction of threedimensional laminar and turbulent boundary layers on bodies of revolution at high angles of attack"
Proc. 2nd Symposium on "Turbulent Shear Flows", July 2-4,1979 Imperial College, London, pp. 15.8-15.13, 1979

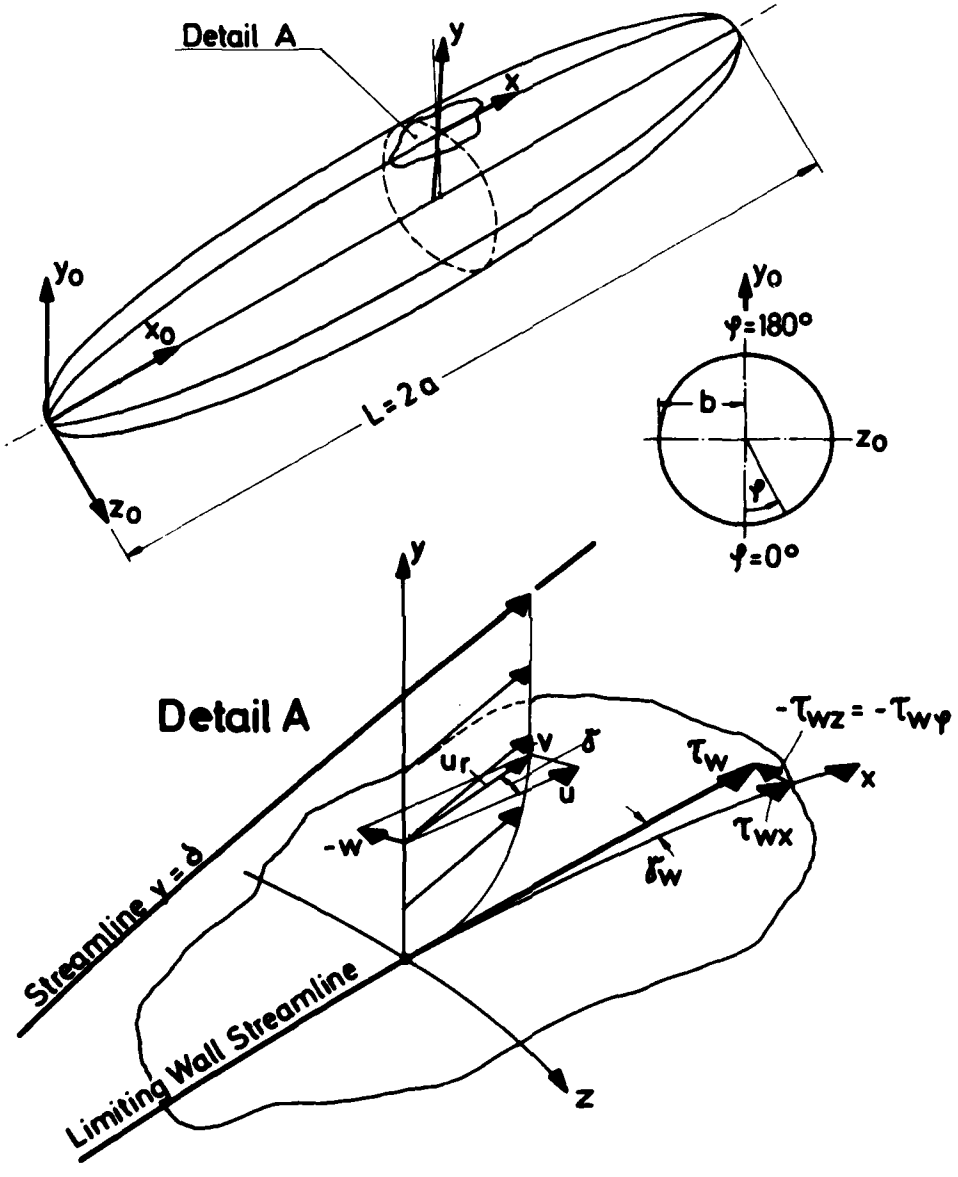

Fig. 1 Co-ordinate Systems Chosen for the Boundary Layer Investigations

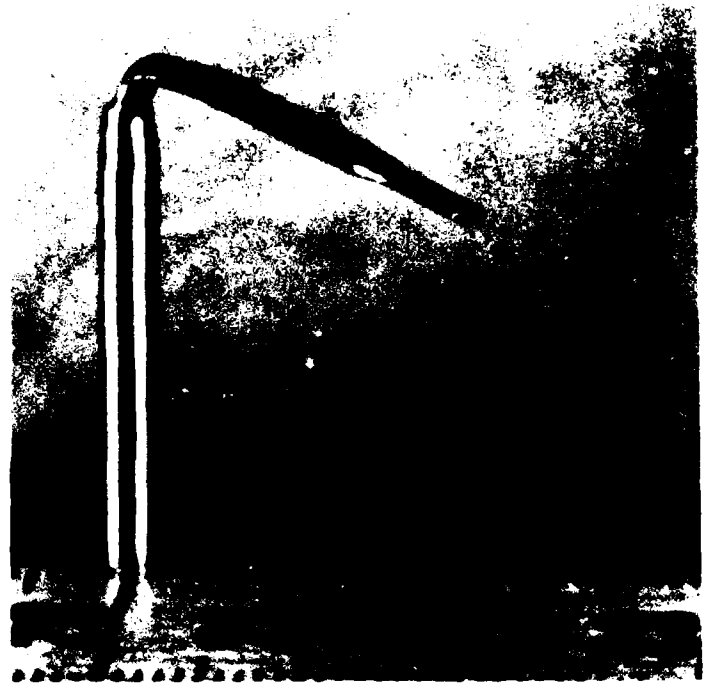

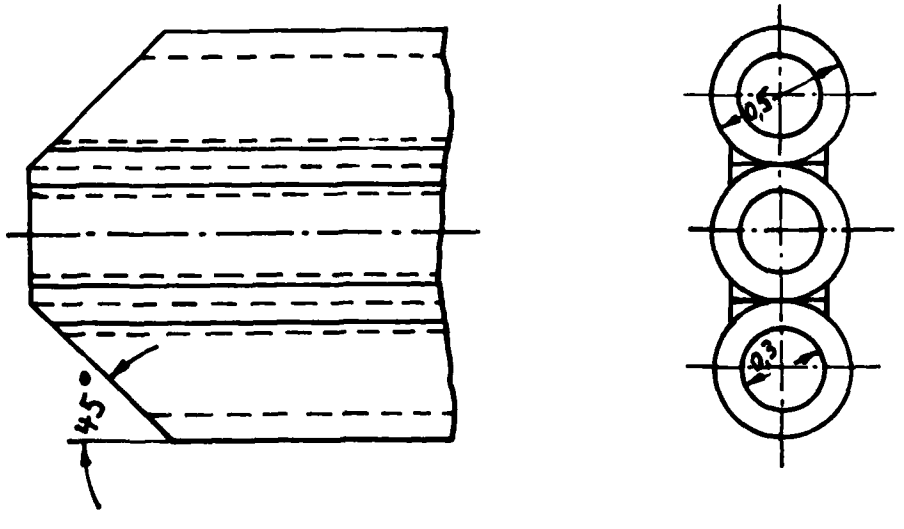

Fig. 2 Three-Hole-Direction Probe for Boundary Layer Measurements

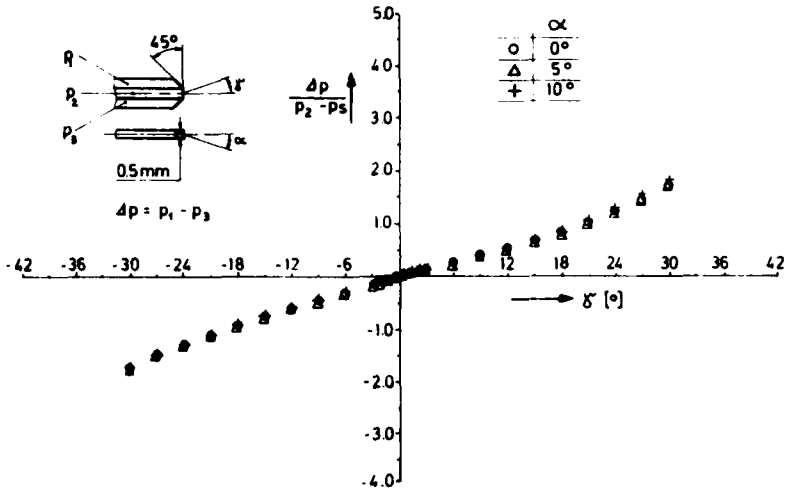

Fig. 3 Directional Sensitivity of the Three-Hole Probe

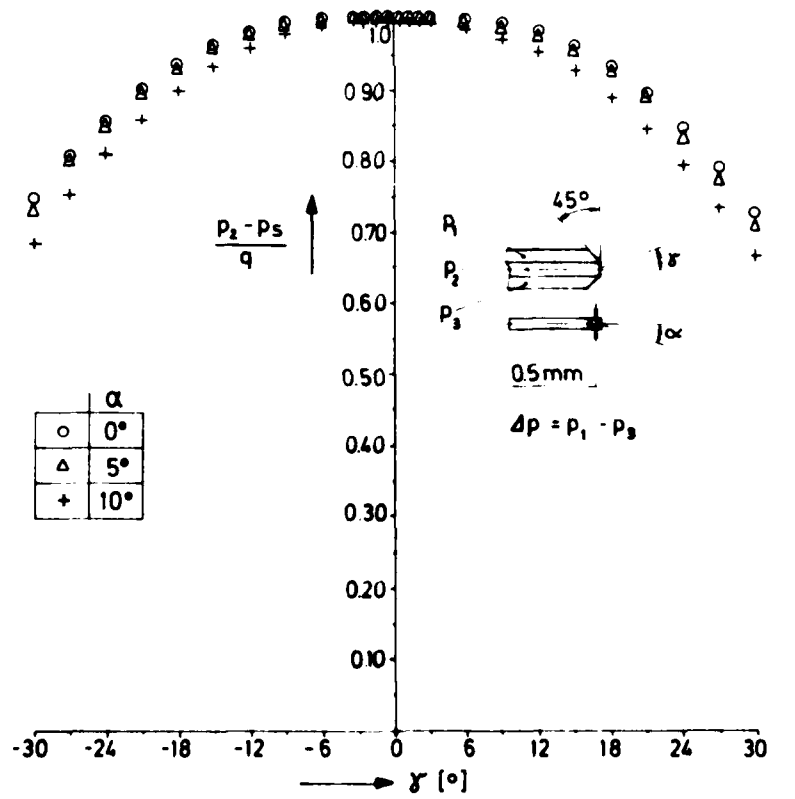

Fig. 4 Directional Sensitivity (α,γ) of the Total Pressure Measurement p_2

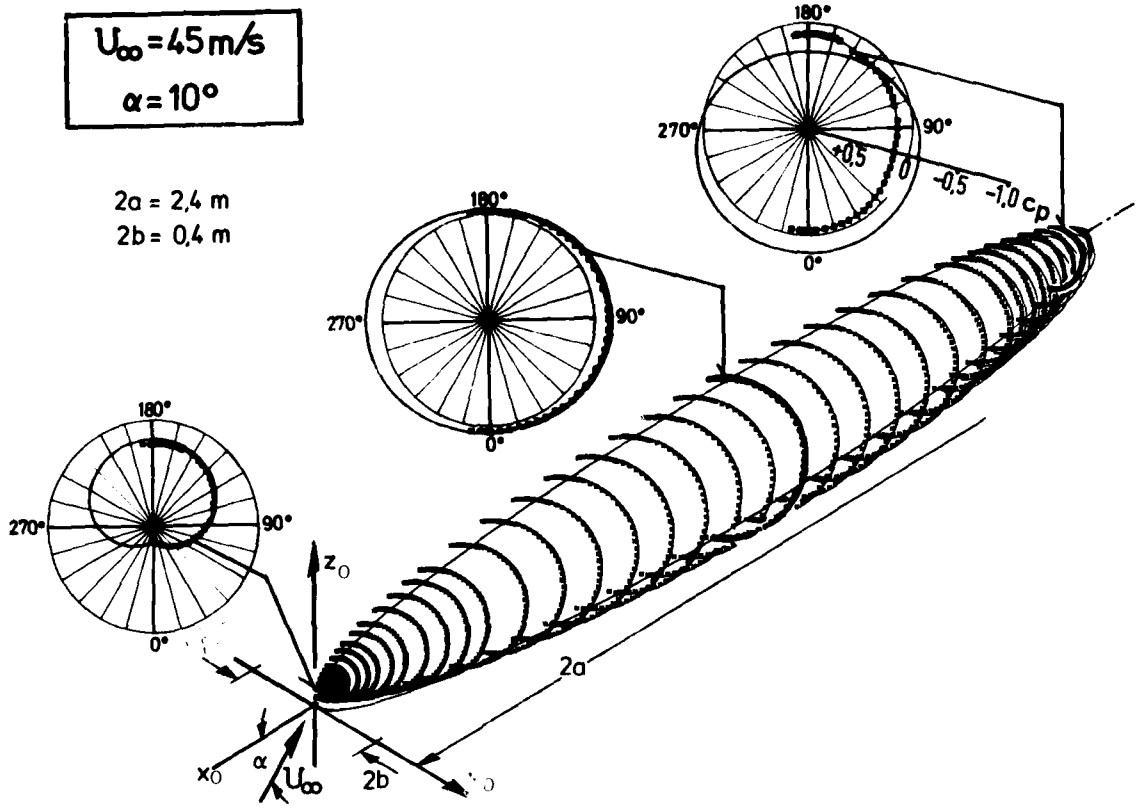

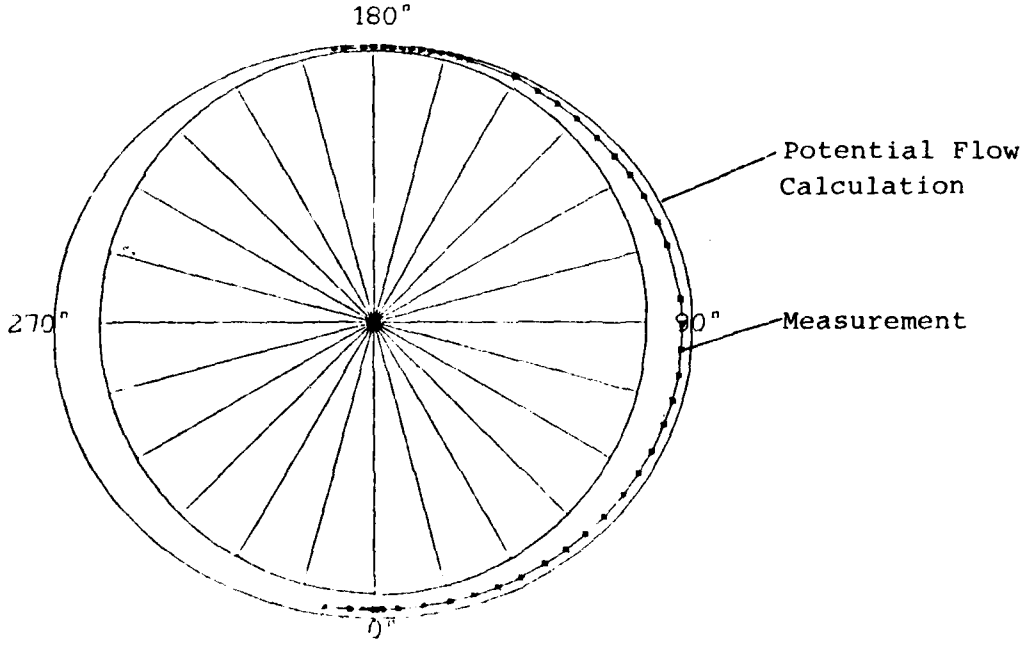

Fig. 5 Surface Pressure Distribution on the Prolate Spheroid at $\alpha = 10°$, Detail $x_o/2a = 0.64$

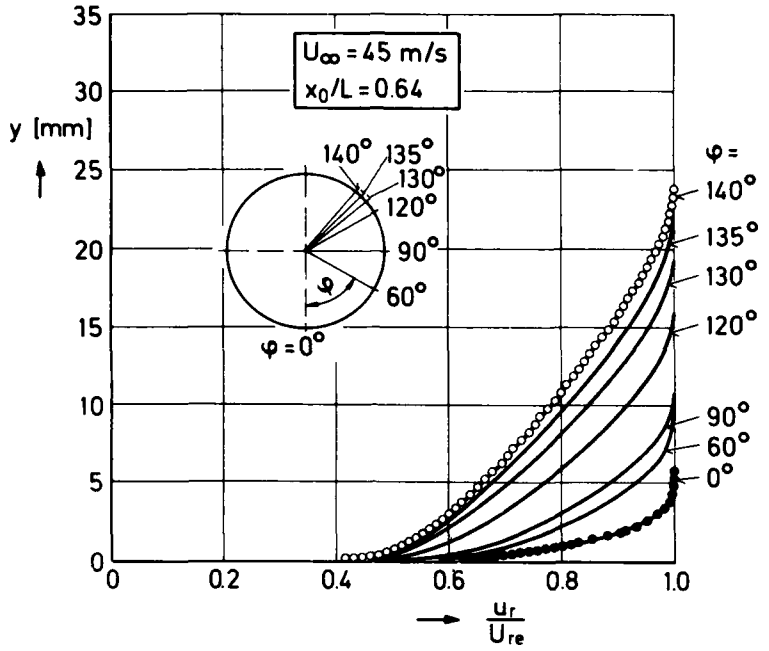

Fig. 6 Distributions of Resultant Velocity Profiles u_r/U_{re} in Boundary Layers at Circumferential Angles φ = 0° - 140°

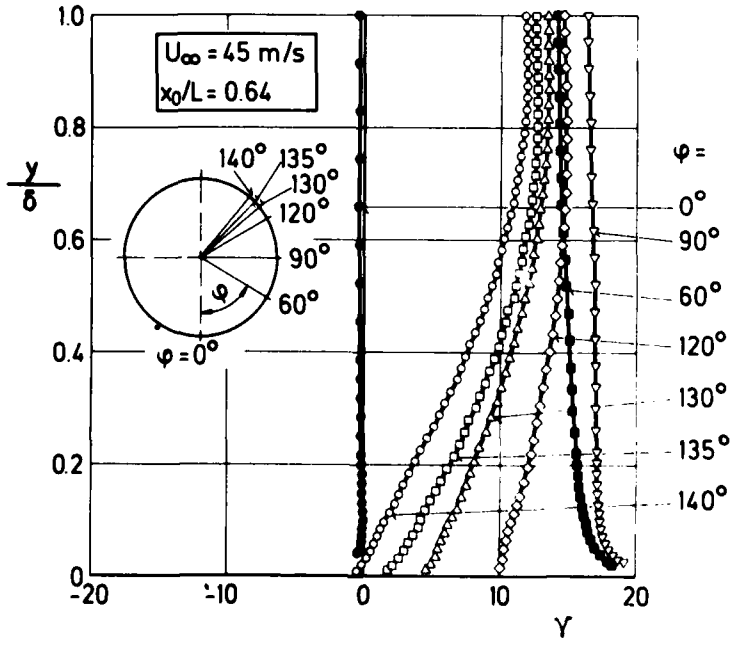

Fig. 7 Distributions of Crossflow Angles γ in Boundary Layers at Circumferential Angles φ = 0° - 140°

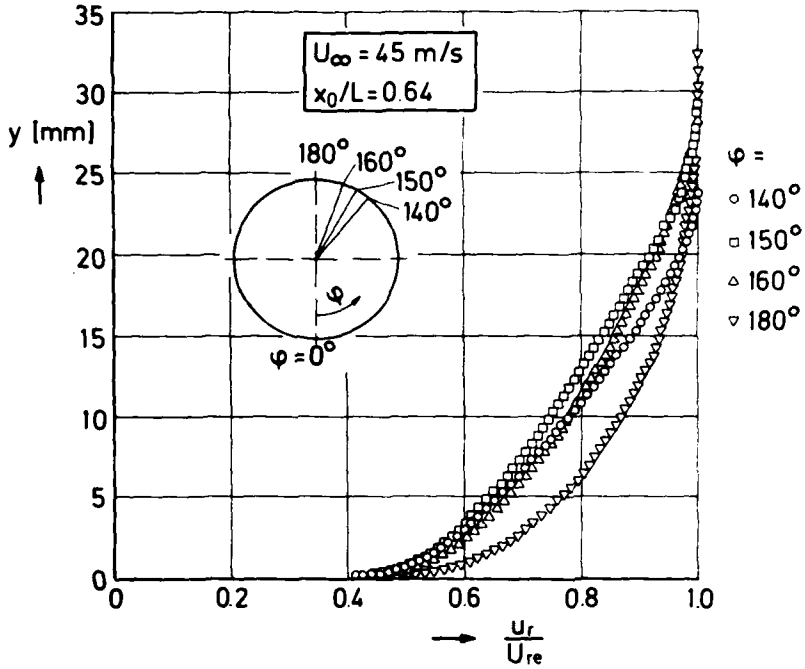

Fig. 8 Distributions of Resultant Velocity Profiles u_r/U_{re} in Boundary Layers at Circumferential Angles φ = 140° - 180°

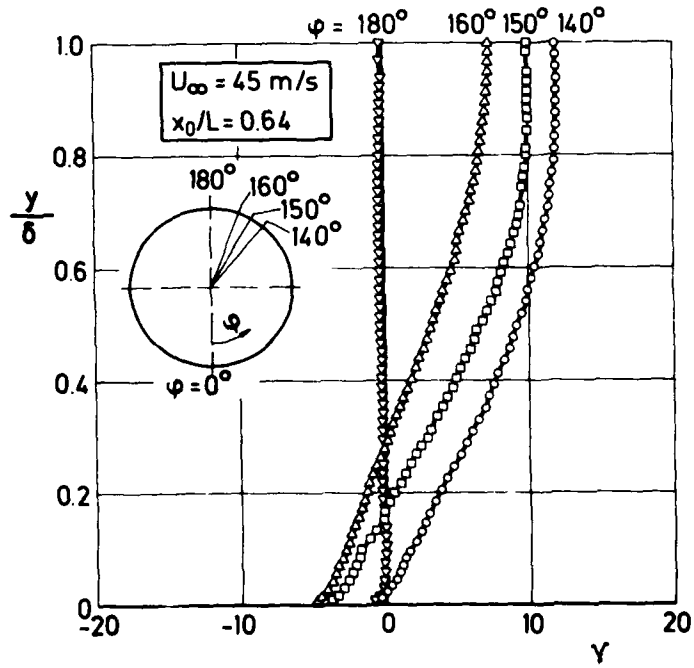

Fig. 9 Distributions of Crossflow Angles Y in Boundary Layers at Circumferential Angles φ = 140° - 180°

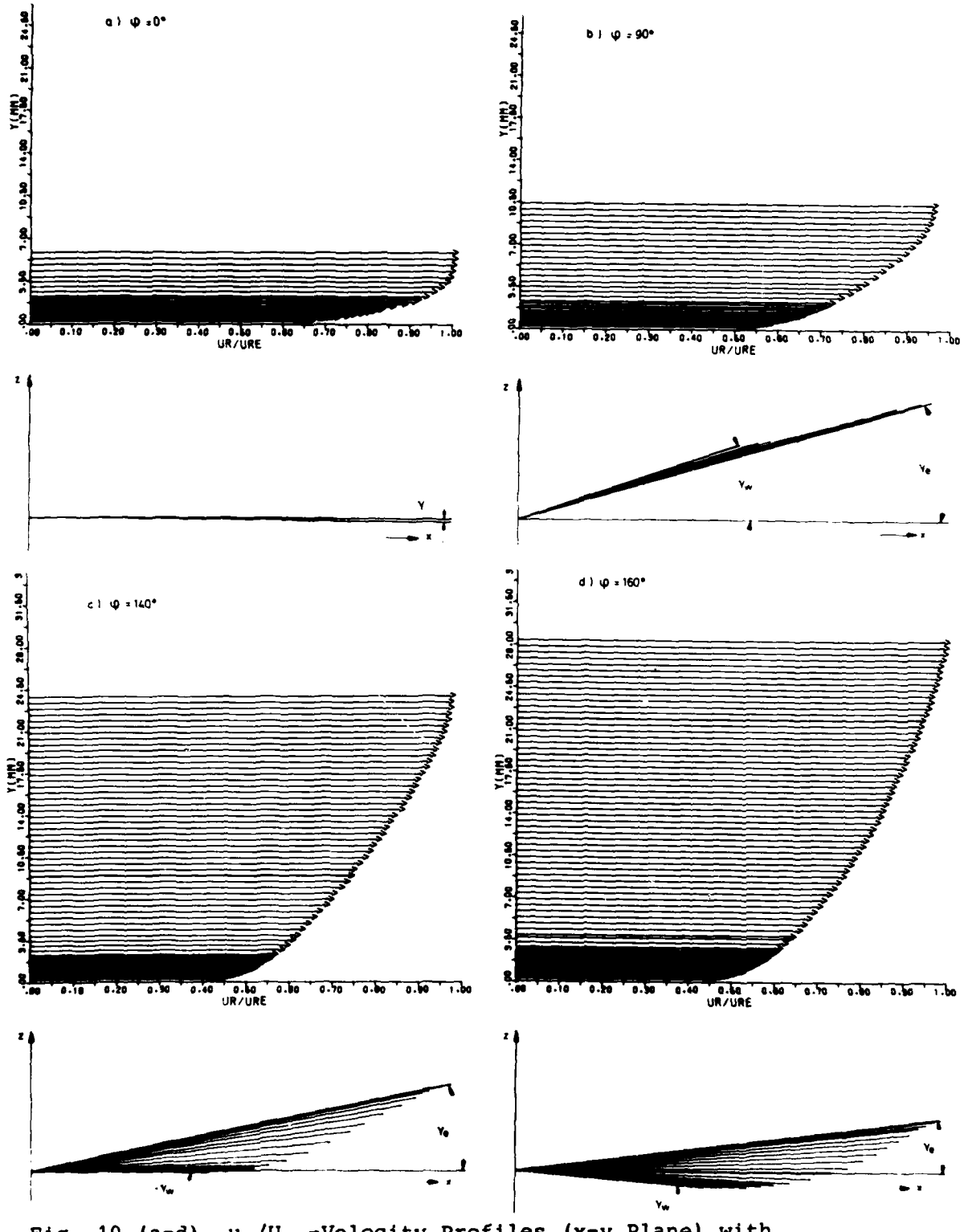

Fig. 10 (a-d) u_r/U_{re}-Velocity Profiles (x-y Plane) with Corresponding Crossflow Angles γ (x-z Plane)

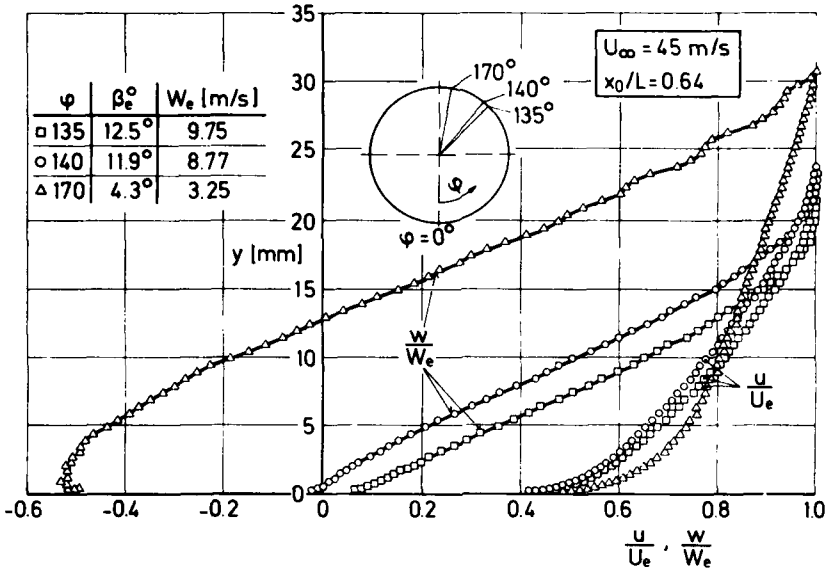

Fig. 11 Boundary Layer Profiles of the Velocity Components u and w in the Region of Zero and Negative Crossflow

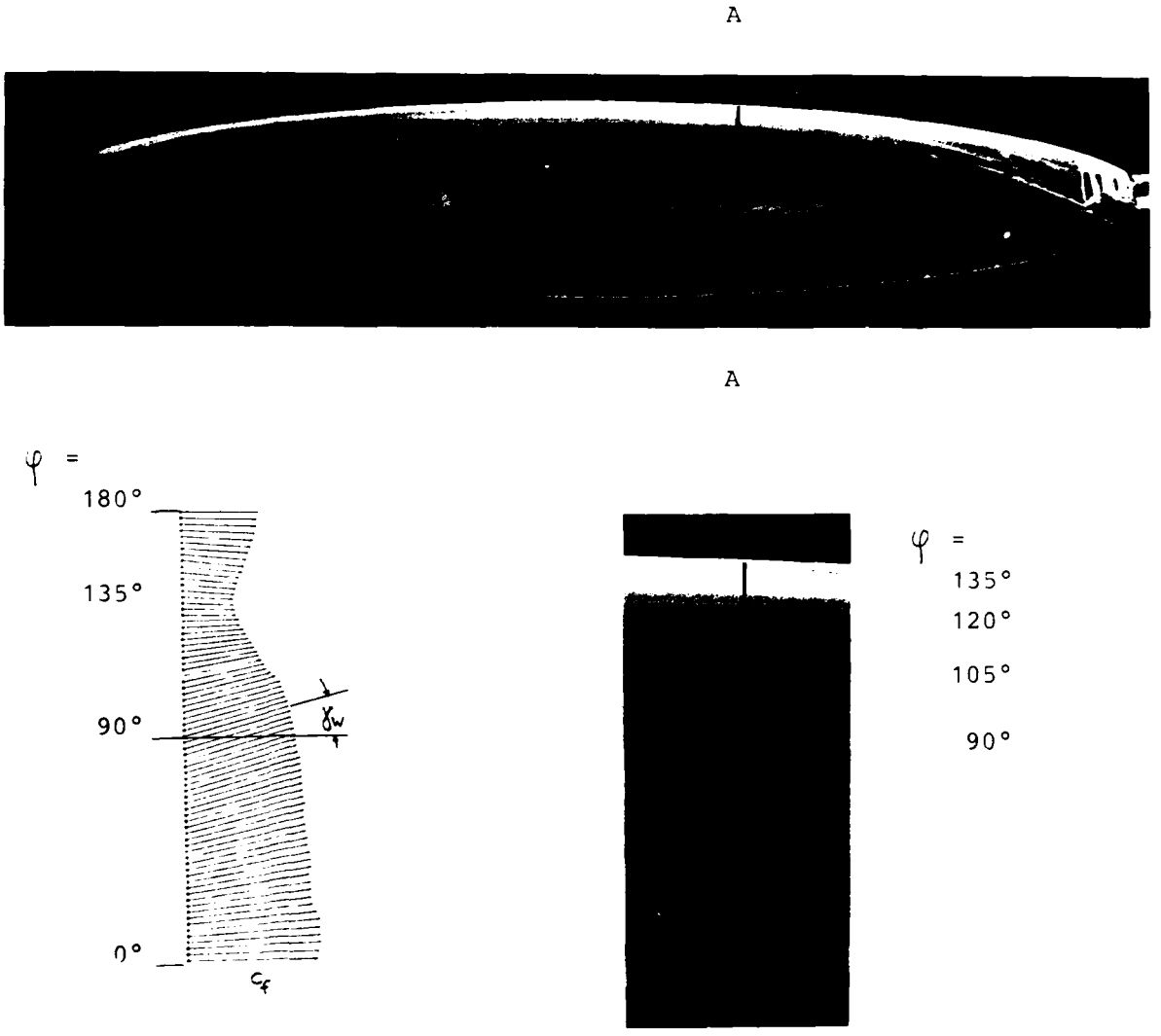

Fig. 12 Oil Flow Pattern and Corresponding measured Wall Shear Stresses in the Cross Section $x_o/2a = 0.64$
(U_∞ = 45 m/s, Re = 7.2 x 10^6, $\alpha = 10^o$)

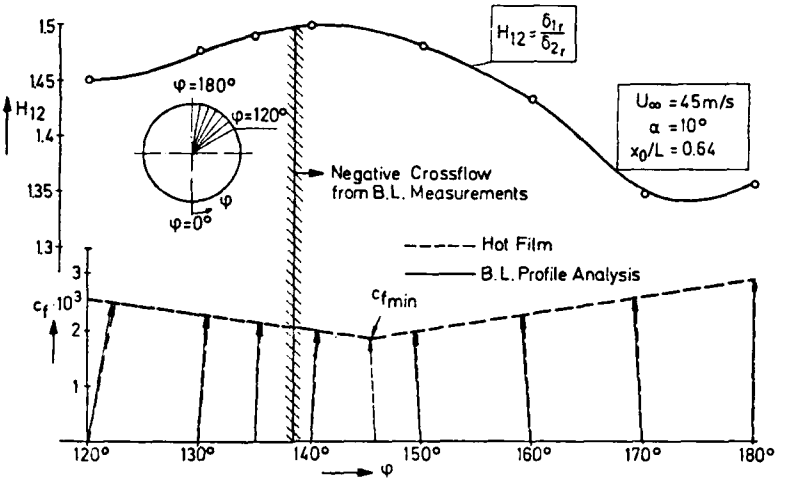

Fig. 13 Wall Shear Stress Vectors c_f and Boundary Layer Shape Parameters H_{12} on the Leeward Side of the Prolate Spheroid (U_∞ = 45 m/s, $x_o/2a$ = 0.64)

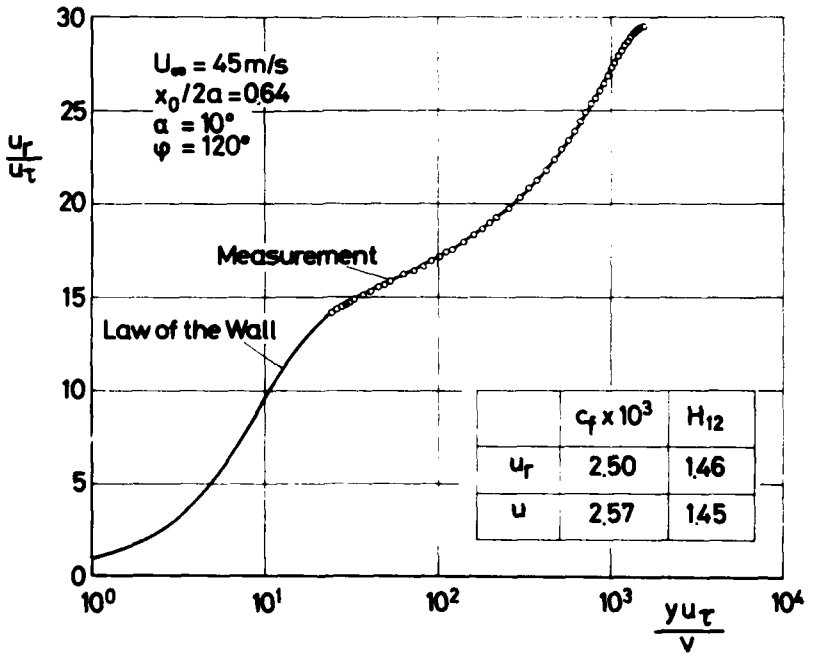

Fig. 14 Logarithm Representation of a Mean Velocity Profile (u_r); Comparison of Skin Friction Coefficients and Shape Parameters for Resultant Velocity u_r and Streamwise Component $u = u_r \cos \gamma$

MEASUREMENTS OF SURFACE ROUGHNESS EFFECTS ON THE HEAT TRANSFER TO SLENDER CONES AT MACH 10

J. A. F. Hill* and R. L. P. Voisinet**
Naval Surface Weapons Center
White Oak, Silver Spring, Maryland 20910

D. A. Wagner***
University of Cincinnati
Cincinnati, Ohio

Abstract

Total skin-friction and local heat-transfer measurements have been obtained with and without sand-grain roughness at Mach 9.9 on a sharp and an 18 percent blunt cone. Based on cone length and free-stream properties, the Reynolds numbers were between 20 x 10^6 and 40 x 10^6. The wall temperature ratio T_w/T_o was approximately 0.26. Three different sizes of grit were tested, of which the larger two were calculated to be in the "fully-rough" flow regime. In all cases the application of roughness increased both the friction and heat transfer relative to the smooth-wall value, the former more than the latter. The results have been compared with two methods for calculating the skin friction and with a modified form of Reynolds analogy applicable to rough surfaces. Boundary-layer profiles for both smooth and rough walls have been obtained from pitot pressure traverses. The velocity profiles have been analyzed in terms of the law of the wall.

Nomenclature

A_B	Model base area
c_f	local skin-friction coefficient
C_{DF}	friction drag coefficient
C_F	average skin-friction coefficient
C_{F_i}	average skin-friction coefficient in incompressible flow
C_{F_o}	average skin-friction coefficient on the smooth wall
C_p	pressure coefficient
h	enthalpy
k	roughness height
ℓ	slant length of sharp cone
M	Mach number
p	pressure
P_o'	pitot pressure
Pr	Prandtl number
q	dynamic pressure
R_N	nose radius
Re_k	roughness Reynolds number $u_\tau k/\nu_w$
$\overline{Re_k}$	average value of roughness Reynolds number
Re_x	Reynolds number based on boundary-layer edge conditions and length x
Re_θ	momentum thickness Reynolds No.
s	arc length from stagnation point along model surface
St	Stanton number
St_o	Stanton number on smooth wall
t	time
T	temperature
T_o	total temperature
u	velocity
u_τ	friction velocity $\sqrt{\tau_w/\rho_w}$
x	distance from cone vertex
Y	distance normal to cone surface
α	parameter in formula (29)
δ_e	boundary-layer thickness
δ^*	boundary-layer displacement thickness
θ	boundary-layer momentum thickness
θ_c	semi-vertex angle of sharp cone
κ	Karman constant
μ	viscosity
ν	kinematic viscosity μ/ρ
ρ	density
τ	shear stress

Subscripts

aw	adiabatic wall
e	boundary-layer edge
w	at wall or based on wall properties
∞	free-stream or based on free-stream conditions

1. Introduction

On a vehicle exposed to a given flow, it has long been recognized that roughening the surface will increase the skin friction and, to a lesser extent, the heat transfer. The literature dealing with incompressible flows, both in pipes and over flat plates, is very extensive. In the last 20 years a number of investigations of compressible flows have also been published.

---

* Aerospace Engineer

** Aerospace Engineer

*** Student

One area of practical concern with this subject has been the aerothermal performance of reentry vehicle nosetips. Here the surface may become rough as material ablates and the effects of this roughness on the boundary layer play a key role in determining the progressive shape changes of the nosetip. A number of experiments have been conducted and some calculation methods[1] have been derived from correlations of the data.

Another potential area of concern is the heat shield on the afterbody of a reentry vehicle. In the past, for ballistic vehicles, the effects of possible heat-transfer augmentation due to roughness have not been critical for heat shield design. In the future, however, for maneuvering vehicles, these effects may become important.

The data base applicable to the afterbody problem is not large. Most of the early supersonic work was done under conditions which were either adiabatic or not too far from it. Recently Keel[2] has measured both the skin friction and heat transfer with large heating rates (T_w/T_o = 0.35) on a sharp cone with sand-grain roughness at free-stream Mach numbers up to 5.

The experiments reported here were conducted to extend the Mach number range of the data base to Mach 10 while maintaining the wall temperature ratio at a value low enough (T_w/T_o = 0.26) to be relevant to reentry conditions. Again the model configuration was conical, and a blunt nose was tested in addition to the sharp cone. The latter is well suited to provide fundamental data for comparison with analytical methods while the former is of course more representative of actual reentry vehicles.

The tests were run "piggy-back" on a tunnel heater development program and the test plan is not as systematic as it could have been if the roughness investigation had been the primary objective. Although the results are therefore incomplete, they do permit the testing of various hypotheses and calculation methods in a flow regime in which experimental data are very scarce.

II. Description of the Experiments

Facility

The tests were conducted in the Hypervelocity Tunnel at the White Oak Laboratory of the Naval Surface Weapons Center. This is a 5-foot tunnel operating at Mach 10 and Mach 14 at high Reynolds numbers. The working fluid is nitrogen, heated only enough to avoid condensation in the nozzle expansion. The volume of hot nitrogen available at either Mach number yields a run time of about one second. Fully stabilized flow suitable for data acquisition is available for about 0.7 seconds.

The data acquisition system samples up to 128 channels at a sampling rate of either 250 Hz or 100 Hz and converts analog signals to 12-bit digital data.

A more complete description of this facility has been given in reference 3.

Model Configurations

The model was a 7-degree half angle cone with two interchangeable noses, sharp and 18% blunt. Figure 1 shows the sharp cone mounted in the test cell and Figure 2 shows the principal dimensions in inches.

Fig. 1 Sharp cone with surface roughness installed in the Hypervelocity Tunnel

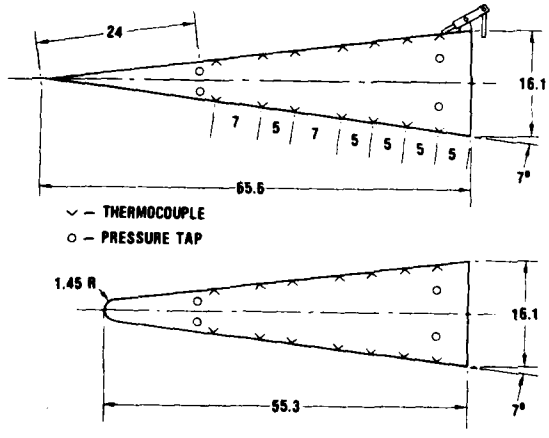

Fig. 2 Model dimensions and instrumentation locations

Rough surfaces were obtained by applying silicon carbide grit to the model skin using an epoxy adhesive with a high thermal conductivity (0.000241 Btu/ft.sec.°F). The nominal grit sizes were 0.011, 0.037, and 0.065 inches. The application procedure was to mount the model on a lathe and to rotate it slowly while applying a thin coat of the adhesive. Grit was then sprinkled on the surface, (with the model still rotating) until no more particles would adhere. To characterize the result, the procedure was repeated on 8-inch-diameter tubing from which sections were cut for photomicrographs, such as shown in Figure 3. These

were then analyzed to obtain the parameters given in the Appendix. However, to be consistent with other investigations using "sand-grain" roughness, the nominal grain size is used as the roughness height for all the results reported in this paper.

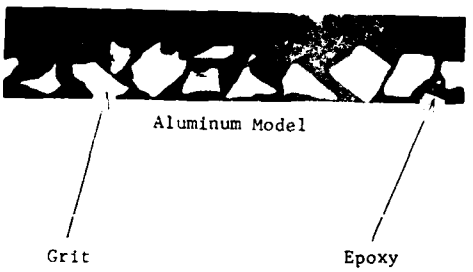

Fig. 3 Photomicrograph of section of rough surface

Instrumentation

The model was mounted on a conventional strain-gage force balance to measure the total drag so that the skin-friction could be obtained as described below.

To measure the heat transfer to the model surface, 14 thermocouples were installed in the aluminum model skin. The nominal wall thickness was 0.090 inches; the actual wall thickness at each thermocouple location was measured and used for data reduction. The thermocouples were installed on two opposite rays of the conical surface so that the measurements could be averaged to eliminate the effects of a small angle of attack.

Rings of four equally spaced pressure taps were installed at two model stations at $s/R_N = 9.82$ and 35.3. These were connected to pressure transducers with short lengths of tubing. The base pressure was measured with two transducers exposed to the cavity inside the model. Their readings were averaged to determine the base pressure.

A boundary-layer probe was installed at the base of the model, mounted on the sting to avoid the inclusion of its drag on the force-balance measurement. The tip was a flattened tube with an opening 0.033 in. x 0.075 in. The tip was approximately 5 inches forward of the model base. The probe was traversed through the boundary layer by a D.C. motor at a speed which could be adjusted from 1 inch/sec. to 4 inch/sec. The lag in the pressure measurement was analyzed by the method described in reference 4 and was found to be small enough to avoid the need for a correction.

Test Conditions and Run Schedule

As noted in the introduction, the test conditions were set by the needs of the heater checkout program. The nominal Mach number was 10, with a supply temperature of about 2100°R chosen to be just hot enough to avoid condensation. Tests were run at two values of the supply pressure, corresponding to unit Reynolds numbers of about 7×10^6 and 4×10^6 per foot. During the one-second run the model wall temperature rose only a few degrees above room temperature, so that the wall temperature ratio T_w/T_o was approximately 0.26.

The test program consisted of 10 runs. Table 1 shows the run schedule matrix by indicating the roughness heights tested on the sharp and blunt configurations. Each entry in the table represents a run at the Reynolds number indicated. These Reynolds numbers are based on free-stream conditions and model length.

Table 1

Test Reynolds Numbers for the Various Roughness Heights on the Sharp and Blunted Cone

Roughness Height (In.)	Sharp Cone Reynolds Number $Re_\infty \times 10^{-6}$	Blunted Cone Reynolds Number $Re_\infty \times 10^{-6}$
0	34.1, 24.1	30.8
0.011	40.0	32.9
0.037	40.9	34.0
0.065	41.6, 22.5	19.8

Data Reduction - Friction Drag Coefficient

The friction drag coefficient for each test was obtained by subtracting the base drag and forebody pressure drag from the total drag measured on the force balance.

For the sharp cone the theoretical inviscid drag coefficient is 0.0343.[5] The average of the eight measured pressure coefficients was within 5% of this value, perhaps due to small misalignments of the model to the flow. For data reduction the mean of the measured and theoretical value was used.

On the blunt cone the theoretical inviscid pressure distribution is as shown in Figure 4.[6]

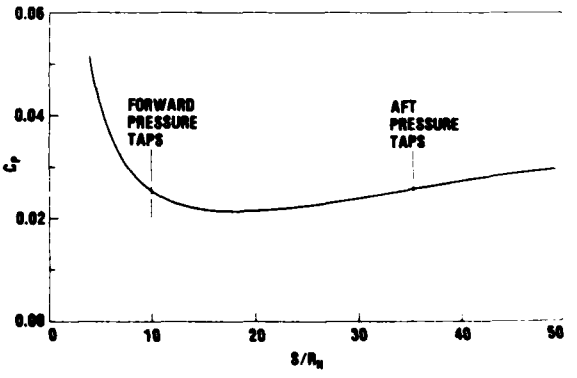

Fig. 4 Surface pressure distribution on the blunted cone

The pressure coefficient at the two pressure tap locations is 0.0256 and the forebody pressure drag coefficient is 0.0530 of which 0.0283 acts on the nose and 0.0247 acts on the frustum. During the tests the averaged measured pressure coefficient at the two instrumented stations was 2%-3% higher than the theoretical value. For data reduction the frustum drag was corrected by the ratio of the pressure coefficients yielding forebody pressure drag coefficients in the range 0.0538-0.0544. These as well as the measured base drag coefficient were then subtracted from the total drag coefficient to yield the friction drag coefficient as for the sharp cone.

Data Reduction - Heat Transfer

The test time in the Hypervelocity Tunnel is long enough that the conventional thin-wall data reduction technique could be used. The heat-transfer rate was computed from

$$\overset{o}{q} = \rho c \delta \frac{dT_w}{dt} \qquad (1)$$

where

ρ is the density of the model wall
c is the specific heat of the model wall
δ is the thickness of the model wall

and the derivative (dT_w/dt) was obtained by fitting a polynominal to the nearly linear portion of the temperature-time history.

The validity of this concept for the rough surfaces was examined before the test by running some calculations with a computer code for transient conduction in multi-layered slabs. Figure 5 is a sample result from such a calculation simulating the largest grit size. There is an initial transient during which a temperature difference is established across the layer of adhesive, after which there is a steady state in which all temperatures rise at the same rate. Once this steady state is established one may write

$$\overset{o}{q} = \overline{\rho c \delta} \frac{dT_w}{dt} \qquad (2)$$

where

$$\overline{\rho c \delta} = (\rho c \delta)_{Al} + (\rho c \delta)_{Epoxy} + (\rho c \delta)_{grit} \qquad (3)$$

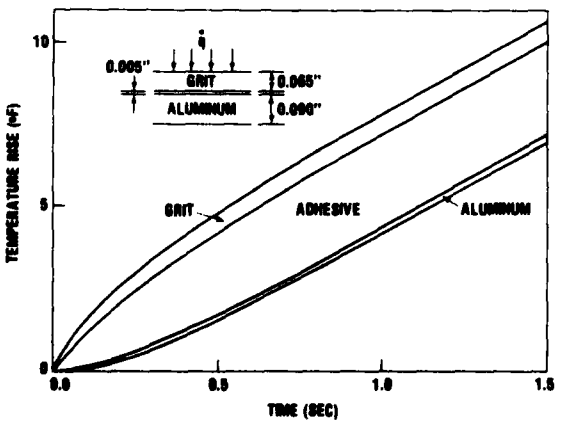

Fig. 5 Response of composite model wall to step input in heat transfer

For these tests the value of $(\rho c \delta)_{Epoxy}$ and $(\rho c \delta)_{grit}$ were obtained by weighing the epoxy and grit applied to the model. This method of course yields an average value and cannot account for variations from one thermocouple station to another. On the other hand the contributions of these terms to $\rho c \delta$ are relatively small, as shown in Table 2. Thus variations in the density of the grit or adhesive can have only very small effects on the computed values of $\overset{o}{q}$ at each thermocouple station.

Table 2

Composite Model Wall Parameters

Material	Thickness of Layer* cm	Heat Capacity cal/cm^2°C	Percent of Total Heat Capacity %
	k = 0.011"		
Aluminum	.2286	.1376	90
Epoxy	.0122	.0083	5
Grit	.0136	.0083	5
	k = 0.037"		
Aluminum	.2286	.1376	86
Epoxy	.0093	.0064	4
Grit	.0269	.0163	10
	k = 0.65"		
Aluminum	.2286	.1376	79
Epoxy	.0103	.0070	4
Grit	.0479	.0289	17

Data Reduction - Boundary-Layer Profiles

Boundary-layer flowfield measurements included the local pitot pressure profiles and a measured cone surface pressure. For the blunt cone case, very little else could be deduced because of the entropy gradients which were superimposed on the flow. For the sharp cone case, however, the static pressure across the boundary layer could be assumed constant with great confidence and Mach number profiles could be obtained. Furthermore, by assuming the temperature-velocity relationship as given by Walz,[7] velocity profiles were obtained. Boundary-layer profiles were then integrated to obtain displacement and momentum thicknesses in the conventional manner.

III. Skin Friction and Heat-Transfer on the Sharp Cone

Relation of the Skin-Friction Coefficients to the Friction Drag

At the high Reynolds numbers used in the experiments, the displacement effect of the boundary layer on the inviscid flow is very small. It is not possible to detect any such effects in our measurements of either the surface pressures or the boundary-layer profiles. Thus the edge conditions for the boundary layers on the sharp cone will be assumed equal to those for the inviscid flow.

Given a uniform boundary-layer edge condition, the variation of local skin-friction coefficient, c_f, along the surface may be calculated by any one of a number of theories. Then the total force along the axis of the cone is

$$F_A = 2\pi\, q_e \cos\alpha_c \sin\alpha_c \int_0^{\ell} c_f \, x \, dx \qquad (4)$$

One may define an average skin-friction coefficient, C_F, such that

$$F_A = C_F\, q_e\, S \cos\alpha_c \qquad (5)$$

where S is the lateral area,

$$S = \pi \ell^2 \sin\alpha_c \qquad (6)$$

The value of C_F may then be obtained as

$$C_F = (2/\ell^2) \int_0^{\ell} C_f x dx \qquad (7)$$

Now the friction-drag coefficient, C_{DF}, is defined such that

$$F_A = C_{DF}\, q_\infty\, A_B \qquad (8)$$

where

$$A_B = \pi \ell^2 \sin^2\theta$$

Therefore

$$C_{DF} = (q_e/q_\infty)\cot\theta_c C_F \qquad (9)$$

For the inviscid flow over a 7-degree cone at Mach 10 this may be written

$$C_{DF} = 18.4\, C_F \qquad (10)$$

A number of analytical methods are available for calculating the variation of c_f along the cone surface. For the smooth cone we have used the method of Van Driest[8] evaluated at our test conditions. Figure 6 shows the ratio of c_f/C_F plotted versus distance from the tip of the cone. The same ratio is also shown for the fully rough flow regime, calculated according to Fenter's[9] formulas.

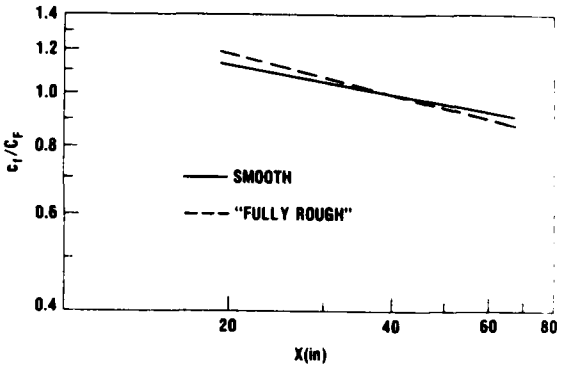

Fig. 6 Ratio of local to average skin friction coefficient

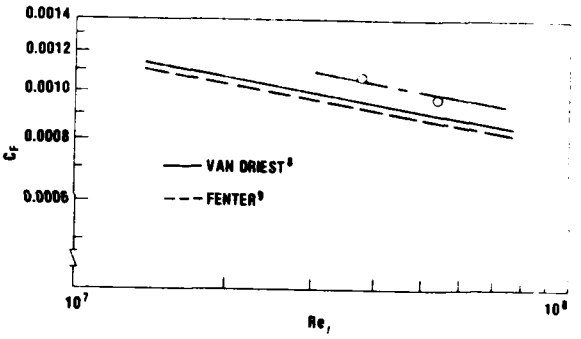

Fig. 7 Average skin friction coefficient versus Reynolds number

Skin Friction on the Smooth Cone

The friction drag on the smooth cone has been measured for two tunnel operating pressures. The results, together with the Reynolds numbers based on cone slant length are given in Table 3.

Table 3 - Skin-Friction Measurements on the Sharp Cone

Nominal Roughness Height k(in.)	Free-Stream Reynolds Number $Re_\infty \times 10^{-6}$	Boundary-Layer Edge Reynolds Number $Re_x \times 10^{-6}$	Roughness Reynolds Number Re_K	Friction Drag Coefficient C_{D_F}	Average Skin-Friction Coefficient C_F
0	34.1	53.4	0	.0179	.00097
0	24.1	37.7	0	.0197	.00107
.011	40.0	62.7	41	.0218	.00119
.037	40.9	64.1	170	.0314	.00171
.065	41.6	65.1	323	.0361	.00196
.065	22.5	35.2	185	.0403	.00219

In Figure 7 these measurements are compared with the formulas of Van Driest[8] and Fenter[9]. The former has been evaluated according to the equations given in reference 10 and the latter is

$$\frac{\psi}{\sqrt{\sigma}}\sqrt{\frac{T_e}{T_w}}\,\frac{1}{\sqrt{c_f}} = 4.13 \log c_f Re_x - 4.13\,\omega \log\frac{T_w}{T_e} + 0.60 \qquad (11)$$

where ω is the exponent in the formula

$$(\mu_w/\mu_e) = (T_w/T_e)^{\omega}$$

and

$$\psi = \sin^{-1}\left(\sqrt{\frac{2\sigma - \lambda}{\lambda^2 + 4\sigma}}\right) + \sin^{-1}\left(\sqrt{\frac{\lambda}{\lambda^2 + 4\sigma}}\right) \qquad (12)$$

with

$$\cdot = (1 + \frac{\cdot-1}{2} M_e^2)(T_e/T_w) \cdot 1 \qquad (13)$$

and

$$\cdot = (\frac{\cdot-1}{2} M_e^2)(T_e/T_w) \qquad (14)$$

This formula yields c_f as a function of x for any given Reynolds number and C_F may then be obtained by integration as described above.

The two formulas, using the same transformation from incompressible to compressible flow yield results which agree quite closely. The experimental data points lie about 10% above the theory. A similar result for this low value of the wall temperature ratio (T_w/T_o 0.26) was obtained by Chien.[11]

Skin Friction on the Rough Cone

The phenomenology of the boundary-layer flow over rough surfaces is generally classified into three flow regimes. These may be identified in terms of a roughness Reynolds number

$$Re_k = u_\tau k/\cdot w \qquad (15)$$

where u_τ is the friction velocity

$$u_\tau = \cdot\sqrt{/\cdot_w} \qquad (16)$$

The value of Re_k is closely related to the ratio of roughness height to the thickness of the laminar sublayer. The three flow regimes are:

$Re_k \cdot 5$	aerodynamically smooth
$5 \cdot Re_k \cdot 70$	transitionally rough
$70 \cdot Re_k$	fully rough

In the aerodynamically smooth regime the size of the roughness elements is too small to affect the flow and the friction and is the same as on a perfectly smooth wall. In the fully rough regime the roughness elements are so much larger than the laminar sublayer that the flow is unaffected by viscosity and hence independent of Reynolds number.

The values of roughness Reynolds number for the experiments have been calculated from the known flow conditions and measured friction coefficients using the formula

$$Re_k = \frac{\cdot_e u_e k}{\mu_w} \sqrt{\frac{c_f}{2} \frac{T_e}{T_w}} \qquad (17)$$

and have been plotted in Figure 8. For the two larger roughness heights the flow is clearly indicated to be in the fully rough regime. For such flows over flat plates or cones with uniform roughness height the skin-friction coefficient depends only on the parameter x/k where x is the distance from the leading edge or nose and k is the roughness height.

The measurements for all the runs are given in Table 3 and those for the two larger roughness heights are plotted versus x/k in Figure 9, using the average value C_F of the skin-friction coefficient. Note first that the two points for x/k = 1000 indicate a decrease in C_F of about 10% as the Reynolds number is doubled. This is contrary to the expected behavior in the fully-rough regime. It may suggest that the flow regime boundaries should be redefined for compressible flows, but this cannot be done on the basis of just these two measurements. The discrepancy could simply be accounted for by a +5% uncertainty in the data, which is quite plausible.

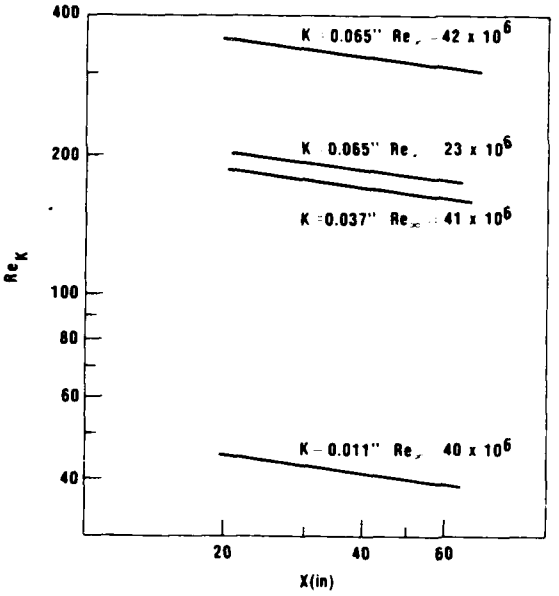

Fig. 8 Roughness Reynolds Number

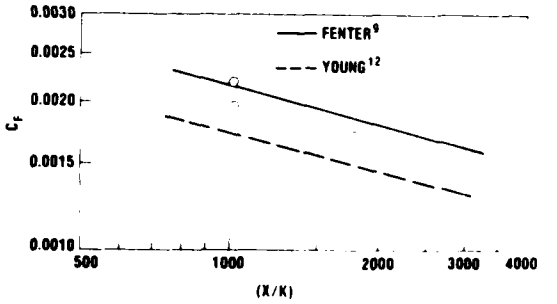

Fig. 9 Average skin friction coefficients versus (x/k)

Also shown in the figure are two analytical predictions of the values of C_F for these flow conditions. Fenter's[9] formula for the local skin friction in the fully-rough flow regime is

$$\frac{\cdot}{\sqrt{\cdot}} \sqrt{\frac{T_e}{T_w}} \frac{1}{\sqrt{c_f}} = 4.13 \log\left(\frac{x}{k} \cdot \overline{c_f}\right) + 2.605 \log (T_w/T_o) + 3.38 \qquad (18)$$

with $\cdot$ and $\cdot$ defined as in (12)-(14). In the range of values of (x/k) of interest here, this may be approximated by the power law formula

$$c_f = 0.0105\ (x/k)^{-.25} \qquad (19)$$

for the nominal flow parameters of our experiments, namely

$$M_e = 8.15 \qquad T_e = 150°R \qquad T_w = 560°R$$

This approximation yields a simple expression for the average friction coefficient C_F in terms of the local coefficient at the base of the cone

$$C_F = (2/1.75)c_f = 1.14\ c_f(\text{base}) \qquad (20)$$

Young's[12] formula represents an extension of Goddard's[13] fundamental work to non-adiabatic flow. It relates the skin friction in compressible flow to that in the corresponding incompressible flow by the relation

$$\frac{C_F}{C_{Fi}} = 0.365\ \frac{T_e}{T_{aw}} + 0.635\ \frac{T_e}{T_w} \qquad (21)$$

To obtain a value of C_F for a given (x/k) one must first obtain the incompressible value C_{Fi}. This may be obtained from Fenter's equation (18) evaluated with $T_e = T_w$ and $\psi/\sqrt{\sigma} = 1$;

$$1/\sqrt{c_f} = 4.13 \log\left[(x/k)\sqrt{c_f}\right] + 3.38 \qquad (22)$$

for the hypothetical case of an incompressible flow over a cone with zero pressure gradient. Note that the corresponding formula for a flat plate;

$$1/\sqrt{c_f} = 4.13 \log\left[(x/k)\sqrt{c_f}\right] + 4.62 \qquad (23)$$

agrees very well with the generally accepted Prandtl-Schlichting[14] law;

$$C_{Fi} = \left[2.87 + 1.58 \log (x/k)\right]^{-2.5} \qquad (24)$$

Figure 9 clearly shows that the effects of compressibility are predicted much better by Fenter's[9] formula than by Young's[12]. Similar results have been noted in some unpublished work at NSWC; Keel's[2] measurements of skin friction in adiabatic flow at $M_e = 2.4$ and 4.7 yield values higher than Goddard's[13] formula

$$C_F/C_{Fi} = T_e/T_{aw} \qquad (25)$$

by about 30%, or slightly more than the amount by which our measurements exceed Young's prediction.

Heat Transfer on the Smooth Surface

The heat-transfer measurements will be discussed in terms of their relation to the skin-friction measurements, using the ratio $2St/c_f$ where both are local values.

The results for the two runs with the smooth surface are shown in Figure 10. The mean value of the Reynolds analogy factor is

$$2St/c_f = 0.98 \qquad (26)$$

This is much lower than the value of about 1.2 generally accepted for supersonic and lower Mach numbers with wall temperatures close to adiabatic. It is, however, consistent with numbers reported by Hopkins and Inouge[10] for cold walls at hypersonic speeds and with the measurements of Keel[2], all of which are near unity.

Heat Transfer on the Rough Surface

It has long been known that the increase in heat transfer due to roughness is less than the corresponding increase in skin friction. Consequently, a simple Reynolds analogy cannot apply to the flow over rough surfaces. The Reynolds analogy factor $2St/c_f$ is expected to decrease with increasing roughness. This effect is illustrated in Figure 11 which shows $2St/c_f$ plotted versus Re_k for the four runs with roughness on the sharp cone.

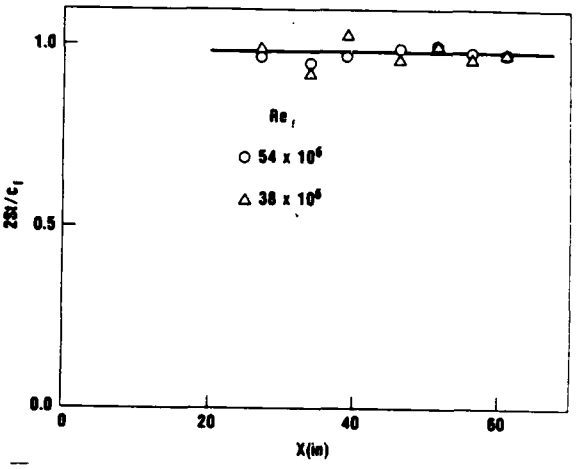

Fig. 10 Reynolds analogy factor on the Smooth Cone

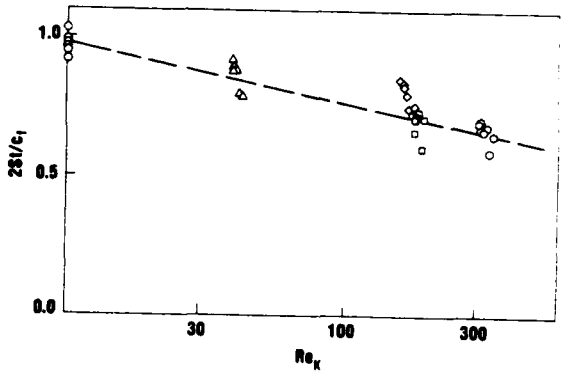

Fig. 11 Reynolds analogy factor versus roughness Reynolds number

Several quantitative analyses of the effect of roughness on the Reynolds analogy factor are available in the literature. We have chosen to compare our results with the work of Owen and Thomson.[15] Their result, modified for compressible flow, may be written

$$\frac{1}{St} = \frac{T_w}{T_e}\frac{U_e}{U_\tau}\left[\frac{U_e}{U_\tau} + \frac{1}{B}\right] \qquad (27)$$

where B is the sublayer Stanton number. In their experiments they obtained correlations for B in the form

$$\frac{1}{B} = \alpha\ Re_k^{0.45}\ P_r^{0.8} \qquad (28)$$

with α varying between 0.45 and 0.7. The modified Reynolds analogy obtained by substituting (28) into (27) is

$$\frac{2St}{c_f} = \left[1 + \alpha\sqrt{\frac{c_f}{2}}\frac{T_w}{T_e}\ Re_k^{0.45}\ P_r^{0.8}\right]^{-1} \qquad (29)$$

A convenient way to try to fit the data to this expression is to plot the quantity

$$\left(\frac{c_f}{2St} - 1\right) \Big/ \sqrt{\frac{c_f}{2}\frac{T_w}{T_e}}$$

versus Re_k as shown in Figure 12. The scatter is quite large, but the trend of the data appears to be consistent with the analysis. Almost all the data can be fitted into a band defined by

$$.45 \leq \alpha \leq 1.3$$

corresponding to a logarithmic mean value of $\alpha = 0.75$.

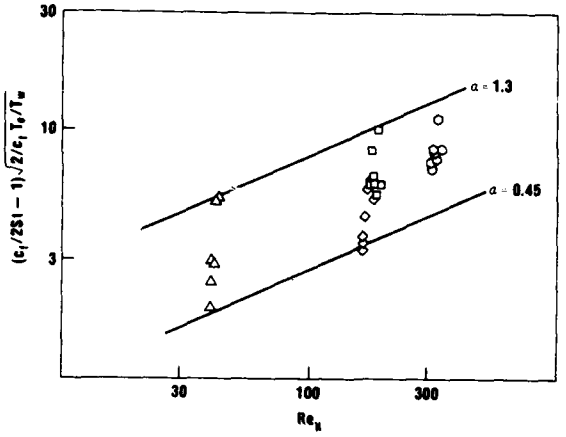

Fig. 12 Heat-transfer parameter versus roughness Reynolds number

This is at the high end of the range of values quoted by Owen and Thomson[15], who do not expect any value of α to be universally applicable.

Augmentation

The data on skin friction and heat transfer for the rough wall may also be shown in terms of augmentation ratios C_F/C_{F_o} and St/St_o, where C_{F_o} and St_o are evaluated for a smooth wall at the same Reynolds number. Considering that in the fully rough regime the variation with Reynolds number of the ratio C_F/C_{F_o} is entirely in C_{F_o}, this concept is clearly not well founded on the phenomenology of the flow over rough surfaces. However, it is used in a number of calculation schemes and may be useful for illustrative purposes.

Figure 13 shows the measured friction augmentation ratios together with some calculated values. They are plotted versus an average value of the roughness Reynolds number defined as

$$\overline{Re_k} = \frac{\rho_e u_e k}{\mu_w}\sqrt{\frac{c_F}{2}\frac{T_e}{T_w}} \qquad (30)$$

The calculations shown are based on Fenter's[9] formulas for the skin friction on cones and have been made for the two values of Reynolds number used in these tests. One set of calculations is purely analytical, using Fenter's formulas for both the smooth and rough wall. This yields an augmentation ratio higher than measured simply because the smooth wall calculation is low, see Figure 7 . In the other set of calculations we have used Fenter's formula for the rough wall and a fit to the data for the smooth wall. These calculations are still somewhat higher than the data but represent the effect of increasing roughness reasonably well.

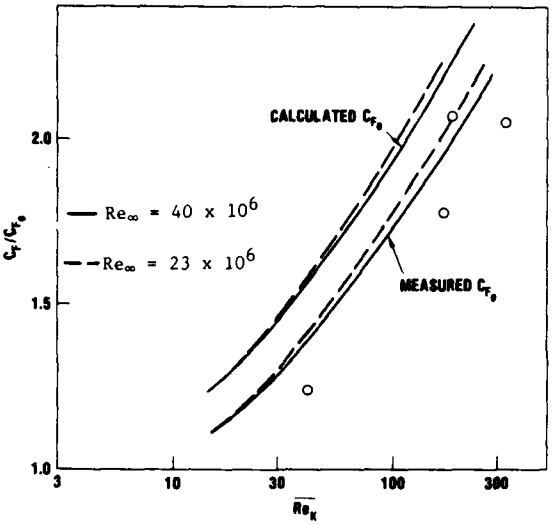

Fig. 13 Skin friction augmentation

Figure 14 shows the measured heat-transfer augmentation ratios together with some calculated values. The latter have been derived from Owen and Thomson's formula (29) using the mean value of α (0.75) derived from Figure 11. The heat-transfer augmentation has been calculated from the friction augmentation using the expression:

$$\frac{St}{St_o} = \frac{2St}{c_f}\frac{C_F}{C_{F_o}}\frac{1}{0.98} \qquad (31)$$

where 0.98 represents the mean value of $2St_o/C_{F_o}$. For this calculation the experimental values of C_F/C_{F_o} have been used, by fitting a curve to the available data.

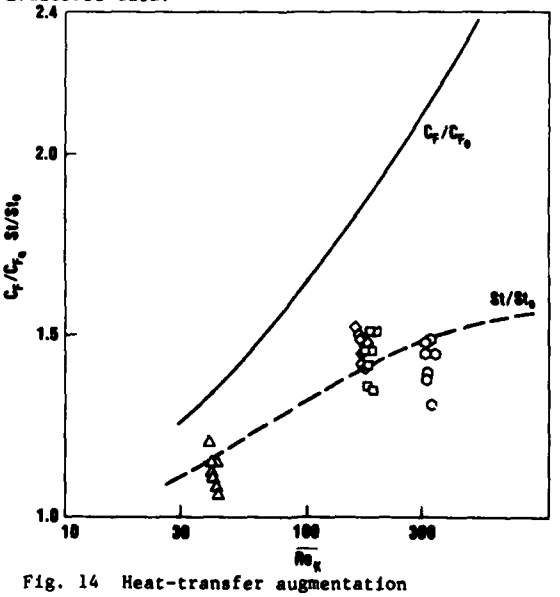

Fig. 14 Heat-transfer augmentation

IV. Skin Friction and Heat Transfer on the Blunted Cone

Interpretation of friction and heat-transfer data on the blunted cone is much less definitive than on the sharp cone for three reasons. First, the friction drag is a much smaller fraction of the total drag and thus subject to a larger uncertainty. Second, the boundary-layer edge conditions are variable rather than uniform. In the absence of an extensive flow-field survey, these edge conditions can only be derived from computations, whose modeling of the flow is necessarily approximate. Third, it was necessary to trip the boundary layer on the model nose in order to obtain turbulent flow over the entire frustum.

Nevertheless it will be possible to discuss the augmentation of the friction due to roughness. As far as the heat transfer is concerned, only the velocity at the boundary-layer edge need be estimated in order to derive a modified Reynolds analogy factor from the data.

Relation of the Skin-Friction Coefficient to the Friction Drag

To avoid the problem of undefined flow conditions at the boundary-layer edge, it is convenient to define a local skin-friction coefficient based on free-stream flow parameters;

$$c_{f_\infty} = 2\tau/\rho_\infty u_\infty^2 \qquad (32)$$

As in the case of the sharp cone, various analytical methods may be used to calculate the variation along the cone surface of the ratio c_{f_∞}/C_{DF}. For the smooth surface we have used the method of reference 16 and obtained the result shown in Figure 15. Note that for a sharp cone with a hypothetical constant value of c_{f_∞} the value of this ratio would be $\tan\theta_c = 0.123$. For the rough surface we have used the RETAS[17] code to compute this ratio for the roughness heights of our experiments. This result is also shown in Figure 15.

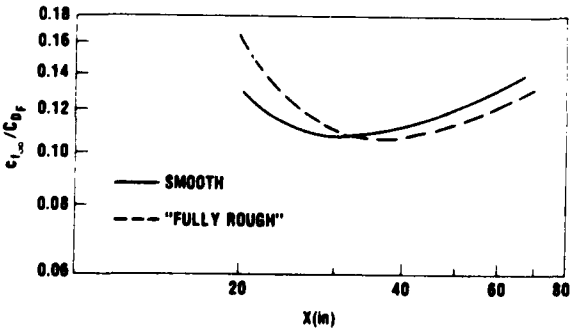

Fig. 15 Ratio of skin-friction coefficient to friction drag coefficient

Friction Drag on the Smooth Cone

The variation with Reynolds number of the friction drag on the smooth cone, calculated by the method of reference 16, is shown in Figure 16. Also shown is the one data point from this test series, which is also given in Table 4.

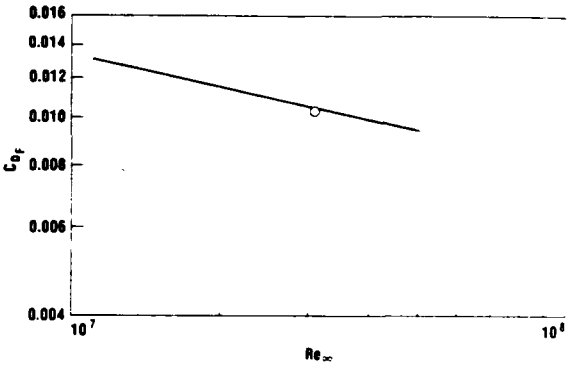

Fig. 16 Friction drag coefficient versus Reynolds number

There is good agreement between the calculations and the measurement. Apparently, the boundary-layer trip used (0.005-inch distributed grit) provides a close approximation to what would be obtained with natural transition.

Not too much significance should be attached to the difference between the situation here, where measurement and calculation agree, and that for the sharp cone, where the measurements are higher than the calculations. The expressions used for the friction coefficients in reference 16 are not as well founded as the Van Driest[18] or Fenter's formulas for the special case of uniform pressure.

Table 4

Skin-Friction Measurements on the Blunted Cone

Nominal Roughness Height k(in.)	Free-Stream Reynolds Number x 10^{-6} Re_∞	Roughness Reynolds Number Re_k	Friction Drag Coefficient C_{DF}
0	30.8	0	.0163
.011	32.9	26	.0111
.037	34	112	.0141
.065	19.8	134	.0283

Friction Drag on the Rough Cone

The roughness Reynolds number on the blunted cone cannot be computed as simply as on the sharp cone. We can write

$$\frac{u_\infty}{u_\tau} = \sqrt{\frac{c_{f_\infty}}{2}}_w \qquad (33)$$

and

$$Re_k = \frac{\rho_w u_k k}{\mu_w} \sqrt{\frac{c_{f_k}}{2}} \frac{\rho_e}{\rho_w} \tag{34}$$

$$= \frac{\rho_\infty u_\infty k}{\mu_w} \sqrt{\frac{T_\infty}{T_w}} \sqrt{\frac{c_{f_k} p}{2 p_\infty}} \frac{w}{\infty}$$

Using values of p_w/p_∞ obtained from the tables in reference 6, values of Re_k have been calculated for the three runs made with rough walls on the blunted cone. These are shown in Figure 17 plotted versus the surface distance from the virtual nose. Again the flow produced by the two larger roughness sizes should be in the fully-rough regime.

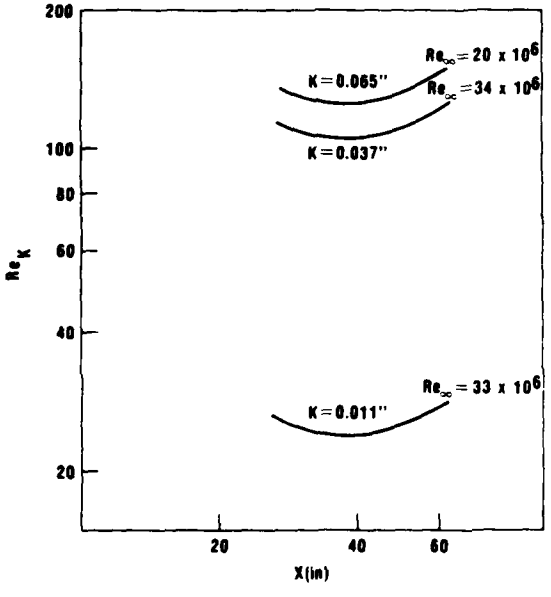

Fig. 17 Roughness Reynolds number

The measurements of friction drag obtained with the rough walls are given in Table 4. The computer code[16] used for the smooth surface cannot handle rough surfaces. The RETAS code[17] can handle rough surfaces but underpredicts the smooth-wall drag by 25%, probably because it does not handle entropy swallowing as well as the code of reference 16. Thus no meaningful direct comparison of these measurements could be obtained from the computer codes available to us. In the subsequent section on augmentation, the ratios of rough-wall to smooth-wall values will be compared with the predictions of the RETAS code.[17]

Heat Transfer on the Smooth Surface

Again we shall discuss the heat-transfer results in terms of the Reynolds analogy factor $2St/c_f$, where both coefficients represent local values of shear stress and heat transfer, divided by local conditions at the boundary-layer edge. As in the case of the skin friction, the Stanton number most conveniently calculated from the measurements is based on free-stream conditions;

$$St_\infty = \frac{q_w}{\rho_\infty u_\infty h} \tag{35}$$

To obtain a Reynolds analogy factor from St_∞ and c_{f_∞} we note that

$$\frac{2St}{c_f} = \frac{u_e q_w}{u_\infty h} \tag{37}$$

whereas

$$\frac{2St_\infty}{c_{f_\infty}} = \frac{u_\infty q_w}{u_\infty h} \tag{38}$$

Therefore

$$\frac{2St}{c_f} = \frac{2St_\infty}{c_{f_\infty}} \frac{u_e}{u_\infty} \tag{39}$$

Values of (u_e/u_∞) required to evaluate this expression can only be obtained from the boundary-layer codes discussed above. There may well be errors in these values, since the codes involve many approximations, and to that extent the Reynolds analogy factors reported here are necessarily approximate. However, the values of (u_e/u_∞) lie in the narrow range

$$0.85 \leq (u_e/u_\infty) \leq 0.95$$

and thus are probably estimated correctly within 5% or less.

Figure 18 shows the values of Reynolds analogy factor obtained from the measurements. The mean value is

$$2St/c_f = 0.90$$

These values are lower than those shown for the smooth cone in Figure 9 and also lower than expected. In view of the difficulty of measuring C_{DF} from the drag data, the difference may not be significant.

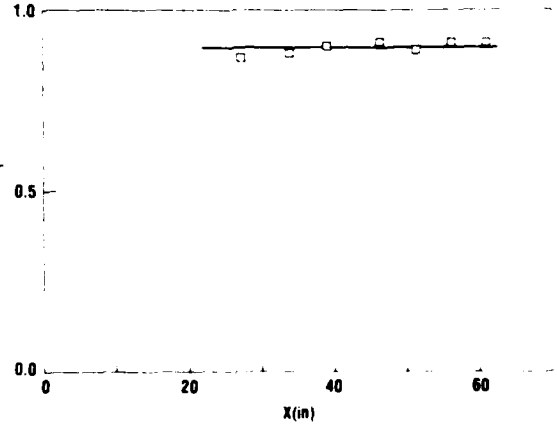

Fig. 18 Reynolds analogy factor on the smooth cone

Heat Transfer on the Rough Surface

As in the case of the skin friction, the Reynolds analogy factor decreases as the roughness Reynolds number increases, see Figure 18. There is quite a great deal of scatter, suggesting that a better correlation might be obtained with some parameter other than Re_k or with some parameter in addition to Re_k.

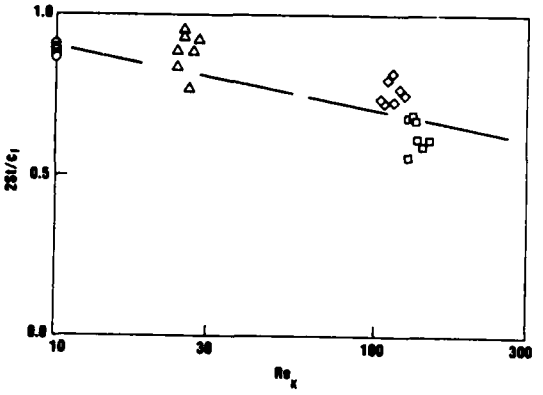

Fig. 19 Reynolds analogy factor versus roughness Reynolds number

The modified Reynolds analogy based on Owen and Thomson's[15] analysis may be rewritten in terms of c_{f_∞} as

$$\frac{2St}{c_f} = \left[1 + \alpha \frac{u_\infty}{u_e}\sqrt{\frac{c_{f_\infty}}{2}\frac{\rho_\infty}{\rho_w}}\, Re_K^{0.45}\, P_r^{0.8}\right]^{-1} \qquad (41)$$

The measured quantity

$$\left(\frac{c_f}{2St} - 1\right) \Big/ \left(\frac{u_\infty}{u_e}\right)\sqrt{\frac{c_{f_\infty}}{2}\frac{\rho_\infty}{\rho_w}}$$

is shown plotted versus Re_K in Figure 19. Estimates of (u_e/u_∞) and p_w/p_∞ have been obtained from the sources described above. The trend is appropriate but the values of α are larger than for the sharp cone. Almost all the data are included in a band defined by

$$0.7 \leq \alpha \leq 2$$

corresponding to a logarithmic mean value of $\alpha = 1.2$.

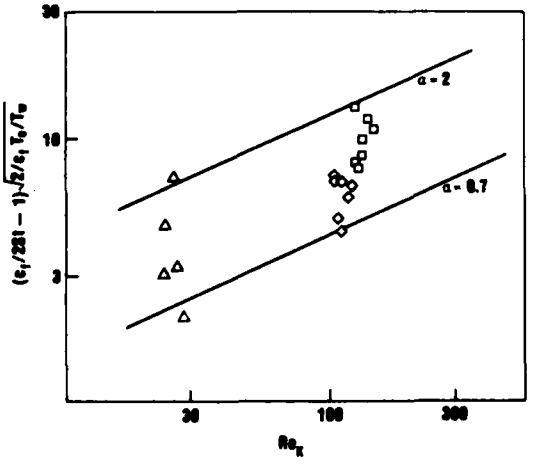

Fig. 20 Heat-transfer parameter versus roughness Reynolds number

Augmentation

Augmentation ratios for the skin friction have been derived from the data by dividing the values of C_{DF} for the rough wall by a smooth-wall value of C_{DF_o} obtained at the same Reynolds number from Figure 15. These ratios have been plotted versus the average value of roughness Reynolds number, Re_k, in Figure 21. Calculated values of the augmentation ratio have been obtained from computations made with the RETAS[17] code, which uses Fenter's[9] skin-friction formulas. It does not predict either the smooth-wall or rough-wall drag very well but does a fair job on the ratio C_F/C_{F_o}.

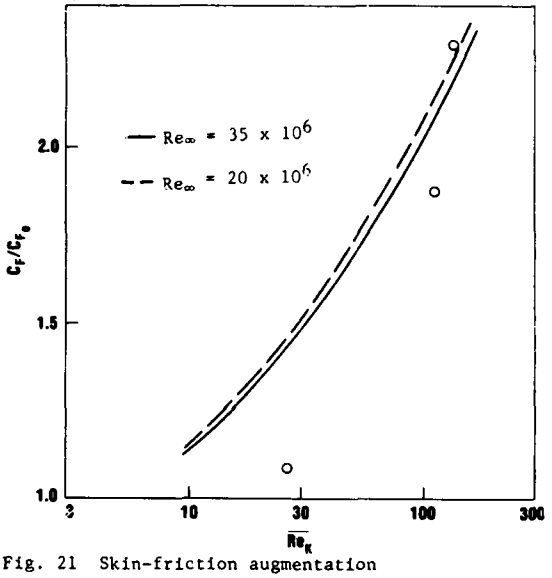

Fig. 21 Skin-friction augmentation

The heat-transfer augmentation ratios are shown in Figure 22, again plotted versus the average value of the roughness Reynolds number, $\overline{Re_k}$. They are shown in terms of Stanton numbers based on free-stream conditions, St_∞ and $St_{\infty o}$. The curve shown has been obtained from the Owen and Thomson formula (41) using the mean value of $\alpha = 1.2$. A curve fitted to the experimental values of C_{DF}/C_{DF_o} has been used for the friction augmentation. The calculations of $St_\infty/St_{\infty o}$ must take into account the different velocity ratios (u_e/u_∞) with and without roughness (this difference is 3%-4%). We have used

$$\frac{St_\infty}{St_{\infty o}} = \left(\frac{2St}{c_f}\right)\frac{C_{DF}}{C_{DF_o}}\,\frac{1}{0.90}\,\frac{(u_e/u_\infty)_{smooth}}{(u_e/u_\infty)_{rough}} \qquad (42)$$

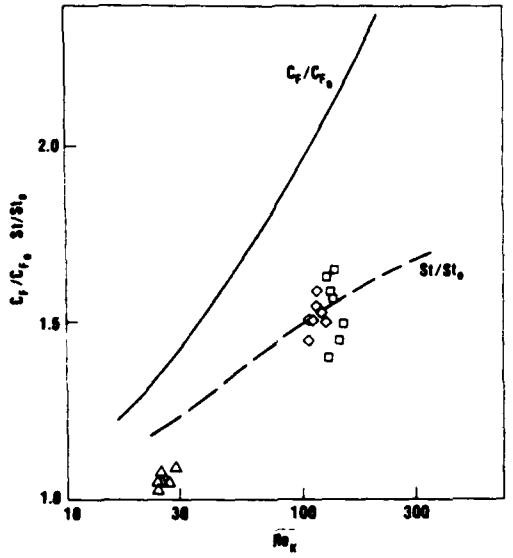

Fig. 22 Heat-transfer augmentation

V. Boundary-Layer Surveys

Pitor Pressure Surveys

Boundary-layer pitot pressure surveys were obtained to verify the establishment of a fully developed turbulent flow and to obtain quantitative values of the boundary-layer parameters for use in the interpretation of the skin-friction results. Boundary-layer survey measurements of this type are generally not available in short duration, high Mach number, high Reynolds number facilities. However, the NSWC Hypervelocity wind tunnel allows sufficient run time for a complete boundary-layer survey during a single run.

Four boundary-layer surveys are presented for discussion; two for the sharp cone and two for the blunted cone with a smooth and a rough surface represented for each. These profiles are illustrated in Figure 23 in the form of a pitot pressure to wall static pressure ratio versus distance from the wall. All profiles show a smooth interference-free flow. The sharp cone results are easily interpreted and boundary-layer thicknesses are easily identified because of the uniform flow outside the boundary layer. The blunt cone results cannot be interpreted in a similar manner because of the severe entropy gradients which are present in the flow. The inviscid trends for the blunt cone case agree with flowfield predictions, but because these effects are so strong, the separation of the boundary layer from the entropy swallowing effects is extremely difficult. As a result of this, the analysis will concentrate on the sharp cone results only.

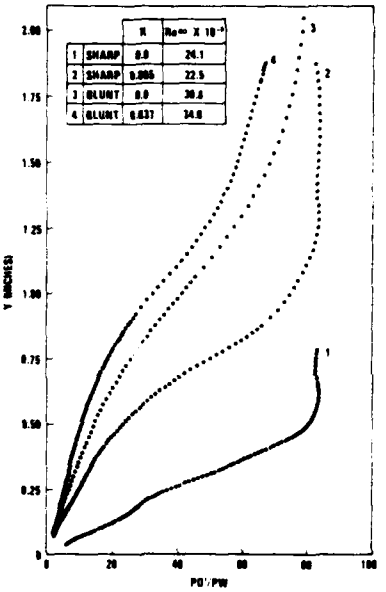

Fig. 23 Boundary-layer pitot pressure surveys

Sharp Cone Velocity Profiles

Velocity profiles for the two sharp cone runs were deduced from the pitot pressure profiles by assuming a constant static pressure through the boundary layer and by introducing a temperature-velocity relationship. These calculations were conducted in a manner as outlined in reference 18. The sharp cone velocity profiles with and without roughness are shown in Figure 24.

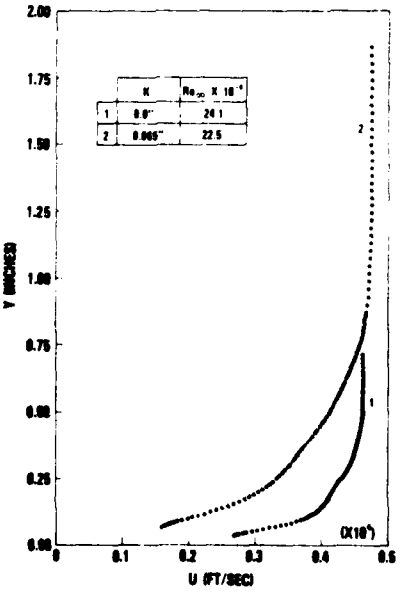

Fig. 24 Sharp cone velocity profiles with and without roughness

The smooth wall profile exhibits fully developed turbulent flow characteristics with a power-law exponent having a value of 7.9. The profile shows a smooth monotonic decrease in velocity from the free-stream to the wall.

The effects of the distributed surface roughness on the boundary-layer development can be observed in the second profile which is shown in Figure 24. The rough wall profile is much thicker than the smooth and its shape is represented by a power profile exponent with a value near 4. Boundary-layer parameters which are tabulated in Table 5 show a corresponding increase in all the boundary-layer integral thicknesses with roughness. Thicknesses are increased by a factor of 2.5 whereas the skin-friction augmentation for this case is 2. External flowfield conditions were nearly identical.

Table 5

A Comparison of Smooth and Rough Boundary-Layer Parameters on the Sharp Cone

Parameter	Smooth	Rough
k	0.0"	0.065"
Me	8.05	8.06
$u_e/\nu_e \times 10^{-6}$	7.75	6.80
Re_θ	8,595	19,861
T_w/T_{aw}	0.34	0.31
δ_e	0.455"	1.106"
δ^*	0.244"	0.615"
θ	0.0133"	0.035"
$c_f \times 10^3$	0.97	1.91
Re_k	0.0	163.

Law of the Wall Analysis

Semi-empirical analyses of turbulent boundary layers are often based on some form of the law-of-the-wall correlation. This analysis provides a means of linking velocity profile and skin-friction measurements and allows for a check of the individual results. The law-of-the-wall is defined most simply in terms of the dimensionless parameters

$$U^+ = \frac{U}{U_\tau} \quad \text{and} \quad Y^+ = \frac{YU_\tau}{\nu_w} \tag{43}$$

Within the turbulent boundary layer, three distinct regions are found to exist; the laminar sublayer, the logarithmic region and the wake or velocity-defect region. The general form of the relationships governing smooth-wall boundary layers is given by:

$$\begin{aligned} U^+ &= Y^+ && \text{for } Y^+ < 11 \\ U^+ &= \frac{1}{\kappa} \ln Y^+ + C && \text{for } Y^+ > 11 \end{aligned} \tag{44}$$

where κ is the Karman constant.

For compressible flows a transformation is utilized to account for the density variation through the boundary layer. The analysis of Van Driest is used in the form:

$$\overline{U^+} = \frac{U_e}{U_\tau A}\left\{\sin^{-1}\left[\frac{2A^2\frac{U}{U_e} - B}{\sqrt{B^2 + 4A^2}}\right] + \sin^{-1}\left[\frac{B}{\sqrt{B^2 + 4A^2}}\right]\right\} \tag{45}$$

where

$$A^2 = \frac{T_{aw} - T_e}{T_w} \qquad B = \frac{T_{aw} - T_w}{T_w}$$

(The law-of-the-wall analysis used herein is described in greater detail in reference 18.)

The effects of roughness on the law-of-the-wall equations has been shown to result solely in a shift in the intercept constant, c, in equation 44. Therefore, the same analysis has been used for both smooth and rough profiles. Law-of-the-wall plots are shown in Figure 25. Shown for comparison are the smooth wall relations given by equations 44 with the constants $\kappa = 0.4$ and $C = 5.1$.

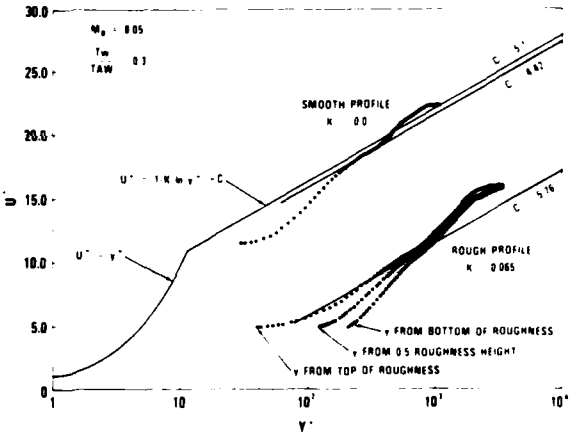

Fig. 25 Law-of-the-Wall velocity profiles

The smooth wall profile shows a general agreement with fully developed turbulent flow relations. A sublayer, logarithmic, and wake region of the profile can all be identified. The sublayer appears at Y^+ values which are relatively large, a trend which is suspected to be due to the cold wall condition and the compressible transformation which is used. However, the real test of the theory lies in the agreement in the logarithmic portion of the profile. The agreement in this region is very good with the value of the constant, C, obtained from a fit of the logarithmic region of the profile, having a value of 4.4 rather than the incompressible value of 5.1.

The rough wall profile is shown in Figure 25 using three different origins for the y coordinate. Since the pitot pressure measurements can only be made to the top of the sand-grain roughness elements, the profile was shifted to an effective origin which was located between the top and

bottom of the roughness elements. An effective origin of 0.5 times the roughness height was used. This value is consistent with other sand-grain results. The rough-wall profile looks similar to the smooth except that it is shifted to lower U^+ values. This trend is consistent with rough-wall results where the shift in the profile is directly related to the value of the roughness Reynolds number. The shift in the rough profile, derived from the difference between the rough and smooth values of C from logarithmic fits, is shown plotted in Figure 26 (from reference 18) as a function of the roughness Reynolds number. The agreement with other sand-grain data, both supersonic and subsonic, is very encouraging.

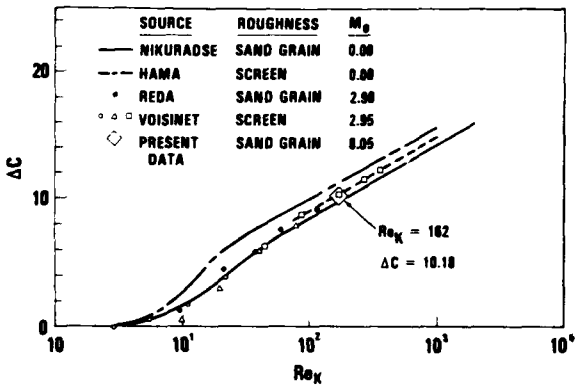

Fig. 26 Shift in the law-of-the-wall constant with roughness

As a result of this law-of-the-wall analysis, the profiles have been shown to be well developed and fully turbulent in nature. Since the value of the local skin-friction coefficient is an inherent part of this analysis, the validity of the skin-friction results is further enhanced.

VI. Conclusions

The skin-friction measurements with smooth walls agree quite well with analytical predictions. On the sharp cone the measurements are higher than the prediction by about 10% which is consistent with previous experiments using cold walls at high Mach numbers.

The heat-transfer measurements with smooth walls yield Reynolds analogy factors of 0.98 on the sharp cone and 0.90 on the blunted cone. The former is consistent with previous measurements under similar conditions. The latter constitutes new information, but it must be noted that the boundary layer was tripped using roughness on the nose of the model.

For all roughness heights the skin friction is larger than on the smooth wall. In the fully rough regime the measurements agree quite well with Fenter's[9] formula but are significantly higher than Young's[12] prediction.

For all roughness heights the heat transfer is larger than on the smooth wall. On both the sharp and blunted cone the Reynolds analogy factor $2St/c_f$ decreases with increasing values of the roughness Reynolds number, Re_k. When the measurements of Reynolds analogy factors are plotted for comparison with a formula due to Owen and Thomson,[15] the trend of the variation with Re_k is confirmed but different values of the numerical constant are found for the sharp and blunted cone and both are higher than those derived from measurements in incompressible flows.

The measured boundary-layer profiles show the expected increase in thickness and change of shape due to roughness. When the profiles obtained on the sharp cone are plotted in law-of-the-wall coordinates, a well-defined logarithmic region is obtained. Both the smooth-wall value of its intercept constant and the shift in its value due to roughness are consistent with results from previous measurements at lower Mach numbers.

References

1. Powars, C. A., "Surface Roughness Effects on Reentry Heating," Aerotherm Report TM-71-10, July 1971.

2. Keel, A. G., Jr., "Influence of Surface Roughness on Skin Friction and Heat Transfer for Compressible Turbulent Boundary Layers," AIAA Paper 77-178, January 1977.

3. Hill, J. A. F., Wardlaw, A. B., Jr., Pronchick, S. W., and Holmes, J. E., "Verification Tests in the Mach 14 Nozzle of the Hypervelocity Tunnel at NSWC (White Oak Lab)," AIAA Paper 77-150, January 1977.

4. Hill, J. A. F., "Stability and Pressure Measurements in the Naval Surface Weapons Center Hypervelocity Tunnel," ICIASF '77 Record, September 1977.

5. Jones, D. J., "Tables of Inviscid Supersonic Flow about Circular Cones at Incidence; γ = 1.4," AGARDOGRAPH 137, November 1969.

6. Morrison, A. M., Solomon, J. M., Ciment, M., and Ferguson, R. E., "Handbook of Inviscid Sphere-Cone Flowfields and Pressure Distributions," NSWC/WOL/TR 75-45, December 1975.

7. Walz, A., Boundary Layers of Flow and Temperature, M.I.T. Press, 1969.

8. Van Driest, E. R., "Problem of Aerodynamic Heating," Aeronautical Engineering Review, Vol. 15, No. 10, October 1956.

9. Fenter, F. W., "The Turbulent Boundary Layer on Uniformly Rough Surfaces at Supersonic Speeds," University of Texas, Defense Research Laboratory Report DRL-437, January 1960.

10. Hopkins, E. J. and Inouye, M., "An Evaluation of Theories for Predicting Turbulent Skin Friction and Heat Transfer on Flat Plates at Supersonic and Hypersonic Mach Numbers," AIAA Journal, Vol. 9, No. 6, June 1971.

11. Chien, K. Y., "Hypersonic, Turbulent, Cold-Wall, Skin-Friction and Heat-Transfer Measurements on an Axisymmetric Sharp Cone," NOLTR 73-108, June 1973.

12. Young, F. L., "Experimental Investigation of the Effects of Surface Roughness on Compressible Turbulent Boundary Layer Skin Friction and Heat Transfer," University of Texas, Defense Research Laboratory Report DRL-532, May 1965.

13. Goddard, F. E., Jr., "Effect of Uniformly Distributed Roughness on Turbulent Skin-Friction Drag at Supersonic Speeds," Journ. Aero. Sciences, Vol. 26, No. 1, January 1959.

14. Schlichting, H., Boundary-Layer Theory, McGraw-Hill, 4th Ed., 1960.

15. Owen, P. R. and Thomson, W. R., "Heat Transfer across Rough Surfaces," Journ. Fluid Mech., Vol. 15, Part 3, March 1963.

16. Hecht, A. M., Nestler, D. E., and Richbourg, D. H., "Application of a Three-Dimensional Viscous Computer Code to Reentry Vehicle Design," AIAA Paper 79-0306, January 1979.

17. Lyons, W. C., Jr. and Brown, H. S., The Drag of Slightly Blunted Slender Cones, NOLTR 68-3, January 1968. See also Wilson, R. E., "Laminar Boundary-Layer Growth on Slightly Blunted Cones at Hypersonic Speeds," Journal Spacecraft and Rockets, Vol. 2, No. 4, July-August 1965.

18. Voisinet, R. L. P., "Influence of Roughness and Blowing on Compressible Turbulent Boundary Layer Flow," NSWC TR 79-153, June 1979. Also, AIAA Paper No. 79-0003, January 1979.

Appendix

Roughness Characterization

The photomicrographs of the replicas of the rough surface were quantitatively characterized in three different ways:

(1) measuring successive peak-to-valley height excursions, Δy_i

(2) measuring successive peak-to-peak displacements along the surface, Δx_i

(3) measuring local surface height, y_i, at 200 equally spaced points along the surface.

For each nominal grain size, the length of the section analyzed was about 15 times the grain size.

From the measurements of peak-to-valley height we computed

$$\bar{K} = (1/n) \sum_1^n \Delta y_i$$

$$K_{RMS} = \left[1/n \sum_1^n (\Delta y_i)^2 \right]^{1/2}$$

From the measurements of peak-to-peak distance we computed

$$\bar{\lambda} = (1/n) \sum_1^n \Delta x_i$$

$$\lambda_{RMS} = \left[1/n \sum_1^n (\Delta x_i)^2 \right]^{1/2}$$

From the equally spaced measurements of surface height we computed

$$\bar{y} = (1/n) \sum_1^n y_i$$

$$y_{MDEV} = (1/n) \sum_1^n (y_i - \bar{y})$$

$$y_{STDEV} = \left[1/n \sum_1^n (y_i - \bar{y})^2 \right]^{1/2}$$

The results of these measurements and computations for the three nominal grain sizes used are given in the following table.

		k = 0.011"	k = 0.037"	k = 0.065"
$\bar{K}$	(in.)	.0083	.0199	.0285
K_{RMS}	(in.)	.0087	.0220	.0326
$\bar{\lambda}$	(in.)	.0231	.0534	.0891
λ_{RMS}	(in.)	.0250	.0586	.0817
y_{MDEV}	(in.)	.0041	.0090	.0146
y_{STDEV}	(in.)	.0049	.0113	.0170

NUMERICAL SIMULATION OF STEADY SUPERSONIC FLOW OVER AN OGIVE-CYLINDER-BOATTAIL BODY

by

W. B. Sturek*

and

L. B. Schiff**

Abstract

A recently reported Parabolized Navier-Stokes code has been employed to compute the supersonic flow field surrounding an ogive-cylinder-boattail body at incidence. The computations were performed for flow conditions where an extensive series of experimental surface pressure and turbulent boundary-layer profile measurements have been obtained. Comparison between the comp tional results and experimental measurements for angles of attack up to show excellent agreement. At angles greater than 6° discrepancies are observed which are tentatively attributed to three-dimensional turbulence modeling errors.

1. Introduction

The use of separate codes for computing the inviscid flow and turbulent boundary-layer development over yawed bodies of revolution has yielded some very good solutions for cone and ogive-cylinder shapes.[1] However, the authors have found that application of these techniques to bodies with boattailed afterbodies has not yielded satisfactory results even at small angle of attack ($\alpha < 4°$).

The PNS method appears to offer an attractive technique for computing flow over bodies with discontinuities in surface curvature (such as occurs at the junction between the cylinder and the boattail) since the inviscid flow and viscous layer are computed simultaneously. Further, the PNS method permits adequate flow-field resolution to be achieved with very reasonable computer costs. This report describes the results of detailed comparisons of PNS computational results to experimental measurements for surface pressures and turbulent boundary-layer profile characteristics of an ogive-cylinder-boattail body at Mach = 3 and angles of attack up to 10°. The PNS code used is that reported by Schiff and Steger.[2]

*U.S. Army Ballistic Research Laboratory/ARRADCOM, Aberdeen Proving Ground, Maryland 21005
**NASA Ames Research Center, Moffett Field, California

2. Overview of Numerical Scheme

A body-conforming ξ, η, ζ, coordinate system (Figure 1) is used which maps the body surface and outer boundary of the flow region in physical space onto coordinate surfaces of the computational space. This transformation simplifies the application of surface boundary conditions and permits the approximation of neglecting streamwise and circumferential viscous terms in high-Reynolds-number flow (see Ref. 2). The resulting steady thin-layer PNS equations can be written in strong conservation-law form in terms of nondimensional variables as

$$\frac{\partial \hat{E}_s}{\partial \xi} + \frac{\partial \hat{F}}{\partial \eta} + \frac{\partial \hat{G}}{\partial \zeta} = \frac{1}{\hat{Re}} \frac{\partial \hat{S}}{\partial \zeta} \tag{1}$$

where

$\xi = \xi(x)$ is the axial (marching) coordinate

$\eta = \eta(x,y,z)$ is the circumferential coordinate

$\zeta = \zeta(x,y,z)$ is the normal coordinate

For turbulent flow computations the coefficients of molecular viscosity and thermal conductivity are computed using the two-layer Cebeci-type eddy viscosity model reported by Baldwin and Lomax.[3] The various constants within the model were set to the values suggested in Ref. 3, with the exception that the turbulent Prandtl number Pr_t was set to 0.8.

Equation (1) is parabolic-like with respect to ξ, and can thus be marched downstream in the ξ direction from an initial data plane (subject to appropriate body and free-stream boundary conditions), under those conditions where the local flow is supersonic. By evaluating the pressure, p_s, which appears in the $\hat{E}_s$ flux vector using the subsonic layer approximation, Eq. (1) can be kept stable for marching for subsonic points as well. If p_s is set equal to the local pressure for supersonic points, and is evaluated from $\partial p_s/\partial \zeta = 0$ (Figure 2) for points within the subsonic viscous layer adjacent to a wall, Eq. (1) can be stably marched for all flows where $U > 0$; that is, for flows without streamwise reversal (see Ref. 2 for associated stability analysis).

The numerical algorithm used to advance Eq. (1) downstream in ξ is a noniterative, implicit, approximately factored finite-difference scheme, analogous to the one developed by Beam and Warming[4] for the solution of the unsteady Navier-Stokes equations. The algorithm is conservative, of second-order accuracy in the marching direction, and can be either second- or fourth-order accurate in the cross-flow plane. The algorithm has been

applied to compute a variety of laminar and turbulent viscous flows and the results have been in excellent agreement with those obtained from more costly time-dependent computations. Full details of the PNS assumption, the associated stability analysis and of the derivation of the algorithm and application of boundary conditions are found in Ref. 2.

In general the initial data plane for the marching method must be supplied from an axiliary computation. However, when treating the flow over conical or pointed bodies, the marching code can be used to generate its own initial data plane. As outlined in Ref. 2, a conical grid is selected and the flow variables are initially set to free-stream values. The solution is marched downstream from an initial station and, after each step, the solution is scaled to place it back at the original station. When no change in the flow variables occur with further marching, a conical solution has been generated.

3. Results

Model Geometry and Experimental Measurements

The dimensions of the ogive-cylinder-boattail model used for this study are shown in Figure 3. The model is 6 calibers long with a 1-caliber, 7° boattail, and closely resembles a modern low-drag artillery projectile.

A number of wind-tunnel experiments have been conducted for this model geometry in order to obtain data for comparison to numerical computations. The data acquired include measurements of wall static pressure, turbulent boundary-layer velocity profiles, surface skin friction, aerodynamic forces, and flow visualization. The test conditions were M = 3 with a tunnel total pressure of 0.298 MPa and tunnel total temperature of 308°K. These conditions produced a free-stream Reynolds number of 7.3×10^6 based on the model length. The boundary layer was tripped near the tip of the model to produce a reliable turbulent flow. All tests were performed using SSWT Number One at the U.S. Army Ballistic Research Laboratory. This facility, which is no longer in operation, was a continuous flow tunnel with a flexible plate nozzle. The test section size was 330 × 380mm (13 × 15 in.).

Comparison Between Computation and Experiment

Computations were performed for a body having the same geometric shape as the experimental model, and for flow conditions duplicating that of the experiment. The tip of the ogive was replaced with a cone tangent to the ogive at x = 15.2mm (see Figure 3). Turbulent conical solutions were generated at that station and used as initial data for the PNS marching code. The present computations used a grid consisting of 36 circumferential points ($\Delta\phi = 10°$) and 50 points radially between the body and the outer boudnary. Computation time on the CDC 7600 computer is 2.3 sec/step with this size grid.

Surface Pressure. The PNS computations are compared to experimental measurements, and to inviscid flow computations made using codes based on MacCormack's predictor-corrector technique (Figures 4-6). Longitudinal surface pressure distributions along the windward and leeward rays are shown in Figure 4 for an angle of attack of 6.3°. The PNS computations exhibit better agreement with experiment in the vicinity of the discontinuities in streamwise surface curvature at the ogive-cylinder and cylinder-boattail junctions than the inviscid computations.

Examples of comparisons of circumferential surface pressure distributions are shown for $\alpha = 6.3°$ in Figure 5 and for $\alpha = 10.4°$ in Figure 6 at two longitudinal stations; one on the cylinder portion of the model near the boattail, the second, midway on the boattail. At $\alpha = 6.3°$ (Figure 5a) the comparison on the cylinder indicates excellent agreement between the PNS computation and experiment and the appearance of a systematic discrepancy between the inviscid computation and experiment for $100° \leqslant \phi \leqslant 150°$. This trend is accentuated for flow on the boattail (Figure 5b). The comparison shown in Figure 6 for $\alpha = 10.4°$ indicates further development of crossflow separation for flow over the boattail and cylinder. The abrupt rise in experimental surface pressure at $\phi \cong 90°$ indicates the location of the crossflow separation point. The inviscid computation predicts a crossflow shock at $\phi \cong 140°$ which is not present in the experimental data. At this incidence the PNS computation is in only fair agreement with the experiment and suggests an upper limit of applicability of the present computational technique of $\alpha = 6°$ for this class of body shapes.

Streamwise Velocity Profiles. A sensitive test of the accuracy of the PNS computational technique applied to this flow is the comparison of measured and computed boundary-layer velocity profiles. Such comparisons are shown in Figures 7 and 8 for two longitudinal stations; station A on the cylinder near the boattail, and station B on the boattail. Each figure shows the velocity profiles for a particular longitudinal station for circumferential stations ranging from the windward to leeward ray in 30° increments. The nondimensional streamwise velocity compounts, u, are plotted versus physical distance y measured radially from the body surface in millimeters, rather than against normalized y/δ. This method of plotting prevents scaling differences between the computation and experiment from giving a false comparison.

Comparison for $\alpha = 6.3°$ are shown in Figures 7 and 8. At this angle of attack the windward side measured and computed profiles are in excellent agreement. However, the discrepancy between the profiles at $\phi = 150P$ is substantial, particularly at the boattail station (Figure 8). Note that this discrepancy is less strongly reflected in the surface pressure distribution at the corresponding station (Figure 5b).

Plots of longitudinal velocity profiles for 10° increments in circumferential position are shown in Figures 9 and 10 for a longitudinal position on the boattail at x = 1.06. Results for $\alpha = 6.3°$ are shown in Figure 9 and $\alpha = 10.4°$ in Figure 10. The significant development of vortical flow from $\alpha = 6.3°$ to $\alpha = 10.4°$ is suggested by the development of the velocity defect in the profiles for $\phi = 120°$ to $\phi = 170°$.

Magnus Force. The PNS technique is particularly attractive for computations of the Magnus effect since, as seen in Figures 4-6, the accuracy for the circumferential and longitudinal distributions of wall pressure are much improved over that obtained using inviscid techniques. This improvement was most significant for the flow over the boattail.

Recently, the PNS code has been used to obtain turbulent viscous results for a spinning model in order to evaluate the Magnus effect. Results obtained to date are limited to M = 3, $\alpha = 2°$, Ω = 20000 RPM for ogive-cylinder and ogive-cylinder-boattail models. The initial results obtained are shown in Figures 11 and 12 where PNS computations are compared to BL-INV computations and experimental data. The total side force consists of contributions of longitudinal velocity wall shear, circumferential velocity wall shear, centrifugal pressure gradient and wall pressure components. The side force is plotted as a function of axial position on the model. The data point at Z/D = 6 is the wind tunnel force measurement. The PNS and BL-INV computations are in fair agreement with the force measurement for the ogive-cylinder model in Figure 11; however, the PNS computation is in significantly better agreement with the experimental point than the BL-INV result for the boattailed model in Figure 12.

5. Concluding Remarks

This paper has described the results of a numerical-computation study in which the parabolized Navier-Stokes marching code recently developed by Schiff and Steger has been exercised for a 6-caliber, ogive-cylinder-boattail shape at incidence. Extensive, detailed comparisons to experimental data at M = 3, $\alpha \leq 10.4°$ have been performed to evaluate the accuracy and stability of the numerical technique.

Comparisons have been made between PNS computations and experiment for surface pressures, velocity profiles and Magnus force. The improved accuracy achieved using the PNS code compared to the BL-INVISCID technique was shown to be of great significance for the flow over the boattail.

REFERENCES

1. Sturek, W. B., et al., "Computations of Magnus Effects for a Yawed, Spinning Body of Revolution," AIAA Journal, Vol. 16, No. 7, July 1978, pp. 687-692.

2. Schiff, L. B., and Steger, J. L., Numerical Simulation of Steady Supersonic Viscous Flow," AIAA Paper 79-0130, 17th Aerospace Sciences Meeting, January 1979.

3. Baldwin, B. S., and Lomax, H., "Thin Layer Approximation and Algebraic Model for Separated Turbulent Flows," AIAA Paper 78-257, 16th Aerospace Sciences Meeting, January 1978.

4. Beam, R., and Warming, R. F., "An Implicit Factored Scheme for the Compressible Navier-Stokes Equations," AIAA Journal, Vol. 16, No. 4, April 1978, pp. 393-402.

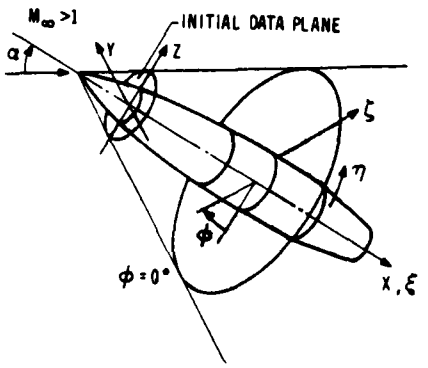

Figure 1. Coordinates and Notation

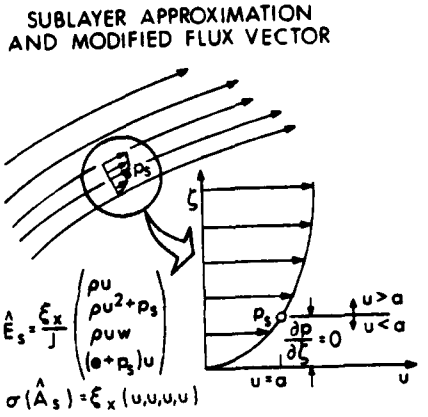

Figure 2. Subsonic Sublayer Approximation

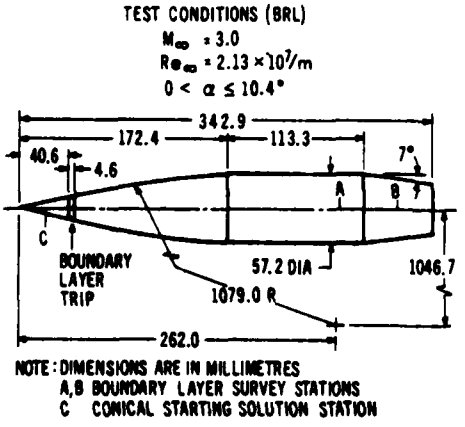

Figure 3. Model Configuration

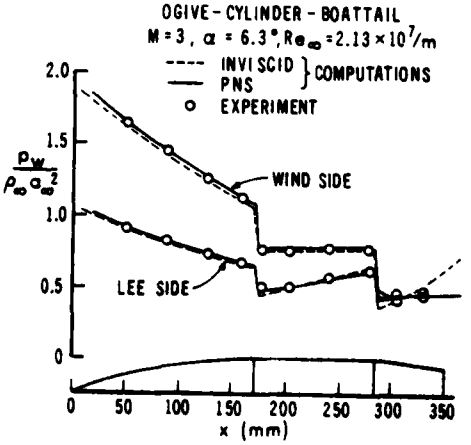

Figure 4. Axial Surface Pressure Distribution; M = 3.0, $\alpha = 6.3°$, $Re_\infty = 2.13 \times 10^6/m$

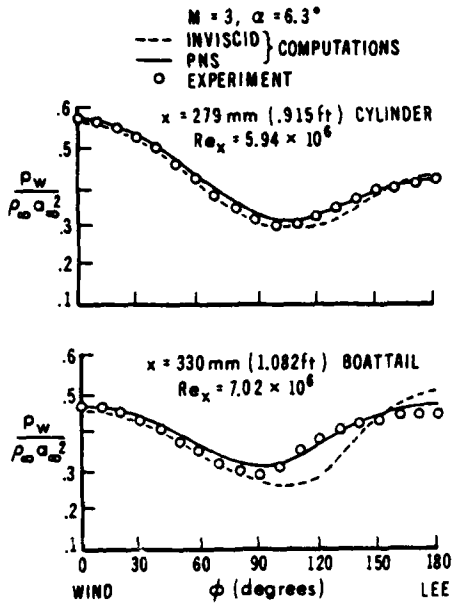

Figure 5. Circumferential Surface Pressure Distribution; M = 3.0, $\alpha = 6.3°$, $Re_\infty = 2.13 \times 10^6/m$

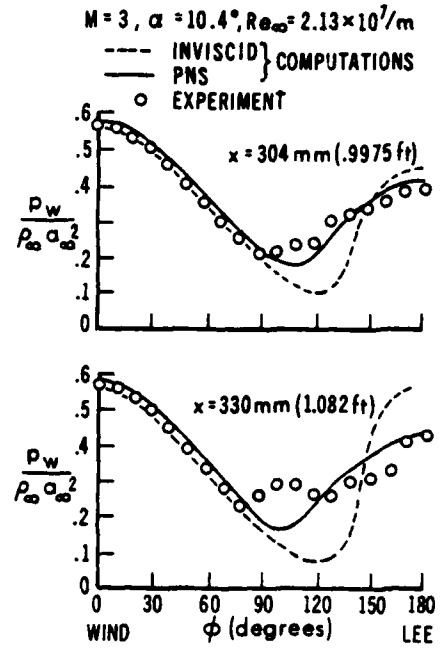

Figure 6. Circumferential Surface Pressure Distribution; M = 3.0, $\alpha = 10.4°$, $Re_\infty = 2.13 \times 10^6/m$

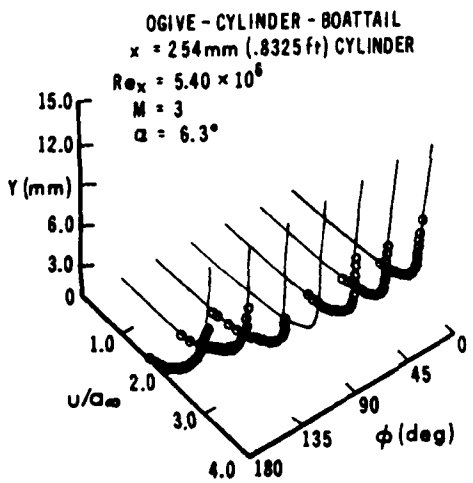

Figure 7. Boundary-Layer Velocity Profiles; M = 3.0, $\alpha = 6.3°$, $Re_\infty = 2.13 \times 10^6/m$, x = 254mm, Cylinder

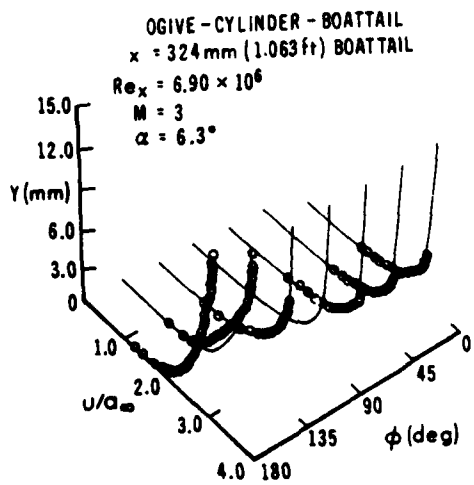

Figure 8. Boundary-Layer Velocity Profiles; M = 3.0, $\alpha = 6.3°$, $Re_\infty = 2.13 \times 10^6/m$, x = 324mm, Boattail

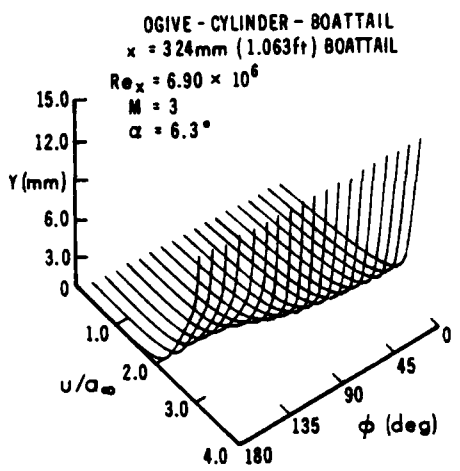

Figure 9. Boundary-Layer Velocity Profiles; M = 3.0, $\alpha = 6.3°$, $Re_\infty = 2.13 \times 10^6$/m, x = 324mm, Boattail

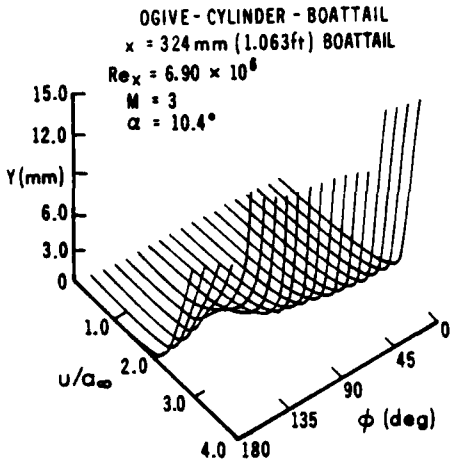

Figure 10. Boundary-Layer Velocity Profiles; M = 3.0, $\alpha = 10.4°$, $Re_\infty = 2.13 \times 10^6$/m, x = 324mm, Boattail

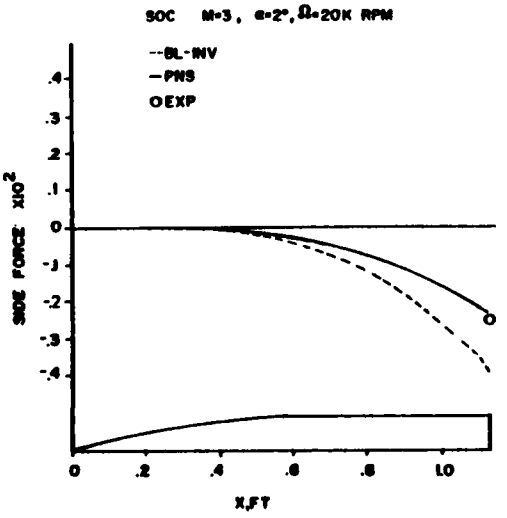

Figure 11. Longitudinal Distribution of Magnus Force; M = 3, $\alpha = 2°$, Ω = 20,000 RPM, Ogive-Cylinder Body

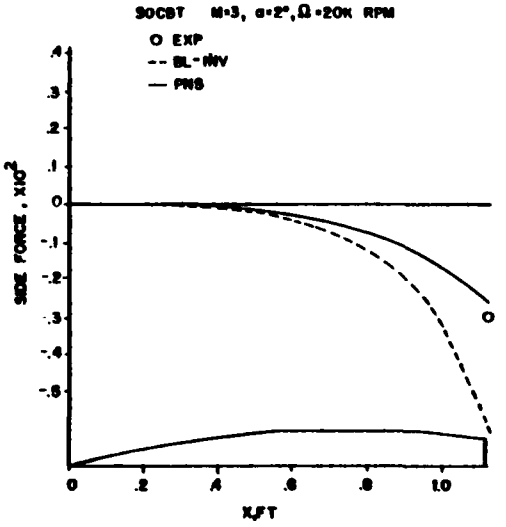

Figure 12. Longitudinal Distribution of Magnus Force; M = 3, $\alpha = 2°$, Ω = 20,000 RPM, Ogive-Cylinder-Boattail Body

A THEORETICAL AND EXPERIMENTAL INVESTIGATION OF A TRANSONIC PROJECTILE FLOW FIELD

by

C. J. Nietubicz*, J. E. Danberg** and G. R. Inger***

Abstract

The transonic flow field about a projectile configuration with a turbulent boundary layer has been studied. A joint theoretical and experimental effort is presented which compares the results of a generalized axisymmetric Navier-Stokes code with a compposite boundary layer interaction solution method and both against experimental data. The longitudinal pressure distribution and velocity profiles at three axial stations are presented for M = .94, and .97 at $\alpha = 0$. Comparison of the boundary layer characteristics which include velocity profiles, displacement thickness and skin friction are presented.

1. Introduction

The aerodynamic characteristics of standard artillery shell from subsonic to supersonic speeds is of major concern in the design of new shell or modifications to existing ones. The possibility that a given shape may have to operate throughout a range of Mach numbers requires a detailed understanding of the flow fields associated with each. Modern computational techniques are now being applied to projectile shapes and the ability to compute the aerodynamics of shell for a wide range of Mach numbers and Reynolds numbers is becoming a reality. Significant accomplishments have been achieved in the supersonic regime. Static and Magnus force coefficients have been computed for standard projectile configurations and experimental data is generally available which shows good comparisons. Transonic flow, however, presents a new complexity for computational analysis. The formation of shock waves, imbedded in the flow field near the surface discontinuities, produces a severe change of the aerodynamic coefficients such as drag and pitching moments. For example, the drag for a projectile shape has been found to change by as much as 100% through a Mach number range of .95 to .97. A change of this magnitude in the aerodynamics makes it essential to be able to understand and compute the features of the flow field which contribute to this effect.

*U.S. Army Ballistic Research Laboratory/ARRADCOM, Aberdeen Proving Ground, Maryland 21005
**University of Delaware, Newark, Delaware 19711
***Virginia Polytechnic Institute and State University, Blacksburg, Virginia 24061

A concentrated theoretical and experimental research program has been ongoing at BRL in order to develop the predictive capabilities required for determining projectile aerodynamics. Supersonic computations using combined inviscid flow field and boundary layer techniques have been developed by Sturek[1], et al., for cone-cylinder and ogive-cylinder configurations. Recent results have been obtained in supersonic flow over a typical boattailed projectile by Schiff and Sturek[2] using modern computational techniques for solving the thin-layer Navier-Stokes equations.

Inviscid transonic computational results have been obtained by Reklis[3], et al., for a secant-ogive-cylinder-boattail shape. This work was then extended to include the viscous boundary layer and modeling of the shock boundary layer interaction regions. A comparison of the composite solution technique with experimental data was presented at the 1979 DEA meeting[4]. The results showed generally good agreement between the theoretical calculation and experiment.

The availability of a new computational technique for solving the thin-layer generalized axisymmetric Navier-Stokes equations and additional experimental data has resulted in a continued analysis of this transonic flow field problem. A discussion of the two computational methods and available experimental data will follow.

2. Generalized Axisymmetric Technique

The Navier-Stokes code which has been used in this study is the η-Invariant or Generalized Axisymmetric version[5]. This code solves the thin-layer Navier-Stokes equations which are cast in strong conservation law form. The equation formulation allows for arbitrary body geometries and are solved using an implicit approximate factorization finite difference scheme. The "thin-layer" approximation[6-7] used here requires that all body surfaces be mapped onto ζ = constant planes and that Re >> 1. Essentially, all the viscous terms in the coordinate directions (here taken as ξ and η) along the body surface are neglected while terms in the ζ or the near normal direction to the body are retained. This approximation is used because, due to computer speed and storage limitations, fine grid spacing can only be provided in one coordinate direction (usually taken as the near normal direction) and the grid spacing available in the other two directions is usually too coarse to resolve the viscous terms.

The thin-layer generalized-axisymmetric Navier-Stokes equations are obtained from the three-dimensional equations by making use of two restrictions: (1) all body geometries are of an axisymmetric type; (2) the state variables and the contravarient velocities do not vary in the circumferential direction. Given the above assumptions the transformed generalized thin-layer Navier-Stokes equations in non-dimensional and strong conservation law form are written as[5]

$$\delta_\tau \hat{q} + \delta_\xi \hat{E} + \delta_\zeta \hat{G} + \hat{H} = Re^{-1}\, \delta_\zeta \hat{S} \qquad (1)$$

where general coordinate transformations

$\xi = \xi(x,y,z,t)$ - longitudinal coordinate

$\zeta = \zeta(x,y,z,t)$ - near Normal coordinate

$\tau = t$ - time

are used.

The vector $\hat{q}$ contains the dependent variables density, ρ, velocity components, u, v and w, and total energy, e. The vectors $\hat{E}$, $\hat{G}$, and $\hat{H}$ contain terms arising from the continuity equation, three momentum equations and energy equation. All viscous terms are contained in the vector $\hat{S}$. The turbulence modeling used is the two layer Cebeci type eddy viscosity model as reported by Baldwin and Lomax[7]

Equation (1) contains only two spatial derivatives but does retain all three momentum equations thus allowing a degree of generality over the standard axisymmetric equations. In particular, the circumferential velocity is not assumed to be zero allowing computations for spinning projectiles or swirl flow to be accomplished.

The numberical algorithm used for equation (1) is a fully implicit, approximately factored finite difference scheme as analyzed by Beam and Warming[8]. The details of the numerical method, algorithm and boundary conditions can be found in Reference 5.

3. Composite Inviscid Flow-Boundary Layer-Shock Interaction Model

Inviscid Flow Region

Inviscid flow calculations were made by methods developed by Reklis, Sturek, and Bailey[3]. The inviscid flow was determined by a numerical solution of the transonic small disturbance equation for the velocity perturbation potential ϕ given by,

$$[(1-M^2) - M^2\ (\gamma+1)\phi_x]\phi_{xx} + \phi_{rr} + \phi_r/r + \phi_{\theta\theta}/r^2 = 0 \qquad (2)$$

where M is the free stream Mach number and γ is the ratio of specific heats for air taken as 1.4 and where the equation is written in cylindrical coordinates. This equation is second order nonlinear partial differential equation of mixed elliptic hyperbolic type. The type of the equation changes to match the physical differences between regions of subsonic and supersonic flow.

Equation (2) can be made to adequately predict the flow about a projectile shape such as that studied here. Certain regions of the flow require some "modeling" however. The wake has been treated in these computations as a solid part of the body slightly smaller in diameter than the base and faired smoothly into the boattail. In order to develop a "conservative" algorithm to solve this equation special care must be taken at transitions between subsonic and supersonic flow. Non-conservative forms of the algorithm, however, often give bette

agreement with experiment because the breakdown in conservation seems to reproduce the effect of the shock boundary layer interaction; the algorithm used here was therefore a non-conservative one for the purposes of constructing a first version of the composite flow model. Consistently, first order boundary condition relations have been used with 120 streamwise grid points along the body length.

Boundary Layer

Boundary layer flow computations were made by methods developed for laminar cone flows by Dwyer and Sanders[9] and extended to more general turbulent flows by Sturek[10], et al. In this technique the boundary layer equations stating principles of conservation of mass, momentum, and energy are solved with an implicit finite difference technique. The solution begins with the development of an approximate boundary layer profile at the tip. The solution is then marched over the body from nose to tail. At each step along the way a two point boundary value system is solved with conditions given at the body surface and at the boundary layer edge. The possibility of body spin is accounted for and care is taken in setting up the difference to maintain stability. Turbulence is accounted for by use of an algebraic type, eddy viscosity, turbulent shear stress model with Van Driest damping. This model has proved suitable for use in cases of supersonic flow and is carried over directly to the transonic regime.

Local Shock-Boundary Layer Interaction Regions

For non-separating interactions (local Mach number roughly less than 1.3 in the Reynolds number range $Re_L \sim 10^6$, - 10^8 a non-asymptotic triple-deck disturbance flow model of the weak normal shock-turbulent interaction is employed. This model has proven very successful in treating a variety of problems involving turbulent boundary layer response to strong adverse pressure gradients and is supported by a large body of transonic and supersonic interaction data[10], its use therefore provides a sound treatment of both the local and downstream effects while avoiding the use of crude empirical "viscous wedge" models whose fundamental dependence on the incoming boundary layer properties is unknown.

The flow model (Figure 1) consists of an inviscid region surrounding a shock discontinuity and an underlying thin viscous disturbance sublayer that contains the upstream influence and skin friction perturbation. An approximate analytic solution is achieved by assuming small linearized-disturbances ahead of and behind the nonlinear shock jump, with a simplified treatment of the detailed shock structure within the boundary layer down to the sonic level. The resulting equations can be solved by operational methods to obtain the interactive pressure rise, displacement thickness growth, and local skin friction solution both upstream and downstream of the shock foot.

The required inputs are the inviscid shock location (about which the interactive solution is "centered"), the corresponding streamwise component of the inviscid flow number and the shape factor from the turbulent boundary layer code. The interactive solution has been inserted as a local module at each shock location to produce a general combined inviscid-boundary layer-interaction solution code. Since the shock location is essentially fixed by the sharp

corners on the body and changes only very slightly due to viscous effects, the shock strength and position are taken from the inviscid calculation. Our interaction solution then allows us to account not only for the rapid displacement thickness growth in each interaction, but also for the attendant local interactive distortion of both the skin friction and profile shape. Moreover, the influence of these changes on the subsequent turbulent boundary layer development downstream is included by appropriate post-interaction reinitialization of the turbulent boundary layer calculation using Walz's composite "Law of the Wall-Law of the Wake" turbulent profile model.

4. Experiment

The experimental data to be described here are an extension of the data reported at the 1979 DEA meeting[4] and at the AIAA Fluid and Plasma Dynamics Conference[11] including new tests at additional survey stations and at Mach Numbers of 0.97 as well as the previous reported data at 0.94.

The wind tunnel measurements were performed in the NASA Langley Research Center 8 foot Transonic Pressure Tunnel (TPT). The tunnel was operated at one atmosphere supply pressure (101.3 kPa) and at a supply temperature of 49.2°C which resulted in a Reynolds number of 13×10^6 1/M. The TPT facility is of slotted wall construction to minimize reflected wave interference effects which were monitored using tunnel wall static pressure taps. The model was sting mounted from the Langley support sector and roll mechanism which allowed measurements at angle of attack and at various roll positions.

The data described here is limited to the zero angle of attack and roll case. Other experiments were performed at 4° angle of attack and at various angles around the model. Preliminary tests for pressure distributions and boundary surveys were carried out on a nonconical afterbody model. The results from these will be reported in the near future.

Model

The tests were made using a model of a typical modern projectile as illustrated in Figure 2. The configuration is an idealization of an artillery projectile consisting of an ogive nose, cylindrical mid-section and 7° conical afterbody or boattail of half a caliber. Turbulent flow was assured by using a sand-grain roughness strip 5 cm from the nose. The 20.2 cm diameter model caused 0.69% blockage of the tunnel which was found acceptable for the measurements carried-out. The afterbody was instrumented with 14 static pressure taps located so as to define the flow conditions in the vicinity of the boattail corner.

Instrumentation

The boundary surveys were made employing the same technique described in 1979. The probing mechanism is shown in Figure 3. Some new probe support arms were designed to increase the traversing distance of the probe tip to approximately 30mm. This was found to be necessary on the lee-side of the model during the previous tests. Separate probe supports were used to reach

the various stations on the model. New arms were constructed so that all wall pressure tap stations between 3 and 9 (see Figure 3) could be investigated. The forward position was expected to be free of the effects of the expansion at the corner of the boattail. Thus the measurement at this station provides a test of our ability to predict the downstream effects of the boundary layer-shock wave interaction which occurs in the region of the ogive-cylinder junction. The most rearward station only 1.27 cm from the model base also provides information about the effects of the afterbody shock.

The probe travel is controlled by an electric motor within the model driving a connecting micrometer lead screw. The control allowed positioning of the probe within ±.03mm. The position of the probe arm was detected using a linear variable differential transducer which was statically calibrated with an optical cathetometer which provided positioning accuracy of ±0.1mm. The probe tip was electrically insulated so that wall contact provides a reference position for calibration in the tunnel.

A major concern in using total head probes at transonic speeds is the possibility of flow interference; thus every attempt was made to reduce exposure of the probing mechanism to the main flow field although some disruption of the base flow is unavoidable. The supersonic region downstream of the boattail corner effectively prevents the upstream propagation of the disturbances caused by the mechanism in wake. This has been verified by viewing a Schlieren picture of the base flow, at Mach No. 0.97 with the station 3 probe installed, where in only weak disturbances can be seen. No significant upstream effects on the wall static pressures were observed when the probe was in the supersonic region behind the boattail corner. Some upstream propagation from the probe was observed when the probe was in the subsonic flow upstream of the corner but the disturbance was only significant with the probe tip within one millimeter of the model surface. In all cases the wall static pressure measured without the probe mechanism installed was used to reduce the pitot probe pressures to Mach numbers.

5. Results

Theoretical and experimental comparisons have been made for surface pressure, velocity profiles, displacement thickness and skin friction. All results shown are for $\alpha = 0°$, $Re = 13 \times 10^6/m$ and $M = .94$ or $M = .97$.

The surface pressure coefficient computed using the Navier-Stokes code is shown in Figure 4 compared to the experimental data. The comparison is seen to be excellent in the vicinity of the expansion but falls off on the boattail. The computational grid contained only 60 points on the body and was severely stretched in the longitudinal direction after the boattail corner. The discrepancy in the comparison on the boattail is attributed to this poor grid resolution.

Velocity profiles are shown in Figure 5 for three axial stations. Stations $x/L = .924$ and .967 are from previous test results while the data at $x/L = .870$ has been obtained from the experiment described in this paper. The Navier-Stokes solution (solid line), composite solution (dotted line) and experimental values compare very well at $x/L = .870$ and .924, however as in the previous report the

results at x/L = .967 show a discrepancy. Shifting the computed free stream velocity indicates that the computed profile shape is consistent with the experimental data. The difference is directly related to a higher observed static pressure in the experiment than obtained in the theoretical calculations.

A calculation of the displacement thickness was made at all stations where velocity profiles were available. A comparison of the theoretical computations and experimental determination of displacement thickness is shown in Figure 6. The composite solution shows a jump in displacment thickness at the shock location and then a gradual increase until the expansion of the corner is felt which produces a decrease in the displacement thickness. The Navier-Stokes results on the other hand show a continuous increase in displacement thickness over the cylinder portion of the model. The experimental results are shown to compare relatively well with the computed values, however, the inability to accurately and consistently determine the boundary layer edge position and velocity in transonic flow, makes any comparison suspect. Additionally the solution of Navier-Stokes type equations does not rely on the computation of a displacement surface for improved flow field prediction.

Similar comparisons have been made for M = .97 in order to determine the applicability of these techniques to Mach number variation. The computed and experimental surface pressure coefficients are again shown in Figure 7 to compare favorably. The velocity profiles at three axial stations for M = .97 are shown in Figure 8. The comparison in this case is shown to be good for all stations. Station x/L = .967 is clearly in the supersonic region at M = .97 as evidenced by schlicren pictures. Disturbances from the probe mechanism are therefore expected to be small in this case. However, for the M = .94 case the supersonic pocket is smaller and interference caused by interaction of the probe and the boattail shock wave is more likely.

A usually severe test of the computational capability is the accurate prediction of the skin friction coefficient. Although, there is no experimental data for comparison, Figure 9 shows the results for both numerical schemes. The expansion about both corners is shown to produce a rapid increase in the skin friction followed by a rapid decrease after the shock. The relative agreement between these two methods, especially in the presence of multiple shocks, is considered to be quite good.

Conclusion

The transonic flow field about a secant-ogive-cylinder-boattailed model has been computed using a generalized axisymmetric Navier-Stokes code and a composite shock boundary layer interaction technique. The computations have been compared to the experimental data at M = .94 and .97 for α = 0. The results show generally good agreement considering the complex double-shocked environment such as exists about a boattailed projectile shape. Difficulties are apparent in the definition and computation of the displacement thickness since the boundary layer edge is difficult to identify.

Additional experimental data is required to fully access the validity of the computational techniques; however, the comparison of the two techniques with the available experimental data shows the correct trends. Navier-Stokes computations have been obtained for a projectile shape at angle of attack and comparisons of these results with the available experimental data and the composite solution technique will be reported in the future.

Acknowledgement

The U.S. Army Research Office supported the measurements reported here under grant DAAG29-78-G0057. The authors wish to thank R. Tschirschitz and E. Krueger for the model design and help furnished during the testing.

REFERENCES

1. W. B. Sturek, et al., "Computations of Magnus Effects for a Yawed, Spinning Body of Revolution", AIAA Journal, Vol. 16, No. 7, July 1978, pp. 687-692.

2. L. B. Schiff and W. B. Sturek, "Numerical Simulation of Steady Supersonic Flow Over Cone Ogive-Cylinder-Boattail Body", AIAA Paper No. 80-0066, January 14-16, 1980.

3. R. P. Reklis, W. B. Sturek and F. L. Bailey, "Computation of Transonic Flow Past Projectiles at Angle of Attack", U.S. Army ARRADCOM Technical Report, ARBRL-TR-02139, February 1979.

4. J. E. Danberg, R. P. Reklis, and G. R. Inger, "Pressure Distributions and Boundary Layer Profiles on a Yawed Projectile at Transonic Speeds", 1979 DEA Meeting, Meersburg, West Germany.

5. C. J. Nietubicz, T. H. Pulliam and J. L. Steger, "Numerical Solution of the Azimuthal-Invariant Thin-Layer Navier-Stokes Equations", AIAA Paper No. 79-0010, January 1979.

6. T. H. Pulliam and J. L. Steger, "On Implicit Finite-Difference Simulations of Three-Dimensional Flow", AIAA Paper No. 78-10, January 1978.

7. B. S. Baldwin and H. Lomax, "Thin Layer Approximation and Algebraic Model for Separated Turbulent Flows", AIAA Paper No. 78-257, January 1978.

8. R. Beam and R. F. Warming, "An Implicit Factored Scheme for the Compressible Navier-Stokes Equations", AIAA Paper No. 77-645, June 1977.

9. H. A. Dwyer and B. R. Sanders, "Magnus Forces on Spinning Supersonic Cones. Part I. The Boundary Layer", AIAA Journal 14, April 1976, p. 498.

10. G. R. Inger, "Transonic Shock-Turbulent Boundary Layer Interaction with Suction or Blowing", AIAA Paper No. 79-0005, New Orleans, Louisiana, January 1979.

11. R. P. Reklis, J. E. Danberg and G. R. Inger, "Boundary Layer Flows on Transonic Projectiles", Paper 79-1551, AIAA 12th Fluid and Plasma Dynamics Conference, Williamsburg, Virginia, 1979.

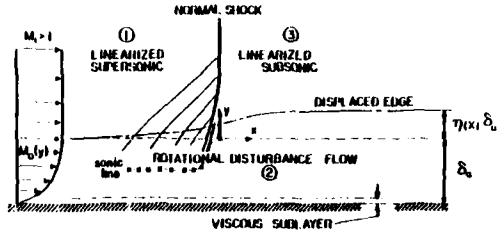

Figure 1. Triple Deck Model of Shock Boundary Layer Interaction

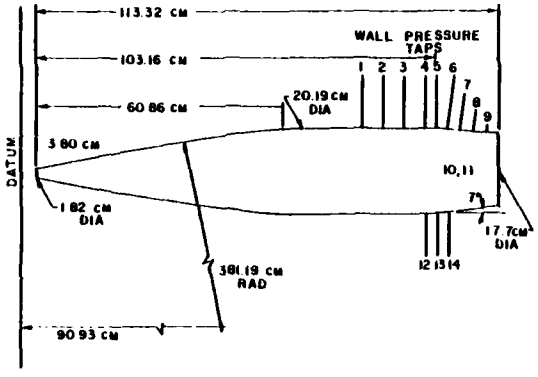

Figure 2. Boattailed Model Configuration

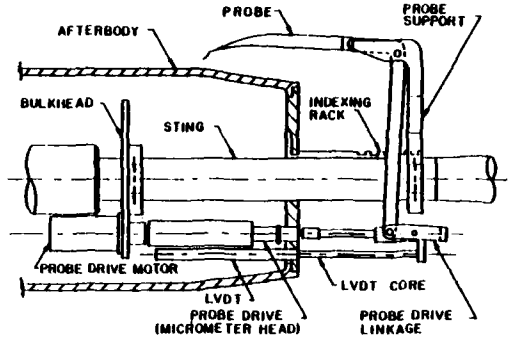

Figure 3. Afterbody of Wind Tunnel Model Showing Probe Support Mechanism

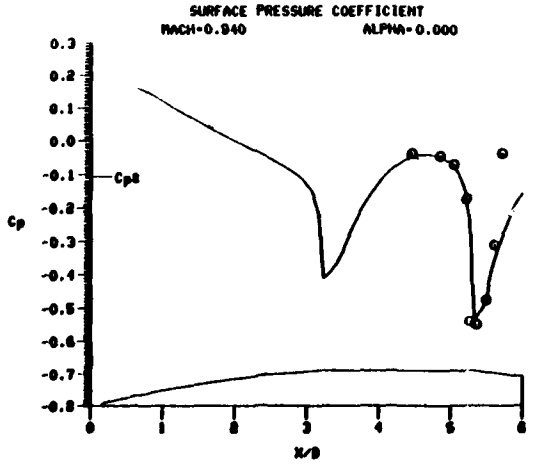

Figure 4. Theoretical and Experimental Comparison of Surface Pressure Coefficient, M = .94

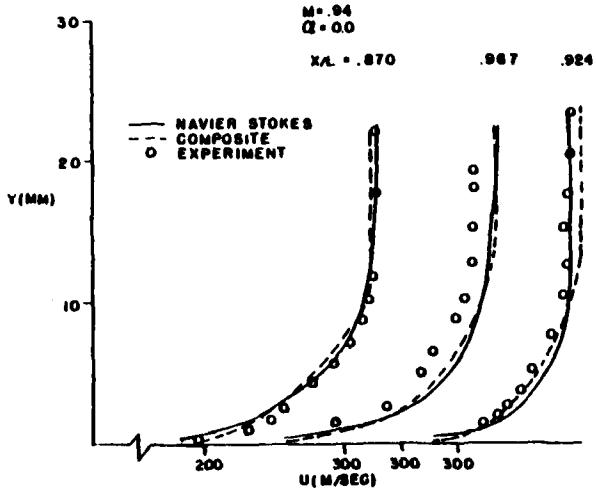

Figure 5. Velocity Profiles at Three Axial Stations, M = .94

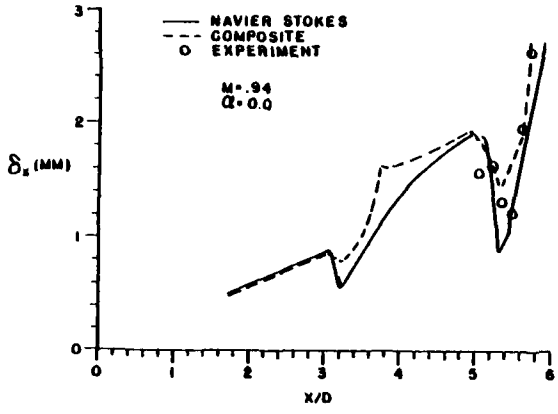

Figure 6. Comparison of Displacement Thickness: Experiment and Theory, M = .94

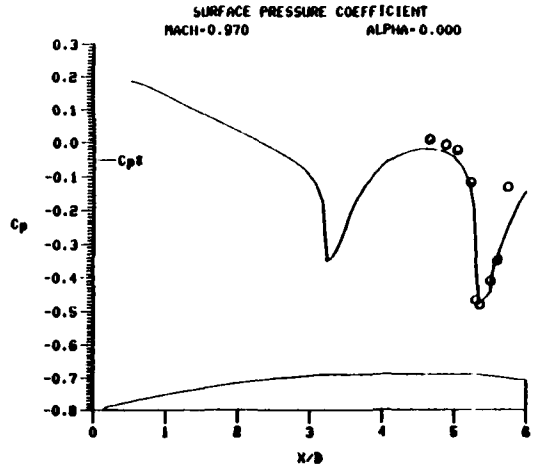

Figure 7. Theoretical and Experimental Comparison of Surface Pressure Coefficient, M = .94

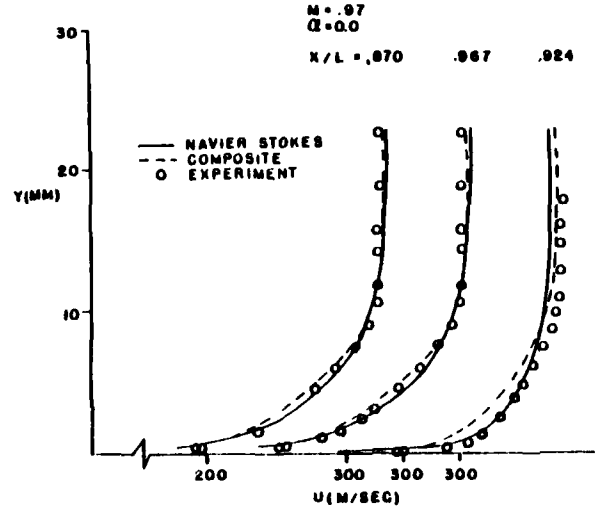

Figure 8. Velocity Profiles at Three Axial Stations, M = .97

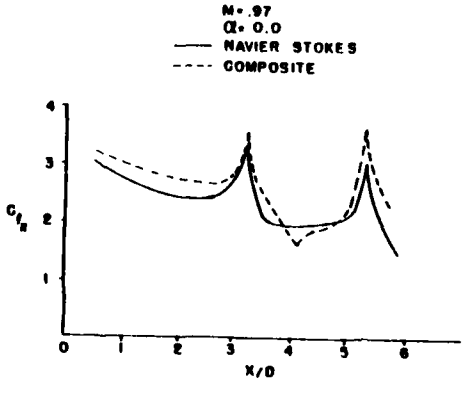

Figure 9. Comparison of Skin Friction Coefficient Between Navier-Stokes and Composite Solution Techniques, M = .97

Three-Dimensional Boundary Layer Calculations for Fuselages

by

J. D. McLean and J. L. Randall

Boeing Commercial Airplane Company

Seattle, Washington 98124

Introduction

A boundary layer grid generation program developed originally for swept wings [1,2] has been modified to generate surface fitted, curvilinear, orthogonal grids for a broad class of fuselage, hull, and nacelle shapes. Outer boundary conditions (velocity vectors) for subsequent three-dimensional boundary layer calculations are interpolated onto the grid from the results of a panel-type potential flow [3] calculation. Provided the flow remains attached, such a calculation yields reasonably accurate results for the entire flow field except over regions of the body where the simple boundary layer approximation breaks down, such as near the tail or near wing-body junctions. In engineering applications the results are useful for predicting:

1) The onset of separation of either the free vortex type or the closed bubble type, and

2) The skin friction field for use in evaluating effects of surface roughness or excrescences.

A future goal of this work is to calculate flows with free vortex separation by coupling the grid generation and boundary layer methods with the Boeing LEV code [4], which was develped originally for delta wing flows with leading edge separation and which is capable of solving for the geometry of the shed vortex sheets.

Grid Generation and Boundary Layer Solution Procedures

For the present analysis, the body shape and the resulting flow field are assumed to have at least a single plane of symmetry. The body shape is defined by columns of geometry data points (panel control points) from the potential flow program, as shown in part (a) of Figure 1. The first step in the construction of the grid is the numerical fitting of longitudinal boundary layer coordinate lines (lines of constant boundary layer coordinate x), as shown in part (b) of Figure 1, which need not generally pass through the potential flow data points. The potential flow velocity vectors defined at the potential flow data points are converted to components parallel and orthogonal to these longitudinal coordinate lines. The orthogonal coordinate lines (lines of constant boundary layer coordinate z) are then constructed numerically segment-by-segment, and, finally, the converted potential flow velocity components are interpolated to the boundary layer grid points. While no procedure of this type can guarantee single-valued grids for general body shapes, the present procedure has yielded usable grids for all of the simple, practical body shapes tried so far.

These grids, by their own nature and because of limitations inherent in the boundary layer solution procedure, must exclude a portion of the body surface that includes the front stagnation point. For most aeronautical

applications this is not a serious drawback because the boundary layer at the nose is usually very thin, and the solution farther aft on the body is insensitive to the initial conditions used at the upstream grid boundary (i.e. the first circumferential grid line). In some special applications, such as flows in which the location of boundary layer transition has a strong effect on the entire flow field, a more precise treatment of the nose region would be required.

The marching scheme used in calculating the boundary layer is illustrated in Figure 2. First, the plane-of-symmetry boundary layer equations are used to calculate the flow along one of the lines of symmetry, and the resulting solution is extrapolated to the next longitudinal coordinate line. The line of symmetry solution then serves as initial conditions for a three-dimensional calculation in which the marching along each circumfercial coordinate line is as shown in part (b) of Figure 2, and the circumferential coordinate lines are taken in sequence, from front to rear.

The finite difference scheme is similar to the one currently used for wing calculations at Boeing [1,2]. When the velocity component u (the circumferential component in this application) is non-negative at all points on a given column, 3-point upwind differences are used in both directions, as shown in part (a) of Figure 3. If the solution is unavailable at the adjacent upwind station in the x direction (e.g. if that station is part of a "forbidden zone," as described below), the alternate form shown on the right in part (a), Figure 3, is used. When u is negative at all points on the column the form shown in part (b), Figure 3, is used, where differencing in the x direction takes place effectively on the previous x-coordinate line. When the u profile crosses over (i.e. when u components of both signs appear on the

same column), the x direction differencing is done in a manner similar to that used in the well-known zig-zag scheme [5], as illustrated in part (c) of Figure 3.

All of the differencing options illustrated in Figure 3 are conditionally stable, i.e. each form is stable only for velocity directions within a particular range consistent with the zones of influence and dependence of the differential equations. If at any point on a particular column the solution produces a velocity direction that is within the stable range of none of the available difference options, the column is flagged as part of a "forbidden zone" such that the column cannot be used in differencing operations at adjacent columns. A forbidden zone can propagate through the solution domain in a manner that depends on the mesh aspect ratio and on the velocity field that emerges as the solution is computed. Under favorable conditions the boundary of a forbidden zone can nearly coincide with any of the various types of three-dimensional separation lines, thus providing a prediction of the separation line location. But a forbidden zone can also be merely a symptom of the failure to specify initial conditions at all of the boundary locations required by a particular velocity field or of a poor choice of mesh aspect ratio for computing negative or cross-over u profiles. The solution near the boundary of a forbidden zone must therefore be examined for the presence of flow field features usually associated with separation, such as the appearance of a large normal velocity component in the outer part of the boundary layer and/or the strong convergence of streamlines near the surface.

Because the finite difference scheme can, conditionally at least, handle both positive and negative u, it is possible to calculate most flows by marching in either direction, i.e., from the windward side to the leeward side or vice versa. This has been done in several cases as a check on the

correctness and accuracy of the program. As an example, results calculatedboth ways for the laminar flow over a 4:1 spheroid at $\alpha = 20^{\circ}$ are shown in Figure 4. For most practical purposes the results are the same, especially with regard to global features such as the separation pattern. The lower limb of the forbidden zone boundary represents an open, free vortex separation line toward the front, joining part of a closed separation bubble in the rear, forming a pattern consistent with that observed experimentally by Han and Patel [6] and computed numerically by Wang [7], Cebeci and Khattab [8], and others. The upper limb of the forbidden zone boundary (toward the leeward symmetry line) is an artifact of the calculation and does not represent a separation line.

In the wing calculations reported earlier [1,2], the special difference formulas for cross-over u profiles (part (c), Figure 3) were not used. When a cross-over u profile appeared, either the positive u (part (a), Figure 3) formulas or negative u (part (b), Figure 3) formulas were chosen on a point-by-point basis, in a manner similar to the scheme reported by Dwyer [9]. This scheme worked well for wing calculations and for many fuselage calculations, provided that only a moderately sized portion of the body surface exhibited cross-over u profiles. For one particular fuselage calculation (Boeing 727-200 fuselage at 0° angle of attack), however, where cross-over u profiles appeared over nearly the entire body surface, the scheme became unstable, and the circumferential distribution of δ^* took on a saw-toothed appearance. This behavior was alleviated by the addition to the program of the special difference formulas for cross-over u profiles (part (c), Figure 3). All of the results discussed in the next section were calculated by the new program, though for all cases except the Boeing 727-200 fuselage at 0° angle of attack there was very little difference between the results of the new program and those of the old program.

Typical Results

Plots illustrating some of the fuselage-type boundary layer flows calculated with the programs thus far are shown in Figures 5-15. In all cases the outer flow boundary conditions were obtained from potential flow calculations for the bare body shape; no displacement effects or vortex shedding effects were included even though separations of various types were predicted in most cases. In all of the calculations for non-zero angles of attack, circumferential marching in the boundary layer solution procedure was carried out from the windward side to the leeward side.

The plots are of two basic types: Streamline plots and contour plots of constant displacement thickness δ^*. In the streamline plots, three-dimensional curves were constructed along the body surface parallel to the appropriate velocity directions. In the plots labeled "Outer-Flow Streamlines" the curves are parallel to the velocity vectors from the potential flow solution, and in the plots labeled "Surface Streamlines" the curves are parallel to the limiting directions of the boundary layer velocity vectors at the surface and are thus parallel to the surface shear stress.

The surface streamline plots provide a convenient way of visualizing the development of separation patterns, especially when studying a series of angles of attack. However, caution should be used in interpreting some features of the streamline patterns. As an example, the surface streamlines for the spheroid at an angle of attack of 5° (Figure 5), have a non-uniformity of spacing through the mid-section where a wide gap appears between the streamlines that emanate from the keel line and those that emanate from the lower part of the nose. This non-uniformity is an artifact of the program

logic; i.e. the streamlines emanating from the nose were drawn at initially wider spacing than those emanating from the keel line, and a careful inspection shows that, when the initial non-uniformity in spacing is taken into account, there is nothing really distinctive happening in this region. At the higher angle of attack of 10° (Figure 6), however, the convergence of streamlines near the top of the body is not the result of any initial non-uniformity and is indicative of an approach to 3-D separation.

The displacement thickness δ^* shown in the contour plots was obtained as a solution to the three-dimensional δ^* equation as described in References 1 and 2. The large blank areas in both the streamline plots and the contour plots coincide with forbidden zones in the solution domain. All of the plots were produced by interactive plotting programs that did not always maintain undistorted scaling; in some cases the vertical scale has been stretched relative to the horizontal scale.

Laminar Boundary Layer on a Spheroid

Figures 5-9 show results calculated for a laminar boundary layer on a 4:1 spheroid at a length Reynolds number of 1.6×10^5 at angles of attack of 0°, 5°, 10°, 15°, and 20°. In all of the non-zero angle of attack cases the lower part of the forbidden zone boundary coincides approximately with a separation line in the flow field. At $\alpha = 5°$ a closed bubble-type separation is indicated, while at $\alpha = 10°$ and higher, an open, free vortex separation line extends increasingly far forward with increasing α. In Figure 9 the δ^* contours for $\alpha = 0°$ display considerable unevenness toward the aft end of the body. The wiggles were found not to be due to any instability in the boundary layer calculations, but were instead found to be in step with the potential

flow paneling. It is not yet known whether the wiggles were caused by non-uniformities in the potential flow velocity vectors or by non-uniformities in the boundary layer grid caused by the use of potential flow geometry data in the construction of the grid. In spite of the non-uniformities of the δ^* contours, the predicted spearation line is quite straight.

Boeing 727-200 Airplane Fuselage

Figures 10-14 show results calculated for a turbulent boundary layer on a Boeing 727-200 airplane fuselage shape without a wing or tail at a length Reynolds number of 2.59×10^8 at angles of attack of 0°, 5°, 10°, and 20°. As in the case of the spheroid, the lower boundary of the forbidden zone approximates a separation line in the flow field, and the progression of the predicted separation pattern with angle of attack can be clearly seen. At α = 5° and 10° the surface streamlines show considerable evidence of convergence and the beginning of a free-vortex separation somewhat forward of the beginning of the forbidden zone. At α = 20° the free vortex separation begins not far aft of the nose. (It should be noted that these program test results are not indicative of the actual flow pattern about the complete airplane, since the wing and its wake - which were omitted - would change the potential flow field considerably.) In Figure 14 it is interesting to note that the δ^* contours over an extensive portion of the middle of the body are aligned longitudinally, as they would be in an infinite yawed clinder flow, even at an angle of attack as low as 5°. At α = 0°, as in the case of the spheroid, the δ^* contours display non-uniformities that appear to be related to the potential flow paneling.

SSPA 720 Ship Hull Model

Figure 15 shows isometric views of the predicted surface streamlines for the SSPA 720 ship hull wind tunnel model examined experimentally by Larsson [10] in turbulent flow at a length Reynolds number of 5 x 10^6, which is one of the required test cases for the Workshop on Ship Hull Boundary Layers to be held in June, 1980 at the Swedish SSPA. Calculations were begun at X/L = .2 using initial conditions supplied by the organizers of the Workshop and ended at X/L = .9, just forward of the rudder post. The flow near the stern displays two interesting regions of flow convergence and possible vortex formation: One near the waterline and another that appears to be related to the sharply rounded corner of the forward hull shape.

Further Developments

In the near future further airplane fuselage boundary layer calculations will be made for a case that includes a wing in the potential flow calculations so that the fuselage will be subjected to a realistic induced velocity field.

A longer term goal is the calculation of viscous-inviscid interaction effects in flows with free-vortex separation of the type illustrated in Figure 16. An iterative procedure is envisioned in which the outer inviscid flow, including the shed vortex sheets, would be calculated by a potential flow panel method capable of solving for the geometry of the vortex sheets, and the boundary layer flow would be calculated by the present boundary layer program. A consistent solution would be sought in which the free vortex separation line prediced by the boundary layer program would agree with the vortex sheet origin assumed in the potential flow calculation. As pointed out

by Smith [11], the convergence to this final solution would have to be carefully controled so that the boundary layer separation predicted at any iteration in the procedure remains to windward of the assumed potential flow vortex.

References

1. McLean, J. D., "Three-Dimensional Boundary Layer Calculations for Swept Wings," AIAA Paper No. 77-3, January 1977.

2. McLean, J. D. and Randall, J. L. Computer Program to Calculate Three-Dimensional Boundary Layer Flows over Wings with Wall Mass Transfer," NASA CR-3123, May 1979.

3. Moran, J., Tinoco, E. N., and Johnson, F. T., "User's Manual Subsonic/Supersonic Advanced Panel Pilot Code," NASA CR-152047, February 1978.

4. Johnson, F. T., Lu, P., Tinoco, E. N., and Epton, M. A., "An Improved Panel Method for the Solution of Three-Dimensional Leading Edge Vortex Flow," NASA CR 159173, to be released.

5. Krause, E., Hirschel, E. H., and Bothmann, T., "Die numerische Integration der Bewegungsgleichungen dreidimensionaler laminarer kompressibler Grenzschichten," Fachtagung Aerodynamik, Berlin 1968, DGLR-Fachbuchreihe, Bd. 3 (Braunschweig 1969), pp. 03-01 - 03-49.

6. Han, T., and Patel, V. C., "Flow Separation on a Spheroid at Incidence," J. Fluid Mech., Vol. 92, Part 4, pp. 643-657, 1979.

7. Wang, K. C., Boundary Layer over a Blunt Body at High Incidence with an Open-Type of Separation," Proc. R. Soc. Lond, A. 340, pp. 33-55, 1974.

8. Cebeci, T. and Khattab, A. A., "Calculation of Three-Dimensional Laminar and Turbulent Boundary Layers with Circumferential Flow Reversal on Bodies of Revolution at Incidence," Viscous and Interacting Flow Field Effects, 4th US-FRG Meeting, Part II, BMVg-FBWT 79-31, 1979.

9. Dwyer, H. A., "A Physically Optimum Difference Scheme for Three-Dimensional Boundary Layers," Proceedings, Fourth International Conference on Numerical Methods in Fluid Dynamics, Boulder, Colorado, June 1974.

10. Larsson, L. "Boundary Layers of Ships, Part III: An Experimental Investigation of the Turbulent Boundary Layer on a Ship Model," SSPA Allman Rapport Nr 46, 1974.

11. Smith, J.H.B., "Inviscid Fluid Models, Based on Rolled-Up Vortex Sheets, For Three-Dimensional Separation at High Reynolds Number," Agard Lecture Series No. 94, Three-Dimensional and Unsteady Separation at High Reynolds Numbers, AGARD-LS-94, 1978.

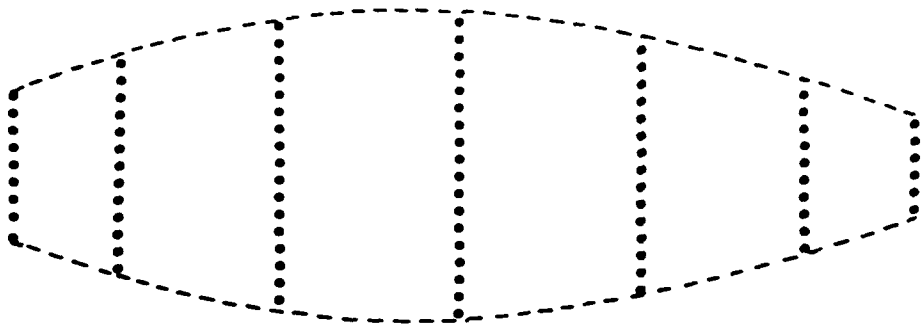

a) BODY SHAPE DEFINED BY GEOMETRY DATA FROM POTENTIAL FLOW PROGRAM

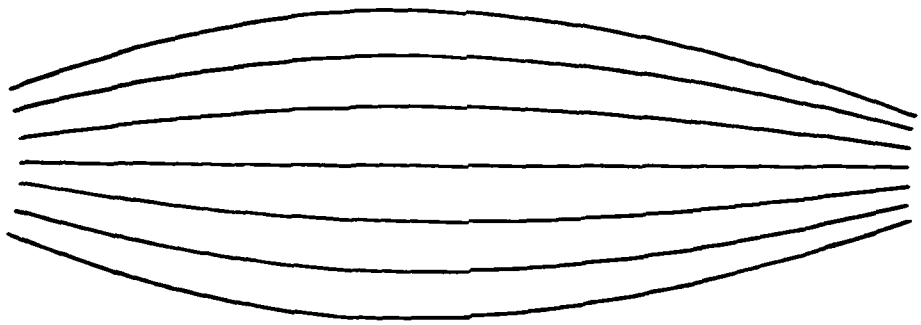

b) LONGITUDINAL CURVILINEAR COORDINATE LINES DEFINED NUMERICALLY

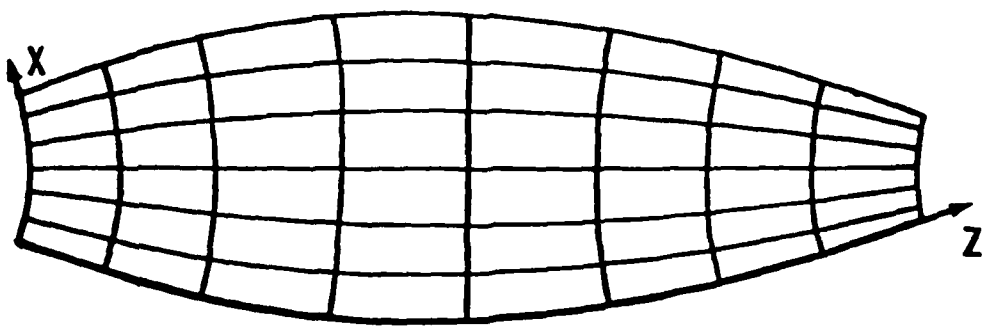

c) ORTHOGONAL COORDINATE LINES CONSTRUCTED NUMERICALLY SEGMENT-BY-SEGMENT

FIGURE 1 CONSTRUCTION OF ORTHOGONAL, CURVILINEAR BOUNDARY LAYER COORDINATE GRID

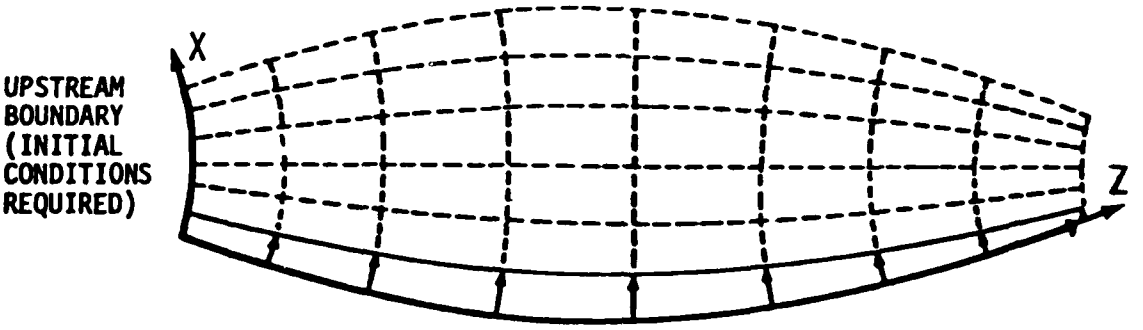

a) CARRY OUT ATTACHMENT LINE ANALYSIS ON ONE LINE OF SYMMETRY AND EXTRAPOLATE SOLUTION TO NEXT LONGITUDINAL COORDINATE LINE.

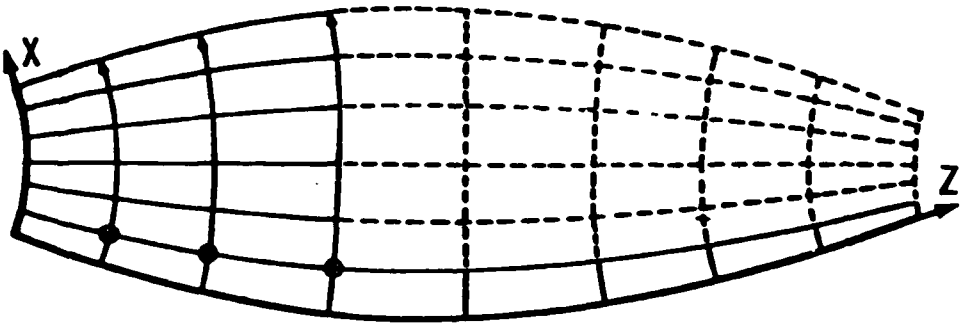

b) MARCH CIRCUMFERENTIALLY IN SECOND RUN, USING PROFILES FROM PART (a) AS INITIAL CONDITIONS.

FIGURE 2 MARCHING SEQUENCE FOR BODY BOUNDARY LAYER CALCULATION

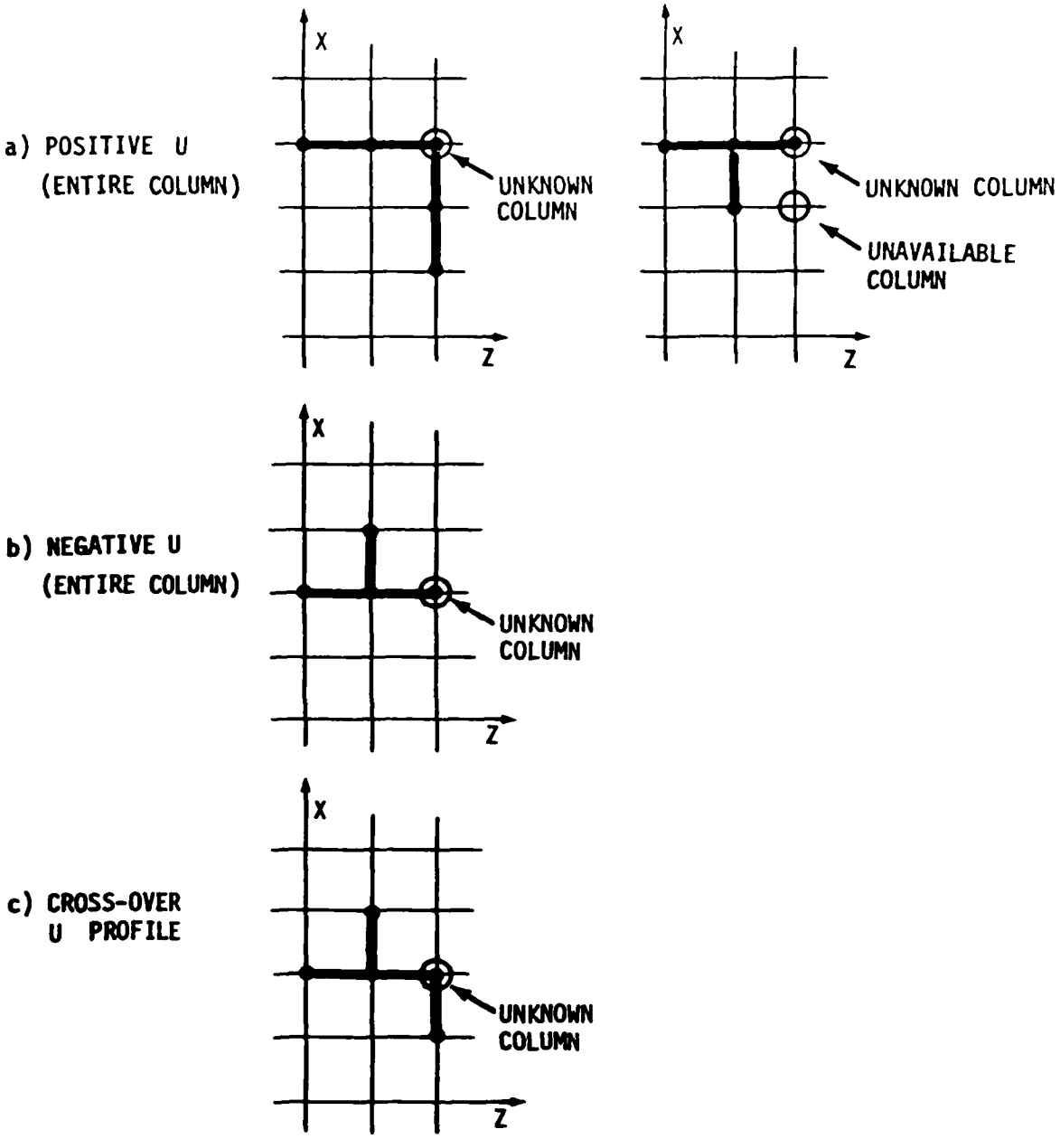

FIGURE 3 GRID POINTS REFERENCED BY FINITE DIFFERENCE FORMULAS

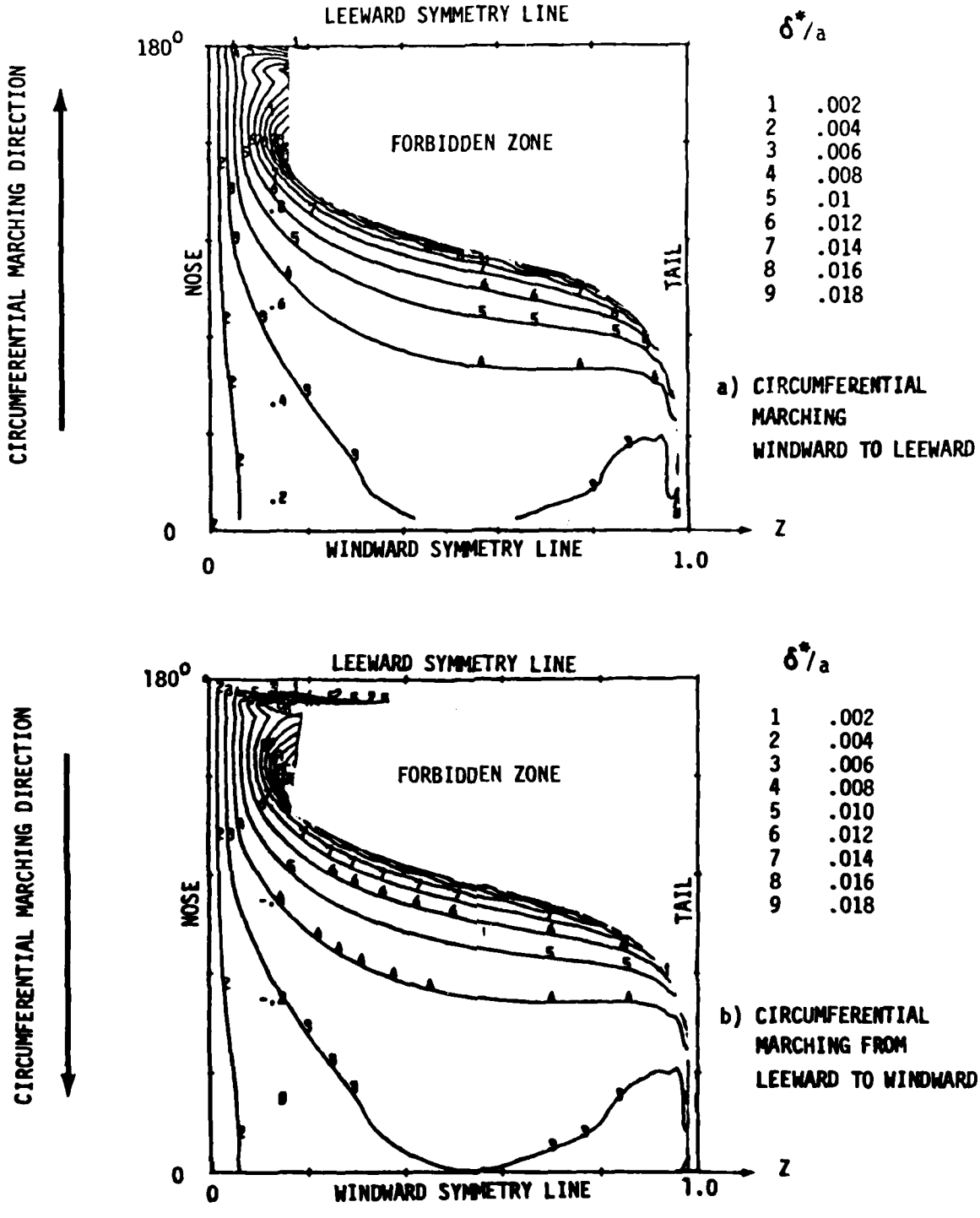

FIGURE 4 CONSTANT δ^* CONTOURS COMPUTED FOR 4.1 SPHEROID AT $\delta = 20^\circ$ WITH CONVENTIONAL AND REVERSE MARCHING DIRECTIONS

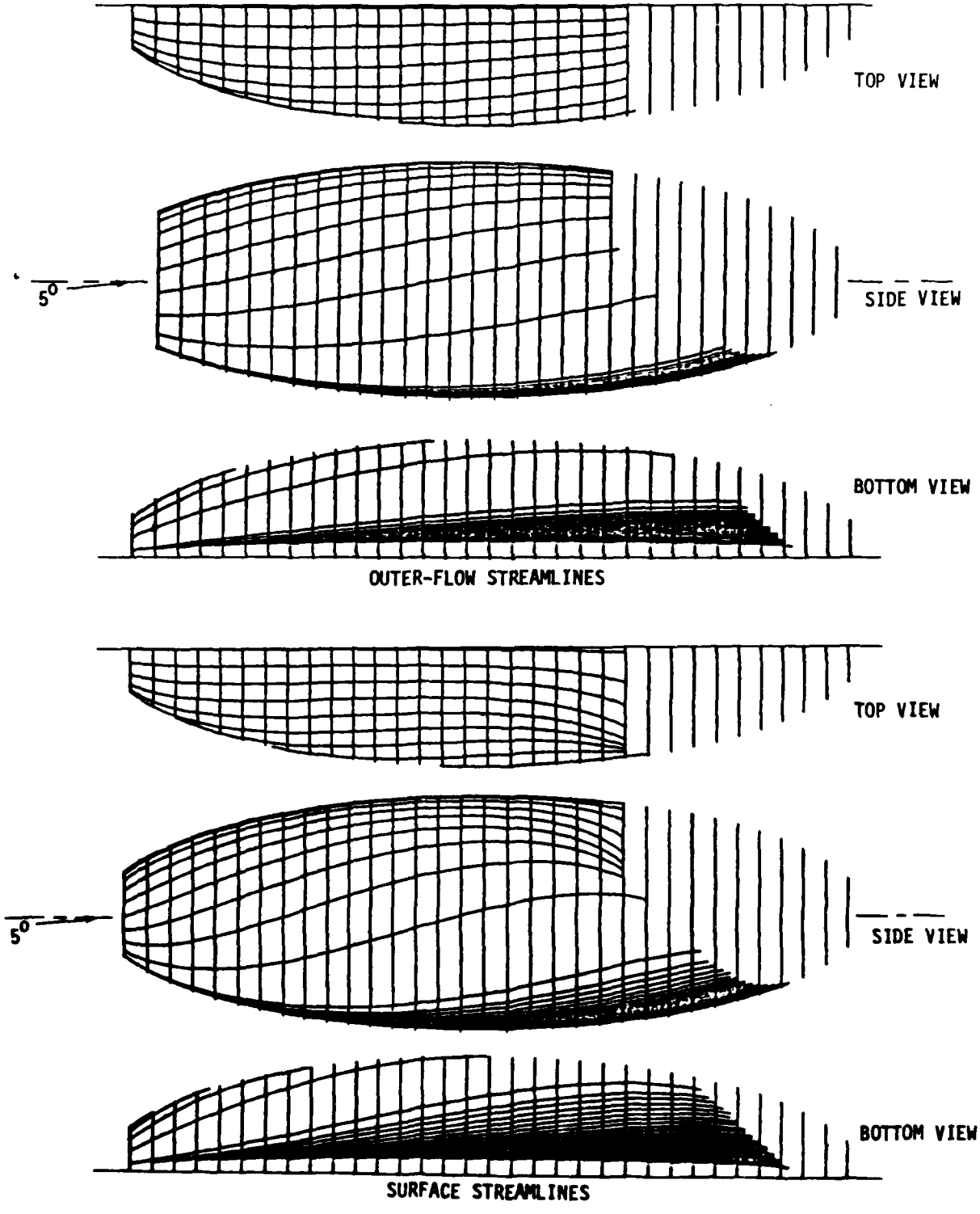

FIGURE 5 PREDICTED STREAMLINES FOR LAMINAR FLOW OVER 4.1 SPHEROID, $\alpha = 5^{\circ}$

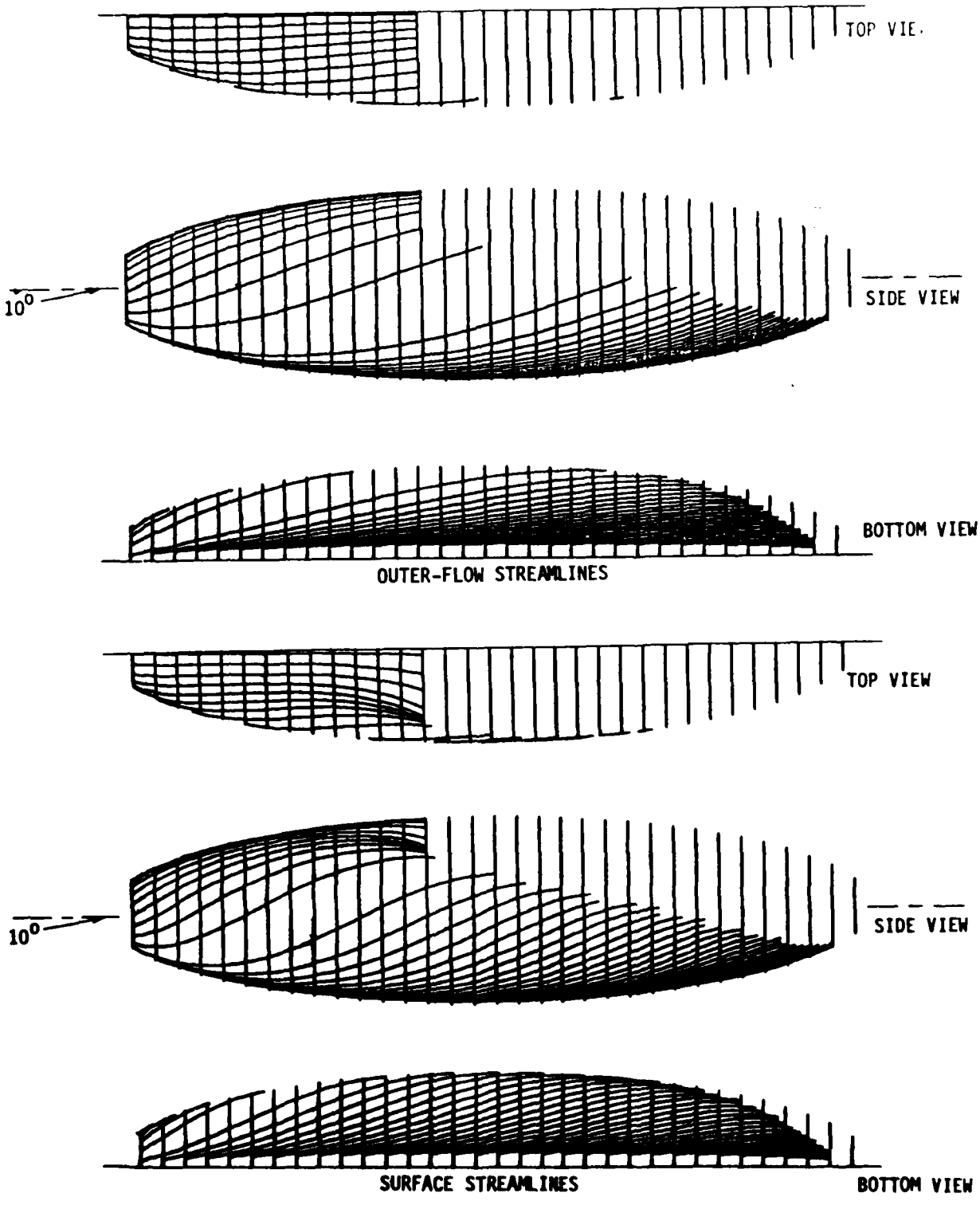

FIGURE 6 PREDICTED STREAMLINES FOR LAMINAR FLOW OVER 4:1 SPHEROID, $\alpha = 10^0$

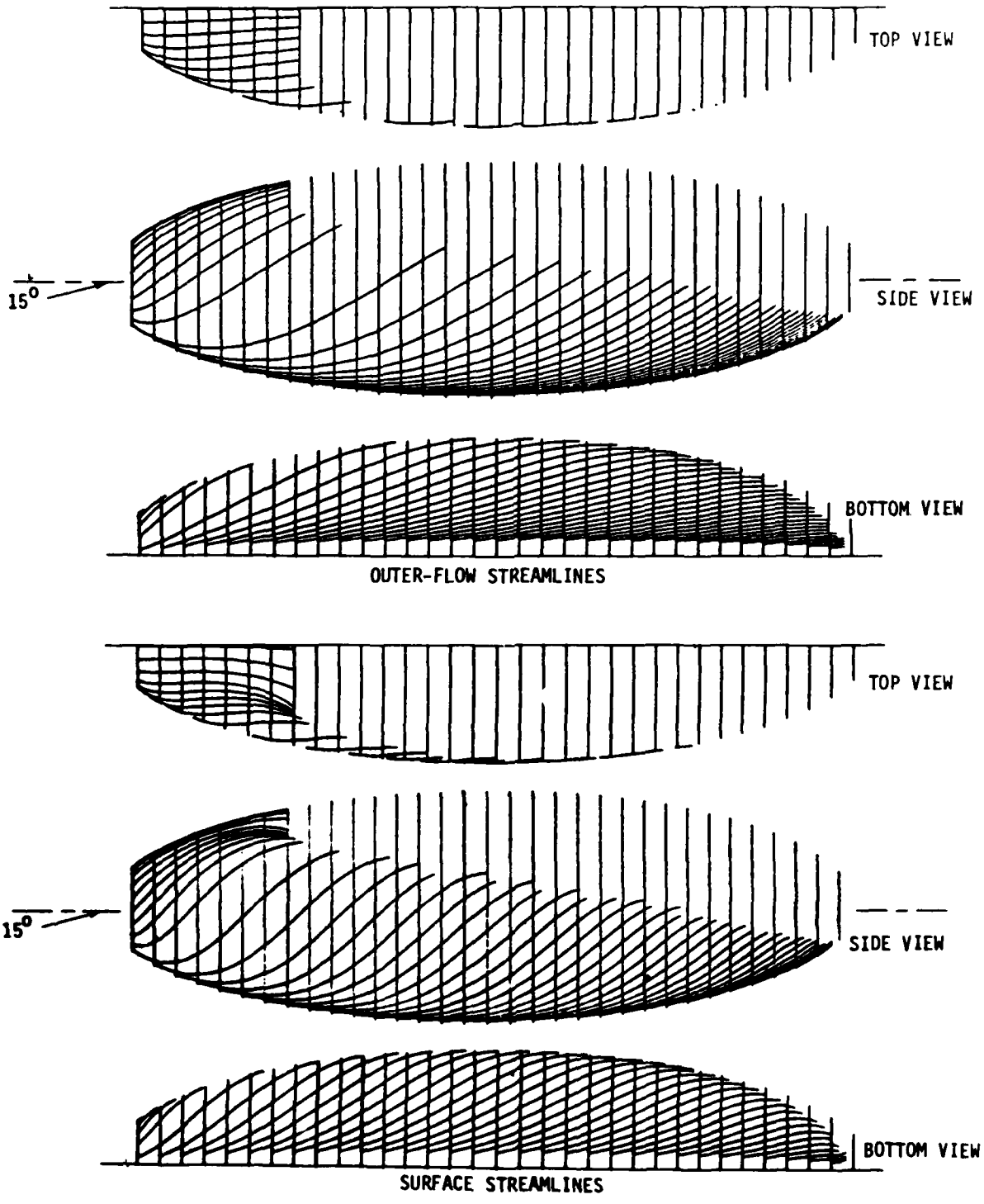

FIGURE 7 PREDICTED STREAMLINES FOR LAMINAR FLOW OVER 4:1 SPHEROID, $\alpha = 15^{0}$

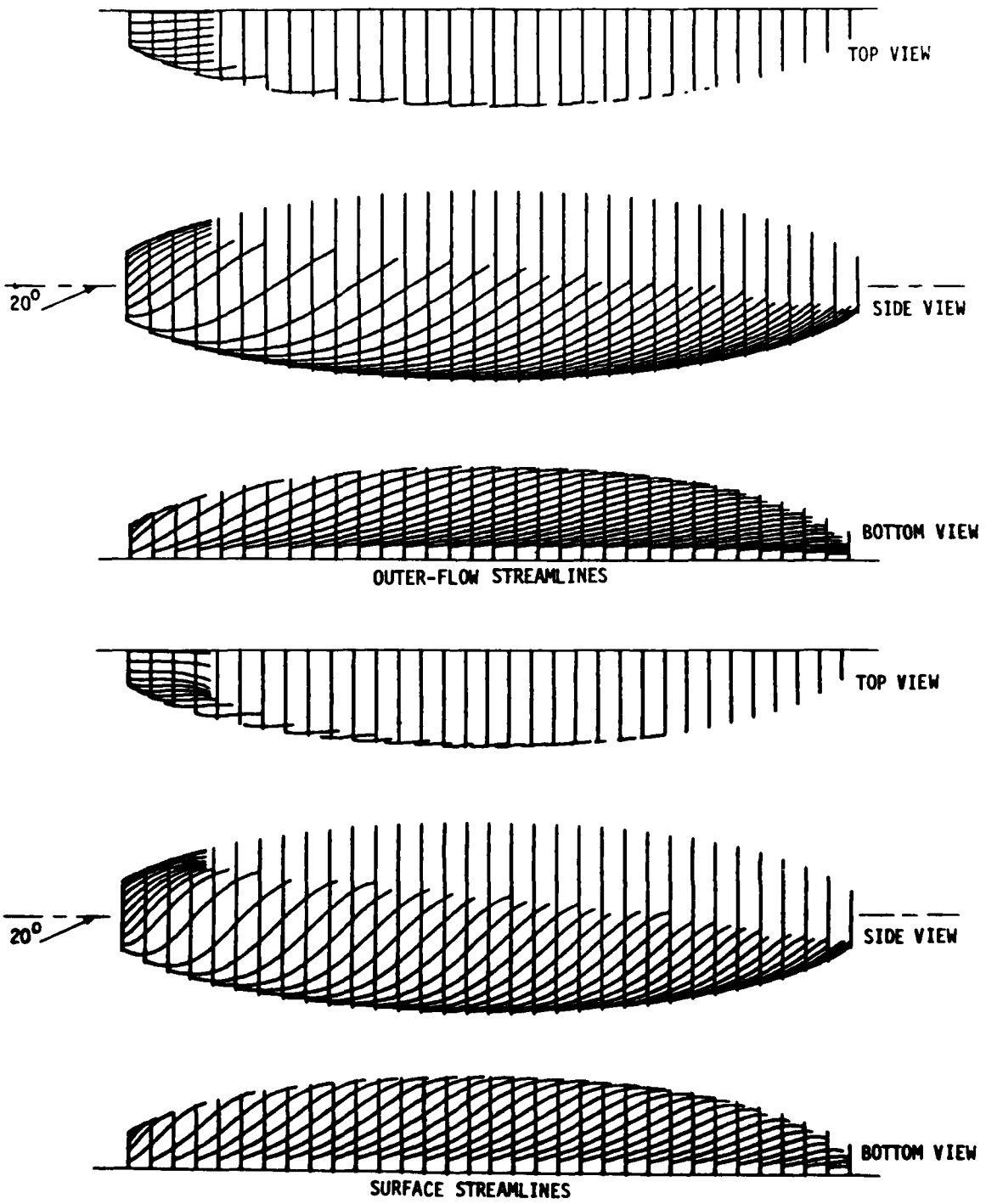

FIGURE 8 PREDICTED STREAMLINES FOR LAMINAR FLOW OVER 4:1 SPHEROID $\alpha = 20^0$

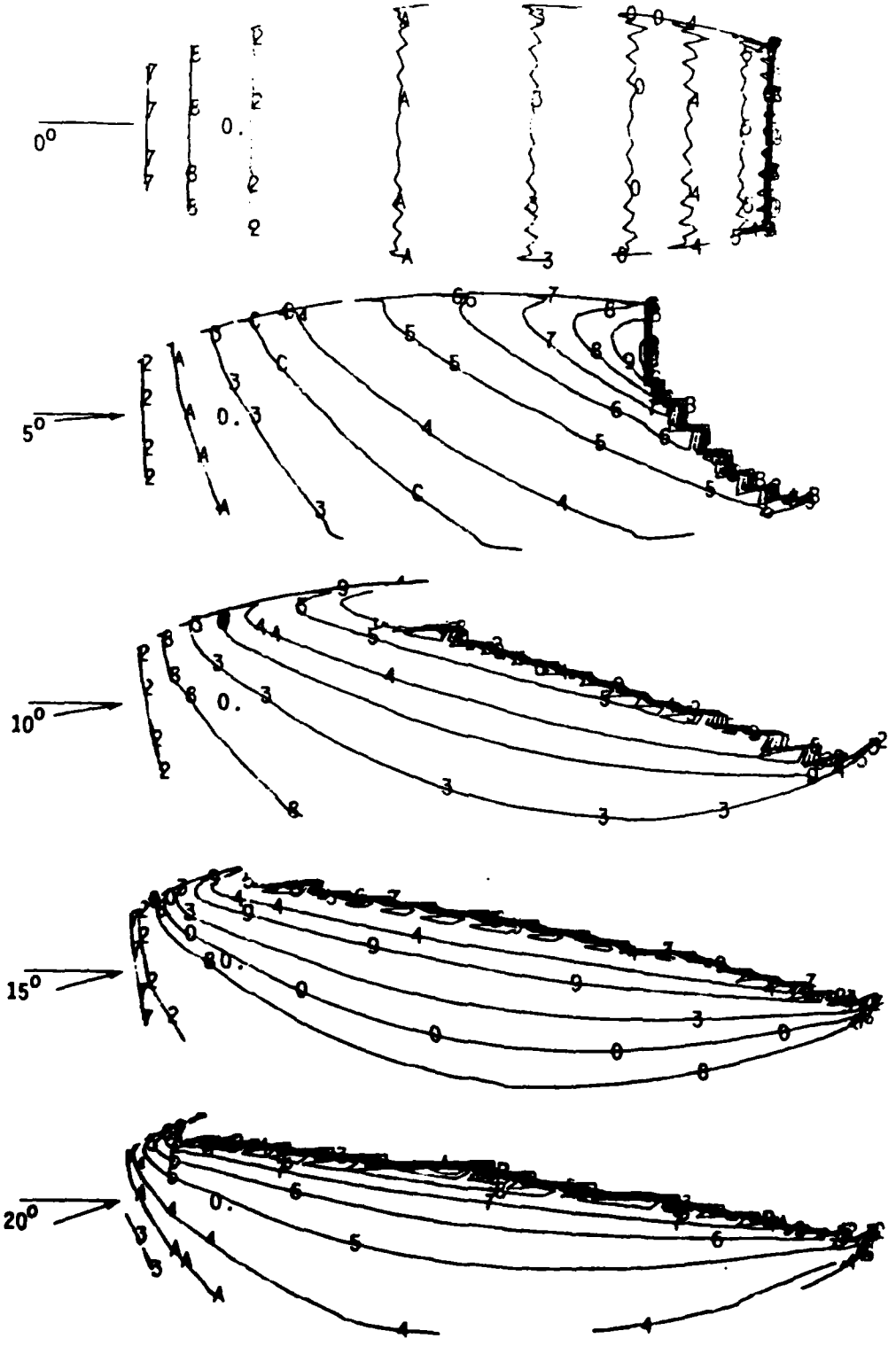

FIGURE 9 PREDICTED δ* CONTOURS FOR LAMINAR FLOW OVER 4:1 SPHEROID

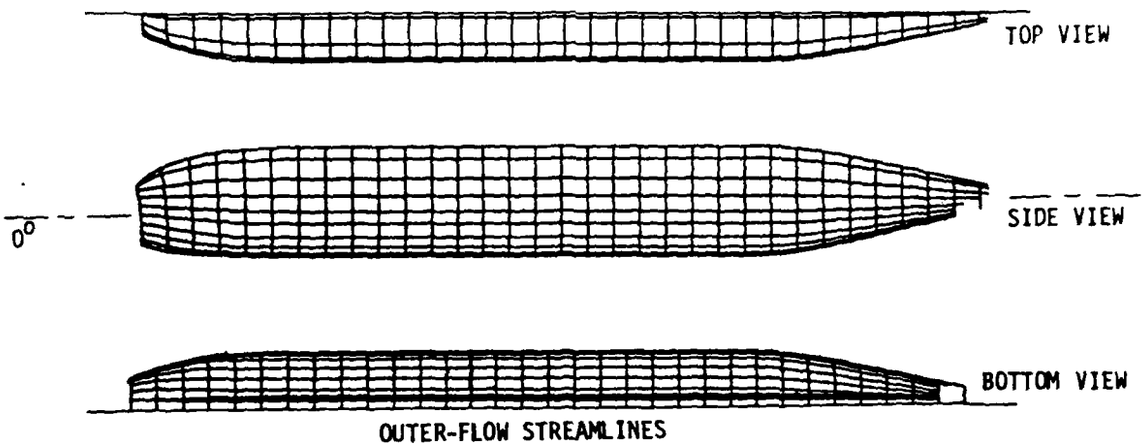

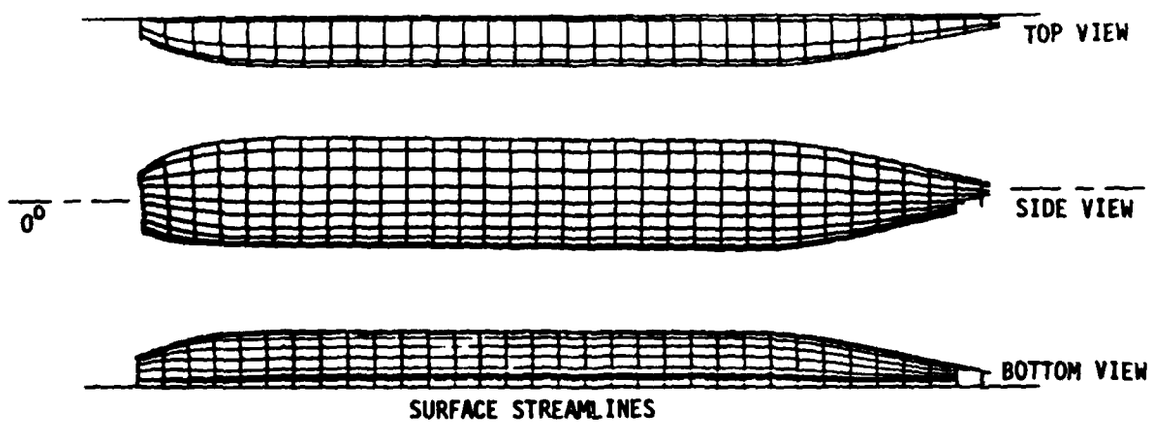

FIGURE 10 PREDICTED STREAMLINES FOR TURBULENT FLOW OVER BOEING 727-200 FUSELAGE, $\alpha = 0^{\circ}$

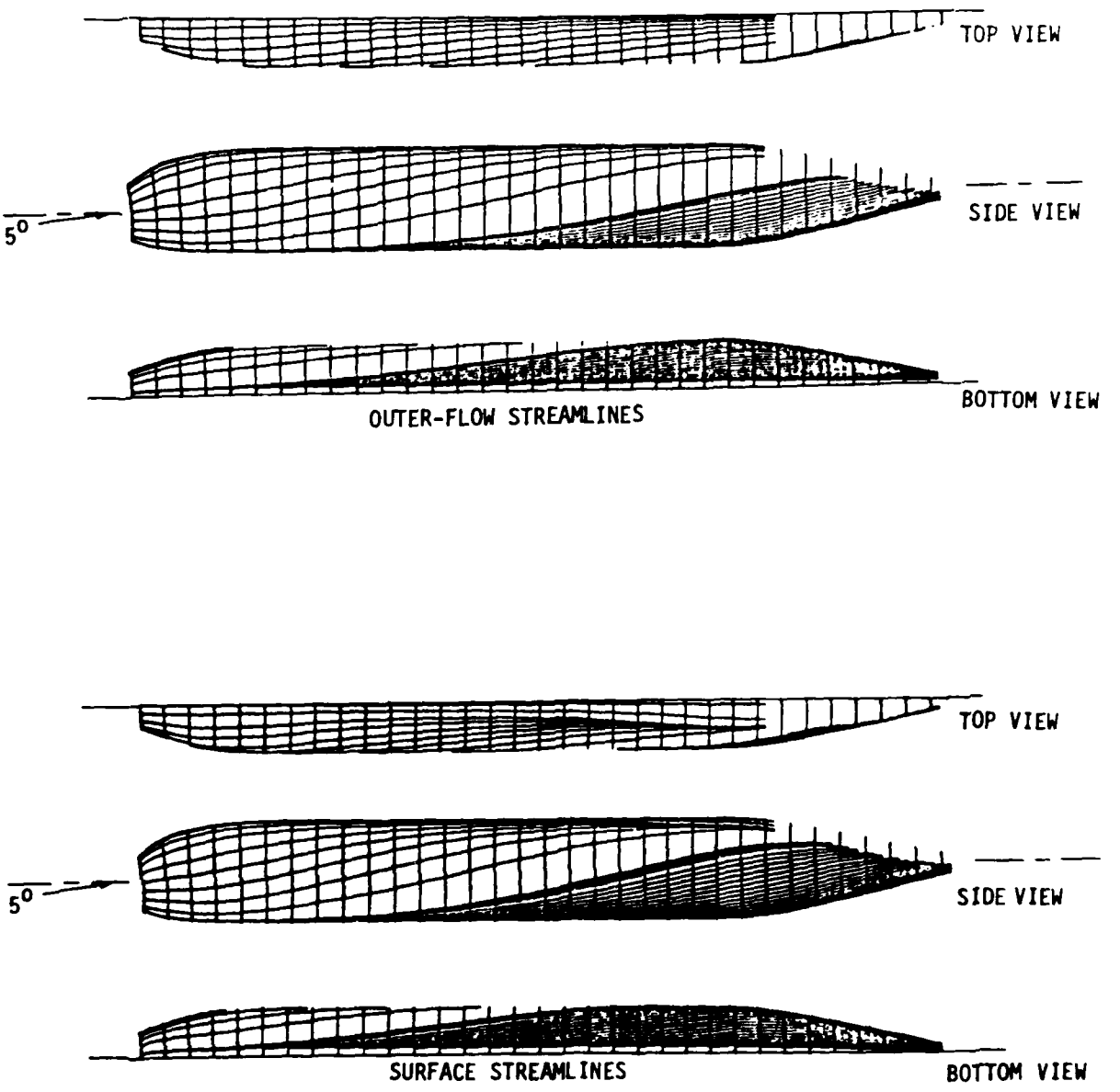

FIGURE 11 PREDICTED STREAMLINES FOR TURBULENT FLOW OVER BOIENG 727-200 FUSELAGE $\alpha = 5^0$

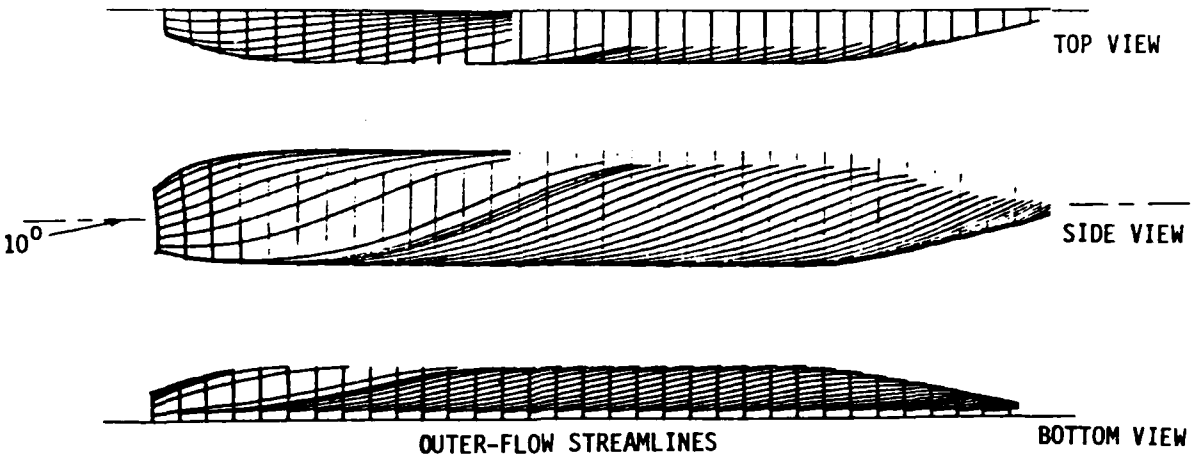

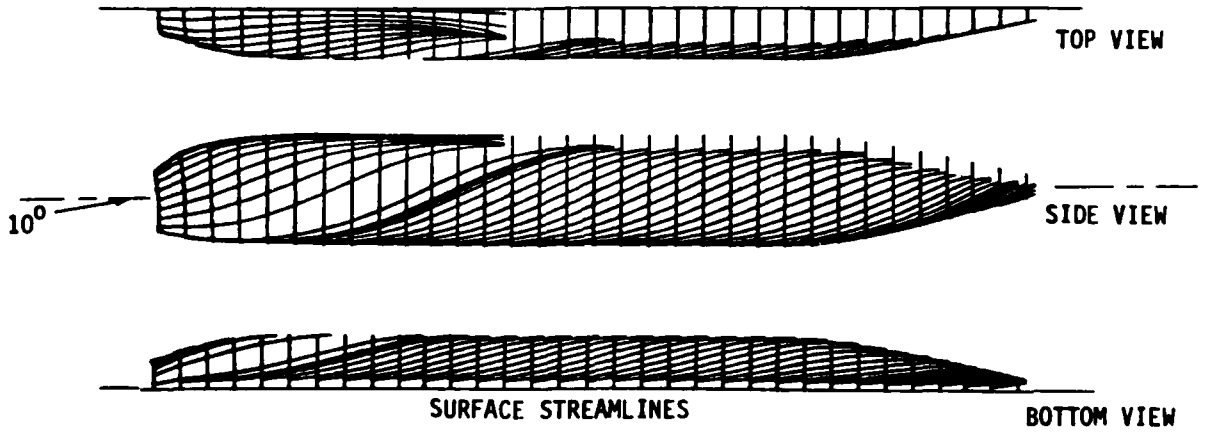

FIGURE 12 PREDICTED STREAMLINES FOR TURBULENT FLOW OVER BOEING 727-200 FUSELAGE, $\alpha = 10^{0}$

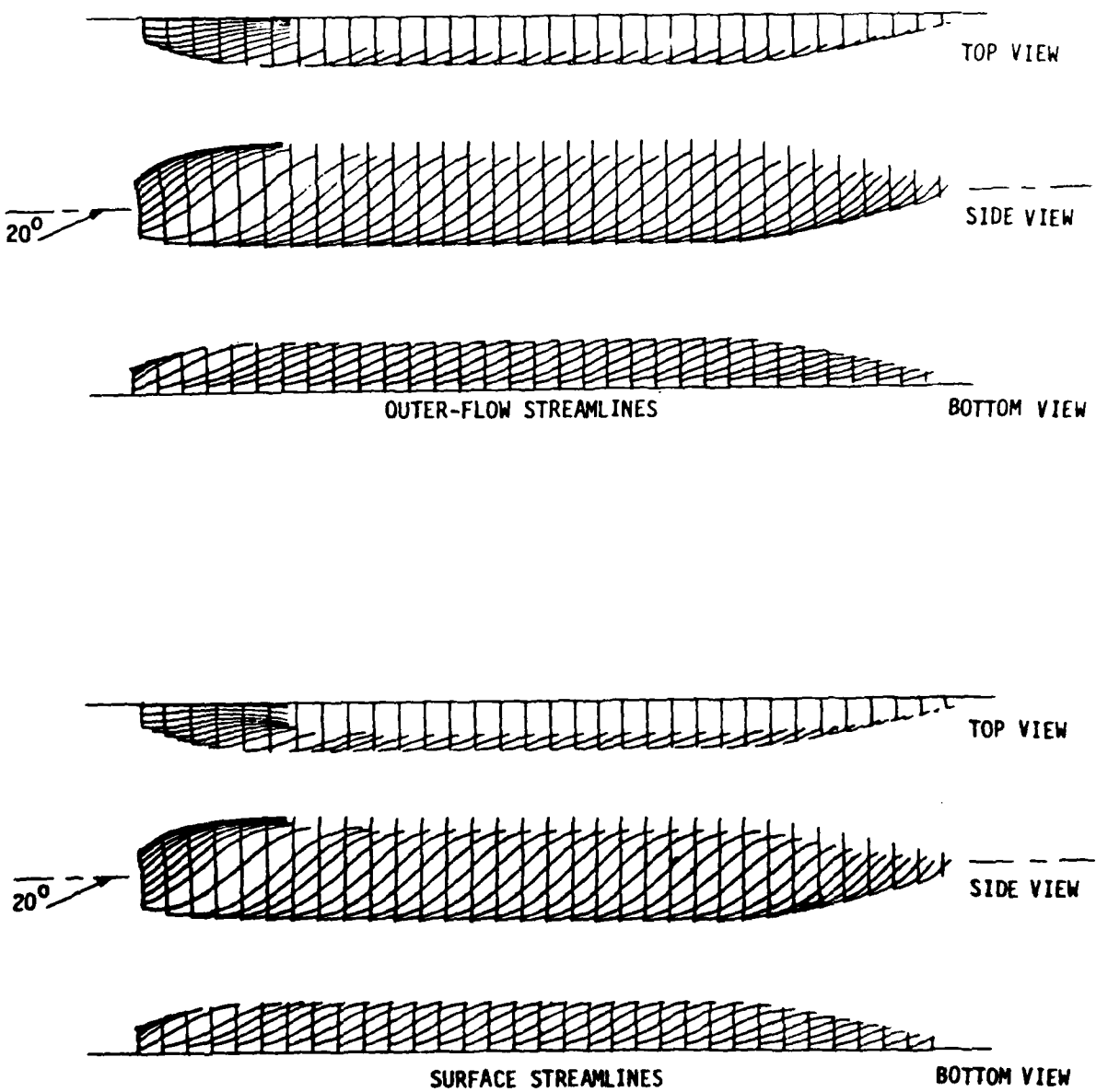

FIGURE 13 PREDICTED STREAMLINES FOR TURBULENT FLOW OVER BOEING 727-200 FUSELAGE, $\alpha = 20^0$

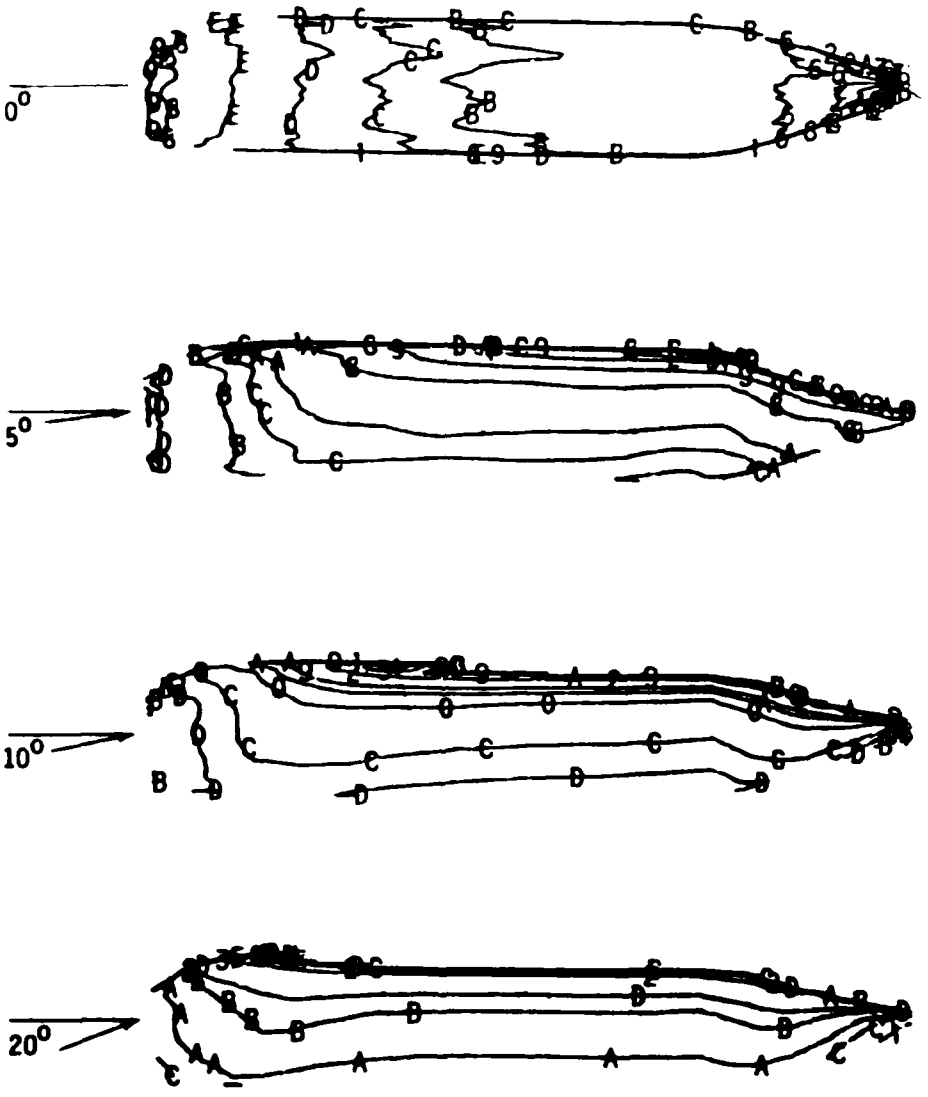

727-200 Fuselage

FIGURE 14 PREDICTED δ^* CONTOURS FOR TURBULENT FLOW OVER BOEING 727-200 FUSELAGE

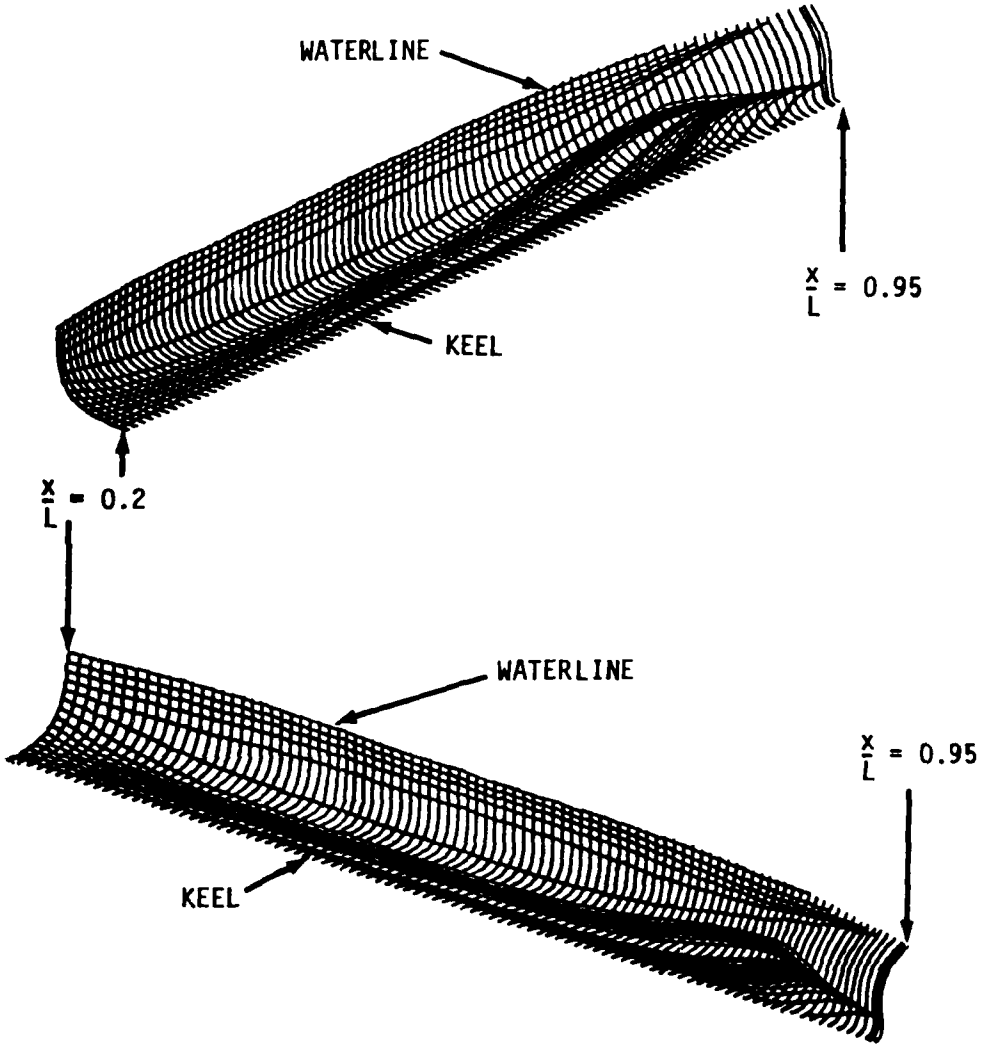

FIGURE 15 PREDICTED SURFACE STREAMLINES FOR SSPA 720 SHIP HULL

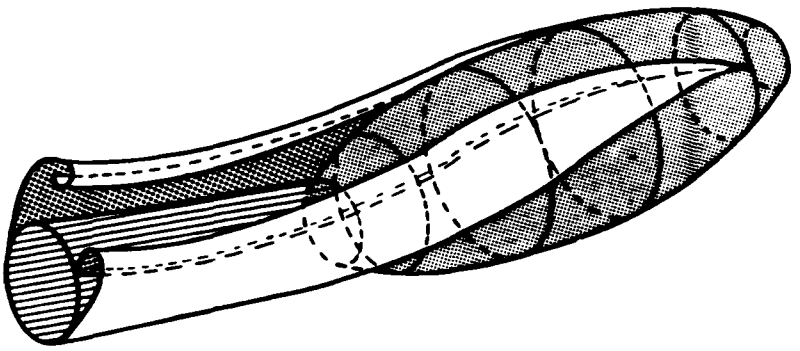

- VORTEX SEPARATION LINE CONSISTENT WITH 3-D BOUNDARY LAYER ANALYSIS
- VORTEX SHEET SHAPE DESIGNED BY PANEL METHOD

FIGURE 16 POSSIBLE FUTURE VISCOUS-INVISCID INTERACTION CALCULATION

SUPERCRITICAL AIRFOIL FLOW CONTROL BY SLOT SUCTION IN THE SHOCK REGION

P. Thiede

Vereinigte Flugtechnische Werke GmbH, Bremen

ABSTRACT

The use of supercritical airfoils at off-design conditions is limited by buffet onset, caused by shock-induced separation. On principle the shock-induced turbulent boundary layer separation can be prevented by slot suction within the shock region, but an efficient suction system can only be brought to bear for supercritical airfoils in connection with a nearly fixed shock position, as realised in an advanced VFW airfoil design.

In this paper, theoretical and experimental investigations of supercritical airfoil flow control by single slot suction within the shock region are presented. In this scope, the slot suction effects are caught by a boundary layer approach, based on the Walz' "amputation principle" at the slot and assuming the validity of the boundary layer approximations outside the slot. This method was used, to optimize the suction coefficient due to the shock-induced separation prevention.

Furthermore, boundary layer and pressure distribution measurements on a supercritical airfoil with a suction slot within the shock region are carried out in the 1 x 1 Meter DFVLR Transonic Tunnel in Göttingen at transonic off-design test conditions. The experimental results confirm the expected buffet onset increase by slot suction in the shock region, but indicate also that the theoretical approach requires further refinement.

INTRODUCTION

Modern supercritical airfoils came up to such a high standard, that tha scope for further design improvements is very small, Fig. 1. However, substantial progress is possible using boundary layer control (Ref. 1), which has not yet reached its full development potential.

Because of the off-design requirements a further increase in the design lift coefficient of a supercritical airfoil is limited by buffet-onset, caused by the bursting of shock-induced seperation bubbles. On principle, the shock-incuced turbulent separation can be prevented by boundary layer suction within the shock region, extending the buffet-boundary beyond the design margin.

Due to the practicability, only the single slot suction is considered in this paper. Because of the limited control region of a suction slot an efficient supercritical airfoil flow control by a single suction slot can only be brought to bear in connection with a nearly fixed shock position at off-design conditions, as realised in an advanced VFW airfoil design (Refs. 2, 3), Fig. 2.

In this paper, theoretical and experimental investigations of the supercritical airfoil flow control by single slot suction within the shock region are outlined. The complete results are published in Ref. 4.

THEORETICAL INVESTIGATIONS

Although the suction slot flow can exactly be described only by the full Navier-Stokes equations, in this scope the slot suction effects are caught by a boundary layer approach, based on the Walz' "amputation principle" at the slot (Ref. 5), and assuming the validity of the boundary layer approximations outside the slot, Fig. 3.

According to the "amputation principle" the turbulent boundary layer velocity profile before the slot is devided into

- the wall layer of the thickness y_S, which will be sucked into the slot
- and the outer profile, which flows along a stagnation line over the slot and forms the initial profile for the boundary layer development behind the slot.

For the prediction of the boundary layer parameters outside the slot, an extended version of the Walz' dissipation integral method (Refs. 6, 7) is used, taking account of the nonequilibrium character of the flow.

Fig. 4 shows predicted boundary layer data on the upper side of the VFW airfoil, prescribing the measured Mach number distribution at buffet-onset conditions, as a function of the suction ratio $\eta_s = v_s/\sigma_{2u_I}$. The suction slot is positioned at the point of beginning shock-induced seperation ($H_{32_I} = 1.545$).

The optimal suction ration for the prevention of the shock-induced separation depends on

- the boundary layer parameter and the local Mach number before the slot
- and the pressure distribution behind the slot.

The present boundary layer approach was used to optimize the suction ratio, assuming a similar solution for the Mach number distribution behind the slot, Fig. 5.

The importance of the suction ratio optimisation lies in the estimation of the limiting ratio, uo to which stronger suction is efficient at all. In consideration of the suction quantity and performance smaller suction ratios than the predicted ones will be of practical interest.

EXPERIMENTS

To confirm the expected buffet-onset increase of a supercritical airfoil by slot suction within the shock region, pressure distribution and boundary layer measurements on the VFW VA-2G airfoil with a single slot are carried out at transonic off-design conditions in the 1x1 Meter DFVLR Transonic Tunnel in Göttingen (Ref. 8). The VFW airfoil was choosen, as it appeared to be suitable for the installation of suction devices because of its nearly stationary shock position at off-design conditions.

Fig. 6 shows the test set up. The airfoil model has a chord length of $c = 200$ mm and a span of $b = 1$ m; the $s = 0.6$ mm wide suction slot is positioned at $x/c = 0.585$. Because of a conical duct within the model the duct velocity is nearly constant. The suction unit for these tests, usually imployed for the suction of the test section walls, is computer controlled.

The boundary layer probe with the probe drive unit, shown in the front view and so far intensively used for boundary layer and wake measurements on supercritical airfoils, as well as the test and data reduction procedures were developed by Stanewsky at the DFVLR and are described in Ref. 9.

Fig. 7 shows the measured lift and drag polar of the VFW airfoil with and without slot suction at $M_\infty = 0.76$. Before the buffet-boundary the influence of the suction on the aerodynamic coefficients is small. But with suction the lift rise can be stretched beyond the buffet-boundary so that a lift increase of more than 15% was obtained with a suction coefficient as low as $c_Q = 0.0006$. Furthermore the extreme drag rise beyond the buffet-boundary was also avoided by slot suction. Contrary to the theoretical results the suction coefficient had only a small influence on the lift and drag coefficients.

Two test cases are discussed here in more detail by means of the experimental results:

1. just before buffet-onset without suction
2. just before buffet-onset with suction.

Fig. 8 shows the measured pressure distributions of the first test case with and without slot suction at $M_\infty = 0.77$ and $\alpha_g = 4^o$. With exception of the slot region there is hardly any remarkable difference between both the distributions, as it can be made more clear by the next fig..

In Fig. 9 the measured boundary layer mean-flow velocity profiles of this test case, evaluated from total and static pressure probe measurements at 11 chordwise stations with and without suction, are plotted. While in the case without suction a shock-induced separation bubble is occuring the separation bubble has completely vanished by slot suction.

In Fig. 10 some measured velocity profiles in the slot region of the suction case are compared with equivalent Coles' wall/wake profiles (Ref. 10). It is obvious, that the actual boundare layer profiles just downstream of the suction slot cannot be well represented by wall/wake profiles, as the outer profile character is existing yet.

Fig. 11 shows the measured pressure distributions of the second test case at $\alpha_g = 5.3^o$, which are drastically different in the cases with and without suction. Without suction the buffet-boundary is clearly exceeded and one has a typical pressure

distribution with buffet-penetration (with an upstream unsteady shock position and a pressure rise at the trailing edge), whereas in the suction case the pressure distribution is of the just before the buffet-boundary typ like at $\alpha_g = 4^o$ without suction.

In Fig. 12 the corresponding boundary layer velocity profiles of this case with and without suction are compared. While without suction as a consequence of the upstream strong shock-boundary layer interaction a very thick but attached boundary layer exists, in the suction case a much thinner boundary layer with a separation bubble some distance behind the slot is evident.

In Fig. 13 measured boundary layer parameter with and without suction are plottet. The strong displacement thickness rise near the trailing edge in the case without suction and the separation bubble dimension in the suction case can be seen.

In Fig. 14 the measured boundary layer data in the slot region of the suction case at $\alpha_g = 5.3^o$ are compared with predicted ones, prescribing the measured pressure distribution. It is obvious that the predicted parameter jump at the slot as a result of the boundary layer concept is unrealistic. Besides, the relaxation process of the turbulent boundary layer behind the slot cannot be well predicted by integral methods, as it had to be suspected by the comparison of actual boundary layer profiles with equivalent wall/wake profiles. In this case the boundary layer prediction further downstream of the suction slot cannot be judged, because the prediction method breaks down when separation occurs.

CONCLUDING REMARKS

The experimental results confirm the expected buffet-onset increase by single slot suction within the shock region on a supercritical airfoil not designed for the special suction requirements. The better the slot positioning is to the shock, the greater is its efficiency.

Therefore, in the future also

- the installation of a multiple suction slot
- and modifications of the airfoil contour in the slot region

should be taken into consideration.

Furthermore, more extensive boundary layer measurements should be carried out, to get more detailed informations about the flow field structure in the slot region.

Further improvements of the theoretical approach to handle the suction effects should be concentrated on the computation of relaxating boundary layer in the slot region by finite-difference methods.

ACKNOWLEDGEMENT

This work was supported by the Ministry of Defence of the Federal Republic of Germany under RüFo contract T/RF 41 / 70021 / 71420.

The experiments were carried out in cooperation with Dipl.-Ing. E. Stanewsky, DFVLR Göttingen. His engagement in preparating, conveying and evaluating the measurements is gratefully acknowledged.

REFERENCES

1. G.V. Lachmann (Editor):
Boundary layer and flow control, Vol. 1 and 2.
Pergamon Press, Oxford, 1961.

2. K.-D. Klevenhusen, R. Hilbig and W. Burgsmüller:
Entwicklung von superkritischen Profilen und Voruntersuchungen zum superkritischen Flügelentwurf, Teil 1.
BMFT-Bericht 523-8891-LFF 34, VFW-Fokker, 1976.

3. R.D. Boehe:
Transsonikmessungen am VFW-F-Profil Va-2 bei der DFVLR Göttingen.
ZKP-Flügelsektion-Ergebnisbericht 8, 1976.

4. P. Thiede, G. Dargel:
Erweiterung des Einsatzbereiches von transsonischen Profilen durch lokale Grenzschichtabsaugung.
BMVg-FBWT RüFo IV T/RF41/70021/71420, VFW, 1980.

5. A, Walz:
Näherungstheorie für Grenzschichtabsaugung durch Einzelschlitze.
DVL-Bericht 184, 1962.

6. A. Walz:
Boundary layers of flow and temperature.
Engl. Ed., MIT Press, Cambridge, Massachusetts, 1969.

7. F. Otte and P. Thiede:
Berechnung ebener und rotationssymmetrischer kompressibler Grenzschichten auf der Basis von Integralbedingungen.
Fortschr.-Bericht VDI-Z, Reihe 7, Nr. 33, 1973.

8. T. Hottner, W. Lorenz-Meyer:
Der Transsonische Windkanal der aerodynamischen Versuchsanstalt Göttingen.
DGLR-Jahrbuch 1968.

9. E. Stanewsky, P. Thiede:
Boundary layer and wake measurements in the trailing edge region of a rear-loaded transonic airfoil.
DEA-Meeting "Viscous and Interacting Flow Field Effects", Meersburg, BMVg-FBWT 79-31, 1979.

10. D.E. Coles:
The law of the wake in the turbulent boundary layer.
J. Fluid Mech. 1, 1956.

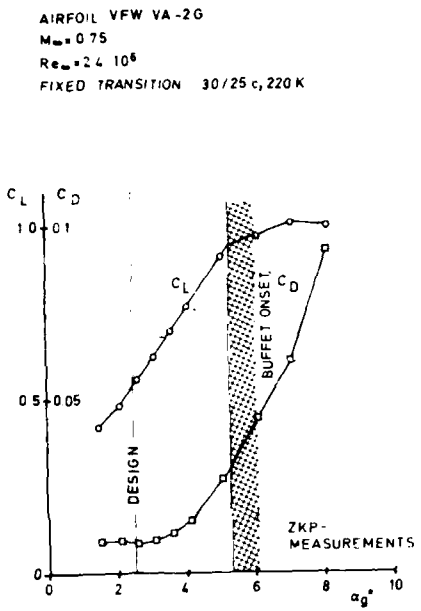

Fig. 1 Lift and drag polar of an advanced supercritical airfoil

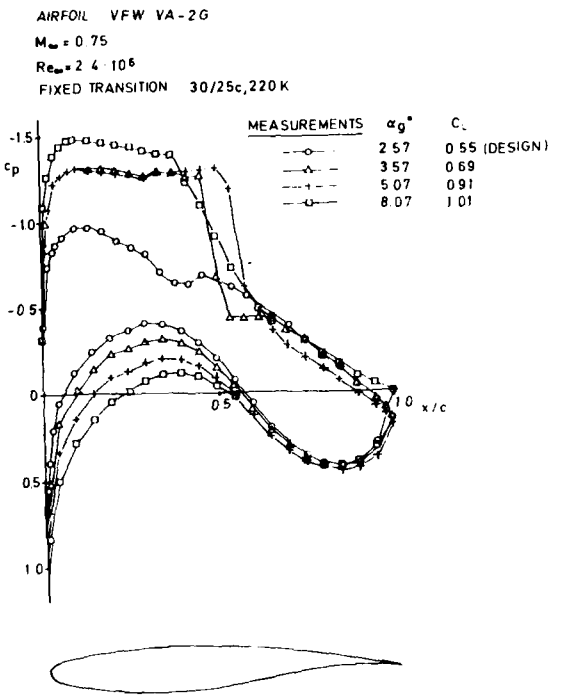

Fig. 2 Off-design pressure distributions of an advanced supercritical airfoil

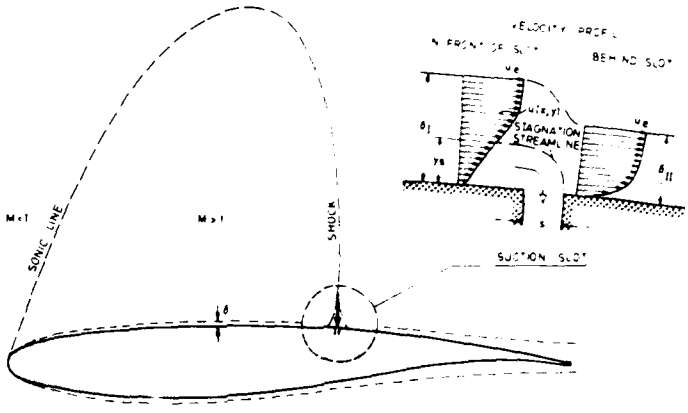

Fig. 3 Supercritical airfoil with suction slot in the shock region

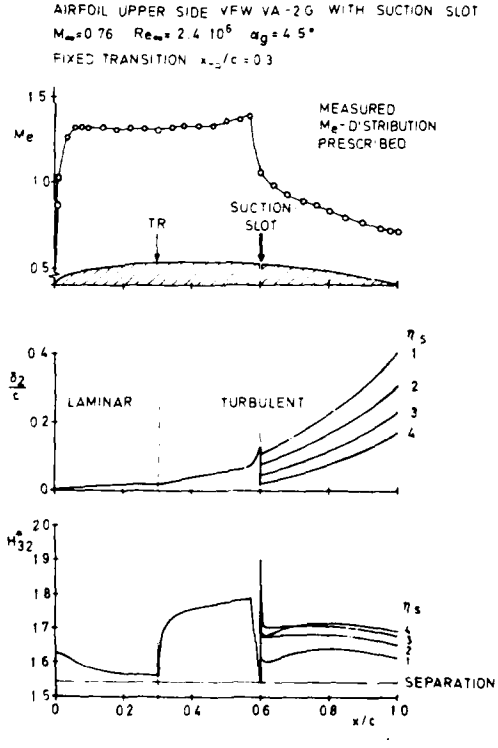

Fig. 4 Predicted boundary layer data dependent on suction ratio

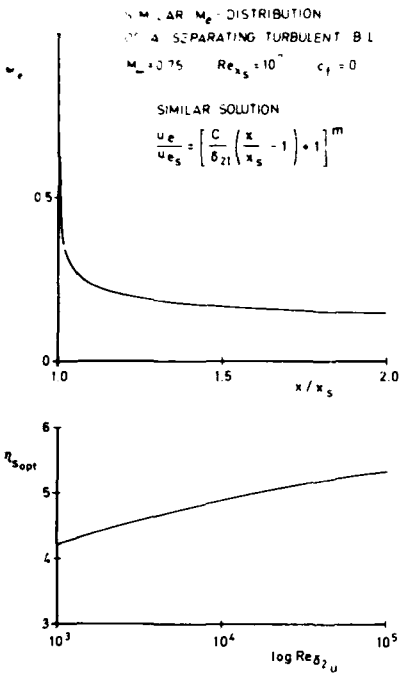

Fig. 5 Predicted optimal suction ratio

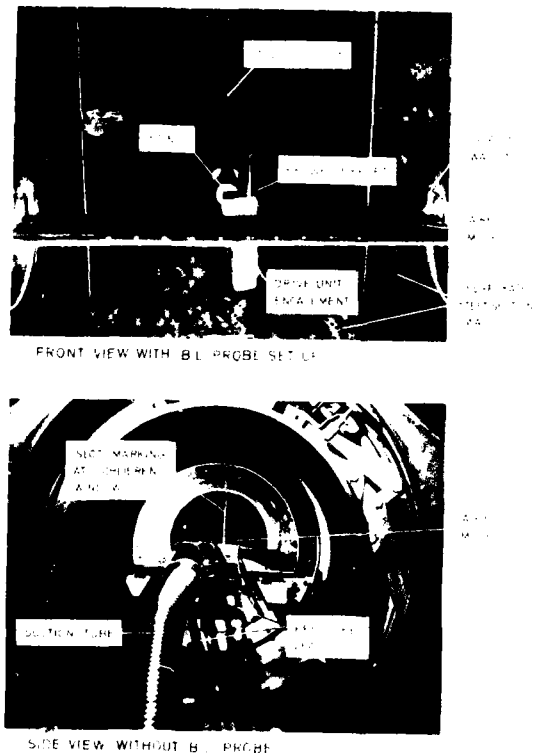

Fig. 6 Test set up in the 1x1 Meter DFVLR Transonic Tunnel in Göttingen

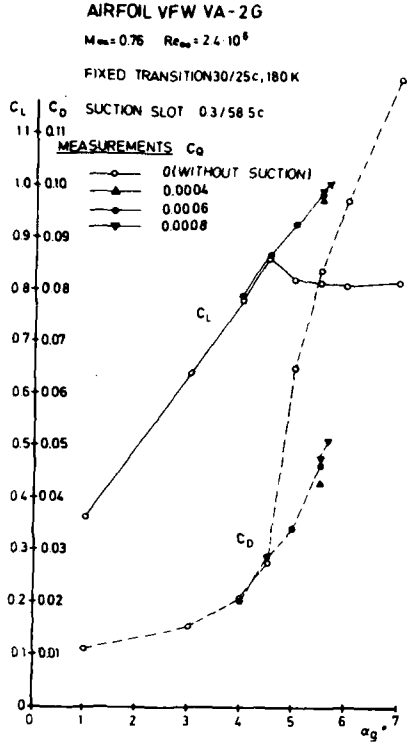

Fig. 7 Supercritical airfoil with suction slot in the shock region. Measured lift and drag polar

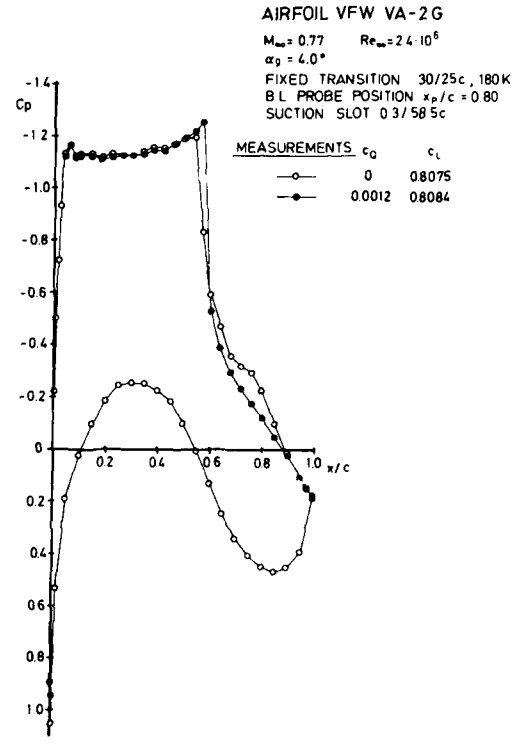

Fig. 8 Supercritical airfoil with suction slot in the shock region. Measured pressure distribution

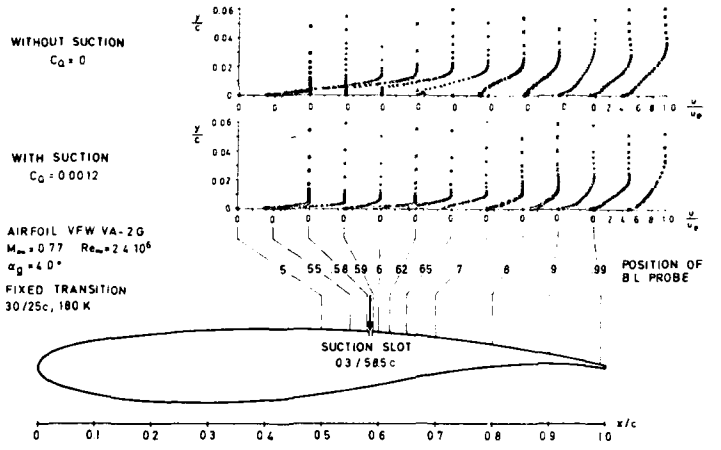

Fig. 9 Supercritical airfoil with suction slot in the shock region. Measured boundary layer velocity profiles

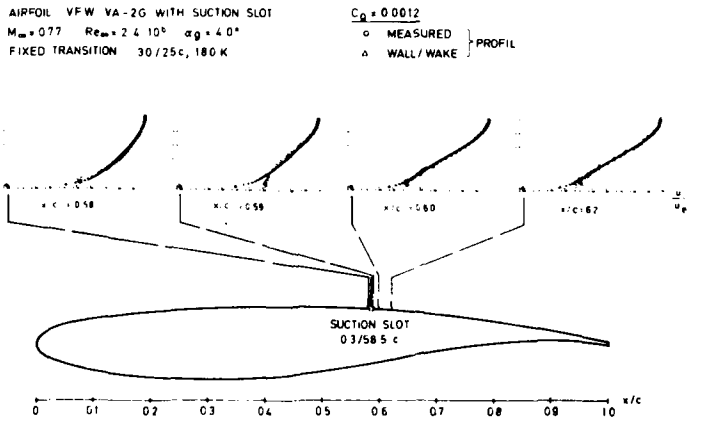

Fig. 10 Comparison of measured boundary layer velocity profiles with equivalent wall/wake profiles

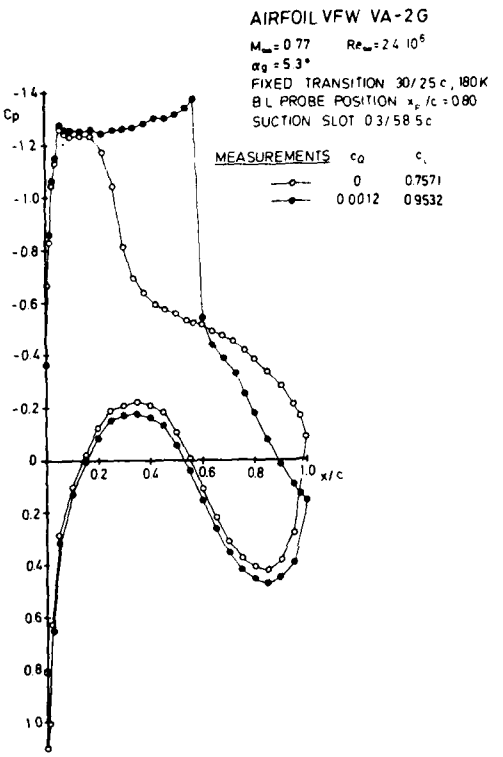

Fig. 11 Supercritical airfoil with suction slot in the shock region. Measured pressure distribution

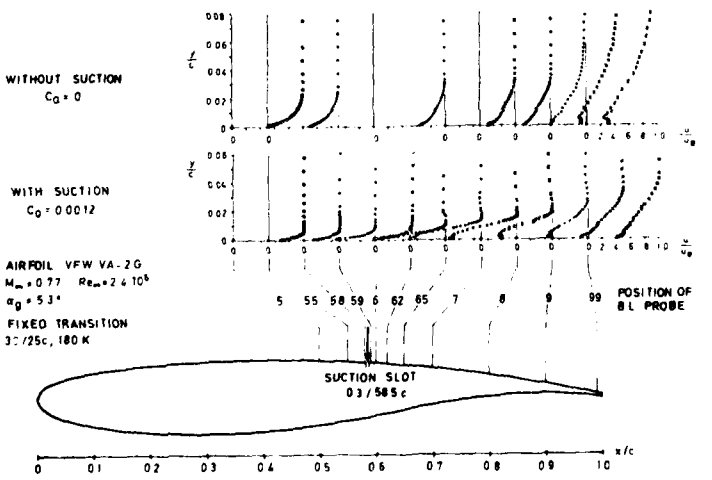

Fig. 12 Supercritical airfoil with suction slot in the shock region. Measured boundary layer velocity profiles

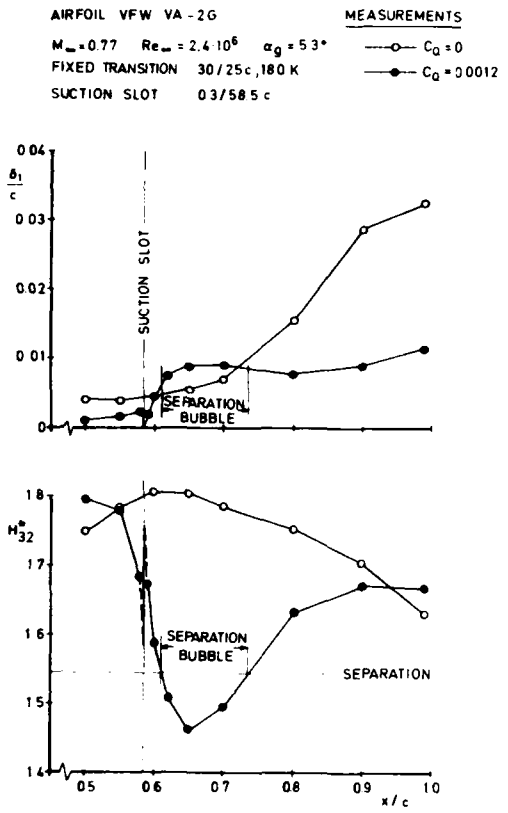

Fig. 13 Supercritical airfoil with suction slot in the shock region. Measured boundary layer data

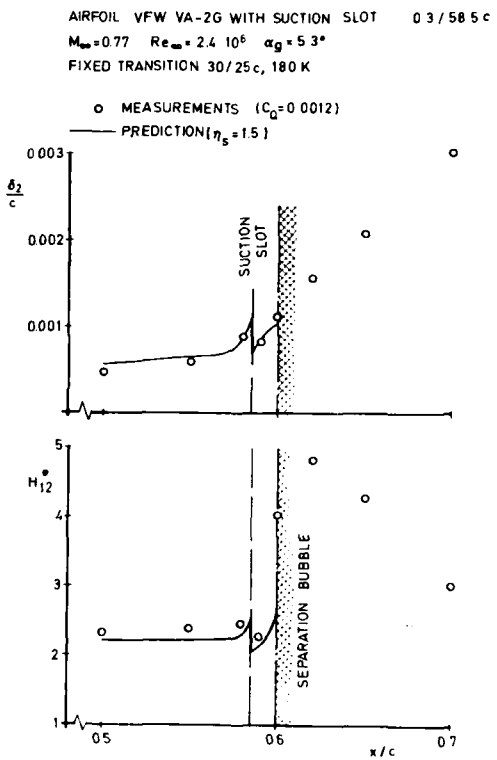

Fig. 14 Comparison of measured and predicted boundary layer data in the shock region

RECENT RESEARCH ON VISCOUS AND INTERACTING FLOW FIELD EFFECTS AT THE UNIVERSITY OF BOCHUM

K. Gersten
S. Kiske
V. Vasanta Ram
P. Wauschkuhn

University of Bochum
Federal Republic of Germany

The following topics of recent research on viscous and interacting flow field effects are discussed: I. Flows with strong viscous-inviscid interaction in the neighbourhood of separation. II. Laser-Doppler velocimeter measurements of separated regions of finite length. III. Prediction method for two-dimensional turbulent flows including separated regions of finite length. IV. Shear layers with disturbed turbulence structure.

I. Flows with Strong Viscous-Inviscid Interaction

In praxi many flows exist where turbulent boundary layers are exposed to strong adverse pressure gradients such, that the flow stays attached only, if the strong viscous-inviscid interaction is taken into account. Examples for such flows are diffusors, flow past slats or slotted flaps and flows in dents or past rounded backward facing steps. The latter is shown as an example in Fig. 1. The geometry is a flat plate of length l followed by a rounded backward facing step of height H and length L. The contour is a polynom of fifth degree such that the curvature of the wall contour is continuous everywhere. The flow is assumed to be incom-

pressible. Potential flow theory would lead to a pressure distribution shown as dotted curve. The turbulent boundary layer under such pressure distribution would separate, as can be seen from the dotted wall shear stress curve. The measurements show a pressure distribution quite different from the one found by potential theory. In particular, the measured pressure gradients are so much smaller that the turbulent boundary does not separate. The experimental pressure distribution can be determined theoretically when the displacement effect of the boundary layer is taken into account. In this particular example, the fictitious contour (contour plus displacement thickness) is quite different from the geometrical contour, and so are the corresponding pressure distributions with the consequence that one pressure distribution leads to boundary layer separation whereas the other one does not. In order to get the correct result the displacement effect has to be taken into account by an iteration procedure. A boundary layer separation during the iteration does not mean necessarily that the final result will show separation. The strategy of the iteration procedure has to be shosen such that in every iteration step separation is avoided if possible. On the boundary between separation and no separation (incipient separation), the wall shear stress curve just touches the abscissa.

In Fig. 2 this boundary of incipient separation is shown for flows past rounded backward facing steps. As can be seen the boundary of incipient separation is shifted drastically to larger step heights if viscous-inviscid interaction is taken into account. By neglecting the interaction separation would be predicted for almost half the step heights compared to the correct critical step heights. There is obviously good agreement of the theoretical

result with experiment, because measurements of configuration ② showed separation, whereas in configuration ②, which corresponds to example shown in Fig. 1, no separation occurs. According to Fig. 2 separation may appear when the step height and/or the thickness of the oncoming boundary layer are increased. The smaller the thickness of the oncoming boundary layer, the larger the critical step heigth of incipient separation.

Similar calculations have been carried out for laminar boundary layers. In Fig. 3 the example of the flow over a dent in a flat plate is shown. Again, without interaction separation would occur, whereas by taking into account the displacement no separation appears. When the depth H of the dent becomes small compared to boundary layer thickness, the calculation procedure reduces to the so-called "Triple-Deck-Concept" [1], where disturbances of the velocity field are restricted mainly to the lower part("lower deck", linear velocity distribution) of the boundary layer. In this limiting case the solution becomes independent of Reynolds number.

The procedure described was applied to predict incipient separation in subsonic diffusors. Detailed results will be given in [2].

II. Laser-Doppler Velocimeter Measurements of Separated Regions of Finite Length

Particular flows are being studied by Laser-Doppler velocimetry where the turbulent boundary layer separates due to the pressure distribution but reattaches after a certain length. As an example, the flow past a rounded backward

facing step is considered which was already marked as measurement (2) in Fig. 2. Typical results of the measurements are shown in Fig. 4. The pressure distribution at the wall shows drastic differences to the potential-flow pressure distribution (see Fig. 1). Between stations (A) and (B) separation occurs. Beyond separation point the pressure is almost constant, but increases again slightly within the rear half of the separation bubble. For four typical stations the mean velocity profiles are shown as measured by LDV-system, which is described in [3]. The so-called dual beam mode with forward scattering was used. Because of back flow and high turbulence intensity frequency shifting (40 MHz) was applied to one of the two laser beams. A counter had to be used for data processing. From the measured velocity distribution the displacement line could be determined. This line is much smoother than the original contour. Therefore, the corresponding pressure distribution has much smaller gradients than potential flow without displacement would predict. One important result from the experiments is that fact, that the pressure gradient perpendicular to the wall is still negligibly small even if the boundary layer separates. Therefore, boundary layer concepts can also be applied to separated regions. The experimental results could be used to model the separated region, which is described in the next section.

III. Prediction Method for Two-dimensional Flows Including Separated Regions of Finite Length

1. Laminar Boundary Layers

The Triple-Deck Concept has also been applied to laminar boundary layers when separation occurs. Fig. 5 shows as an example the flow over a dent in a flat plate similar

to the example in Fig. 3. However, the ratio of depth to length of the dent is six times larger, i.e. H/L = 0,048. The resulting pressure distribution shows a very similar form as that in Fig. 4. The integral

$$\int_{-\infty}^{+\infty} c_p(x)\,dx$$

is always equal to zero because of vertical momentum balance. It is worth mentioning that the wall shear stress distribution shows an overshoot, i.e. the wall shear stress just beyond reattachment is higher than the asymptotic value far downstream. In Fig. 6 the corresponding stream lines are shown in the lower-deck coordinate system. Although separation occurs the dent is still quite slight, which can be seen from the geometry of the dent in physical coordinates.

2. Turbulent Boundary Layers

In principal, a prediction method for turbulent flows including separated regions would work the same way as the method described in Section I. The main additional difficulty arises in the modelling of the separated region. One connection between the displacement line and the pressure distribution is given - as before - by the inviscid potential theory. The other connection is supplied by the "boundary layer" calculation of the viscous part of the flow. In case of flows with separated regions this "boundary-layer calculation" is divided into three parts, see Fig. 7, namely the regions in front of the separation bubble, the region of the separation bubble, and the region beyond the separation bubble. The first and the third region can be covered by ordinary prediction methods for attached

tubulent boundary layers. The main problem left is a prediction method for calculating the displacement distribution within the bubble region and the bubble length. Therefore, our work is now concentrated on developing a proper model for the separated region. This combined theoretical and experimental (see Section II) research is still in progress.

As a first step, we started with the following simple engineering approach which is demonstrated in Fig. 7:

a) It is assumed that the geometry of the bubble (dividing stream line) is universal if properly scaled. This geometry is shown in Fig. 7, taken from experiment. The ratio of height to length of the bubble is assumed to be a constant, namely H/L = 0,08. This is in agreement with the results in [4].

b) The free shear layer between the separated region and the inviscid outer flow is approximated by the simple shear layer solution of a free jet boundary where the displacement thickness increases proportional to the coordinate, the gradient being approximately $d\delta_1/dx = 0{,}05$

c) The location of the reattachment point and, hence, the bubble length are determined by using the same reattachment criterion as in [3], in which it is assumed that the total pressure on the dividing streamline is constant near reattachment.

The flow diagram of the calculation procedure is shown in Fig. 8. The final result of the iteration process is reached when the distributions of pressure and desplacement thickness generate each other, by inviscid theory as well as by "boundary layer" calculation including modelling of the separated region. More sophisticated models of the separated region are just under consideration.

IV. Shear Layers with Disturbed Turbulence Structure

In the 1979 DEA-meeting held at Meersburg a simple method was proposed to handle the wall-bounded shear flow subject to a step jump in surface roughness. The method hinges upon the existence of an internal layer whose characteristic is a scaling behaviour different from the rest of the shear layer. When such an internal layer is identifiable the concept of "entrainment of fluid belonging to a region of turbulent flow of one scale into a region of another scale" achieves importance.

A study of available literature shows that the divisibility of a shear layer into subregions characterized by their scaling behaviour is feasible even when the disturbance originates at a location within the body of the shear layer, not necessarily at the wall. A schematic diagram of such a flow is shown in Fig. 9 . Layer 1 is characterized by the friction velocity $u_{\tau a}$ where $\rho u^2_{\tau a} = \tau_w$ is the wall shear stress. The characteristic quantity for layer 5 is $u_{\tau b}$, the scale for the velocity defect $U_\infty - u$. In layer 3, say in the wake of a disturbance at $(x = x_c , y = y_c)$, a velocity defect $U_c - u$ may be expected to scale with a friction velocity $u_{\tau c}$, where U_c is the velocity in the undisturbed shear layer at the location of the disturbance. Layers 2 and 4 bridge regions of different scales, 1-3 and 3-5 respectively. The velocity in the disturbed shear layer can then be written als follows:

<u>Layer 1:</u> $\delta_s < y < \delta_1 \; : \; u = u_{\tau a} F_1(\xi_1) \; , \quad \xi_1 = \frac{y}{\delta_1}$ (1a)

<u>Layer 2:</u> $\delta_1 < y < \delta_2 \; : \; u = u_{\tau a} F_{2a} + u_{\tau c} F_{2c}$ (1b)

Layer 3: $\delta_2 < y < \delta_3$: $u = U_c - u_{\tau c} F_3(\xi_3)$,

$$\xi_3 = \frac{y - 0.5(\delta_3 + \delta_2)}{(\delta_3 - \delta_2)} \qquad (1c)$$

Layer 4: $\delta_3 < y < \delta_4$: $u = u_{\tau c} F_{4c} + u_{\tau b} F_{4b}$ (1d)

Layer 5: $\delta_4 < y < \delta_5$: $u = U_\infty - u_b F_5(\xi_5)$, $\xi_5 = \frac{y}{\delta_5}$ (1e)

The velocity profiles in layers 1 and 5 are taken to be of the same form as in the undisturbed shear layer. In layer 3, when the disturbance is "wake like" (or jet like), $u_{\tau c}$ is taken to scale in the same manner as the wake (or jet) in a uniform stream, i.e., $u_{\tau c} = C \cdot (x - x_c)^{-1/2}$. The functions F_{2a} , F_{2c} , F_{4c} and F_{4b} are taken to be simple expressions of the following forms (eqn.2) that guarantee the proper scaling behaviour at the interfaces 1-2, 2-3, 3-4 and 4-5.

$$F_{2a} = F_1(\delta_1/\delta_5) + [A_{1a} - F_1(\delta_1/\delta_5)][(y-\delta_1)/(\delta_2-\delta_1)]$$

$$- A_{1a}[(y-\delta_1)/(\delta_2-\delta_1)]^2 \qquad (2a)$$

$$F_{2c} = [\frac{U_c}{u_{\tau c}} - F_3(-\frac{1}{2})] + [A_{1c} - \frac{U_c}{u_{\tau c}} + F_3(-\frac{1}{2})]$$

$$[(y-\delta_2)/(\delta_1-\delta_2)] - A_{1c}[(y-\delta_2)/(\delta_1-\delta_2)]^2 \qquad (2b)$$

$$F_{4c} = \left[\frac{U_c}{u_{\tau c}} - F_3\left(\frac{1}{2}\right)\right] + \left[B_{1c} - \frac{U_c}{u_{\tau c}} + F_3\left(\frac{1}{2}\right)\right]\left[(y-\delta_3)/(\delta_4-\delta_3)\right]$$

$$- B_{1c}\left[(y-\delta_3)/(\delta_4-\delta_3)\right]^2 \qquad (2c)$$

$$F_{4b} = \left[\frac{U_c}{u_{\tau b}} - F_5\left(\frac{\delta_4}{\delta_5}\right)\right] + \left[B_{1b} - \frac{U_\infty}{u_{\tau b}} + F_5\left(\frac{\delta_4}{\delta_5}\right)\right]$$

$$\left[(y-\delta_4)/(\delta_3-\delta_4)\right] - B_{1b}\left[(y-\delta_4)/(\delta_3-\delta_4)\right]^{+2} \qquad (2d)$$

The velocity profiles (eqs.(1a-1e)) substituted into the momentum integral equation involves six unkowns $u_{\tau a}$, δ_1, δ_2, δ_3, δ_4, δ_5. The five auxiliary relations may be obtained by considering the entrainment of turbulent flow of one scale into another and invoking their scaling behaviour as follows.

$$\frac{d}{dx}\int_{\delta_4}^{\delta_5} u\,dy + u(\delta_4)\frac{d\,\delta_4}{dx} - v(\delta_4) = u_{\tau b}\,F_{e\,\delta_5} \qquad (3a)$$

$$\frac{d}{dx}\int_{\delta_3}^{\delta_4} u\,dy + u(\delta_3)\frac{d\,\delta_3}{dx} - v(\delta_3) = (u_{\tau c} - u_{\tau b})F_{e\,\delta_4} \qquad (3b)$$

$$\frac{d}{dx}\int_{\delta_2}^{\delta_3} u\,dy + u(\delta_2)\frac{d\,\delta_2}{dx} - v(\delta_2) = (u_{\tau c} - u_{\tau b})F_{e\,\delta_3} \qquad (3c)$$

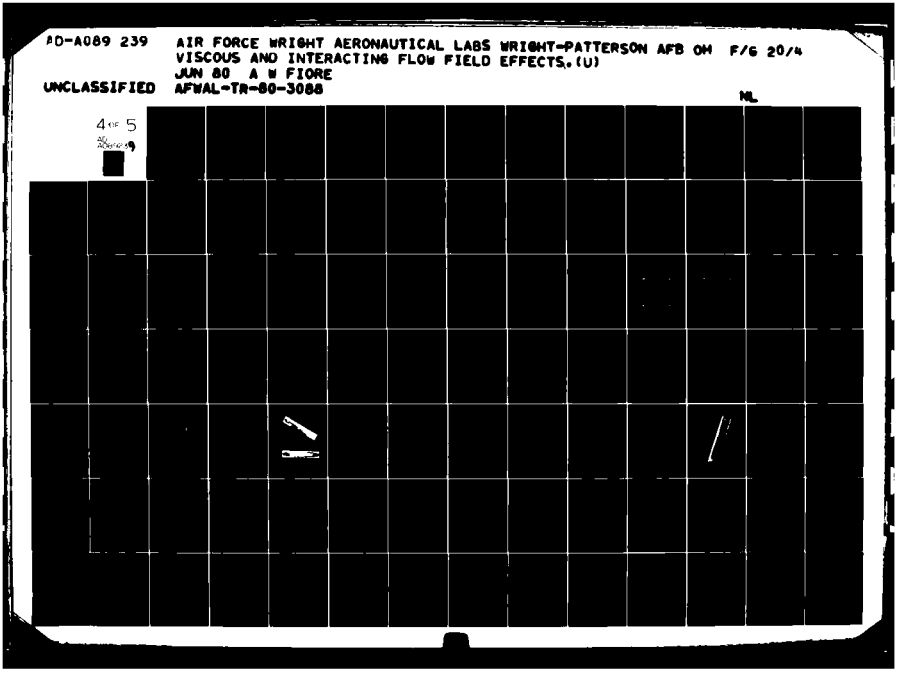

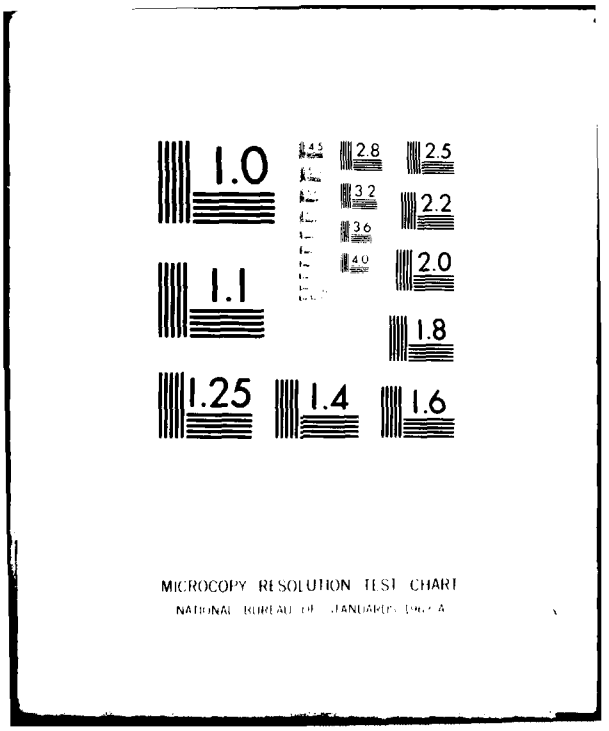

$$\frac{d}{dx}\int_{\delta_1}^{\delta_2} u\,dy + u(\delta_1)\frac{d\,\delta_1}{dx} - v(\delta_1) = (u_{\tau c} - u_{\tau a})F_{e\,\delta_2} \qquad (3d)$$

$$\frac{d}{dx}\int_{0}^{\delta_1} u\,dy = (u_{\tau c} - u_{\tau a})F_{e\,\delta_1} \qquad (3e)$$

The momentum integral equation

$$U_\infty^2 \frac{d}{dx}\int_{0}^{\delta_5} u(U_\infty - u)dy - u_{\tau a}^2 = 0 \qquad (4)$$

together with the five entrainment relations (eqn.(3a)-(3e)) with u given by eqn.(1a)-(1e) constitute a set of equations for the six unknowns $u_{\tau a}$, δ_1 , δ_2 , δ_3 , δ_4 and δ_5 .

Status of work and open problems

Studies up to now at the Ruhr University Bochum indicate that the set of equations (3,4) would be in a position to describe the shear layer with a disturbed turbulence structure if the multi-layered structure is identifiable. However, with the state of experimental evicence available today it is hard to say a priori what kind of a disturbance would produce such a multi-layered structure in the flow.

A further point which our studies have shown to be of crucial importance, concerns the choice of the quantities $F_{e\delta_1}$, $F_{e\delta_2}$, $F_{e\delta_3}$, $F_{e\delta_4}$, $F_{e\delta_5}$ in the entrainment relations.

Fig. 10 taken for the relatively simple case of the disturbance originating at the wall (rough → smooth) serves to illustrate this point. In this case only two entrainment relations are required which are as follows [5], DEA-meeting 1979):

$$\frac{d}{dx}\int_{\delta_1}^{\delta} u\,dy + u(\delta_1)\frac{d\,\delta_1}{dx} - v(\delta_1) = u_{\tau a}\,F_{e\delta}$$

$$\frac{d}{dx}\int_{0}^{\delta_1} u\,dy = (u_{\tau a} - u_{\tau b})F_{e\delta_1} \qquad (5)$$

The figure shows results for the wall-shear stress and for the growth of the internal layer with $F_{e\delta} = 0.3$ and $F_{e\delta_1} = 1.2$. It is apparent that $F_{e\delta}$ and $F_{e\delta_1}$ may be choosen to be constant, but they are far from being identical. Since, in the present case of the disturbed shear layer with a multi-layered structure five quantities $F_{e\delta_1}$, $F_{e\delta_2}$, $F_{e\delta_3}$, $F_{e\delta_4}$, $F_{e\delta_5}$ are involved it is clear that a deeper study of the mechanism governing entrainment is necessary. At the Ruhr University Bochum this is being persued along lines suggested by A.A. Townsend [6].

References

[1] K. Gersten: Method of matched asymptotic expansion. Lecture Series on "Mathematical Methods in Fluid Mechanics". Von Karman Institute, Brussels, February 1980.

[2] K. Gersten, H. Herwig, P. Wauschkuhn: Theoretical and experimental investigation of two-dimensional flows with separated regions of finite length. Proceedings of AGARD-Symposium on "Computation of Viscous-Inviscid Interaction" in Colorado Springs, Sept. 1980.

[3] K. Gersten, P. Wauschkuhn: Recent research work on separated flows at the University of Bochum. Viscous and Interacting Flow Field Effects, 4th US-FRG-Meeting, 1979, BMVg-FBWT 79-31, 396-407.

[4] W.R. Briley, H. McDonald: Numerical Prediction of Incompressible Separation Bubbles. J. Fluid Mech. 69 (1975), 4, 631-656.

[5] V. Vasanta Ram, S. Kiske: The wall-bounded shear layer with a disturbed turbulence structure. Proceedings of 4th US-FRG DEA-Meeting 1979, BMVg-FBWT 79-31, 481-499.

[6] A.A. Townsend: The structure of turbulent shear flow, Cambridge University Press, 1976 (2nd Ed.).

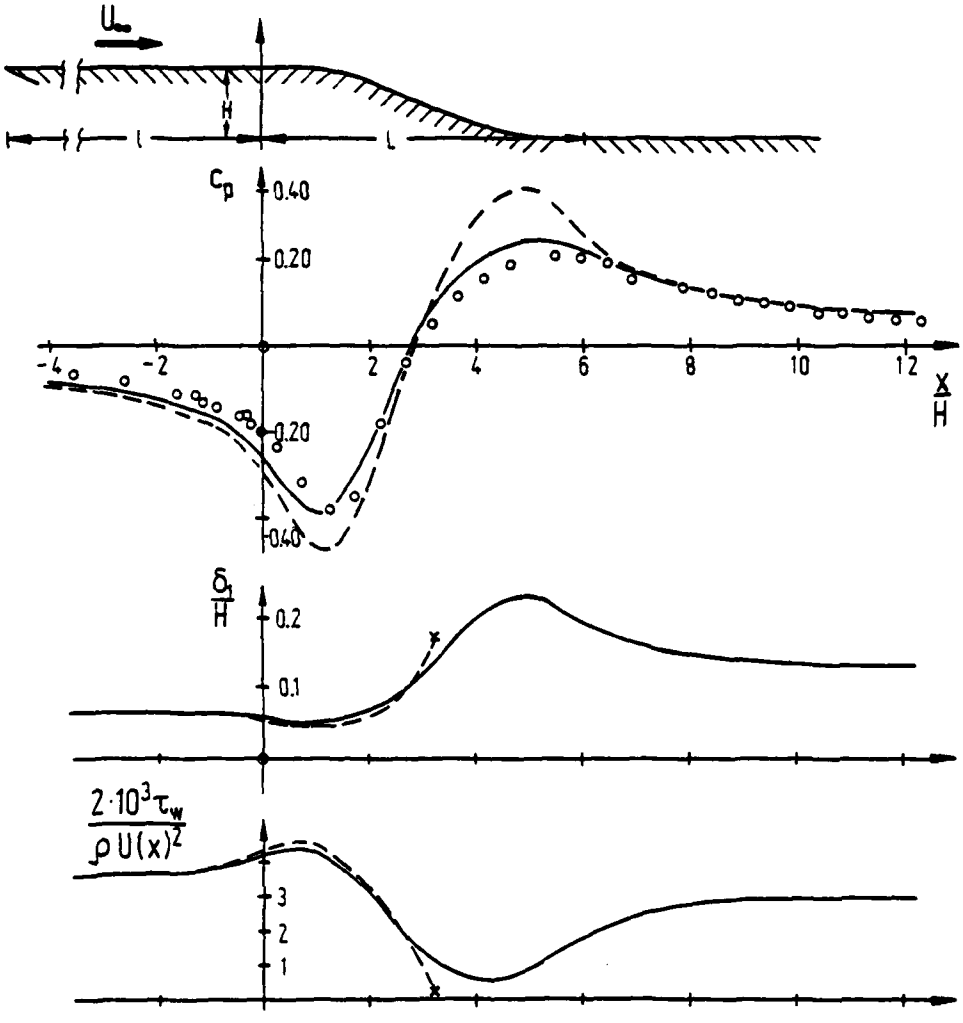

Figure 1. Viscous-Inviscid Interaction of the Flow past a Rounded Backward Facing Step (Turbulent Boundary Layer)

- o Measurement
- ---Theory Neglecting Interaction
- —Theory Including Interaction

$l/L = 5.3$ $H/L = 0.166$

$Re_l = 1.6\cdot10^6$ $Re_H = 5\cdot10^4$

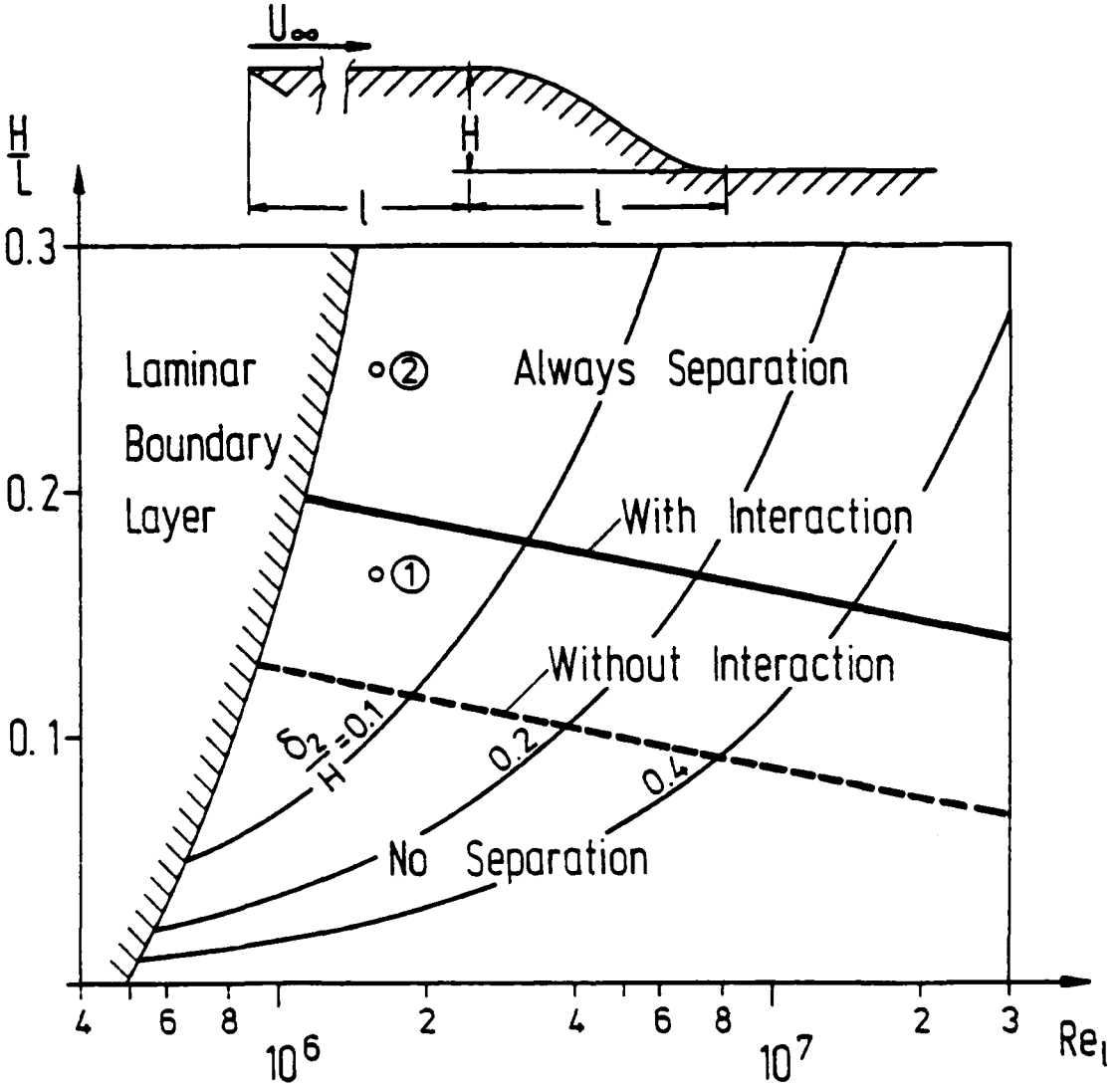

Fig. 2: Viscous - Inviscid Interaction of the Flow past a Rounded Backward Facing Step (Turbulent Boundary Layer). Boundary between Separation and No Separation.

$Re_L = 3.2 \cdot 10^5$ ○ Measurements

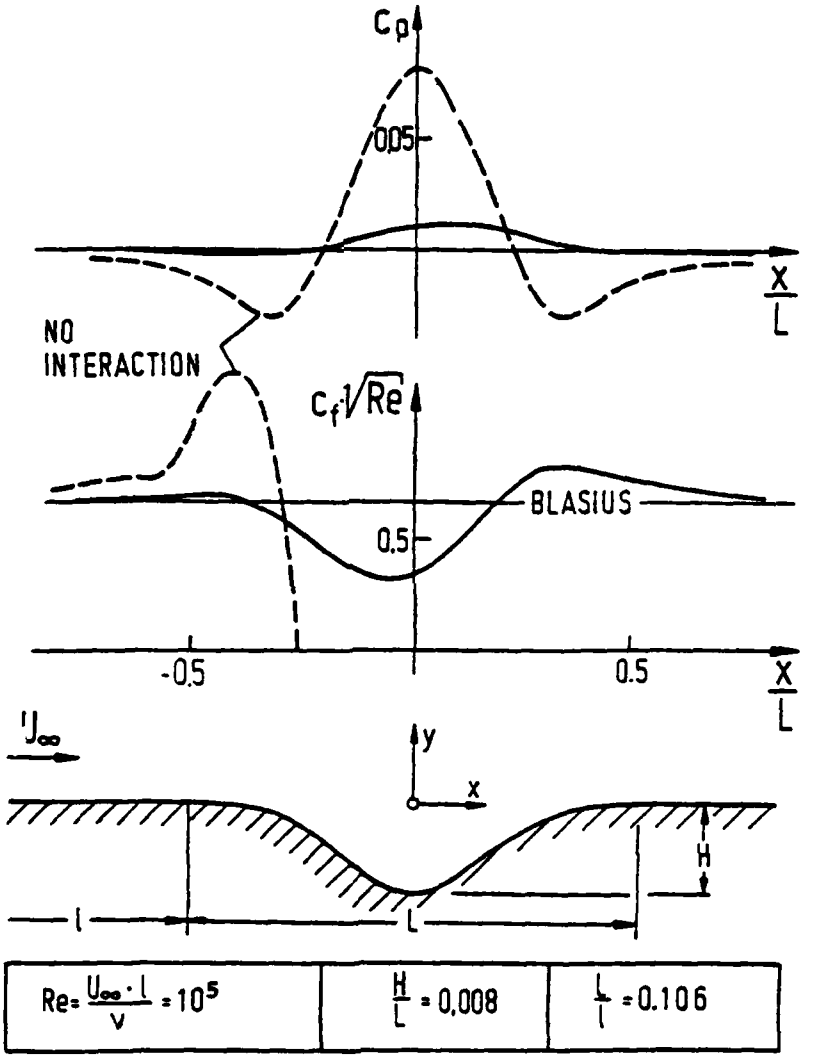

$Re = \frac{U_\infty \cdot l}{\nu} = 10^5$	$\frac{H}{L} = 0.008$	$\frac{L}{l} = 0.106$

Fig. 3: Boundary-Layer Flow over a Dent in a Flat Plate (No Separation)
Laminar Boundary Layer
---Without Interaction
——With Interaction

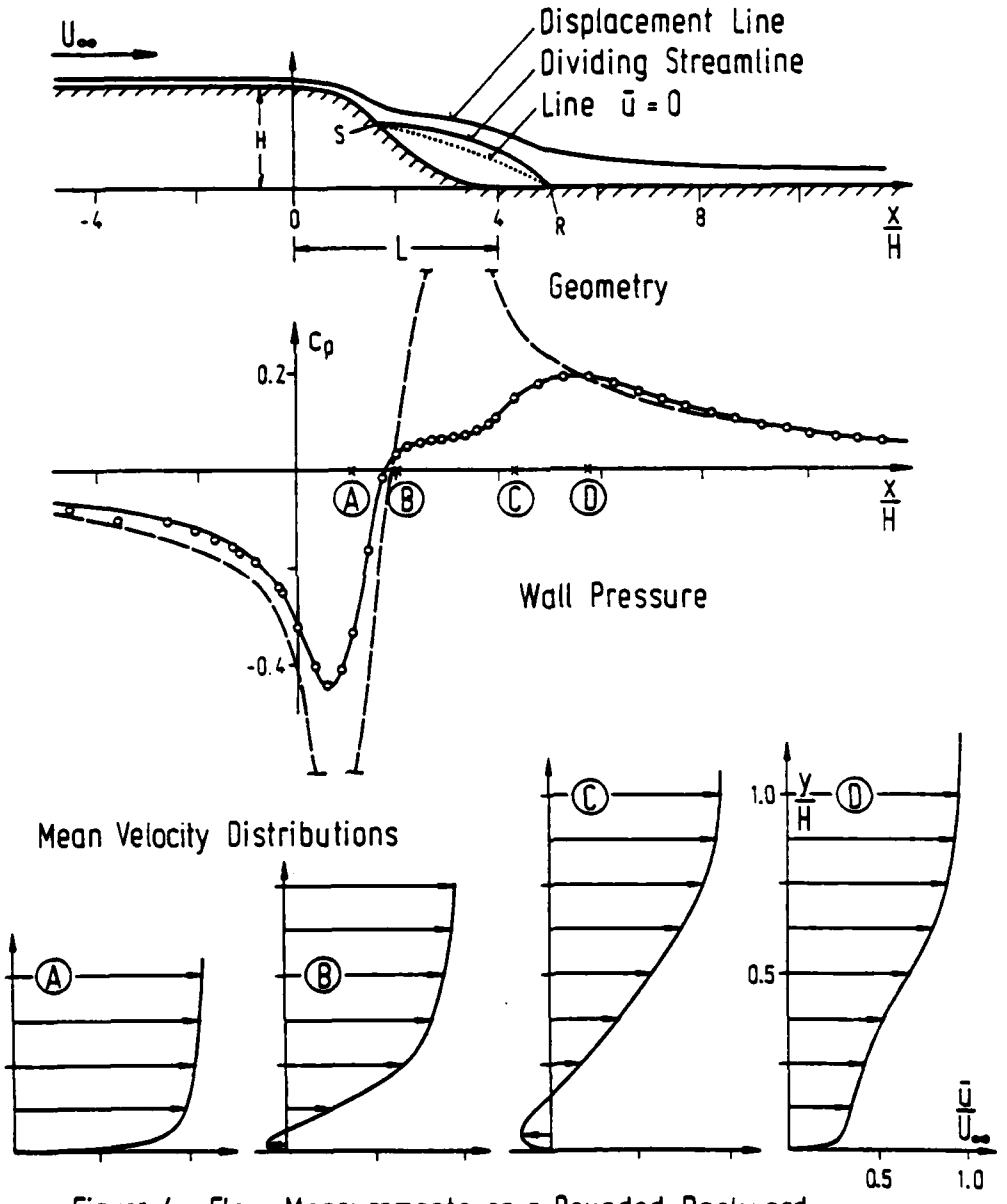

Figure 4: Flow Measurements on a Rounded Backward Facing Step with Separation
$H/L = 0.25$
$Re_l = 1.6 \cdot 10^6$

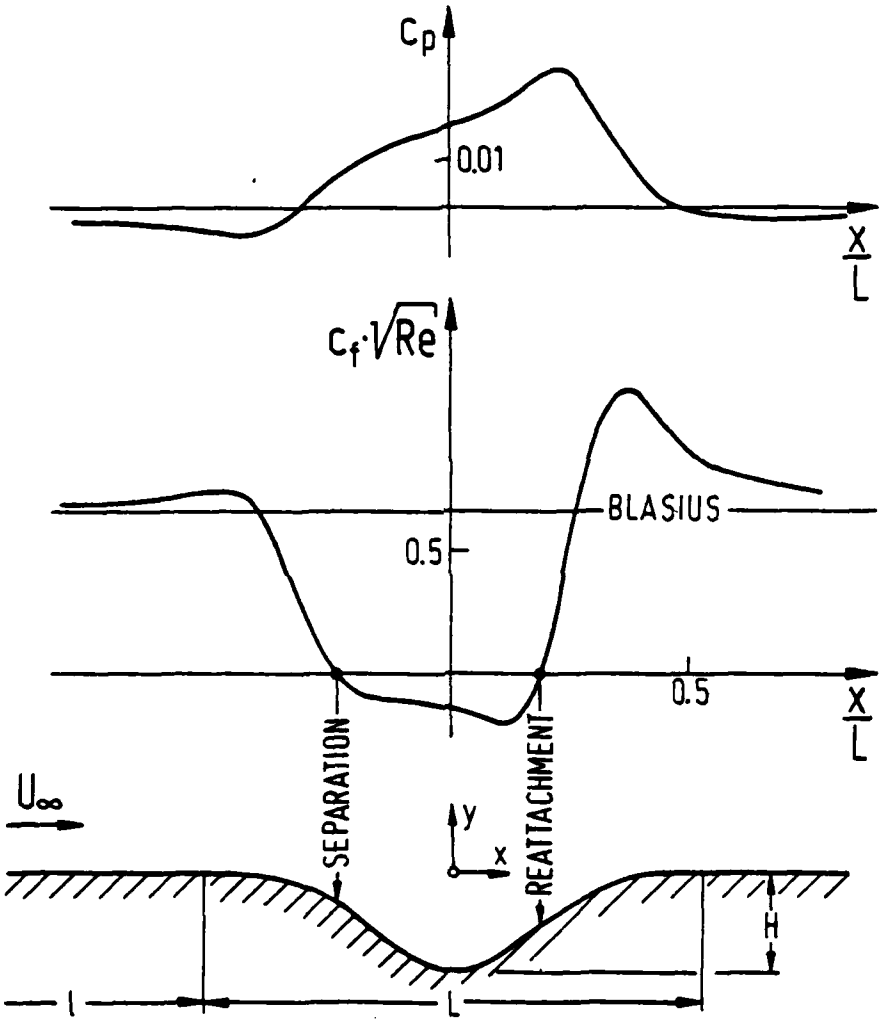

$Re = \frac{U_\infty \cdot l}{\nu} = 10^5$	$\frac{H}{l} = 0.048$	$\frac{L}{l} = 0.106$

Fig.5: Boundary-Layer Flow over a Dent in a Flat Plate (With Separation)

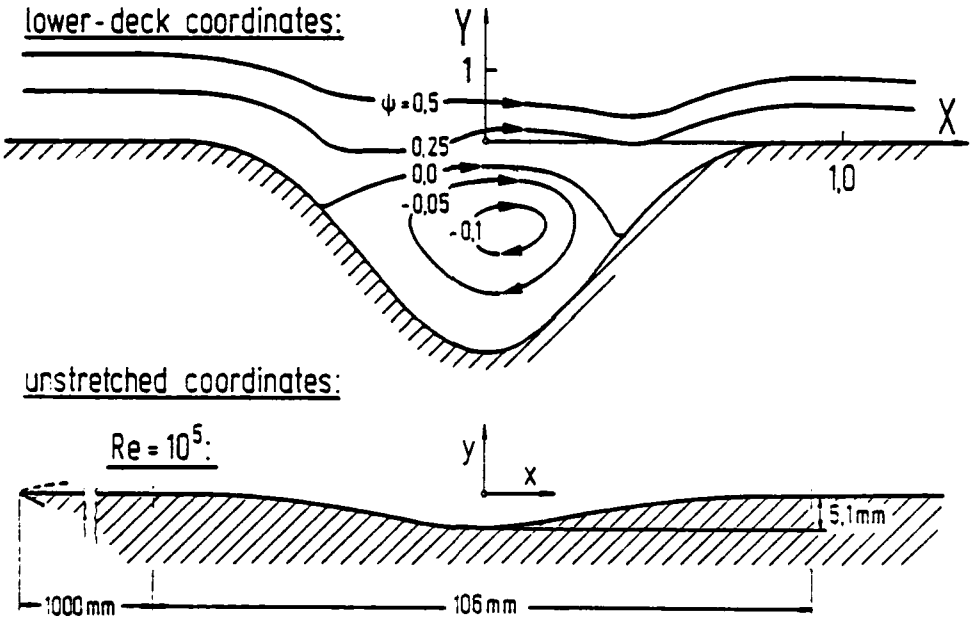

Fig. 6: Boundary-layer Flow over a Dent in a Flat Plate

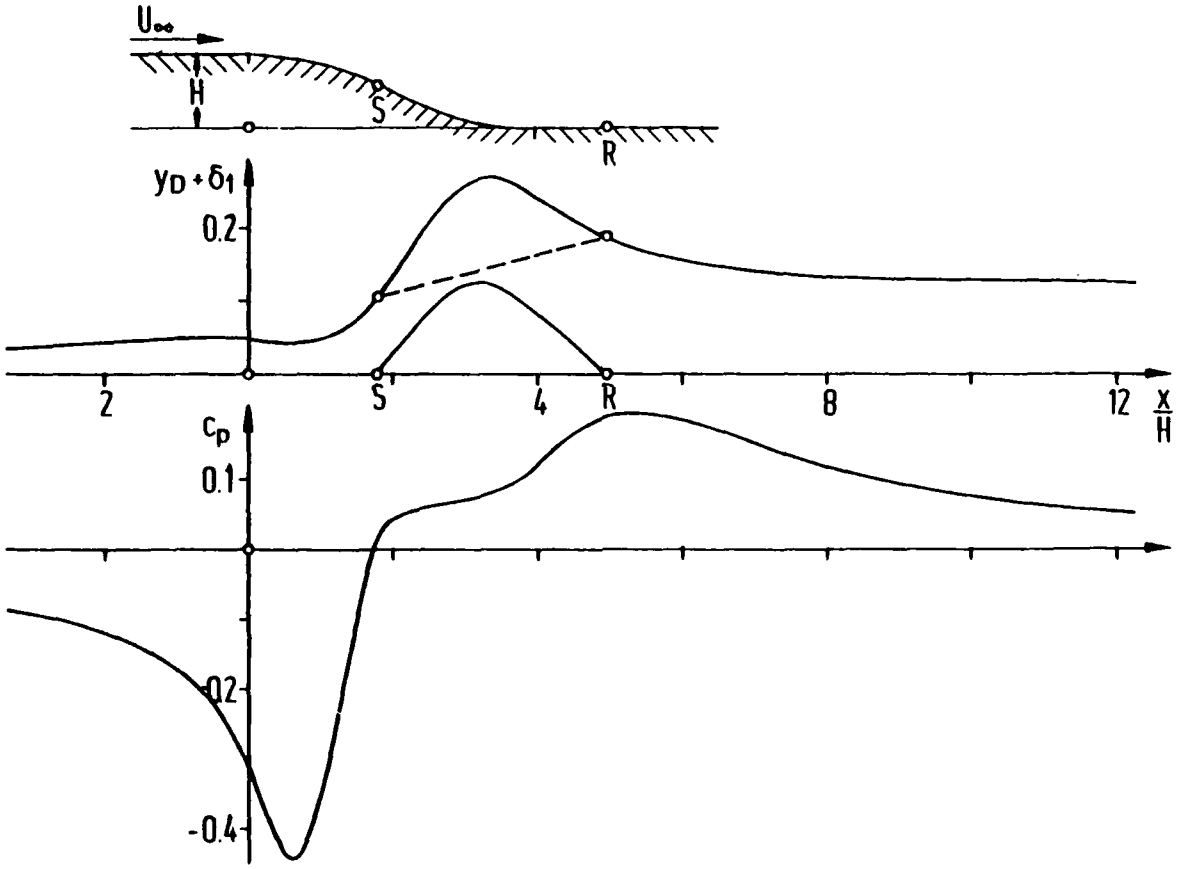

Fig. 7: Viscous - Inviscid Interaction for Turbulent Flows with Separated Regions of Finite Length

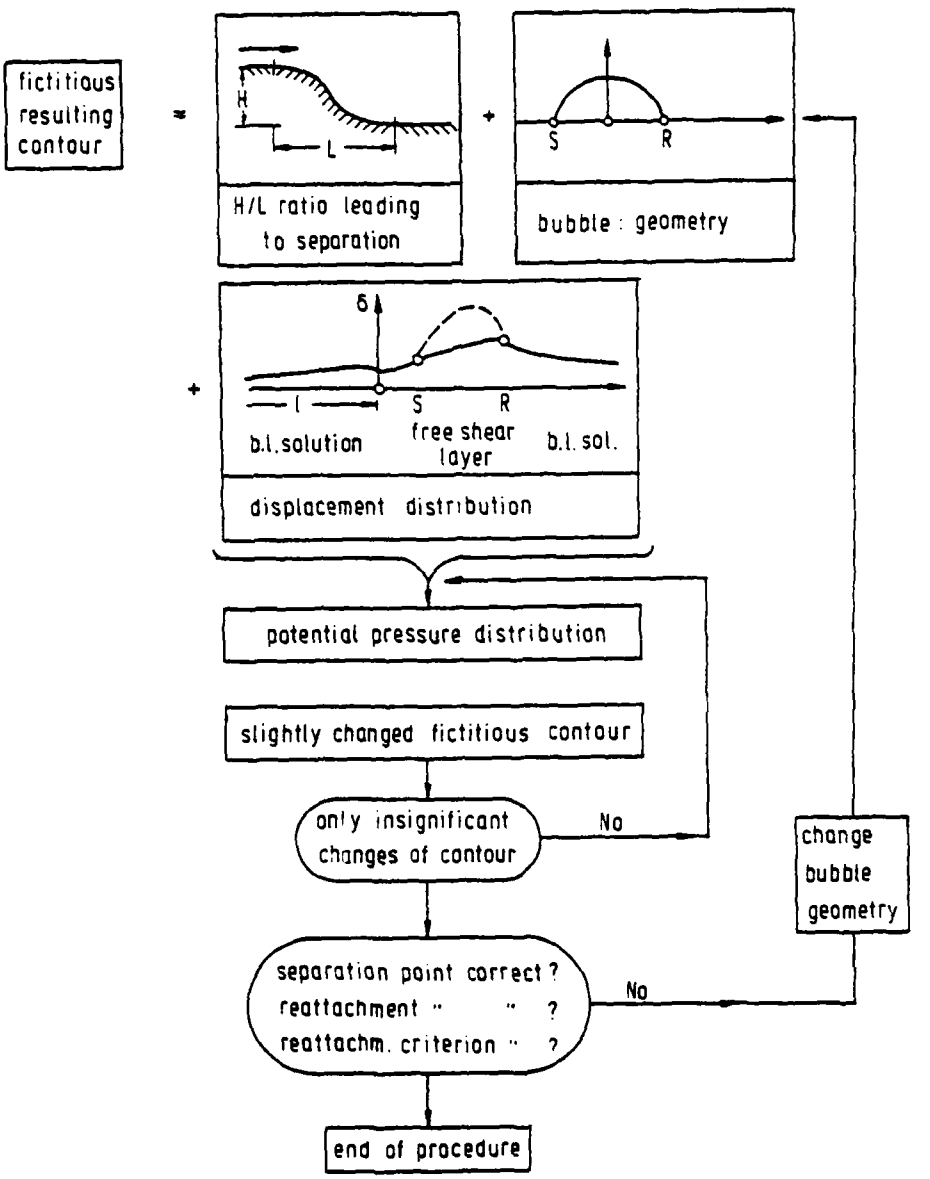

Fig. 8: Schematic Prediction Procedure of Separating Flow Including Viscous - Inviscid Interaction

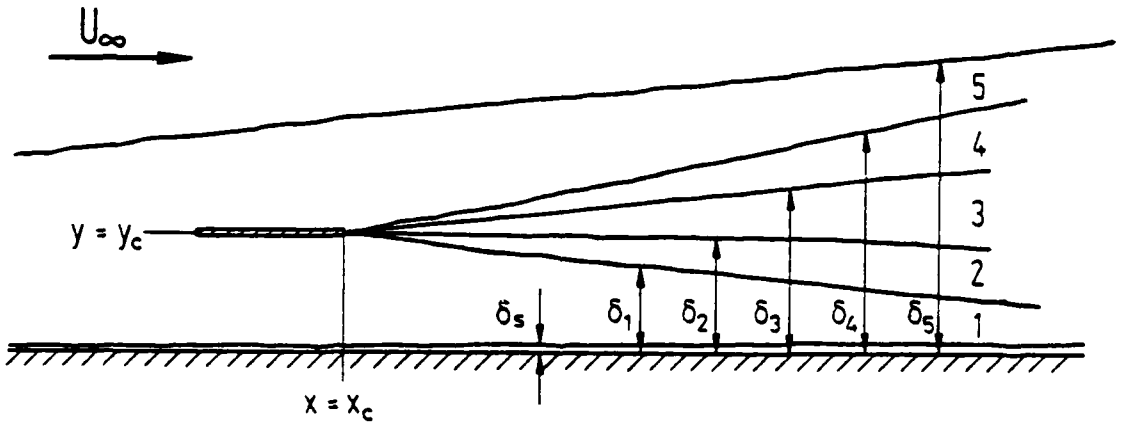

Fig.9: Layer Structure in Disturbed Shear Layer

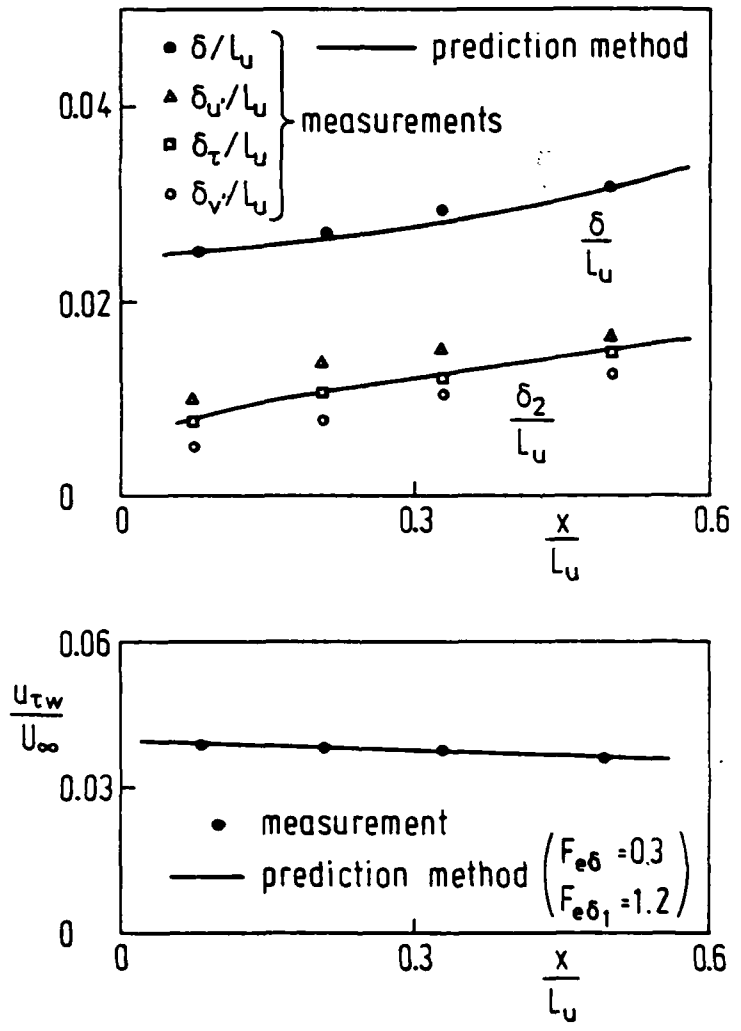

Fig.10: Turbulent boundary layer rough→smooth
Comparison of prediction method with measurements

CALCULATION OF THREE-DIMENSIONAL BOUNDARY LAYERS ON BODIES OF REVOLUTION AT INCIDENCE.

Gert R. Schneider
Deutsche Forschungs- und Versuchsanstalt für Luft- und Raumfahrt
Aerodynamische Versuchsanstalt Göttingen
Bunsenstraße 10, 3400 Göttingen, W - Germany

SUMMARY

A numerical method has been developed for computing three-dimensional incompressible laminar and turbulent boundary layers on bodies of revolution at incidence. The boundary layer calculation is carried out in a streamline coordinate system; the coordinates are fixed to the streamlines and equipotential lines of the inviscid flow.

For the prolate spheroid selected as a special test case for three-dimensional boundary layer calculations the velocity components of the inviscid flow and the development of equipotential lines over the surface are known in a closed analytical form. The development of the streamlines over the surface is calculated by a numerical procedure. The boundary layer equations are integrated by an implicit finite difference method. For the turbulent cases the unknown Reynolds shear - stress terms are modeled by an algebraic three-dimensional mixing length model which is based on an anisotropicaly distributed eddy viscosity.

For the laminar case and different angles of incidence the development of boundary layer parameters are predicted in streamline direction. For this case a comparison with experimental data is used. For the turbulent case the calculations are in preparation.

NOMENCLATURE

x, r, φ	cylindrical coordinates
u_x, u_φ	velocity components in cylindrical coordinates
U	velocity of potential flow
U_∞	velocity of undisturbed flow
q_∞	dynamic head, $q_\infty = \rho_\infty U_\infty/2$
α	angle of incidence of the body
a	major axis of the ellipsoid
b	minor axis of the ellipsoid
Φ, ψ, z	system of rectangular streamline coordinates
u, v, w	velocity components in streamline coordinates
τ_Φ, τ_ψ	shear stress components in streamline coordinates
c_f	local skin friction coefficient, $c_f = \tau_w/(\frac{\rho}{2} U^2)$
δ_2	streamwise momentum thickness, $\delta_2 = \int_0^\delta (1 - \frac{u}{U}) \frac{u}{U} dz$
H_{12}	streamwise shape parameter, $H_{12} = \frac{1}{\delta_2} \int_0^\delta (1 - \frac{u}{U}) dz$
Re	Reynolds number, $Re = \frac{U_\infty \cdot a}{\nu}$
Re_{ref}	reference Reynolds number, $Re_{ref} = \frac{U_\infty \cdot L_{ref}}{\nu}$
L_{ref}	reference length of the experimental investigation, $L_{ref} = 2\ a$
γ_w	cross flow angle at the wall relative to the x-direction

β_w cross flow angle at the wall relative to the outer streamline

INTRODUCTION

In recent years, a number of methods have been developed in order to compute three-dimensional boundary layers.

There are no exact solutions for turbulent boundary layer flows. The governing equations, obtained by means of physical assumptions, can be solved only by numerical methods. Consequently, the problem of solving the turbulent boundary layer equations is both physical and mathematical or numerical. The numerical methods can be divided into two groups - i.e. integral and differential methods. In both groups, calculations can be carried out only if empirical assumptions are made regarding the turbulence.

A systematic comparison between existing methods of calculating three-dimensional turbulent boundary layers was made at the Euromech Kolloquium No. 60 (Trodheim Trials) [1]. The results of the comparison are given and discussed by L.F. East [2].

The quality of a method of calculation must first be judged by experiment. One test case is the NLR infinite swept wing experiment of B. Van den Berg and A. Elsenaar [3].

The experimental observations show that the vector of the shear stress is in general not parallel to the vector of the mean velocity gradient. Following these observations a generalized three-dimensional mixing length model based on an anisotropically distributed eddy viscosity is given by G.R. Schneider [4]. The comparisons with experiments show an improvement of the prediction over the

isotropic calculations. The idea of non-isotropic turbulence in a thin shear layer was transferred by J.C. Rotta [5] to more complex turbulence models, and he was able to show that the generalized mixing length model is a member of a family of turbulence models.

In the special case of the infinite swept wing the numerical method is independent of the second surface coordinate and is similarly constructed as in the two-dimensional case. One reason for the experimental investigation on a body of revolution by H.U. Meier and H.-P. Kreplin [6] at the DFVLR was to give more experimental information in the field of three-dimensional turbulent boundary layers and to give additional information about the Reynolds shear stresses for the closure assumptions.

The laminar boundary layer development on bodies of revolution at incidence (ellipsoids) using differential methods has been extensively studied by K.C. Wang [7,8,9,10,11,12], W. Geißler [13], F.G. Blottner and M.A. Ellis [14] and T. Cebeci et al. [15,16,17, 18]. Integral methods have been developed by E.A. Eichelbrenner and A. Oudart [19], H.W. Stock and H.P. Horton [20]. The three-dimensional mixing length model refers to the local mean streamline. A finite difference method is used based on an orthogonal coordinate system represented by the streamlines and potential lines of the outer inviscid flow. In the present study the differential method of W. Geißler [13,21] which is based on a finite difference scheme of M.G. Hall [22] is used to calculate the three-dimensional boundary layer of the DFVLR ellipsoid.

INVISCID PROBLEM AND STREAMLINE COORDINATES

An ellipsoid of revolution about the major axis of an ellipse is also known as a prolate spheroid.

It is described in a cylindric polar coordinate system (x, r, φ) by

$$x^2 + F^2 r^2 = 1 \quad ; \quad F = \frac{a}{b} \geq 1$$

a and b are the semi-major and semi-minor axes.

Now x and φ denote the surface coordinates along the meridional and circumferential direction.

All length values are non-dimensionalized with respect to the semi-major axis a. The corresponding metric coefficients h_x and h_φ are given by

$$h_x = \sqrt{\frac{1 + x^2(b^2 - 1)}{1 - x^2}}$$

$$h_\varphi = r = b\sqrt{1 - x^2} \quad ; \quad b = \frac{1}{F} \leq 1 \quad .$$

The inviscid velocity components on the surface of a prolate spheroid at incidence α can be derived with the potential of the flow given by H. Lamb [23].

This surface potential Φ which is non-dimensionalized with respect to $U_\infty \cdot a$ may be written

$$\Phi = A_1 x - r A_2 \cos \varphi$$
$$A_1 = V_o \cos \alpha$$
$$A_2 = V_{90} \sin \alpha$$

$$V_o = \frac{(1 - b^2)^{3/2}}{(1 - b^2)^{1/2} - \frac{b^2}{2} \ln \left\{ \frac{1 + (1 - b^2)^{1/2}}{1 - (1 - b^2)^{1/2}} \right\}}$$

$$V_{90} = \frac{2 V_o}{2 V_o - 1} \quad .$$

The velocity components are given by

$$u_x = \frac{1}{h_x} \frac{\partial \Phi}{\partial x} = A_1 \cos \gamma + A_2 \sin \gamma \cos \varphi$$

$$V_\varphi = \frac{1}{h_\varphi} \frac{\partial \Phi}{\partial_\varphi} = A_2 \sin \varphi$$

$$U = \sqrt{u_x^2 + v_\varphi^2}$$

$$\cos \gamma = \frac{1}{h_x} \quad .$$

The absolute value $|x_o|$ of the x-coordinate of the stagnation point is given by

$$|x_o| = \frac{A_1}{\sqrt{A_1^2 + b^2 A_2^2}}$$

with the potential $\Phi_o = -\frac{A_1}{|x_o|}$ at the stagnation point. A standard form for the potential in the range $0 \leq \tilde{\Phi} \leq 1$ is defined by

$$\tilde{\Phi} = \frac{1}{2} \left(\frac{\Phi_o - \Phi}{\Phi_o} \right)$$

with $\frac{\Phi}{\Phi_o} = - |x_o| \cdot x + \cos\varphi \sqrt{1 - x_o^2} \sqrt{1 - x^2}$.

$$\tilde{\Phi} = \frac{1}{2} \left(|x_o| \cdot x - \cos\varphi \sqrt{1 - x_o^2} \sqrt{1 - x^2} + 1 \right)$$

Setting Φ = const. a family of equipotential lines result. These equipotential lines are ellipses which are nearly perpendicular to the free stream velocity and the centre of these ellipses are all on the line given by the front and the rear stagnation points of the prolate spheroid.

With h_Φ and h_ψ being the metric coefficients for the streamline coordinates the actual differential lengths along the equipotential lines become

$$d n = h_\psi \, d\psi$$

and along the streamlines

$$d s = h_\Phi \, d \Phi \ .$$

The metric coefficient h_Φ is defined by

$$h_\Phi = \frac{1}{U} \ .$$

The metric coefficient h_ψ must be calculated by a numerical procedure.

The surface streamlines are calculated starting from a selected equipotential line near the front stagnation point. The differential equations for the streamlines in the form

$$\frac{d x}{d s} = \frac{u_x}{h_x U} \ , \qquad \frac{d \varphi}{d s} = \frac{v_\varphi}{h_\varphi U}$$

are integrated numerically by a Runge - Kutta method.

With this numerical procedure a complete set of streamline coordinates can be calculated. The mesh sizes formed by the streamlines and equipotential lines must be controlled by the Courant - Friedrich - Levy stability condition. This condition is based on the concept of the zone of dependence. To fulfill the stability condition the streamlines have to be reorientated several times along equipotential lines.

More information about the construction of a streamline coordinate system about a prolate spheroid is given by W. Geißler [21] and K.C. Wang [24].

BOUNDARY LAYER EQUATIONS AND THE TURBULENCE MODEL

The boundary layer equations for steady three-dimensional incompressible flow are given in terms of the streamline coordinates (Φ, ψ, z) and their corresponding velocities (u, v, w) in dimensionless form. z is normal to the body surface.

The equation of continuity is

$$\frac{\partial u}{h_\Phi \partial \Phi} + \frac{\partial v}{h_\psi \partial \psi} + \frac{\partial w}{\partial z} - K_1 u - K_2 v = 0$$

The equation of momentum in Φ-direction is

$$u \frac{\partial u}{h_\Phi \partial \Phi} + v \frac{\partial u}{h_\psi \partial \psi} + w \frac{\partial u}{\partial z} - K_2 uv + K_1 v^2 = U \frac{\partial U}{h_\Phi \partial \Phi} + \frac{\partial (\frac{\tau_\Phi}{\rho})}{\partial z} .$$

The equation of momentum in ψ-direction is

$$u \frac{\partial v}{h_\Phi \partial \Phi} + v \frac{\partial v}{h_\psi \partial \psi} + w \frac{\partial v}{\partial z} - K_1 uv + K_2 (u^2 - U^2) = \frac{\partial (\frac{\tau_\psi}{\rho})}{\partial z}$$

The boundary conditions are

$$z = 0 \qquad u = 0 \qquad v = 0 \qquad w = 0$$

$$z = \infty \qquad u = U \qquad v = 0 \quad .$$

The local curvature parameters K_1 and K_2 are defined as follows

$$K_1 = - \frac{1}{h_\psi h_\Phi} \frac{\partial h_\psi}{\partial \Phi} \quad ; \qquad K_2 = - \frac{1}{h_\Phi h_\psi} \frac{\partial h_\Phi}{\partial \psi} \quad .$$

The Reynolds shear stress terms are described by the general mixing length model developed for three-dimensional flows by G. R. Schneider [4].

The shear stress terms are given by

$$\frac{\tau_\Phi}{\rho} = (\varepsilon + \frac{1}{Re}) \frac{\partial u}{\partial z} - (1 - T)\, \varepsilon \frac{v}{u_r} h$$

$$\frac{\tau_\psi}{\rho} = (\varepsilon + \frac{1}{Re}) \frac{\partial v}{\partial z} + (1 - T)\, \varepsilon \frac{u}{u_r} h \quad .$$

The scalar eddy viscosity ε assumes the following form

$$\varepsilon = L^2 \{ (\frac{\partial u}{\partial z})^2 + (\frac{\partial v}{\partial z})^2 - (1 - T) h^2 \}^{1/2}$$

where the function h summarizes the expression

$$h = \frac{v}{u_r} \frac{\partial u}{\partial z} - \frac{u}{u_r} \frac{\partial v}{\partial z}$$

$u_r = (u^2 + v^2)^{1/2}$ is the resultant mean velocity .

For the mixing length $L = F \cdot l$ the formula by R. Michel et al. [25] is used.

$$\frac{l}{\delta} = \frac{l_e}{\delta} \tanh \left(\frac{\varkappa}{l_e/\delta} \frac{z}{\delta} \right)$$

$$\frac{l_e}{\delta} = \text{const} = 0.08, \qquad \varkappa = 0.41$$

δ is the boundary layer thickness.

In the neighbourhood of the viscous sublayer at the wall, and at the edge of the boundary layer the mixing length l is multiplied by a dimensionless corrective function

$$F = 1 - \exp(-\omega)$$

$$\omega = \mathrm{Re} \cdot l \sqrt{\frac{\tau}{\rho}} \; / \; 10.66$$

$\frac{\tau}{\rho} = \sqrt{(\frac{\tau_\Phi}{\rho})^2 + (\frac{\tau_\psi}{\rho})^2}$ is the local value of the shear stress.

The three-dimensional turbulence model described here is fixed by the numerical values of the two dimensionless parameters T and l_e/δ .

The value T is a measure for the anisotropy of the eddy viscosity in planes where z = const. T has the value $0 < T \leq 1$. The special case of isotropic eddy viscosity distribution is represented by T = 1.0.

NUMERICAL METHOD

The boundary layer equations will be solved in physical coordinates. An implicit finite difference scheme of the Crank-Nicholson type investigated by M.G. Hall [22] and also used by W. Geißler [13] is introduced.

In contrast to the two-dimensional case, this method is not always stable. A numerical stability condition, namely the Courant - Friedrich - Levy condition, must be satisfied through the boundary layer.

To start the numerical calculation initial boundary layer profiles near the front stagnation point over two successive equipotential lines are constructed with the stagnation point boundary layer solution of L. Howarth [26].

The differential quotients are approximated by finite differences around the central point of the difference scheme.

Since the velocity profiles of turbulent boundary layer flows vary greatly near the wall, the spaces between grid points for forming the difference expressions for the derivatives in the z-direction must be very small in this region.

With a coordinate transformation similar to that described by G. R. Schneider [4] the variably spaced z-coordinate is transformed into a new coordinate divided into equal intervals. For the z-direction for all calculation stations the same number of grid points is used. This means that all distances normal to the surface are referenced to the boundary layer thickness δ .

The three difference equations are linearized and decoupled by an iterative procedure. The starting values for this iterative procedure are extrapolated from the values of the last two upstream stations.

The computation process marches from netpoint to netpoint along the equipotential lines including both lines of symmetry. For each equipotential line the calculations are started at the line of symmetry on the windward side.

The numerical calculation can be extended over the body surface until a point is reached, where the stability condition is violated. The computation can be extended downstream of the first numerical instability point by always marching along equipotential lines until numerical instability occurs.

The so determined instability line is interpreted as a separation line of the free vortex layer type. The separation line ends at the windward symmetry line of the potential flow, where reversed flow occurs in the boundary layer.

COMPUTATIONAL RESULTS

For all calculations a prolate spheroid with $F = \frac{a}{b} = 6$ is used. This is the form of the body of revolution selected for the experimental program at the DFVLR. For comparison between the prediction and measurements a reference Reynolds numer $Re_{ref} = U_\infty \cdot L_{ref}/\nu$ is defined. This reference Reynolds number is formed with the reference length $L_{ref} = 2\,a$ of the experimental investigation.

a. laminar case

In the laminar case the boundary layer equations are independent of the Reynolds number Re if the quantities z and w are multiplied by $Re^{1/2}$. To take this into consideration for the numerical method the Reynolds number Re must be set equal to one in the shear stress terms. The velocity components in equipotential and streamline direction, together with the boundary layer thickness are calculated for each equipotential line by the numerical boundary layer method. Each equipotential line is described by the standard form potential $\tilde{\Phi}$. The velocity components are used to calculate four characteristic boundary layer parameters all relative to the direction of external streamline.

These parameters are the cross flow angle at the wall β_w, the local skin friction coefficient

$$c_f = \frac{\tau_w}{\frac{\rho}{2} U^2}$$

and the two integral boundary layer parameters, the momentum thickness

$$\delta_2 = \int_0^{\delta} (1 - \frac{u}{U}) \frac{u}{U} \, dz$$

and the shape parameter

$$H_{12} = \frac{1}{\delta_2} \int_0^{\delta} (1 - \frac{u}{U}) \, dz$$

In Fig. 1 to 16 the development of the selected four characteristic boundary layer parameters over the ellipsoid at different angles of attack $\alpha = 5^{\circ}$, 10°, 15° and 30° are given for the ellipsoid F = 6. The development of these boundary layer parameters are similar to that calculated by W. Geißler [21] and by H.W. Stock [27]. The last one uses an integral prediction method. With an increase in the angle of incidence the separation line moves in the upstream direction.

In Fig. 17 to 19 the calculated streamline coordinate systems are given for $\alpha = 10^{\circ}$, 15° and 30°. The number of new orientations increases with larger incidence. In these figures the location of the free vortex layer separation lines are plotted in a side view of the body.

In Fig. 20 to 25 the predicted dimensionless wall shear stress values are compared with the measured values. The comparison is made for $\alpha = 10^{\circ}$ and $\alpha = 30^{\circ}$ angle of attack and the following three measurement stations of the DFVLR experiment

station 3 with x/a = - 0.554
station 6 with x/a = - 0.040
station 9 with x/a = + 0.476.

These selected stations represent the behavior of the flow situation in the front, in the middle and in the back part of the ellipsoid. In Fig. 26 to 31 a comparison between the predicted and measured cross flow angle at the wall $\gamma_w = \gamma_e + \beta_w$ are given for the same angles of attack and the same three measuring stations. The angle γ_w is related to the direction of the x-axis of the body oriented coordinate system of the DFVLR experiment. The comparison between the predicted and the measured values shows that all the τ_w-values are overpredicted and that with an increase in the angle of incidence the difference to the measured values increases. For the γ_w-values and $\alpha = 10^o$ the predicted values are over the measured values, the difference is small. For $\alpha = 30^o$ the situation is contrary to the $\alpha = 10^o$ values. The difference is greater and the measured values are over the calculated values. These discrepancies are a result of the difference between the pressure distribution used for the numerical calculations and the pressure distribution given by the experiment. These differences grow by increasing the angle of attack. The predicted separation points follow roughly the experimental trend.

b. turbulent case

For the turbulent case the calculations are underway and will be reported upon later. In this case the boundary layer equations are not independent of the Reynolds number Re. And therefore the mesh widths must decrease, if the Reynolds number Re is increased. The first test calculations confirmed this effect. This seems to be a disadventage of the physical coordinates selected for these calculations.

CONCLUDING REMARKS

For the laminar flow there are no problems with the selected numerical method. The difference between predicted and measured wall shear stress values is a result of the difference between the theoretical pressure distribution used for the numerical calculations and the pressure distribution given by the experiment. It seems to be promising to recalculate the laminar boundary layer flow with the measured pressure distributions for a comparison test with the experimental data of the DFVLR experiment.

For the turbulent flow it seems that in the numerical method a similarity transformation must be investigated for the streamline coordinates to reduce computer time and storage for future calculations.

REFERENCES

[1] Fanneloep, T.K.
Krogstadt, P.A.
Three-Dimensional Turbulent Boundary Layers in External Flows: A Report on Euromech 60
J. Fluid Mech. 71 (1975), pp. 815-826

[2] East, L.F.
Computation of Three-Dimensional Turbulent Boundary Layers
FFA TN AE-1211 (1975), pp. 1-86

[3] Van den Berg, B.
Elsenaar, A.
Measurements in a Three-Dimensional Incompressible Turbulent Boundary Layer in an Adverse Pressure Gradient Under Infinite Swept Wing Conditions.
NLR TR 72092 U (1972), pp. 1-31

[4] Schneider, G.R. — Die Berechnung der turbulenten Grenzschicht am schiebenden Flügel unendlicher Spannweite mittels eines dreidimensionalen Mischungswegmodells.
DLR-FB 77-73 (1977/78), S. 1-61
English Translation:
Calculation of the Turbulent Boundary Layer on an Infinite Swept Wing Using a Three-Dimensional Mixing Length Model
ESA-TT-534, July 1979

[5] Rotta, J.C. — A Family of Turbulence Models for Three-Dimensional Thin Shear Layers
Proceedings: 1st Symposium on Turbulent Shear Flows, April 18-20, 1977, University Park, Pennsylvania/USA, Vol.I, pp. 10.27 to 10.34

[6] Meier, H.U.
Kreplin, H.-P. — Experimental Investigation of the Transition and Separation Phenomena on a Body of Revolution.
Proceedings: 2nd Symposium on Turbulent Shear Flows, July 2-4, 1979, Imperial College, London Vol.II, pp. 15.1 to 15.7

[7] Wang, K.C. — Three-Dimensional Boundary Layer Near the Plane of Symmetry of a Spheroid at Incidence.
J. Fluid Mech. Vol.43, pp. 187-209, (1970)

[8] Wang, K.C. — Separation Patterns of Boundary Layers over an Inclined Body of Revolution
AIAA J. Vol. 10, pp. 1044-1050 (1972)

[9] Wang, K.C. — Boundary Layer over a Blunt Body at High Incidence with a Open-Type of Separation.
Proc. Roy. Soc., London, A340, pp. 33-55, (1974)

[10] Wang, K.C. — Boundary Layer over a Blunt Body at Low Incidence with Circumferential Reversed Flow
J. Fluid Mech. Vol.72, pp. 49-65, (1975)

[11] Wang, K.C. — Laminar Boundary Layer over a Body of Revolution at Extremely High Incidence
Phys. Fluid, Vol. 17, p. 1381-1385, (1974)

[12] Wang, K.C. — Laminar Boundary Layer Near the Symmetry Plane of a Prolate Spheroid
AIAA J., Vol.12, p. 949-958, (1974)

[13] Geißler, W. — Berechnung der dreidimensionalen laminaren Grenzschicht an schrägangeströmten Rotationskörpern mit Ablösung
Ing. Archiv 43 (1974) S. 413-425

[14] Blottner, F.G.
Ellis, M.A. — Finite-Difference Solution of the Incompressible Three-Dimensional Boundary Layer Equations for a Blunt Body
Computer & Fluids Vol.1, pp. 133-158(1979)

[15] Cebeci, T.
Khattab, A.A.
Stewartson, K. — Prediction of the Three-Dimensional Laminar and Turbulent Boundary Layers on Bodies of Revolution at High Angles of Attack.
Proceedings: 2nd Symposium on Turbulent Shear Flows, July 2-4, 1979, Imperial College, London Vol.II, pp. 15.8 to 15.13

[16] Cebeci, T.
Khattab, A.A.
Stewartson, K. — Studies on Three-Dimensional Laminar and Turbulent Boundary Layer on Bodies of Revolution at Incidence. I. Nose Separations.
AIAA-Paper 79-138 (1979)

[17] Cebeci, T. — Progress in the Calculation of Three-Dimensional Boundary Layers on Bodies of Revolution at Incidence
Aeromech. Div. Air Force Flight Dyn.Lab. Wright-Patterson Air Force Base, Ohio/USA
Technical Report AFFDL-TR-78-111(1978)

[18] Hirsh, R.S.
Cebeci, T.
Calculation of Three-Dimensional Boundary Layers with Negative Cross Flow on Bodies of Revolution
AIAA-Paper 77-683 (1977)

[19] Eichelbrenner, E.A.
Oudart, A.
Méthode de la couche limite tridimensionelle Application à un corps fuselé incliné sur le vent
ONERA Publ. 76 (1955)

[20] Stock, H.W.
Horton, H.P.
Ein Integralverfahren zur Berechnung dreidimensionaler, laminarer, kompressibler adiabater Grenzschichten.
Dornier Bericht Do 79-22/B (1979)

[21] Geißler, W.
Berechnung der laminaren, dreidimensionalen Grenzschicht an unsymmetrisch umströmten Rotationskörpern mittels Differenzenverfahren.
DFVLR-AVA-Bericht IB 251-73A19 (1973)

[22] Hall, M.G.
A Numerical Method for Calculating Steady Three-Dimensional Laminar Boundary Layers.
RAE TR 67145 (1967)

[23] Lamb, H.
Hydrodynamics
Cambridge University Press (1932)

[24] Wang, K.C.
Three-Dimensional Laminar Boundary Layer over Body of Revolution at Incidence.
Part 1. Method of Calculation
RIAS TR 68-14 (1968)

[25] Michel, R.
Cousteix, J.
Quermard, C.
Application d'un schéma améliore de longueur de mélange à l'étude des couches limites turbulentes tridimensionelles.
AGARD Meeting on Turbulent Shear Flows, London Sept. 1971,
AGARD CP 93 (1972)

[26] Howarth, L. The Boundary Layer in Three-Dimensional Flow, Part 2: The Flow Near a Stagnation Point.
Phil. Mag. 42 (1951) pp. 1433-1440

[27] Stock, H.W. Three-Dimensional Boundary Layers on Wings and Bodies of Revolution.
Aeromech. Div. Air Force Flight Dyn.Lab.
Wright-Patterson Air Force Base, Ohio/USA
Technical Report AFFDL-TR-78-111(1978)

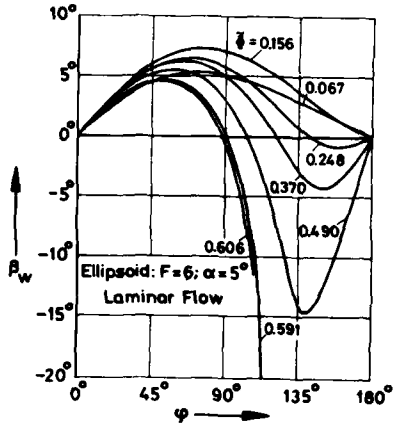

Fig. 1 α = 5° angle of attack

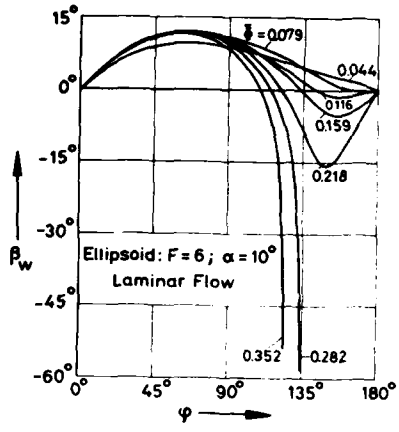

Fig. 2 α = 10° angle of attack

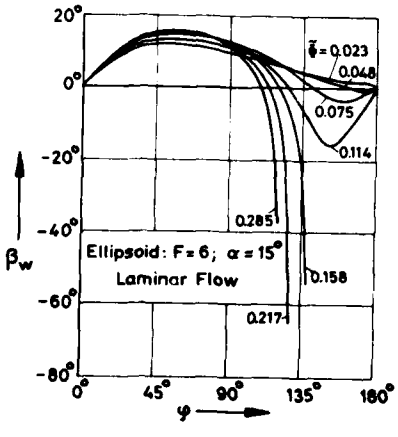

Fig. 3 α = 15° angle of attack

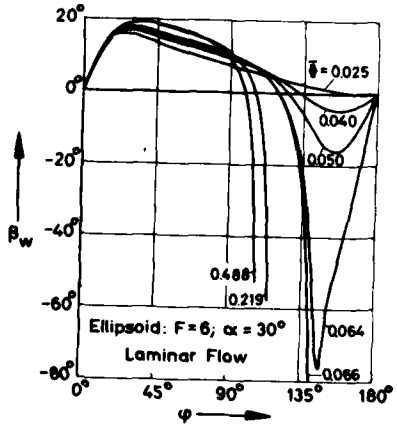

Fig. 4 α = 30° angle of attack

Curve of the cross flow angle at the wall relative to the direction of the external streamline for different equipotential lines ($\tilde{\Phi}$ = const.)

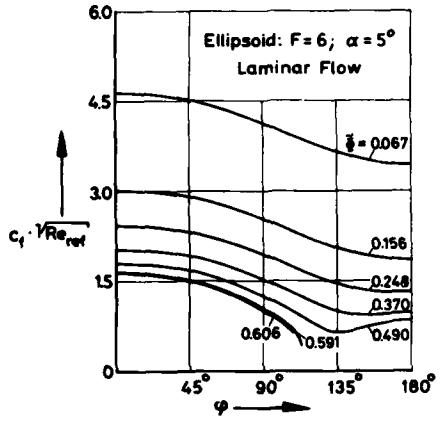

Fig. 5 α = 5° angle of attack

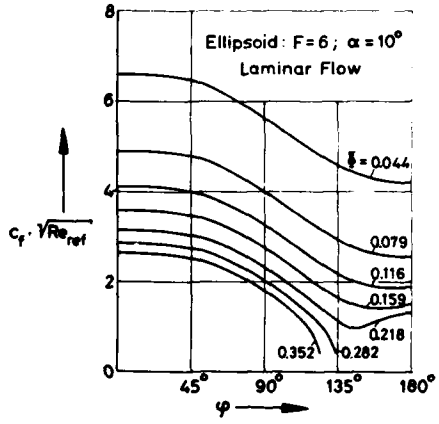

Fig. 6 α = 10° angle of attack

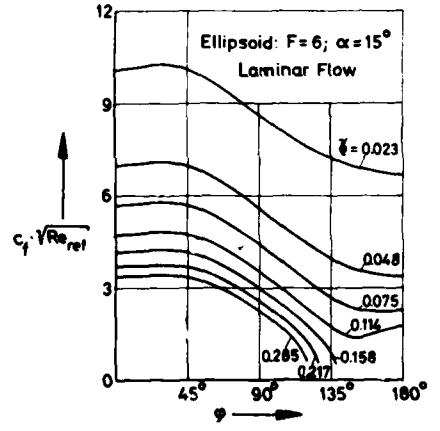

Fig. 7 α = 15° angle of attack

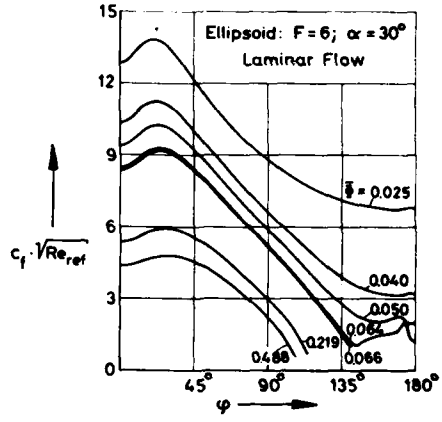

Fig. 8 α = 30° angle of attack

Curve of the local skin friction coefficient relative to the external streamline for different equipotential lines ($\tilde{\Phi}$ = const.)

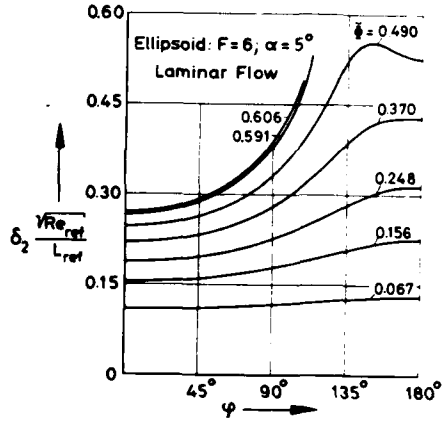

Fig. 9 α = 5° angle of attack

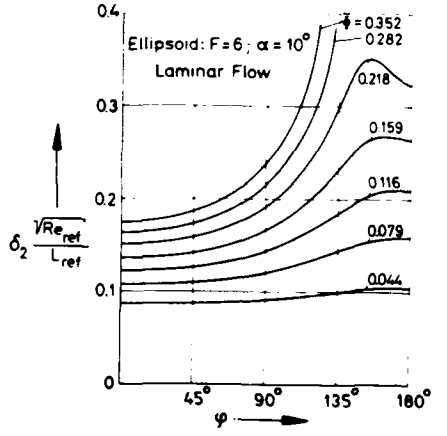

Fig. 10 α = 10° angle of attack

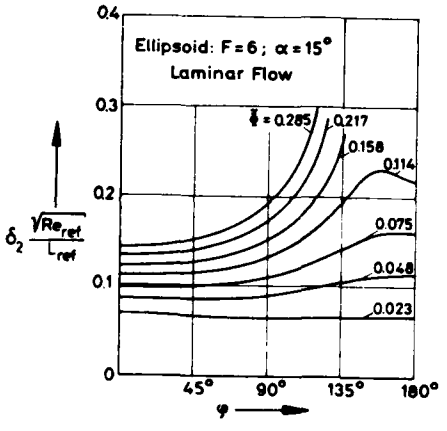

Fig. 11 α = 15° angle of attack

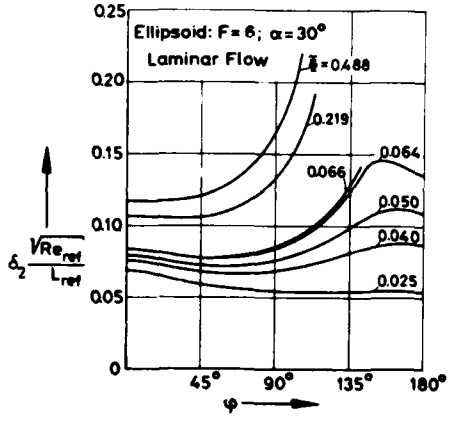

Fig. 12 α = 30° angle of attack

Curve of the streamwise momentum thickness for different equipotential lines ($\bar{\Phi}$ = const.)

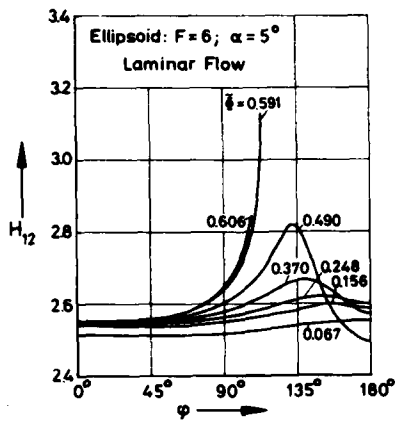

Fig. 13 α = 5° angle of attack

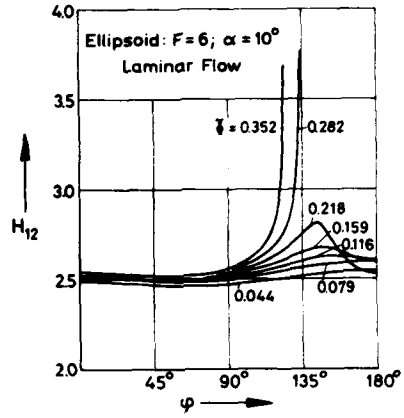

Fig. 14 α = 10° angle of attack

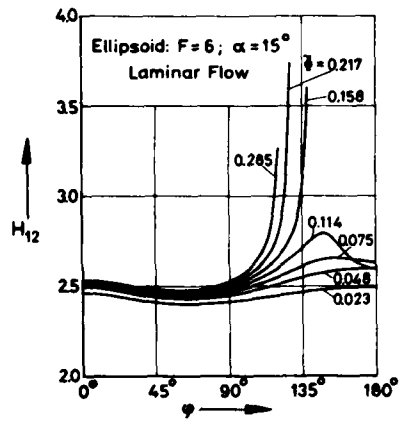

Fig. 15 α = 15° angle of attack

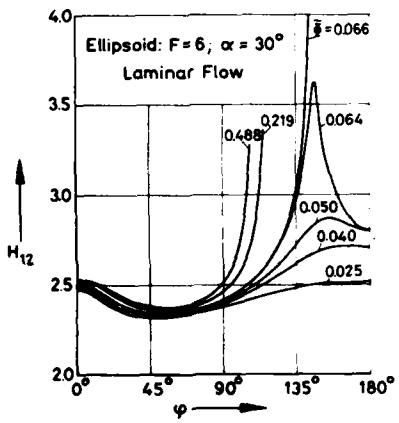

Fig. 16 α = 30° angle of attack

Curve of the streamwise shape parameter for different equipotential lines ($\tilde{\Phi}$ = const.)

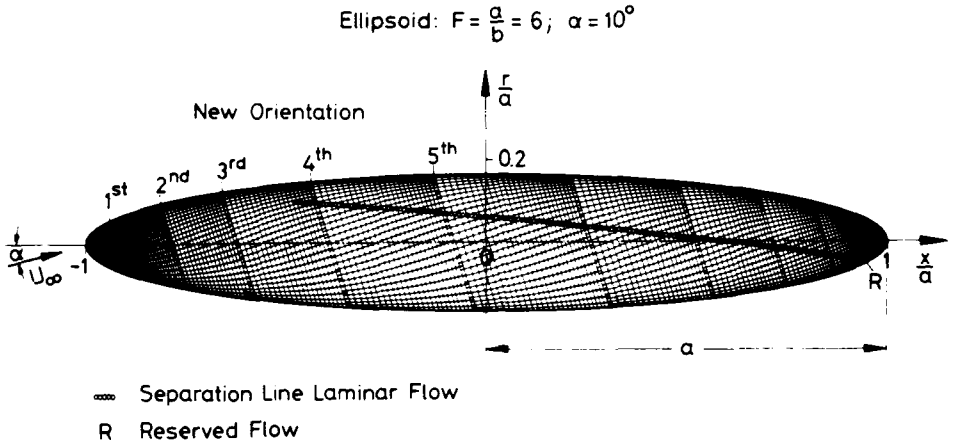

Fig. 17 Streamline net with the separation line for an ellipsoid of revolution at $\alpha = 10^{\circ}$ angle of attack.

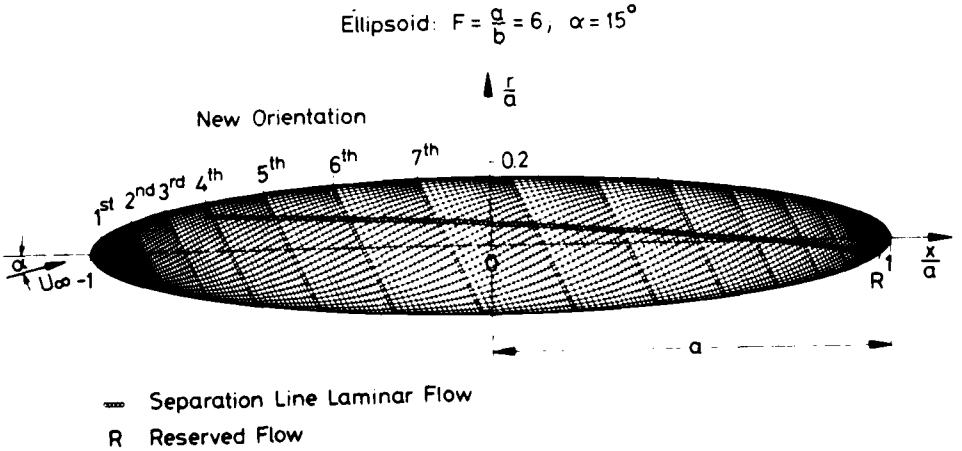

Fig. 18 Streamline net with the separation line for an ellipsoid of revolution at $\alpha = 15^{\circ}$ angle of attack.

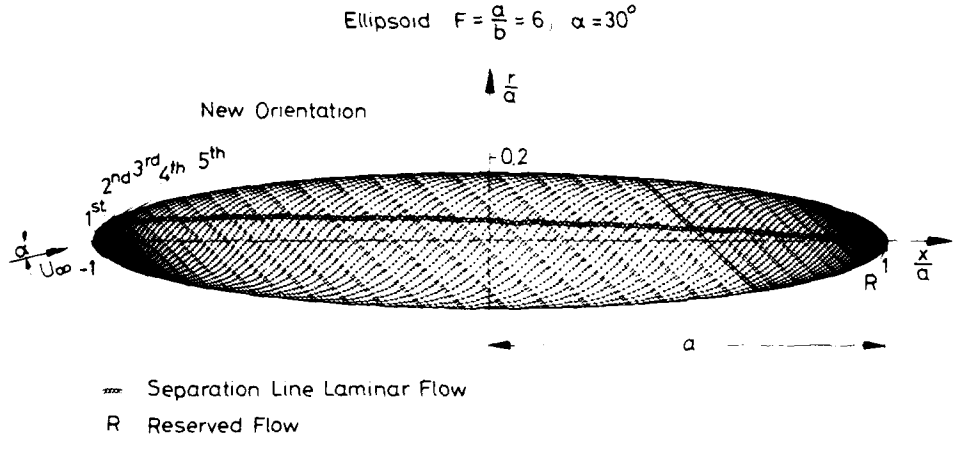

Fig. 19 Streamline net with the separation line for an ellipsoid of revolution at α = 30° angle of attack.

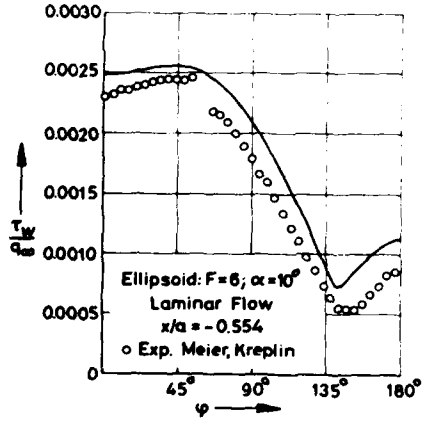

Fig. 20 α = 10° angle of attack

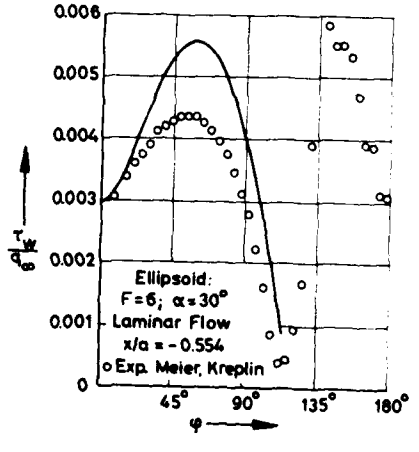

Fig. 21 α = 30° angle of attack

Comparison between the calculated and measured wall shear stress values at measuring station 3 with x/a = - 0.554.

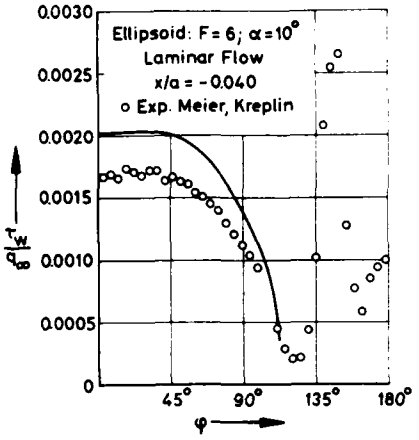

Fig. 22 α = 10° angle of attack

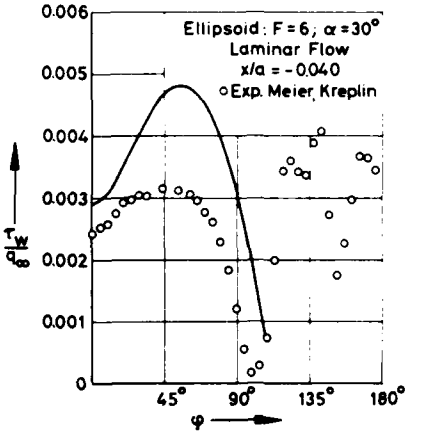

Fig. 23 α = 30° angle of attack

Comparison between the calculated and measured wall shear stress values at measuring station 6 with x/a = - 0.040.

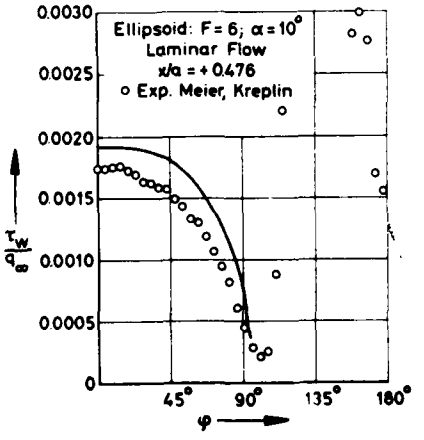

Fig. 24 α = 10° angle of attack

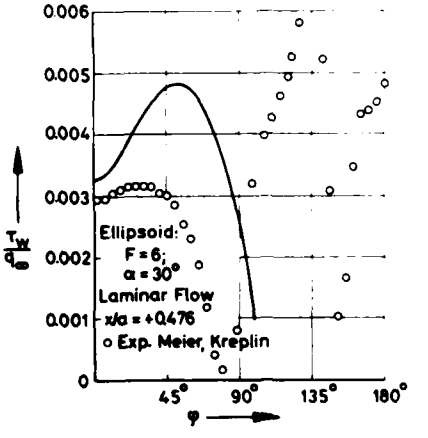

Fig. 25 α = 30° angle of attack

Comparison between the calculated and measured wall shear stress values at measuring station 9 with x/a = + 0.476.

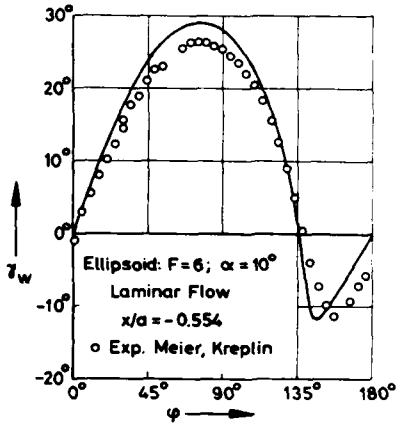

Fig. 26 α = 10° angle of attack

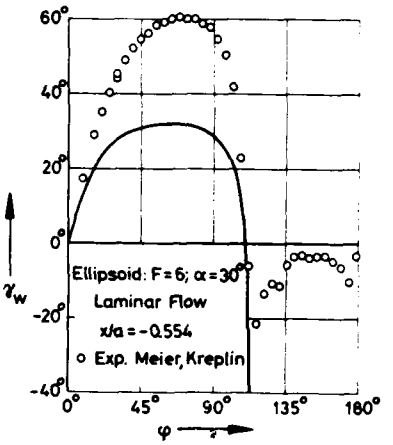

Fig. 27 α = 30° angle of attack

Comparison between the calculated and measured cross flow angles at the wall at measuring station 3 with x/a = - 0.554.

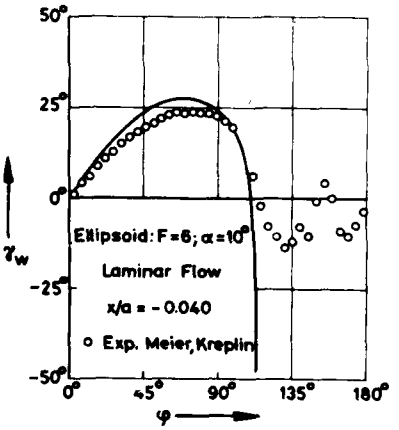

Fig. 28 α = 10° angle of attack

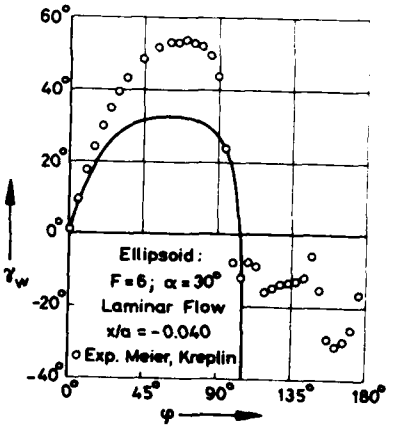

Fig. 29 α = 30° angle of attack

Comparison between the calculated and measured cross flow angles at the wall at measuring station 6 with x/a = - 0.040.

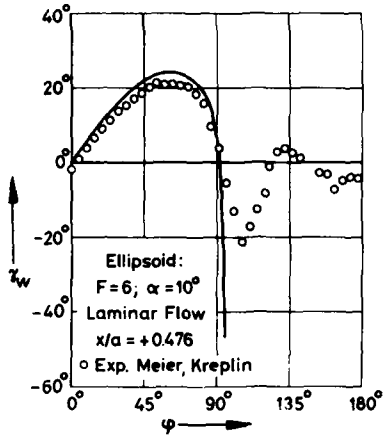

Fig. 30 α = 10° angle of attack

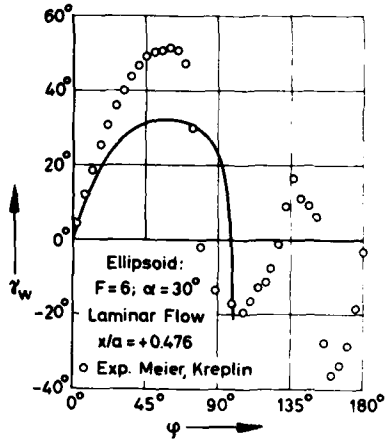

Fig. 31 α = 30° angle of attack

Comparison between the calculated and measured cross flow angles at the wall at measuring station 9 with x/a = + 0.476.

EXPERIMENTAL DETERMINATION OF WALL SHEAR STRESS VECTORS ON AN INCLINED PROLATE SPHEROID

H.-P. Kreplin*)
H. Vollmers**)
H.U. Meier*)

Deutsche Forschungs- und Versuchsanstalt
für Luft- und Raumfahrt e.V.
Aerodynamische Versuchsanstalt Göttingen

*) Institut für Experimentelle Strömungsmechanik
**) Institut für Theoretische Strömungsmechanik

Abstract

Surface hot film probes were applied to measurements of the local wall shear stress (magnitude and direction) on a prolate spheroid at incidence in subsonic flow. Distributions of wall shear stress vectors are presented for two angles of incidence (α = 10°, 30°) and two free stream velocities (U_∞ = 10 m/s, 45 m/s). The limiting streamlines at the model surface were derived from the integration of the measured shear stress directions. The limiting streamlines as well as the wall shear stress distributions lead to detailed information about the boundary layer transition and separation.

1. Introduction

At the last DEA-meeting (1979) the development and application of a new measuring technique for the measurement of the wall shear stress on a body of revolution was described (Ref.[1]). It was demonstrated that V-surface hot film probes enable us to measure the magnitude, direction and fluctuating components of the local wall shear stress. In order to obtain an overall picture of the surface flow on an inclined prolate spheroid this technique was applied to the determination of the boundary layer transition and separation.

2. Test Set Up and Data Reduction

As described at the last DEA-meeting, Ref. [1], the experiments were carried out at the 1 : 6 prolate spheroid in the 3m x 3m Low Speed Wind Tunnel of the DFVLR-Göttingen. The model is now equipped with 12 surface hot film probes in the cross-sections specified in Fig. 1. Two additional probes were mounted on the afterbody of the ellipsoid in order to investigate the flow in this regime.

Due to the V-configuration of the two films of a hot film probe the magnitude and direction of the local wall shear stress can be determined. The hot film calibration and data reduction procedure was described in detail in Ref. [1]. In principle the hot film signals were related to calculated local wall shear stress values based on the potential pressure distribution and the experimentally determined transition locations for axisymmetric flow conditions. In order to increase the accuracy of the calibration the present calibration procedure

is now based on the measured instead of the potential pressure distribution.

Obviously the directional sensitivity of the hot film probes could not be derived from a direct calibration on the prolate spheroid. For this reason this calibration was carried out on a flat tunnel wall in a two-dimensional turbulent boundary layer. As demonstrated in Ref. [2] a linear relation between the yaw angle γ_w and the hot film output signals was found for $-40° \leq \gamma_w \leq +40°$. This linear relationship was applied to the 12 hot film surface probes in the present data reduction procedure.

While an error bound for the magnitude of the wall shear stress obviously depends on several parameters like

- Reynolds number
- temperature sensitivity
- surface curvature
- pressure gradient
- flow direction

the determination of the wall shear stress direction is more accurate ($\Delta\gamma_w \approx \pm 2°$).

3. Results and Discussion

3a. Wall Shear Stress Measurements

The reported experiments were performed for angles of incidence $\alpha = 10°$ and $30°$ at the free stream velocities $U_\infty = 10$ m/s and 45 m/s. The corresponding Reynolds numbers, based on the model length 2a, were $Re = 1.6 \times 10^6$ and 7.2×10^6.

In Fig. 2 the circumferential distribution of wall shear stress vectors in a central cross-section ($x_o/2a = 0.48$) of the prolate spheroid at $\alpha = 30°$ and $U_\infty = 45$ m/s together with typical instationary wall shear stress signals is shown. A systematic sketch of the flow around the body in this cross-section is given in order to assist an interpretation of the wall shear stress distribution. Starting from the windward line of symmetry ($\varphi = 0°$) a laminar boundary layer is developing up to $\varphi \approx 50°$, followed by a transitional boundary layer which becomes fully turbulent at $\varphi \approx 70°$. This is indicated by the significant increase of the wall shear stress and corresponding fluctuating components. The region of the three-dimensional boundary layer separation is characterized by:

- The circumferential wall shear stress component becomes zero ($\tau_w = 0$).
- The wall shear stress magnitude reaches a minimum.

Due to the fact that in this case we consider only one cross-section of the body for a fixed model orientated coordinate system the exact location of the boundary layer separation cannot be determined. For this reason the enveloping limiting streamlines on the body surface have been calculated from the measurements in all 12 cross-sections as will be shown later.

In addition, the vortex flow pattern characterized by the reattachment and secondary boundary layer separation is clearly indicated by the measured wall shear stress vectors. The large c_f-values on the lee-side result from the induced velocities due to the separated vortex flow.

In Figs. 3a and 3b wall shear stress distributions for the angle of incidence $\alpha = 10°$ and free stream velocities $U_\infty = 10$ m/s and 45 m/s are shown, respectively. For $U_\infty = 10$ m/s (Fig. 3a) the boundary layer is laminar up to separation in all cross-sections. It should be mentioned that the maximum wall shear stresses for this test case are in the order of $\tau_w = 0.25$ N/m², which is equivalent to 0.0025 p/cm². This clearly indicates the difficulties for shear stress measurements at such low Reynolds numbers and characterizes the limitations of this measuring technique. However, this test case was carried out to obtain qualitative as well as quantitative information about the surface flow which has been calculated by several authors.

With increased free stream velocity ($U_\infty = 45$ m/s) the laminar boundary layer becomes turbulent in the cross-section $x_o/2a = 0.3$ at $\varphi \approx 70°$ (compare the interpretation of the wall shear stress distribution shown in Fig. 2). In the cross-section $x_o/2a = 0.64$ the flow is fully turbulent. Applying the definition of an open and closed separation introduced by Wang [3], the open separation, clearly illustrated in Fig. 3a, is only indicated in Fig. 3b by the change in sign of the crossflow angle γ_w. This implies the existence of negative crossflow in the model oriented co-ordinate system, which was confirmed by boundary layer velocity profile measurements [4].

In Figs. 4a and 4b the wall shear stress distributions for the high angle of incidence ($\alpha = 30°$) are shown.Again for a free stream velocity $U_\infty = 10$ m/s the boundary layer is laminar in all cross-sections up to separation. At $U_\infty = 45$ m/s in contrast to the low incidence an open boundary layer separation is evident.

As found already in Ref. [1] this separation is due to a laminar boundary layer in the nose region while beyond $x_o/2a \approx 0.2$ a turbulent boundary layer separation is indicated. Obviously the separation occurs in the laminar case at smaller circumferential angles φ compared to the turbulent case. This consequently results in a deflection of the separation "line" (Fig. 4b) which can also be observed from oil flow patterns shown later.

For Figs. 3a - 4b we have to mention that

- the hot films cannot distinguish between positive and negative flow direction, a flow problem which is not relevant for our test conditions and this can be excluded,

- the circumferential shear stress component becomes zero at smaller angles φ than the wall shear stress minima occur.

3b. Integration of the Wall Shear Stress Directions

For better intuition and a more illustrative picture of the flow field near the surface the limiting streamlines were determined by an integration of the direction field of the wall shear stress.

The measurements at the 12 cross-sections were used to generate a B-spline approximation of the field of directions of the wall shear stress [5]. From this approximation the direction can be evaluated at any point on the spheroid between the first and last cross-section.

The locations of the limiting streamlines were determined by a

numerical integration of the differential equation

$$\tan \gamma_w = \frac{\tau_{w\varphi}}{\tau_{ws}} = \frac{b(2ax_o - x_o^2)}{\sqrt{a^2(2ax_o - x_o^2) + b^2(x_o - a)^2}} \quad \frac{d\varphi}{dx_o} .$$

corresponding to the coordinates defined in Fig. 1. The integration was started at given points which are marked in the following figures. It proceedes in equidistant steps of about 2.5 mm on the model surface in the direction, evaluated from the shear stress direction field, i.e. tangentially to the local streamline.

This calculation procedure was applied for the wall shear stress distributions presented in Figs. 3a - 4b. As stated already, the exact locations of the boundary layer separation cannot be detected from these distributions. If an open separation is characterized by an envelope of limiting streamlines, then this method enables us to determine separation lines as well as regions of reattached flow. For this reason the following conclusions can be deduced from the streamline patterns shown in Figs. 5 - 8*).

In the laminar flow case at $\alpha = 10°$ (Fig. 5) two enveloping streamlines caused by the primary and secondary boundary layer

*) It should be noted that the separation is not indicated by the concentration of streamlines - which mainly depends on the number of "starting points" - but by the convergence of streamlines resulting in an envelope.

separation are clearly indicated. With conventional techniques it is not possible to perform visualizations of the surface flow at these low Reynolds numbers. A primary open boundary layer separation was observed in Ref. [6] on an 1 : 4.3 prolate spheroid at even lower Reynolds numbers. No mentioning of a secondary separation is given in this article.

The calculated limiting streamline pattern obtained for a higher Reynolds number at the same angle of incidence (Fig. 6) is more difficult to interprete, because it is not characterized by such significant enveloped streamlines. Additional information about the boundary layer in the cross-section $x_o/2a = 0.64$ is given in [4].

If the model is inclined to $\alpha = 30°$a free stream velocity of $U_\infty = 10$ m/s generates a laminar boundary layer separation as demonstrated in Fig. 4a. Due to the stronger cross flow components this separation occurs at smaller circumferential angles φ compared to $\alpha = 10°$. The region between the primary and secondary separation line shows divergent streamlines, which indicate flow reattachment.

The validity of these experimentally obtained streamline patterns is confirmed in Fig. 8 ($\alpha = 30°$, $U_\infty = 45$ m/s) by a comparison with oil flow patterns obtained at the same Reynolds number. Except for the nose region the interpretation of this figure leads to analogous conclusions as discussed before. It should be noted that at $\alpha = 30°$ at least one third of the flow near the surface is not accessible by conventional boundary layer calculation procedures.

4. Summary of the Results and Conclusions

The results of the investigation can be summarized as follows:

- The wall shear stress vector distributions obtained from surface hot film measurements give a clear indication of the laminar-turbulent boundary layer transition. The circumferential shear stress component vanishes - in the coordinate system used - before the locations of the shear stress minimum. This holds true for laminar as well as turbulent boundary layers.

- The limiting streamline patterns derived from the measured wall shear stress distributions are in excellent agreement with oil flow patterns. The results make it possible to determine the envelopes of limiting streamlines which characterize the so-called open three-dimensional boundary layer separation. For the flow conditions $\alpha = 10°$, $U_\infty = 10$ m/s ($Re = 1.6 \times 10^6$) a secondary boundary layer separation occurs which is not reported so far in the literature. At $\alpha = 30°$ and $U_\infty = 10$ m/s the primary separation is laminar all over the body. Increasing the free stream velocity to $U_\infty = 45$ m/s results in a laminar separation in the nose region. Further downstream the boundary layer becomes turbulent.

The investigation lead to the following conclusions:

The results presented here should provide a sufficient data base for the testing of existing three-dimensional boundary layer calculation procedures. However, it is known, that three-dimensional turbulence models applied to date have to be improved, in particular for strong

cross flows and regions of boundary layer separation. For this reason detailed investigations of the boundary layer flow developing on the prolate spheroid are carried out at the DFVLR-AVA in Göttingen.

5. References

[1] Meier, H.U.; Kreplin, H.-P.
"Experimental investigation of the transition and separation phenomena on a body of revolution"
Proc. 2nd Symposium on "Turbulent Shear Flows", July 2-4, 1979, Imperial College, London, pp. 15.1 - 15.7, 1979
see also: Proc. 4th US-FRG DEA Meeting "Viscous and Interacting Flow Field Effects"
Forschungsbericht aus der Wehrtechnik BMVg-FBWT 29-31, pp. 258 - 273, 1979

[2] Kreplin, H.-P.; Meier, H.U.; Maier, A.,
"Wind Tunnel Model and Measuring Techniques for the Investigation of Three-Dimensional Turbulent Boundary Layers"
Proc. AIAA 10th Aerodynamic Testing Conference, San Diego, California, April 19-21, 1978; AIAA-Paper 78-781, 1978

[3] Wang, K.C.
"Separation patterns of boundary layer over an inclined body of revolution"
AIAA Journ., Vol. 10, pp. 1044 - 1050, 1972

[4] Meier, H.U.; Kreplin, H.-P.
"Experimental study of boundary layer velocity profiles on a prolate spheroid at low incidence in the cross section $x_o/L = 0.64$"
Proc. 5th US-FRG DEA-Meeting "Viscous and Interacting Flow Field Effects", Naval Academy, Annapolis/Maryland, April 16-18, 1980, to be published.

[5] Müller-Wichards, D.
"Behandlung von Kurven und Oberflächen mit Hilfe von Splines"
DFVLR-Report IB 230-80-R01, 1980

[6] Taeyoung Han; Patel, V.C.
"Flow separation on a spheroid at incidence"
J.Fluid Mech. Vol. 92, pp. 643 - 657, 1979

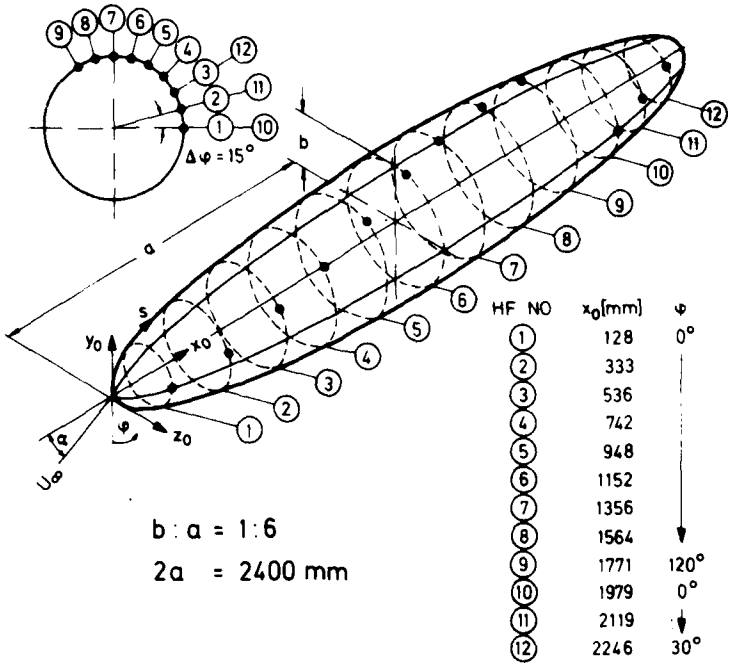

Fig. 1 Prolate spheroid equipped with surface hot film probes in 12 cross-sections

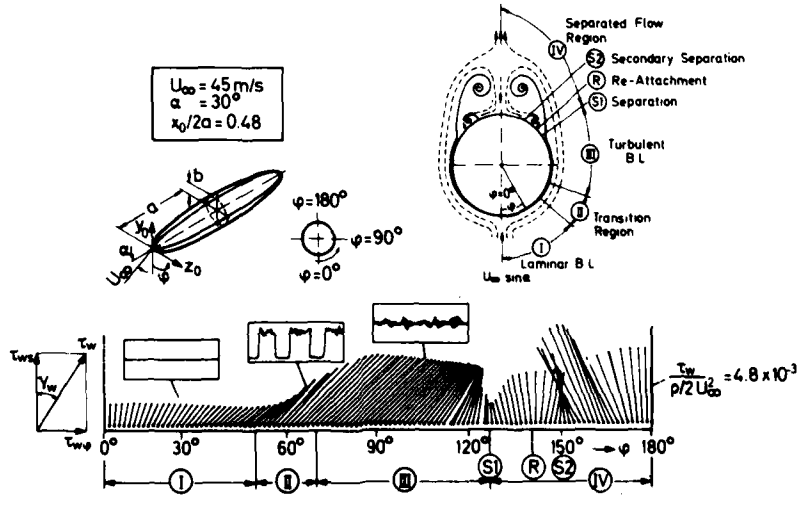

Fig. 2 Measured wall shear stress vectors in the central cross-section, $x_0/2a = 0.48$, at $\alpha = 30°$, $U_\infty = 45$ m/s and a systematical sketch of the flow field around a prolate spheroid at high incidence

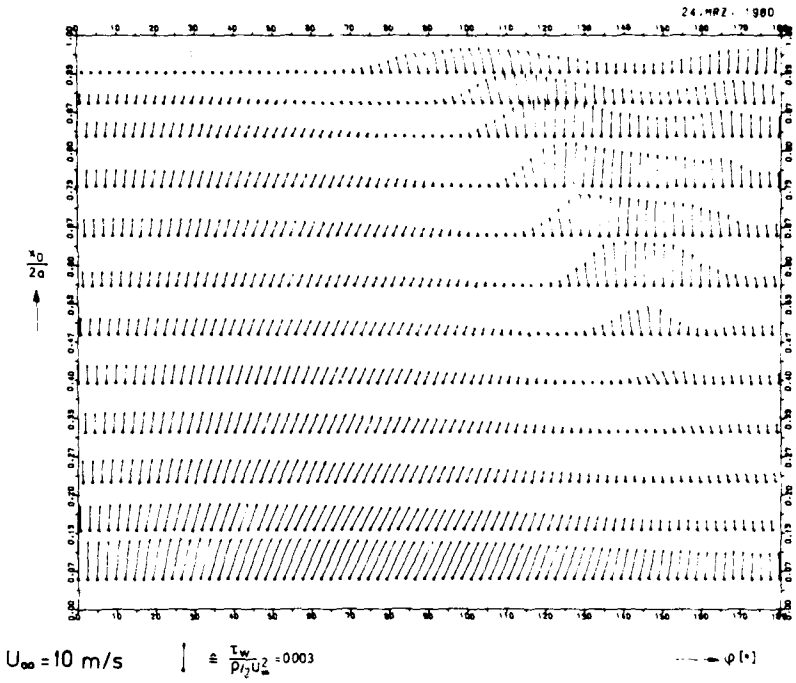

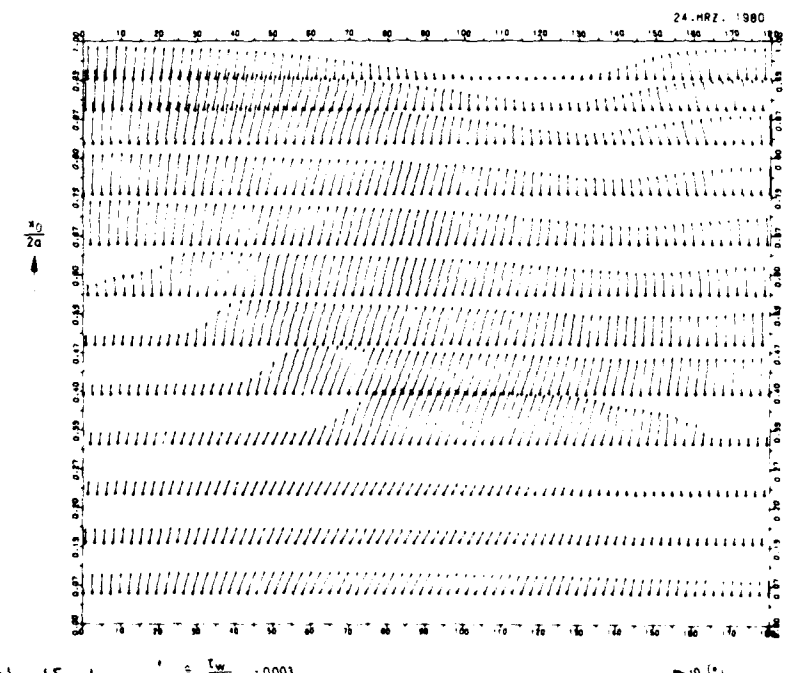

Fig. 3a, b Distributions of wall shear stress vectors on the prolate spheroid at α = 10°

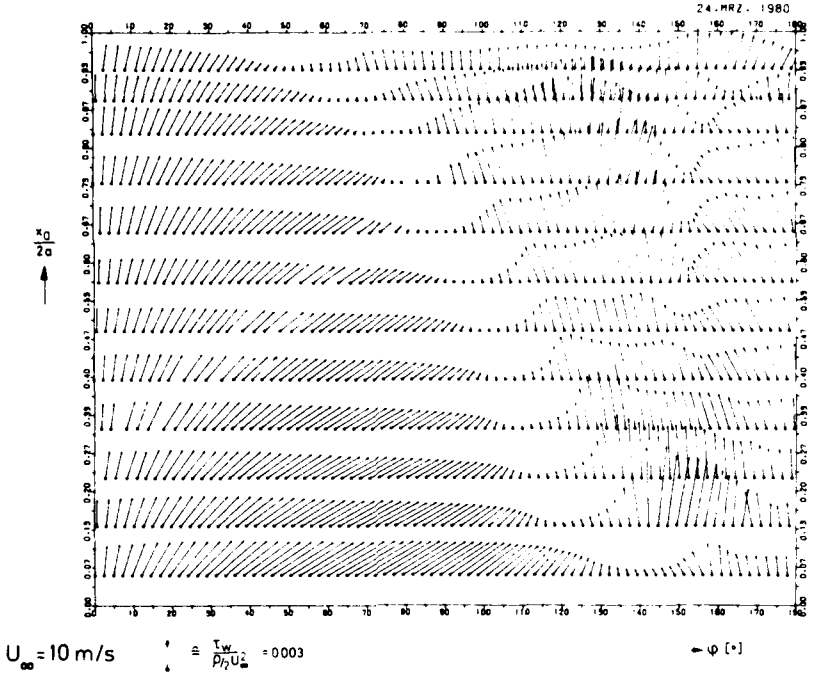

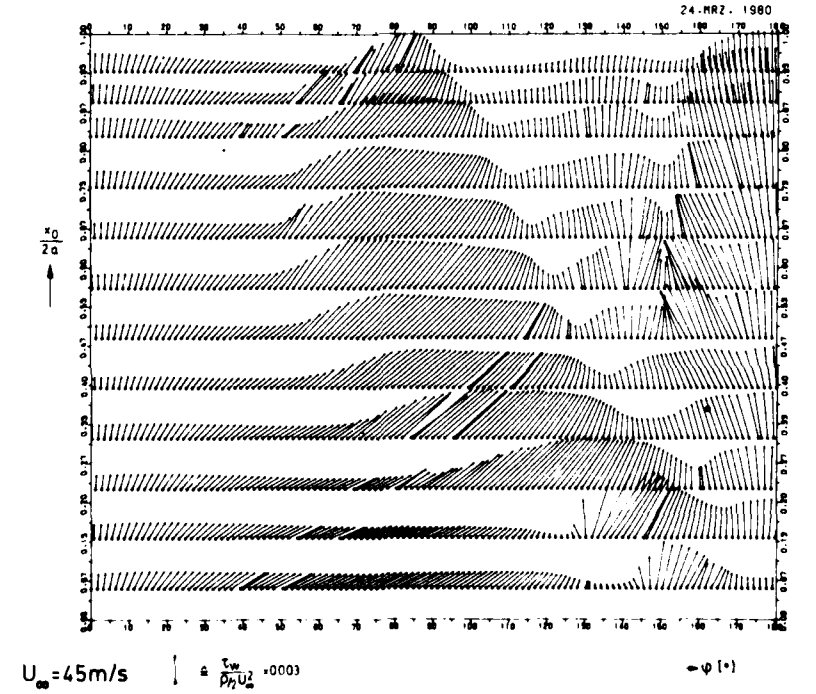

Fig. 4a, b Distributions of wall shear stress vectors on the prolate spheroid at $\alpha = 30°$

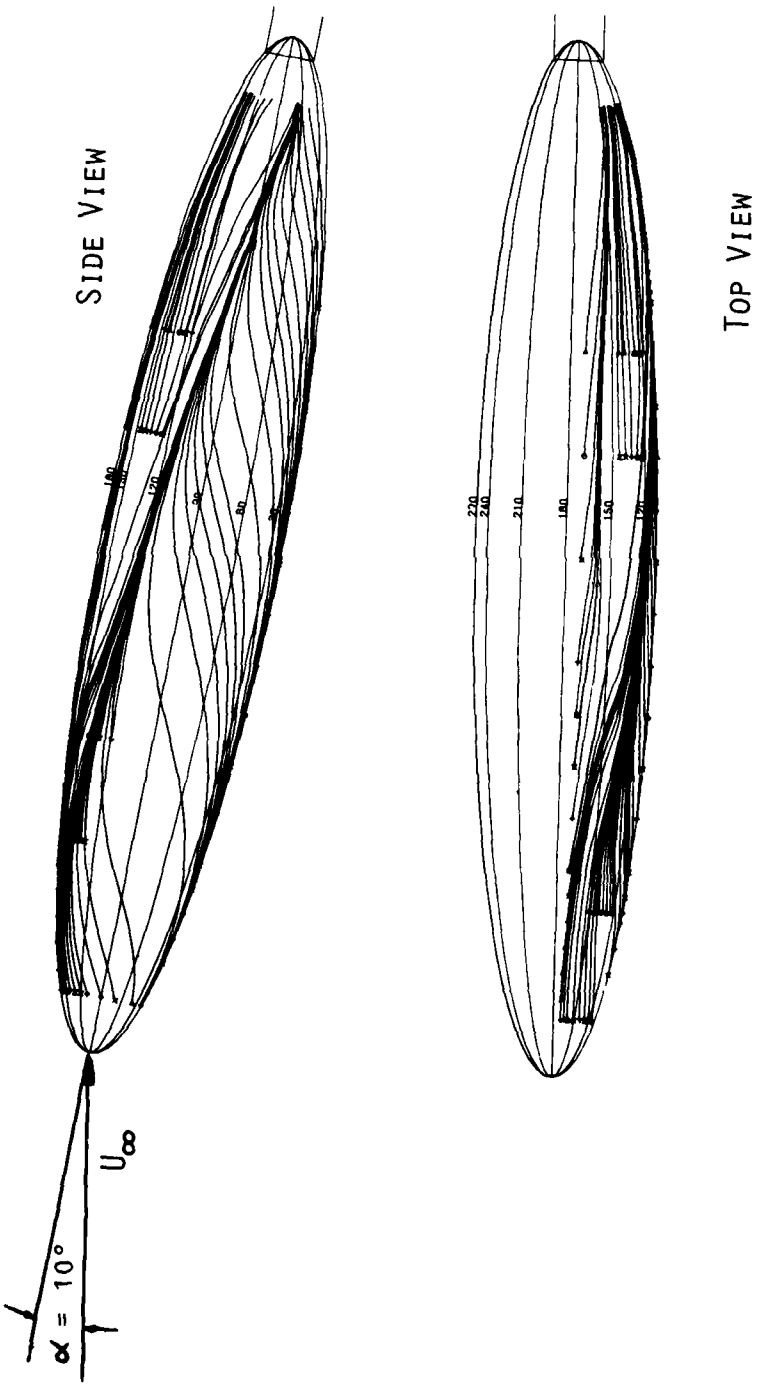

Fig. 5 Limiting streamlines, α = 10°, U_∞ = 10 m/s

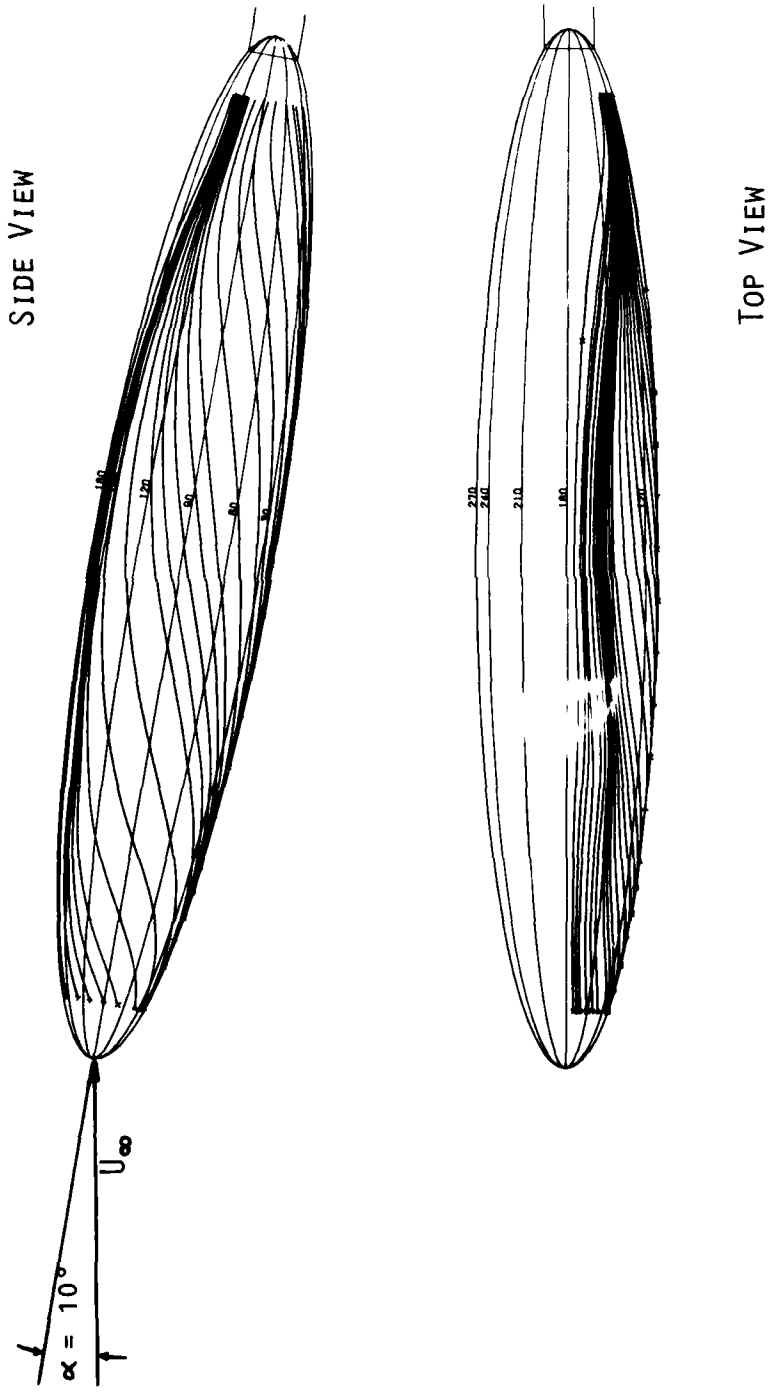

Fig. 6 Limiting streamlines, $\alpha = 10°$, $U_\infty = 45$ m/s

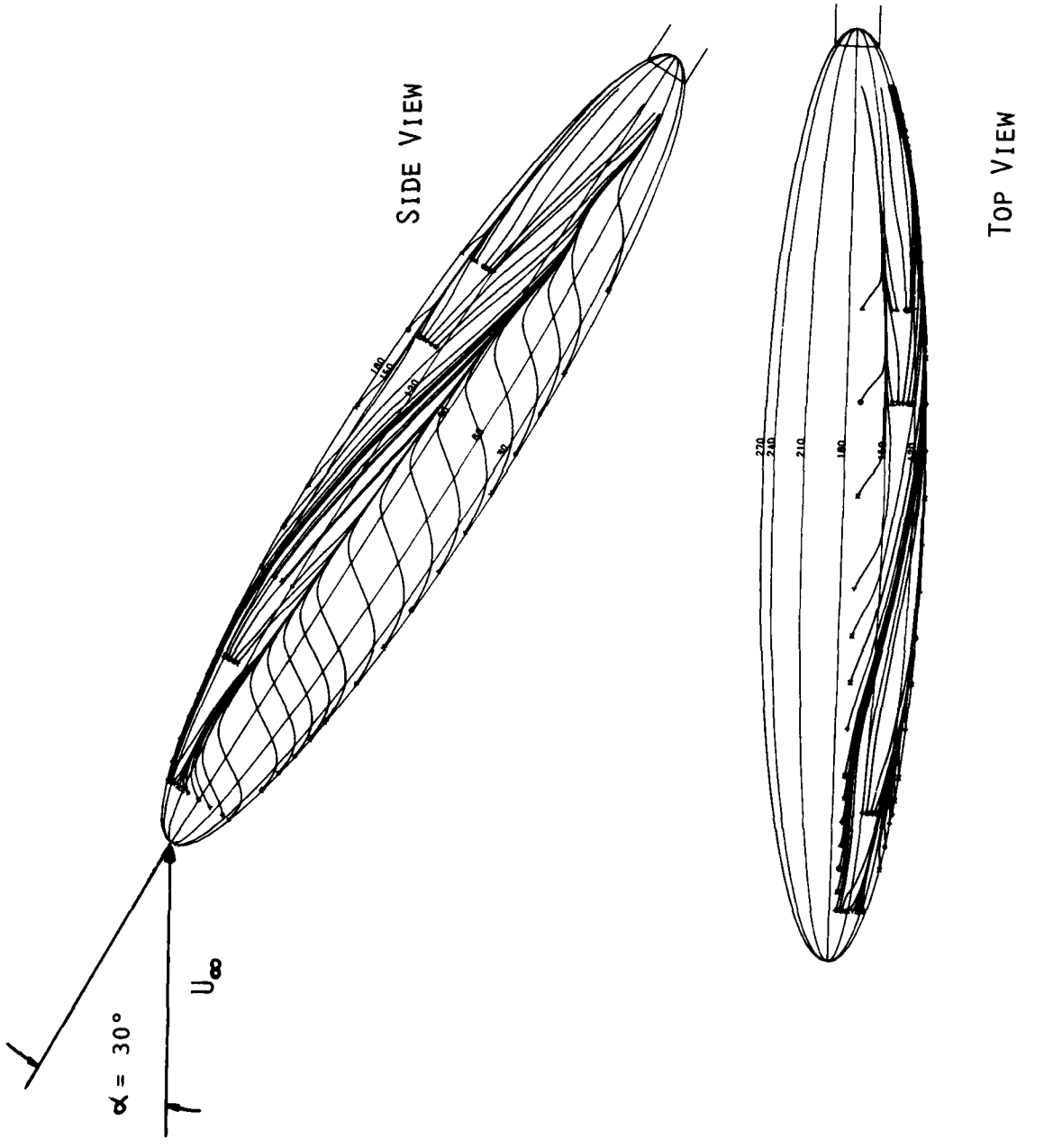

Fig. 7 Limiting streamlines, $\alpha = 30°$, $U_\infty = 10$ m/s

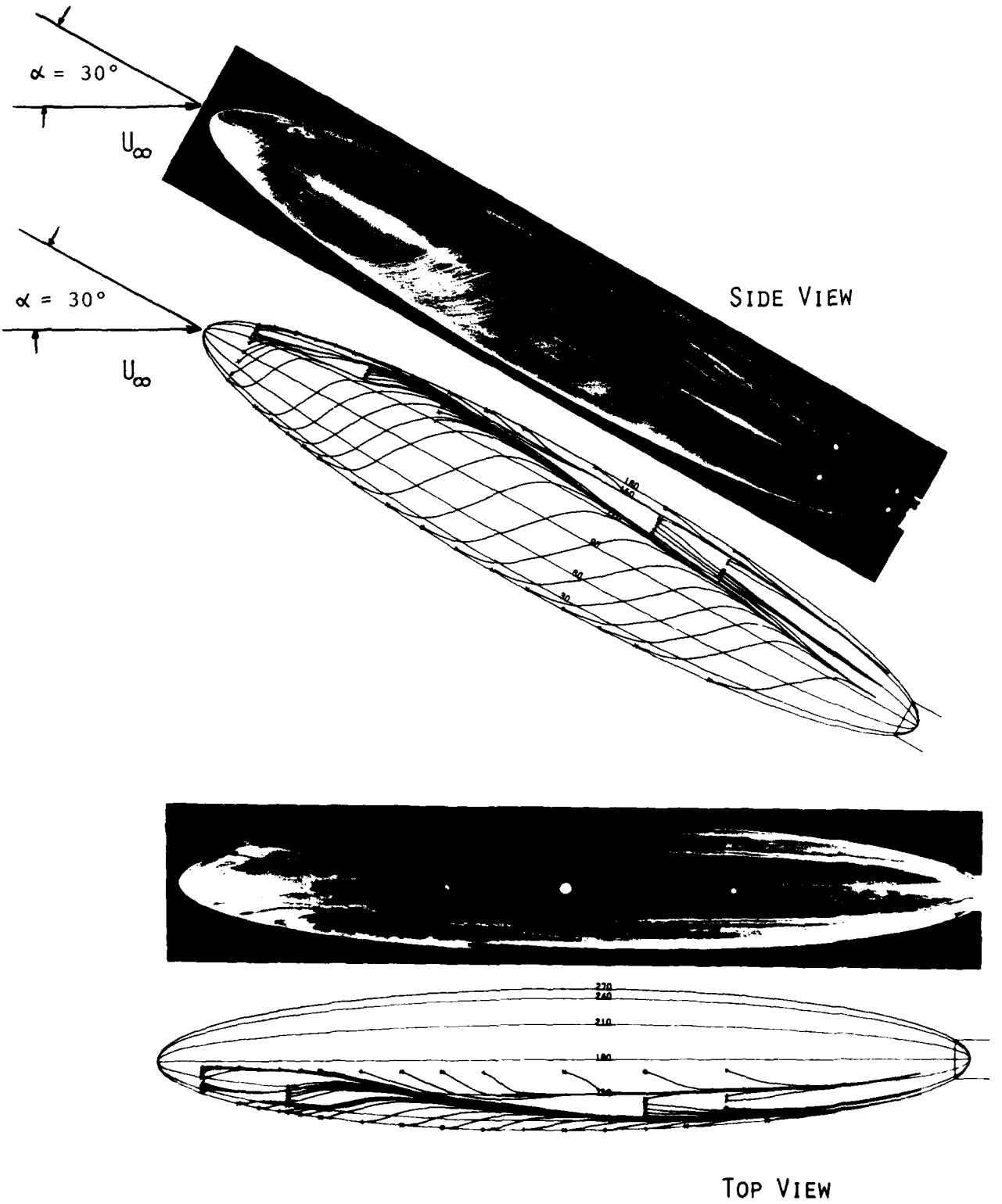

Fig. 8 Limiting streamlines and oil flow patterns
$\alpha = 30°$, $U_\infty = 45$ m/s

Calculation of Viscous, Sonic Flow over Hemisphere-Cylinder at 19 deg Incidence-- The Capturing of Nose Vortices

by

T. Hsieh

Naval Surface Weapons Center

White Oak, Silver Spring, Maryland 20910

Introduction

In Ref. 1 an experimental investigation of separated flow about a hemisphere-cylinder at 0- to 19-deg incidence in the Mach number range from 0.6 to 1.5 was reported. Among the many separation phenomena, of great interest is the appearance of nose vortex pair standing on the leeside of the forebody at α = 19 deg as indicated by the oil flow pictures taken from wind tunnel testing. The nose vortex pair also appears to be most pronounced at M_∞ = 1. Although physical explanation has been given to the mechanism of formation of the nose vortices, an effort of numerical simulation of viscous sonic flow over hemisphere-cylinder at 19 deg incidence based on the computer code developed by Pulliam and Steger (Ref. 2) is reported in this paper. The purpose of present work is twofold: first, to confirm the physical reasoning concerning the formation of nose vortices made previously and secondly, to assess the capability of the numerical simulation of a complicated three dimensional separated flow.

Description of Separated Flowfield

In Fig. 1, the experimentally observed surface flow pattern in the leeside of a hemisphere-cylinder (1 in. in diameter and 10 in. in length) at M_∞ = 1 and α = 19 deg is present. The flowfield is assumed to be symmetric with respect to the pitching plane throughout this paper. The flow breaks away on the leeside of the hemispherical nose near the shoulder and a standing vortex, which features a simultaneous reversal of flow in both the meridianal and circumferential direction is formed. Further downstream, there is a flow reattachment region. From there on, the cross flow separation forms the primary and secondary separation lines as shown. It is important to emphasize that the standing vortex is most pronounced and covers over a relatively large area in

sonic flow than that at subsonic or supersonic free stream condition. Since only a limited number of grid points can be provided by the computer to resolve the flowfield in the numerical simulation, the choice of $M_\infty = 1$ and $\alpha = 19$ deg case will improve the chance of success (note that in Ref. 2, the results of $M_\infty = 1.2$ and $\alpha = 19$ deg was reported but no comments were made concerning the nose vortices although experimental results indicated the existence of small nose vortices).

The mechanism and condition for the formation of the nose vortices can be understood as follows. As shown in Fig. 2, at low incidence only primary separation line in region I is formed far downstream, Fig. 2a. This is the case of open-type separation defined by Wang[3]. As the incidence increases, the nose separation region II starts to develop. When the nose separation bubble is small, the flow reattaches. The limiting streamline is shown in Fig. 2b. At moderate incidence, the nose separation bubble grows and becomes open, meanwhile, the primary separation line moves forward (a secondary separation line can also appear at this stage). The fluid in region II near the pitching plane must flow upstream, whereas that near the limiting streamline AA (Fig. 2c) must flow downstream and a condition is provided for the reversal of surface flow in both meridianal and circumferential components. Therefore, the nose vortices (a pair) are formed. It should be noted the direction of the vortex is counterclockwise (on the left side of the pitching plane when facing upstream). At still higher incidence, which is beyond the experimental range, it is believed that separation region I and II will merge to form a closed-type separation region as sketched in Fig. 2d. Then the nose vortices will disappear. Based on this reasoning, the nose vortices occur only during the transition from an open separation to a completely closed

separation in the presence of an open nose separation bubble. A three dimensional sketch of the flowfield with the presence of the nose vortices is given in Fig. 2e.

Numerical Results

The computer code (AIR3D) of Pulliam and Steger solves the three dimensional unsteady Navier-Stokes equations with "thin layer" approximation, i.e. all the viscous terms in the streamwise and circumferential directions are neglected. The numerical method is based on the implicit factored scheme of Beam and Warming[4]. A turbulent and transitional model due to Baldwin and Lomax[5] is also included in the code. For detail, please refer to Ref. 2, 4 and 5. In this note, only the procedure of utilizing the computer code to obtain the results present herein will be briefly described.

The computations were carried out using an IBM 370/165 computer with double precision. A 48 (meridianal direction) x 15 (circumferential direction) x 20 (normal direction) grid is used for inviscid flow and 30 x 15 x 36 for viscous flow. Two preparation runs were performed for inviscid flow at the following conditions: (I) $M_\infty = 1.4$, $\alpha = 19$ deg and (II) $M_\infty = 1.0$ and $\alpha = 0$. The surface pressure distribution for case I is compared to the calculation of Weiland[6] as shown in Figure 3 and that for case II is compared to the full potential solution of South and Jameson[7] and experimental data[8] as shown in Figure 4. Figures 3 and 4 establish the accuracy of the computer code and the computation domain to be used for the viscous flow computation.

To see the effects of viscosity (i.e. via the "thin layer" approximation) and of numerical turbulence model, three calculations were performed for the case of sonic flow over a hemisphere-cylinder at 19 deg incidence, namely: (i) inviscid flow; (ii) viscous, laminar flow; and (iii) viscous, transitional flow (corresponding to the experimental condition). The computed results for

the surface pressure distribution are present and compared to the experimental data as shown in Figure 5. In the windwardside, ϕ = 180 deg, the agreement among all results are good. The inviscid results agree slightly better with experiments. As one moves toward the leeward side, it is noted that the inviscid results first follow the general trend of the experimental data better than the viscous results till $\phi \simeq 60$ deg and then the viscous results agree better with the experimental data for the rest of the flowfield in the leeside separated region. There is only slight difference in the calculated surface pressure between the results of laminar and transitional model, most significantly in the portion near the nose. The fact that the results of transitional model deviate further from the experimental data than the laminar case strongly suggests that the turbulence model used in the computer code is not sufficient to describe the separated three dimensional flow. Of course, the limited grid points used in the computation also contribute to the deviation between computation and experiments.

Of great interest is the calculated surface flow pattern as shown in Fig. 6 obtained by plotting the velocity vector projection on the unwrapped cylindrical surface at $\Delta R = 0.00005R$ above the body surface (on body surface $\Delta R = 0$ the velocity is zero as required for viscous computation). It is seen that most of the features of separated flow as depicted in Fig. 1 are captured qualitatively, including the nose vortices. (That the secondary separation line was not captured is perhaps due to insufficient grid points.) The important significances of the present calculation are: (1) the appearance of nose vortices as observed experimentally is confirmed by numerical calculation, (2) the "thin layer" approximation of Navier-Stokes equations is capable of depicting a complicated three dimensional separated flow, and (3) to improve the numerical results one needs a better turbulence and transitional flow model and a larger computer.

References

1. Hsieh, T., "An Investigation of Separated Flow about a Hemisphere-Cylinder at 0- to 19-deg Incidence in the Mach Number Range from 0.6 to 1.5," AIAA Paper 77-179 or AEDC-TR-76-112, Nov. 1976.

2. Pulliam, T. H. and Steger, J. L., "On Implicit Finite Difference Simulations of Three Dimensional Flow," AIAA Paper 78-10, 1978.

3. Wang, K. C., "Separation Patterns of Boundary Layer over an Inclined Body of Revolution," AIAA J., Vol. 10, Aug. 1972, pp. 1044-1050.

4. Warming, K. F. and Beam, R., "On the Construction and Application of Implicit Factored Schemes for Conservation Laws," SIAM, ATNS Proceedings, Vol. 11, 1978, pp. 85-129.

5. Baldwin, B. S. and Lomax, H., "Thin Layer Approximation and Algebraic Model for Separated Turbulent Flow," AIAA Paper 78-257, 1978.

6. Weiland, C., "Calculation of Three Dimensional Stationary Supersonic Flow Fields by Applying the 'Progonka' Process to a Conservative Formulation of the Governing Equations," J. of Computational Physics, Vol. 29, No. 2, Nov. 1978, pp. 173-198.

7. South, J. C., Jr. and Jameson, A., "Relaxation Solution for Inviscid Axisymmetric Transonic Flow over Blunt or Pointed Bodies," Proceedings of AIAA Computational Fluid Dynamic Conference, July 19-20, 1973.

8. Hsieh, T., "Flow Field Study about a Hemisphere-Cylinder in the Transonic and Low Supersonic Mach Number Range," AIAA J., Vol. 13, No. 10, Oct. 1975, pp. 1411-1413.

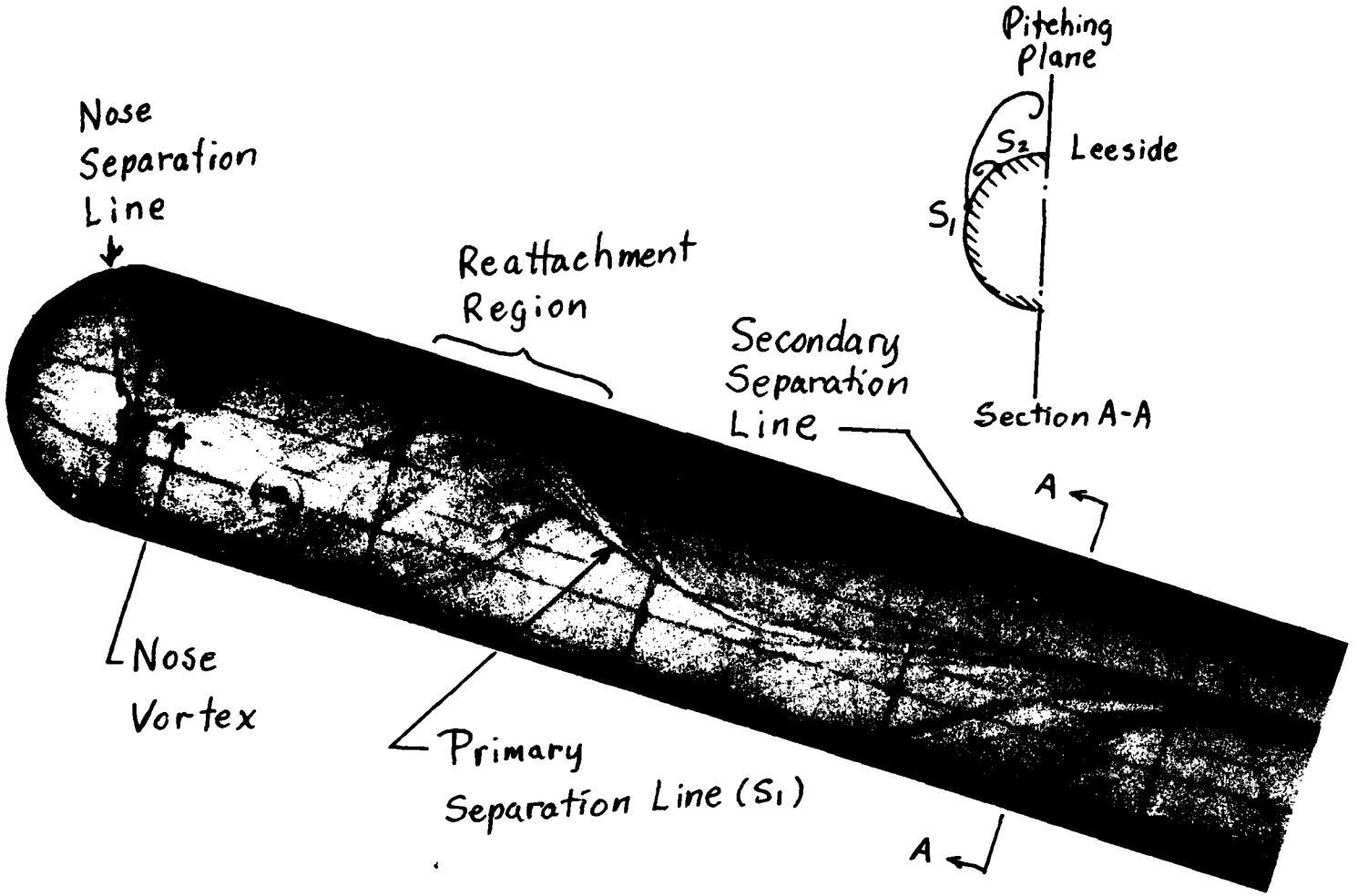

Fig. 1 Oil Flow Picture Showing the Surface Flow Pattern about a Hemisphere-Cylinder, $M_\infty = 1.0$, $\alpha \approx 19$ deg

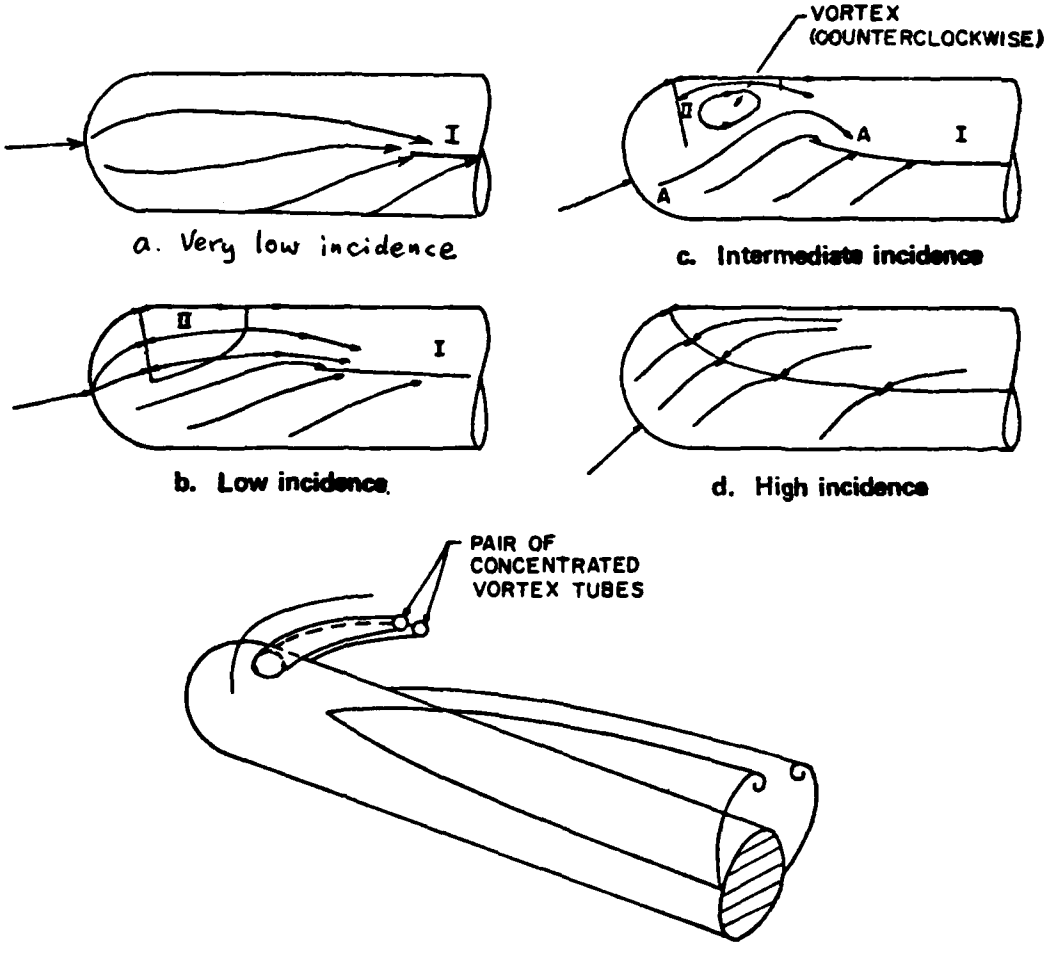

Fig. 2 Mechanism and Condition for the Formation of the Nose Vortices

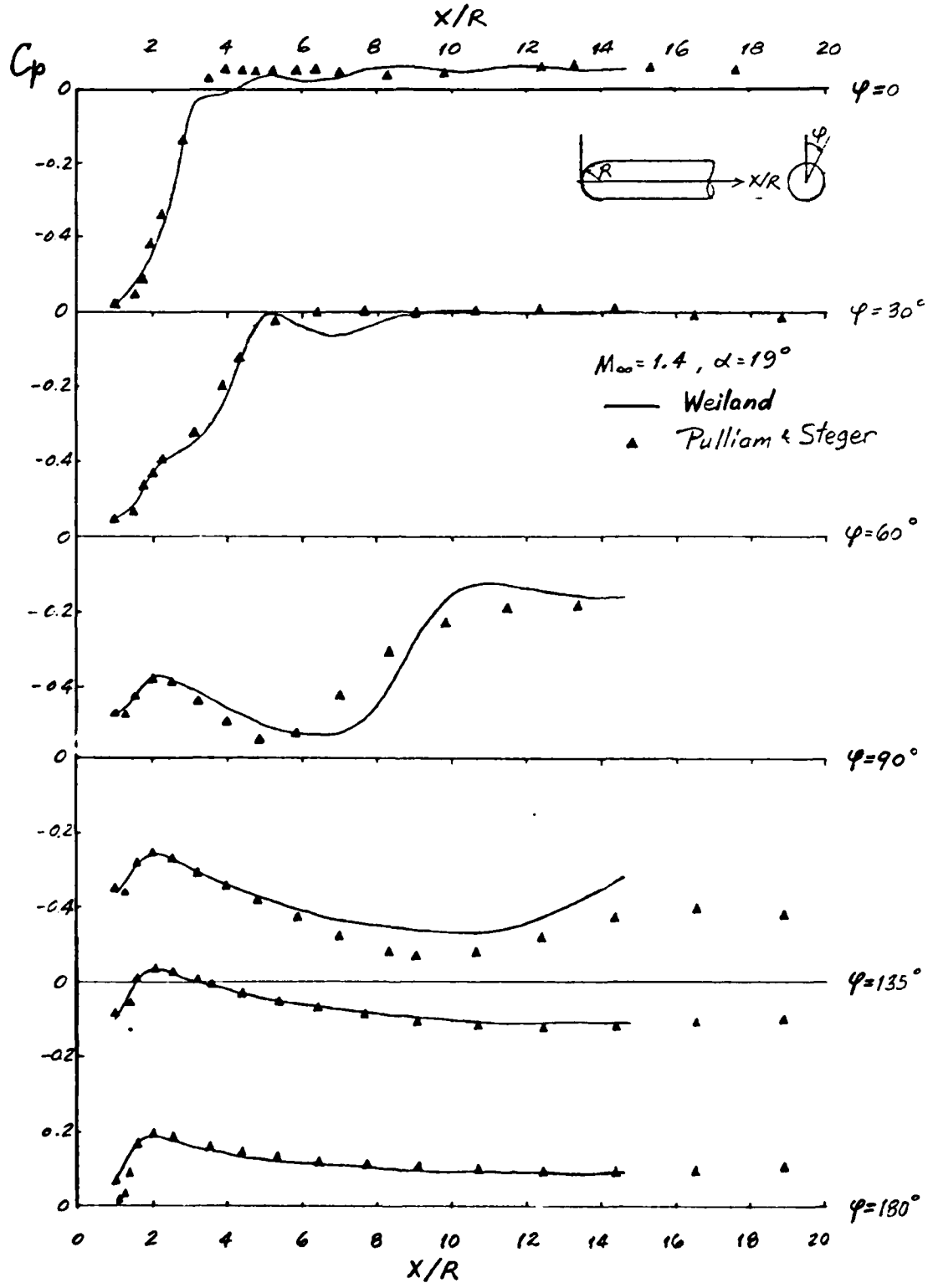

Fig. 3 Surface Pressure Distribution for Inviscid Flow over a Hemisphere-Cylinder

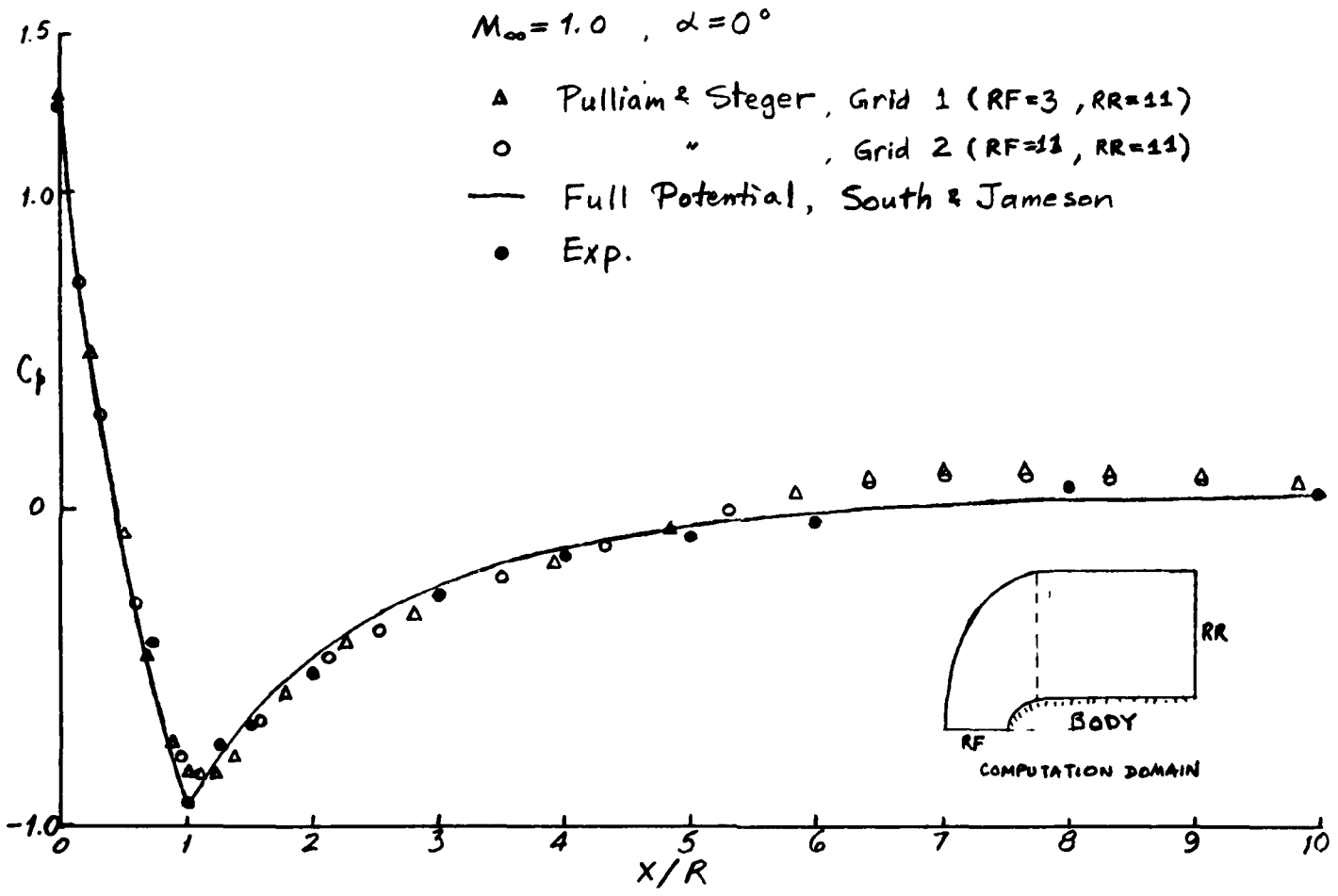

Fig. 4 Surface Pressure Distribution for Inviscid Flow over a Hemisphere-Cylinder

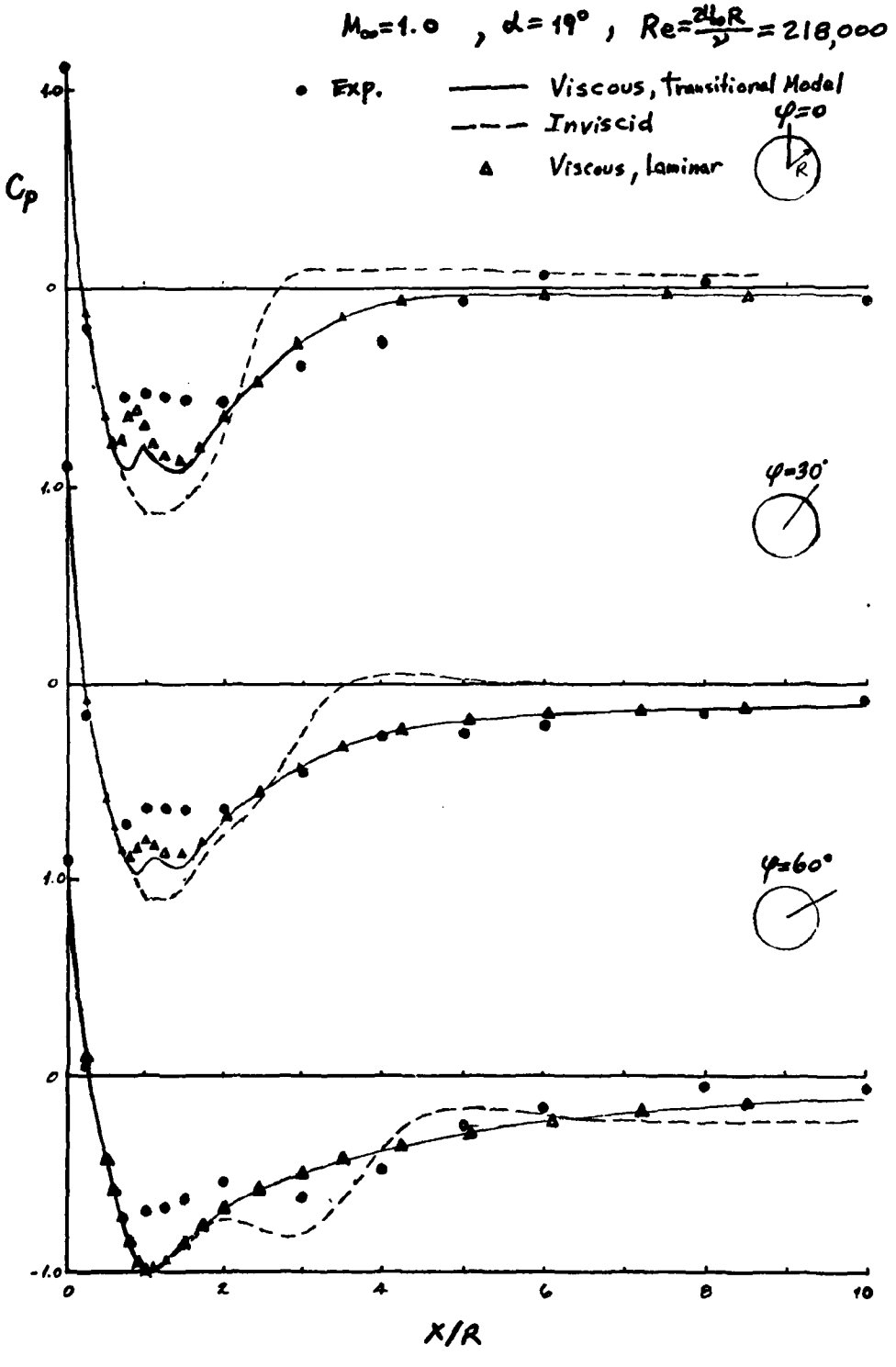

Fig. 5 Comparison of Surface Pressure Distribution for a Hemisphere-Cylinder

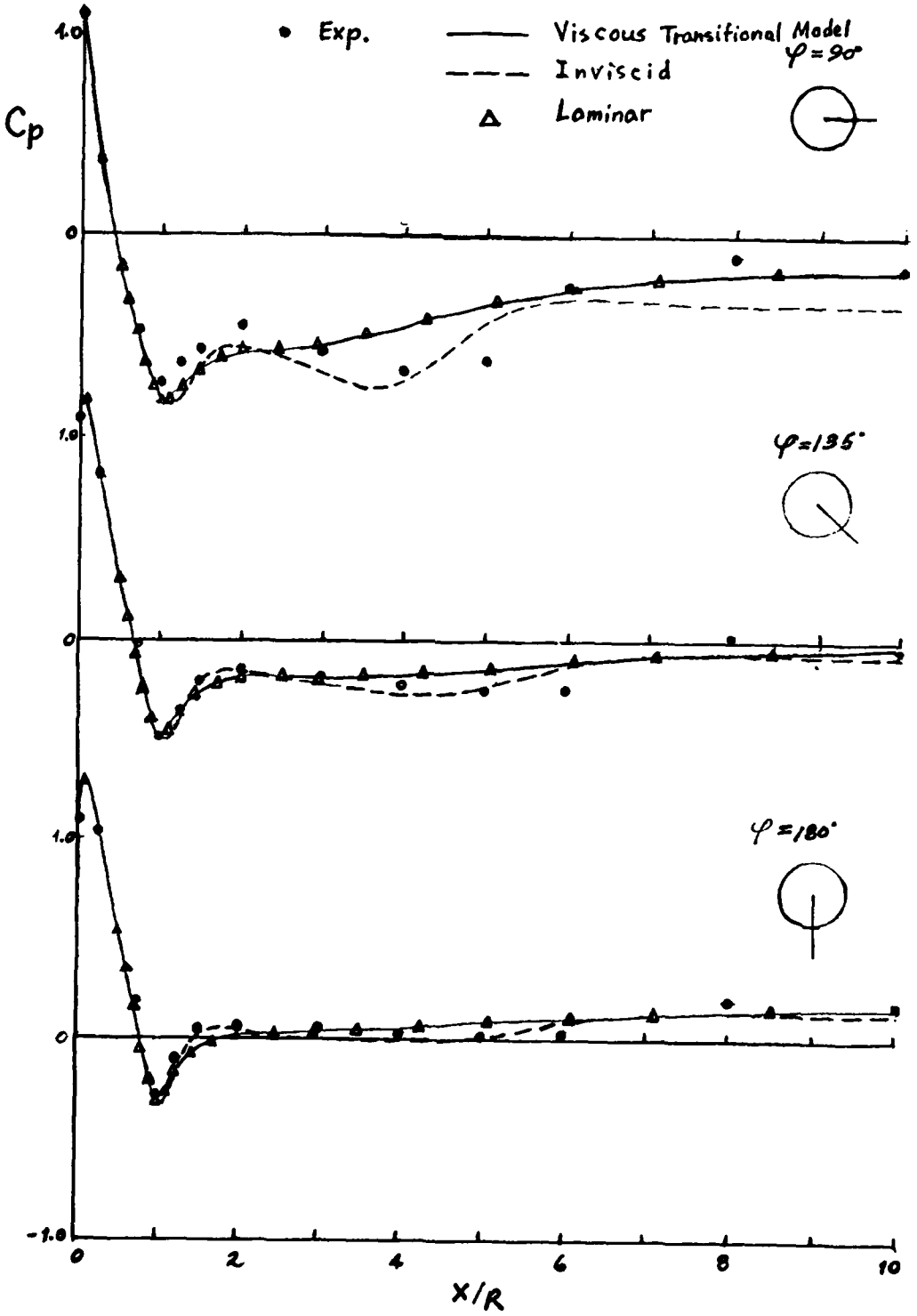

Fig. 5 Concluded

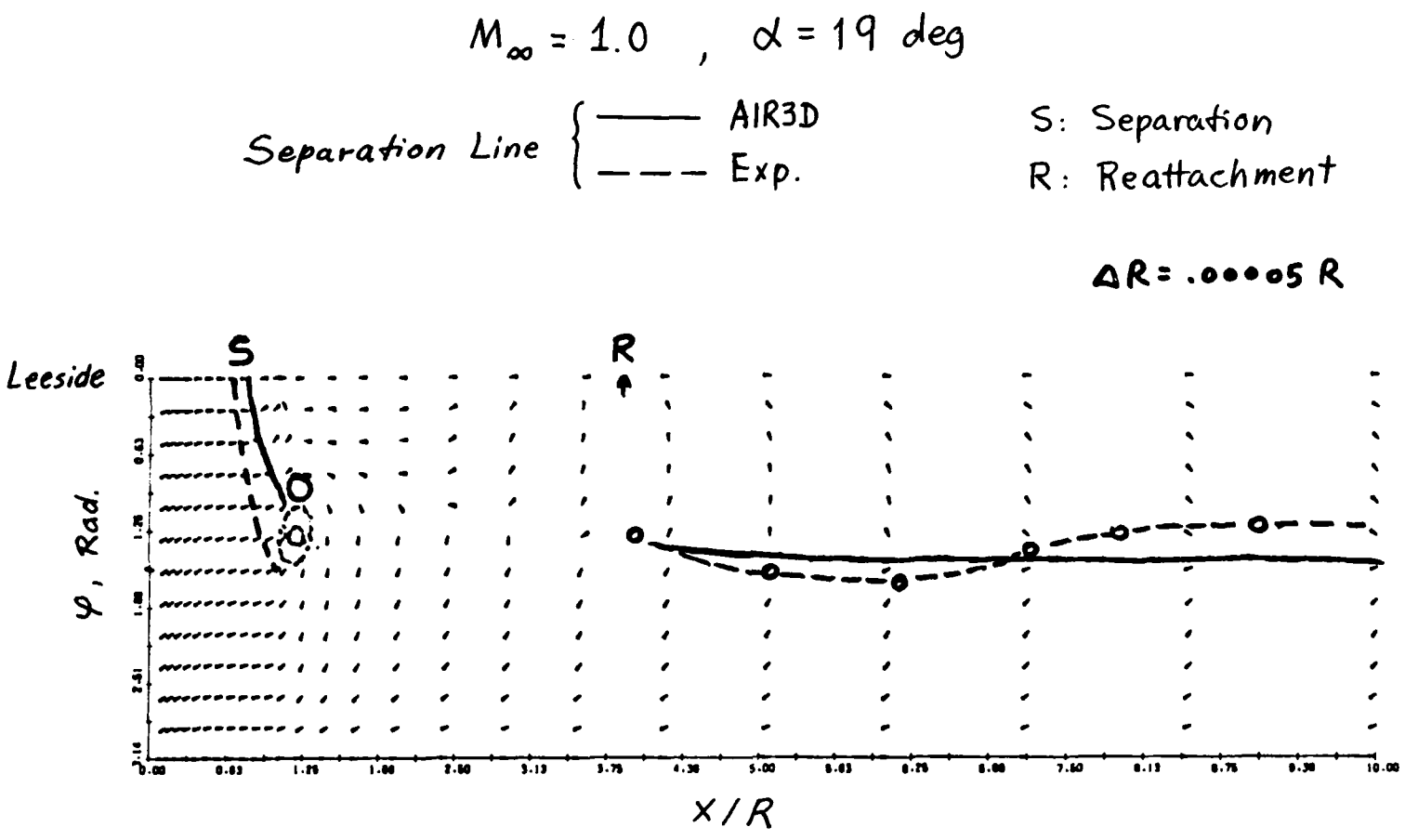

Fig. 6 Calculated and Measured Surface Flow Pattern

A Non-Orthogonal Coordinate System for Calculating Boundary Layers along Lines of Symmetry

Roger Grundmann

DFVLR-AVA Göttingen

Summary

The three-dimensional boundary layer equations for steady, laminar or turbulent, compressible flows along lines of symmetry on bodies at high incidences have been derived for a body-oriented, curved, non-orthogonal coordinate system. The advantage of using such a coordinate system is that there is no need to transform the governing equations in order to eliminate the geometrical singularity at the pole of the body. This singularity arises if a polar or elliptic coordinate system is used as usually done. For an ellipsoid of revolution some boundary layer calculations were carried through, and the comparison with other results, theoretical as well as experimental, was in good agreement.

Introduction

Boundary layer calculation along lines of symmetry on bodies have to be treated three-dimensional. This is because the flow around a body at high incidence moves from the windward side to the leeward side, and due to continuity effects, the upper boundary layer has to be thicker than the lower one. If the crossflow influence would be neglected, that would mean the flow problem is handled two-dimensionally.

This physical effect could not be reproduced by the calculations. To calculate this flow, different coordinate systems have been applied. WANG [1], HIRSH and CEBECI [2] used the surface oriented elliptic coordinate system for which for example LAMB [3] gave the inviscid solution. This system unfortunately reveals a geometrical singularity at the pole of the ellipsoid, which causes undefined terms in the governing equations. Flows at high incidences can not be computed without taking considerable effort in transforming these equations.

In the latest literature describing the calculation of the boundary layer along the line of symmetry on an ellipsoid of revolution for extremely high incidences, CEBECI, KHATTAB and STEWARTSON [4] put their interest in eliminating the geometrical singularity at the pole of the ellipsoid by still using the elliptic coordinates. A transformation is found, by which new independent coordinates replace the elliptic ones. The analytical effort is considerable.

The purpose of this paper is to show, that the use of surface oriented, curved, non-orthogonal coordinate systems reduces the effort in transforming nearly completely.

Geometrical conditions

The coordinate system used in the nose region of the ellipsoid is a modified spherical system, for which the radius is a variable depending on the shape of the ellipsoid. The connection between the Cartesian and the new coordinate system is described in the following, supported by fig. 1. Here the origin of the Cartesian systems has to be situated in the center of the ellipsoid.

$$x = r \cos \theta \cos \varphi$$

$$y = r \cos \theta \sin \varphi$$

$$z = r \sin \theta$$

The radius r is a function of the new independent variables θ and φ and of the axes of the ellipsoid a and b.

$$r = a\,b\,[b^2 \cos^2 \theta \cos^2 \varphi + a^2 (\cos^2 \theta \sin^2 \varphi + \sin^2 \theta)]^{-1/2}$$

Governing equations

The differential equations formulating the three-dimensional boundary layer flow in the Euclidian space written in tensor notation were reported in the proceedings of the last DEA-Meeting. This notation enables the user to apply these equations to any curved, non-orthogonal, surface oriented coordinate system, that is ordered by his flow problem. Additionally the analytical and later the numerical effort can be kept small by using this notation, because here the terms of the differential equations are composed of tensorial quantities and not, as usually done, of physical quantities. The latter causes the additional differentiation of the elements of the metric tensor, which are dependent as well on the independent variables, and so some more terms have to be computed. If one prefers the computation in the tensorial formulation the results of this can easily be transformed in the physical state.

Boundary conditions

The ellipsoid is one of the very few bodies for which the three-dimensional inviscid velocity distribution is given analytically. The total surface potential ϕ, see ref. [1], can be written as follows.

$$\phi = Bx + Cz$$

with $B = (1 + k_a) \cos \alpha$

$$C = (1 + k_c) \sin \alpha$$

$$k_a = \frac{\frac{1}{2e} \ln \frac{1 + e}{1 - e} - 1}{\frac{1}{1 - e^2} - \frac{1}{2e} \ln \frac{1 + e}{1 - e}}$$

$$k_c = \frac{1}{1 + 2 k_a}$$

$$e = (1 - \frac{b^2}{a^2})^{\frac{1}{2}}$$

Here α is the angle of incidence. This potential is given in Cartesian coordinates and can be transformed into the new surface oriented coordinates.

$$\phi = B r \cos \theta \cos\varphi + C r \sin \theta$$

The surface velocity components can be developed by the following formula

$$\text{grad } \phi = \phi_{,i}\, a^{ij}\, \bar{a}_j \qquad i,j = 1,2$$

$\bar{a}_j$ is the base vector and a^{ij} is the inverse metric tensor of the surface.

$$|a^{ij}| = \frac{1}{D} \begin{vmatrix} a_{22} & -a_{12} \\ -a_{21} & a_{11} \end{vmatrix}$$

$$\text{with } D = a_{11}\, a_{22} - a_{12}^2$$

Now the inviscid velocity component u_e in the downstream direction and the cross flow velocity gradient A_e, which are the boundary conditions at the outer edge of the boundary layer, become

$$u_e = \frac{1}{a_{11}} \frac{\partial \phi}{\partial \Theta}$$

$$A_e = \frac{\partial v}{\partial \varphi}\bigg|_e = \frac{1}{a_{22}} \left(\frac{\partial^2 \phi}{\partial \varphi^2} - \frac{\partial a_{12}}{\partial \varphi}\, u_e\right)$$

The boundary conditions on the wall are as usual

$$u_w = 0$$

$$A_w = \frac{\partial v}{\partial \varphi}\bigg|_w = 0$$

Because the solution scheme is developed for the equations describing compressible flows, the boundary conditions for the temperature also have to be defined. The value of the temperature on the outer edge of the boundary layer is

$$T_e = 1 + \frac{u_\infty^2}{2c_p T_\infty} (1 - u_e^2)$$

The value at the wall is by choice

$$T_w = T_w(\theta) \quad \text{or} \quad \left.\frac{\partial T}{\partial n}\right|_w = 0$$

Solution scheme

The governing equations were discretized in the sense of an implicit difference scheme. The difference molecule was chosen in such a way that the three unknown values have to be computed using the three known values. The discretization center was placed in the middle of the molecule, so that the truncation error was the square of the step size in the main flow direction as well as in the normal direction.

This solution scheme follows the RICHTMYER algorithm applied to a three component solution vector consisting of the main velocity component the cross flow velocity gradient, and the temperature. The normal velocity component is computed separately by integrating the continuity equation. At least one iteration is necessary.

Numerical results

To prove the reliability of the solution scheme, the calculation of the boundary layer along the line of symmetry on an ellipsoid with the axis ratio b/a = 1/4 at zero incidence was first done. Here the common elliptic coordinate system was used. In this case the singularity at the nose

is identical with the stagnation point and so the calculation can easily be started. The computation stops immediately upon reaching the separation point. In fig. 2 a comparison with other theoretical results made by WANG [1] and HIRSH and CEBECI [2] was carried out. The dimensionless wall shear stress $c_f \, Re^{1/2}$ is plotted against the dimensionless x-axis. The present results are identical with those of ref. [2].

CEBECI, KHATTAB and STEWARTSON [4] made computations of the boundary layer along the symmetry line in the nose region. They used the elliptic coordinate system, which was transformed by trigonometric functions so that the nose singularity was eliminated. They gave results for an ellipsoid with "zero thickness". This limiting case could be computed due to the transformation.

In fig. 3 the results of the present method are given for an ellipsoid with the axis ratio of b/a = 1/6. The dimensionless wall shear stress $c_f \, Re^{1/2}$ is plotted against the angle ϑ, beginning at the stagnation point, leading around the nose and ending at a predetermined point on the leeward side. These results are qualitatively in agreement with those of ref. [4]. The quantitative comparison was impossible because a body with "zero thickness" could not be simulated with the present method. But generally it can be confirmed, that an incidence greater than $\alpha = 41^{\circ}$ causes separation immediately at the nose.

Measurements have been made by MEIER and KREPLIN [5] on the ellipsoid with the axis ratio b/a = 1/6. One example is given in fig. 4 for the windward side at an incidence of

$\alpha = 10^{o}$. The dimensionalized wall shear stress τ_w against the dimensionless x-axis is compared with theoretical result made by GEISSLER [6], STOCK [7], and the present method. The agreement between all these results is again very good.

Concluding Remarks

The solution of the boundary layer equations along the line of symmetry of an inclined ellipsoid causes difficulties, if the common elliptic coordinate system is applied. A geometrical singularity arises at the pole of the ellipsoid and causes undefined coefficients in the governing equations. Additionally the inviscid velocity distributions have changes in sign at the pole. That means, if the solution procedure is started at the stagnation point going ahead to the pole, the step over the pole becomes impossible. In ref. [4] this difficulty was overcome by introducing a trigonometrical transformation in the governing equations, which makes a lot of analytical effort.

In the present paper it has been shown, that the use of the tensorial notation of the governing equations lightens the analytical and numerical effort. Surface oriented coordinate systems, no matter how complicated they may be, curved and non-orthogonal, can be applied, if the flow problem demands them. Unpleasant geometrical singularities, additional transformations and three-dimensional interpolations can be avoided in this way. The results shown clearly prove this. Turbulent boundary layer calculations were not performed because the flow in the nose region, which was the purpose of the paper, is in general laminar.

References

[1] WANG, K.C.
Three-Dimensional Boundary Layer Near the Plane of Symmetry of a Spheroid at incidence.
J. Fluid Mech. Vol. 43 (1970), part 1, pp. 187-209.

[2] HIRSH, R.S.
CEBECI, T.
Calculation of Three-Dimensional Boundary Layers with Negative Cross Flow on Bodies of Revolution.
AIAA-Paper 77-683, 1977.

[3] LAMB, H.
Hydrodynamics.
Cambridge University Press, 1932.

[4] CEBECI, T.
KHATTAB, A.K.
STEWARTSON, K.
Studies on Three-Dimensional Laminar and Turbulent Boundary Layers on Bodies of Revolution at Incidence. I. Nose Separation.
AIAA-Paper 79-138, 1979.

[5] MEIER, H.U.
KREPLIN, H.P.
Experimental Investigation of the Transition and Separation Phenomena on a Body of Revolution.
BMVg-FBWT 79-31, pp. 258-273.

[6] GEISSLER, W.
Berechnung der laminaren, dreidimensionalen Grenzschicht an unsymmetrisch umströmten Rotationskörpern mittels Differenzenverfahren.
DFVLR FB-251-73 A 19, 1973.

[7] STOCK, H.W.
Laminar Boundary Layers on Inclined Ellipsoids.
Dornier GmbH, Aktenvermerk BF 30/ 1511-79.

Figures

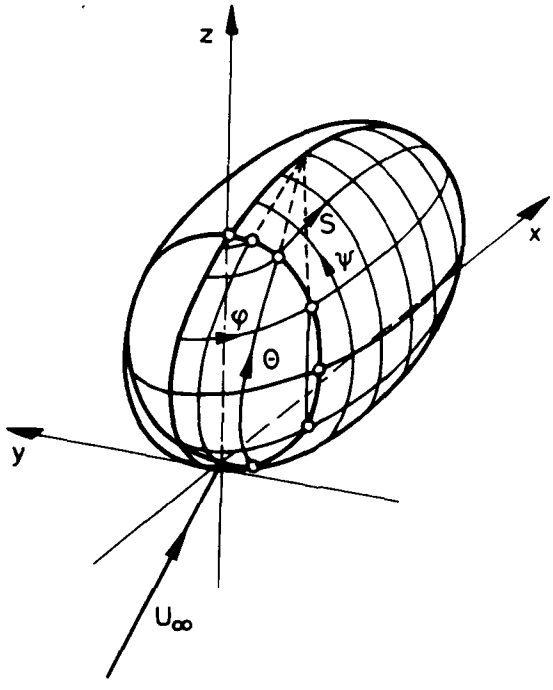

fig. 1. Spherical coordinate system fixed on an ellipsoid.

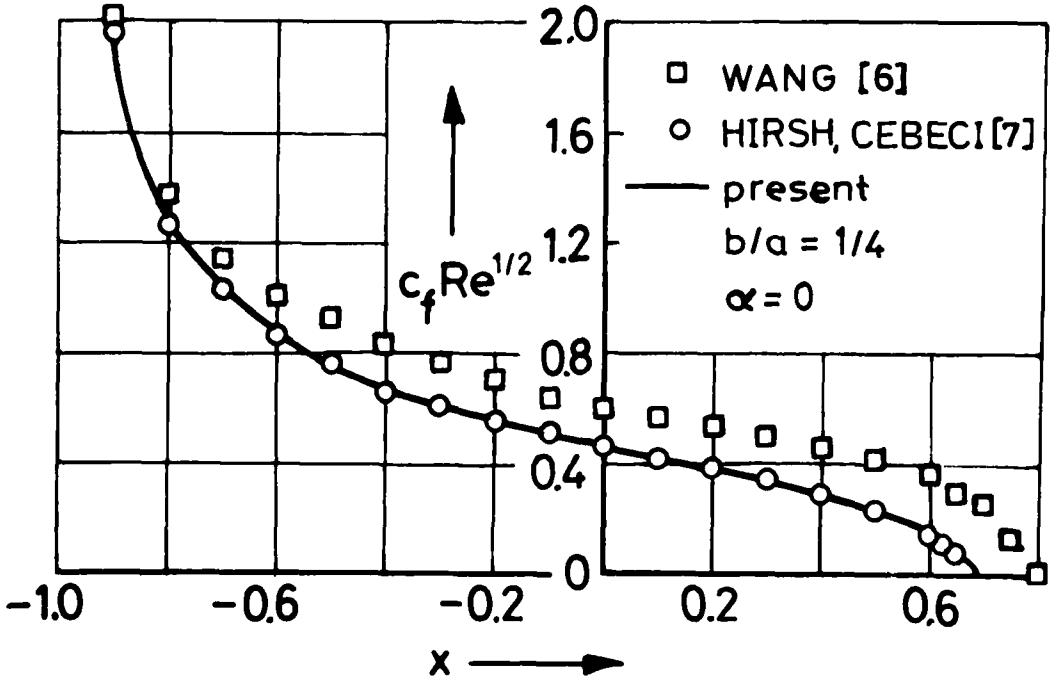

fig. 2. Dimensionless wall shear stress along the symmetry line of an ellipsoid at zero incidence, b/a = 1/4.

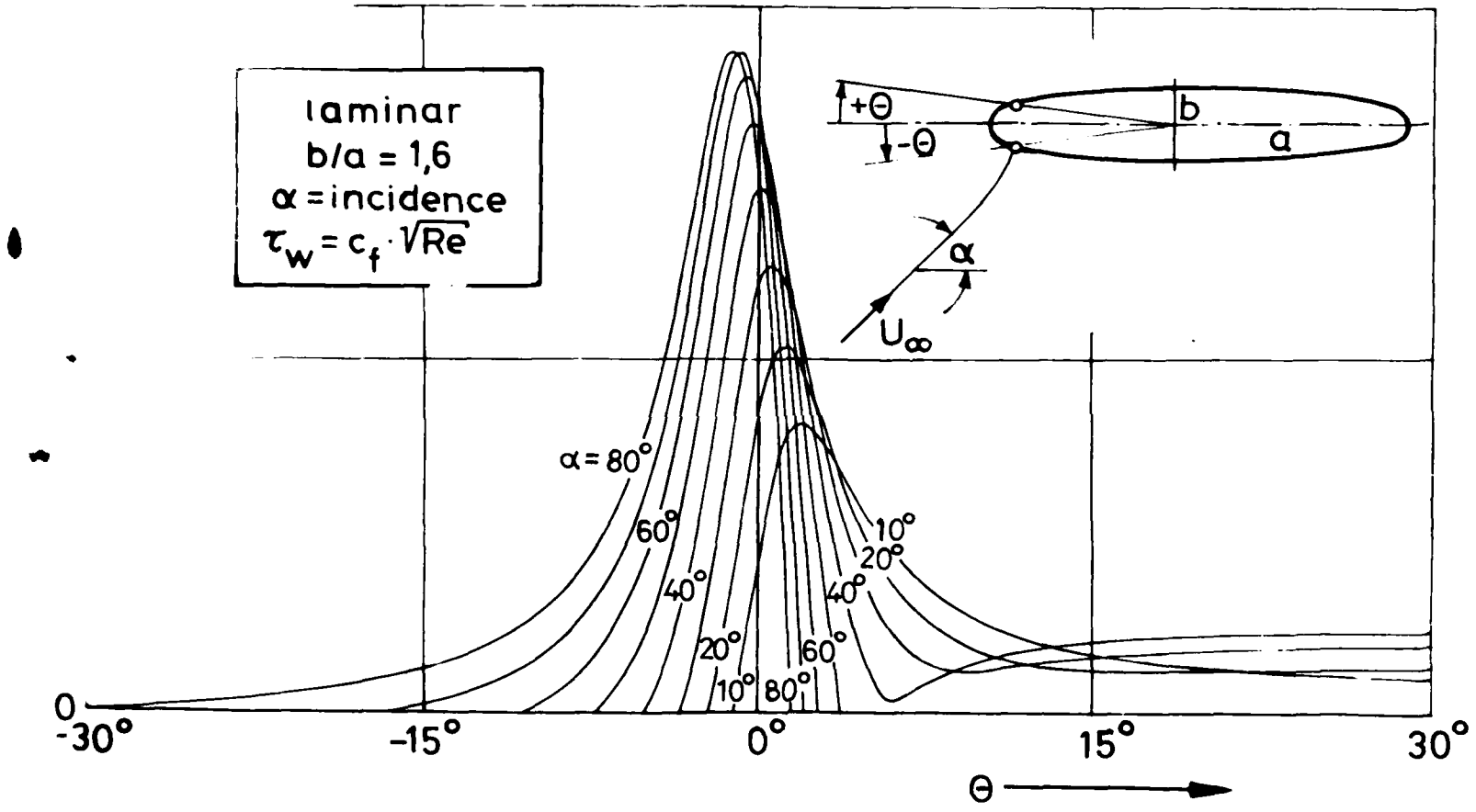

fig. 3. Dimensionless wall shear stress along the leeward symmetry line of an ellipsoid at different incidences, b/a = 1/6.

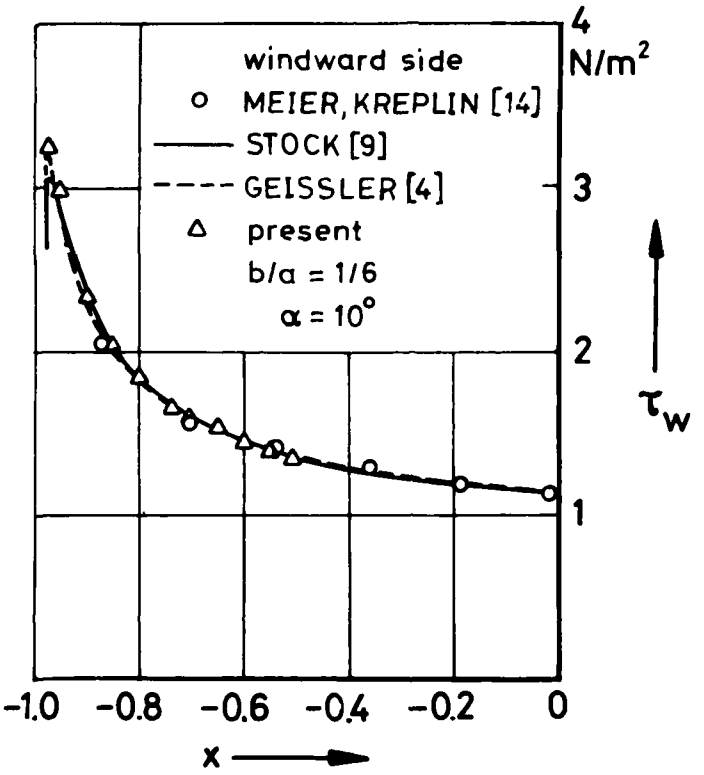

fig. 4. Dimensional wall shear stress along the windward symmetry line of an ellipsoid at incidence, $\alpha = 10^{o}$, $b/a = 1/6$.

Mean Velocities and Reynolds Stresses Measured in a Three-dimensional Boundary Layer

Udo Mueller *
Aerodynamisches Institut, RWTH Aachen
Aachen, Germany

A steady, incompressible boundary layer about a plane wall was tripped at the leading edge and deflected laterally by baffle plates. A three-dimensional flow developed in which the velocity component in mean-flow direction was decelerated and the one in cross-flow direction was accelerated. At 21 stations profiles of the time-averaged velocities and of the Reynolds stresses as well as the wall shear stresses were measured, the pressure distribution was mapped out at the outer edge of the boundary layer. Main results of measured profiles of mean and fluctuating velocities as well as deduced eddy viscosities, mixing lenths and the ratio of resultant shear stress to kinetic turbulent energy were reported in ref.[1] Supplementary in this paper a comparison of mean-velocity profiles with the law-of-the-wall and a survey of efforts to reduce the experimental errors of hot-wire measurements are described. Additionally tables with all measured data are provided.

Introduction

Actual and future problems in fluid mechanics require prediction methods for three-dimensional turbulent boundary layers. As a general description of the turbulent momentum transfer is not yet available, empirical laws for describing the time-averaged motion will still have to be used. These assumptions are usually limited to special classes of flows, but they are espected to be valid within certain ranges of varying initial-and boundary conditions. Because of the insufficient understanding of three-dimensional

---

* present address: NASA Ames Research Center, Experimental Fluid Dynamic Branch, Moffett Field, California 94o35

turbulent boundary layers measured data are urgently needed for testing calculation methods and closure assumptions. So an experimental investigation into such a flow was started at the Aerodynamic Institute, Aachen. Profiles of mean velocities and of Reynolds stresses were measured at 21 stations revealing the downstream development of the boundary-layer flow. With the measured data the validity of closure assumptions with respect to the present flow field was checked.

Description of the experiment

The experiment was carried out in a boundary layer about a plane wall. By means of baffle plates the flow was deflected laterally, fig. 1, inducing pressure gradients in both tangential directions. A boundary-layer velocity profile typical for the pressure-driven flow is schematically depicted in fig. 2. Different coordinate systems are also defined in this figure. The boundary layer which was tripped at the leading edge developed from a nearly two-dimensional flow to a full three-dimensional one with differences in the directions of wall- and outer-edge streamlines up to 30°. The streamlines indicated in fig. 1 include the investigated area. At 21 measuring stations marked by crosses profiles of mean velocities and of all Reynolds stresses as well as the wall shear stresses were measured. The pressure distribution was mapped out with a Prandtl tube at the outer edge of the boundary layer. The unit Reynolds number was $1.95 m^{-1}$.

The measuremts were carried out with a goose-neck shaped probe support according to Johnston[2]. Single and X-hot-wire probes as well as pressure probes could be moved relative to the wall and could also be rotated around the longitudinal axis, as described in ref.[1], in order to get a sufficient number of measured data.

Measured mean velocities and Reynolds stresses

In fig. 3 the profiles of the velocity $\overline{U}_{C1}$ which is defined by the direction of the wall shear stress, fig.2, are compared with the law-of-the-wall of two-dimensional flows. The friction velocity u_τ was measured with a Preston tube and was evaluated with the calibration of Patel[3]. These values and those obtained from Clauser charts agree within errors of 5 percent. Additionally the wall shear stresses were inferred

according to an extension of the Ludwieg-Tillmann[4] formula and that of Fernholz[5] as proposed by Johnston[6]. The results are compared in table 1.

Typical profiles of the measured Reynolds stresses of the local coordinate systems x_m, y_m, z_m, defined by $\overline{W_m} = 0$, are displayed in fig. 4 revaling the down-stream development. The maxima of the $\overline{u_m v_m}$-correlations were shifted away from the wall according to the positive pressure gradients. The transverse shear stress $\overline{v_m w_m}$ increased continuously and reached the order of magnitude of the $\overline{u_m v_m}$-correlation.

From the measured data profiles of eddy viscosities and mixing lengths for both tangential directions as well as the ratio of resultant shear stress to turbulent kinetic energy were deduced. Typical results were reported in ref. [1]

Accuracy of hot-wire measurements

The turbulence quantities evaluated with the measured data can strongly be impaired by experimental inaccuracies. The efforts of reducing the errors of hot-wire measurements will be described in detail in a separate paper and are summarized here, see also ref.[1]. When using miniature hot-wire probes it proved to be necessary to calibrate each wire individually with respect to magnitude and direction of the velocity vector. The coolings of the wires were described by an effective velocity

$$\overline{U_c^2} = \overline{U_{N1}^2} + k^2\overline{U_T^2} + h^2\overline{U_{N2}^2} .$$

$\overline{U_T}$ is the velocity component tangential to the hot wire while both $\overline{U_{N1}}$ und $\overline{U_{N2}}$ are perpendicular to the wire axis, one lying in the plane of the prongs and the other normal to it. The calibration curves of the non-constant sensitivity k together with h = 1.2 were taken into account in the data reduction. In fig. 5 profiles of measured Reynolds stresses are compared to those determined with the empirical cooling law of ref.[7] Especially the cross-correlations proved to be sensitive indicated by errors up to 15 percent. At each spatial point 16 different r m s -measurements were carried out in order to diminish experimental random scatter and to check the spatial resolution. Additionally, in separate measurements the accuracy of the conventional linearized evaluation of the Reynolds stresses was checked against increasing turbulence levels. The method

developed in the thesis[8] takes into account the triple velocity correlations usually neglected. Both methods are compared in fig. 6 regarding the same set of measured data. It was found that in the present investigation with turbulence levels below 23 percent the application of the conventional method was justified. The remaining experimental uncertainties in the measured Reynolds stresses were estimated to be $\pm$ 10 percent and $\pm$ 15 percent concerning the transverse shear stress $\overline{v_m w_m}$.

All measured data, i.e. mean velocities, Reynolds stresses, pressure distribution, wall shear stresses and integral parameters are summarized in the tables printed below.

References

1 Mueller, U.,Krause, E.,: Measurements of Mean Velocities and Reynolds Stresses in an Incompressible Three-Dimensional Turbulent Boundary Layer. Second Symposium on Turbulent Shear Flows, July 2-4, Imperial College, London, 1979.

2 Johnston, J.P.,: Measurements in a Three-Dimensional Turbulent Boundary Layer Induced by a Swept, Forward Facing Step. JFM (1970),42,P3,p.823.

3 Patel, V.C.,: Calibrations of the Preston Tube and Limitations on its Use in Pressure Gradients. JFM (1965), 23, P1, p.185.

4 Ludwieg, H.,Tillmann, W.,: Untersuchung ueber die Wandschubspannung in turbulenten Reibungsschichten. Ing.-Archiv (1949), 17, p.288.

5 Fernholz, H.,: Halbempirische Gesetze zur Berechnung turbulenter Grenzschichten nach der Methode der Integralbedingungen.Ing.-Archiv(1964),33,p.384.

6 Johnston, J.P.,: On the Three-Dimensional Turbulent Boundary Layer Generated by Secondary Flow. J.Basic Eng. (1960), 82, p.233.

7 Champagne, F.H., Sleicher, C.A.,: Turbulence Measurements with Inclined Hot-Wires.Part 2.Hot-Wire Response Equations. JFM (1967), 28, P1,p.177.

8 Mueller, U.,: Messung von Reynoldsschen Spannungen und zeitlich gemittelten Geschwindigkeiten in einer dreidimensionalen Grenzschicht mit nichtverschwindenden Druckgradienten. Dissertation RWTH Aachen, 1979.

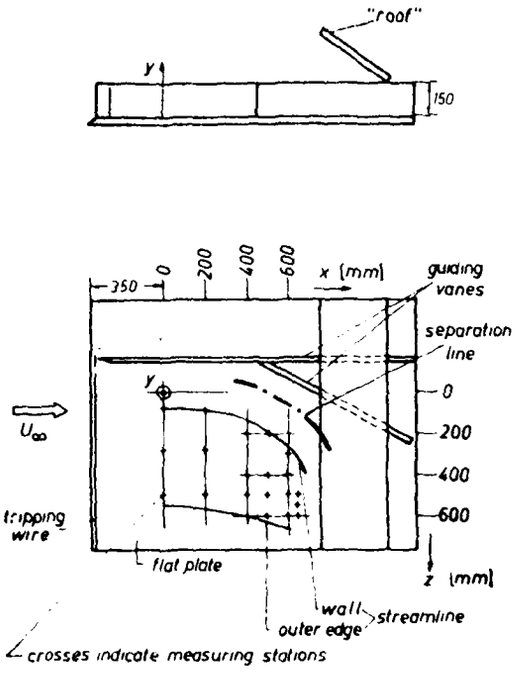

Fig.1 Schematic of experimental setup

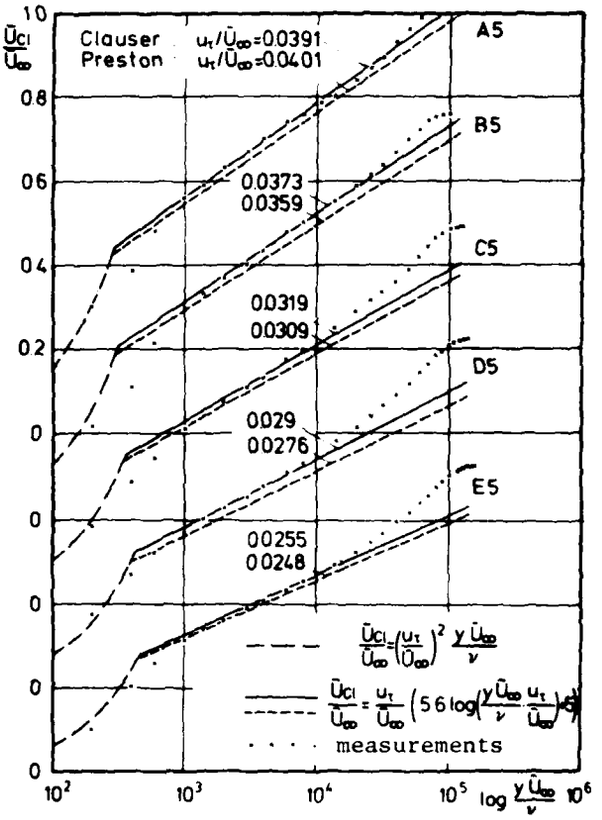

Fig.3 Clauser chart

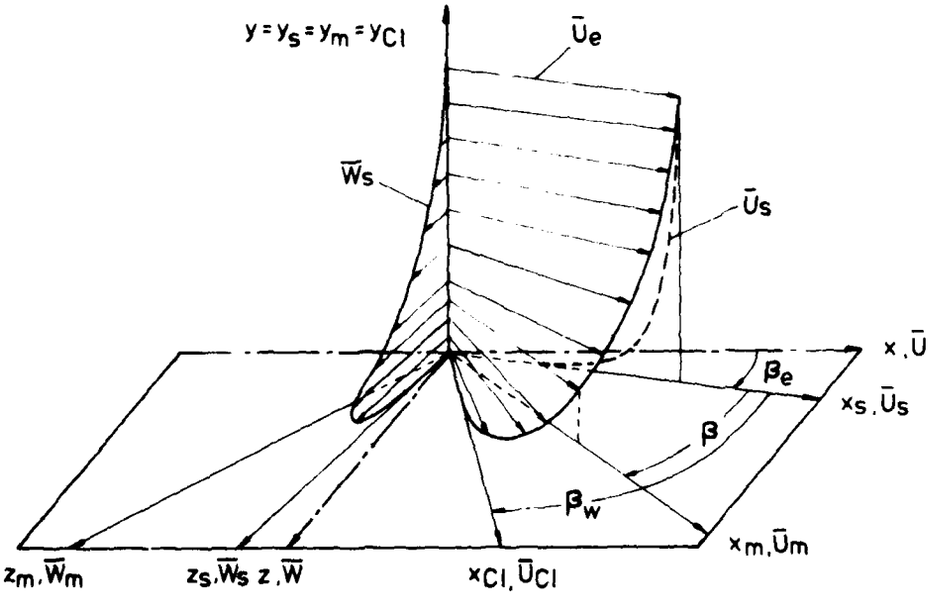

Fig. 2 Three-dimensional velocity profiles and coordinate systems used

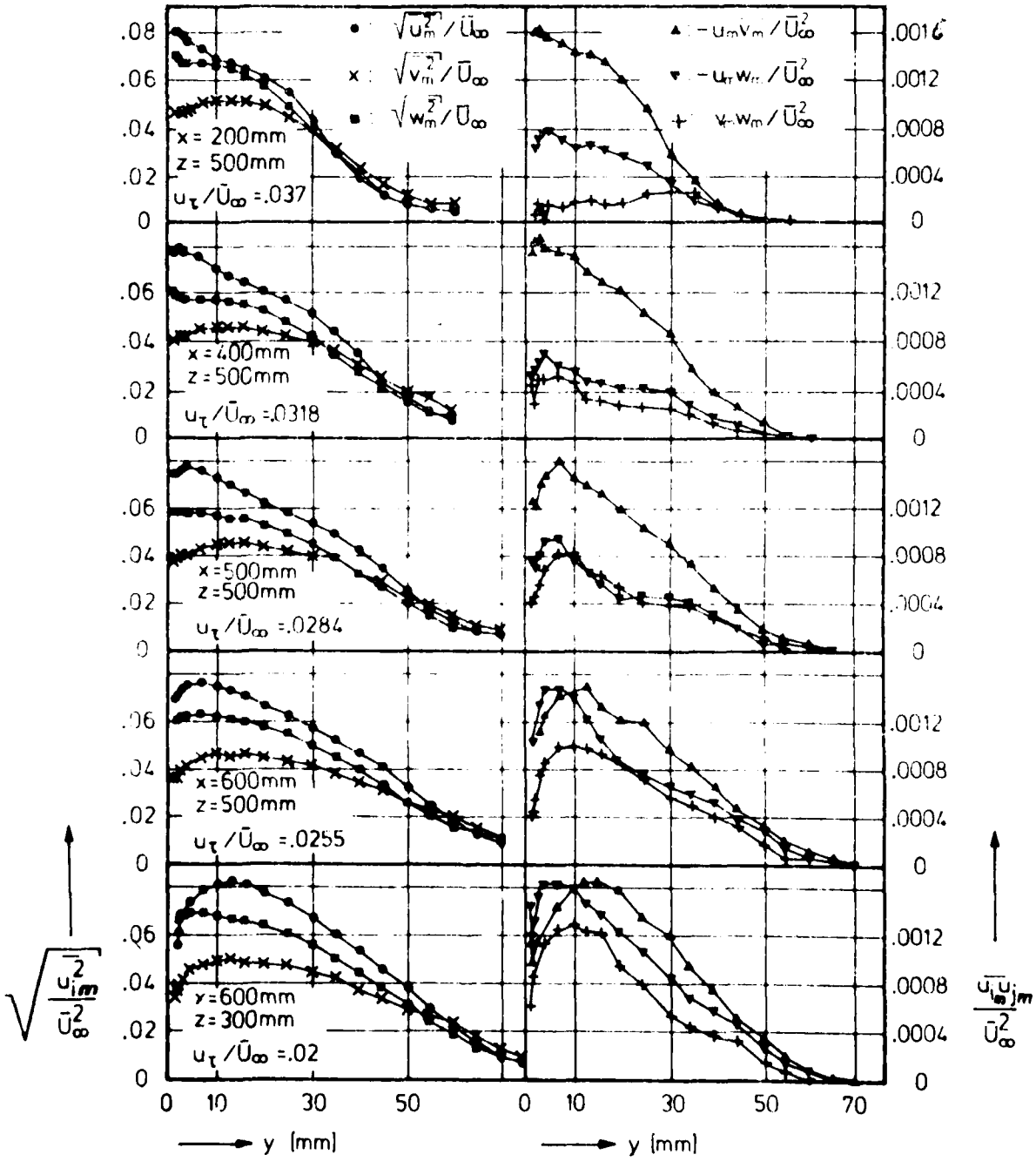

Fig. 4 Measured Reynolds stresses

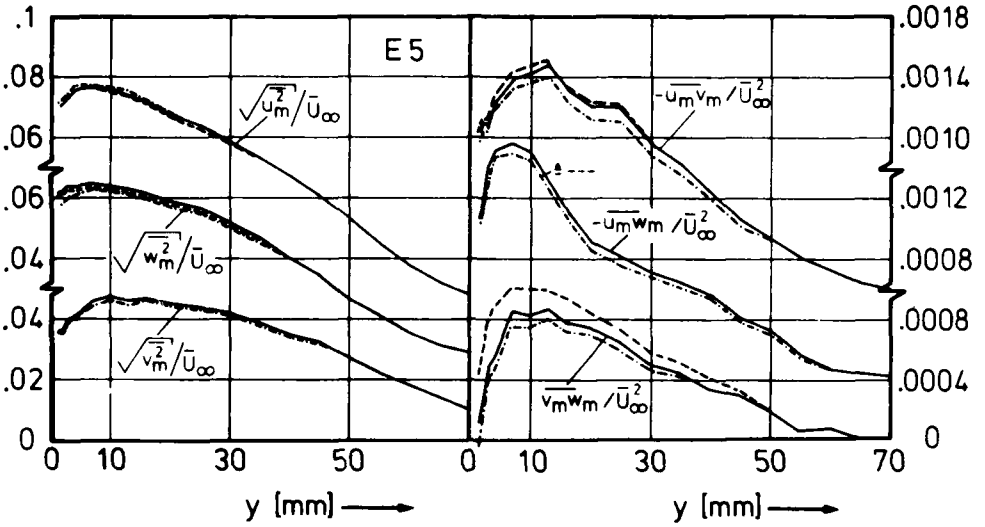

Fig.5 Influence of hot-wire cooling law on Reynolds stresses

-·-·- k=0.2 ; h=1 (ref.7)

——— $k=k(\overline{U}_m,\overline{V}_m)$; h=1

- - - $k=k(\overline{U}_m,\overline{V}_m)$; h=1.2 (actual calibration)

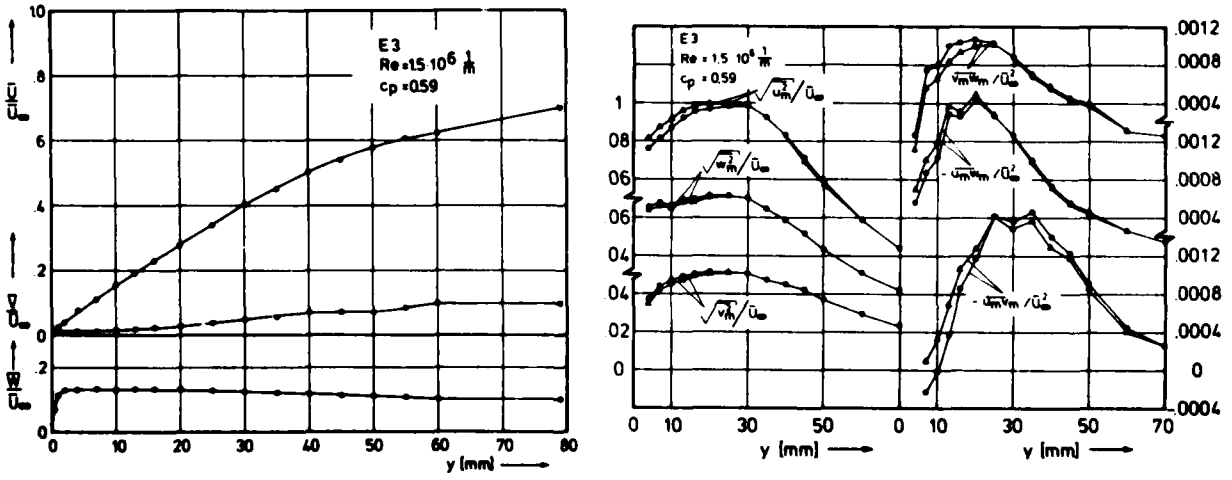

a) b)

Fig.6 Measurements close to separation

a) Mean velocities

b) Reynolds stresses evaluated with conventional method (▲) and that of ref.8 (●)

Table 1 Wall shear stresses and integral thicknesses

Nr.	x (mm)	z (mm)	$\bar{U}_e/\bar{U}_\infty$	$u_\tau/\bar{U}_\infty$ Preston	$u_\tau/\bar{U}_\infty$ ref.4	$u_\tau/\bar{U}_\infty$ ref.5	$u_\tau/\bar{U}_\infty$ Clauser	δ (mm)	δ_1 (mm)	δ_2 (mm)	θ_{11} (mm)	θ_{12} (mm)	θ_{21} (mm)	θ_{22} (mm)	e_1 (mm)	e_2 (mm)
A1	0	84	.9885	.03710	.04012	.03955	.04045	33.95	3.76		2.95				2.66	
A3	0	284	.9821	.03862	.04055	.03995	.04045	35.00	3.52		2.78				2.55	
A5	0	484	.9984	.03912	.03964	.03909	.04013	34.55	4.13		3.21				2.91	
B1	200	100	.9045	.03179	.03422	.03384	.03408	33.70	4.57	-0.07	3.36	0.02	-0.05	-0.001	2.98	0.02
B3	200	300	.9260	.03433	.03600	.03558	.03600	31.50	3.97	-0.66	2.96	0.09	-0.60	-0.012	2.63	0.08
B5	200	500	.9627	.03593	.03697	.03648	.03726	42.30	5.07	-0.25	3.90	0.06	-0.19	-0.005	3.52	0.05
C2	400	200	.8149	.02521	.02845	.02816	.02803	57.75	8.14	-1.60	5.86	0.39	-1.21	-0.073	5.12	0.32
C4	400	400	.8648	.02897	.03145	.03109	.03121	50.40	6.90	-1.08	5.12	0.37	-1.51	-0.089	4.52	0.31
C5	400	500	.9012	.03093	.03246	.03208	.03185	54.40	7.33	-1.34	5.48	0.33	-1.32	-0.063	4.84	0.27
C7	400	600	.9430	.03392	.03452	.03410	.03471	58.70	6.55	-1.05	4.92	0.25	-0.79	-0.047	4.41	0.21
D2	500	200	.7620	.02089	.02377	.02360	.02261	67.90	12.34	-3.46	8.10	1.10	-2.36	-0.284	6.81	0.88
D4	500	400	.8174	.02536	.02755	.02730	.02611	59.35	9.12	-2.80	6.38	0.70	-2.10	-0.196	5.51	0.57
D5	500	500	.8529	.02759	.02986	.02955	.02900	57.50	8.58	-2.44	6.22	0.65	-1.79	-0.186	5.41	0.53
D7	500	600	.8987	.03093	.03137	.03106	.03217	53.70	7.59	-2.24	5.44	0.54	-1.70	-0.166	4.77	0.45
E3	600	300	.7262	.01944	.02093	.02077	.01879	69.65	15.14	-4.79	9.14	1.79	-3.00	-0.543	7.45	1.24
E4	600	400	.7614	.02240	.02418	.02400	.02293	66.25	12.16	-4.73	7.98	1.49	-3.24	-0.552	6.63	1.19
E5	600	500	.8025	.02475	.02666	.02644	.02548	65.00	11.28	-4.38	7.73	1.33	-3.05	-0.522	6.52	1.04
E7	600	600	.8544	.02819	.02934	.02907	.02866	60.60	9.70	-3.79	6.84	1.12	-2.67	-0.484	5.91	0.88
F5	650	500	.7712	.02378	.02578	.02558	.02452	71.65	12.84	-6.30	8.86	1.94	-4.35	-0.940	7.15	1.49
F6	650	550	.8014	.02566	.02692	.02671	.02580	68.50	12.49	-6.43	8.33	1.97	-4.46	-1.042	6.91	1.50
F7	650	600	.8254	.02738	.02824	.02801	.02707	68.95	11.83	-6.18	8.12	1.80	-4.36	-0.959	6.75	1.36

$$\delta_1 = \int_0^\infty \left(1 - \frac{\bar{U}_S}{\bar{U}_e}\right) dy \qquad \delta_2 = \int_0^\infty -\frac{\bar{w}_S}{\bar{U}_e}\, dy \qquad \theta_{11} = \int_0^\infty \left(1 - \frac{\bar{U}_S}{\bar{U}_e}\right)\frac{\bar{U}_S}{\bar{U}_e}\, dy$$

$$\theta_{12} = \int_0^\infty \left(1 - \frac{\bar{U}_S}{\bar{U}_e}\right)\frac{\bar{w}_S}{\bar{U}_e}\, dy \qquad \theta_{21} = \int_0^\infty -\frac{\bar{U}_S\bar{w}_S}{\bar{U}_e^2}\, dy \qquad \theta_{22} = \int_0^\infty -\frac{\bar{w}_S^2}{\bar{U}_e^2}\, dy$$

$$e_1 = \int_0^\infty \frac{1}{2}\left(1 - \frac{\bar{U}_S^2+\bar{w}_S^2}{\bar{U}_e^2}\right)\frac{\bar{U}_S}{\bar{U}_e}\, dy \qquad e_2 = \int_0^\infty \frac{1}{2}\left(1 - \frac{\bar{U}_S^2+\bar{w}_S^2}{\bar{U}_e^2}\right)\frac{\bar{w}_S}{\bar{U}_e}\, dy$$

Table 2 Mean velocities and Reynolds stresses

1 : y (mm) ; 2 : $\bar{U}/\bar{U}_\infty$; 3 : $\bar{v}/\bar{U}_\infty$;
4 : $\bar{w}/\bar{U}_\infty$; 5 : $\beta = \beta + \beta_0(1^\circ)$; 6 : $\varepsilon = \tan^{-1}(\bar{v}_m/\bar{U}_m)$;
7 : $10\sqrt{\bar{u}^2}/\bar{U}_\infty^2$; 8 : $10\sqrt{\bar{v}^2}/\bar{U}_\infty^2$; 9 : $10\sqrt{\bar{w}^2}/\bar{U}_\infty^2$;
10 : $100\cdot\overline{uv}/\bar{U}_\infty^2$; 11 : $1000\cdot\overline{uw}/\bar{U}_\infty^2$; 12 : $1000\cdot\overline{vw}/\bar{U}_\infty^2$.

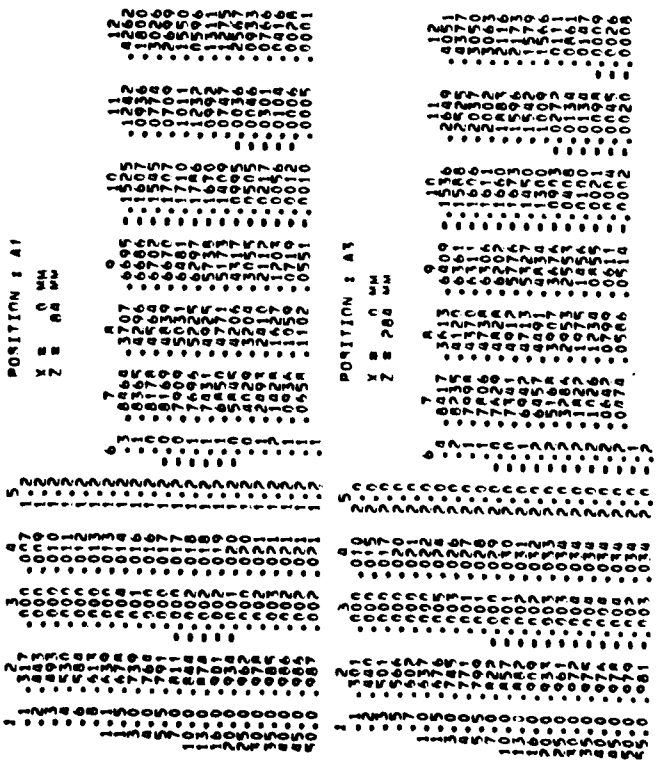

Table 3 Pressure distribution

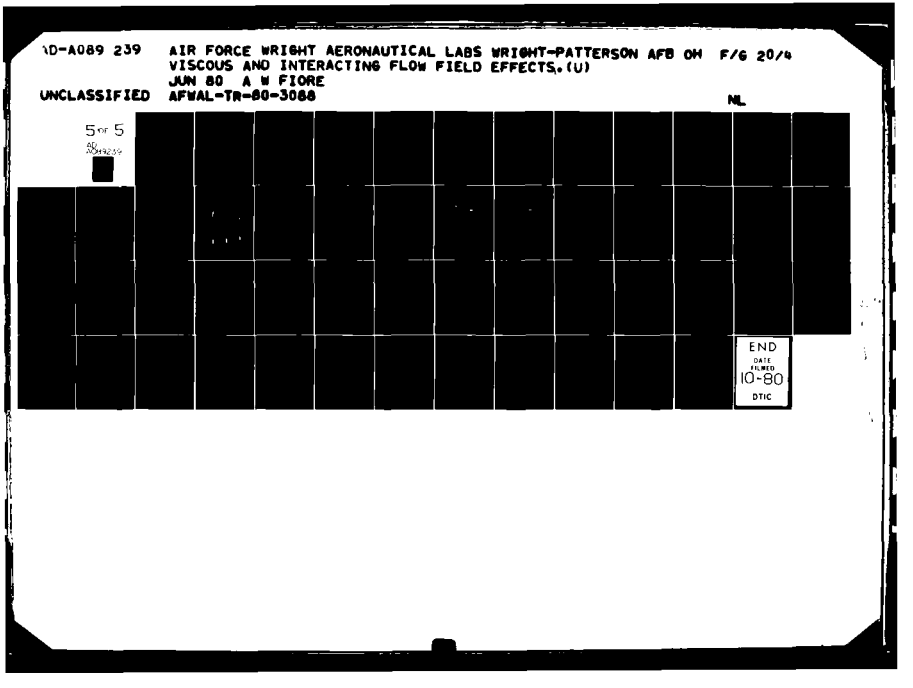

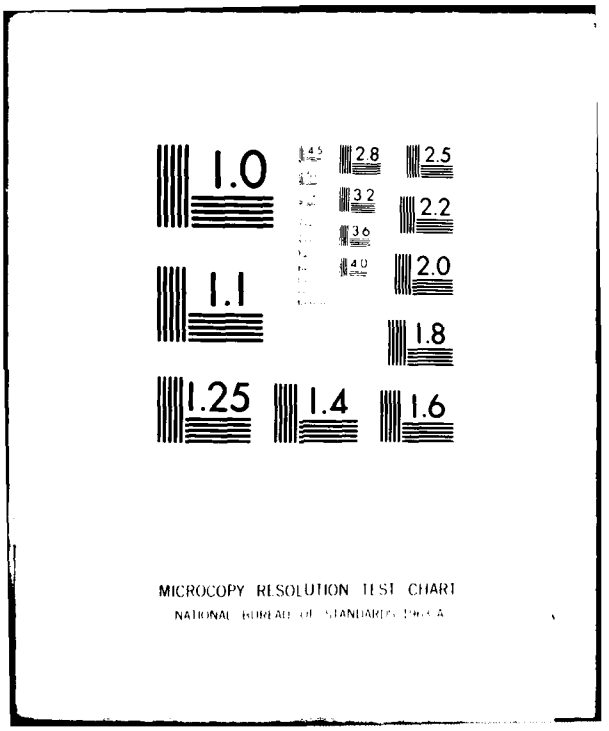

SEPARATION AND VORTEX PATTERN ON A SPHEROID AT INCIDENCE

W. Haase
Dornier GmbH, Friedrichshafen

ABSTRACT

Results are given for threedimensional laminar incompressible flowfields past prolate spheroids at incidence. In addition to last year's DEA present paper is concerned with a 4:1 spheroid at Reynoldsnumbers up to $0.8 \cdot 10^5$ (based on length of spheroid). Furthermore vorticity- and pressure distributions are given.

INTRODUCTION

This work is concerned with three-dimensional laminar separation phenomena of the boundary layer over an inclined body of revolution. It is a continuation of results [6] presented at the DEA-Meeting in Meersburg last year and especially investigates the high Reynoldsnumber case as well as pressure distributions in the entire flowfield.

Analysed flowfield patterns clearly demonstrate separation phenomena resulting in a combinuation of a free vortex layer type and a bubble type separation. Navier-Stokes solutions are compared with experiments by HAN/PATEL [7] and boundary

layer calculations by WANG [12, 13], Stock [11] and GEISSLER [2, 3]. Contrarily to these methods, integration of the Navier-Stokes equations does not require any assumptions at all.

Navier-Stokes calculations allow to predict complete surface pattern as well as direction and strength of trailing vortices whose effect on downstream flow conditions can be severe. Due to their direction of rotation these trailing vortices cause a thinning of boundary layer at the plane of symmetry, see e.g. STOCK [11].

DISCUSSION OF SURFACE FLOW PATTERN

For better physical understanding a brief discussion is given dealing with the conception of three-dimensional laminar separation.

In the two-dimensional case it is easy to specify separation phenomena because the boundary layer separates at one single point. At that point the first-order boundary layer equations become singular and the tangential flow components at the surface is reversed. Therefore, the downstream flow regime is inaccessible for boundary layer calculations.

For three-dimensional flow problems it is much more complicate to give a definition for separation. In most previous studies concerned with three-dimensional separation, e.g. LIGHTHILL [8], MASKELL [9], WANG [12], ZAKKAY/MIYAZAWA/WANG [14], authors correlate separation with an observation of limiting streamlines.

Separation lines are defined as follows, HAN/PATEL [7]:

- lines on which components of wall shear stress tends to zero
- limiting streamlines joining singular points
- envelope of limiting streamlines
- lines dividing surface flow pattern into special domains.

Each definition is only valid under certain conditions but none is universally valid.

To describe the physical flow phenomena more precisely a body-oriented coordinate system is given in Fig. 1; nevertheless, present calculations were carried out in a cartesian coordinate system. Furthermore, Fig. 1 shows the surface flow pattern for an inclined spheroid for a mediate angle of attack as first pointed out by WANG [13]. Streamlines starting from the front stagnation point (FS) approach the solid part of curve R_1R_2 designated as the separation line of free vortex layer type. In the area of the dotted part of R_1R_2 streamlines still penetrate from region A to region B but the line itself indicates the location of zero circumferential skin friction. Specifically we define the complete curve R_1R_2 to be the line where $(\partial v/\partial\theta)_w$ vanishes. Following WANG [12] and HAN/PATEL [7] the solid part of R_1R_2 is called a separation line under the condition of "not too small" angles of attack. At vanishing incidence no separation occurs just behind the line of zero circumferential skin friction, but at medium and high angles of attack, the boundary layer is so much thickened before reaching R_1R_2 that separation of the free vortex layer occurs right after R_1R_2 forming two symmetri-

cally trailing vortices. Together with the negativ circumferential velocity component v which is derivable from boundary layer calculations, these vortices cause a thinning of the boundary layer along the line of symmetry.

In region B the main flow velocity component u remains unchanged. However, behind line S_1S_2 u is reversed, too. We define that part of the spheroid as region C. While R_1 and R_2 are regular points because only one limiting streamline passes through, S_1 is a saddle point. Additionally, FS, RS and S_2 are nodal points satisfying the topological law of LIGHTHILL [8], stating that the number of nodal points must exceed the number of saddle points by two.

In opposite to WANG's proposals and calculations, HAN/PATEL [7] found by flow field observations, that R_2 may intersect the line of closed separation S_1S_2, forming an R_{2_I} and $R_{2_{II}}$ on the opposite side of the body. Again these nodal points together with FS and RS exceed the number of saddle points (S_1 and S_2 (!)) by two and verify the topological law.

The numerical calculations of Navier-Stokes equations are quite similar to the observed flowfield configuration presented by HAN/PATEL.

NAVIER-STOKES RESULTS

To underline the foregoing discussion three-dimensional flowfield configurations for a spheroid with axis ratio a:b = 4:1 are given, obtained from Navier-Stokes calculations. Flow is assumed to be incompressible and laminar.

To give an overlook to the entire flowfield around an spheroid at incidence ($\alpha = 30^{\circ}$) Fig. 2 shows the flowfield pattern for the plane of symmetry (Fig. 2 a,b) as well as some crossflow velocity plots (Fig. 2c - 2h).

Results are based to a Reynoldsnumber of Re = 1000 (Re = $U_{\infty} \cdot 2a/\nu$; a = semi-major axis of spheroid). Into Fig. 2a three lines are inserted, denoted by I, II and III. Line I characterizes the locus of open separation, identical with a separation of the free vortex layer type. Along this line the boundary layer rolls up into a longitudinal vortex. Line II enclose the region of bubble type separation, e.g. reversed u-velocityand it is evident from Fig. 2b, that the leeward separation point S_1 lies very close near the rear end of the body. A more exact graph of these separation lines is given in Fig. 3. Projected into the plane of symmetry - as well as the previous lines - curve III demonstrates the path of the longitudinal trailing vortex. The path was found to be positioned close to the body's shape, and the whole vortex will be lifted up due to chosen Reynolds number and angle of attack.

Remember, line III represents the projection of the vortex path, and its lift-up is in fact not controverse to the direction of the velocity vectors in that region. These velocity vectors are pointing towards the end of the spheroid, indicating the thinning of boundary layer at the plane of symmetry and are caused by the direction of rotation of the two symmetric vortices.

All three lines can be constructed with help of crossflow velocity plots; some of them are presented in Fig. 2c-2d, their positions x/2a along the major axis of the spheroid is indicated by vertical arrows in Fig. 2a.

Fig. 2c shows the crossflow pattern near the leading edge at x/2a = 0.09; x measured from the body's tip. At the windward side velocity vectors are pointed downwards due to a main flow directed tangential to the body's shape. In Fig. 2d the secondary vortex is not fully developed, but very small (negativ) v-components near the symmetry plane indicate the vortex's starting point at that station x/2a = 0.4. Further downstream - Fig. 2e: x/2a = 0.7 - this vortex is clearly to be seen and is directed normally from the plane of symmetry not changing its height in the z-direction. Due to the convergent back part of the body, that vortex is lengthened as shown in Fig. 2f at the station x/2a = 0.95, changing the vortex path by no means as shown in Fig. 2e. The flow pattern just behind the spheroid is shown in Fig. 2g at x/2a = 1.05, the secondary vortex remains unchanged.

Nevertheless, downstream - Fig. 2h, x/2a = 1.31 - it is forced to lift up due to the main flow direction and at the same time it is directed towards the symmetry plane again. Furthermore, the shape of that vortex has been rounded because of viscous effects.

These viscous effects are also responsible for a vanishing of the secondary vortex downstream of station x/2a = 1.6, indicated by the dotted part of line III in Fig. 2a. Only wake velocity-profiles can be identified looking at crossflow patterns downstream of x/2a = 1.6.

In addition to given explanations, Fig. 3 states a more precise documentation of separation lines and vortex pathes in side- and top view respectively.

To underline the previous discussion of threedimensional separation, in Fig. 4 lines of constant vorticity (Fig. 4a) and constant pressure (Fig. 4b) are presented, each for the plane of symmetry when flow comes from the bottom of left. Especially in Fig. 4a one can examine the conical region of convected vorticity behind the spheroid. The value 0.001 denotes vanishing vorticity and the corresponding lines act as boundaries dividing the flow regime into a rotation free outer region and another one which is affected with vorticity. Following the 1.28-line along the body, again the thinning of the symmetry plane boundary layer can be examined, because that line is directed towards the body downstream of the main cross-section of the spheroid. Additionally the distribution of the pressure coefficient is given in Fig. 4b.

The procedure, especially for calculating pressure in the entire computational domain had been presented first by HAASE/ELSHOLZ [4] and HAASE/HINDENBERG [5] and is comparable with proceedings presented by MASON/SYKES [10].

That procedure integrates the pressure differential equation directly in the whole domain, including the interior of the body. Therefore pressure calculations can be made without further body boundary conditions, these are implicitly contained in the coefficients of the differential equations because of the non-slip conditions.

To emphasize that procedure, in Fig. 4a,b and in the following Figures 4c-4h lines of constant vorticity and pressure are additionally drawn inside of body's shape, however these lines are of no physical interest. Latter figures show the development of vorticity (left hand part) and pressure (right hand part) for various cross-sections. At the lower side of sphe-

roid's cross-sections one can determine the growth of the boundary layer thickness, while on the upper half only the development of vorticity is visible. In other words: The complete -0.3-vorticity-line cannot be interpreted as the outer part of a boundary layer due to that large stretching, but nevertheless it helps to demonstrate the differences between flow regimes controlled by diffusion and or convection.

From the corresponding pressure results in Fig. 4c-4h, it is evident that pressure-lines are nearly normal to the body surface in the front part of the spheroid, see Fig. 4c ($x/2a = 0.09$). Therefore, the boundary layer assumptions with $\partial p/\partial n = 0$ are valid in that flow regime and this in fact is trivial, because the boundary flow is accelerated in the corresponding part of the spheroid.

In Fig. 4d the normal derivative of pressure only vanishes in the lower half of body cross-section, but is at variance to that at the upper half due to the beginning of open separation at station $x/2a = 0.4$. The influence of flow separation on the pressure distribution (or vice versa) can easily be verified by observing the -0.2-pressure line in the next two Figures 4e and 4f at $x/2a = 0.50$ and 0.70 respectively.

Fig. 5 shows flow pattern in the symmetry plane as well as zero circumferential skin friction lines, separation lines, and the vortex paths in top and side view; free stream Reynoldsnumber is $0.8 \cdot 10^5$ and the angle of attack equals $\alpha = 5^\circ$. Present results are compared with boundary layer calculations by WANG [12] (for $\alpha = 6^\circ$) and with measurements

of HAN/PATEL [7] (a:b = 4.3:1). The separation line II denoting bubble type separation disagree with the calculations by WANG, while comparison of separation points S_1 and S_2 with calculations and observations are not too bad. That is quite the same for the line of open separation (curve I).

In comparison with Fig. 3 the vortex paths (III) is positioned much closer to the body, following its shape until reaching the end. This may be attributed to a thinner boundary layer compared with the Re = 1000 case and to a smaller angle of attack.

These effects can also be verified using Fig. 6, which shows the $\alpha = 15^{\circ}$ case for the same Reynolds number and axis ratio. Lines of open separation are compared with finite difference results by GEISSLER [2] and an integral approach by STOCK [11]. The agreement between present results and calculations by these authors is only qualitatively acceptable. There are in fact two main reasons for such discrepancies. At first, some of these disagreements may be attributed to the use of the potential pressure distributions in the boundary layer calculations since the actual pressure distribution is significantly changed by the complex flow patterns including the strong interactions with trailing vortices.

Furthermore, using cartesian coordinates for noncartesian bodies causes problems in the sense of meshpoint clustering near the body and therefore it is not trivial to calculate lines of separation. Nevertheless, cartesian coordinate systems denote a worthy tool in predicting complex flow field configurations and more than that, they are easy to handle, e.g. see DAWSON/MARCUS [1] or MASON/SYKES [10].

The last two figures, show the locations of the leeward separation point S_1 (Fig. 7) and the windward separation point S_2 (Fig. 8) for a 4:1 spheroid at Re = $0.8 \cdot 10^5$ as a function of the angle of attack. They are compared with experiments by WILSON [15], HAN/PATEL [7] and calculated values by WANG [12].

ACKNOWLEDGEMENT

Present work was performed at Technische Universität Berlin and partially sponsored by the Deutsche Forschungsgemeinschaft. The author is greatly indepted to Prof. Dr.-Ing. A. Walz for his guidance.

REFERENCES

[1] Dawson, Ch., Marcus, M.
DMC - A Computer Code to Simulate Viscous flow about Arbitrarily Shaped Bodies.
Proc. of 1970 Heat Transfer and Fluid Mechanics Institute, pp. 323-338. Stanford, California: Stanford University Press, 1970.

[2] Geissler, W.
Berechnung der laminaren Ablösung an unsymmetrisch umströmten Rotationskörpern mittels Differenzenverfahren.
DFVLR-AVA Bericht Nr. IB 251-73 A 31 (1973).

[3] Geissler, W.
Berechnung der laminaren dreidimensionalen Grenzschicht an unsymmetrisch umströmten Rotationskörpern mittels Differenzenverfahren.
DFVLR-AVA Bericht Nr. IB 251-73 A 19 (1973).

[4] Haase, W., Elsholz, E.
Some New Results on Calculating Three-Dimensional Viscous Flows. Techn. Report AFFDL-TR-77-61 (1977), pp. 47-53.

[5] Haase, W., Hindenberg, J.
Die Lösung der zweidimensionalen Navier-Stokes-Gleichung für Strömungen um beliebige Körperkonfigurationen
DLR-FB 77-16 (1977), S. 107-118.

auch erschienen als:
The solution of the Two-Dimensional Navier-Stokes Equations for Flows about Arbitrary Configurations. ESA-TT-498 (1979), pp. 157-173.

[6] Haase, W.
Some Remarks on Separation Pattern over an Inclined Body of Revolution.
BMVG-FBWT 79-31 (1979).

[7] Han, T., Patel, V.C.
Flow Separation on a Spheroid at Incidence.
J. Fluid Mech. (1979), Vol. 92, Part 4, pp. 643-657.

[8] Lighthill, M.J.
Laminar Boundary Layers
Editor: L. Rosenhead, Oxford University Press, Oxford, England (1963).

[9] Maskell, E.C.
Flow Separation in Three Dimensions. RAE Rept. AERO 2565, Nov. 1955, Royal Aircraft Establishment, Bedford, England

[10] Mason, P.J., Sykes, R.I.
Three-Dimensional Numerical Integrations of the Navier-Stokes Equations for Flow over Surface-Mounted Obstacles.
J. Fluid Mech., Vol. 91, Part 3 (1979), pp. 433-450.

[11] Stock, H.W.
Laminar Boundary Layers on Inclined Ellipsoids.
ZFW: zur Veröffentlichung vorgelegt.

[12] Wang, K.C.
Separation Patterns of boundary Layerover an inclined Body of Revolution.
AIAA Journal (1972), Vol. 10, No. 8, pp. 1044-1050.

[13] Wang, K.C.
Three-Dimensional Boundary Layer near the Plane of Symmetry of a Spheroid at Incidence.
J. Fluid Mech., Vol 43, Part 1, (1970), pp. 187-209.

[14] Zakkay, V., Miyazawa, M., Wang, C.R.
Lee Surface flow phenomena over Spaceshuttle at large Angles of Attack at Ma = 6.
NASA Contractor Report, No. 132501 (1974).

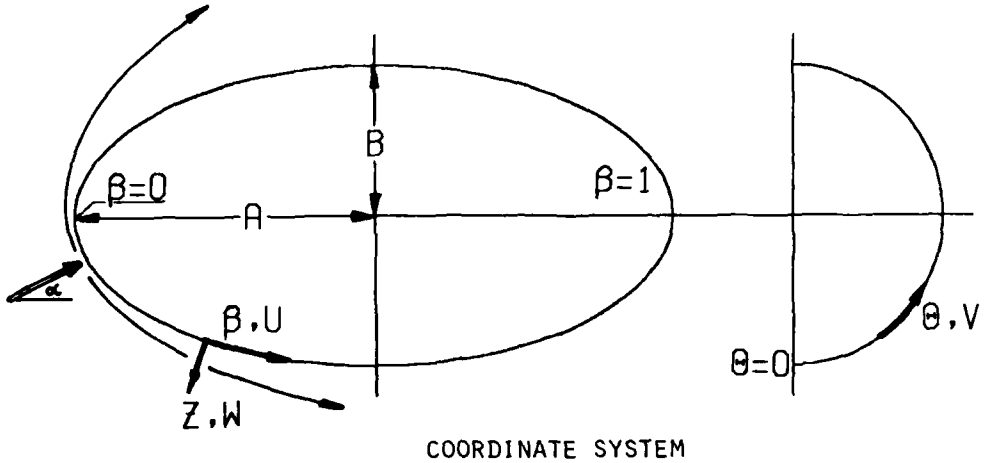

COORDINATE SYSTEM

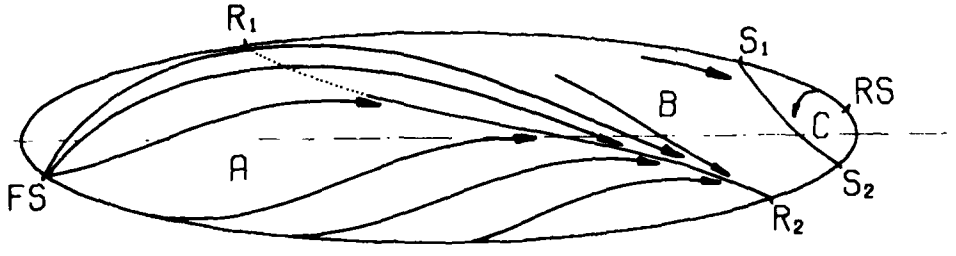

SIDE VIEW

TOP VIEW

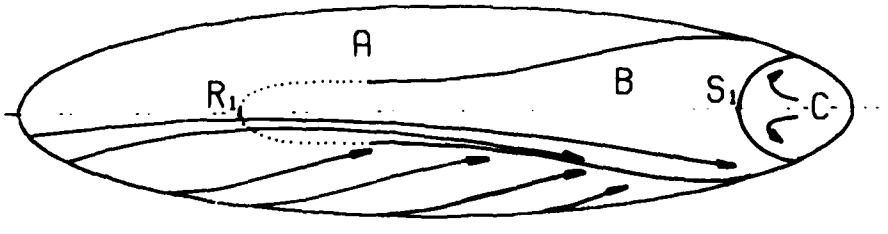

FIG.1: COORDINATE SYSTEM, LIMITING STREAMLINES AND LINES OF SEPARATION FOR AN INCLINED SPHEROID

A)

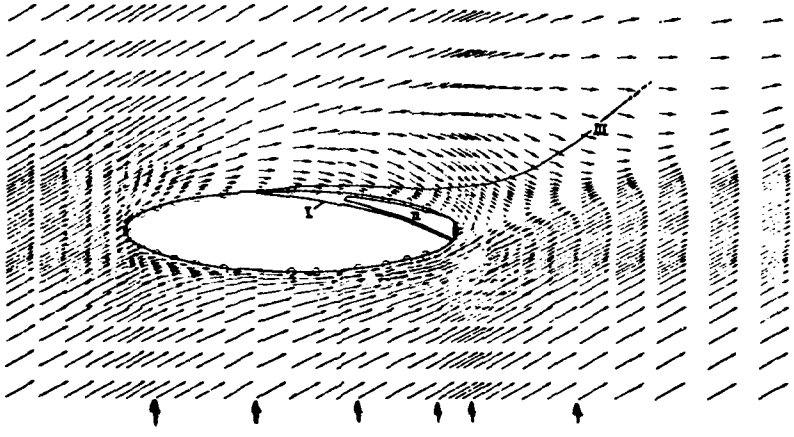

B)

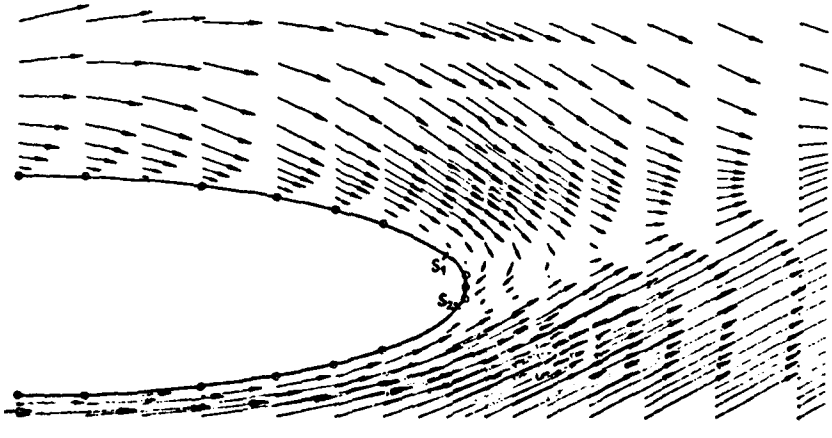

FIG. 2 A,B: VELOCITY-VECTOR PLOT OF THE PLANE OF SYMMETRY
(α = 30°, RE = 1000, A:B = 4:1)

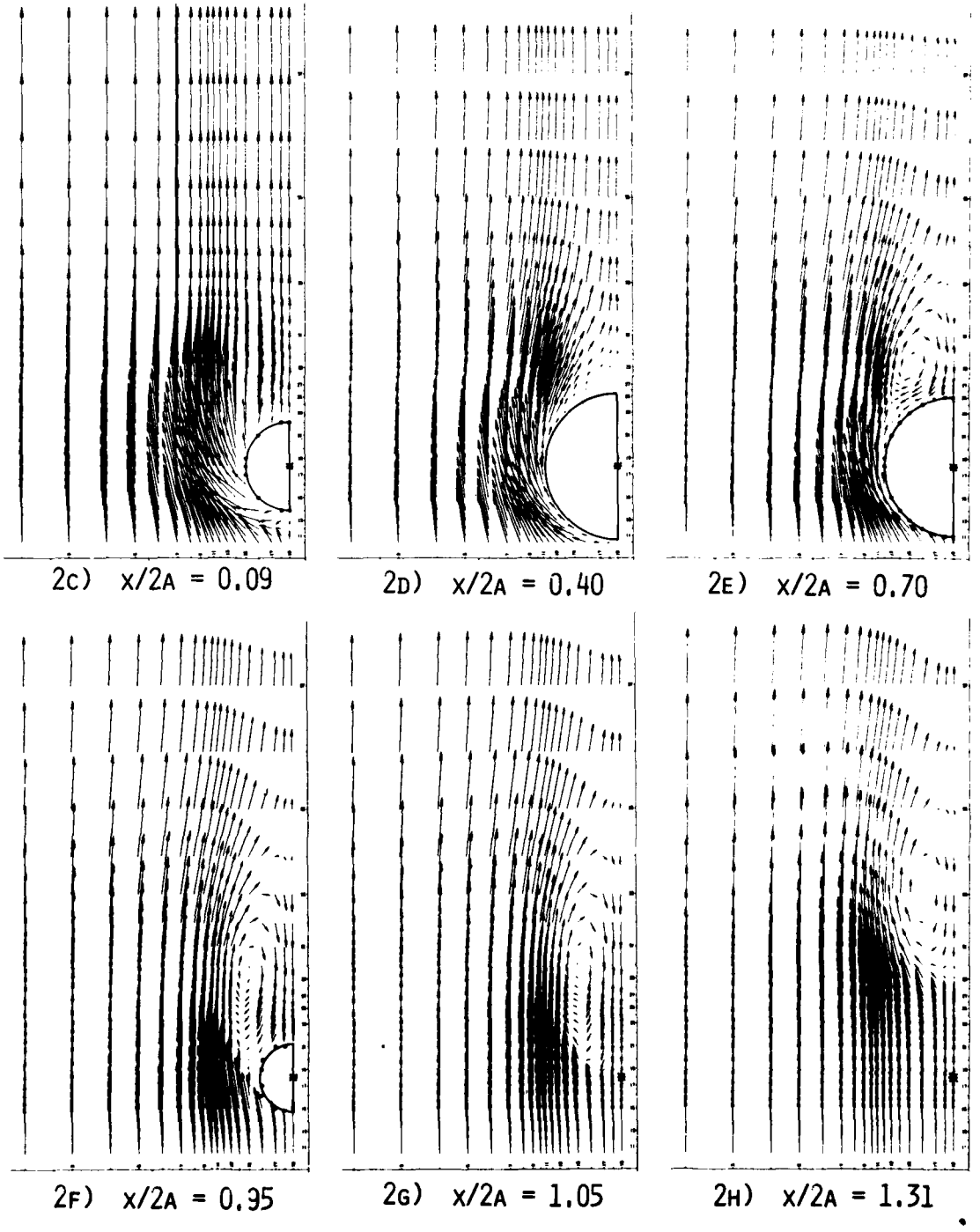

FIG. 2 C-H: CROSSFLOW VELOCITY-VECTOR PLOT
($\alpha = 30^0$, RE = 1000, A:B = 4:1)

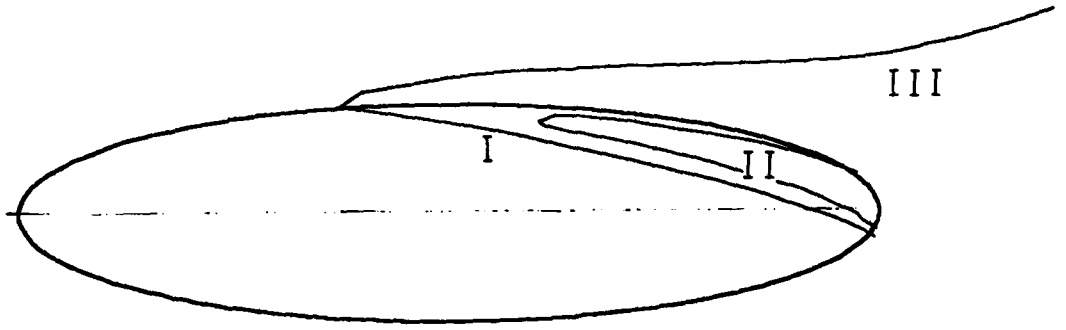

SIDE VIEW

TOP VIEW

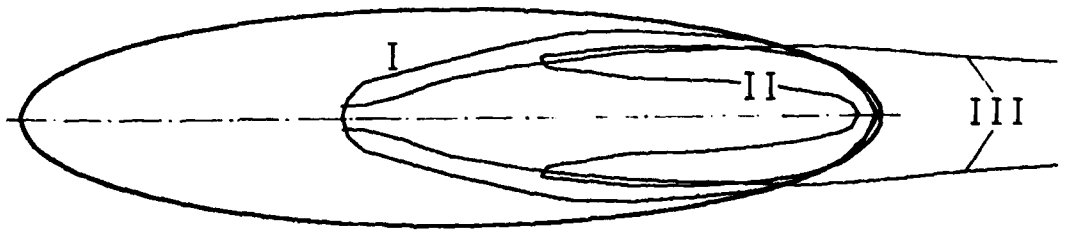

I = $C_{F,\theta}$ = 0-LINE

II = $C_{F,\beta}$ = 0-LINE

III = PATH OF VORTEX

FIG. 3: C_F = 0-LINES AND PATH OF TRAILING VORTICES
($\alpha = 30^0$, RE = 1000, A:B = 4:1)

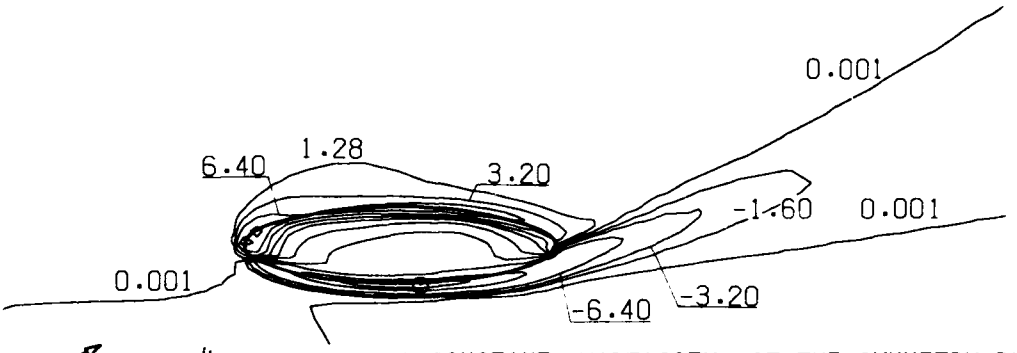

FIG. 4 A: LINES OF CONSTANT VORTICITY AT THE SYMMETRY PLANE
($\alpha = 30^0$, RE = 1000, A:B = 4:1)

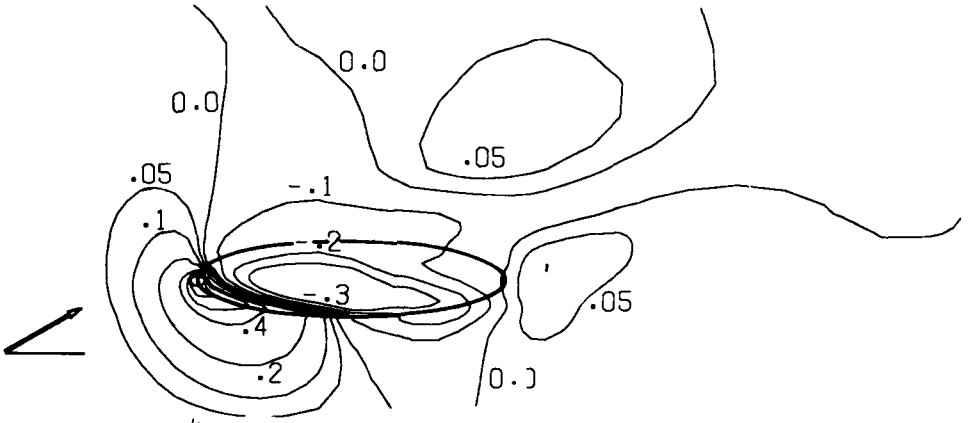

FIG. 4 B: LINES OF CONSTANT PRESSURE COEFFICIENT

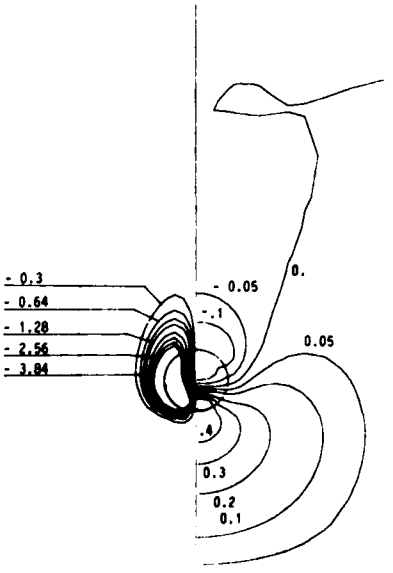

4 C) x/2A = 0.09

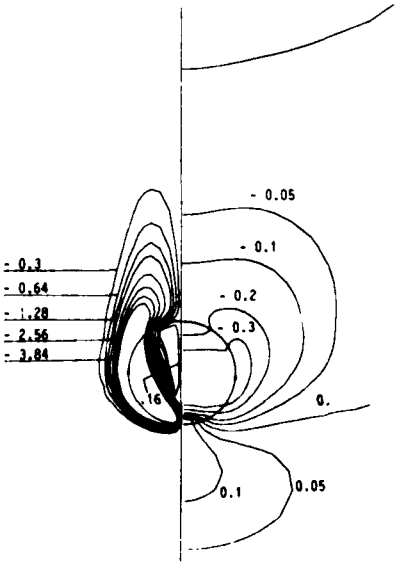

4 D) x/2A = 0.40

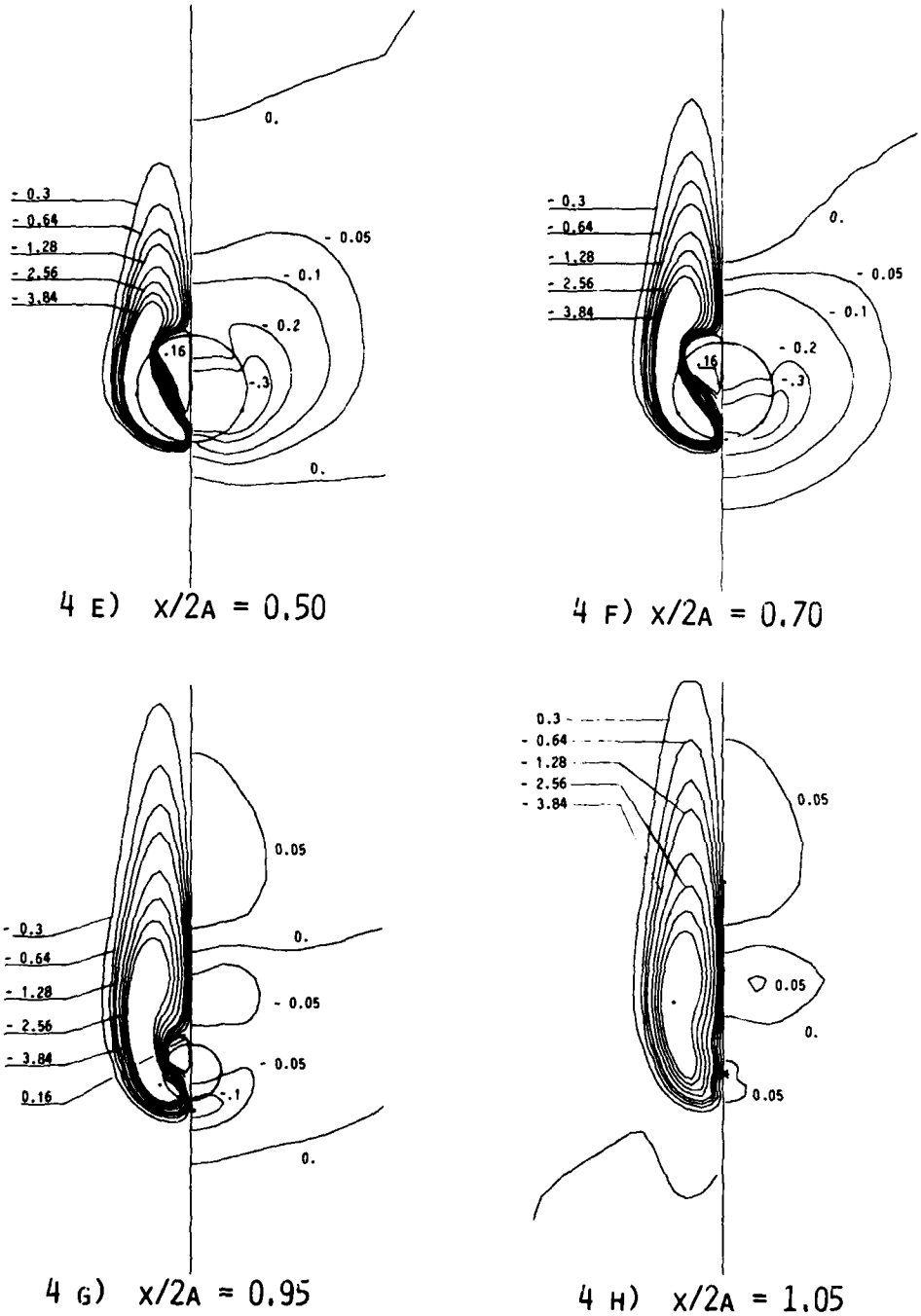

FIG. 4 C-H: LINES OF CONSTANT VORTICITY (LEFT HAND SIDE) AND PRESSURE COEFFICIENT (RIGHT HAND SIDE) AT VARIOUS CROSS SECTIONS ($\alpha = 30^0$, RE = 1000, A:B = 4:1)

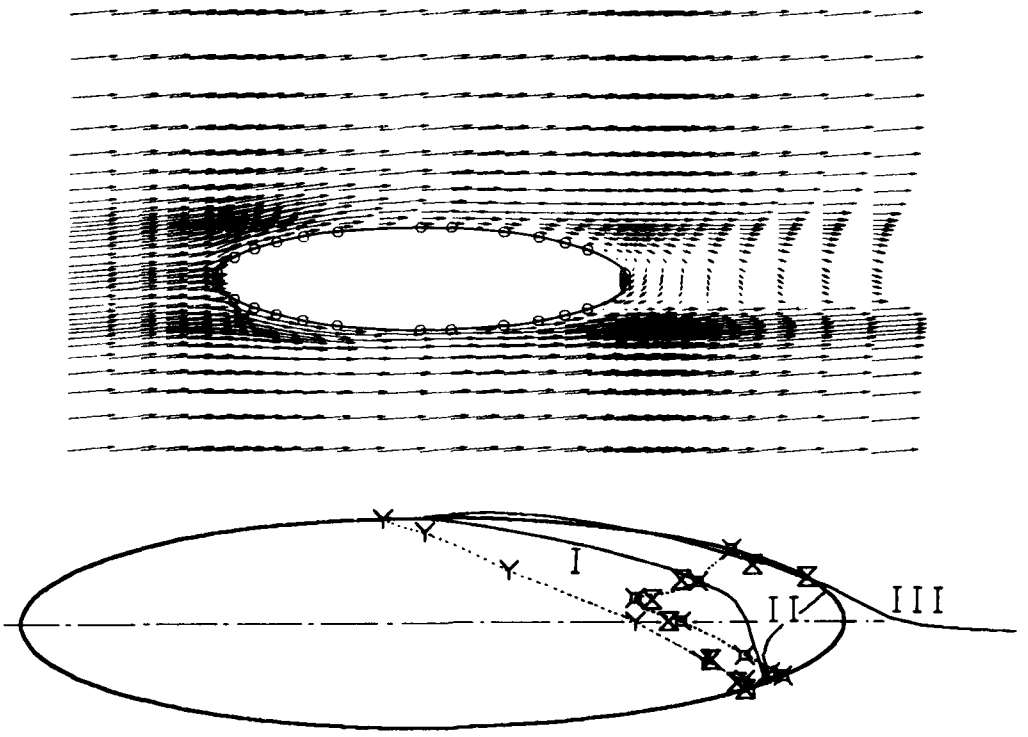

SIDE VIEW

TOP VIEW

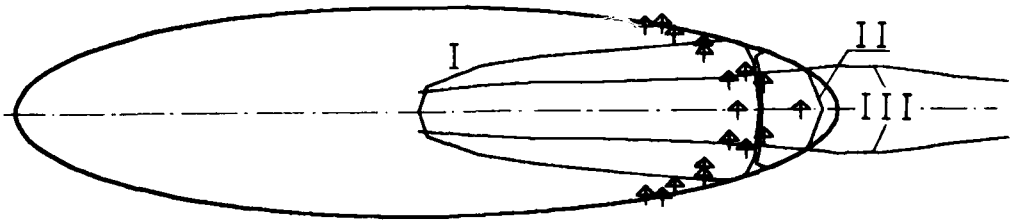

PRESENT WORK I = $C_{F,\theta}$ = O-LINE
II = $C_{F,\beta}$ = O-LINE
III = PATH OF VORTEX

WANG (CALCULATION, $\alpha = 60$)

HAN/PATEL (MEASUREMENT, A:B = 4.3:1)

FIG. 5: VELOCITY-VECTOR PLOT OF SYMMETRY PLANE, C_F = O-LINES AND PATH OF TRAILING VORTICES
($\alpha = 50$, RE = 0.8×10^5, A:B = 4:1)

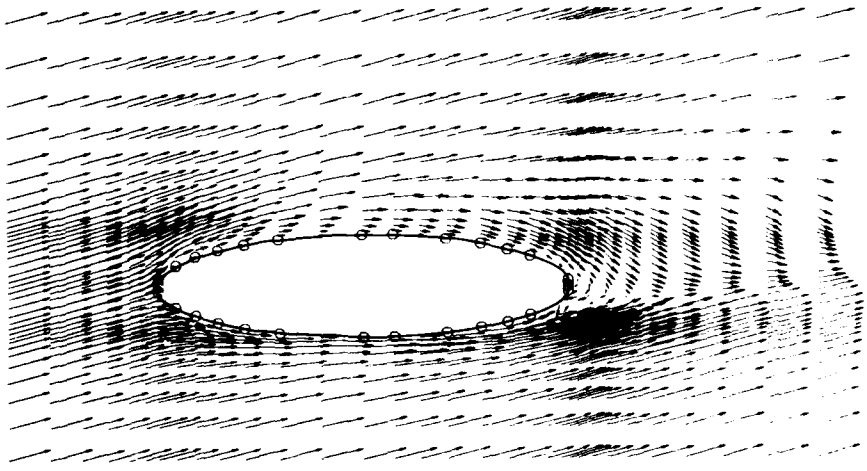

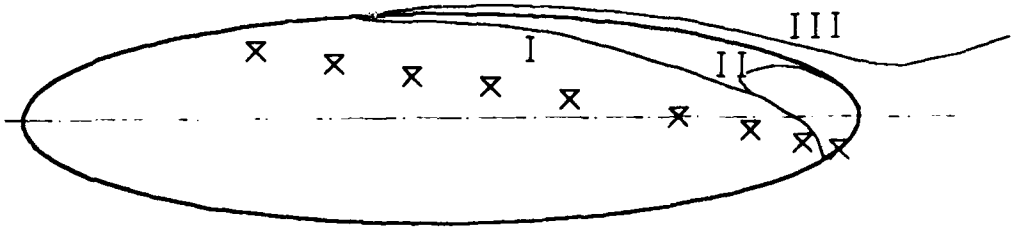

SIDE VIEW

TOP VIEW

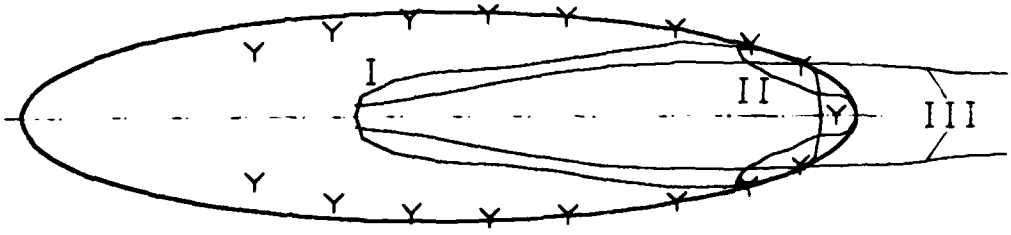

— PRESENT WORK I = $C_{F,\theta}$ = 0-LINE
II = $C_{F,\beta}$ = 0-LINE
III = PATH OF VORTEX

XY STOCK AND GEISSLER (BOUNDARY LAYER CALCULATION)

FIG. 6: VELOCITY-VECTOR PLOT OF SYMMETRY PLANE, C_F = 0-LINES AND PATH OF TRAILING VORTICES
(α=15°, RE = 0.8 x 10^5, A:B = 4:1)

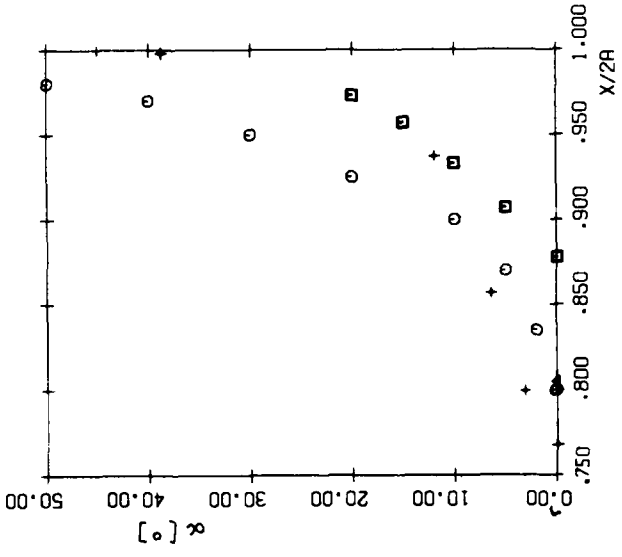

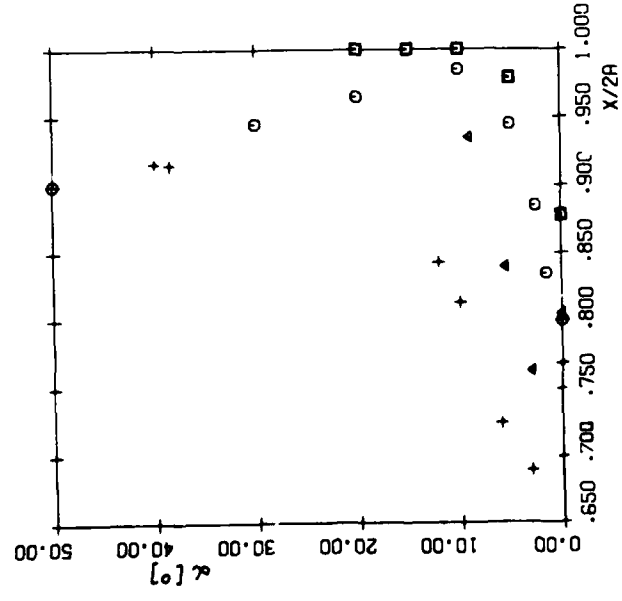

- PRESENT WORK
- HAN/PATEL (MEASUREMENT, A:B = 4.3:1)
- WILSON (MEASUREMENT)
- WANG (BOUNDARY LAYER CALCULATION)

FIG. 7: LOCATION OF LEEWARD SEPARATION POINT s1 ($Re = 0.8 \times 10^5$, A:B = 4:1)

FIG. 8: LOCATION OF WINDWARD SEPARATION POINT s1 ($Re = 0.8 \times 10^5$, A:B = 4:1)

EXPERIMENTS ON VORTEX IMPINGEMENT ON CONTROL FINS

J. D. Gillerlain, Jr.
U. S. Naval Academy, Annapolis, Maryland 21402

W. J. Yanta
Naval Surface Weapons Center, Silver Spring, Maryland 20910

Abstract

Accurate prediction of the aerodynamic behavior of missiles and aircraft experiencing vortex impingement on control surfaces becomes more essential as high angle-of-attack maneuvering requirements increase. Detailed knowledge of the three-dimensional viscous flowfield, as determined from windtunnel experiments, is required in order to develop predictive methods based on the vortex-fin interaction. Tests were conducted in the U. S. Naval Academy Aerodynamics Laboratory subsonic windtunnel using a rectangular fin model adjustable for angle-of-attack. The impinging vortex was generated at different positions upstream of the fin at the juncture of two adjacent airfoils set at equal but opposite angles-of-attack. Force, moment, and pressure distribution data were obtained for one freesteam velocity and one vortex strength. Flow visualization tests utilized the fluorescent mini-tuft technique. The three-dimensional flowfield was surveyed using a laser Doppler velocimeter. The status of the experimental program is updated, and the direction of future work is discussed.

Foreword

This paper is included in a session entitled "Research Updates." Part of the project was outlined in Reference (1) at the 4th U. S. - German DEA Meeting held in Meersburg. The introduction and background are included here for completeness, and the status of the work is reported.

Introduction

The accurate prediction of vortex-control fin interactions is especially important for both missiles and aircraft. As maneuvering requirements become more severe, both types of vehicles must fly at larger angles-of-attack. Consequently, vortices from noses, canard control surfaces, or fuselages begin to interact more and more with rearward fins or tail surfaces. Therefore, in the design of these vehicles it becomes increasingly important to accurately model the aerodynamic characteristics of the vortex-fin interaction. One objective of this investigation is to develop predictive methods for the aerodynamic behavior of missiles and aircraft experiencing vortex impingement on control surfaces. Detailed information about the three-dimensional (3-D) viscous flowfield, as determined from windtunnel experiments, is to be obtained in order to model the vortex-fin interaction and to provide a basis for developing predictive methods.

Background

The literature in this area is fairly extensive. However, except for work reported in References (2) and (3), there is a definite lack of detailed experimental data which adequately describe both the pressure distributions on the fin and the external flowfield about the fin. Because of the difficulty in determining the 3-D flowfield in sufficient detail, most of the reported work has assumed a constant vorticity acting over the fin, and has made no attempt to account for the effect of the fin on the incoming vortex. With the development of the laser Doppler velocimeter (LDV), it is possible to measure actual 3-D flowfields without disturbing the flow. The LDV has been used to measure leeward flowfields behind bodies at angles-of-attack up to 50°; for example, see Reference (4). In addition, a recently developed flow visualization method

reported in Reference (5) appears to present an improved tuft technique. The method uses very fine nylon mono-filaments which are rendered visible by fluorescence photography. The tufts do not appear to significantly alter the flowfield. Experimental results from this program will lead to predictive methods which may be compared with existing methods. Reference (6) presents a viscous numerical analysis coupled with a vortex lattice lifting surface theory which has proved to be quite successful in describing fin flowfields with vortex interactions.

Approach

A control fin model, consisting of a rectangular fin with cylindrical leading and trailing edges, was mounted in the U. S. Naval Academy Aerodynamics Laboratory subsonic windtunnel as shown schematically in Figure 1. A single vortex was generated at different positions upstream of the fin as the trailing vortex generated at the juncture of two adjacent NACA 0015 airfoils set at equal but opposite angles-of-attack, δ. The strength, Γ, of the vortex may be varied by adjusting δ. A single δ-setting of 5° has been used in all tests to date. The freesteam velocity was 150 ft/sec (45 m/sec). The angle-of-attack, α, of the control fin was varied from -10° to +10° in 5° increments. The position of the vortex upstream of the fin was varied by moving the generator vertically, and by moving the generator juncture laterally by rearranging end sections of the airfoil.

Details of the control fin and the vortex generator are shown schematically in Figure 2. Several geometrically identical fin models were fabricated. One was an aluminum pressure distribution model with 50 pressure taps arranged in five rows. Another was a phenolic model with a 0.5-inch by 0.5-inch (1.27 cm by 1.27 cm) square mesh of nylon tufts which were applied by means of liquid

adhesive. The fluorescence photography used selective light filtration utilizing a high intensity, short duration flash with both exciter and barrier filters to produce high contrast. Both of these models were mounted on the six-degree-of-freedom windtunnel balance system.

In the 3-D flowfield measurements using the LDV system described in Reference (7), a phenolic fin model was mounted on the windtunnel sidewall on a glass port to provide a forward scatter optical path. The port was rotatable to vary the fin angle-of-attack. The vortex generator was mounted vertically from floor to ceiling in the windtunnel. Data have been obtained for the single freestream velocity and single vortex strength for two upstream positions of the generated vortex, one on and one off fin centerline, and for fin angles-of-attack of -10°, 0° and 10°. Three-dimensional LDV measurements were made upstream of the fin through the vortex core, and in planes at three chordwise stations along the fin on both the windward and leeward sides.

Status and Plans

Data reduction and analysis is in progress. The data reduction will concentrate on (1) determination of the vortex strength from numerical integration of the LDV data, (2) determination of the effects of vortex impingement on aerodynamic coefficients from force and moment data, (3) comparison of forces obtained from pressure distribution data with windtunnel force balance data, and (4) determination of vorticity contours and velocity vector diagrams in the 3-D flowfield from LDV data. It is expected that selected initial results will be presented in a forthcoming paper (Reference (8)). A data report is planned for completion by fall of 1980. Further testing is planned using different vortex strengths. In addition, some investigations of vortex meander and vortex breakdown over the fin are being considered. Some analytical modeling may be

undertaken to arrive at a formulation based on vortex strength and location. Such modeling of the vortex-fin interaction will contribute to the development of predictive methods for the aerodynamic behavior of missiles and aircraft experiencing vortex impingement on control surfaces.

Summary

Force, moment, pressure distribution, and flow visualization data have been obtained for one freestream velocity and one vortex strength for ten vortex generator upstream positions and five fin angles-of-attack. In addition, 3-D flowfield LDV measurements have been completed for two upstream positions of the generated vortex and for three fin angles-of-attack. The LDV measurements were obtained upstream of the fin and in planes at three chordwise stations on the fins on both the windward and leeward sides. Data reduction and analysis is in progress.

References

(1) Gillerlain, J. D. Jr. and Yanta, W. J., "Vortex-Fin Interaction Flow Field Measurements," 4th U. S. - German DEA Meeting, BMVg-FBWT 79-31, Teil II, pp. 408-417.

(2) Smith, W. G. and Lazzeroni, F. A., "Experimental and Theoretical Study of a Rectangular Wing in a Vortical Wake at Low Speed," NASA TN D-339, Oct 1960.

(3) McMillan, O. J., Schwind, R. G., and Nielsen, J. N., "Rolling Moments in a Trailing Vortex Flowfield," NEAR TR 129, Feb 1977.

(4) Yanta, W. J. and Wardlaw, A. B., "Laser Doppler Velocimeter Measurements of Leeward Flowfields Behind Bodies at Large Angle of Attack," AIAA 77-660, Jun 1977.

(5) Crowder, J. P., "Fluorescent Mini-Tufts for Non-Intrusive Flow Visualization," MDC Report J7374, Feb 1977.

(6) Scruggs, R. M. and Nash, J. F., "Vortex/Jet/Wing Interactions by Viscous Numerical Analysis," Paper No. 10, AGARD Conference Proceedings No. 204 on Prediction of Aerodynamic Loading.

(7) Yanta, W. J. and Wardlaw, A. B., "Measurement of the Unsteady Flow Field About and Body Forces on a Tangent-Ogive Body at High Angles-of-Attack," 4th U. S. - German DEA Meeting, BMVg-FBWT 79-31, Teil II, pp. 418-431.

(8) Gillerlain, J. D., Jr. and Yanta, W. J., "Vortex-Fin Interaction Flow Field Measurements," AIAA 80-1332, to be presented at the AIAA 13th Fluid and Plasma Dynamics Conference to be held July, 1980.

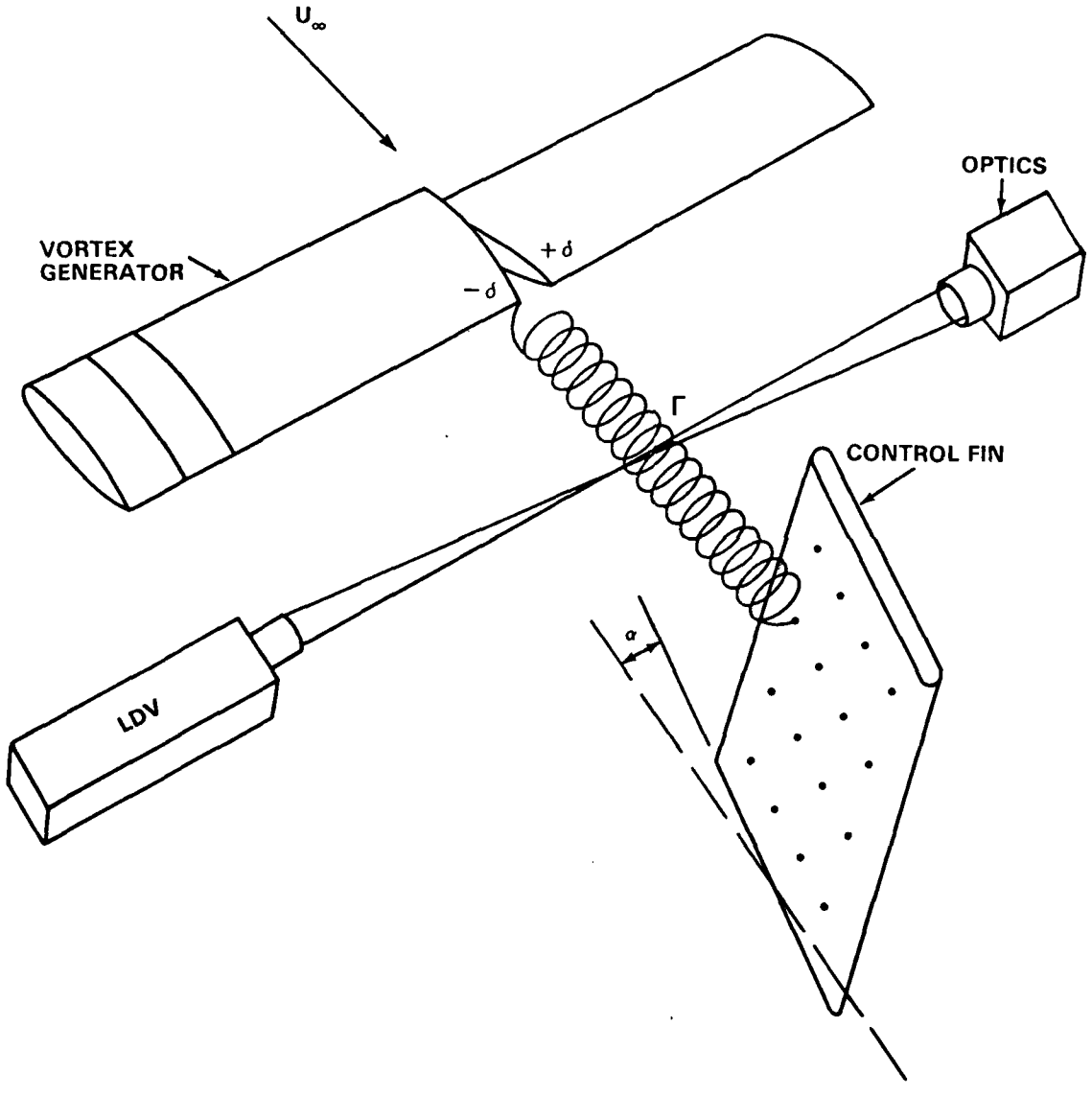

FIGURE 1. EXPERIMENTAL SETUP

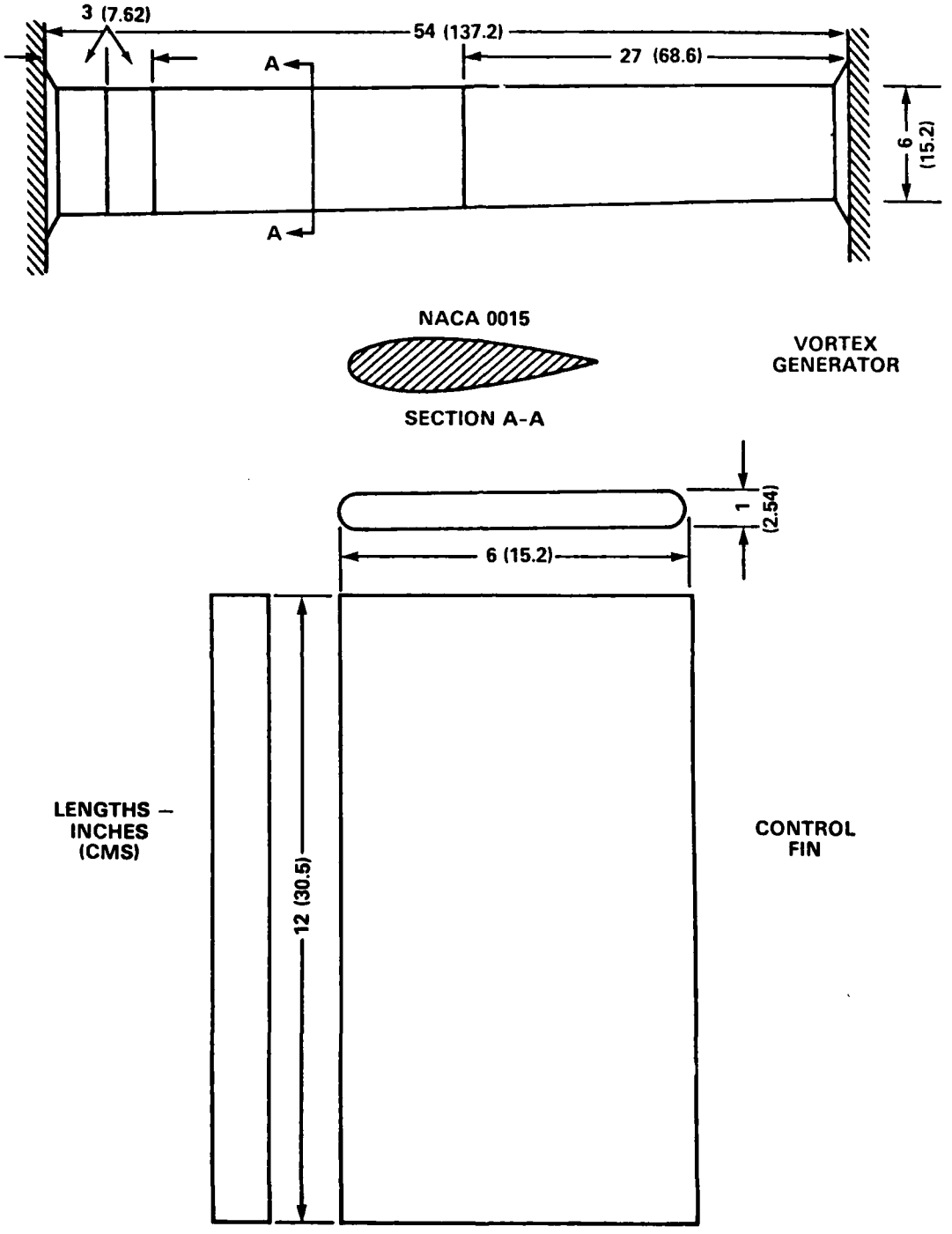

FIGURE 2. THE MODELS

COMPUTATION OF THE BOUNDARY LAYER AND SEPARATION LINES ON INCLINED ELLIPSOIDS AND OF SEPARATED FLOWS ON INFINITE SWEPT WINGS*

H.W. Stock, Dornier GmbH, Friedrichshafen, FRG**

Summary:

Integral methods are used to predict the attached boundary layer flow on inclined ellipsoids. The boundary layer quantities and the vortex separation lines (open type of separation) are compared to the results of finite difference methods.

Symmetry plane calculations allow the computation of the windward and leeward separation points (closed type of separation). The influence of the angle of attack and of the axis ratio of the ellipsoids on the position of the separation point is investigated.

Results of an inverse method for the prediction of turbulent separated flows on infinite swept wings are compared to available measurements.

LIST OF SYMBOLS

a	Major axis of the ellipsoid
b	Minor axis of the ellipsoid
b,c	Parameters of the laminar crossflow velocity profiles
c_f	Skin friction component in streamwise direction
c_{f_x}, c_{f_y}	Component of the resultant skin friction in x- and y-direction
c_p	Pressure coefficient
F	Thickness ratio a/b
H	Shape parameter of the streamwise velocity profile $H = \theta_{11}/\delta_1^*$
H_x	Shape parameter of the chordwise velocity profile $H_x = \theta_x/\delta_x^*$
H_y	Shape parameter of the spanwise velocity profile $H_y = \theta_y/\delta_y^*$

* This work was supported by the Ministry of Defence of the Federal Republic of Germany under RüFo contract T/RF41/80052/81451

** Senior Research Scientist, Theoretical Aerodynamics Group

Re	Reynolds number $Re = \frac{U_\infty a}{\nu}$
S	Streamwise direction
S	Stagnation point
u,U	Velocity component in x- and streamwise direction
v,V	Velocity component in y- and cross-flow direction
X,Y,Z	Carthesian Coordinates
x,y	Chordwise and spanwise direction
α	Angle of attack
α	Angle between the x- and streamwise direction
α^*	Angle of attack, for which the jump in the separation point location occurs
β	Falkner-Skan pressure gradient parameter
β	Limiting streamline angle, angle between the projection of the streamwise direction onto the surface and the resultant skin friction direction
δ	Boundary layer thickness
δ^*	Three-dimensional displacement thickness
$\overline{\delta}^*$	Dimensionless three-dimensional displacement thickness $\overline{\delta}^* = \delta^* \sqrt{Re}/2a$
δ_x^*	Displacement thickness of the velocity profile in x-direction $\delta_x^* = \int_0^\delta (1-\frac{u}{u_e})\, dz$
δ_y^*	Displacement thickness of the velocity profile in y-direction $\delta_y^* = \int_0^\delta (1-\frac{v}{v_e})\, dz$
δ_1^*	Displacement thickness of the streamwise velocity profile $\delta_1^* = \int_0^1 (1-\frac{U}{U_e})\, dz$
$\overline{\delta_1^*}$	Dimensionless displacement thickness of the streamwise velocity profile $\overline{\delta_1^*} = \delta_1^* \sqrt{Re}/2a$

δ_2^* Displacement thickness of the cross-flow velocity profile

$$\delta_2^* = - \int_0^\delta \frac{V}{U_e} \, dz$$

η Similarity variable of the similar solutions of the laminar boundary layer

η_δ Value of η for which $\frac{U}{U_e} = 0.99$

θ Circumferential coordinate

θ' Circumferential coordinate (Elliptical coordinates)

θ_{11} Momentum thickness of the streamwise velocity profile

$$\theta_{11} = \int_0^\delta \frac{U}{U_e} \left(1 - \frac{U}{U_e}\right) dz$$

$\overline{\theta}_{11}$ Dimensionless momentum thickness of the streamwise velocity profile

$$\overline{\theta}_{11} = \theta_{11} \sqrt{Re}/2a$$

θ_{12} Momentum thickness

$$\theta_{12} = \int_0^\delta \frac{V}{U_e} \left(1 - \frac{U}{U_e}\right) dz$$

θ_{22} Momentum thickness of the cross-flow velocity profile

$$\theta_{22} = - \int_0^\delta \left(\frac{V}{U_e}\right)^2 dz$$

μ Kinematik viscosity

ν Dynamic viscosity

τ_w Resultant wall shear stress

$$\tau_w = \mu \left[\left(\frac{\partial U}{\partial z}\right)_w^2 + \left(\frac{\partial V}{\partial z}\right)_w^2\right]^{1/2}$$

τ_w Dimensionless resultant wall shear stress

$$\overline{\tau}_w = \tau_w \frac{2a}{\mu U_\infty} \sqrt{Re}$$

ψ Meriodinal coordinate

ψ' Meridional coordinate (Elliptical coordinates)

Subscripts

e Condition at the outer edge of the boundary layer

w Conditions at the wall

∞ Unperturbed flow conditions.

1. INTRODUCTION

In recent years, a number of difference and integral methods have been developed to compute attached laminar and turbulent, three-dimensional boundary layers. Although some are developed to treat general problems, most treat either of two specific classes of problems, i.e., flows on wings, or flows past bodies of revolution. Results of the development of three-dimensional, compressible boundary layers on wings using difference methods are given in [1-4] and integral methods in [5-6]. The first subject of the present paper is the study of laminar boundary layer flows on inclined ellipsoids using an integral method [6] which is applicable to general problems.

Boundary layer calculations in the symmetry plane on the windward and leeward side of a threedimensional configuration represent a fairly inexpensive way to get a rough idea of the viscous flow field. Furthermore, the calculation supplies boundary layer data in the symmetry plane in regions which may be inaccessible for a conventional three-dimensional computation. The second part of the paper investigates the laminar flow in the symmetry plane of inclined ellipsoids.

In spite of the advances in computer technology and numerical methods, the numerical solutions of the Navier-Stokes equations are today still very expensive and for some applications not necessary. It seems reasonable to compute flows with limited regions of separated flow and no strong viscous-inviscid interactions with the boundary layer concept. The solutions of the two-dimensional, steady boundary layer equations get singular [32,] at the separation point, where the skin friction vanishes. It is impossible in the direct problem - calculation of the boundary layer for a prescribed pressure distribution - to generate solutions downstream the separation point. Catherall and Mangler [34] have numerically shown that no singular behaviour occurs at separation in the inverse problem - calculation of the inviscid outer flow for a prescribed boundary layer quantity. Furhtermore it is shown in [34] that downstream of separation the downstream marching integration technique can be maintained.

In the past several two-dimensional inverse difference [7-8] and integral boundary layer methods [9-14] were developed for the computation of separated flows. In the third part of the present work the concept of the inverse method is extended to the infinite swept wing situation using an integral method [35].

2. THREE-DIMENSIONAL LAMINAR BOUNDARY LAYERS ON INCLINED ELLIPSOIDS

2.1 Applied Integral Method and Calculation Procedure

The surface of the ellipsoid is a nondevelopable surface, which means that the boundary layer computation can hardly be made in a Cartesian coordinate system. A possible system is given by the streamline coordinate system, which leads to orthogonal, curvilinear coordinates. However, this system requires the knowledge of the external flow in great detail.

For small angles of attack the stagnation point is very close to the nose of the ellipsoid and elliptical coordinates become fairly attractive, as shown in the upper part of fig. 1. However, for large angles of attack, the stagnation point moves away from the nose of the body, as shown in the lower part of fig. 1, and elliptical coordinates are not applicable.

The coordinate system, proposed by J. Grashof [15], in the lower part of fig. 1 is applied for the present study. Here the coordinates are determined by the intersection with the body surface of planes, which are parallel to the tangential planes in the stagnation points. The angle ψ is one coordinate which becomes a measure for the distance along the axis S ÷ S. The angle θ is measured from the windward side to the leeward side. The windward symmetry line is represented by $\theta = 0^0$ and the leeward symmetry line by $\theta = 180^0$. The advantage of that coordinate system is that the geometric and aerodynamic singularities coincide in the stagnation points. Fig. 2 gives an idea of the computational grid.

Details of the applied integral method are given in Ref. [6]. The method is written in non-orthogonal, curvilinear coordinates and uses a one parameter (a) profile family (similar solutions) for the streamwise velocity profiles, fig. 3, and a two parameter (b and c) profile family for the cross-flow velocity profiles, fig. 4, (6^{th} order polynomial). The momentum thickness of the mainstream velocity profile θ_{11} is used as physical scaling parameter for the boundary layer. For the solution of the problem the ψ- and θ-momentum integral equations and the ψ- and θ-moment of momentum integral equations are used. The calculation is started at $\psi = 9^0$, which means 0,6 % of the distance S ÷ S, fig. 1, downstream of the forward stagnation point. Along the line $\psi = 9^0$ initial conditions are supplied, using the similar solutions of the boundary layer together with the Mangler [16] transformation.

The integration is done from the windward to the leeward stagnation point, which corresponds to ψ from 0^0 to 180^0. Along the symmetry lines, where for ψ = const a and θ_{11} are symmetric and b and c are antimetric, the derivatives

$$\frac{\partial a}{\partial \theta} \text{ and } \frac{\partial \theta_{11}}{\partial \theta}$$

are identical zero. The quantities

$$\frac{\partial b}{\partial \theta} \text{ and } \frac{\partial c}{\partial \theta}$$

are evaluated on the windward symmetry line by forward differences and on the leeward symmetry line by backward differences.

The inviscid flow field is determined by a potential flow solution, see Lamb [17]. This solution does not take into account the influence of the

free vortices and the flow separation at rear part of the body on the wall pressure distribution. Despite these deficiencies it is assumed that the pressure distribution in the front part of the body, where the boundary layer development is calculated, is not altered drastically due to viscous interaction. This statement is validated by wall pressure measurements on inclined ellipsoids.

2.2 Results

2.2.1 Comparison with finite difference solutions

The present computations are compared to the results of Geissler [18], who solved the boundary layer equations in streamline coordinates using a finite difference method. The momentum thickness $\bar{\theta}_{11}$, the displacement thickness $\bar{\delta}_1^*$ (both based on the mainstream velocity profile) and the resultant wall shear $\bar{\tau}_w$ are compared for the ellipsoid F = 6 at $\alpha = 10^0$ in fig. 5.

Unfortunately Geissler did not present cross-flow quantities and the limiting streamline angle β; β is shown nevertheless. The agreement, considering the complexity of the flow, is very satisfactory, especially in the curves 1-3. When approaching separation (see chapter 2.2.4), curve 5 in fig. 5, the gradients get very large on the leeward side of the body, θ from 90^0 to 180^0, and some disagreement can be observed. In the windward part of the body, θ from 0^0 to 90^0, the agreement for all curves is perfect. The maximum values of the boundary layer thickness show up on the side of the ellipsoid not in the leeward symmetry line. Especially the displacement thickness $\bar{\delta}_1^*$ produces sharp peaks. The value of θ, where this happens, differs not by too much in both methods. The rapide increase of the thicknesses is accompagnied by a sharp decrease in the resultant skin friction $\bar{\tau}_w$. Its minimum appears at about the same θ value, where the maxima of the thicknesses do occur. The limiting streamline angle β shows in that region large negative values.

The sharp peak in β, which means a rapide change in the resultant skin friction direction, indicates that the skin friction of the mainstream velocity profile is going to vanish. Under these circumstances the pressure gradient perpendicular to the mainstream direction can produce such drastic changes in the flow direction close to the wall.

In fig. 6 the resultant skin friction $\bar{\tau}_w$ is given for the windward symmetry plane ($\theta = 0^0$) and plotted vs. X/a. The ellipsoid F = 4 is calculated at zero and 30^0 incidence. For the zero incidence case the present calculations are compared to the results of Wang [19] and Hirsh and Cebeci [20], both finite difference methods. The integral method is in almost perfect agreement with Cebeci's method, except that the integral calculation predicts separation some distance downstream. Wang's results show a certain difference. A similar situation can be seen for the case of 30^0 incidence. Here the integral method is in perfect agreement with Geissler's results [21]. Wang's computations shown again a disagreement.

2.2.2 Comparison with experiments

Recently at the DFVLR in Göttingen an experimental program was started to measure boundary layer flows on inclined ellipsoids. The first measurements of the resultant skin friction using a hot film device are presented by Meier and Kreplin [22]. For the ellipsoid F = 6 at 5^0 and 10^0 incidence

the results are shown in fig. 7 in three stations. The deviation of the computation from the measurements in station 1 is at most 17 %, which is not too much considering the difficulties involved in skin friction measurements. The agreement in stations 2 and 3 is excellent. The calculation predicts for $\alpha = 10^0$ in station 3 a minimum of τ_w at about $\theta = 150^0$. The measurements seem to indicate a minimum in the same location.

The skin friction distribution for $\alpha = 10^0$ on the windward side ($\theta = 0^0$) is plotted vs. X/a in fig. 8. The calculation of Geissler [21] predicts an almost identical behaviour. The measurements of Meier and Kreplin [22] are given too up to X/a = 0.15. The boundary layer was shown to stay laminar up to this point. The agreement between calculations and measurements is perfect.

2.2.3 Displacement surface

The three-dimensional displacement thickness δ^* is calculated by a supplementary equation, which is solved simultaneously with the boundary layer equations [6]. In fig. 9 the dimensionless three-dimensional displacement thickness $\bar{\delta}^*$ is plotted for different stations ψ vs. θ, using θ as polar angle. Only the thickness $\bar{\delta}^*$ is given, the thickness of the ellipsoid is not represented.

In fig. 9 the results for the ellipsoid F = 6 are given for $\alpha = 5^0$, 10^0 and 15^0. The curves from 1 to 9 for $\alpha = 5^0$ and from 1 to 6 for $\alpha = 10^0$ and 15^0 give an idea of the displacement surface development. The curves 9 and 6 respectively give the last results of the attached layer, downstream of these curves a free vortex layer separation, see chapter 2.2.4, is indicated.

The displacement surface grows everywhere in the downstream direction, especially on the sides of the ellipsoids, except on the leeward symmetry line, when approaching the free vortex separation. Here the displacement surface decreases in downstream direction. The reason is, that the growth on the sides is such drastic that the boundary layer material, which is fed into the growing layer, stems partly from the leeward boundary layer material.

At separation the vorticity inside the boundary layer will be shed into the free stream forming two vortices. The deformation of the displacement surface just before separation seems to indicate the direction of rotation of the shedded vortices. They are counterrotating and rotate, view in the free stream direction, left on the right hand side and vice versa.

The effect of the angle of incidence is to move the separation region upstream (decreasing ψ_{Sep}). Furthermore, the relative lateral extension of the displacement surface is decreasing with incidence and the relative extension in the crossflow direction of the inviscid flow is increasing. The boundary layer material is blown away from the windward to the leeward side.

2.2.4 Free Vortex Layer Separation Lines

The phenomenon of separation in three-dimensional steady flow is reviewed recently in Ref. [23] and gives an idea of the complexity of that problem, as compared to the easiness of the definition of separation in two-dimensional steady flow. Maskell [24] gave definitions of three-dimensional separation, which can be referred to the present study.

Maskell [24] decribes two types of separation, the closed and open type. In the closed type the separation line is closed around the body and passes through the singular points of the limiting streamlines, where the total skin friction vanishes. A distinct reversed flow region develops, in which the streamlines originate from the rear stagnation point. The streamlines in the attached region originate from the front stagnation point. In contrast, the separation line of the open type is not closed and does not originate or terminate at singular points. The limiting streamlines on both sides of the separation line originate from the same front stagnation point. However, in either case, the separation line is determined by the appearance of an envelope of limiting streamlines.

Geissler [18, 21] has determined the location of the free vortex separation line, where numerical instabilities occur in his method.

Wang [25] determines the location of the free vortex layer separation line by identifying that line with the position where cf_θ', the circumferential skin friction component, vanishes. He argues that the limiting streamlines approaching the zero-cf_θ' line, make a sharp turn and merge into the zero-cf_θ' line so that the letter virtually becomes an envelope of the limiting streamlines. Although this envelope is located slightly above the zero-cf_θ' line, he does not make such a distinction, because they are such close to each other.

In the present integral method the free vortex separation line is positioned, where the mainstream skin friction component vanishes. This line coincides with the points, where the limiting streamlines make a sharp turn. Thus, the separation lines evaluated by the present method should be almost identical to the separation lines determined by Wang [25].

The direction of the resultant skin friction with the present method is given in fig. 10 for the ellipsoid F = 6 at 5^o angle of attack. The direction is plotted in 12 stations ψ = const, which are indicated in the figure. In station 7 the onset of separation is predicted for $\theta \sim 120^o$. The flow field downstream of station 6 was evaluated only on the windward part of the body in order to determine the free vortex separation line. The plot of the resultant skin friction direction gives an idea of the limiting streamline behaviour and shows clearly the appearance of an envelope of the limiting streamlines.

In fig. 11 the calculated free vortex separation lines for the ellipsoids F = 2, 4 and 6 at different angles of incidence are compared to the calculations of Geissler [18, 21]. The agreement in circumferential and meridional direction is excellent. The effect of the angle of incidence is to move the separation line upstream and downstream if the geometric parameter F decreases.

A special feature shows up for the ellipsoid F = 2. At the rear end of the separation line close to the windward side Geissler indicated a reversed flow region (closed type of separation), which produces a sudden change in the separation line inclination. In this part of the body the two types of separation, open and closed, may merge. Indeed, Wang [25] discussed the possibility that the two types of separation must intersect for certain geometries and angles of attack. The present integral method predicts in almost the same region the same behaviour.

3. LAMINAR BOUNDAR LAYER SEPARATION IN THE SYMMETRY PLANE OF INCLINED ELLIPSOIDS

The separation point motion on the windward and leeward side will be investigated as a function of the ellipsoid geometry and the angle of attack.

3.1 Applied Integral Method

Details of the applied integral method are given in Ref. [30]. The method uses the same velocity profile families as the approach described in chapter 2.1. Following Moore's idea [31] for the solution of the symmetry plane problem, the continuity equation, the ψ-momentum equation and the θ-momentum equation differentiated with respect to θ are used. This set of equations leads in the integral approach [30] to the ψ-momentum and moment of momentum integral equations and to the differentiated θ-momentum and moment of momentum integral equations.

3.2 Results

Fig. 12 gives the results for ellipsoids at 12^0 angle of attack as a function of the aspect ratio b/a. The finite difference results are taken from Wang [19]. The results for a sphere b/a = 1 from Ref. [26] are given too. Wang's computations for the sphere may be incorrectly represented. Extrapolating Wang's data to b/a = 1 on the windward side ($\theta = 0^0$) agreement may be found with the results of Ref. [26]. Doing the same on the leeward side ($\theta = 180^0$) a slight discrepancy may be seen.

The integral method predicts for b/a = 1 separation slightly upstream of the exact location (3.5^0 in terms of ψ). The overall trend of the separation point motion is well represented when compared to Wang's results.

Fig. 13 shows for the geometry F = 4 the separation point location as a function of the angle of attack. On the windward side the present results are in almost perfect agreement with those of Wang [19]. On the leeward side both boundary layer methods calculate an upstream motion of the separation point for small angles of attack and a downstream motion for larger angles. Round about 40^0 both methods predict a jump of the separation point from the rear part of the body to the front part.

Measurements [28, 29] and Navier-Stokes solutions [27] are shown for comparison. Wilson [29] observed for small angles of attack an upstream motion of the separation point, which was not indicated in the experiments of Ref. [28]. The difference between the boundary layer solutions and the measurements and Navier-Stokes solutions may be mainly due to the fact that for the boundary layer calculations the potential flow pressure distribution was used which does not take into account the influence of the viscous-inviscid interaction.

Fig. 14 shows the pressure coefficient on the leeward side of the ellipsoid F = 4 up to separation. It is clearly to be seen that the boundary layer can withstand increasingly larger pressure gradients in the rear part of the ellipsoid for increasing angles of attack. For $\alpha = 40^0$ the laminar boundary layer can overcome the pressure recovery nearly right down to the rear stagnation point ($c_p = 1.0$). In the nose region of the ellipsoid the suction peak gets more pronounced if the angle of attack is increasing and the recompression downstream of the suction peak will lead finally to nose separation of the flow.

Fig. 15 shows the momentum thickness and the shape parameter of the mainstream velocity profiles.

Taking the shape parameter H as a measure to indicate flow separation ($H \sim 4.1$) the lower part of fig. 15 demonstrates that in the nose region the flow is on the verge to separate for an angle of attack of 40^0. For angles α larger than 40^0 the flow separates at the nose. These features demonstrate why the separation point jumps from the rear part of the body to the front part. Downstream the peak in H for $\alpha < 40^0$ the flow relaxes and at the rear part of the ellipsoid H increases again leading to separation.

Another effect of the angle of attack, fig. 15 is to thicken the momentum thickness θ_{11} in the nose region and to thin θ_{11} in the rear part. Considering that the pressure gradient $\partial c_p/\partial \psi$ is everywhere positive except in the nose region, fig. 14, the decreasing values for θ_{11} can only be explained by a three-dimensional flow effect. (In two-dimensional flow a boundary layer and hence the momentum thickness will grow even steeper for adverse pressure gradients). The reason is that on the leeward side on the aft part of the ellipsoid the boundary layer flow close to the surface is severely divergent. This statement is supported by the results for the limiting streamline angle β, fig. 5, since the gradient $\partial\beta/\partial\theta$ for $\theta = 180^0$ is considerably increasing in downstream direction.

Fig. 16 describes for different thickness ratios $F \geq 2.165$ the separation point motion on the leeward side as a function of α. For small angles of attack the separation point moves upstream for values of $F < 5$ and slowly downstream for $F \geq 5$. The angle of attack α^*, for which the jump of the separation point from the rear to front part of the body occurs, gets smaller for thicker ellipsoids, decreasing at the same time the jump distance. For slender ellipsoids the flow separates further downstream and after the jump further upstream. Finally, for ellipsoids $F \leq 2.165$ no more jump is predicted, fig. 17.

In fig. 18 the shape parameter distribution is shown for the ellipsoids $F = 2.17 \div 6$ at the angle of attack α^*.

It is clearly to be seen that the relaxation process of the boundary layer downstream the peak in H is getting progressively less pronounced for thicker ellipsoids. For curve 1 in fig. 18 for the ellipsoid $F = 2.17$ the flow stays almost separated downstream the peak in H and finally separates only a small distance downstream the peak. From these results it is understable why for thickness ratios $F \leq 2.17$ no more jump does occur.

Fig. 19 finally shows α^* as a function of b/a and it may be argued that for extremely slender ellipsoids there exist a limiting value of α^* round about 42^0-43^0.

4. TURBULENT SEPARATED BOUNDARY LAYERS ON INFINITE SWEPT WINGS

4.1 Applied Integral Method

A newly developed integral method [35] which calculates turbulent separated flows on infinite swept wings is applied. The method uses the two parameter Coles profile family for the streamwise velocity profiles which are extended to flows describing separated profiles in a similar way as in Ref. [9,11]. Cross flow velocity profiles are not described by the Mager [36] or Johnston [37] empirical approach. It is assumed that the velocity profile in spanwise direction can be represented by a flat plate velocity profile. Knowing the angle α, fig. 20, and the streamwise velocity profiles it is an easy matter of geometry to evaluate the cross-flow velocity profiles To describe turbulence, the entrainment concept was applied together with a Lag-Entrainment formulation [38].

4.2 Results

The integral method was tested up to now only for the van den Berg and Elsenaar [39] test case. They measured the turbulent boundary layer development on a swept flat plate to avoid surface curvature effects on the turbulence structure. The boundary layer develops from a two-dimensional zero pressure gradient layer to a three-dimensional separation. The desired pressure distribution on the plate was induced by an appropriately shaped body near the plate. Care was taken to simulate flow conditions that occur on infinite swept wings.

Fig. 21 shows the measured velocity profilles in the spanwise direction. Separation was indicated in the measurements around station 8. It can be seen that the $v/_{ve}$ profiles do not change considerably from the flat plate situation (station 1) to the separated state (station 10). The continuous line is the Coles profile for a flate plate and gives a reasonable representation of all the measured velocity profiles. Fig. 22 shows the displacement thickness δ^*, which is based on the velocity profiles in chordwise direction. The continuous line is the smoothed curve which is used as input to the inverse method. Fig. 23 gives the momentum thicknesses θ_{11} and θ_{12} and fig. 24 the momentum thickness θ_{22} and the displacement thickness δ_2^*, the latter quantities are based on the cross-flow velocity profiles. θ_{22} and δ_2^* are in good agreement with the measurements considering the crude approach on which the cross-flow profiles are based. The limiting streamline angle β is given in fig. 25. Three different shape parameters H, H_x and H_y are given in fig. 26. H is the shape parameter of the streamwise velocity profile, H_x and H_y are the shape parameters of the profiles in x- and y-direction respectively. H_y stays constant in the measurements, which furthermore supports the assumption that in spanwise direction the velocity profiles are close to those on a flat plate. Comparison of the skin friction with measurements is given in fig. 27, c_{f_x} and c_{f_y} being the components of the resultant skin friction in x- and y-direction and c_f being the skin friction in streamwise direction. Separation is indicated by definition for an infinite swept wing at the location where c_{f_x} vanishes. As may be seen the experimentally observed separation location is well predicted by the calculation.

Finally fig. 28 represents the results of the inverse method. The magnitude of the resultant velocity vector at the outer edge of the boundary layer U_e

and its position α are given. The agreement between measurements and calculations is fairly good.

5. CONCLUSIONS

The laminar boundary layer development on inclined ellipsoids is calculated for different body geometries and angles of attack. The thicknesses of the boundary layer, the skin friction parameter and the limiting streamline angle are compared to finite difference solutions. The agreement is shown to be good. The computation of the skin friction reproduces the measurements in good agreement. The displacement surface on inclined ellipsoids is shown up to separation of the free vortices. The deformation of the displacement surface close to separation seems to indicate the direction of rotation of the shedded vortices. The free vortex separation lines calculated by the integral method are shown to be in good agreement with the finite difference results.

The separation point motion on the windward- and leeward side of inclined ellipsoids was investigated changing the ellipsoid geometry and the angle of attack. The results agree well with finite difference computations. It is shown that the jump of the separation point on the leeward side from the rear part of the body to front part does occur for ellipsoids $F \geq 2.17$ at a certain angle of attack α^*. For larger thickness ratios F the angle α^* is increasing and the jump distance is increasing too. For ellipsoids $F < 2.17$ no more jump is predicted anymore.

A newly developed inverse integral method for turbulent separated boundary layers on infinite swept wings was compared to one test case. The results seem to be encouraging.

REFERENCES

[1] T. CEBECI, K. KAUPS, J.A. RAMSEY
A General Method for Calculating Three-Dimensional Compressible Laminar and Turbulent Boundary Layers on Arbitrary Wings
NASA CR-2777 (1977)

[2] J.D. McLEAN
Three-Dimensional Turbulent Boundary Layer Calculations for Swept Wings
AIAA Paper No. 77-3 (1977)

[3] W. KORDULLA
Investigations Related to the Inviscid-Viscous Interaction in Transonic Flow about Finite 3-D Wings
AIAA Paper No. 77-209 (1977)

[4] J.F. NASH
An Explicit Scheme for the Calculation of Three-Dimensional Turbulent Boundary Layers, J. Basic Eng. 94 D, No. 1, p. 131, (1972)

[5] D.A. HUMPHREYS
Comparison of Boundary Layer Calculations for a Wing:
The May 1978
Stockholm Workshop Test Case
FFA TN AE-1522 (1979)

[6] H.W. STOCK, H.P. HORTON
Ein Integralverfahren zur Berechnung dreidimensionaler, laminarer, kompressibler, adiabater Grenzschichten
Submitted for publication in ZFW

[7] J.E. CARTER
Inverse Solutions for Laminar Boundary Layers Flows with Separation and Reattachment
NASA TR R-447, (1975)

[8] T. CEBECI
An Inverse Boundary Layer Method for Compressible Laminar and Turbulent Boundary Layers
AIAA J. Vol. 13, Nr. 9, S. 709-717, (1976)

[9] G.D. KUHN, J.N. NIELSEN
Prediction of Turbulent Separated Boundary Layers
AIAA J. Vol. 12, Nr. 7, S. 881-882, (1974)

[10] W.W. BOWER
Analytical Procedure for Calculation of Attached and Separated Subsonic Diffuser Flow
AIAA J. Vol. 13, Nr. 1, S. 49-56, (1976)

[11] G.M. ASSASSA, B. GAY
Prédiction numérique des écoulements turbulents au voisinage du point de décollement
Entropie, Vol. 14, S. 29-38, (1978)

[12] L.F. EAST, P.D. SMITH, P.J. MERRYMAN
Prediction of the Development of Separated Turbulent Boundary Layers by the Lag-Entrainment Method
RAE TN Nr. 77046, (1977)

[13] J.C. Le BALLEUR, J. MIRANDE
Etude Expérimentele et Théorique du Recollement Bidimensional Turbulent Incompressible
ONERA T.P. Nr. 1975-16, (1975)

[14] P. THIEDE
Extension of the Boundary Layer Concept to the Calculation of Two-Dimensional Separated Flows
BMVg-FBWT 77-20, (1977)

[15] J. GRASHOF
Private Communication

[16] W. MANGLER
Zusammenhang zwischen ebenen und rotationssymmetrischen Grenzschichten in kompressiblen Flüssigkeiten
ZAMM, Vol. 28, p. 97 (1948)

[17] H. LAMB
Hydrodynamics
Cambridge University Press (1932)

[18] W. GEISSLER
Berechnung der laminaren, dreidimensionalen Grenzschicht an unsymmetrisch umströmten Rotationskörpern mittels Differenzenverfahren
DFVLR IB-251-73 A 19 (1973)

[19] K.C. WANG
Laminar Boundary Layer Near the Symmetry Plane of a Prolate Spheroid
AIAA J., Vol. 12, p. 949 (1974)

[20] R.S. HIRSH, T. CEBECI
Calculation of Three-Dimensional Boundary Layers With Negative Cross Flow on Bodies of Revolution
AIAA Paper No. 77-683 (1977)

[21] W. GEISSLER
Berechnung der laminaren Ablösung an unsymmetrisch umströmten Rotationskörpern mittels Differenzenverfahren
DFVLR-IB 251-73 A31 (1973)

[22] H.U. MEIER, H.P. KREPLIN
Experimental Investigation of the Transition and Separation Phenomena on a Body of Revolution
DEA-Meeting on Boundary Layer Effects (1979)
To be published as FBWT

[23] J.H.B. SMITH
A Review of Separation in Steady, Three-Dimensional Flow
AGARD CP No. 168 Paper 31 (1975)

[24] E.C. MASKELL
Flow Separation in Three-Dimensions
RAE-Rep. Aero 2565 (1955)

[25] K.C. WANG
Boundary Layer over a Blunt Body at High Incidence with a Open-Type of Separation
Proc. Roy. Soc., London, A340, p. 33 (1973)

[26] H. SCHLICHTING
Grenzschichttheorie
G. Braun Publishers, Karlsruhe, West Germany (1951)

[27] W. HAASE
Separation and Vortex Pattern on a Spheroid at Incidence
DEA-Meeting on Viscous and Interacting Flow Field Effects, Annapolis (1980)
To be published as AFFOL Report

[28] T. HAN, V.C. PATEL
Flow Separation on a Spheroid at Incidence
J. Fluid. Mech., Vol. 9?, part 4, p. 693-657 (1979)

[29] G.R. WILSON
Experimental Study of Laminar Boundary Layers on a Body of Revolution
Master's Thesis GAM/AE/71-4, Air Force
Inst. of Technology, Wright-Patterson
Air Force Base, Ohio (1971)

[30] H.W. STOCK
Laminar Boundary Layer Development in the Symmetry Plane of Inclined Prolate Spheroids
Will be submitted for publication in AIAA J.

[31] F.K. MOORE
Three-Dimensional Laminar Boundary Layer Flow
J.A.S. Vol. 20, p. 525-534 (1953)

[32] S. GOLDSTEIN
On Laminar Boundary Layer Flow Near a Position of Separation
Quart. J. Mech. Appl. Math., 1, p. 43-69, (1948)

[33] S.N. BROWN, K. STEWARTSON
Laminar Separation
Annual Review of Fluid Mechanics,
Annual Reviews Inc., S. 45-72, (1969)

[34] D. CATHERALL, K.W. MANGLER
The Integration of Two-Dimensional Laminar Boundary Layer Equations Past the Point of Vanishing Skin Friction
J. Fluid. Mech., Vo. 26, S. 163-182, (1966)

[35] H.W. STOCK
Ablöseverhalten von Grenzschichten an dreidimensionalen Flügeln
Dornier-Bericht, 79/41B, (1979)

[36] A. Mager
Generalisation of Boundary Layer Momentum Integral Equations to Three-dimensional Flows, Including those of Rotating Systems
NACA Rep. 1067, (1952)

[37] J.P. JOHNSTON
On the Three-dimensional Turbulent Boundary Layer Generated by Secondary Flow
J. of Basic Eng. Vol. 82, S. 223-250, (1960)

[38] H.P. HORTON
Entrainment in Equilibrium and Non-Equilibrium Turbulent Boundary Layers
Hawker Siddely Aviation Ltd., Hatfield, Rep. Nr. Research/ 1094/HPH, (1969)

[39] B. VAN DEN BERG und A. ELSENAAR
Measurements in a Three-Dimensional Incompressible Turbulent Boundary Layer in an Adverse Pressure Gradient under Infinite Swept Wing Conditions
NLR TR 72092 U, (1972)

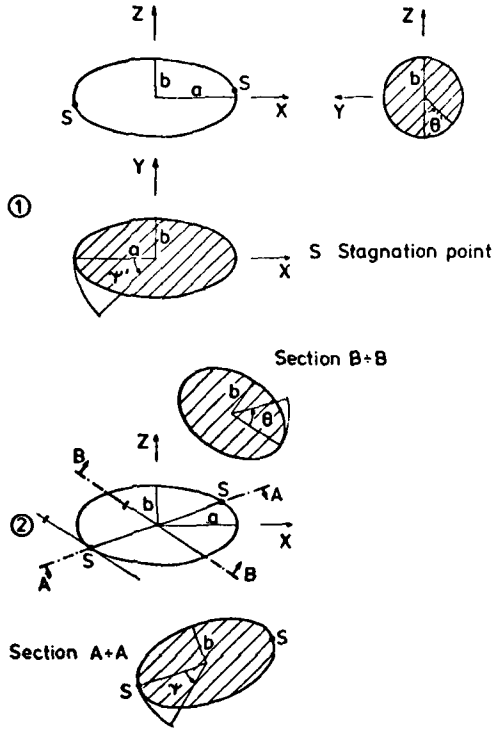

Fig. 1 Coordinate systems for the boundary layer calculation on ellipsoids (1 elliptical coordinates, 2 present coordinates)

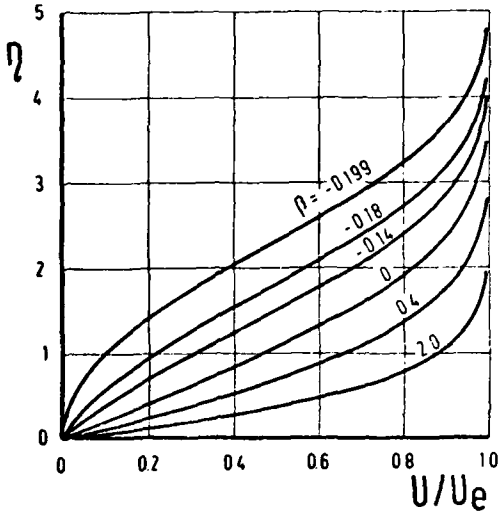

Fig. 4 Cross-flow velocity profiles

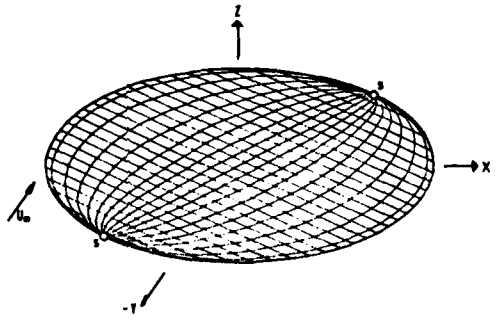

Fig. 2 Computational grid

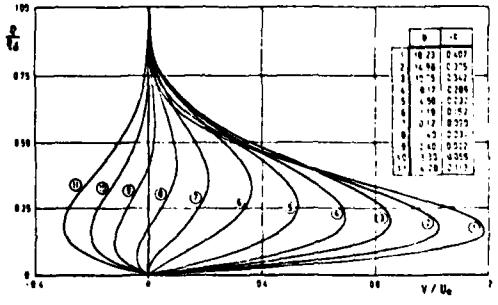

Fig. 3 Streamwise velocity profiles

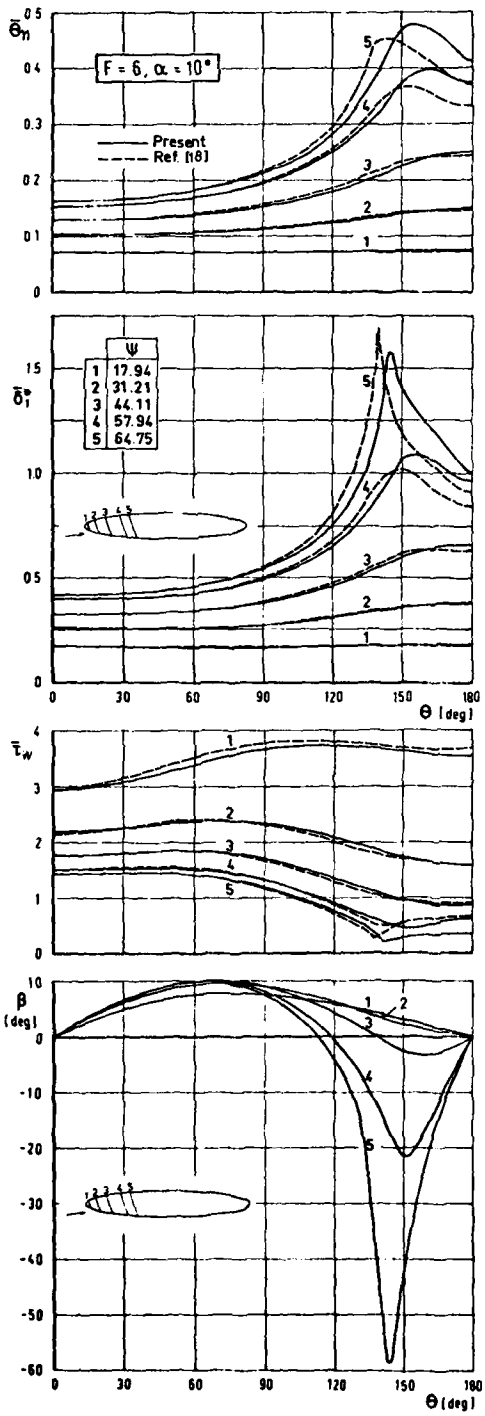

Fig. 5 Distribution of the momentum thickness $\bar{\theta}_{11}$ and the displacement thickness $\bar{\delta}_1^*$ of the streamwise velocity profile, the resultant skin friction $\bar{\tau}_w$ and the limiting streamline angle β

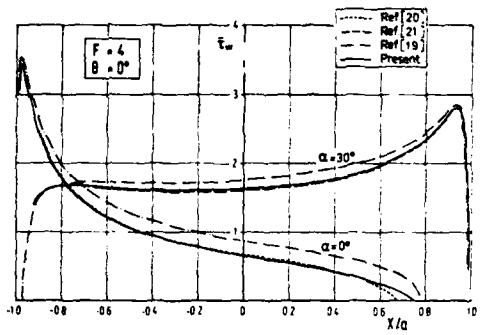

Fig. 6 The development of the skin friction $\bar{\tau}_w$ on the windward symmetry line for 0° and 30° degree angle of attack

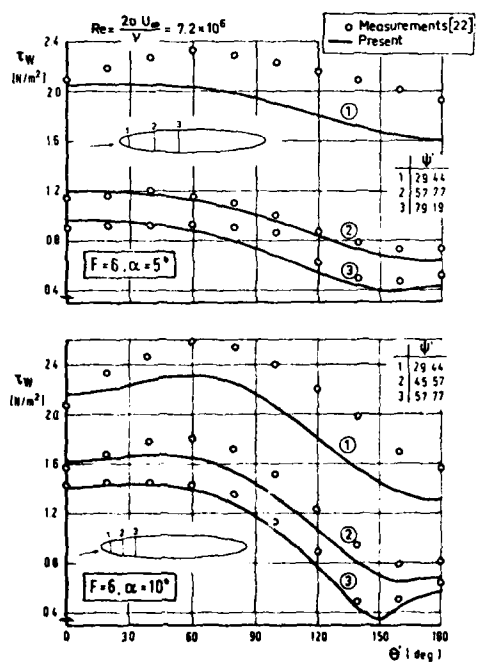

Fig. 7 Comparison of the calculated resultant skin friction $\bar{\tau}_w$ with measurements [22]

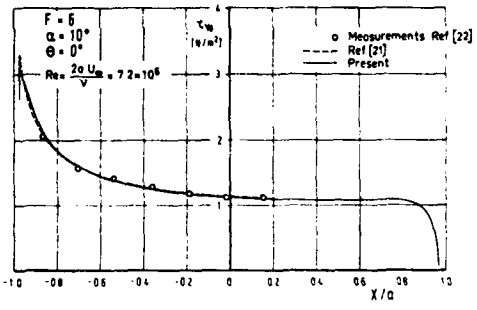

Fig. 8 Comparison of the calculated skin friction τ_w with measurements [22]

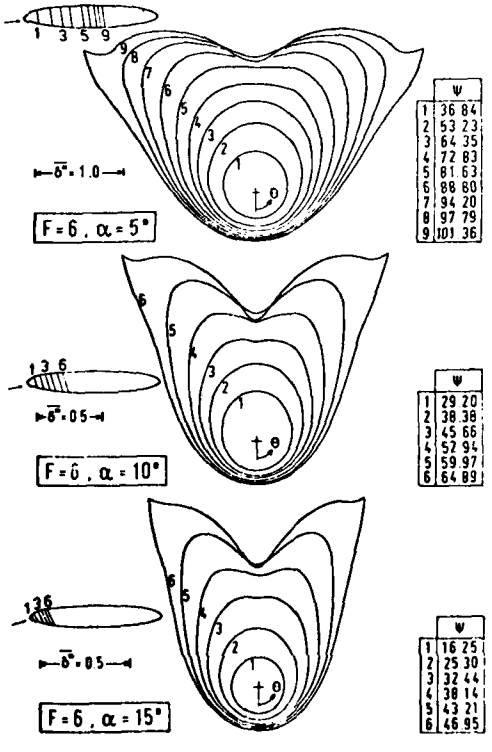

Fig. 9 The displacement surface development on the ellipsoid for three different angles attack

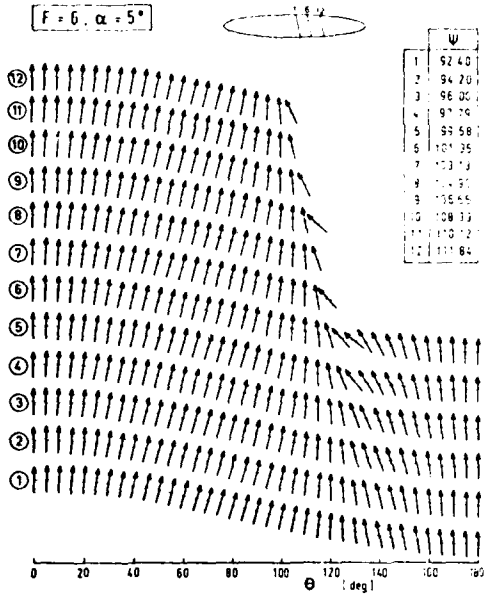

Fig. 10 Distribution of the direction of the resultant skin friction

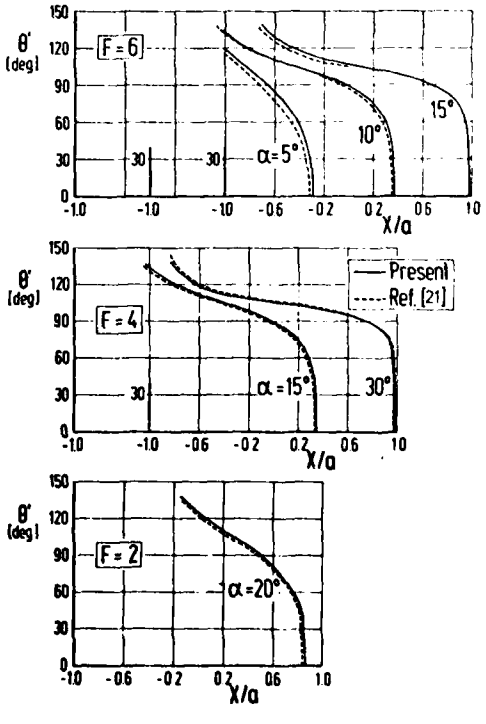

Fig. 11 The free vortex separation line for three different configurations

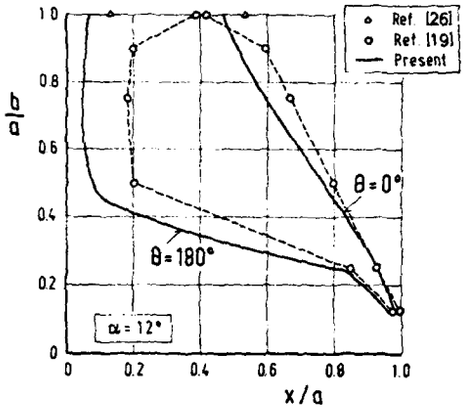

Fig. 12 The separation point location for different ellipsoid geometries at 12° angle of attack

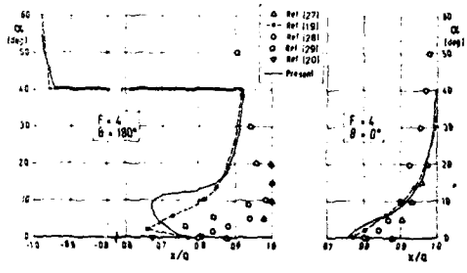

Fig. 13 The separation point location of the ellipsoid F = 4 as a function of the angle of attack

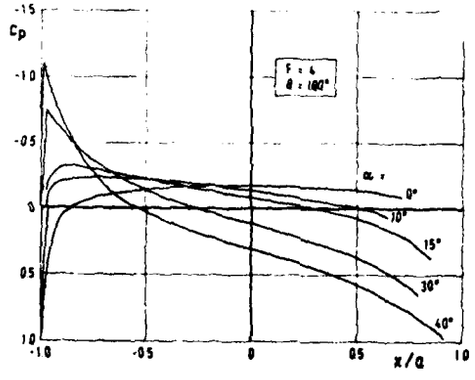

Fig. 14 Pressure distribution on the ellipsoid F = 4 at different angles of attack

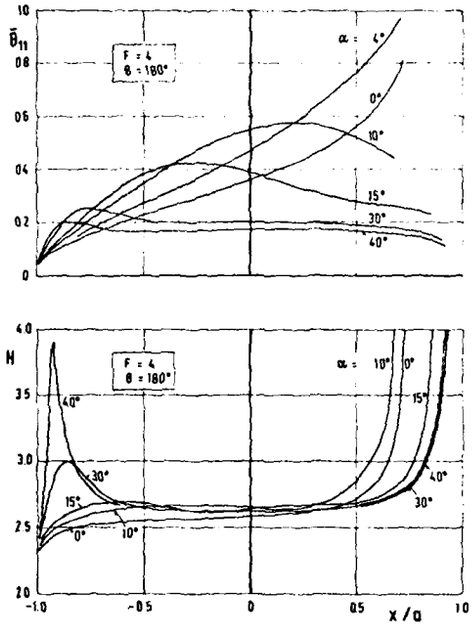

Fig. 15 Distribution of the momentum thickness $\bar{\theta}_{11}$ and the shape parameter H of the streamwise velocity profile

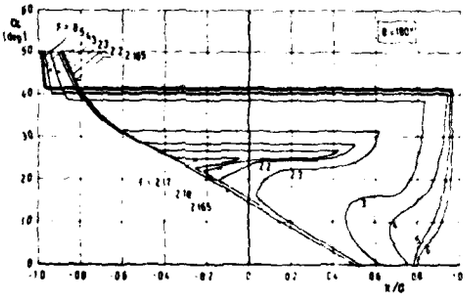

Fig. 16 The separation point location on the leeward side of the ellipsoids, F = 2.165 ÷ 6, as a function of the angle of attack

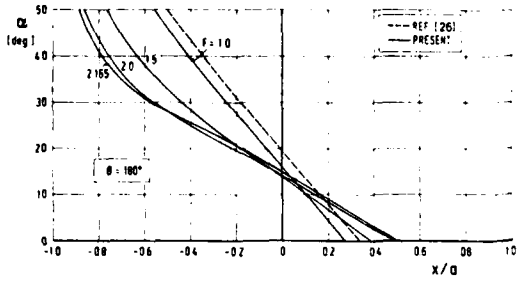

Fig. 17 The separation point location on the leeward side of the ellipsoids, F = 1 ; 2.165, as a function of the angle of attack

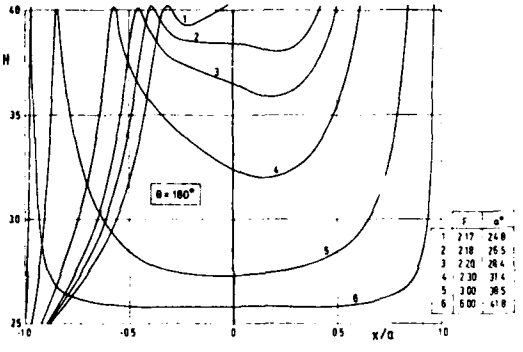

Fig. 18 The shape parameter distribution on the leeward side of the ellipsoids, F = 2.17 ; 6, at the angle of attack α*

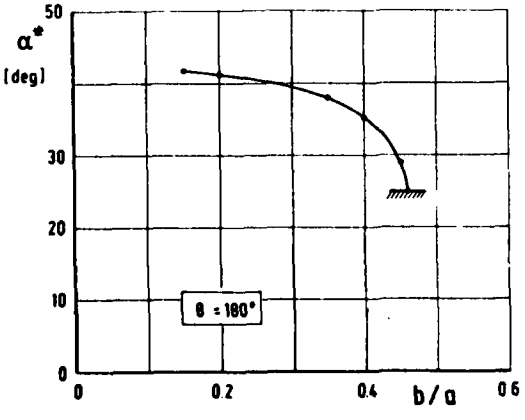

Fig. 19 The angle of attack α* as function of the aspect ratio of the ellipsoids

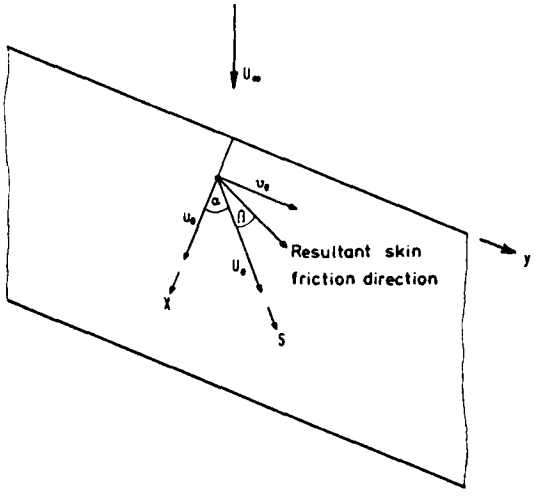

Fig. 20 Skematic sketch on an infinite swept wing

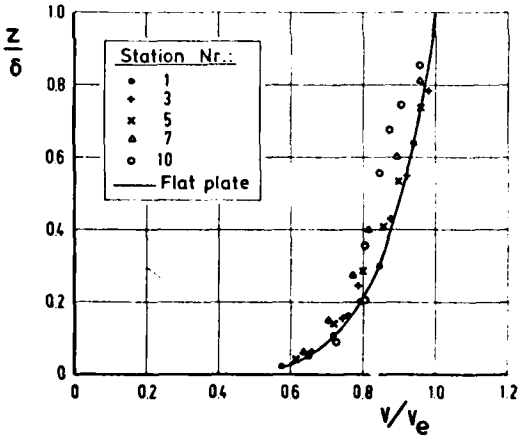

Fig. 21 Comparison of the measured velocity profiles in spanwise direction and the flat plate velocity profiles

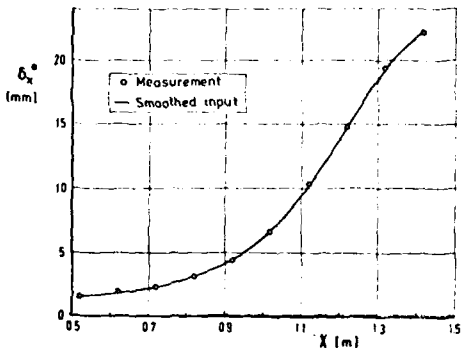

Fig. 22 Distribution of the displacement thickness δ_x^*, used as input to the inverse method

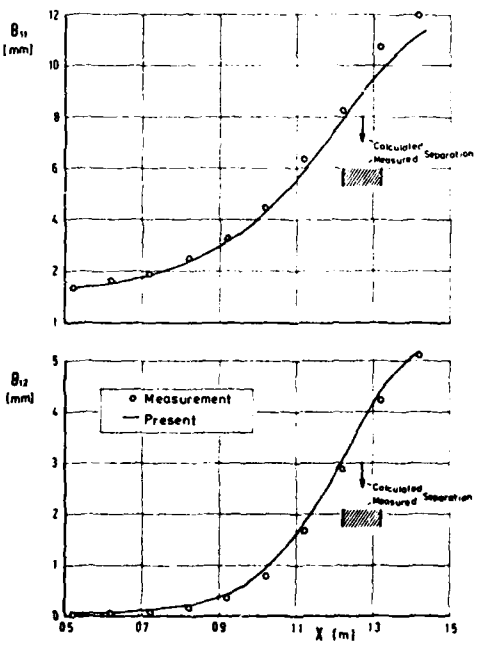

Fig. 23 Comparison of the momentum thicknesses θ_{11} and θ_{12} with measurements

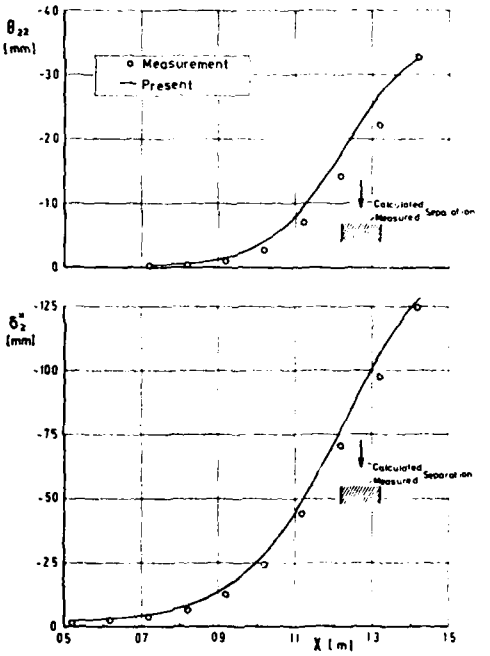

Fig. 24 Comparison of the momentum thickness θ_{22} and the displacement thickness δ_2^* with measurements

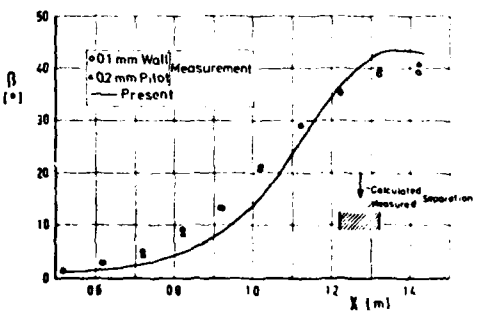

Fig. 25 The limiting streamline angle β compared to measurements

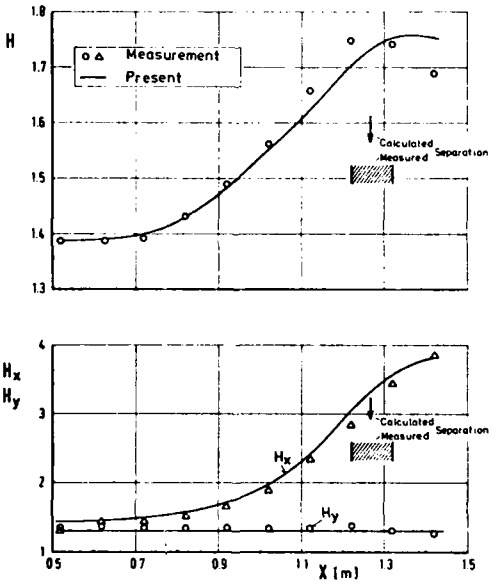

Fig. 26 The distribution of the shape parameters H, H_x and H_y compared to measurements

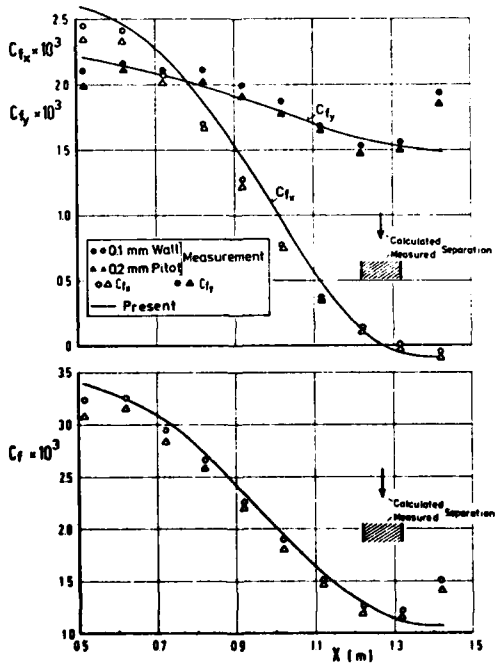

Fig. 27 Comparison of the skin friction components c_f, c_{f_x} and c_{f_y} with measurements

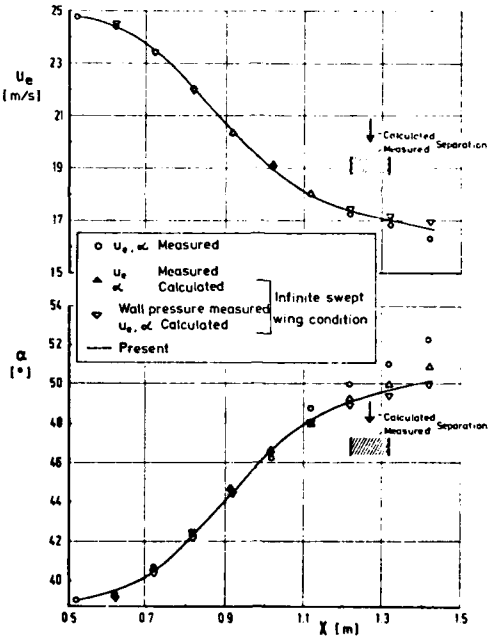

Fig. 28 The resultant velocity at the outer edge of the boundary layer U_e and its position α as compared to measurements.

*U.S.Government Printing Office: 1980 — 657-084/59

END

DATE
FILMED

10-80

DTIC